Roberto Sabadini · Bert Vermeersen
Gabriele Cambiotti

Global Dynamics of the Earth

Applications of Viscoelastic Relaxation Theory to Solid-Earth and Planetary Geophysics

Second Edition

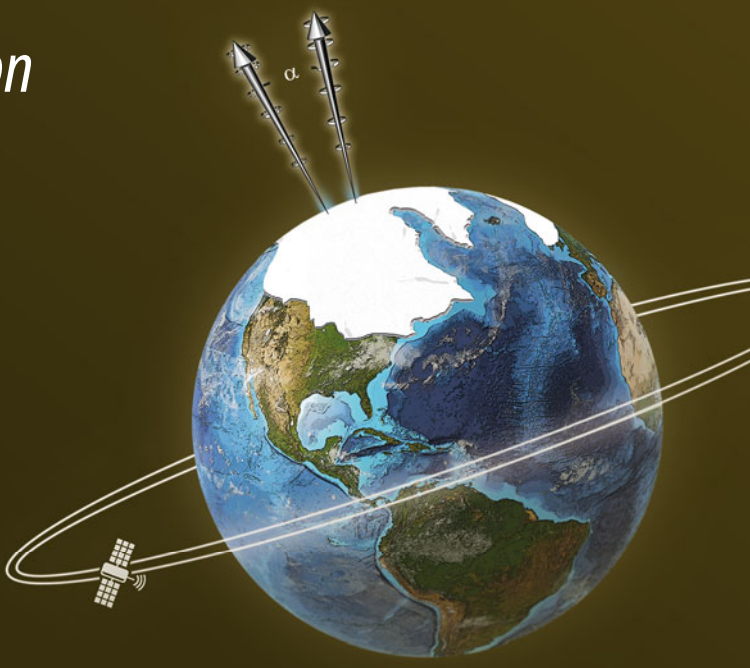

Springer

Global Dynamics of the Earth: Applications of Viscoelastic Relaxation Theory to Solid-Earth and Planetary Geophysics

Roberto Sabadini · Bert Vermeersen
Gabriele Cambiotti

Global Dynamics of the Earth: Applications of Viscoelastic Relaxation Theory to Solid-Earth and Planetary Geophysics

Second Edition

Springer

Roberto Sabadini
Section of Geophysics
University of Milan
Milan
Italy

Gabriele Cambiotti
University of Milan
Milan
Italy

Bert Vermeersen
Delft University of Technology
Delft
The Netherlands

and

NIOZ/Utrecht University
Utrecht
The Netherlands

This book is a revised and updated edition of the book "Global Dynamics of the Earth", Series: Modern Approaches in Geophysics, vol. 20, published in hardbound and paperback editions (ISBN 978-1-4020-1267-9 and 978-1-4020-1268-6) by Kluwer Academic Publishers Dordrecht, 2004.

ISBN 978-94-017-7550-2 ISBN 978-94-017-7552-6 (eBook)
DOI 10.1007/978-94-017-7552-6

Library of Congress Control Number: 2016934439

Cover figure: Cover figure of the first edition of the book, amended by Creativebrain, Milan, Italy

Printed on acid-free paper

This Springer imprint is published by Springer Nature
The registered company is Springer Science+Business Media B.V. Dordrecht

To Giulia and Armanda

—Roberto Sabadini

Foreword to the Second Edition

With this book we provide graduate students with the mathematical techniques necessary to solve some basic problems related to the deformation of the Earth by a variety of geophysical and geological processes involving the rheological behavior of the mantle. We deal with global processes involving the deformation of the Earth as a whole, as in rotation dynamics, or, on a smaller scale, with the response of the planet to the redistribution of surface loads and seismic sources associated with earthquakes faulting the lithosphere.

When we had the idea for this book, our major concern was to write something that could be used by students to write their own codes for solving problems in linear viscoelasticity and, at the same time, to tell them what we have learned in rotation dynamics and related processes like induced sea-level changes.

Now we realize that we can go beyond the original scope of our work and consider it as a tool for gaining an in-depth physical insight into the complex relations among the various processes involving our planet, from surface and deep mantle processes to rotation instabilities and, eventually, long timescale climate variability.

In the following decades, major advancements in our understanding of the dynamics and evolution of the Earth as an integrated system, including a variety of geophysical processes that affect the life of human beings, will come from joint efforts in geophysics and geodesy, from a tight link between the mathematical modeling of geophysical phenomena and the constraints provided by the gravity field, of its time-dependent and static components at long and short wavelengths, and by the geodetically detected crustal deformation. Our book provides the mathematical formulation to establish the link between geophysics and geodesy.

Our book opens up new perspectives on the physics of the Earth's interior, looking at our planet in an integrated fashion and focusing on the geophysical and geodetic techniques that record, over a broad spectrum of spatial wavelengths, the ongoing modifications in the shape and gravity of the Earth. Basic issues related to the rheological properties of the Earth's mantle and to its slow deformation will be understood, within the framework of an analytical normal mode theory;

fundamentals of this theory are developed in the first, tutorial part, while a wide range of applications are considered in the second part. With respect to the first edition, we improved substantially our formalism for viscoelastic relaxation, implementing the compressible model, starting from a new analytical compressible solution that, although within some simplifying assumptions, is a step ahead with respect to previous ones, allowing the reader to understand some basic aspects of viscoelastic compressible relaxation. The formalism is now completely self-contained, and all the aspects from viscoelastic relaxation, Earth's deformation at various spatial and temporal scales, rotation, and gravity are now framed within a unitary self-consistent theory.

Although the first edition contained already some applications to other planets in our Solar System, notably on Polar Wander, we have added a chapter on deformation and stresses of icy moons. Since the publication of the first edition, we learned that also planetary scientists have used the theory and models of our book for solid planets and moons. Many icy moons around Jupiter and Saturn are thought to possess relatively large shallow low-viscosity zones under their icy crusts, perhaps even in the form of inviscid water layers. Shallow low-viscosity zones introduce additional complications in theory and modeling. Apart from this, tidal interaction is the dominant forcing mechanism for moons around the giant planets in the Solar System. The reader can find both theory and models for such tidal-forced objects that have shallow low-viscosity or water layers in Chap. 9.

In the study of the physics of the Earth's interior, this book bridges the gap between seismology and geodynamics, making a step ahead in this respect compared to the first edition, by introducing the new physics of the gravitational effects of large earthquakes at subduction zones, nowadays made possible by the new gravity data from space missions.

Our hope is of course that not only graduate students but also researchers working in the fields touched upon by this book may find it useful for their own work and teaching.

Milan — Roberto Sabadini
Delft — Bert Vermeersen
Milan — Gabriele Cambiotti
February 2016

Foreword to the First Edition

With this book we provide graduate students with the mathematical techniques necessary to solve some basic problems related to the deformation of the Earth by a variety of geophysical and geological processes involving the rheological behavior of the mantle. We deal with global processes involving the deformation of the Earth as a whole, as in rotation dynamics, or, on a smaller scale, with the response of the planet to the redistribution of surface loads and seismic sources associated with earthquakes faulting the lithosphere.

When we had the idea for this book, our major concern was to write something that could be used by students to write their own codes for solving problems in linear viscoelasticity and, at the same time, to tell them what we have learned in rotation dynamics and related processes like induced sea-level changes.

Now we realize that we can go beyond the original scope of our work and consider it as a tool for gaining in-depth physical insight into the complex relations among the various processes involving our planet, from surface and deep mantle processes to rotation instabilities and, eventually, long time scale climate variabilities.

In the following decades, major advancements in our understanding of the dynamics and evolution of the Earth as an integrated system, including a variety of geophysical processes that affect the life of human beings, will come from joint efforts in geophysics and geodesy, from a tight link between the mathematicalmodeling of geophysical phenomena and the constraints provided by the gravity field, of its time dependent and static components at long and short wavelengths, and by the geodetically detected crustal deformation. Our book provides the mathematical formulation to establish the link between geophysics and geodesy.

Our book opens up new perspectives on the physics of the Earth's interior, looking at our planet in an integrated fashion and focusing on the geophysical and geodetic techniques that record, over a broad spectrum of spatial wavelengths, the ongoing modifications in the shape and gravity of the Earth. Basic issues related to the rheological properties of the Earth's mantle and to its slow deformation will be understood, within the framework of an analytical normal mode theory;

fundamentals of this theory are developed in the first, tutorial part, while a wide range of applications are considered in the second part.

In the study of the physics of the Earth's interior, this book bridges the gap between seismology and geodynamics.

Our hope is of course that not only graduate students but also researchers working in the fields touched upon by this book may find it useful for their own work and teaching.

Milan — Roberto Sabadini
Delft — Bert Vermeersen
December 2003

Acknowledgments

This book project could never have been conceived, written, and completed without the help of many. We thank Petra van Steenbergen at Springer for the continuous support and the advice she gave during the years we worked on the book.

We thank Hermes Jara-Orué for providing us with essential contents and assistance for Chap. 9.

We thank David A. Yuen from the University of Minnesota, U.S.A. and Gennaro Corrado, from the University of Napoli "Federico II", Italy, for their careful review of the manuscript.

Thanks also to our students from different Countries, from the University of Milano, from the Delft University of Technology, and from the University of the Chinese Academy of Sciences in Beijing, for useful discussions.

Contents

Chapter 1
Viscoelastic Relaxation Theory, Momentum and Poisson Equations

Abstract This chapter deals with the expansion in spheroidal and toroidal harmonics of the momentum and Poisson equations, for spherical, self-gravitating, stratified, viscoelastic planets. For the linear viscoelastic Maxwell rheology, the Correspondence Principle is considered for obtaining the viscoelastic solution from the equivalent elastic problem. Both normal mode and complex contour integration techniques are used for anti-transforming the field from the s-domain to the time domain. Boundary conditions at the surface of the planet, at the core-mantle boundary and at the internal interfaces between layers of different elastic and density characteristics, are obtained. Point sources for loads and dislocations, the latter limited to the spheroidal component for applications to gravity modeling, are expanded in spherical harmonics for Green function derivation.

1.1 Rheological Models

In modeling a particular geophysical phenomenon, the choice of the rheology used depends on (1) mathematical difficulty, (2) the quality of the geophysical data which the calculations of the model are required to match and (3) our knowledge of the rheological behavior of the medium at hand. Over the last few decades a considerable amount of knowledge has been gained about mantle rheology in terms of the values of rheological parameters and deformation mechanisms. For instance, what is most important, as far as mantle convection is concerned, is clearly the strong temperature dependence of the viscosity which the laboratory-derived values of the activation energy and volume seem to suggest. This intense interest in understanding convection in a fluid with markedly temperature-dependent viscosity is attested by the recent fundamental studies by geophysicists using analytical, numerical and experimental methods. In what follows, however, rather than discussing topics of mantle rheology and mantle convection, for which we refer to the book by Ranalli (1995), we will try to address the main questions that are at issue in attempting to study transient and long time scale geodynamic phenomena in a wide arc of time scales, ranging from years, characteristic of post-seismic deformation, to hundreds of millions

R. Sabadini et al., *Global Dynamics of the Earth: Applications of Viscoelastic Relaxation Theory to Solid-Earth and Planetary Geophysics*,
DOI 10.1007/978-94-017-7552-6_1

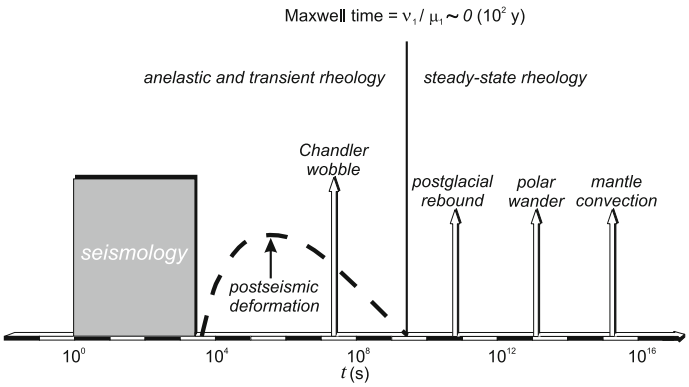

Fig. 1.1 Diagram illustrating the relation of the characteristic time scale for several geophysical phenomena to the Maxwell time τ of the mantle defined as $\tau = \nu_1/\mu_1$—with ν_1 and μ_1 denoting respectively the steady state mantle viscosity and rigidity—which separates the steady state and the transient regimes of mantle creep

of years as in the case of true polar wander driven by subduction, making use of the relaxation theory in viscoelasticity with different models of mantle rheology. In Fig. 1.1 we sketch the entire geodynamic spectrum spanning the whole range of phenomenological time scales. One of the key questions is whether one can devise a constitutive law which can satisfactorily model all these phenomena, from the anelastic transient regime to the steady-state domain.

The appropriate constitutive relation which is to be employed in analyzing transient geodynamic phenomena, such as post glacial rebound (PGR) or Glacial Isostatic Adjustment (GIA), is currently a matter of controversy in geophysics. Advocates of non-linear rheology (e.g. Melosh 1980) use as supporting arguments the laboratory data of single-crystal olivine whose power law index is about three (Goetze 1978; Durham and Goetze 1977). But there is now mounting evidence that at the stress levels in post glacial rebound (less than 10^2 bar) the creep mechanism may in fact be linear for polycrystalline aggregates (Relandeau 1981) since grain boundary processes, such as Coble creep, may become dominant. There are also recent theoretical studies indicating that the power law index changes gradually with stress and hence the transition stress which marks the boundary between linear and non-linear behavior is not as sharply defined as has previously been thought (Greenwood et al. 1980). Indeed, a proper mathematical formulation of the mixed initial and boundary-value problems associated with non-linear viscoelasticity is a formidable one, fraught with numerical difficulties. It is also important to note that there is no unambiguous evidence in either the post glacial rebound event or in other types of geodynamic data which absolutely requires a non-linear viscoelastic rheology, in spite of claims to the contrary. For these reasons, geophysicists tend to prefer the simple linear models in viscoelasticity, which allow for a considerably simpler mathematical treatment of the dynamics. Moreover, the linear approach also allows

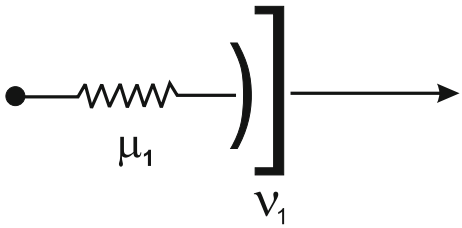

Fig. 1.2 Mechanical analog of Maxwell rheology. The elastic response is governed by the shear modulus μ_1 of the spring while the long-term creep is controlled by the viscosity ν_1 of the dashpot

one to study easily the potentially interesting effects of the interaction between transient and steady-state rheologies. The simplest viscoelastic model which can describe the Earth as an elastic body for short time scales and as a viscous fluid for time scales characteristic of continental drift is that of a linear Maxwell solid. Figure 1.2 shows a standard one-dimensional spring and dashpot analog of the Maxwell rheology. The speed for shear wave propagation depends on the square root of the instantaneous rigidity μ_1, whereas the strength of mantle convection depends inversely upon the magnitude of the steady-state viscosity ν_1.

A powerful method of solving transient problems of linear viscoelasticity has been the use of the Correspondence Principle (Peltier 1974), which allows one to employ the elastic solution of a given problem in the Laplace-transformed version of the corresponding viscoelastic problem. The Correspondence Principle for the Maxwell rheology and viscoelastic relaxation theory is introduced hereafter in this chapter.

1.2 Mathematics

The following mathematical model describes the response of a self-gravitating Earth's model to external forces, loads seated at its surface or interior and dislocations. We will assume that the rheological laws (relating stress to strain and strain rate) are linear and that the strain is infinitesimal. We do not deal with non-linear constitutive equations and finite strain theory, but that does not imply that these are not important for the Earth Sciences. However, for a wide spectrum of solid Earth relaxation processes, we can neglect both.

For long time scale processes the inertial forces vanish and the conservation of linear momentum requires that the body force $\mathbf{F}$ per unit volume acting on the infinitesimal element of the continuum body is balanced by the stress acting on the surface of the element. At any instant of time t, we thus have for the Cauchy stress tensor $\boldsymbol{\sigma}$ acting on the infinitesimal element

$$\nabla \cdot \boldsymbol{\sigma} + \mathbf{F} = \mathbf{0} \tag{1.1}$$

that is the momentum equation that must be solved within the whole volume of the Earth.

The body force $\mathbf{F}$ accounts for gravitation due to the Earth, internal and surface loads, and external bodies responsible for tidal forces. It also accounts for all kinds of other contributions like centrifugal and seismic forces. We decompose the body force $\mathbf{F}$ into a non-conservative force $\mathbf{M}$ (i.e., the equivalent body force for shear dislocations, Eq. (1.221)) and a conservative force that we express in terms of the gradient of the potential ϕ

$$\mathbf{F} = \mathbf{M} - \left(\rho + \rho^L\right) \nabla\phi \tag{1.2}$$

where ρ and ρ^L are the densities of the Earth and loads, and the potential ϕ consists of the gravitational potentials of the Earth, ϕ^E, and loads, ϕ^L, and the tidal, ϕ^T, and centrifugal, ϕ^C, potentials. Note that each term in Eqs. (1.1) and (1.2) has the dimension of N/m^3, or force per unitary volume.

$$\phi = \phi^E + \phi^L + \phi^T + \phi^C \tag{1.3}$$

The gravitational potentials ϕ^E and ϕ^L are due to the density of the Earth ρ and loads ρ^L, respectively, while the tidal potential is due to the density of external bodies ρ^T. They satisfy the following Poisson equations

$$\nabla^2\phi^E = 4\,\pi\,G\,\rho \tag{1.4}$$

$$\nabla^2\phi^L = 4\,\pi\,G\,\rho^L \tag{1.5}$$

$$\nabla^2\phi^T = 4\,\pi\,G\,\rho^T \tag{1.6}$$

where G is the universal gravitational constant. Note that the density ρ^T of external bodies, responsible for the tidal potential ϕ^T, does not enter the momentum equation (1.1) via Eq. (1.2) because, by definition, external bodies do not load the Earth, i.e., the balance of forces acting on external bodies does not involve surface forces from the Earth. The centrifugal potential ϕ^C due to the Earth's rotation is defined by

$$\phi^C = \frac{1}{2}\left[(\boldsymbol{\omega}\cdot\boldsymbol{r})^2 - \omega^2\,r^2\right] \tag{1.7}$$

where $\boldsymbol{\omega}$ and $\boldsymbol{r}$ are the angular velocity of the Earth and the position vector, and $\omega = |\boldsymbol{\omega}|$ and $r = |\boldsymbol{r}|$ are the rotation rate and the radial distance from the Earth's centre.

The potential ϕ thus solves the Poisson equation

$$\nabla^2\phi = 4\,\pi\,G\,\left(\rho + \rho^L + \rho^T\right) - 2\,\omega^2 \tag{1.8}$$

where the latter term in the right-hand side (RHS) results from the Laplacian of the centrifugal potential, $\nabla^2\phi^C = -2\,\omega^2$. Differently from the momentum equation (1.1), which must be solved only within the volume of the Earth, the Poisson equation (1.8) must be solved also outside the Earth.

Within the Lagrangian approach, we describe the deformed Earth in terms of displacements of the particles of the continuum body

$$\boldsymbol{r} = \boldsymbol{x} + \boldsymbol{u}(\boldsymbol{x}, t) \tag{1.9}$$

where t is the time, and $\boldsymbol{x}$ and $\boldsymbol{r}$ denote the initial and current positions of the particle subjected to the displacement $\boldsymbol{u}$. Following the work of Wolf (1991), we then introduce the decomposition of scalar, vector and tensor fields into initial fields, (i.e., the fields at the initial time), and local and material incremental fields

$$f(\boldsymbol{r}, t) = f_0(\boldsymbol{r}) + f^{\Delta}(\boldsymbol{r}, t) \tag{1.10}$$

$$f(\boldsymbol{r}, t) = f_0(\boldsymbol{x}) + f^{\delta}(\boldsymbol{x}, t) \tag{1.11}$$

where f stands for the generic field. The initial field f_0 (denoted with the subscript 0) describes the initial state of the undeformed Earth. The local incremental field f^{Δ} (denoted with the superscript Δ) is the increment of the field at point $\boldsymbol{r}$ with respect to the initial field at the same position $\boldsymbol{r}$. The material incremental field f^{δ} (denoted with the superscript δ) is the increment of the field at point $\boldsymbol{r}$ with respect to the initial field at point $\boldsymbol{x}$, which is the initial position of the particle that is currently located at $\boldsymbol{r}$, Eq. (1.9).

Local and material incremental fields only differ for the so called advective incremental field, which is the difference between the initial field evaluated at the current and initial positions of the particle. Particularly, within the assumption of infinitesimal deformations, this difference is a first–order term that cannot be neglected

$$f^{\delta} = f^{\Delta} + \boldsymbol{u} \cdot \boldsymbol{\nabla} f_0 \tag{1.12}$$

This relation holds both in Lagrangian and Eulerian formulations, i.e., when the incremental fields are functions of the initial and current positions of the particle, because differences among incremental fields are of the second order and can be ignored.

Because the undeformed Earth is in non-rotating hydrostatic equilibrium, the initial potential ϕ_0 is the gravitational potential due to the initial density ρ_0, i.e., the density of the undeformed Earth, and satisfies the Poisson equation

$$\nabla^2 \phi_0 = 4\,\pi\, G\, \rho_0 \tag{1.13}$$

Also, the initial Cauchy stress tensor $\boldsymbol{\sigma}_0$ is the initial hydrostatic stress

$$\boldsymbol{\sigma}_0 = -p_0\, \mathbf{1} \tag{1.14}$$

where $\mathbf{1}$ and p_0 are the identity matrix and the initial hydrostatic pressure, entering with the minus sign according to the convention that stress are positive when they act in the same direction as the outward normal to the surface. From the momentum

equation at the initial time, we thus find the condition of non-rotating hydrostatic equilibrium

$$-\nabla p_0 - \rho_0 \nabla \phi_0 = \mathbf{0} \tag{1.15}$$

In the following, we describe perturbations of the Cauchy stress tensor $\boldsymbol{\sigma}$ in terms of the material increment

$$\boldsymbol{\sigma}(\boldsymbol{r}, t) = -p_0(\boldsymbol{x})\, \mathbf{1} + \boldsymbol{\sigma}^{\delta}(\boldsymbol{x}, t) \tag{1.16}$$

for which the constitutive equations of elastic and viscoelastic materials hold and are expressed as functions of strain and strain rate. Differently, the natural choice for perturbations of the total potential ϕ and the density of the Earth ρ are the local increments

$$\phi(\boldsymbol{r}, t) = \phi_0(\boldsymbol{r}) + \phi^{\Delta}(\boldsymbol{r}, t) \tag{1.17}$$

$$\rho(\boldsymbol{r}, t) = \rho_0(\boldsymbol{r}) + \rho^{\Delta}(\boldsymbol{r}, t) \tag{1.18}$$

Then, in view of Eqs. (1.13) and (1.15) and after substitution of Eqs. (1.2) and (1.16)–(1.18) into Eqs. (1.1) and (1.8), we obtain the incremental momentum and Poisson equations

$$\nabla \cdot \boldsymbol{\sigma}^{\delta} + \nabla (\boldsymbol{u} \cdot \nabla p_0) - \rho^{\Delta} \nabla \phi_0 - \rho_0 \nabla \phi^{\Delta} - \rho^{L} \nabla \phi_0 + \mathbf{M} = \mathbf{0} \tag{1.19}$$

$$\nabla^2 \phi^{\Delta} = 4\pi G \left(\rho^{\Delta} + \rho^{L} + \rho^{T}\right) - 2\omega^2 \tag{1.20}$$

in which only first-order terms enter. The first term in Eq. (1.19) describes the contribution from the material incremental stress and the second term accounts for the advection of the initial hydrostatic pressure

$$p_0(\boldsymbol{r}) = p_0(\boldsymbol{x}) + \boldsymbol{u}(\boldsymbol{x}, t) \cdot \nabla p_0(\boldsymbol{x}) \tag{1.21}$$

after Eq. (1.15) is applied at $\boldsymbol{r}$

$$-\nabla p_0(\boldsymbol{r}) - \rho_0(\boldsymbol{r}) \nabla \phi_0(\boldsymbol{r}) = \mathbf{0} \tag{1.22}$$

The third term describes the buoyancy forces due to density changes (i.e., compressibility), the fourth term describes the gravity perturbations (i.e., self–gravitation) due to any kind of forcing, and the fifth and sixth terms account for the weight of loads and non-conservative forces.

For self–gravitating Earth's models, the local incremental potential ϕ^{Δ} must be obtained self–consistently together with the local incremental density ρ^{Δ}. This couples the momentum and Poisson equations, Eqs. (1.19)–(1.20), via the continuity equation of mass written as

$$\rho^{\Delta} = -\nabla \cdot (\rho_0 \boldsymbol{u}) = -\rho_0 \Delta - \boldsymbol{u} \cdot \nabla \rho_0 \tag{1.23}$$

Here, the first term of the RHS describes the density perturbation due to the volume variation Δ of the particle

$$\Delta = \nabla \cdot \boldsymbol{u} \tag{1.24}$$

and the second term the advection of the initial density field. In this respect, the first term of the RHS of Eq. (1.23) is the material incremental density ρ^{δ}

$$\rho^{\delta} = -\rho_0 \, \Delta \tag{1.25}$$

1.2.1 The Linear Maxwell Solid

The equations above need to be supplemented by the constitutive equation describing how material incremental stress and strain (or strain rate) are related to each other. Within the first–order perturbation theory, the strain tensor $\boldsymbol{\epsilon}$ is defined by

$$\boldsymbol{\epsilon} = \frac{1}{2} \left[\nabla \otimes \boldsymbol{u} + (\nabla \otimes \boldsymbol{u})^T \right] \tag{1.26}$$

where $\otimes$ and T stand for the algebraic product and the transpose. This representation of the strain tensor is based on the dyadic formulation, following Ben-Menahem and Singh (2000), and it is equivalent to its usual definition in terms of its Cartesian components ϵ_{ij}

$$\epsilon_{ij} = \frac{1}{2} \left(\frac{\partial u_i}{\partial x_j} + \frac{\partial u_j}{\partial x_i} \right) \tag{1.27}$$

where x_1, x_2 and x_3 are the Cartesian coordinates. The dyadic formulation allows to deal with stress and strain tensors without choosing a specific coordinate system, and to obtain general expressions for the gradient and curl of vectors and the divergence of tensors that hold in any coordinate system. In Appendix A some basic results of dyadic and vector identities are provided, to which we refer to make easier for the reader, in particular, the expansion of the momentum equations in spherical harmonics.

In the following, we will assume linear and isotropic constitutive equations and we focus on the viscoelastic rheology. We also assume that perturbations are isentropic and isochemical because viscoelastic relaxation processes of the Earth occur on time scales much smaller than those of heat diffusion and changes in the chemical composition of the rock. Particularly, we consider the viscoelastic Maxwell rheology defined by the following constitutive equation

$$\boldsymbol{\sigma}^{\delta} = \kappa \, \Delta \, \mathbf{1} + 2 \, q \star \partial_t \boldsymbol{\epsilon}_D \tag{1.28}$$

where ∂_t and $\star$ stand for the partial derivative with respect to time t and the time convolution

$$(q \star \partial_t \boldsymbol{\epsilon}_D)(t) = \int_0^t q(t - t')\, \partial_{t'} \boldsymbol{\epsilon}_D(t')\, dt' \tag{1.29}$$

and κ, q and $\boldsymbol{\epsilon}_D$ are the adiabatic bulk modulus, the shear relaxation function and the deviatoric strain tensor

$$\boldsymbol{\epsilon}_D = \boldsymbol{\epsilon} - \frac{\Delta}{3}\mathbf{1} \tag{1.30}$$

In this respect, the first and second terms in the RHS of Eq. (1.28) describe isotropic and deviatoric material incremental stresses, respectively, and, particularly, the factor $\kappa\,\Delta$ multiplying the identity matrix $\mathbf{1}$ corresponds to the negative of the material incremental pressure

$$p^{\delta} = -\kappa\,\Delta \tag{1.31}$$

as it can be understood after substitution of Eq. (1.28) into Eq. (1.16).

For the Maxwell solid, the shear relaxation function takes the following form

$$q(t) = \begin{cases} \mu\, \exp\left(-\frac{t}{\tau}\right) & t \geq 0 \\ 0 & t < 0 \end{cases} \tag{1.32}$$

where τ is the Maxwell time defined by the ratio between viscosity and rigidity (Lamé parameter)

$$\tau = \frac{\nu}{\mu} \tag{1.33}$$

By means of the Maxwell rheology, we describe the transition from the elastic to the Newtonian fluid behavior of the Earth that occurs on the timescale given by the Maxwell time τ. Despite the constitutive equations of both elastic and Newtonian fluid bodies relating stress at a given time to only strain and strain rate at that time, the Maxwell rheology relates the viscoelastic stress at a given time to the whole strain rate history before that time, as pointed out by the time convolution between the shear relaxation function and the deviatoric strain rate in Eq. (1.28).

Note that the Maxwell solid does not account for bulk relaxation because the adiabatic bulk modulus κ is simply a constant. The latter is defined starting from the differential form of the density state function $\rho(p, s, c)$ that describes the density of a particle as function of its pressure p, entropy s and chemical composition c

$$d\rho = \left.\frac{\partial \rho}{\partial p}\right|_{s,c} dp + \left.\frac{\partial \rho}{\partial s}\right|_{p,c} ds + \left.\frac{\partial \rho}{\partial c}\right|_{p,s} dc \tag{1.34}$$

We choose the entropy as thermodynamic quantity rather than the temperature as we are focusing on isentropic perturbations. By considering the differentials $d\rho$, dp, ds and dc as perturbations with respect to the initial state of the particle, they

actually correspond to material incremental fields ρ^δ, p^δ, s^δ and c^δ. Thus, within the assumption of isentropic and isochemical pertubations (i.e., for $s^\delta = 0$ and $c^\delta = 0$), we obtain

$$\rho^\delta = \left.\frac{\partial \rho}{\partial p}\right|_{s_0, c_0} p^\delta \tag{1.35}$$

where the subscript 0 denotes initial fields. By making use of Eqs. (1.25) and (1.31) into Eq. (1.35), we thus obtain the definition of the adiabatic bulk modulus κ entering the consitutive equation (1.28) in terms of the partial derivative of the density with respect to the pressure at the initial state

$$\frac{\rho_0}{\kappa} = \left.\frac{\partial \rho}{\partial p}\right|_{s_0, c_0} \tag{1.36}$$

1.2.2 Compressible and Incompressible Earth's Models

By definition, there are no volume changes Δ within incompressible materials. Instead, they occur within compressible materials. This makes differences both in the style of deformation and in the interpretation of density stratifications at the initial state of hydrostatic equilibrium.

During the deformations, incompressible materials must be able to react to isotropic stresses. From Eq. (1.31), we thus require that the bulk modulus κ is infinitely large in order that the incremental pressure p^δ remains finite in the limit of Δ going to zero and of κ going to infinity (Love 1911, Sect. 154)

$$p^\delta = \lim_{\Delta \to 0 \kappa \to \infty} (-\kappa \, \Delta) \tag{1.37}$$

In this respect, the bulk modulus is sometimes called modulus of incompressibility. On the contrary, compressible materials are characterized by a finite bulk modulus.

Incompressible and compressible Earth's models also differ in their initial state of hydrostatic equilibrium, once the compression of the Earth due to its own weight (i.e., self-compression) is accounted for self-consistently. To better understand this issue, let us consider the initial density $\rho_0 = \rho(p_0, s_0, c_0)$ as function of the initial pressure p_0, entropy s_0 and chemical composition c_0 and take its gradient

$$\nabla \rho_0 = \left.\frac{\partial \rho_0}{\partial p}\right|_{s_0, c_0} \nabla p_0 + \left.\frac{\partial \rho_0}{\partial s}\right|_{p_0, c_0} \nabla s_0 + \left.\frac{\partial \rho_0}{\partial c}\right|_{p_0, s_0} \nabla c_0 \tag{1.38}$$

Let us also assume that the Earth's model is spherically symmetric, an assumption that we will adopt later in this book. The initial density, entropy and chemical composition only depend on the radial distance from the Earth's centre r and, thus, we have

$$\nabla \rho_0 = \partial_r \rho_0 \, \boldsymbol{e}_r \quad \nabla s_0 = \partial_r s_0 \, \boldsymbol{e}_r \quad \nabla c_0 = \partial_r c_0 \, \boldsymbol{e}_r \tag{1.39}$$

and, from the condition of hydrostatic equilibrium, Eq. (1.15), the gradient of the initial pressure yields

$$\nabla p_0 = -\rho_0 \nabla \phi_0 = -\rho_0 \, g \, \boldsymbol{e}_r \tag{1.40}$$

where $\mathbf{e}_r$ and g are the unit vector pointing outward the Earth's centre and the gravity acceleration for a spherically symmetric Earth

$$g(r) = \frac{4\pi G}{r^2} \int_0^r \rho_0(r') \, r'^2 \, dr' \tag{1.41}$$

Then, Eq. (1.38) can be arranged as follows

$$\partial_r \rho_0 = -\frac{\rho_0^2 \, g}{\kappa} + \gamma \tag{1.42}$$

where γ is the compositional coefficient given by

$$\gamma = \left.\frac{\partial \rho}{\partial s}\right|_{p_0, c_0} \partial_r s_0 + \left.\frac{\partial \rho}{\partial c}\right|_{p_0, s_0} \partial_r c_0 \tag{1.43}$$

Equation (1.42) is named the generalized Williamson–Adams equation (Wolf and Kaufmann 2000; Cambiotti and Sabadini 2010). The first term in the RHS shows how compressibility, via the bulk modulus κ, characterizes the initial density profile of the Earth. A finite bulk modulus yields a negative density gradient $\partial_r \rho_0$ and the initial density increases with depth accordingly to compression of the Earth due to its own weight (i.e., self–compression). The second term, the compositional coefficient γ, takes into account the departure from the self–compression due to non-adiabatic and chemically heterogeneous stratifications, i.e., when the gradient of the initial entropy, $\partial_r s_0$, and chemical composition, $\partial_r c_0$, differ from zero. Their contribution does not amount to more than 10–20 % of the actual density gradient of the Earth (Birch 1952, 1964; Wolf and Kaufmann 2000) and it occurs likely in the outermost layers of the Earth, like the transition zone and the lithosphere. The core and the lower mantle, instead, deviate marginally from the adiabatic and chemically homogeneous stratification.

Afterwards, we will call compressional stratifications or we will say that a layer of the Earth is in a neutral state of equilibrium if the stratification is adiabatic and chemically homogeneous ($\gamma = 0$). Instead, we will refer to non-adiabatic and chemically heterogeneous stratifications ($\gamma \neq 0$) as compositional stratifications.

1.2.3 The Correspondence Principle

The Laplace transform of a function $f(t)$ is formally defined by

$$\mathcal{L}[f] = \int_0^\infty f(t) e^{-st} dt, \tag{1.44}$$

with $\mathcal{L}$, t and s being the Laplace transform operator, time and Laplace variable (which has dimension of inverse time). Introducing $\tilde{f}(s) = \mathcal{L}[f]$ for brevity, it is straightforward to show that the Laplace transform of the time derivative of the function $f(t)$ yields

$$\mathcal{L}[\partial_t f] = s\, \tilde{f}(s) - f(0) \tag{1.45}$$

and that the Laplace transform of the time convolution of two functions $f(t)$ and $h(t)$ yields the product of the Laplace transforms $\tilde{f}(s)$ and $\tilde{h}(s)$

$$\mathcal{L}[f \star h] = \tilde{f}(s)\, \tilde{h}(s) \tag{1.46}$$

with $\star$ denoting the time convolution operator and s the Laplace variable.

In the following we will consider external forcing and loading that act on the Earth starting immediately after the initial time, at $t = 0^+$, and we restrict our attention on right-handed functions that differ from zero only for $t > 0$

$$f_+(t) = f(t)\, H(t - 0^+) \tag{1.47}$$

Here $H(t)$ is the Heaviside function. It is a discontinuous function, whose value is zero for negative arguments and one for positive arguments, and its derivative yields the Dirac delta function $\delta(t)$

$$\partial_t H(t) = \delta(t) \tag{1.48}$$

The Laplace transform of the right-handed function $f_+(t)$ is the same of the original function $f(t)$

$$\tilde{f}_+(s) = \tilde{f}(s) \tag{1.49}$$

while its Laplace transform yields

$$\mathcal{L}[\partial_t f_+(t)] = s\, \tilde{f}(s) \tag{1.50}$$

because the second term of the RHS of Eq. (1.45) disappears due to the step-like discontinuity of $f_+(t)$ at $t = 0^+$. From now on, we intend time-dependent functions describing forcings and perturbations as right-handed functions, even though the subscript $+$ will be omitted in order to not overwhelm the text.

Exercise 1 Prove that the time convolution between the exponential $e^{-t/\tau}$, with τ as a constant (the Maxwell time), and the Heaviside function $H(t)$ yields

$$e^{-t/\tau} \star H = \tau \left(1 - e^{-t/\tau}\right) \tag{1.51}$$

Exercise 2 Prove that the Laplace transforms of the Dirac delta, $\delta(t)$, and Heaviside, $H(t)$, functions and of the exponential $e^{-t/\tau}$ yield

$$\mathcal{L}[\delta(t)] = 1 \quad \mathcal{L}[H(t)] = \frac{1}{s} \quad \mathcal{L}\left[e^{-t/\tau}\right] = \frac{1}{s + \frac{1}{\tau}} \tag{1.52}$$

By making use of Eq. (1.50), the Laplace transform of the constitutive equation for the Maxwell solid, Eq. (1.28), yields

$$\tilde{\boldsymbol{\sigma}}^{\delta}(s) = \kappa\, \tilde{\Delta}(s)\, \mathbf{1} + 2\, \hat{\mu}(s)\, \tilde{\boldsymbol{\epsilon}}_D(s) \tag{1.53}$$

with $\hat{\mu}(s)$ being the following function of the Laplace variable s

$$\hat{\mu}(s) = \frac{\mu\, s}{s + \frac{1}{\tau}} \tag{1.54}$$

Note that Eq. (1.53) has the same form of the Hooke's law for linear elastic solids

$$\boldsymbol{\sigma}^{\delta} = \kappa\, \Delta\, \mathbf{1} + 2\, \mu\, \boldsymbol{\epsilon}_D \tag{1.55}$$

where $\hat{\mu}(s)$ and the Laplace transforms of the fields are replaced by the shear modulus μ and the same fields in the time domain. So we can derive equations for viscoelastic bodies in the Laplace domain from elastic body equations. Particularly, after Laplace transformation, the momentum and Poisson equations for the viscoelastic body are formally equivalent to those for the elastic solid. We thus solve the equivalent elastic problem in the Laplace domain and, only at the last stage, we will perform the inverse Laplace transform of the solution to obtain the viscoelastic solution in the time domain. In this respect, we will also refer to the viscoelastic solution in the Laplace domain as the associated elastic solution.

The so-called Correspondence Principle (Peltier 1974; Wu and Peltier 1982) states that the time dependent viscoelastic solution of the momentum and Poisson equations can be found in a unique way after the inverse Laplace transformation of the associated elastic solution. In the light of this analogy between the elastic and viscoelastic problems, afterwards we will omit the tilde to denote Laplace transforms and we do not distinguish between the shear modulus μ and the function $\hat{\mu}(s)$, Eq. (1.54). In this respect, the following results can be seen both as the solution of the elastic static problem and the associated viscoelastic solution.

1.3 Expansion in Spherical Harmonics

In the following we will consider spherically symmetric Earth's models composed of several concentric layers as the core, the lower and upper mantle and the lithosphere. Within each layer the material parameters, consisting of the initial density ρ_0, the bulk modulus κ, the shear modulus μ and the viscosity ν, are continuous functions of the only radial distance from the Earth's centre r. At the internal boundaries separating two layers of the Earth, these parameters may have step-like discontinuities due to the specific chemical compositions and phases of the rock of each layer.

The most widely used spherically symmetric Earth's model is the Preliminary Reference Earth Model PREM (Dziewonski and Anderson 1981) that specifies the material parameters of the main layers of the Earth in terms of polynomials of the radial distance from the Earth's centre r. It thus accounts for the continuous variations of the material parameters and discontinuities at the interfaces between the layers. As it concerns the rheology, we will consider models with a fluid core, a viscoelastic mantle, with viscosity of about 10^{21} Pa s, and an elastic or viscoelastic (but more viscous than the mantle) lithosphere of about 100 km.

The spherical symmetry of the Earth's model is herein exploited to further simplify the incremental momentum and Poisson equations and discuss fundamental aspects of the style of deformation. We thus consider the spherical reference frame and we denote with r, θ and φ the radial distance from the Earth's centre, the colatitude and the longitude; $\boldsymbol{e}_r$, $\boldsymbol{e}_\theta$ and $\boldsymbol{e}_\varphi$ denote the respective unit vectors. We also recall that the gradient and Laplacian operators in spherical coordinates are

$$\boldsymbol{\nabla} = \boldsymbol{e}_r \frac{\partial}{\partial r} + \boldsymbol{e}_\theta \frac{1}{r} \frac{\partial}{\partial \theta} + \boldsymbol{e}_\varphi \frac{1}{r \sin\theta} \frac{\partial}{\partial \varphi} \tag{1.56}$$

$$\nabla^2 = \frac{\partial^2}{\partial r^2} + \frac{2}{r} \frac{\partial}{\partial r} + \frac{1}{r^2} \left(\frac{\partial^2}{\partial \theta^2} + \cot\theta \frac{\partial}{\partial \theta} + \frac{1}{\sin^2\theta} \frac{\partial^2}{\partial \varphi^2} \right) \tag{1.57}$$

In view of the spherical symmetry, the initial density, potential and pressure only depend on the radial distance from the Earth's centre r and their gradients have no angular components, as already shown in Eqs. (1.39)–(1.40). The incremental momentum and Poisson equations (1.19)–(1.20) become

$$\boldsymbol{\nabla} \cdot \boldsymbol{\sigma}^\delta - \rho_0 \boldsymbol{\nabla} (g \boldsymbol{u} \cdot \boldsymbol{e}_r) + \rho_0 \Delta g \boldsymbol{e}_r - \rho_0 \boldsymbol{\nabla} \phi^\Delta - \rho^L g \boldsymbol{e}_r + \mathbf{M} = \mathbf{0} \tag{1.58}$$

$$\nabla^2 \phi^\Delta = -4\pi G (\rho_0 \Delta + \partial_r \rho_0 \boldsymbol{u} \cdot \boldsymbol{e}_r) + 4\pi G \left(\rho^L + \rho^T \right) - 2\omega^2 \tag{1.59}$$

We also introduce the spherical harmonic expansions of the potential ϕ and the decomposition of the displacement $\boldsymbol{u}$ into spheroidal, $\boldsymbol{u}_S$, and toroidal, $\boldsymbol{u}_T$, displacements

$$\phi^\Delta(r, \theta, \varphi) = \sum_{\ell=0}^{\infty} \sum_{m=-\ell}^{\ell} \Phi_{\ell m}(r) Y_{\ell m}(\theta, \varphi) \tag{1.60}$$

$$\boldsymbol{u} = \boldsymbol{u}_S + \boldsymbol{u}_T \tag{1.61}$$

with

$$\boldsymbol{u}^S(\boldsymbol{r}) = \sum_{\ell=0}^{\infty} \sum_{m=-\ell}^{\ell} \left[U_{\ell m}(r)\, \boldsymbol{R}_{\ell m}(\theta, \varphi) + V_{\ell m}(r)\, \boldsymbol{S}_{\ell m}(\theta, \varphi) \right] \tag{1.62}$$

$$\boldsymbol{u}^T(\boldsymbol{r}) = \sum_{\ell=0}^{\infty} \sum_{m=-\ell}^{\ell} W_{\ell m}(r)\, \boldsymbol{T}_{\ell m}(\theta, \varphi) \tag{1.63}$$

Here, $Y_{\ell m}$ are the spherical harmonics of degree $\ell = 0, \ldots, \infty$ and order $m = -\ell, \ldots, \ell$, and $\boldsymbol{R}_{\ell m}$, $\boldsymbol{S}_{\ell m}$ and $\boldsymbol{T}_{\ell m}$ are the spherical harmonic vectors defined by

$$\boldsymbol{R}_{\ell m} = Y_{\ell m}\, \boldsymbol{e}_r \tag{1.64}$$

$$\boldsymbol{S}_{\ell m} = r\, \boldsymbol{\nabla} Y_{\ell m} = \partial_\theta Y_{\ell m}\, \boldsymbol{e}_\theta + \frac{\partial_\varphi Y_{\ell m}}{\sin\theta}\, \boldsymbol{e}_\varphi \tag{1.65}$$

$$\boldsymbol{T}_{\ell m} = \boldsymbol{\nabla} \times (\boldsymbol{r}\, Y_{\ell m}) = \frac{\partial_\varphi Y_{\ell m}}{\sin\theta}\, \boldsymbol{e}_\theta - \partial_\theta Y_{\ell m}\, \boldsymbol{e}_\varphi \tag{1.66}$$

with $\boldsymbol{r} = r\, \boldsymbol{e}_r$ being the position vector. Also, the scalars $\Phi_{\ell m}$, $U_{\ell m}$, $V_{\ell m}$ and $W_{\ell m}$ are the respective spherical harmonic coefficients and we will simply refer to them as the potential, the radial and tangential spheroidal displacements, and the toroidal displacement. Note that the spherical harmonic vectors $\mathbf{S}_{00}$ and $\mathbf{T}_{00}$ yield zero and, in this respect, tangential spheroidal and toroidal displacements of harmonic degree $\ell = 0$ do not contribute to deformations. Thus, we can set the respective spherical harmonic coefficients to zero, $V_{00} = W_{00} = 0$.

Further details about spherical harmonics and spherical harmonic vectors are discussed in Ben-Menahem and Singh (2000). Here we only explicit the definition of spherical harmonics

$$Y_{\ell m}(\theta, \varphi) = P_{\ell m}(\cos\theta)\, e^{i\, m\, \varphi} \tag{1.67}$$

where $P_{\ell m}$ are the associated Legendre polynomials. The latter, for $m \geq 0$, are given by

$$P_{\ell m}(x) = \frac{1}{2^\ell\, \ell!} \left(1 - x^2\right)^{m/2} \frac{d^{\ell+m} \left(x^2 - 1\right)^\ell}{dx^{\ell+m}} \tag{1.68}$$

and, for $m < 0$,

$$P_{\ell -m}(x) = (-1)^m \frac{(\ell - m)!}{(\ell + m)!}\, P_{\ell m}(x) \tag{1.69}$$

We also recall that the spherical harmonics are eigenfunctions of the angular part of the Laplacian operator in spherical coordinates, Eq. (1.57), so that

$$\nabla^2 Y_{\ell m} = \frac{1}{r^2}\left(\frac{\partial^2}{\partial\theta^2} + \cot\theta\,\frac{\partial}{\partial\theta} + \frac{1}{\sin^2\theta}\,\frac{\partial^2}{\partial\varphi^2}\right) Y_{\ell m} = -\frac{\ell(\ell+1)}{r^2}\,Y_{\ell m} \tag{1.70}$$

Spherical harmonics are normalized as

$$\int_\Omega Y_{\ell m} Y^*_{\ell' m'} d\Omega = N_{\ell m}\delta_{\ell l'}\delta_{m m'} \tag{1.71}$$

where $N_{\ell m}$ denotes the normalization factor.

$$N_{\ell m} = \frac{4\,\pi}{2\,\ell+1}\,\frac{(\ell+m)!}{(\ell-m)!} \tag{1.72}$$

1.3.1 Volume Changes and Surface Forces

After substitution of Eqs. (1.61)–(1.63) into (1.24), we obtain the spherical harmonic expansions of the volume change Δ

$$\Delta = \boldsymbol{\nabla}\cdot\boldsymbol{u} = \sum_{\ell=0}^{\infty}\sum_{m=-\ell}^{\ell} \chi_{\ell m}\,Y_{\ell m} \tag{1.73}$$

where the scalar $\chi_{\ell m}$ is given by

$$\chi_{\ell m} = \partial_r U_{\ell m} + \frac{2}{r}\,U_{\ell m} - \frac{\ell\,(\ell+1)}{r}\,V_{\ell m} \tag{1.74}$$

Exercise 3 Prove Eq. (1.74). Make use of the operator identities you find in Appendix A.

It is noteworthy that the toroidal displacement does not contribute to volume changes, i.e., $\boldsymbol{\nabla}\cdot\boldsymbol{u}_T = 0$. Furthermore, because the toroidal displacement has no component along $\boldsymbol{e}_r$, it does not contribute to the advection of the initial density field of the Earth's models, which can be only radial for Eq. (1.39). This means that the local incremental density is only due to spheroidal deformations

$$\rho^\Delta = -\rho_0\,\boldsymbol{\nabla}\cdot\boldsymbol{u}_S - \partial_r\rho_0\,\boldsymbol{u}_S\cdot\boldsymbol{e}_r \tag{1.75}$$

and that toroidal deformations do not directly contribute to the local incremental gravitational potential ϕ^Δ. Actually, as we will show in a while, toroidal deformations are completely decoupled from spheroidal deformations and perturbations of the gravitational potential. They can be studied separately.

Let us now consider the spherical harmonic expansion of the material incremental stress $\boldsymbol{\sigma}^{\delta} \cdot \boldsymbol{e}_r$ acting on a surface element with outward normal $\boldsymbol{e}_r$. From the definition of the strain tensor, Eq. (1.26), and the Hooke's law, Eq. (1.55) or, equivalently, the constitutive equation for the Maxwell solid in the Laplace domain, Eq. (1.53), after some straightforward algebra we obtain

$$\boldsymbol{\sigma}^{\delta} \cdot \boldsymbol{e}_r = \lambda \, \Delta \, \boldsymbol{e}_r + \mu \, [\nabla \, (\boldsymbol{u} \cdot \boldsymbol{e}_r) - (\nabla \boldsymbol{e}_r) \cdot \boldsymbol{u} + (\boldsymbol{e}_r \cdot \nabla) \, \boldsymbol{u}] \tag{1.76}$$

where λ is the second Lamé parameter that is expressed in terms of the shear modulus μ (also known as first Lamé parameter) and the bulk modulus κ

$$\lambda = \kappa - \frac{2}{3} \, \mu \tag{1.77}$$

Then, by substituting the spherical harmonic expansions for displacements and volume changes, Eqs. (1.61)–(1.63) and (1.73), we obtain

$$\boldsymbol{\sigma}^{\delta} \cdot \boldsymbol{e}_r = \sum_{\ell m} (R_{\ell m} \, \mathbf{R}_{\ell m} + S_{\ell m} \, \mathbf{S}_{\ell m} + T_{\ell m} \, \mathbf{T}_{\ell m}) \tag{1.78}$$

where the spherical harmonic coefficients $R_{\ell m}$, $S_{\ell m}$ and $T_{\ell m}$ are given by

$$R_{\ell m} = \lambda \, \chi_{\ell m} + 2 \, \mu \, \partial_r U_{\ell m} \tag{1.79}$$

$$S_{\ell m} = \mu \left(\partial_r V_{\ell m} + \frac{U_{\ell m} - V_{\ell m}}{r} \right) \tag{1.80}$$

$$T_{\ell m} = \mu \left(\partial_r W_{\ell m} - \frac{W_{\ell m}}{r} \right) \tag{1.81}$$

We will refer to $R_{\ell m}$ and $S_{\ell m}$ as the radial and tangential spheroidal stresses and to $T_{\ell m}$ as the toroidal stress.

1.3.2 Spheroidal and Toroidal Deformations

The results of this Sect. 1.3.2 are based on the dyadic formalism, exploited in Appendix A. The divergence of the material incremental Cauchy stress tensor, assuming the elastic or the viscoelastic rheology, Eqs. (1.53) and (1.55), and using the definition of the strain tensor, Eq. (1.26), can be arranged as follow

$$\nabla \cdot \boldsymbol{\sigma}^{\delta} = \lambda \, \nabla \Delta + \Delta \, \nabla \lambda + \mu \, \left(\nabla^2 \boldsymbol{u} + \nabla \Delta \right) + \nabla \mu \cdot (\nabla \boldsymbol{u} + \boldsymbol{u} \nabla) \tag{1.82}$$

which simplifies into

$$\nabla \cdot \boldsymbol{\sigma}^{\delta} = (\lambda + \mu)\,\nabla\Delta + \partial_r\lambda\,\Delta\,\boldsymbol{e}_r + \mu\,\nabla^2\boldsymbol{u} + \partial_r\mu\,[2\,\partial_r\boldsymbol{u} + \boldsymbol{e}_r \times (\nabla \times \boldsymbol{u})] \quad (1.83)$$

owing to the spherical symmetry of the Earth's model, i.e., $\nabla\mu = \partial_r\mu\,\boldsymbol{e}_r$ and $\nabla\lambda = \partial_r\lambda\,\boldsymbol{e}_r$.

Exercise 4 Prove Eq. (1.83). Make use of the dyadic identities of Appendix A.

By making use of Eq. (1.83), expanding it in spherical harmonics together with Eq. (1.59), we finally obtain the spherical harmonic coefficients of the radial and tangential spheroidal components of the momentum equation,

$$\begin{aligned} &-\rho_0\,\partial_r\Phi_{\ell m} - \rho_0\,\partial_r\,(g\,U_{\ell m}) + \rho_0\,g\,\chi_{\ell m} + \partial_r\,(\lambda\,\chi_{\ell m} + 2\,\mu\,\partial_r U_{\ell m}) \\ &+\frac{1}{r^2}\,\mu\,[4\,r\,\partial_r U_{\ell m} - 4\,U_{\ell m} + \ell(\ell+1)(3\,V_{\ell m} - U_{\ell m} - r\,\partial_r V_{\ell m})] \\ &- \rho^L_{\ell m}\,g + m^R_{\ell m} = 0 \end{aligned} \quad (1.84)$$

$$\begin{aligned} &-\frac{\rho_0}{r}\,\Phi_{\ell m} - \frac{\rho_0}{r}\,g\,U_{\ell m} + \frac{\lambda}{r}\,\chi_{\ell m} + \partial_r\left[\mu\,\left(\partial_r V_{\ell m} + \frac{1}{r}U_{\ell m} - \frac{1}{r}\,V_{\ell m}\right)\right] \\ &+\frac{1}{r^2}\,\mu\,[5\,U_{\ell m} + 3\,r\,\partial_r V_{\ell m} - V_{\ell m} - 2\,\ell(\ell+1)\,V_{\ell m}] + m^S_{\ell m} = 0 \end{aligned} \quad (1.85)$$

the toroidal component,

$$\partial_r\left[\mu\,\left(\partial_r W_{\ell m} - \frac{W_{\ell m}}{r}\right)\right] + \mu\,\left(\frac{3}{r}\,\partial_r W_{\ell m} - \frac{1+\ell(\ell+1)}{r^2}\,W_{\ell m}\right) + m^T_{\ell m} = 0 \quad (1.86)$$

and the Poisson equation

$$\nabla^2_r\Phi_{\ell m} = -4\,\pi\,G\,(\rho_0\,\chi_{\ell m} + U_{\ell m}\,\partial_r\rho_0) + 4\,\pi\,G\,\left(\rho^L_{\ell m} + \rho^T_{\ell m}\right) \quad (1.87)$$

where $\rho^L_{\ell m}$, $\rho^T_{\ell m}$, $m^R_{\ell m}$, $m^S_{\ell m}$ and $m^T_{\ell m}$ are the spherical harmonic coefficients of the densities of loads and external bodies, and of the non-conservative forces

$$\rho^L = \sum_{\ell=0}^{\infty}\sum_{m=-\ell}^{\ell}\rho^L_{\ell m}\,Y_{\ell m} \quad (1.88)$$

$$\rho^T = \sum_{\ell=0}^{\infty}\sum_{m=-\ell}^{\ell}\rho^T_{\ell m}\,Y_{\ell m} \quad (1.89)$$

$$\mathbf{M} = \sum_{\ell=0}^{\infty}\sum_{m=-\ell}^{\ell}\left(m^R_{\ell m}\,\mathbf{R}_{\ell m} + m^S_{\ell m}\,\mathbf{S}_{\ell m} + m^T_{\ell m}\,\mathbf{T}_{\ell m}\right) \quad (1.90)$$

and ∇_r^2 is the radial part of the Laplacian operator ∇^2

$$\nabla_r^2 = \partial_r^2 + \frac{2}{r}\,\partial_r - \frac{\ell(\ell+1)}{r^2} \tag{1.91}$$

Exercise 5 Prove Eqs. (1.84)–(1.86), making use of Appendix A.

Expansion of Eqs. (1.84), (1.85) and (1.86) can be easily derived by making use of the vector identities shown in Appendix A, based on the dyadic formalism, to which we refer for whom willing to undertake the job of deriving these equations starting from Eq. (1.83).

The radial and tangential spheroidal components of the momentum equation, Eqs. (1.84)–(1.85), and the Poisson equation, Eq. (1.87), are decoupled from the toroidal component of the momentum equation, Eq. (1.86). In this respect, spheroidal and toroidal deformations can be studied separately. Furthermore, it is also noteworthy that spheroidal perturbations are triggered by all kind of forcing that we are considering (loads and tidal, centrifugal and seismic forces), while toroidal deformations are triggered only by seismic forces. This reflects the fact that loading, tidal and centrifugal forcings are axially symmetric.

Equations (1.84)–(1.87) hold only for harmonic degree ℓ greater than 0. They can be extended to the case of harmonic degree $\ell = 0$ with the care of omitting the tangential spheroidal and toroidal components of the momentum equation, Eqs. (1.85)–(1.86), and setting to zero the tangential spheroidal coefficients of the displacement, $V_{00} = 0$, in the radial component of the momentum equation and Poisson equation, Eqs. (1.84) and (1.87). In this respect, the case of harmonic degree $\ell = 0$ would require a specific treatment that we do not discuss as it has little relevance for the geophysical processes considered in this book. Also the case of harmonic degree $\ell = 1$ would require a specific treatment, although for different reasons related to the fact that perturbations of harmonic degree $\ell = 1$ may involve a net shift of the centre of mass of the Earth. For the readers who may be interested in these issues, we refer to Farrell (1972) for surface load problems as in the case of ice sheet loading, to Sun and Okubo (1993) for earthquake forcing and to Greff-Lefftz (2011) for internal loads and tidal and centrifugal forcing.

Regardless these specific treatments for perturbations of harmonic degrees $\ell = 0$ and $\ell = 1$, however, we note that the perturbation of the total gravitational potential (including contributions from both mass rearrangement of the Earth and from surface and internal loads) for these harmonic degrees must be zero in order that the mass and the centre of mass of the system are preserved.

1.4 Spheroidal Deformations

The radial and tangential spheroidal components of the momentum equation and the Poisson equation constitute a system of three differential equations of second order in the unknowns $U_{\ell m}$, $V_{\ell m}$ and $\Phi_{\ell m}$. This differential system must be solved

for each harmonic degree, except $\ell = 0$ $\ell = 1$ as anticipated, from the centre to the surface of the Earth where proper boundary conditions uniquely determine the solution. Analytical solutions of these differential equations will be considered in Chap. 2, with some restrictions on the material parameters of the Earth's model. Here, in order to define proper boundary conditions and compute numerical solutions of the viscoelastic problem for general spherically symmetric Earth's models, we cast these differential equations into the form of six differential equations of the first–order that are suitable for numerical integration in the radial variable r by means of algorithms like Runge-Kutta. We therefore introduce the spheroidal 6–vector solution $\boldsymbol{y}_{\ell m}$

$$\boldsymbol{y}_{\ell m} = (U_{\ell m},\ V_{\ell m},\ R_{\ell m},\ S_{\ell m},\ \Phi_{\ell m},\ Q_{\ell m})^T \tag{1.92}$$

where the first and second components are the radial and tangential displacements, the third and fourth components the radial and tangential stresses, the fifth component the potential and the sixth component the so called 'potential stress'. The latter is defined by

$$Q_{\ell m} = \partial_r \Phi_{\ell m} + \frac{\ell + 1}{r}\, \Phi_{\ell m} + 4\,\pi\, G\, \rho_0\, U_{\ell m} \tag{1.93}$$

and its meaning will be clarified in Sect. 1.6.2, when we discuss the boundary conditions at the internal interfaces and at the surface of the Earth.

From the radial and tangential spheroidal components of the momentum equation, Eqs. (1.84)–(1.85), the Poisson equation, Eq. (1.87), and the definition of radial, tangential and potential stresses, Eqs. (1.79)–(1.80) and (1.93), after some straightforward algebra we obtain the following linear differential system for the spheroidal vector solution

$$\frac{d\,\boldsymbol{y}_{\ell m}(r)}{dr} = \mathbf{A}_\ell(r)\, \boldsymbol{y}_{\ell m}(r) - \boldsymbol{f}_{\ell m}(r) \tag{1.94}$$

where $\mathbf{A}_\ell$ is the 6×6–matrix depending on the material parameters of the Earth's model, on the radial distance from the Earth's centre r and on the harmonic degree ℓ

$$\mathbf{A}_\ell(r) =$$

$$\begin{pmatrix}
-\frac{2\,\lambda}{r\,\beta} & \frac{\ell(\ell+1)\,\lambda}{r\,\beta} & \frac{1}{\beta} & 0 & 0 & 0 \\
-\frac{1}{r} & \frac{1}{r} & 0 & \frac{1}{\mu} & 0 & 0 \\
\frac{4}{r}\left(\frac{3\,\kappa\,\mu}{r\,\beta} - \rho_0\, g\right) & \frac{\ell(\ell+1)}{r}\left(\rho_0\, g - \frac{6\,\kappa\,\mu}{r\,\beta}\right) & -\frac{4\,\mu}{r\,\beta} & \frac{\ell(\ell+1)}{r} & -\frac{\rho_0\,(\ell+1)}{r} & \rho_0 \\
\frac{1}{r}\left(\rho_0\, g - \frac{6\,\mu\,\kappa}{r\,\beta}\right) & \frac{2\,\mu}{r^2}\left[\ell(\ell+1)\left(1+\frac{\lambda}{\beta}\right) - 1\right] & -\frac{\lambda}{r\,\beta} & -\frac{3}{r} & \frac{\rho_0}{r} & 0 \\
-4\,\pi\, G\, \rho_0 & 0 & 0 & 0 & -\frac{\ell+1}{r} & 1 \\
-\frac{4\,\pi\, G\, \rho_0\,(\ell+1)}{r} & \frac{4\,\pi\, G\, \rho_0\, \ell(\ell+1)}{r} & 0 & 0 & 0 & \frac{\ell-1}{r}
\end{pmatrix} \tag{1.95}$$

with

$$\beta = \lambda + 2\,\mu \tag{1.96}$$

The non-homogeneous term $\boldsymbol{f}_{\ell m}$ of the differential system (1.94) accounts for terms related to massive bodies other than the Earth and seismic forces. Remembering that for tidal and centrifugal forcings we provide in the following a formulation in terms of boundary conditions at the Earth's surface, we have

$$\boldsymbol{f}_{\ell m} = \rho^L_{\ell m}\, \boldsymbol{f}^L_\ell + \boldsymbol{m}_{\ell m} \tag{1.97}$$

with

$$\boldsymbol{f}^L_\ell = \left(0,\, 0,\, -\frac{(2\,\ell+1)\,g}{4\,\pi\,r^2},\, 0,\, 0,\, -\frac{(2\,\ell+1)\,G}{r^2}\right)^T \tag{1.98}$$

where the third, fifth an sixth components of $\boldsymbol{f}^L_\ell$ are those of the vector

$$\boldsymbol{b}^L(r) = \left(-\frac{(2\,\ell+1)\,g(r)}{4\,\pi\,r^2},\, 0,\, -\frac{(2\,\ell+1)\,G}{r^2}\right)^T \tag{1.99}$$

defined in Sect. 1.6.1, Eq. (1.129), for an arbitrary depth r rather than at the Earth's surface and

$$\boldsymbol{m}_{\ell m} = \left(0,\, 0,\, m^R_{\ell m},\, m^S_{\ell m},\, 0,\, 0\right)^T \tag{1.100}$$

Exercise 6 Verify that, with the above definition of the spheroidal vector solution (1.92), the matrix $\boldsymbol{A}(r)$ entering the system of differential equations (1.94) takes the form given in Eq. (1.95).

Exercise 7 Verify that, with the above definition of the spheroidal vector solution (1.92), the spheroidal forcing vector takes the form given by Eqs. (1.97)–(1.98), once the harmonic expansion for the point-load source in Eq. (1.216) appearing in Sect. 1.10.1 is taken into account.

1.5 Toroidal Deformations

Similarly to the case of spheroidal deformations, we define the toroidal 2-vector solution $\boldsymbol{y}_{\ell m}$ as follows

$$\boldsymbol{y}_{\ell m} = (W_{\ell m},\, T_{\ell m})^T \tag{1.101}$$

where the first and second components are the toroidal displacement and stress, respectively. The component (1.86) of the momentum equation can be cast into a linear differential system like Eq. (1.94)

$$\frac{d\,\boldsymbol{y}_{\ell m}(r)}{dr} = \mathbf{A}_\ell(r)\,\boldsymbol{y}_{\ell m}(r) - \boldsymbol{f}_{\ell m}(r) \tag{1.102}$$

where now $\boldsymbol{y}_{\ell m}$ and $\mathbf{A}_\ell$ are the toroidal 2−vector solution (1.101) and the following 2×2-matrix

$$\mathbf{A}_\ell = \begin{pmatrix} \frac{1}{r} & \frac{1}{\mu} \\ \frac{\mu(\ell(\ell+1)-2)}{r^2} & -\frac{3}{r} \end{pmatrix} \tag{1.103}$$

and the dishomogeneous term $\mathbf{f}_{\ell m}$ only accounts for toroidal components of seismic forces

$$\boldsymbol{f}_{\ell m} = \boldsymbol{m}_{\ell m} \tag{1.104}$$

with

$$\boldsymbol{m}_{\ell m} = \left(0,\, m_{\ell m}^T\right)^T \tag{1.105}$$

1.6 Boundary Conditions

In order to obtain the solution of the associated elastic problem, the above equations must be solved within each viscoelastic layer of the Earth's model and supplemented by proper boundary conditions at the bottom and top interfaces. Each layer is bounded by another viscoelastic layer, or by the fluid outer core, or by the Earth's surface. For each kind of interface we thus need to specify proper boundary conditions.

In the following, we denote the number of layer of the Earth's model with N and the radial distance from the Earth's centre of the top interface of the jth layer with r_j. We order the layers in such a way that $r_{j-1} < r_j$ for $j = 2, \ldots N$. Particularly, r_j are interfaces within the viscoelastic mantle for $j = 2, \ldots, N-1$, while r_1 and r_N are the core and Earth's radii, also denoted by r_C and a, respectively.

1.6.1 The Earth's Surface

We begin by considering the Earth's surface boundary conditions. We distinguish between massive bodies outside the Earth and loads seated at the Earth's surface or its interior. By definition, the load density ρ^L is zero outside the Earth

$$\rho^L(r > a) = 0 \tag{1.106}$$

while the density of external bodies ρ^T is zero within a sphere of radius a_T containing the Earth

$$\rho^T(r < a_T) = 0 \tag{1.107}$$

with a_T greater than the Earth's radius, $a_T > a$.

We write the load density ρ^L as the sum of the density of internal loads ρ^I and the surface density of loads seated at the Earth's surface σ^L

$$\rho^L(r) = \rho^I(r) + \sigma^L\,\delta(r-a) \tag{1.108}$$

where δ is the Dirac delta function.

For internal loading and tidal, centrifugal and seismic forcings, the Earth's surface is stress free. For the case of surface loading, instead, the tangential stress $S_{\ell m}$ is still zero while the radial stress $R_{\ell m}$ must compensate the weight of the surface density

$$R_{\ell m}(a^-) = -g(a)\,\sigma^L_{\ell m} \tag{1.109}$$

where $\sigma^L_{\ell m}$ are the spherical harmonic coefficients of the surface density σ^L.

An additional condition can be found for the potential stress $Q_{\ell m}$. By applying the Gauss theorem at the incremental Poisson equation (1.20) within a volume embedded in an infinitesimal pill-box at the Earth's surface, we obtain

$$\partial_r\phi^\Delta(a^-) = \partial_r\phi^\Delta(a^+) - 4\,\pi\,G\,\rho_0(a^-)u(a^-)\cdot e_r - 4\,\pi\,G\,\sigma^L \tag{1.110}$$

where we have assumed that the initial density ρ_0 is zero outside the Earth (i.e., we neglect the atmosphere)

$$\rho_0(r > a) = 0 \tag{1.111}$$

Equation (1.110) expresses the radial derivative of the potential within the Earth, a^-, in terms of the radial derivative of the potential outside the Earth, a^+, and contributions from perturbations of the Earth's surface topography and surface loading. After spherical harmonic expansion, Eq. (1.110) can be arranged as follows

$$Q_{\ell m}(a^-) = \partial_r\Phi_{\ell m}(a^+) + \frac{\ell+1}{a}\,\Phi_{\ell m}(a^+) - 4\,\pi\,G\,\sigma^L_{\ell m} \tag{1.112}$$

where we have used the fact that the potential is continuous across any interface

$$\Phi_{\ell m}(a^+) = \Phi_{\ell m}(a^-) \tag{1.113}$$

The first term in the RHS of Eq. (1.112) can be further specified by considering the dependence of the potential on the radial distance from the Earth's centre. First, we distinguish between gravitational, tidal and centrifugal potentials as in Eq. (1.3). From Eqs. (1.106) to (1.107), the Poisson Eqs. (1.5)–(1.6) for the gravitational and tidal potentials become Laplace equations outside the Earth and within the sphere of radius a^T containing it, respectively. After spherical harmonic expansion, we thus obtain

$$\nabla_r^2\Phi^G_{\ell m} = 0 \quad (r > a) \tag{1.114}$$

$$\nabla_r^2\Phi^T_{\ell m} = 0 \quad (r < a_T) \tag{1.115}$$

where $\Phi^G_{\ell m}$ and $\Phi^T_{\ell m}$ are the spherical harmonic coefficients of the gravitational and tidal potentials, ϕ^G and ϕ^T, respectively. By imposing the regularity conditions at the infinity (in the limit for $r \to \infty$) and the centre of the Earth ($r = 0$), the solutions of the above Laplacian equations read

$$\Phi^G_{\ell m}(r) = \Phi^G_{\ell m}(a) \left(\frac{r}{a}\right)^{-\ell-1} \quad (r > a) \tag{1.116}$$

$$\Phi^T_{\ell m}(r) = \Phi^T_{\ell m}(a) \left(\frac{r}{a}\right)^{\ell} \quad (r < a_T) \tag{1.117}$$

Here $\Phi^G_{\ell m}(a)$ and $\Phi^T_{\ell m}(a)$ must be intended as constants of integration. The gravitational potential at the Earth's surface $\Phi^G_{\ell m}(a)$ will be obtained solving the viscoelastic problem, while the tidal potential $\Phi^T_{\ell m}(a)$ is prescribed by the external bodies for which we are solving the problem

$$\Phi^T_{\ell m}(a) = -\frac{4\pi\, G\, a}{2\,\ell + 1} \int_{a_T}^{\infty} \rho^T_{\ell m}(r) \left(\frac{a}{r}\right)^{\ell-1} dr \tag{1.118}$$

as for Eq. (3.17) and thereafter for this case of external bodies.

After expansion in spherical harmonics of Eq. (1.7) we obtain for the centrifugal potential ϕ^C from Eq. (3.25) evaluated with respect to $\hat{\mathbf{n}}$

$$\phi^C(r, \theta, \varphi) = \Phi^C_{00}(r)\, Y_{00}(\theta, \varphi) + \sum_{m=-2}^{2} \Phi^C_{2m}(r)\, Y_{2m}(\theta, \varphi) \tag{1.119}$$

where the spherical harmonic coefficients Φ^C_{00} anc Φ^C_{2m} are given by

$$\Phi^C_{00}(r) = -\frac{\omega^2\, r^2}{3} \tag{1.120}$$

$$\Phi^C_{2m}(r) = \frac{\omega^2\, r^2}{3} \frac{(2-m)!}{(2+m)!}\, Y^*_{2m}(\theta_C, \varphi_C) \quad (m = -2, \ldots, 2) \tag{1.121}$$

while the others are zero, $\Phi^C_{\ell m} = 0$ for $\ell = 1, 3, \ldots, \infty$. Here, θ_C, φ_C are the colatitude and longitude of the angular velocity $\boldsymbol{\omega}$. Note that the $\ell = 2$ spherical harmonic coefficients Φ^T_{2m} and Φ^C_{2m} share the same dependence on r, i.e., r^2. In this respect, the following treatment will be done assuming

$$\Phi^C_{\ell m}(r) = \Phi^C_{\ell m}(a) \left(\frac{r}{a}\right)^{\ell} \tag{1.122}$$

because we do not consider $\ell = 0$ perturbations and $\Phi^C_{\ell m}(a) = 0$ for $\ell = 1, 3, \ldots, \infty$.

By using these results, Eq. (1.112) becomes

$$Q_{\ell m}(a^-) = \frac{2\,\ell+1}{a}\,\left(\Phi^T_{\ell m}(a) + \Phi^C_{\ell m}(a)\right) - 4\,\pi\,G\,\sigma^L_{\ell m} \tag{1.123}$$

where the terms related to the gravitational potential $\Phi^G_{\ell m}$ in the RHS cancel each other via Eq. (1.116)

$$\partial_r \Phi^G_{\ell m}(a^+) = -\frac{\ell+1}{a}\,\Phi^G_{\ell m}(a) \tag{1.124}$$

and the radial derivatives of the tidal and centrifugal potentials have been obtained from Eqs. (1.117) and (1.122)

$$\partial_r \Phi^T_{\ell m}(a^+) = \frac{\ell}{a}\,\Phi^T_{\ell m}(a) \tag{1.125}$$

$$\partial_r \Phi^C_{\ell m}(a^+) = \frac{\ell}{a}\,\Phi^C_{\ell m}(a) \tag{1.126}$$

In summary, for the forcings that we are considering, the tangential stress $S_{\ell m}$ is zero at the Earth's surface while the radial, $R_{\ell m}$, and potential, $Q_{\ell m}$, stresses are constrained by Eqs. (1.109) and (1.123). We collect these findings in the following compact form, assuming a unitary surface density anomaly as appropriate in Green functions generation as done in Chap. 2, accounting for the spherical harmonic components of the point load given by Eq. (1.216)

$$\mathbf{P}_1\,\boldsymbol{y}(a^-) = \boldsymbol{b} \tag{1.127}$$

where $\mathbf{P}_1$ is the projector for the third, fourth and sixth components of the spheroidal vector solution, and $\boldsymbol{b}$ is the 3–vector

$$\boldsymbol{b} = \sigma^L_{\ell m}\boldsymbol{b}^L + \left(\Phi^T_{\ell m}(a) + \Phi^C_{\ell m}(a)\right)\,\boldsymbol{b}^T \tag{1.128}$$

with

$$\boldsymbol{b}^L = \begin{pmatrix} -\frac{(2\,\ell+1)\,g(a)}{4\,\pi\,a^2} \\ 0 \\ -\frac{(2\,\ell+1)\,G}{a^2} \end{pmatrix} \tag{1.129}$$

$$\boldsymbol{b}^T = \begin{pmatrix} 0 \\ 0 \\ \frac{2\,\ell+1}{a} \end{pmatrix} \tag{1.130}$$

To keep similar expressions for the spheroidal and toroidal components at the Earth's surface, in the following we will denote by $\mathbf{P}_1$ and $\mathbf{P}_2$ the projectors over the second constrained component of the toroidal vector solution, namely the stress, and

respectively over the unconstrained first component of the toroidal vector solution, the displacement, similarly to the spheroidal part.

At the Earth's surface, the toroidal counterpart of Eq. (1.127) must furnish a stress-free boundary condition, which means $\boldsymbol{b} = 0$ where the latter is a one dimensional vector.

1.6.2 Chemical Boundaries

Between two viscoelastic layers, we assume a chemical boundary where the material does not cross the interface. Internal interfaces where the material does cross the interface undergoing a phase change, are named phase-change boundaries. Chemical boundaries are adequate for viscoelastic deformation on timescale comparable or smaller than those of ice ages, hundreds of thousand years, although the lower-upper mantle interface is likely to be partly a chemical and partly a phase-change boundary: this possibility is controversial and we simply ignore it. Phase-change boundaries are certainly appropriate for mantle convection studies when modeling whole mantle circulation. In Chaps. 3 and 7, we will consider the impact of mantle convection on the rotational stability of Earth: in this case, however, we will use a simplified phase-change interface to model the whole mantle circulation, by assuming that the density is constant through the interface, in such a way to mimic the behavior of a more realistic phase-change boundary accross which the material is not subject to any isostatic restoring force when crossing the phase-change interface, since its density changes according to the background value.

At chemical boundaries, there is no cavitation and no slip between two adjacent layers, and the stress components are continuous. By definition, also the potential perturbation is continuous while its radial derivative is discontinuous at density contrast interfaces. This results applying the Gauss theorem at the incremental Poisson equation (1.20) within a volume embedded in an infinitesimal pill-box at an internal interface

$$\partial_r \phi^{\Delta}(r_j^+) - \partial_r \phi^{\Delta}(r_j^-) = -4\,\pi\, G\, \Delta\rho_j\, \boldsymbol{u}(r_j) \cdot \boldsymbol{e}_r \tag{1.131}$$

where $\Delta\rho_j$ is the density contrast between the two layers (that is positive if the inner layer is denser than the outer layer)

$$\Delta\rho_j = \rho_0(r_j^+) - \rho_0(r_j^-) \tag{1.132}$$

Equation (1.131) shows that topography perturbations of the internal interfaces affect the local incremental potential in terms of the surface density given by product of the radial displacement and the density contrast. This product describes the local incremental density localized at the internal interfaces. After spherical harmonic expansion, Eq. (1.131) can thus be arranged in the continuity condition for the potential stress

$$Q_{\ell m}(r_j^+) = Q_{\ell m}(r_j^-) \tag{1.133}$$

In the light of the above remarks, all the components of the spheroidal and toroidal vector solutions are continuous at chemical boundaries

$$\boldsymbol{y}_{\ell m}(r_j^+) = \boldsymbol{y}_{\ell m}(r_j^-) \tag{1.134}$$

1.6.3 Core-Mantle Boundary

The conditions at the core-mantle boundary (CMB) have been disputed among geophysicists since the work of Longman (1962, 1963). This controversy focuses on the treatment of the continuity conditions for the radial deformation at the CMB for the case in which the fluid core deviates from the neutral state of equilibirum, i.e., when the core stratification is non-adiabatic and chemically heterogeneous. Indeed, as we are going to show, for such stratifications the solution of the momentum and Poisson equations leads to the conclusion that radial and geoid displacements coincide. This also implies that no isostatic compensation of the mantle bumping into the core would be possible and this is not the case of reality. This problem was named the Longman (1962) paradox. Differently, the Longman (1962) paradox does not subsist if the core is in a neutral state of equilibrium, and the CMB conditions are derived in a straightforward way.

According to Sect. 1.2.2, in order to discriminate between the neutral state of equilibrium from departures due to non-adiabatic and chemically heterogeneous stratifications, we consider the generalized Williamson-Adams equation (1.42): the neutral state of equilibrium (or compressional stratification) is characterized by a zero compositional coefficient ($\gamma = 0$), while non-adiabatic and chemically heterogeneous stratifications by a non-zero compositional coefficient ($\gamma \neq 0$).

We deal with the fluid core as an inviscid body, in which there is no deviatoric stress. Only the ℓ dependence must be considered, in absence of m dependent forcing. The material incremental stress is given by the material incremental hydrostatic stress

$$\boldsymbol{\sigma}^{\delta}(\boldsymbol{x}, t) = -p^{\delta}\,\mathbf{1} = \kappa\,\Delta\,\mathbf{1} \tag{1.135}$$

and the radial and tangential stresses become

$$R_\ell = \kappa\,\chi_\ell \tag{1.136}$$

$$S_\ell = 0 \tag{1.137}$$

The CMB is a chemical boundary through which the material does not cross. Differently from solid–solid interfaces, for which all the components of the spheroidal vector solution must be continuous at the interface, the CMB is a free–slip boundary where the solid mantle can slip over the inviscid core without tangential stresses, Eq. (1.137). We thus write the spheroidal vector solution at the bottom of the solid mantle as

$$\boldsymbol{y}(r_C^+) = \begin{pmatrix} U_\ell(r_C^-) \\ 0 \\ R_\ell(r_C^-) \\ 0 \\ \Phi_\ell(r_C^-) \\ Q_\ell(r_C^-) \end{pmatrix} + C_2 \begin{pmatrix} 0 \\ 1 \\ 0 \\ 0 \\ 0 \\ 0 \end{pmatrix} \tag{1.138}$$

where the tangential stress is set to zero and we consider the tangential displacement as a constant of integration denoted by C_2.

The inviscid core can be dealt with either as an elastic body with the shear modulus μ set to zero (Longman 1963) or as a viscoelastic body in the Laplace domain, with the Laplace variable s set to zero (Wu and Peltier 1982), since $\hat{\mu}(0) = 0$ from Eq. (1.54). We thus obtain the radial and tangential components of the momentum equation for the inviscid body from Eqs. (1.84) to (1.85) setting $\mu = 0$

$$\frac{\partial_r R_\ell}{\rho_0} - \partial_r (g\, U_\ell) + g\, \chi_\ell - \partial_r \Phi_\ell = 0 \tag{1.139}$$

$$\frac{R_\ell}{\rho_0} - g\, U_\ell - \Phi_\ell = 0 \tag{1.140}$$

where we have assumed that the bulk modulus κ does not depend on the radius r. We omit the terms related to the forcing because they do not contribute within the core.

Following the treatment of Longman (1962), we subtract the radial derivative of the second equation from the first equation

$$\frac{\kappa}{\rho_0^2} \left(\partial_r \rho_0 + \frac{\rho_0^2\, g}{\kappa} \right) \chi_\ell = 0 \tag{1.141}$$

The quantity within the bracket in the LHS depends only on the material parameter of the Earth's model and, after comparison with Eq. (1.42), corresponds to the compositional coefficient γ. Furthermore, by making use of Eqs. (1.140)–(1.141) for eliminating the radial displacement and volume changes into the Poisson equation (1.87), the latter becomes a second order differential equation in the only potential $\Phi_{\ell m}$

$$\nabla_r^2 \Phi_\ell = 4\,\pi\, G\, \partial_r \rho_0\, \frac{\Phi_\ell}{g} \tag{1.142}$$

In the limit $r \to 0$ the solution of the above differential equation $\psi_\ell(r)$ satisfies

$$\lim_{r \to 0} r^{-\ell}\, \psi_\ell(r) = 1 \tag{1.143}$$

since around the Earth's centre within a small volume $\partial_r \rho_0 = 0$ holds, so that the solution $\psi_\ell(r)$ satisfies the Laplace equation, must be regular at the $r = 0$, and is thus proportional to r^ℓ.

When the density in the core is not constant, Eq. (1.142) must be solved numerically and depends on the harmonic degree ℓ and on the density ρ_0 via the ratio between the initial density gradient and gravity, $\partial_r \rho_0 / g$. By denoting the regular solution as ψ_ℓ such that it satisfies the limit given by Eq. (1.143) we write the potential Φ_ℓ as

$$\Phi_\ell(r) = C_1 \, \psi_\ell(r) \tag{1.144}$$

where C_1 is a constant of integration. If $\partial_r \rho_0 = 0$, we simply have $\Phi_\ell(r) = C_1 r^\ell$.

Solutions of the radial and tangential components of the momentum equation, Eqs. (1.139)–(1.140), are perturbed states of hydrostatic equilibrium, where perturbed equipotential, isobaric and equal density surfaces coincide (Chinnery 1975). For compressional stratification, Eq. (1.141) is identically satisfied for any volume change χ_ℓ because the compositional coefficient is zero, $\gamma = 0$. This means that Eqs. (1.139)–(1.140) are not linearly independent. We thus restrict our attention only on the tangential component, Eq. (1.140), from which we constrain the radial stress (or the volume change from Eq. (1.136)) in terms of the gap between radial displacements and geoid perturbations

$$R_\ell = \rho_0 \, g \left[U_\ell - \left(- \frac{\Phi_\ell}{g} \right) \right] = \rho_0 \, g \, C_3 \tag{1.145}$$

that we consider as a constant of integration, C_3, which is equivalent to assume that the pressure is constant within the core in the state of hydrostatic equilibrium. This allows us to obtain the radial displacement and the potential stress in terms of the constants of integration C_1 and C_3

$$U_\ell = -C_1 \, \frac{\psi_\ell}{g} + C_3 \tag{1.146}$$

$$Q_\ell = C_1 \, q_\ell + 4 \pi \, G \, \rho_0 \, C_3 \tag{1.147}$$

where q_ℓ is defined by

$$q_\ell = \partial_r \psi_\ell + \frac{\ell + 1}{r} \, \psi_\ell - \frac{4 \pi \, G \, \rho_0}{g} \, \psi_\ell \tag{1.148}$$

By making use of Eqs. (1.144)–(1.147) into the CMB conditions, Eq. (1.138), we thus express the spheroidal vector solution at the bottom of the solid mantle as

$$\boldsymbol{y}_\ell(r_C^+) = \mathbf{I}_C \, \mathbf{C} \tag{1.149}$$

where $\mathbf{I}_C$ is the core-mantle boundary (CMB) matrix

$$\mathbf{I}_C = \begin{pmatrix} -\psi_\ell(r_C)/g(r_C) & 0 & 1 \\ 0 & 1 & 0 \\ 0 & 0 & g(r_C)\,\rho_0(r_C^-) \\ 0 & 0 & 0 \\ \psi_\ell(r_C) & 0 & 0 \\ q_\ell(r_C) & 0 & 4\pi\, G\, \rho_0(r_C^-) \end{pmatrix} \tag{1.150}$$

and $\mathbf{C}$ is the vector of constants of integration

$$\mathbf{C} = (C_1, C_2, C_3) \tag{1.151}$$

As we will see in Sect. 1.7, these constants of integration must be determined using the boundary condition at the Earth's surface for the stress components of the spheroidal vector solution. Once obtained, the perturbed state of the solid mantle is completely determined. Differently, the perturbed state of the core is determined only for some aspects. Indeed, the constants of integrations only determine the potential within the core, the radial displacement and the radial stress at the CMB. Other information about the core, instead, remain undetermined within the present assumptions. Particularly, below the CMB, we do not know volume changes, displacements and radial stresses.

For compositional stratifications ($\gamma \neq 0$) the above boundary conditions must be reconsidered. In this case, Eq. (1.141) constrains volume variation χ_ℓ to be zero

$$\chi_\ell = 0 \tag{1.152}$$

From Eq. (1.136), this also constrain the radial stress to zero and, from Eq. (1.140), radial displacements and geoid perturbations must coincide

$$U_\ell = -\frac{\Phi_\ell}{g} \tag{1.153}$$

This condition means that all particles located at a given equipotential surface at the initial state of hydrostatic equilibrium (which defines a material interface) must be displaced over the same perturbed equipotential surface (Chinnery 1975). This constrains to zero the constant of integration C_3 entering the radial stress, Eq. (1.145), and one should conclude that isostatic compensation at the CMB is thus impossible for an inviscid core with compositional stratification. This problem was named Longman (1962) paradox and debated in the seventies by many authors, among which Smylie and Mansinha (1971), Pekeris and Accad (1972) and Chinnery (1975).

By considering perturbations of the inviscid core in the frequency ω-domain, Pekeris and Accad (1972) obtained the static solution as the limit case of the dynamic problem for $\omega \to 0$. They pointed out that static volume variations are indeed zero for compositional stratifications, with the exception of an infinitesimally thin layer

just below the CMB where volume variations may occur. Thus, Eq. (1.153) does not hold in this thin boundary layer and isostatic compensation of the above solid mantle is obtained by a non-zero gap between radial displacements and geoid perturbations. In light of this, CMB conditions for compressional and compositional stratifications are formally equivalent, although isostatic compensation is achieved in very different ways: for compressional stratifications, perturbations involve the whole core, while, for compositional stratifications, they are confined in a thin boundary layer just below the CMB.

Smylie and Mansinha (1971) and Chinnery (1975) obtained CMB conditions for compositional stratifications by assuming that radial displacement can be discontinuous at the CMB. This discontinuity, howevfer, should not be intended literally. Indeed, in view of Eq. (1.153), these authors considered geoid perturbations within the inviscid core as radial displacements and, thus, the discontinuity actually corresponds to a non-zero gap between radial displacement and geoid perturbations, in agreement with the finding of Pekeris and Accad (1972). In this respect, we also note that the arguments of Denis (1989) (see their Sect. 5.3) against CMB conditions of Smylie and Mansinha (1971) and Chinnery (1975) were incorrect. Particularly, we refer to when Denis (1989) writes that the analogy of the mantle bumping into the core like a boat on a lake is misleading since (i) the boat problem is a local problem, while the static-core problem is a global one, and (ii) water level around the boat can rise by a finite amount, while the fluid core cannot since it is closed by an elastic or viscoelastic membrane, the above solid mantle. Indeed, it is not physically sound thinking that the boat problem cannot be solved as a global problem, where forces acting on and within the lake are also balanced, and for the simple geometrical reason that Longman (1962) paradox concerns only perturbations of harmonic degrees greater than 0, which do not affect the total volume of the core.

For toroidal perturbations the toroidal stress component T_ℓ is zero at the CMB, as the core is assumed to be inviscid, while the toroidal displacement is unconstrained

$$W_\ell(r_C) = C \tag{1.154}$$

with C as an integration constant. We thus write the CMB conditions for the toroidal solution vector as in Eq. (1.149), with the exception that $\boldsymbol{C}_c = C$ and that $\mathbf{I}_C$ is defined by

$$\mathbf{I}_C = \begin{pmatrix} 1 \\ 0 \end{pmatrix} \tag{1.155}$$

In view of this we thus have

$$\boldsymbol{y}_\ell(r_C^+) = \mathbf{I}_C \, \boldsymbol{C}_c \tag{1.156}$$

which is formally identical to Eq. (1.149).

1.7 Elastic and Viscoelastic Solutions

The general solution of the differential system (1.94) or (1.102) reads

$$\mathbf{y}_{\ell m}(r) = \mathbf{\Pi}_\ell(r, r_0)\mathbf{y}_0 - \int_{r_0}^{r} \mathbf{\Pi}_\ell(r, r')\, \boldsymbol{f}_{\ell m}(r')\, dr' \tag{1.157}$$

where $\mathbf{y}_0$ is the Cauchy datum at the radius r_0

$$\mathbf{y}_{\ell m}(r_0) = \mathbf{y}_0 \tag{1.158}$$

and $\mathbf{\Pi}_\ell$ is the so called propagator matrix. The latter is the 6×6-matrix for the spheroidal case and the 2×2-matrix for the toroidal case that solve the following homogeneous differential system

$$\frac{d\mathbf{\Pi}_\ell(r, r')}{dr} = \mathbf{A}_\ell(r)\, \mathbf{\Pi}_\ell(r, r') \tag{1.159}$$

with the Cauchy datum at the radius r' given by the identity matrix $\mathbf{1}$

$$\mathbf{\Pi}_\ell(r', r') = \mathbf{1} \tag{1.160}$$

For the toroidal case, the forcing term is limited to the seismic sources. In this respect, each column of the propagator matrix is one of the six linearly independent solution of the homogeneous differential system

$$\frac{d\mathbf{y}_{\ell m}}{dr} = \mathbf{A}_\ell\, \mathbf{y}_{\ell m} \tag{1.161}$$

When the integration of Eq. (1.159) in a viscoelastic layer of the Earth's model arrives at an internal chemical boundary, we impose the continuity of the propagator and we continue the integration in the new layer according to Eq. (1.134)

$$\mathbf{\Pi}_\ell(r_j^+, r') = \mathbf{\Pi}_\ell(r_j^-, r') \tag{1.162}$$

In this way the spheroidal and toroidal vector solutions $\boldsymbol{y}_{\ell m}$, Eq. (1.157), satisfy the conditions for the chemical boundaries between the viscoelastic layers of the Earth's model.

We impose CMB conditions in the general solution (1.157) by choosing the bottom of the mantle as the radius from which the integration starts, $r_0 = r_C^+$, and equating the Cauchy datum $\mathbf{y}_0$ to the RHS of Eq. (1.149) or (1.156)

$$\mathbf{y}_{\ell m}(r_C^+) = \mathbf{y}_0 = \mathbf{I}_C\, \mathbf{C} \tag{1.163}$$

This yields

$$\mathbf{y}_{\ell m}(r) = \mathbf{\Pi}_\ell(r, r_C^+)\mathbf{I}_C\mathbf{C} - \mathbf{w}(r) \tag{1.164}$$

where, for brevity, we have defined

$$\mathbf{w}(r) = \int_{r_C^+}^{r} \mathbf{\Pi}_\ell(r, r')\, \boldsymbol{f}_{\ell m}(r')\, dr' \tag{1.165}$$

without the explicit dependence on ℓ, m to not overwhelm the following equations.

The three constants of integration $\mathbf{C}$ entering the CMB conditions are estimated by imposing the boundary conditions at the Earth's surface (1.127). From Eq. (1.164) and by recalling that the vector solution in the LHS of Eq. (1.127) refers to the solution just below the Earth's surface, we write

$$\mathbf{P}_1\mathbf{y}_{\ell m}(a^-) = \mathbf{P}_1\left(\mathbf{\Pi}_\ell(a^-, r_C^+)\mathbf{I}_C\mathbf{C} - \mathbf{w}(a^-)\right) = \boldsymbol{b} \tag{1.166}$$

where $\boldsymbol{b}$ is zero for the toroidal part being the Earth's surface stress free.

Note that $\mathbf{w}$ is evaluated at a^-, i.e., the integration from the bottom of the mantle entering Eq. (1.165) ends just below the Earth's surface, a^-. This means that surface loadings do not actually contribute to the integral since their effect is already accounted for by the Earth's surface boundary condition via the $\boldsymbol{b}$ term, Eq. (1.128). In other words, the vector solution always must be intended as evaluated below the Earth's surface a because it refers to perturbations of the Earth, and only the density of internal loads and seismic forces contribute to the vector $\mathbf{w}$. The dishomogeneous term $\boldsymbol{f}_{\ell m}$ does not thus include those terms that are zero within the Earth, i.e., the surface density $\sigma^L_{\ell m}$ and the density of external bodies $\rho^T_{\ell m}$

$$\boldsymbol{f}_{\ell m} = \rho^I_{\ell m}\, \boldsymbol{f}^L + \boldsymbol{m}_{\ell m} \tag{1.167}$$

in agreement with Eq. (1.97) where the superscript I for internal loads is used rather than the more general L; the toroidal case is limited to the solely seismic term denoted by the second term in the RHS.

Then, using Eq. (1.166) for obtaining the constants of integration $\mathbf{C}$

$$\mathbf{C} = (\mathbf{P}_1\, \mathbf{\Pi}_\ell(a, r_C)\, \mathbf{I}_C)^{-1}\ (\mathbf{P}_1\, \mathbf{w}(a) + \boldsymbol{b}) \tag{1.168}$$

where now the minus sign is omitted in a^- and the plus sign is omitted in r_C^+, Eq. (1.164) becomes

$$\mathbf{y}_{\ell m}(r) = \mathbf{\Pi}_\ell(r, r_C)\mathbf{I}_C\ (\mathbf{P}_1\, \mathbf{\Pi}_\ell(a, r_C)\, \mathbf{I}_C)^{-1}\ (\mathbf{P}_1\, \mathbf{w}(a) + \boldsymbol{b}) - \mathbf{w}(r) \tag{1.169}$$

This is the solution of the associated elastic problem that uniquely determines the spheroidal deformations and the perturbations of the potential within the Earth, as well as the radial and tangential spheroidal stresses and the potential stress, in response to internal and surface loading, and tidal, centrifugal and seismic forcings.

1.7.1 Load and Tidal Love Numbers

Within the perspective of applications of the present theory to the modeling of geodetic observations, we consider the solution, denoted by $\mathbf{K}$, for the radial and tangential spheroidal displacements and local incremental potential at the Earth's surface

$$\mathbf{K}_{\ell m}(a) = \begin{pmatrix} U_{\ell m}(a) \\ V_{\ell m}(a) \\ \Phi_{\ell m}(a) \end{pmatrix} \tag{1.170}$$

From Eq. (1.169) we obtain

$$\mathbf{K}_{\ell m}(a) = \mathbf{P}_2\, \mathbf{y}_{\ell m}(a) = \mathbf{B}_\ell(a)\ (\mathbf{P}_1\, \mathbf{w}(a) + \boldsymbol{b}) - \mathbf{P}_2\, \mathbf{w}(a) \tag{1.171}$$

where $\mathbf{P}_2$ is the projector for the first, second and fifth components of the spheroidal vector solution and, for brevity, we have defined

$$\mathbf{B}_\ell(r) = \mathbf{P}_2 \boldsymbol{\Pi}_\ell(r, r_C) \mathbf{I}_C\ (\mathbf{P}_1\, \boldsymbol{\Pi}_\ell(a, r_C)\, \mathbf{I}_C)^{-1} \tag{1.172}$$

Seismic forces need a specific treatment of the non-conservative force $\mathbf{M}$ entering the dishomogeneous term $\boldsymbol{f}_{\ell m}$, Eq. (1.97), via the vector $\boldsymbol{m}_{\ell m}$. We first deal only with loadings and external potentials and we set the seismic forcing to zero in the non homogeneous term $\boldsymbol{f}_{\ell m}$, postponing to Sect. 1.10.2 the discussion on fault discontinuities.

We then introduce the so called Love numbers $\boldsymbol{k}$. They are non-dimensional Green functions that linearly relate the perturbations $\mathbf{K}$ to internal and surface loads, and tidal and centrifugal potentials

$$\mathbf{K}_{\ell m}(a) = \mathbf{N}_L \int_{r_C}^{a} \boldsymbol{k}_\ell^L(r)\ \left(\delta(r-a)\, \sigma_{\ell m}^L + \rho_{\ell m}^I(r)\right) dr$$

$$+ \mathbf{N}_T\, \boldsymbol{k}^T\ \left(\Phi_{\ell m}^T(a) + \Phi_{\ell m}^C(a)\right) \tag{1.173}$$

where the surface density contribution entering the $\mathbf{b}$ vector as in Eq. (1.128) has been included in the integrand and $\mathbf{N}_L$ and $\mathbf{N}_T$ are the dimensional diagonal matrices

$$\mathbf{N}_L = \frac{G}{a}\, \mathrm{Diag}[1/g(a),\ 1/g(a),\ 1] \tag{1.174}$$

$$\mathbf{N}_T = \mathrm{Diag}[1/g(a),\ 1/g(a),\ 1] \tag{1.175}$$

where $\boldsymbol{k}^L$ and $\boldsymbol{k}^T$ are load and tidal Love numbers, respectively, that we obtain from comparison among Eqs. (1.97), (1.128), (1.165), (1.171) and (1.173), remembering that $\mathbf{w} = 0$ for tidal and centrifugal loadings.

$$\boldsymbol{k}_\ell^L(r) = \mathbf{N}_L^{-1}\ (\mathbf{B}_\ell(a)\,\mathbf{P}_1 - \mathbf{P}_2)\,\boldsymbol{\Pi}_\ell(a,r)\,\boldsymbol{f}_\ell^L(r) \tag{1.176}$$

$$\boldsymbol{k}_\ell^L(a) = \mathbf{N}_L^{-1}\,\mathbf{B}_\ell(a)\,\boldsymbol{b}^L \tag{1.177}$$

$$\boldsymbol{k}_\ell^T = \mathbf{N}_T^{-1}\,\mathbf{B}_\ell(a)\,\boldsymbol{b}^T \tag{1.178}$$

It is noteworthy that Eq. (1.177) can be also obtained from Eq. (1.176) for $r = a$. We note here that the Love number is function of the material stratification of the Earth's models and the harmonic degree ℓ via the propagator matrix $\boldsymbol{\Pi}_\ell$, but not on the order m. Note also that perturbations due to tidal and centrifugal forces share the same Green function, the tidal Love number $\boldsymbol{k}_\ell^T(a)$, and that the load Love number $\boldsymbol{k}_\ell^L(r)$ depends on the radial distance from the Earth's centre r where the load is sitting.

1.7.2 Application of the Correspondence Principle

The components of the load and tidal Love numbers consist of the so called radial, tangential and gravitational Love numbers, that we denote by h_ℓ, l_ℓ and k_ℓ, respectively. They are defined by

$$\boldsymbol{k}_\ell^L(r) = \begin{pmatrix} h_\ell^L(r) \\ l_\ell^L(r) \\ -(r/a)^\ell - k_\ell^L(r) \end{pmatrix} \tag{1.179}$$

$$\boldsymbol{k}_\ell^L(a) = \begin{pmatrix} h_\ell^L(a) \\ l_\ell^L(a) \\ 1 + k_\ell^L(a) \end{pmatrix} \tag{1.180}$$

Due to the term $(r/a)^\ell$ and the unit in the third components, the gravitational Love numbers $k_\ell^L(r)$ and $k_\ell^L(a)$ describe only the gravitational potential that is due to density perturbations of the Earth, without including the direct contributions from load densities and external potentials.

Equation (1.173) can be seen as the solution of the static elastic problem or the associated elastic solution, i.e., the solution of the viscoelastic problem in the Laplace domain accordingly to the Correspondence Principle. In the first case, the fields are in the time domain and the propagator matrix depends on the shear modulus μ. Then Eq. (1.173) can readily be used for modeling elastic perturbations at the Earth's surface, for which the Love number $\boldsymbol{k}_\ell$ is named elastic $\boldsymbol{k}_E$, denoted by the subscript E, now on omitting the ℓ, m in $\mathbf{K}$ and ℓ in $\boldsymbol{k}$ to not overwhelm the writing of the Love numbers, since we want to emphasize their elastic component and the residues corresponding to the s-singularities. In the second case, we must intend formulas as in the Laplace domain, where fields are the Laplace transform of fields and the

propagator matrix $\mathbf{\Pi}_\ell$ depends on the function $\hat{\mu}(s)$ of the Laplace variable s defined by Eq. (1.54), rather than the shear modulus μ. We then define the viscoelastic Love number $\boldsymbol{k}$ in the time domain in terms of its Laplace transform $\tilde{\boldsymbol{k}}(s)$ that we obtain from Eqs. (1.176)–(1.178)

$$\tilde{\boldsymbol{k}}^L(r,s) = \mathcal{L}\left[\boldsymbol{k}^L(r,t)\right] = \mathbf{N}_L^{-1}\ \left(\mathbf{B}_\ell(a)\,\mathbf{P}_1 - \mathbf{P}_2\right)\mathbf{\Pi}_\ell(a,r)\ \boldsymbol{f}^L(r)\big|_{\mu=\hat{\mu}(s)} \tag{1.181}$$

$$\tilde{\boldsymbol{k}}^T(a,s) = \mathcal{L}\left[\boldsymbol{k}^T(t)\right] = \mathbf{N}_T^{-1}\,\mathbf{B}_\ell(a)\,\boldsymbol{b}^T\big|_{\mu=\hat{\mu}(s)} \tag{1.182}$$

where we have indicated the dependence on the Laplace variable s via the function $\hat{\mu}(s)$ that substitutes the shear modulus μ. Note that we do not have given $\tilde{\boldsymbol{k}}^L(a,s)$ as for Eq. (1.177), since it can be obtained from Eq. (1.181) when the r-dependence of $\boldsymbol{f}^L(r)$ is $\delta(r-a)$ for surface density anomalies. $\hat{\mu}(s)$ affects the propagator matrix $\mathbf{\Pi}_\ell$ and also the matrix $\mathbf{B}_\ell$, Eq. (1.172). Note that the limit of Eqs. (1.181)–(1.182) for $|s| \to \infty$ converges to the elastic Love numbers $\boldsymbol{k}_E^L$ and $\boldsymbol{k}_E^T$

$$\lim_{|s|\to\infty} \tilde{\boldsymbol{k}}^L(r,s) = \boldsymbol{k}_E^L(r) \tag{1.183}$$

$$\lim_{|s|\to\infty} \tilde{\boldsymbol{k}}^T(s) = \boldsymbol{k}_E^T \tag{1.184}$$

because the limit of $\hat{\mu}(s)$ for $|s| \to \infty$ converges to the shear modulus μ, Eq. (1.54)

$$\lim_{|s|\to\infty} \tilde{\mu}(s) = \mu \tag{1.185}$$

With these definitions, the associated elastic solution in the Laplace domain becomes

$$\begin{aligned}\tilde{\mathbf{K}}(s) = \mathbf{N}_L \int_{r_C}^{a} \tilde{\boldsymbol{k}}^L(r,s)\ \left(\delta(r-a)\,\tilde{\sigma}_{\ell m}^L(s) + \tilde{\rho}_{\ell m}^I(r,s)\right) dr \\ + \mathbf{N}_T\,\tilde{\boldsymbol{k}}^T(s)\ \left(\tilde{\Phi}_{\ell m}^T(a,s) + \tilde{\Phi}_{\ell m}^C(a,s)\right)\end{aligned} \tag{1.186}$$

and, after inverse Laplace transform of the product of two functions, Eq. (1.46), we obtain the viscoelastic perturbations $\mathbf{K}$ in the time domain as the time convolution of the viscoelastic Love number $\boldsymbol{k}$ and the time histories of the forcing terms

$$\begin{aligned}\mathbf{K}(t) = \mathbf{N}_L \int_{r_C}^{a} \boldsymbol{k}^L(r,t) \star \left(\delta(r-a)\,\sigma_{\ell m}^L(r,t) + \rho_{\ell m}^I(r,t)\right) dr \\ + \mathbf{N}_T\,\boldsymbol{k}^T(t) \star \left(\Phi_{\ell m}^T(a,t) + \Phi_{\ell m}^C(a,t)\right)\end{aligned} \tag{1.187}$$

The viscoelastic Love numbers, with $\boldsymbol{k}$ standing for $\boldsymbol{k}^L$ and $\boldsymbol{k}^T$, must be obtained by inverse Laplace transformation of Eqs. (1.181)–(1.182). The inverse Laplace transform is formally defined by complex integration along the Bromwich path

$$\boldsymbol{k}(t) = \mathcal{L}^{-1}\left[\tilde{\boldsymbol{k}}(s)\right] = \frac{1}{2\,\pi\,i}\int_{c-i\infty}^{c+i\infty} \tilde{\boldsymbol{k}}(s)\,e^{s\,t}\,ds \tag{1.188}$$

The real constant c is chosen such that the singularities of the integrand $\tilde{\boldsymbol{k}}(s)\,e^{s\,t}$ are either all on the left or all on the right side of the vertical line running from $c-i\infty$ to $c+i\infty$. Closing the contour with a half-circle C_R of radius R (either on the left of the line or on the right, depending on where the singularities are situated) leads to the following complex contour integration

$$\boldsymbol{k}(t) = -\frac{1}{2\,\pi\,i}\lim_{R\to\infty}\int_{C_R} \tilde{\boldsymbol{k}}(s)\,e^{s\,t}\,ds + \frac{1}{2\,\pi\,i}\oint_{\Gamma} \tilde{\boldsymbol{k}}(s)\,e^{s\,t}\,ds \tag{1.189}$$

where Γ is an arbitrary closed contour which contains all the singularities. By considering Eqs. (1.183)–(1.184), and that the inverse Laplace transform of the unit 1 yields the Dirac delta $\delta(t)$, it is easy to show that the first term of the RHS of Eq. (1.189) becomes $\boldsymbol{k}_E\,\delta(t)$, so that Eq. (1.189) can be written as follows

$$\boldsymbol{k}(t) = \boldsymbol{k}_E\,\delta(t) + \frac{1}{2\,\pi\,i}\oint_{\Gamma} \tilde{\boldsymbol{k}}(s)\,e^{s\,t}\,ds \tag{1.190}$$

This representation of the viscoelastic Love number separates the instantaneous elastic response of the viscoelastic Earth's model to the imposition of loading and external potentials from the following response due to viscoelastic relaxation of the deviatoric stress. We mantain this distinction by defining the viscous Love number $\boldsymbol{k}_V$

$$\boldsymbol{k}_V(t) = \frac{1}{2\,\pi\,i}\oint_{\Gamma} \tilde{\boldsymbol{k}}(s)\,e^{s\,t}\,ds \tag{1.191}$$

and writing the Love numbers $\boldsymbol{k}$ as

$$\boldsymbol{k}(t) = \boldsymbol{k}_E\,\delta(t) + \boldsymbol{k}_V(t) \tag{1.192}$$

1.8 The Relaxation Spectrum

The singularities of the integrand $\tilde{\boldsymbol{k}}(s)\,e^{s\,t}$ within the complex closed contour Γ arise from different sources. The first source of singularities arises when the differential system (1.159) is non–uniformly Lipschitzian, not satisfying the Lipschitz condition

$|f(r) - f(r')| \leq K\,|r - r'|\,, \forall\,(r, r') \in [r_C, a]$ and K a positive constant, due to the singularities of the propagator matrix $\mathbf{\Pi}_\ell$: inspection of the function $\hat{\mu}(s)$ and of the elements of the matrix $\mathbf{A}_\ell$, defined in Eqs. (1.54) and (1.95), leads to the conclusion that the differential system is not-uniformly Lipschitzian for $s = 0$, $s = -\tau^{-1}$ and $s = -\varsigma^{-1}$, where ς is the so called compressional transient time (Cambiotti et al. 2009; Cambiotti and Sabadini 2010) defined by

$$\varsigma = \tau\left(1 + \frac{4\,\mu}{3\,\kappa}\right) \tag{1.193}$$

which makes singular some elements of the $\mathbf{A}_\ell$ matrix given by Eq. (1.95), being responsible for $\beta = 0$ in Eq. (1.96) once $\hat{\mu}(s)$, Eq. (1.54), is considered.

We denote the set of non–uniformly Lipschitzian zones as $\mathcal{N}$

$$\mathcal{N} = \{0\} \cup \mathcal{N}_\tau \cup \mathcal{N}_\varsigma \tag{1.194}$$

with

$$\mathcal{N}_\tau = \left\{ s \in \mathbb{R} \,\middle|\, s = -\frac{1}{\tau(r)} \quad \forall\, r \in [r_C, a] \right\} \tag{1.195}$$

$$\mathcal{N}_\varsigma = \left\{ s \in \mathbb{R} \,\middle|\, s = -\frac{1}{\varsigma(r)} \quad \forall\, r \in [r_C, a] \right\} \tag{1.196}$$

This singularity at the origin of the Laplace domain occurs because $\hat{\mu}(s = 0) = 0$ and the momentum equation becomes the equation for the inviscid body. This demands a specific treatment, like that discussed in Sect. 1.6.3 for the inviscid core. Cambiotti and Sabadini (2010) show that the origin of the Laplace domain is not a singularity if the stratification of the mantle is compressional ($\gamma = 0$), while it is the cluster point of a infinite denumerable set of roots if the stratification is compositional ($\gamma \neq 0$).

The second source of singularities comes from the determination of the constants of integration $\mathbf{C}$ using the boundary conditions at the Earth's surface, Eq. (1.168). Indeed, the inverse of the 3×3-matrix

$$[\mathbf{P}_1\,\mathbf{\Pi}_\ell(a, r)\,\mathbf{I}_C]_{\mu=\hat{\mu}(s)} \tag{1.197}$$

may be singular for some values of the Laplace variable s. In this respect, we recast the matrix $\mathbf{B}_\ell$ as follows

$$\mathbf{B}_\ell(r)|_{\mu=\hat{\mu}(s)} = \frac{(\mathbf{P}_2\,\mathbf{\Pi}_\ell(r, r_C)\,\mathbf{I}_C)\;(\mathbf{P}_1\,\mathbf{\Pi}_\ell(a, r_C)\,\mathbf{I}_C)^\dagger\big|_{\mu=\hat{\mu}(s)}}{D(s)} \tag{1.198}$$

where $\dagger$ stands for the matrix of complementary minors, and $D(s)$ is the so called secular determinant

$$D(s) = \det\,(\mathbf{P}_1\,\mathbf{\Pi}_\ell(a, r)\,\mathbf{I}_C)|_{\mu=\hat{\mu}(s)} \tag{1.199}$$

The singularities thus occur for the solutions of the so called secular equation

$$D(s) = 0 \tag{1.200}$$

when the secular determinant entering the denominator of Eq. (1.198) is zero. Tanaka et al. (2006) proved that these solutions, satisfying Eq. (1.200), must be on the real axis of the Laplace domain, i.e., $\Im s = 0$. We denote the set of these singularities as $\mathcal{S}$

$$\mathcal{S} = \{s \in \mathbb{R} |\ D(s) = 0\} \tag{1.201}$$

Experience and analytical proofs have lead to the conclusion that the solution of the secular equation (1.200) are finite or, at the most, infinite denumerable (they may have cluster points belonging to the non-uniformly Lipschitzian zone $\mathcal{N}$). Furthermore, they are first-order roots and, in this respect, the Love numbers in the Laplace domain have first-order poles at these roots. This is the simplest type of singularity we deal with by means of the residue theorem derived in Appendix B on analytical functions. Particularly, each root contributes to the complex integration along the closed contour Γ entering Eq. (1.191) for

$$\oint_{\Gamma_j} \boldsymbol{k}(s)\, e^{s\,t} ds = \boldsymbol{k}_j\, e^{s_j\, t} \tag{1.202}$$

where s_j and Γ_j denote the jth first-order pole and the closed path containing only this root, and $\boldsymbol{k}_j$ is the residue

$$\boldsymbol{k}_j = \lim_{s \to s_j} (s - s_j)\boldsymbol{k}(s) \tag{1.203}$$

on the basis of the residue theorem.

This shows that each root s_j is associated with a response of the viscoelastic Earth's model due to the imposition of loading and external potentials. These responses are called normal modes and have characteristic relaxation times t_j given by the inverse of the root s_j. They describe the transition from the elastic to fluid behavior due to viscoelastic relaxation of deviatoric stress. The roots s_j depend generally on the material parameters of all the layers of the viscoelastic Earth's model and on the harmonic degree ℓ (and thus must be determined for each harmonic degree). It turns out that the roots s_j are negative but density inversion at the internal interfaces between the layers of the model, when the density of the layers is lower than that of the neighboring layer above (Plag and Jüttner 1995; Vermeersen and Mitrovica 2000; Cambiotti and Sabadini 2010), and unstable compositional stratifications, for positive compositional coefficients $\gamma > 0$ (see Chap. 2; Cambiotti et al. 2009; Cambiotti and Sabadini 2010), trigger positive normal mode roots s_j. According to Eq. (1.202), these positive roots are responsible for the divergence of the displacements and the potential at large timescales, called Rayleigh-Taylor instabilities. If that is the case, unstable convective motions will be triggered in the Earth's model and the theory as

developed in this book breaks down on timescales comparable with the characteristic relaxation time of Rayleigh-Taylor instabilities, $t_j = -1/s_j$.

For simple layered incompressible models, the total number of normal modes is finite and can be determined by means of the following rules:

- At each boundary between two viscoelastic layers, one buoyancy mode is triggered if the densities on both sides of the boundary are different. Buoyancy modes between two mantle layers are usually labelled Mi, with $i = 1, 2, \ldots$. At the same boundary, two additional relaxation modes are triggered if the Maxwell times of both sides of the boundary are different. These paired modes are called transient viscoelastic modes as they have relatively short relaxation times and therefore usually labelled Ti^+ and Ti^-, with $i = 1, 2, \ldots$.
- If one side of the boundary is elastic and the other is viscoelastic, as the interface between the elastic lithosphere and the viscoelastic mantle, one buoyancy mode and one transient viscoelastic mode are triggered, labelled M0 and L0 in this case, the first due to the density contrast between the atmosphere and the viscoleatic mantle beneath the lithosphere.
- If the lithosphere is viscoelastic or we consider the viscoelastic upper mantle as the outermost layer, the viscoelastic Earth's surface contributes with a buoyancy mode that is also labelled M0, confusingly with one of the two transient viscoelastic modes that are triggered at the interface between the elastic lithosphere and the viscoelastic mantle.
- The core-mantle boundary contributes with one buoyancy mode, labelled C0.

Density contrasts thus provide the most important modal contributions, the buoyancy modes, and the amplitude of the former, and the depth where they are located, determine the characteristic time scale over which the density contrast interface adjusts once displaced by any geophysical forcing. Each mode contrbution, due to density, viscosity, elasticity contrasts, or due to compressional dilatation and contraction, as hereinafter, has its own clear and simple physical explanation.

Compressible layered models and the self-compressed compressible sphere share the same normal modes of layered incompressible models (Sect. 2.3) and additional relaxations modes associated to compressibility (Han and Wahr 1995; Cambiotti et al. 2009; Cambiotti and Sabadini 2010):

- Each viscoelastic compressible layer triggers two modes. These paired modes are called transient compressible modes as they have relatively short relaxation times and usually labelled Zi^+ and Zi^-, with $i = 1, 2, \ldots$. Within the same layer, also an infinite denumerable set of modes is triggered. They are called dilatational modes, labelled D$_j$, with $j = 1, \ldots, \infty$, and their characteristic times converge to the compressional transient time ς in the limit for $j \to \infty$

$$\lim_{j \to \infty} s_{\mathrm{D}_j} = -\varsigma^{-1} \tag{1.204}$$

The normal modes defined above complete those for compressible Earth's models with compressional stratifications ($\gamma = 0$), i.e. when the initial density stratification is

due to the only self-compression of the Earth. Instead, compositional stratifications ($\gamma \neq 0$) trigger another infinite denumerable set of buoyancy modes with very long characteristic times. They are called compositional modes, labelled C_j, with $j = 1, \ldots, \infty$. These modes can be both stable, $s_{\mathrm{C}_j} < 0$, and unstable, $s_{\mathrm{C}_j} > 0$, and their poles s_{C_j} monotonically converge to the origin of the Laplace domain for $j \to \infty$

$$\lim_{j \to \infty} s_{\mathrm{C}_j} = 0 \tag{1.205}$$

The stable case will be carefully discussed in Chap. 2. In the unstable case, instead, the compositional modes describe Rayleigh-Taylor instabilities that occur on timescales of the order of the shortest characteristic time $t_{\mathrm{C}_1} = -1/s_{\mathrm{C}_1}$, with $j = 1$.

The presence of dilatational and compositional modes arises theoretical and computational problems in obtaining all the contributions from normal modes, Eq. (1.202). However, it is sufficient to detect the first few of these modes in order that the Green functions converge to the exact ones. In fact, for $j \to \infty$, the residues $\boldsymbol{k}_{\mathrm{D}_j}$ and $\boldsymbol{k}_{\mathrm{C}_j}$ of dilatational and compositional modes go to zero sufficiently fast so that their summation converges once the first few of them are taken into account (Cambiotti et al. 2009; Cambiotti and Sabadini 2010).

Modal components to the deformation and gravity, resulting from the Correspondece Principle, provide us a clear physics and makes it possible a deep comprehension of the intimate nature of the viscoelastic behaviour of the Earth, which would be impossible to attain for example via standard integration in time.

It is thus possible, with the above rules, to determine the total number of modes of equation (1.200). This is of importance as solving this equation has to be done numerically. However, this root-solving is the only non-analytical part of the viscoelastic relaxation method when incompressible models, as in Chap. 2, Sect. 2.3, are considered.

The root-solving procedure usually consists of two parts: grid-spacing, followed by a bisection algorithm. In the grid-spacing part, the s-domain is split into a number of discrete intervals. For each s-value at a boundary of an interval, the value of the determinant expressed by Eq. (1.200) is calculated, after which this value is multiplied with the value of the determinant of the s-value of the boundary next to it. If this product is positive, then the determinant has not changed in sign (or has changed an even number of times). If the product is negative, then we are sure that there is (at least) one root inside the interval bounded by the two s-values for which the determinant was calculated. In that case, the interval is split up in two parts, and the procedure of determining the product of the determinant of the bounding s-values is repeated. The interval where the determinant changes sign will result again in a negative product, and for this interval the procedure of cutting the interval in two, etc., is repeated. Thus the s-value where the determinant (1.199) is equal to zero becomes progressively better estimated with each further step in this bisection algorithm. Of course, it can happen that the determinant (1.199) changes sign over a small s-interval twice or even more times. It is thus necessary to choose small grids in the s-domain (in practice, it appears that especially the two modes of each

T-mode pair have inverse relaxation times (s-values) that are very close to each other). Only after the complete number (determined with the rules above) of roots/modes of equation (1.200) has been found can one be sure that the complete signal will be retrieved after inverse-Laplace transformation. For this final step in the relaxation modeling procedure we use the so-called method of complex contour integration. Those readers who are not acquainted with this technique will find an overview in Appendix B.

1.8.1 Modal and Non-modal Contributions

The Love number $\tilde{\boldsymbol{k}}(s)$ has thus two different types of not analyticity. The first comes from a denumerable set of poles $s_j \in \mathcal{S}_0$. The second comes from the continuous set $\mathcal{N}$ of the Maxwell and compressional transient times τ and ς. Accordingly to Fang and Hager (1995), we will refer to these contributions as the "modal" and "non-modal" contributions, respectively. The modal contribution can be explicited in the viscoelastic Love number by making use of the residue theorem as in Eq. (1.202)

$$\boldsymbol{k}(t) = \sum_{s_j \in \mathcal{S}_0} \boldsymbol{k}_j \, e^{s_j t} + \frac{1}{2\pi i} \oint_{\Gamma} \boldsymbol{k}_N(s) \, ds + \boldsymbol{k}_E \, \delta(t) \tag{1.206}$$

Here, $\tilde{\boldsymbol{k}}_N(s)$ stands for the non-modal contribution that we cannot further explicit and must be obtained by complex integration along the closed contour Γ.

The non-modal contribution is inherently associated with the continuous variations of the Maxwell and compressional transient times. Indeed, as discussed in Spada et al. (1992a), Han and Wahr (1995), Vermeersen and Sabadini (1997) and Cambiotti et al. (2009), these singularities do not contribute to the perturbations in the time domain if there are only isolated points in the Laplace s-domain. This is the case for layered Earth's models, where the elastic parameter and the viscosity are constant within each layer, because the Maxwell and compressional transient times do not vary within each layer. Equation (1.191) thus becomes

$$\boldsymbol{k}_V(t) = \sum_{s_j \in \mathcal{S}_0} \boldsymbol{k}_j \, e^{s_j t} \tag{1.207}$$

On the contrary, we have verified that a not zero contribution comes from the set $\mathcal{N}$ when it is continuous (Cambiotti and Sabadini 2010; Cambiotti et al. 2010) and we must evaluate the complex contour integration along the contour Γ in Eq. (1.206).

1.9 The Complex Contour Integration

For applications of the present theory for modelling perturbations in the time domain, we do not need to investigate any time the relaxation spectrum. We just need to know where the singularities are located in order to choose the closed contour Γ that contains them, and then perform the complex contour integration in Eq. (1.191). This approach was implemented by Tanaka et al. (2006) for modelling post-seismic perturbations due to the December 2004 Sumatran earthquake. In the following we describe some aspects necessary for obtaining stable numerical codes able to compute the viscoelastic response in a wide range of time scales, from the instantaneous elastic response to the billion year time scales.

Figure 1.3 shows the contour Γ (dashed line) that we use in Eq. (1.191) and the contour of Tanaka et al. (2006) (solid line). The difference consists in the fact that our contour is situated on the half space with positive real part of the Laplace variable s, $\Re s > 0$, only for the semi–circle of radius R

$$R = \max\left\{5\, s_{C1},\, 10^{-5}\,\mathrm{kyr}^{-1}\right\} \tag{1.208}$$

where s_{C1} is the largest positive pole of the first compositional mode due to unstable compositional stratifications. The factor 5 and the lower bound $10^{-5}\,\mathrm{kyr}^{-1}$ in Eq. (1.208) have been chosen in order to avoid numerical instability in the radial Gill-Runge-Kutta integration of the differential system (1.159) near the pole s_{C1} and the origin of the Laplace domain, $s = 0$. This choice reduces the numerical instability in the numerical evaluation of Eq. (1.191) due to the term $e^{\Re s\, t}$, which diverges in the limit $t \to \infty$ if $\Re s > 0$. The pole s_{C1} is obtained by means of a root-finding algorithm, which can be applied safely in the positive half of the real axis because

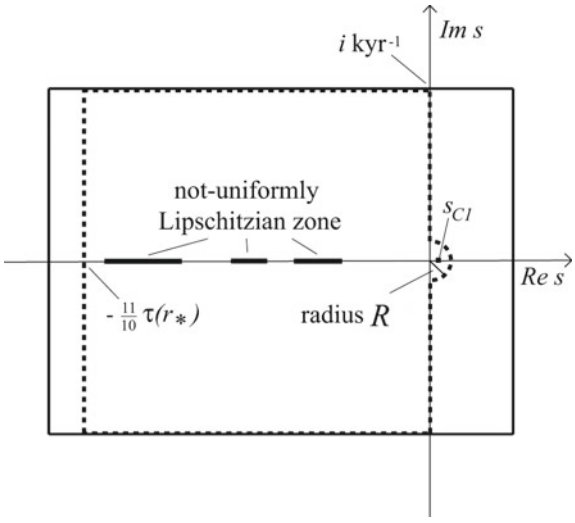

Fig. 1.3 The closed contour Γ and that used in Tanaka et al. (2006) (*dashed* and *solid lines*, respectively)

the non–uniformly Lipschitzian zone $\mathcal{N}$ is situated in the negative half, by definition, Eq. (1.194).

The value Z defining the lowest $\Re s < 0$ of the contour Γ is chosen as

$$Z = -\frac{11}{10}\,\frac{1}{\tau(r_*)} \tag{1.209}$$

where r_* is the radius at which the Maxwell relaxation time τ assumes its smallest value. Singularities can in fact be composed only of isolated poles $s_j \in \mathcal{S}_0$ if $\Re s < -\tau(r_*)$, and our experience has shown that there are no poles such that $s_j < -\tau(r_*)$.

We choose $1\,\mathrm{kyr}^{-1}$ for the greatest and lowest $\Im s$ of the contour Γ. Increasing the time t, numerical instabilities may occur due to the sign oscillations of $e^{i\Im s\,t}$ near the imaginary axis, for small $\Re s$. Indeed, elsewhere the term $e^{\Re s\,t}$ goes rapidly to zero increasing t, since $\Re s < 0$, and this damps the oscillations of $e^{i\,\Im s\,t}$. To avoid the numerical instability near the imaginary axis, particularly for those s with $\Re s \geq 0$, we proceed as follows. We adopt an adaptive Cavalieri-Simpson method to evaluate the contour integral entering Eq. (1.191) and, at each stage, we increase artfully the sampling of the integrand $\tilde{\boldsymbol{k}}(s)$ by using the same second order interpolating polynomial on which the Cavalieri-Simpson method is based. In this way the number of steps at which $\tilde{\boldsymbol{k}}(s)$ is effectively evaluated depends only on the smoothness or stiffness of $\tilde{\boldsymbol{k}}(s)$ along the contour Γ, rather than on the condition $t\,\Im s \ll 2\,\pi$ proposed by Tanaka et al. (2006). The time scale at which the numerical instability due to the oscillation of $e^{i\Im s\,t}$ occurs is increased by about 1–2 orders of magnitude, under the same number of effective evaluations of $\tilde{\boldsymbol{k}}(s)$.

1.10 Point Sources

1.10.1 Point Loads

In order to obtain the Green functions for radial and tangential displacements and gravitational potential perturbations due to loading, we consider a point-like load with mass M_L located at the point $\boldsymbol{r}_L$ along the polar axis. Such a point-like mass has the following density distribution, in terms of the Dirac delta δ

$$\rho^L(\boldsymbol{r}) = M_L\,\delta(\boldsymbol{r} - \boldsymbol{r}_L) \tag{1.210}$$

and it is responsible for the gravitational potential

$$\phi^L(\boldsymbol{r}) = -\frac{G\,M_L}{|\boldsymbol{r} - \boldsymbol{r}_L|} \tag{1.211}$$

Note the negative sign opposite with the definition usually followed in geodesy, as for Eq. (1) in Chao and Gross (1987): our definition is in agreement with

Eq. (1.2) where, in physics, the force is the negative of the gradient of the potential. In the following we shall make use of the expansions in Legendre polynomials of Eqs. (1.210)–(1.211)

$$\rho^L(r,\theta) = \sum_{\ell=0}^{\infty} \rho_\ell^L(r)\, P_\ell(\cos\theta) \tag{1.212}$$

$$\phi^L(r,\theta) = \sum_{\ell=0}^{\infty} \Phi_\ell^L(r)\, P_\ell(\cos\theta) \tag{1.213}$$

where the scalars ρ_ℓ^L and Φ_ℓ^L depend solely on the radial distance r from the Earth's centre and on the harmonic degree ℓ. By considering that the three-dimensional Dirac delta in spherical coordinates is given by

$$\delta(\boldsymbol{r} - \boldsymbol{r}_L) = \frac{\delta(r - r_L)}{r^2}\, \frac{\delta(\theta)\,\delta(\varphi - \varphi_L)}{\sin\theta} \tag{1.214}$$

with $\boldsymbol{r}_L = (r_L, 0, \varphi_L)$, and that

$$\frac{\delta(\theta)\,\delta(\varphi - \varphi_L)}{\sin\theta} = \sum_{\ell=0}^{\infty} \frac{2\,\ell + 1}{4\,\pi}\, P_\ell(\cos\theta) \tag{1.215}$$

we have

$$\rho_\ell^L(r) = M_L\, \delta(r - r_L)\, \frac{2\,\ell + 1}{4\,\pi\, r^2} \tag{1.216}$$

Furthermore, by considering that the inverse of the distance between the observation, $\boldsymbol{r}$, and load, $\boldsymbol{r}_L$, points in spherical coordinates reads

$$\frac{1}{|\boldsymbol{r} - \boldsymbol{r}_L|} = \frac{1}{\sqrt{r^2 + r_L^2 - 2\,r\,r_L\,\cos\theta}} \tag{1.217}$$

and that the generating function of the Legendre polynomials is

$$\frac{1}{\sqrt{1 + x^2 - 2\,x\,\cos\theta}} = \sum_{\ell=0}^{\infty} x^\ell\, P_\ell(\cos\theta) \tag{1.218}$$

with $x \leq 1$, we have

$$\Phi_\ell^L(r) = \begin{cases} -\frac{G\,M_L}{r_L}\left(\frac{r}{r_L}\right)^{\ell} & r \leq r_L \\ -\frac{G\,M_L}{r_L}\left(\frac{r}{r_L}\right)^{-(\ell+1)} & r \geq r_L \end{cases} \tag{1.219}$$

to be compared with Eqs. (1.116)–(1.117).

Exercise 8 Expand a disk load of angular radius α, sitting at the radial distance r_L along the polar axis, in Legendre polynomials. Make use of the Legendre equation, satisfied by the Legendre polynomials, that you can obtain from Eq. (1.70): you will get Eq. (19) of Sabadini et al. (1982).

1.10.2 Fault Discontinuities

Earthquakes yield a discontinuity in the displacement across the fault plane, where the rock fractures. By denoting with $d\boldsymbol{S} = dS\,\boldsymbol{n}$ an infinitesimal surface element of the fault plane of area dS and unit normal vector $\boldsymbol{n}$, we thus impose the following condition for displacements due to earthquakes

$$\delta\boldsymbol{u} = \delta u\,\boldsymbol{v} = \lim_{\epsilon\to 0}\left[\boldsymbol{u}(\boldsymbol{r}_0 + \epsilon\,\boldsymbol{n}) - \boldsymbol{u}(\boldsymbol{r}_0 - \epsilon\,\boldsymbol{n})\right] \tag{1.220}$$

where $\boldsymbol{r}_0$ is the position of the infinitesimal surface element, and $\delta\boldsymbol{u} = \delta u\,\boldsymbol{v}$ is the displacement discontinuity of length δu and direction $\boldsymbol{v}$. Discontinuities which are parallel to the fault plane ($\boldsymbol{v}\cdot\boldsymbol{n} = 0$) are called tangential (or shear) displacement dislocations. Discontinuities which are normal to the fault plane ($\boldsymbol{v}\cdot\boldsymbol{n} = 1$) are called tensile dislocations. Between the two types of dislocations, we will focus only on the former as it is responsible for the main contribution to co- and post-seismic perturbations.

Smylie and Mansinha (1971), Manshina (1979) and Ben-Menahem and Singh (2000) have shown that the effect of dislocations is equivalent to including an extra body force $\mathbf{M}$ in the momentum equation. For shear dislocations, the equivalent body force is the double couple

$$\mathbf{M} = M\ (\boldsymbol{n}\otimes\boldsymbol{v} + \boldsymbol{v}\otimes\boldsymbol{n})\cdot\nabla_0\delta(\boldsymbol{r} - \boldsymbol{r}_0) \tag{1.221}$$

where M is the moment of each couple given by

$$M = \mu(r_0)\,\delta u\,dS \tag{1.222}$$

and the gradient operator ∇_0 operates on the coordinates of the seismic source point $\boldsymbol{r}_0 = (r_0, \theta_0, \varphi_0)$. In order to understand the definition of the equivalent body force $\mathbf{M}$, Eq. (1.221), we rewrite it as the sum of two single couples $\mathbf{M}_{n,v}$ and $\mathbf{M}_{v,n}$

$$\mathbf{M} = \mathbf{M}_{n,v} + \mathbf{M}_{v,n} \tag{1.223}$$

The single couple $\mathbf{M}_{n,v}$ (and similarly $\mathbf{M}_{v,n}$) is given by two opposite point-like forces of magnitude F and direction $\boldsymbol{v}$ located at points $\boldsymbol{r}_0 \pm \epsilon/2\,\boldsymbol{n}$

$$\mathbf{M}_{n,v} = F\,\boldsymbol{v}\,\delta(\boldsymbol{r} - (\boldsymbol{r}_0 + \epsilon/2\,\boldsymbol{n})) - F\,\boldsymbol{v}\,\delta(\boldsymbol{r} - (\boldsymbol{r}_0 - \epsilon/2\,\boldsymbol{n})) \tag{1.224}$$

and, in the limit for F going to infinity and ϵ going to zero, it yields

$$\mathbf{M}_{n,v} = M\, \boldsymbol{n}\, \boldsymbol{v} \cdot \nabla_0 \delta(\boldsymbol{r} - \boldsymbol{r}_0) \tag{1.225}$$

Here, we have assumed that the product between F and ϵ remains finite and it coincides with the seismic moment M given by Eq. (1.222)

$$M = \lim_{F \to \infty, \epsilon \to 0} F\, \epsilon \tag{1.226}$$

In order to obtain the forcing $\boldsymbol{m}_{\ell m}$, Eq. (1.100), entering the differential system (1.94) via the dishomogeneous term $\boldsymbol{f}_{\ell m}$, Eq. (1.97), we must expand in spherical harmonics the expression for the double couple, Eq. (1.221). First we recast Eq. (1.221) as follows

$$\mathbf{M} = M\, \boldsymbol{n} \cdot [\boldsymbol{v} \cdot \nabla_0 \otimes (\delta(\boldsymbol{r} - \boldsymbol{r}_0)\, \mathbf{1})] + M\, \boldsymbol{v} \cdot [\boldsymbol{n} \cdot \nabla_0 \otimes (\delta(\boldsymbol{r} - \boldsymbol{r}_0)\, \mathbf{1})] \tag{1.227}$$

where we have utilized $\nabla_0 \delta(\boldsymbol{r} - \boldsymbol{r}_0) \otimes \mathbf{1} = \nabla_0 \otimes (\delta(\boldsymbol{r} - \boldsymbol{r}_0)\, \mathbf{1})$, based on $\nabla \otimes (u\, \mathbf{1}) = \nabla u \otimes \mathbf{1}$.

The above expression for the double couple is convenient as the spherical harmonic expansion of the three-dimensional Dirac delta $\delta(\boldsymbol{r} - \boldsymbol{r}_0)$ multiplied by the unit diadyc $\mathbf{1}$ yields

$$\delta(\boldsymbol{r} - \boldsymbol{r}_0)\, \mathbf{1} = \frac{\delta(r - r_0)}{r^2} \sum_{\ell=0}^{\infty} \sum_{m=-\ell}^{\ell} \frac{1}{N_{\ell m}} \left[\boldsymbol{R}_{\ell m}(\theta, \varphi)\, \boldsymbol{R}^*_{\ell m} \theta_0, \varphi_0) \right.$$

$$\left. + \boldsymbol{S}_{\ell m}(\theta, \varphi)\, \boldsymbol{S}^*_{\ell m}(\theta_0, \varphi_0) + \boldsymbol{T}_{\ell m}(\theta, \varphi)\, \boldsymbol{T}^*_{\ell m}(\theta_0, \varphi_0) \right] \tag{1.228}$$

according to Eqs. (F.17) and (F.25) of Ben-Menahem and Singh (2000) and the asterisc standing for the complex conjugate.

The Green functions for the displacement and the gravitational potential perturbation due to the seismic forcing are obtained by considering the infinitesimal fault plane $d\boldsymbol{S}$ located along the polar axis, i.e., taking the limit of Eq. (1.227) for the colatitude θ_0 and longitude φ_0 of the seismic source going to zero. In view of this, we shall use the following limits

$$\lim_{\theta_0, \varphi_0 \to 0} \boldsymbol{e}_\theta(\theta_0, \varphi_0) = \boldsymbol{x}_1 \tag{1.229}$$

$$\lim_{\theta_0, \varphi_0 \to 0} \boldsymbol{e}_\varphi(\theta_0, \varphi_0) = \boldsymbol{x}_2 \tag{1.230}$$

$$\lim_{\theta_0, \varphi_0 \to 0} \boldsymbol{e}_r(\theta_0, \varphi_0) = \boldsymbol{x}_3 \tag{1.231}$$

where $\boldsymbol{x}_j$ are the Cartesian unit vectors of the geographical reference ($\boldsymbol{x}_1$ points to the Greenwich meridian while $\boldsymbol{x}_3$ points to the north pole, i.e., coincides with the present-day rotation axis), and

$$\lim_{\theta_0,\varphi_0\to 0} Y^*_{\ell m}(\theta_0,\varphi_0) = \delta_{m0} \tag{1.232}$$

$$\lim_{\theta_0,\varphi_0\to 0} \frac{\partial Y^*_{\ell m}(\theta_0,\varphi_0)}{\partial\theta_0} = \frac{1}{2}\left[\ell(\ell+1)\,\delta_{m1} - \delta_{m(-1)}\right] \tag{1.233}$$

$$\lim_{\theta_0,\varphi_0\to 0} \frac{1}{\sin\theta_0}\frac{\partial Y^*_{\ell m}(\theta_0,\varphi_0)}{\partial\varphi_0} = \frac{i}{2}\left[\ell(\ell+1)\,\delta_{m1} + \delta_{m(-1)}\right] \tag{1.234}$$

$$\lim_{\theta_0,\varphi_0\to 0} \frac{\partial}{\partial\theta_0}\left(\frac{\partial Y^*_{\ell m}(\theta_0,\varphi_0)}{\partial\varphi_0}\right) = -\frac{i}{4}\left[\frac{(\ell+2)!}{(\ell-2)!}\,\delta_{m2} - \delta_{m(-2)}\right] \tag{1.235}$$

Then, by making use of Eq. (1.228) into Eq. (1.227) and by considering the limit of the latter for θ_0 and φ_0 going to zero in order to locate the double couple along the polar axis, we obtain

$$\mathbf{M} = M\sum_{\ell=0}^{\infty}\sum_{m=-\ell}^{\ell}\left[m^R_{\ell m}(r)\,\boldsymbol{R}_{\ell m}(\theta,\varphi) + m^S_{\ell m}(r)\,\boldsymbol{S}_{\ell m}(\theta,\varphi) + m^T_{\ell m}(r)\,\boldsymbol{T}_{\ell m}(\theta,\varphi)\right] \tag{1.236}$$

where

$$m^R_{\ell m}(r) = \frac{1}{N_{\ell m}}\lim_{\theta_0,\varphi_0\to 0}\left\{\boldsymbol{n}\cdot\left[\boldsymbol{v}\cdot\nabla_0\left(\frac{\delta(r-r_0)}{r^2}\,\boldsymbol{R}^*_{\ell m}(\theta_0,\varphi_0)\right)\right]\right.$$
$$\left.+\boldsymbol{v}\cdot\left[\boldsymbol{n}\cdot\nabla_0\left(\frac{\delta(r-r_0)}{r^2}\,\boldsymbol{R}^*_{\ell m}(\theta_0,\varphi_0)\right)\right]\right\} \tag{1.237}$$

$$m^S_{\ell m}(r) = \frac{1}{\ell(\ell+1)\,N_{\ell m}}\lim_{\theta_0,\varphi_0\to 0}\left\{\boldsymbol{n}\cdot\left[\boldsymbol{v}\cdot\nabla_0\left(\frac{\delta(r-r_0)}{r^2}\,\boldsymbol{S}^*_{\ell m}(\theta_0,\varphi_0)\right)\right]\right.$$
$$\left.+\boldsymbol{v}\cdot\left[\boldsymbol{n}\cdot\nabla_0\left(\frac{\delta(r-r_0)}{r^2}\,\boldsymbol{S}^*_{\ell m}(\theta_0,\varphi_0)\right)\right]\right\} \tag{1.238}$$

$$m^T_{\ell m}(r) = \frac{1}{\ell(\ell+1)\,N_{\ell m}}\lim_{\theta_0,\varphi_0\to 0}\left\{\boldsymbol{n}\cdot\left[\boldsymbol{v}\cdot\nabla_0\left(\frac{\delta(r-r_0)}{r^2}\,\boldsymbol{T}^*_{\ell m}(\theta_0,\varphi_0)\right)\right]\right.$$
$$\left.+\boldsymbol{v}\cdot\left[\boldsymbol{n}\cdot\nabla_0\left(\frac{\delta(r-r_0)}{r^2}\,\boldsymbol{T}^*_{\ell m}(\theta_0,\varphi_0)\right)\right]\right\} \tag{1.239}$$

In the following we will do not discuss further the toroidal component of the seismic force, since our book is particularly devoted to the latest developments of gravity measurements from space in terms of the gravity signature, depending solely on the spheroidal part, from giant earthquakes at subduction zones.

By writing the unit direction $\boldsymbol{v}$ of the slip and the unit normal $\boldsymbol{n}$ to the infinitesimal fault plane in terms of dip, α, and slip, γ, angles

$$\boldsymbol{v} = \cos\gamma\, \boldsymbol{x}_1 + \sin\gamma\, \cos\alpha\, \boldsymbol{x}_2 + \sin\gamma\, \sin\delta\, \boldsymbol{x}_3 \tag{1.240}$$

$$\boldsymbol{n} = -\sin\alpha\, \boldsymbol{x}_2 + \cos\alpha\, \boldsymbol{x}_3 \tag{1.241}$$

after some straightforward algebra, Eqs. (1.237)–(1.238) can be cast as follows

$$m^{X}_{\ell m}(r) = \frac{\delta(r-r_0)}{r^2\, r_0}\, m^{(0)X}_{\ell m}(r) + \frac{\partial}{\partial r}\left(\frac{\delta(r-r_0)}{r^2}\right) m^{(1)X}_{\ell m}(r) \tag{1.242}$$

where X denotes the spheroidal radial, $X = R$, and tangential, $X = S$, components of the seismic force, and $m^{(x)X}_{\ell m}$, for $x = 0, 1$ and $X = R, S$, is given by

$$m^{(0)R}_{\ell 0} = -\frac{2\,\ell+1}{4\,\pi}\, \sin 2\delta\, \sin\gamma \tag{1.243}$$

$$m^{(0)R}_{\ell 1} = \frac{2\,\ell+1}{8\,\pi}\, (\cos\delta\, \cos\gamma - i\, \cos 2\alpha\, \sin\gamma) \tag{1.244}$$

$$m^{(0)R}_{\ell 2} = 0 \tag{1.245}$$

$$m^{(1)R}_{\ell 0} = -\frac{2\,\ell+1}{4\,\pi}\, \sin 2\alpha\, \cos\gamma \tag{1.246}$$

$$m^{(1)R}_{\ell 1} = 0 \tag{1.247}$$

$$m^{(1)R}_{\ell 2} = 0 \tag{1.248}$$

$$m^{(0)S}_{\ell 0} = \frac{2\,\ell+1}{8\,\pi}\, \sin 2\delta\, \sin\gamma \tag{1.249}$$

$$m^{(0)S}_{\ell 1} = \frac{2\,\ell+1}{8\,\pi\,\ell\,(\ell+1)}\, (-\cos\delta\, \cos\gamma + i\, \cos 2\delta\, \sin\gamma) \tag{1.250}$$

$$m^{(0)S}_{\ell 2} = \frac{2\,\ell+1}{16\,\pi\,\ell\,(\ell+1)}\, (2\,i\, \sin\delta\, \cos\gamma + \sin 2\delta\, \sin\gamma) \tag{1.251}$$

$$m^{(1)S}_{\ell 0} = 0 \tag{1.252}$$

$$m_{\ell 1}^{(1)S} = \frac{2\,\ell + 1}{8\,\pi\,\ell\,(\ell + 1)}\,(-\cos\delta\,\cos\gamma + i\,\cos 2\delta\,\sin\gamma) \tag{1.253}$$

$$m_{\ell 2}^{(1)S} = 0 \tag{1.254}$$

with i being the imaginary unit. The scalars $m_{\ell m}^{(0)X}$ and $m_{\ell m}^{(1)X}$ of order $|m| > 2$ are zero and their expression for $m = -1, -2$ are obtained by the above expressions by considering that

$$m_{\ell -m}^{X} = (-1)^m\,\frac{(\ell - m)!}{(\ell + m)!}\,\bar{m}_{\ell m}^{X} \tag{1.255}$$

In view of these results, the vector $\boldsymbol{m}_{\ell m}$, Eq. (1.100), which describes the seismic force and enters the differential system (1.94) via the dishomogeneous term $\boldsymbol{f}_{\ell m}$, Eq. (1.97), takes the following form

$$\boldsymbol{m}_{\ell m}(r) = \frac{M}{r^2}\left(\frac{\delta(r - r_0)}{r_0}\,\boldsymbol{m}_{\ell m}^{(0)} + \frac{\partial\delta(r - r_0)}{\partial r}\,\boldsymbol{m}_{\ell m}^{(1)}\right) \tag{1.256}$$

where the vectors $\boldsymbol{m}_{\ell m}^{(x)}$, for $x = 0, 1$, are given by

$$\boldsymbol{m}_{\ell m}^{(x)} = \left(0, 0, m_{\ell m}^{(x)R}, m_{\ell m}^{(x)S}, 0, 0\right)^T \tag{1.257}$$

The differential system (1.94) for the seismic problem thus becomes

$$\frac{d\mathbf{y}_{\ell m}}{dr} = \mathbf{A}_{\ell m}\,\mathbf{y}_{\ell m} - \frac{M}{r^2}\left(\frac{\delta(r - r_0)}{r_0}\,\boldsymbol{m}_{\ell m}^{(0)} + \frac{\partial\delta(r - r_0)}{\partial r}\,\boldsymbol{m}_{\ell m}^{(1)}\right) \tag{1.258}$$

that is solved by

$$\boldsymbol{y}_{\ell m}(r) = \boldsymbol{\Pi}_\ell(r, r_C)\,\mathbf{I}_C\,\mathbf{C} - \mathbf{w}(r) \tag{1.259}$$

Here, $\mathbf{w}$ is defined by Eq. (1.165) and, for the seismic force, yields

$$\mathbf{w}(r) = \frac{M}{r_0^2}\,H(r - r_0)\,\boldsymbol{\Pi}_\ell(r, r_0)\left[\frac{\boldsymbol{m}_{\ell m}^{(0)}}{r_0} + \frac{2\,\boldsymbol{m}_{\ell m}^{(1)}}{r_0} + \boldsymbol{A}_\ell(r_0)\,\boldsymbol{m}_{\ell m}^{(1)}\right] \tag{1.260}$$

It is important to note the second term within the brackets of the RHS of Eq. (1.260). This term results from the fact that the expression for $\boldsymbol{m}_{\ell m}$ obtained above, Eq. (1.256), which is similar to that obtained by Smylie and Mansinha (1971) and Manshina (1979) (but for some convention about spherical harmonics), also depends on the radial variable r rather than on the only radius of the seismic source r_0. If this dependence is omitted, the theory for the seismic source of Smylie and Mansinha (1971) and Manshina (1979) yields

$$\mathbf{w}_{\ell m}(r) = \frac{M}{r_0^2}\, H(r - r_0)\, \mathbf{\Pi}_\ell(r, r_0) \left[\frac{\boldsymbol{m}_{\ell m}^{(0)}}{r_0} + \mathbf{A}_\ell(r_0)\, \boldsymbol{m}_{\ell m}^{(1)} \right] \tag{1.261}$$

and it would differ from that discussed in Takeuchi and Saito (1972). References to Smylie and Mansinha (1971) and Manshina (1979) should not neglect this subtle dependence and use Eq. (1.260) rather than Eq. (1.261).

Both spheroidal radial, $R_{\ell m}$, and tangential, $S_{\ell m}$, components of stress must be zero at the Earth's surface, as well as the potential stress $Q_{\ell m}$. Then, the Earth's surface boundary conditions are those for a free surface

$$\mathbf{P}_1\, \boldsymbol{y}_{\ell m}(a) = \mathbf{0} \tag{1.262}$$

After elimination of the constants of integration $\mathbf{C}$ imposing the free Earth's surface boundary conditions (1.262) from Eq. (1.259), the solution $\mathbf{K}$ for the radial and tangential spheroidal displacements and local incremental potential at the Earth's surface becomes

$$\boldsymbol{K} = (\mathbf{B}_\ell\, \mathbf{P}_1 - \mathbf{P}_2)\ \mathbf{w}(a) \tag{1.263}$$

according to Eq. (1.171).

References

Ben-Menahem, A. and S.J. Singh (2000). *Seismic waves and sources*. 2nd. Dover Publications, Inc., Mineola, New York.

Birch, F. (1952). "Elasticity and constitution of the Earth's interior". In: *J. Geophys. Res*. 57, pp. 227–286.

Birch, F. (1964). "Density and composition of mantle and core". In: *J. Geophys. Res*. 69, pp. 4377–4388.

Cambiotti, G., V.R. Barletta, A. Bordoni, and R. Sabadini (2009). "A comparative analysis of the solutions for a Maxwell Earth: the role of the advection and buoyancy force". In: *Geophys. J. Int*. 176, pp. 995–1006.

Cambiotti, G., Y. Ricard, and R. Sabadini (2010). "Ice age true polar wander in a compressible and non-hydrostatic Earth". In: *Geophys. J. Int*. 183, pp. 1248–1264.

Cambiotti, G. and R. Sabadini (2010). "The compressional and compositional stratifications in Maxwell Earth models: the gravitational overturning and the long-period tangential flux". *In: Geophys. J. Int*. 180, pp. 475–500.

Chao, B.F. and R.S. Gross (1987). "Changes in the Earth's rotation and low-degree gravitational field induced by earthquakes". In: *Geophys. J. R. Astropys. Soc*. 91, pp. 569–596.

Chinnery, M.A. (1975). "The static deformation of an earth with a fluid core: a physical approach". In: *Geophys. J. R. astr. Soc*. 42, pp. 461–475.

Denis, C. (1989). "The hydrostatic figure of the Earth, in Gravity and Low Frequency Geodynamics (chap. 3)". In: ed. by R. Teisseyre. Vol. 4. Elsevier, Amsterdam.

Durham, W.B. and C. Goetze (1977). "Plastic flow of oriented single crystals of olivine. 1. Mechanical data". In: *J. Geophys. Res*. 82, pp. 737–753.

Dziewonski, A.M. and D.L. Anderson (1981). "Preliminary reference Earth model". In: *Phys. Earth Planet. Inter*. 25, pp. 297–356.

Fang, M. and B.H. Hager (1995). "The singularity mystery associated with a radially continuous Maxwell viscoelastic structure". In: *Geophys. J. Int*. 123, pp. 849–865.

Farrell, W.E. (1972). “Deformation of the Earth by surface loads”. In: *Rev. Geophys*. 10, pp. 761–797.
Goetze, C. (1978). “The mechanisms of creep in olivine”. In: *Phil. Trans. Roy. Soc. London* 288, pp. 99–119.
Greenwood, G.W., H. Jones, and T. Sritharan (1980). “On the transition between dislocation and diffusion creep”. In: *Philos. Mag*. A 41, pp. 871–872.
Greff-Lefftz, M. (2011). “Length of day variations due to mantle dynamics at geological timescale”. In: *Geophys. J. Int*. 187, pp. 595–612.
Han, D. and J. Wahr (1995). “The viscoelastic relaxation of a realistically stratified earth, and a further analysis of postglacial rebound”. In: *Geo-phys. J. Int*. 120, pp. 278–311.
Longman, I.M. (1962). “A Green’s function for determining the deformation of the earth under surface mass loads-1. Theory”. In: *J. Geophys. Res*. 67, pp. 845–850.
Longman, I.M. (1963). “A Green’s function for determining the deformation of the earth under surface mass loads-2. Computations and numerical results”. In: *J. Geophys. Res*. 68, pp. 485–496.
Love, A.E.H. (1911). *Some Problems of Geodynamics*. Dover reprint, New York, 1967.
Manshina, L., D.E. Smylie, and C.H. Chapman (1979). “Seismic excitation of the Chandler wobble revisited”. In: *Geophys. J. R. Astron Soc*. 59, pp. 1–17.
Melosh, H.J. (1980). “Cratering Mechanics: Observational, Experimental and Theoretical”. In: *Ann. Rev. Earth Planet. Sci*. 8, pp. 65–93.
Pekeris, C.L. and Y. Accad (1972). “Dynamics of the Liquid Core of the Earth”. In: *Phil. Trans. R. Soc. Lond. A* 273, pp. 237–260.
Peltier, W.R. (1974). “The impulse response of a Maxwell Earth”. In: *Rev. Geophys. Space Phys*. 12, pp. 649–669.
Plag, H.-P. and H.-U. Jüttner (1995). “Rayleigh-Taylor instabilities of a self-gravitating Earth”. In: *J. Geodyn*. 20, pp. 267–288.
Ranalli, G. (1995). *Rheology of the Earth: Deformation and Flow Processes in Geophysics and Geodynamics*. Chapman and Hall.
Relandeau, C. (1981). “Rheology”. In: *Geophys. Res. Lett*. 8, pp. 733–736.
Sabadini, R., D.A. Yuen, and E. Boschi (1982). “Polar wandering and the forced responses of a rotating, multilayered, viscoelastic planet”. In: *J.Geophys. Res*. 87, pp. 2885–2903.
Smylie, D.E. and L. Mansinha (1971). “The elasticity theory of dislocations in real earth models and changes in the rotation of the earth”. In: *Geophys. J. Roy. Astron. Soc*. 23, pp. 329–354.
Spada, G., Y. Ricard, and R. Sabadini (1992a). “Excitation of true polar wander by subduction”. In: *Nature* 360, pp. 452–454.
Sun, W. and S. Okubo (1993). “Surface potential and gravity changes due to internal dislocations in a spherical Earth, 1, Theory for a point dislocation”. In: *Geophys. J. Int*. 114, pp. 569–592.
Takeuchi, H. and M. Saito (1972). “Seismic surface waves”. In: *Methods Comput. Phys*. 11, pp. 217–295.
Tanaka, Y., J. Okuno, and S. Okubo (2006). “A new method for the computation of global viscoelastic post-seismic deformation in a realistic Earth model (I)—vertical displacement and gravity variation”. In: *Geophys. J. Int*. 164, pp. 273–289.
Vermeersen, L.L.A. and J.X. Mitrovica (2000). “Gravitational stability of spherical self-gravitating relaxation models”. In: *Geophys. J. Int*. 142, pp. 351–360.
Vermeersen, L.L.A. and R. Sabadini (1997). “A new class of stratified viscoelastic models by analytical techniques”. In: *Geophys. J. Int*. 129, pp. 531–570.
Wolf, D. (1991). “Visco-elastodynamics of a stratified compressible planet: incremental field equations and short- and long-time asymptotes”. In: *Geophys. J. Int*. 104, pp. 401–417.
Wolf, D. and G. Kaufmann (2000). “Effects due to compressional and compositional density stratification on load-induced Maxwell viscoelastic perturbations”. In: *Geophys. J. Int*. 140, pp. 51–62.
Wu, P. and W.R. Peltier (1982). “Viscous gravitational relaxation”. In: *Geophys. J. R. Astron. Soc*. 70, pp. 435–485.

Chapter 2
Incompressible and Compressible Analytical Viscoelastic Models

Abstract In this chapter we will derive the analytical solutions for two most representative cases of Earth's models: the stratified viscoelastic incompressible model and the self-compressed viscoelastic compressible sphere. Within the scheme of the Correspondence Principle, these analytical solutions make possible to gain a deep insight into the relaxation spectra of incompressible and compressible Earth's models, via normal modes or complex contour integration. Love numbers, for surface, unitary, constant loads, are finally explored during their time evolution.

2.1 Analytical Solution

By considering the general solution for the spheroidal and toroidal vector solution $\mathbf{y}_{\ell m}$ given by Eq. (1.169) in Chap. 1, its analytical expression can be obtained once specified the analytical expressions for the core-mantle boundary matrix $\mathbf{I}_C$ and the propagator matrix $\mathbf{\Pi}_\ell$. This is possible by imposing some restrictions on the material parameters of the Earth's model that will be introduced later. Here, we recall that the vector $\mathbf{b}$, Eq. (1.128), describes the Earth's surface boundary conditions and it differs from zero only for surface loading and tidal forcing, while the vector $\mathbf{w}$, Eq. (1.165), describes internal loading and seismic forcing.

2.2 Green Functions for Incompressible and Compressible Stratified Viscoelastic Earth's Models

Four major layers build our Earth's models, the lithosphere, the upper and lower mantle and the core. Each one of these layers can in principle be subdivided into other layers, but this four-layer scheme continues to be valid, since any further stratified model would continue to carry an elastic lithosphere, a viscoelastic upper mantle, a viscoelastic lower mantle and an inviscid core. Thus from the point of view of rheology, the Maxwell Model of Fig. 1.2 will be appropriate for the upper and lower

R. Sabadini et al., *Global Dynamics of the Earth: Applications of Viscoelastic Relaxation Theory to Solid-Earth and Planetary Geophysics*,
DOI 10.1007/978-94-017-7552-6_2

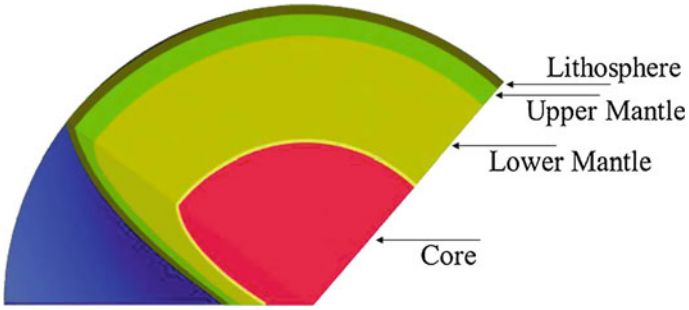

Fig. 2.1 Schematic Earth's model, including the lithosphere, *gray*, the upper mantle, *dark green*, the lower mantle, *light green*, and the core, *red*

mantle, the green layers of Fig. 2.1, while the lithosphere would be characterized solely by the spring of Fig. 1.2.

The core will always be inviscid, and we will not consider the differentiation between the inner and the outer core. When dealing with other planetary bodies, as Europa in Chap. 9, we will modify the outermost layers, in such a way to account for an icy "lithosphere" and a fluid global ocean underneath, and the mantle will also be considered different from the Earth's one in terms of its dimension. Earth's models can be differentiated in many more layers than those of Fig. 2.1, but the major discontinuities in density, at the CMB and upper-lower mantle, remain fixed at 3485 and 5701 km from the centre of the planet. It is worthwhile to remind that the mantle layers are green in our cartoon of the Earth since olivine and pyroxene, the major constituents of the mantle, carry beautiful green colors in the visible frequency range, as observed in samples lifted at the Earth's surface from the mantle by tectonic processes. Peridot (i.e., the gem variety of olivine—The Egyptians fashioned peridot beads as long as 3500 years ago!) is used in jewelry, which makes our planet a precious source of gemstones in the Universe!

2.2.1 Core-Mantle Boundary (CMB) Matrix

In order to specify the core-mantle boundary (CMB) matrix, Eq. (1.150), we must obtain the solution ψ_ℓ of the Poisson equation for the inviscid core, Eq. (1.142), that satisfies the regularity condition at the Earth's centre, Eq. (1.143). Within the assumption of an homogeneous core, i.e., with a constant density profile, the Eq. (1.142) becomes the Laplace equation for ψ_ℓ because its right-hand side yields zero

$$\nabla_r^2 \psi_\ell = 0 \tag{2.1}$$

This equation admits two independent solutions

$$\psi_\ell(r) = c\, r^\ell + c^*\, r^{-(\ell+1)} \tag{2.2}$$

where c and c^* are two integration constants. However, by considering the regularity condition at the Earth's centre, Eq. (1.143), we are left only with

$$\psi_\ell(r) = r^\ell \tag{2.3}$$

and the quantity q_ℓ defined in Eq. (1.148) yields

$$q_\ell(r) = 2\,(\ell - 1)\, r^{\ell-1} \tag{2.4}$$

where we used the following expression for the gravity within an homogeneous sphere of density ρ_C

$$g(r) = \frac{4\,\pi}{3}\, G\, \rho_C\, r \tag{2.5}$$

Then, in the case of an homogeneous core, we can further specify the general expression of the CMB matrix, Eq. (1.150), as follows

$$\mathbf{I}_C = \begin{pmatrix} -r^\ell / g(r_C) & 0 & 1 \\ 0 & 1 & 0 \\ 0 & 0 & g(r_C)\,\rho_C \\ 0 & 0 & 0 \\ r^\ell & 0 & 0 \\ 2\,(\ell-1)\, r^{\ell-1} & 0 & 4\,\pi\, G\, \rho_C \end{pmatrix} \tag{2.6}$$

This is Eq. (63) of Sabadini et al. (1982).

2.2.2 Propagators and Fundamental Matrices

As already argued in Sect. 1.7, the propagator matrix solves the homogeneous system given by Eq. (1.159), with the Cauchy datum and the continuity condition across internal interfaces of radius r_j, as in Eqs. (1.160) and (1.162). In this chapter we derive the fundamental solutions for an incompressible model and for the self-compressed compressible sphere, which allow us to build the propagator.

Considering that the solution of a system of N homogeneous first order differential equations can be expressed as a linear combination of N independent solutions, both spheroidal and toroidal vector solutions $\mathbf{y}_\ell$ of the homogeneous differential system within the same layer, say the jth viscoelastic layer,

$$\frac{d\mathbf{y}_\ell(r)}{dr} = \mathbf{A}_\ell(r)\, \mathbf{y}_\ell(r) \quad r_{j-1} < r < r_j \tag{2.7}$$

can be expressed as follows

$$\boldsymbol{y}_\ell(r) = \mathbf{Y}_\ell(r)\,\boldsymbol{C} \quad r_{j-1} < r < r_j \tag{2.8}$$

where $\mathbf{Y}_\ell$ is the fundamental 6×6- or 2×2-matrix, whose columns are independent solutions of the spheroidal or toroidal homogeneous differential system (2.7) in the jth layer, and $\boldsymbol{C}$ is a vector of integration constants. Note that only the harmonic degree ℓ enters, being the order m dependence due to the non-homogeneous forcing. This allows us to cast the propagator matrix $\mathbf{\Pi}_\ell(r, r')$, when r and r' belong to the jth layer of the Earth's models, in the following form

$$\mathbf{\Pi}_\ell(r, r') = \mathbf{Y}_\ell(r)\,\mathbf{Y}_\ell^{-1}(r') \quad r_{j-1} < r < r_j \tag{2.9}$$

in such a way that it solves the homogeneous differential system (2.7) and satisfies the Cauchy datum $\mathbf{\Pi}_\ell(r', r') = \mathbf{1}$. When r and r' belong to different layers, say jth and ith layers, with $j > i$, the propagator matrix can be obtained using the continuity condition Eq. (1.134) at the chemical interfaces between these two layers, i.e. $\boldsymbol{y}_\ell(r_k^+) = \boldsymbol{y}_\ell(r_k^-)$ at r_k for $k = i, \ldots, j-1$. We thus obtain, from Eqs. (1.134), (2.8) and (2.9)

$$\mathbf{\Pi}_\ell(r, r') = \mathbf{\Pi}_\ell(r, r_j) \left(\prod_{k=i+1}^{j} \mathbf{\Pi}_\ell(r_k, r_{k-1}) \right) \mathbf{\Pi}_\ell(r_i, r') \tag{2.10}$$

In order to obtain an analytical expression for the propagator matrix $\mathbf{\Pi}_\ell$ we thus need to obtain the linear independent solutions of the homogeneous differential system (2.7) in each layer of the Earth's model. They can be obtained analytically both for incompressible and compressible Earth's models with some restrictions on the material parameters, leading to incompressible models, or on the density profile, leading to a new analytical compressional model. Particularly, for layered models we will require that the two Lamé parameters are constant in each layer of the Earth, i.e., $\partial_r \lambda = 0$ and $\partial_r \mu = 0$. Furthermore, rather than solving Eq. (2.7), we will consider the original momentum and Poisson equations, after spherical harmonic expansion, Eqs. (1.84)–(1.87), where the forcing terms will be omitted because we are now interested in the solution of the homogeneous problem.

In order to simplify the following treatment, it is useful to introduce the quantity H_ℓ defined by

$$H_\ell = \partial_r V_\ell + \frac{V_\ell - U_\ell}{r} \tag{2.11}$$

and to consider the radial (1.84), tangential (1.85) and toroidal (1.86) components of the momentum equation (without the forcing terms) multiplied by $1/\rho_0$, r/ρ_0 and $1/\mu$, respectively, and cast them as follows within the assumption of constant elastic parameters

$$\frac{\beta}{\rho_0}\,\partial_r \chi_\ell \; - \partial_r (g\,U) + g\,\chi_\ell - \partial_r \Phi_\ell + \frac{\mu}{\rho_0}\,\frac{\ell(\ell+1)}{r}\,H_\ell = 0 \tag{2.12}$$

$$\frac{\beta}{\rho_0}\,\chi_\ell - g\,U_\ell - \Phi_\ell + \frac{\mu}{\rho_0}\,\partial_r (r\,H_\ell) = 0 \tag{2.13}$$

$$\nabla_r^2 W_\ell = 0 \tag{2.14}$$

It is interesting to note that the terms β/ρ_0 nd μ/ρ_0 entering Eqs. (2.12) and (2.13) correspond to the square of the compressional and shear wave velocities.

The Poisson equation without the forcing terms becomes

$$\nabla_r^2 \Phi_\ell = -4\,\pi\,G\;(\rho_0\,\chi_\ell + U_\ell\,\partial_r \rho_0) \tag{2.15}$$

Exercise 9 Verify that the spheroidal radial (1.84) and tangential (1.85), and toroidal tangential (1.86) components of the momentum equation can be cast as in Eqs. (2.12)–(2.14)

2.3 Layered Incompressible Models

In the case of incompressibility, volume variations Δ are constrained to zero

$$\chi_\ell = 0 \tag{2.16}$$

From Eq. (1.74), we then express the tangential displacement V_ℓ as function of the radial displacement U_ℓ

$$V_\ell = \frac{r\,\partial_r U_\ell + 2\,U_\ell}{\ell(\ell+1)} \tag{2.17}$$

and the quantity H_ℓ defined in Eq. (2.11) becomes

$$H_\ell = \frac{\nabla_r^2 (U_\ell\,r)}{\ell(\ell+1)} \tag{2.18}$$

Furthermore, as pointed out in Sect. 1.2.2, incompressible materials are characterized by an infinitely large bulk modulus κ in order that they are able to react to isotropic stresses. We thus require that the product $\kappa\,\chi_\ell$ remains finite in the limit of χ_ℓ going to zero and of κ going to infinity (Love 1911, Sect. 154). We define this limit with the quantity p_ℓ according to Eqs. (1.31) and (1.37)

$$p_\ell = \lim_{\chi_\ell \to 0\,\kappa \to \infty} -\kappa\,\chi_\ell \tag{2.19}$$

Note that the same limit for $\lambda\,\chi_\ell$ and $\beta\,\chi_\ell$ converges to p_ℓ since $\mu\,\chi_\ell$ goes to zero. In view of this, the radial stress component R_ℓ, Eq. (1.79), becomes

$$R_\ell = -p_\ell + 2\,\mu\,\partial_r U_\ell \tag{2.20}$$

We also assume that the initial density is homogeneous within each layer of the Earth's model

$$\partial_r \rho_0 = 0 \tag{2.21}$$

even though it may differ from a layer to another, due to the specific chemical composition and phase of each layer of the Earth. From the generalized Williamson-Adams equation (1.42), this corresponds to the case in which the compositional coefficient γ defined in Eq. (1.43) is zero, i.e., every incompressible layer is in a neutral state of equilibrium.

In view of Eqs. (1.75), (2.16) and (2.21), there are no local density perturbations ρ^Δ within the layers, and the Poisson equation (2.15) becomes the Laplace equation

$$\nabla_r^2 \Phi_\ell = 0 \tag{2.22}$$

and it admits two independent solutions which takes the following form

$$\Phi_\ell = c_3\, r^\ell + c_3^*\, r^{-(\ell+1)} \tag{2.23}$$

where r^ℓ and $r^{-(\ell+1)}$ are the regular and irregular solutions at the Earth's centre, respectively. Here c_3 and c_3^* are two constants of integration and the subscript 3 is used for convenience.

The absence of local density perturbations ρ^Δ within the layers does not mean that there are no gravitational perturbations Φ_ℓ^Δ. Indeed, density perturbations occur at the Earth's surface, as well as at any internal chemical interfaces separating two neighboring layers of the Earth, where the density contrast $\Delta\rho_j$ differs from zero

$$\Delta\rho_j = \rho_0(r_j^+) - \rho_0(r_j^-) \tag{2.24}$$

Here r_j is the radius of the interface, with the superscripts $+$ and $-$ indicating that the density is evaluated just above and below of the interface. Indeed, within the assumption of infinitesimal perturbations, the radial displacement $u_r(r_j, \theta)$ of the interface (i.e., the perturbation of the topography of the interface) yields a surface density anomaly given by the negative of the product between the density contrast $\Delta\rho_j$ and the radial displacement $u_r(r_j, \theta)$

$$\rho^\Delta = -\Delta\rho_j\, u_r(r_j, \theta)\, \delta(r - r_j) \tag{2.25}$$

with δ being the Dirac delta function. Equation (2.25) can be also obtained from the right-hand side of Eq. (1.75) by considering that the radial derivative of a function

with a step-like discontinuity at $r = r_j$ yields the Dirac delta $\delta(r - r_j)$ multiplied by the value of the step, the density contrast $\Delta\rho_j$ in our case

$$\partial_r \rho_0 = \Delta\rho_j \, \delta(r - r_j) \tag{2.26}$$

For each interface there is a surface density perturbation that contributes to the gravitational perturbation via the Poisson equation and it affects the momentum equation in terms both of gravity perturbations and buoyancy forces, i.e., the fourth and third terms in Eq. (1.19). Note that the effects of these surface density perturbations are already accounted for by the way in which we have defined the potential flux $Q_{\ell m}$, Eq. (1.123), and by the requirement that it is continuous across the internal interfaces.

In view of Eqs. (2.16) and (2.19), the radial (2.12) and tangential (2.13) components of the momentum equation simplify into

$$\partial_r \Gamma_\ell + \frac{\mu}{\rho_0} \frac{\ell(\ell+1)}{r} H_\ell = 0 \tag{2.27}$$

$$\Gamma_\ell + \frac{\mu}{\rho_0} \partial_r (r \, H_\ell) = 0 \tag{2.28}$$

where Γ_ℓ is defined by

$$\Gamma_\ell = -\frac{p_\ell}{\rho_0} - g \, U_\ell - \Phi_\ell \tag{2.29}$$

By applying the operator $\partial_r + 2/r$ to Eq. (2.27) and subtracting Eq. (2.28) multiplied by $\ell(\ell+1)/r^2$ we obtain

$$\nabla_r^2 \Gamma_\ell = 0 \tag{2.30}$$

the terms in H_ℓ canceling each other

$$\left(\partial_r + \frac{2}{r}\right) \frac{\ell(\ell+1) \, H_\ell}{r} - \frac{\ell(\ell+1)}{r^2} \partial_r (r \, H_\ell) = 0 \tag{2.31}$$

Since Γ_ℓ satisfies the Laplace equation (2.30), it thus takes the following form, with the same dependence of Φ_ℓ obtained in Eq. (2.23) on the radial distance r from the Earth's centre

$$\Gamma_\ell = -\frac{\mu}{\rho_0} c_1 \, r^\ell - \frac{\mu}{\rho_0} c_1^* \, r^{-(\ell+1)} \tag{2.32}$$

where c_1 and c_1^* are two constants of integration that have been multiplied by $-\mu/\rho_0$ for convenience, as it will be apparent in the following. Then, by substituting this solution into Eq. (2.27) and by making use of Eq. (2.18), we obtain a dishomogeneous differential equation of the second order in U_ℓ

$$\nabla^2 (U_\ell \, r) = c_1 \, \ell \, r^\ell - c_1^* \, (\ell + 1) \, r^{-(\ell+1)} \tag{2.33}$$

It is solved by the two particular solutions

$$U_\ell = c_1 \frac{\ell\, r^{\ell+1}}{2(2\,\ell+3)} + c_1^* \frac{(\ell+1)\, r^{-\ell}}{2(2\,\ell-1)} \tag{2.34}$$

and by the two linearly independent solutions of the homogeneous differential equation, i.e., when c_1 and c_1^* are set to zero in Eq. (2.33),

$$U_\ell = c_2\, r^{\ell-1} + c_2^*\, r^{-(\ell+2)} \tag{2.35}$$

Summing up all the contributions, we obtain

$$U_\ell = c_1 \frac{\ell\, r^{\ell+1}}{2(2\,\ell+3)} + c_2\, r^{\ell-1} + c_1^* \frac{(\ell+1)\, r^{-\ell}}{2(2\,\ell-1)} + c_2^*\, r^{-(\ell+2)} \tag{2.36}$$

and, using this into Eq. (2.17), the tangential displacement V_ℓ yields

$$V_\ell = c_1 \frac{(\ell+3)\, r^{\ell+1}}{2\,(2\,\ell+3)(\ell+1)} + c_2 \frac{r^{\ell-1}}{\ell} + c_1^* \frac{(2-\ell)\, r^{-\ell}}{2\,\ell(2\,\ell-1)} - c_2^* \frac{r^{-(\ell+2)}}{\ell+1} \tag{2.37}$$

Exercise 10 Verify that the radial, R_ℓ, tangential, S_ℓ, and potential, Q_ℓ, stress components of the spheroidal solution $\boldsymbol{y}$, as defined in Eqs. (2.20), (1.80) and (1.93), respectively, take the form

$$\begin{aligned} R_\ell = {} & c_1 \tfrac{\ell\,\rho_0\, g\, r + 2\left(\ell^2-\ell-3\right)\mu}{2\,(2\,\ell+3)}\, r^{\ell} + c_2\, [\rho_0\, g\, r + 2\,(\ell-1)\,\mu]\, r^{\ell-2} \\ & + c_3\, \rho_0\, r^{\ell} + c_1^* \tfrac{(\ell+1)\,\rho_0\, g\, r - 2\left(\ell^2+3\,\ell-1\right)\mu}{2\,(2\,\ell-1)}\, r^{-(\ell+1)} \\ & + c_2^* [\rho_0\, g\, r - 2\,(\ell+2)\,\mu]\, r^{-(\ell+3)} + c_3^*\, \rho_0\, r^{-(\ell+1)} \end{aligned} \tag{2.38}$$

$$\begin{aligned} S_\ell = {} & c_1 \tfrac{\ell\,(\ell+2)}{(2\,\ell+3)(\ell+1)} \mu\, r^{\ell} + c_2 \tfrac{2\,(\ell-1)}{\ell} \mu\, r^{(\ell-2)} \\ & + c_1^* \tfrac{(\ell^2-1)}{\ell\,(2\,\ell-1)} \mu\, r^{-(\ell+1)} + c_2^* \tfrac{2\,(\ell+2)}{\ell+1} \mu\, r^{-(\ell+3)} \end{aligned} \tag{2.39}$$

$$\begin{aligned} Q_\ell = {} & c_1 \tfrac{2\pi G \rho_0 \ell}{2l+3} r^{\ell+1} + c_2\, 4\,\pi\, G\, \rho_0\, r^{\ell-1} + c_3 (2\,\ell+1)\, r^{\ell-1} \\ & + c_1^* \tfrac{2\,\pi\, G\, \rho_0\, (\ell+1)}{2l-1}\, r^{-l} + c_2^* 4\,\pi\, G\, \rho_0\, r^{-(l+2)} \end{aligned} \tag{2.40}$$

For each layer of the Earth's model (assuming that each layer has material parameters ρ_0 and μ which are constant inside it), on the basis of Eqs. (2.23), (2.36)–(2.37) and (2.38)–(2.40), the spheroidal vector solution $\boldsymbol{y}$ can be written as

$$\boldsymbol{y}_\ell(r) = \mathbf{Y}_\ell(r)\, \boldsymbol{C}_\ell \tag{2.41}$$

where $\mathbf{Y}_\ell$ is the fundamental matrix

$$\mathbf{Y}_\ell(r) = \begin{pmatrix} \frac{l r^{l+1}}{2(2l+3)} & r^{l-1} & 0 \\ \frac{(l+3) r^{l+1}}{2(2l+3)(l+1)} & \frac{r^{l-1}}{l} & 0 \\ \frac{(l\rho_0 g r + 2(l^2-l-3)\mu) r^l}{2(2l+3)} & (\rho_0 g r + 2(l-1)\mu) r^{l-2} & \rho_0 r^l \\ \frac{l(l+2)\mu r^l}{(2l+3)(l+1)} & \frac{2(l-1)\mu r^{l-2}}{l} & 0 \\ 0 & 0 & r^l \\ \frac{2\pi G \rho_0 l r^{l+1}}{2l+3} & 4\pi G \rho_0 r^{l-1} & (2l+1) r^{l-1} \end{pmatrix} \cdots$$

$$\cdots \begin{pmatrix} \frac{(l+1) r^{-l}}{2(2l-1)} & r^{-l-2} & 0 \\ \frac{(2-l) r^{-l}}{2l(2l-1)} & -\frac{r^{-l-2}}{l+1} & 0 \\ \frac{(l+1)\rho_0 g r - 2(l^2+3l-1)\mu}{2(2l-1) r^{l+1}} & \frac{\rho_0 g r - 2(l+2)\mu}{r^{l+3}} & \frac{\rho_0}{r^{l+1}} \\ \frac{(l^2-1)\mu}{l(2l-1) r^{l+1}} & \frac{2(l+2)\mu}{(l+1) r^{l+3}} & 0 \\ 0 & 0 & \frac{1}{r^{l+1}} \\ \frac{2\pi G \rho_0 (l+1)}{(2l-1) r^l} & \frac{4\pi G \rho_0}{r^{l+2}} & 0 \end{pmatrix} \tag{2.42}$$

and $\boldsymbol{C}_\ell$ is the vector of integration constants

$$\boldsymbol{C}_\ell = \left(c_1, c_2, c_3, c_1^*, c_2^*, c_3^*\right)^T \tag{2.43}$$

The regular and singular part of the fundamental matrix are the first three columns and last three columns respectively, the first going to zero at the Earth's centre and they are given by Eqs. (46) and (48) in Sabadini et al. (1982), where the singular part of the incompressible solution was given for the first time for a stratified viscoelastic Earth. The asterisk for denoting the part of the vector of integration constant multiplying the singular part of the fundamental matrix is also taken from Sabadini et al. (1982).

Each column of the fundamental matrix $\mathbf{Y}_\ell$ represents an independent solution of the linear differential system (1.161) in the incompressible case, i.e., in the limit of the matrix $\mathbf{A}$ defined in Eq. (1.95) for the bulk modulus κ going to infinity

$$\partial_r \mathbf{Y}_\ell = \left(\lim_{\kappa \to \infty} \mathbf{A}_\ell\right) \mathbf{Y}_\ell \tag{2.44}$$

Note that, from Eqs. (1.77) and (1.96), also λ and β go to infinity

The analytical expression of the fundamental solution (2.42), which includes the regular and singular part at the Earth's centre was first obtained in Sabadini et al. (1982), after the regular part was given first in Wu and Peltier (1982), their Eqs. (30a)–(30d). The reader should note that the terms of the third and sixth columns of the fundamental matrix $\mathbf{Y}_\ell(r)$ have the opposite sign with respect to the corresponding terms in Eqs. (46) and (48) of Sabadini et al. (1982) due to the sign definition of the ϕ gravitational potential in this book with respect to Sabadini et al. (1982), to match herein the definition of the perturbation of the gravitational potential in agreement

with Eqs. (1.60) and (1.2). The results are of course the same, for both Sabadini et al. (1982) and what we show in this book: we now simply avoid a somehow confusing artificial change of sign in the definition of the gravitational potential. Several works and results from other groups streamed from this fundamental solution describing a self-gravitating, viscoelastic, stratified Earth. It should be noted on the other hand, that some applications of $\mathbf{Y}_\ell(r)$, as for the case of co-seismic deformation, is not appropriate because in that case the effects of compressibility play a key role, but this will be analyzed in Chap. 5.

The inverse of the fundamental matrix $\mathbf{Y}_\ell$ has the form

$$\mathbf{Y}_\ell^{-1}(r) = \mathbf{D}_\ell(r)\,\bar{\mathbf{Y}}_\ell(r) \tag{2.45}$$

with $\mathbf{D}_\ell$ being a diagonal matrix with elements

$$\begin{aligned}&\mathrm{diag}\,[\mathbf{D}_\ell(r)]\\ &\quad = \frac{1}{2\,\ell+1}\left(\frac{\ell+1}{r^{\ell+1}}\,,\ \frac{\ell(\ell+1)}{2(2\,\ell-1)r^{\ell-1}}\,,\ -\frac{1}{r^{\ell-1}}\,,\ \ell r^{\ell}\,,\ \frac{\ell(\ell+1)}{2(2\,\ell+3)}r^{\ell+2}\,,\ r^{\ell+1}\right)\end{aligned} \tag{2.46}$$

and

$$\bar{\mathbf{Y}}_\ell(r) \;=\; \begin{pmatrix} \frac{\rho g r}{\mu} & -2(\ell+2) & 2\,\ell(\ell+2) & -\frac{r}{\mu} & \frac{\ell r}{\mu} & \frac{\rho r}{\mu} & 0 \\ -\frac{\rho g r}{\mu}+\frac{2(\ell^2+3\,\ell-1)}{\ell+1} & -2(\ell^2-1) & \frac{r}{\mu} & \frac{(2-\ell)r}{\mu} & -\frac{\rho r}{\mu} & 0 \\ 4\pi G\rho & 0 & 0 & 0 & 0 & -1 \\ \frac{\rho g r}{\mu} & +2(\ell-1) & 2(\ell^2-1) & -\frac{r}{\mu} & -\frac{(\ell+1)r}{\mu} & \frac{\rho r}{\mu} & 0 \\ -\frac{\rho g r}{\mu}-\frac{2(\ell^2-\ell-3)}{l} & -2\,\ell(\ell+2) & \frac{r}{\mu} & \frac{(\ell+3)r}{\mu} & -\frac{\rho r}{\mu} & 0 \\ 4\pi G\rho r & 0 & 0 & 0 & 2\,\ell+1 & -r \end{pmatrix} \tag{2.47}$$

Although it would be quite laborious to derive such an analytical compact form of a 6×6 inverse matrix by hand, this can be done nowadays by means of an algebraic software package like *Mathematica*. It was first done by (Spada et al. 1990, 1992). Of course, it is not difficult to show analytically that $\mathbf{Y}_\ell(r)\,\mathbf{Y}_\ell^{-1}(r) = \mathbf{1}$, with $\mathbf{1}$ being the identity matrix, by hand! With respect to (Spada et al. 1990, 1992), the elements of $\mathbf{D}_\ell(r)$ and $\bar{\mathbf{Y}}_\ell(r)$ are changed accordingly to account for our own definition of the sign of the perturbation of the gravitational potential.

2.4 Relaxation Times for Incompressible Earth's Models

In order to gain insights into the physics of the relaxation processes, it is important to take a close look at the relaxation times corresponding to the modes excited by discontinuities in the physical parameters of simple Earth's models. We will consider the spheroidal case. Equations (2.42) and (2.45) allow us to build the propagator, Eq. (2.9), and to derive the normalized secular determinant $D(s)$, Eq. (1.199).

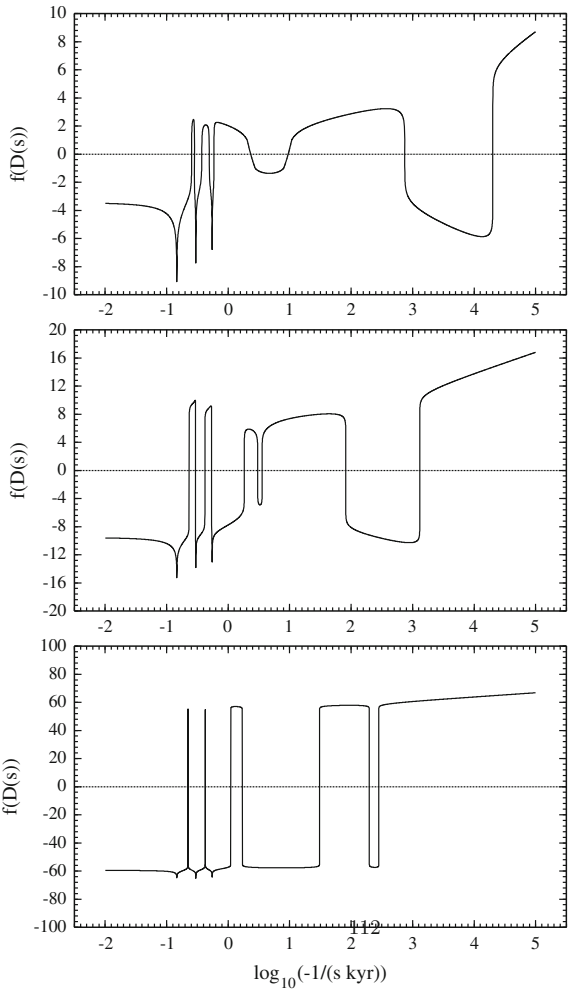

Fig. 2.2 With s normalized by 1 kyr, plot of the function defined as $f(D_\ell(s)) = sgn(D_\ell(s)) \times log(|D_\ell(s)|)$ if $|D(s)| > 10.0$ and $f(D_\ell(s)) = D_\ell(s)/10.0)$ if $|D_\ell(s)| \leq 10.0$ as function of $\log(-1/(\text{s} \times \text{kyr}))$ and its zero crossings, providing the relaxation times $T_i = -1/s_i$, for the 5-layer incompressible model of Table 2.1 and $l = 2, 10, 100$ from *top* to *bottom*. This calculation and corresponding figure have been kindly provided by Shuang Yi, from the Key Laboratory of Computational Geodynamics from the University of the Chinese Academy of Sciences (UCAS), January 2015

Figure 2.2, kindly provided by S. Yi (personal communication), portrays $f(D_\ell(s)) = sgn(D_\ell(s)) \times log(|D_\ell(s)|)$ if $|D(s)| > 10.0$ and $f(D_\ell(s)) = D_\ell(s)/10.0)$ if $|D_\ell(s)| \leq 10.0$ as function of $\log(-1/(s \times kyr))$, which means that s, negative, expressed in 1/s is normalized by 1 kyr = 3.153×10^{10} s, for the harmonic degrees $\ell = 2$, 10 and 100, from top to bottom and for the 5-layer, incompressible Earth's model displayed in Table 2.1. The zero crossings are the relaxation times corresponding to the normal modes $T_i = -1/s_i$ of the 5-layer Earth's model. According to the rules established in Sect. 1.8 for counting the normal modes for incompressible models, Fig. 2.2 portrays 9 zero crossings, or normal modes of the secular determinant $D(s)$ as expected for the five-layer model of Table 2.1: four transient modes $T1$–$T4$ are triggered at the two interfaces between the viscoelastic layers, at 5951 and

Table 2.1 Parameters for the 5-layer fixed-boundary contrast Earth's model

Layer	r (km)	ρ (kg/m^3)	ν (Pa s)	μ (N/m^2)	
1	6371 – 6251	3070	Elastic	5.76×10^{10}	Lithosphere
2	6251 – 5951	3070	10^{21}	5.76×10^{10}	Shallow upper mantle
3	5951 – 5701	3850	10^{21}	1.06×10^{11}	Transition zone
4	5701 – 3480	4970	10^{21}	2.16×10^{11}	Lower mantle
5	3480 – 0	10,750	Inviscid	0	Inviscid fluid core

r is the distance with respect to the centre of the Earth, ρ the density of the layer, and μ the rigidity

5701 km, because their Maxwell times are different (from Table 2.1); two buoyancy modes, $M1$ and $M2$ are triggered at these two interfaces between viscoelastic layers, $M1$ at 5701 and $M2$ at 5951 km; the density contrast between the viscoelastic mantle and the outer atmosphere triggers the mantle mode $M0$, the rheological contrast between the viscoelastic mantle and the elastic lithosphere triggers $L0$ and finally the density contrast between the mantle and the core triggers the core mode $C0$, giving a final total count of nine modes. The slowest modes have been named $M1$ and $M2$ by Wu and Peltier (1982) and are associated with the two internal chemical boundaries at 670 and 420 km. These $M1$ and $M2$ modes will be quoted several times in the book when dealing with the geophysical processes affected by the slow readjustment of the 670 and 420 km density discontinuities.

The longest T_i correspond to the buoyancy $M2$ and $M1$ modes in the extreme right of the abscissa, and for $\ell = 2$ they are $T_{M2} = 2.01 \times 10^7$ yr, $T_{M1} = 7.44 \times 10^5$ yr, due to density contrasts between viscoelastic internal layers. To the left, towards shorter times, we catch the core mode $C0 = 9.48 \times 10^3$ yr, the mantle mode $M0 = 2.33 \times 10^3$ yr, the lithospheric mode $L0 = 5.89 \times 10^2$ yr and then, at the shortest times, the couple of transient relaxation times $T1$–$T4$, 4.92×10^2, 3.73×10^2, 2.83×10^2 and 2.55×10^2 yr. Increasing the harmonic degree at $\ell = 10$ the transient relaxation times remain constant, while the three modes $L0$, $M0$ and $C0$ move to the right, towards longer times, while $M1$ and $M2$ do the opposite. When $\ell = 100$ the transient modes merge together and the two adjacent modes become indistinguishable at this scale, apparently reducing the nine modes to seven modes. The lithospheric mode $L0$ moves towards the slowest $M1$, $M2$ modes, while the latter get close to one another. Figure 2.3, kindly provided by S. Yi (personal communication), shows for the same Earth's model of Table 2.1 the relaxation times as a function of the harmonic degree from $\ell = 2$ to $\ell = 100$, in order to provide a more precise determination of the zero crossings and relaxation time values with respect to Fig. 2.2.

Figure 2.3 portrays in detail the relaxation times for $\ell = 2$–100, which in Fig. 2.2 are shown solely for $\ell = 2$, 10 and 100. This representation allows us to perceive that each viscoelastic mode follows its own peculiar branch for varying harmonic degree ℓ, so the $M1$, $M2$ modes become faster with increasing ℓ compared to their slowest $\ell = 2$ counterparts. The $\ell = 100$ $M2$ for example is faster by almost two orders of magnitude compared to $\ell = 2$, from about twenty million years to three hundred thousand years. On the opposite, the $C0$ mode becomes slower, while the

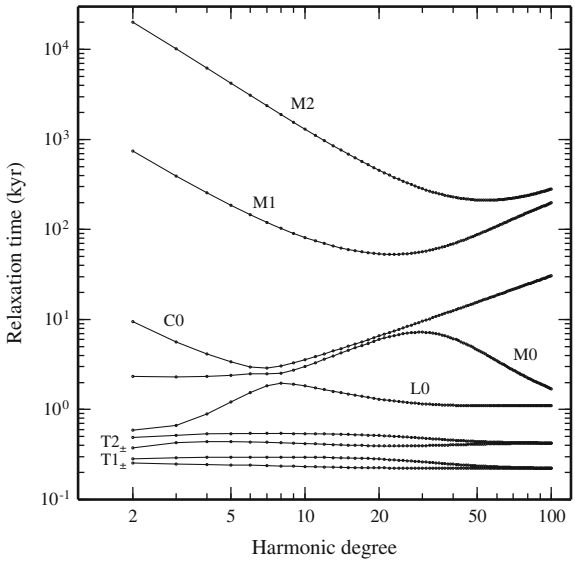

Fig. 2.3 Relaxation times T_i in kyr for the 5-layer incompressible model of Table 2.1 and $l = 2$–100. As for Fig. 2.2, this calculation and corresponding figure have been kindly provided by Shuang Yi, from UCAS, January 2015

$M0$ mode is the slowest for $\ell = 30$, about seven thousand years compared to two 2.5 thousand years for $\ell = 2$, becoming fast again for $\ell = 100$. The $L0$ mode becomes slower for increasing ℓ in a non monotonic way, and the transient modes become indistinguishable in pairs. This result shows the richness in time scales caused by the Earth's stratification and wavelength decomposition.

We now have a closer look at the relaxation times as a function of the harmonic degree ℓ as in Fig. 2.3 but for 5-layer Earth's models with varying viscosity ratio between the lower and upper mantle and between the transition zone and the upper mantle. The relaxation times for these 5-layer models are shown in Figs. 2.4 and 2.5 as a function of the harmonic order ℓ, for varying ratio $B = \nu_2/\nu_1$ between the lower and upper mantle viscosity from 1 to 200, and for varying ratio $C = \nu_3/\nu_1$ between the viscosity of the transition zone and that of the upper mantle by the same amount. All the ℓ patterns resemble that of Fig. 2.3.

The relaxation times $T_i = -1/s_i$ are expressed in years, ranging from $\ell = 2$ to $\ell = 100$. Figure 2.4 deals with a viscosity increase in the lower mantle, with the ratio B between the lower and upper mantle viscosity ranging from 1 to 200. OM stands for an old viscosity model in which the upper mantle viscosity is fixed at 10^{21} Pa s, while NM stands for a new viscosity model in which ν_1 is fixed at 0.5×10^{21} Pa s, in agreement with the recent analyses by Lambeck et al. (1990), Vermeersen and Sabadini (1999), Devoti et al. (2001) based on postglacial rebound modeling from different perspectives, sea-level changes in the far field and long-wavelength geopotential variations. These models are chemically stratified at 420 and 670 km depth and the viscosity is uniform in the whole upper mantle; this stratification supports nine relaxation modes.

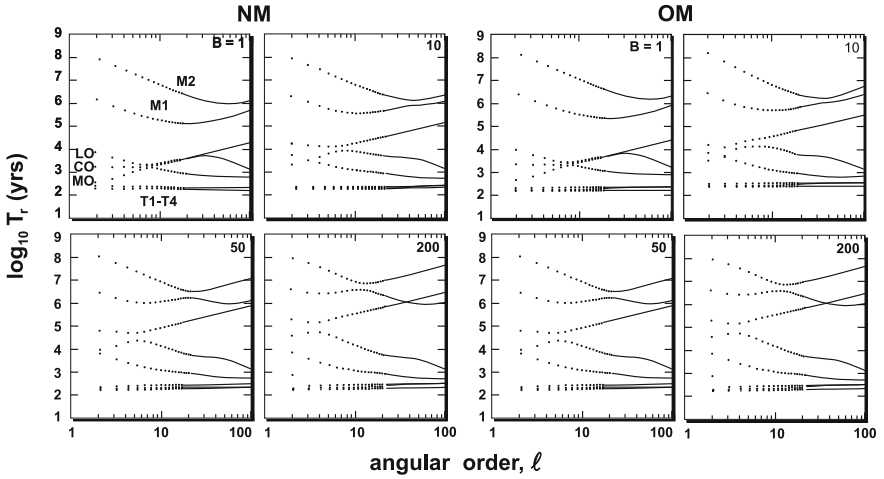

Fig. 2.4 Relaxation times in years as a function of the harmonic degree ℓ and varying lower mantle viscosity. The parameter $B = \nu_2/\nu_1$ is varied from 1 to 200. *OM* corresponds to $\nu_1 = 10^{21}$ Pa s, while *NM* corresponds to $\nu_1 = 0.5 \times 10^{21}$ Pa s (Fig. 2 in Spada et al. 1992)

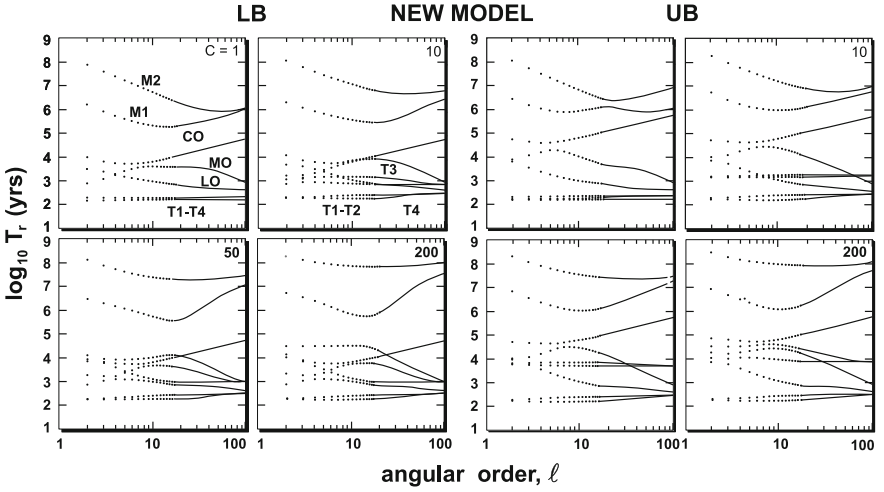

Fig. 2.5 Relaxation times in years as a function of the harmonic degree ℓ and varying lower mantle viscosity. The parameter $C = \nu_3/\nu_1$ is varied from 1 to 200. *LB* corresponds to $\nu_1 = 0.5 \times 10^{21}$ Pa s and $\nu_2 = 2 \times 10^{21}$ Pa s, while *UB* corresponds to $\nu_1 = 0.5 \times 10^{21}$ Pa s and $\nu_2 = 2 \times 10^{22}$ Pa s (Fig. 3 in Spada et al. 1992)

At low degrees, Fig. 2.4, the transient times $T_1 - T_4$ are followed by the lithospheric ($L0$) mode and by the core ($C0$) and mantle ($M0$) modes, as portrayed in the panel NM by $B = 1$, with $B = \nu_2/\nu_1$ denoting the ratio between the lower to upper mantle viscosity. When B is increased from 1 to 200, all the curves are moved upward toward

slower relaxation times. This upward migration occurs first for longer wavelengths, say lower than $\ell = 10$, followed by the shorter ones, which are less affected by lower mantle viscosity. For shorter wavelengths only the $M1$, $M2$ and core modes have slower relaxation times, while the lithospheric and mantle modes are rather unaffected, the deformation at such high harmonic degrees being concentrated in the upper mantle and thus unaffected by lower mantle viscosity variations. The NM curves, in the left panel, can be obtained from their counterparts in the right panel by a uniform downward shift towards faster relaxation times, in agreement with the lowering of the global mantle viscosity of this model.

Figure 2.5 shows the effects of a viscosity increase in the transition zone for the new model NM, with $C = \nu_3/\nu_1$ denoting the ratio between the viscosity in the transition zone ν_3 with respect to the viscosity in the upper mantle. These models, with a stiff transition zone at the upper lower mantle boundary, are based on the laboratory studies by Karato (1989) and Meade and Jeanloz (1990), which suggest that the transition zone may form a layer of relatively high viscosity between the upper and lower mantle. Panel LB, with LB standing for lower branch, corresponds to an upper mantle viscosity of 0.5×10^{21} Pa s and to $\nu_2 = 2 \times 10^{21}$ Pa s in the lower mantle, while UB, with UB standing for upper branch, corresponds to the same upper mantle viscosity and to a higher lower mantle viscosity of $\nu_2 = 2 \times 10^{22}$ Pa s. LB and UB for the lower mantle viscosity stand for the two possible viscosity solutions when true polar wander data and variations in the long-wavelength gravity field are used to constrain the viscosity of the lower mantle (see Chaps. 4 and 5). Viscosity increase in the hard layer influences all the modes for all the models, in particular the $M1$ and $M2$ modes, which is not surprising as these modes are excited by the discontinuities that bound the region where the viscosity is varied. With respect to the previous figure, all the modes are now affected by the viscosity increase in the transition layer which, lying close to the surface, is also able to affect the short wavelength, high-degree modes.

Exercise 11 Making use of the analytical fundamental solution for the incompressible, homogeneous Earth's model, show that the loading Love number k_2^L can be cast in the following form in the Laplace transform domain

$$k_2^L(s) = \frac{-1}{(1 + \hat{\mu}(s))} \tag{2.48}$$

while the tidal Love number k_2^T becomes

$$k_2^T(s) = \frac{3/2}{(1 + \hat{\mu}(s))} \tag{2.49}$$

where $\hat{\mu}(s)$ is given by Eq. (1.54), with the elastic μ multiplied by the normalization factor $19/(2\rho g(a)a)$, valid for $\ell = 2$.

2.5 The Self-compressed, Compressible Sphere

Cambiotti and Sabadini (2010) found the analytical solution of viscoelastic perturbations in the Laplace domain for a specific self-gravitating compressible Maxwell Earth's model, called "self-compressed compressible sphere". This model is composed of an incompressible inviscid core and a compressible Maxwell mantle with constant shear modulus, μ, bulk modulus, κ, and viscosity, ν. In order to account for the self-compression of the mantle at the initial state of hydrostatic equilibrium, the initial density profile within the mantle varies with the radial distance from the Earth's centre r according to

$$\rho_0(r) = \begin{cases} \frac{3\alpha}{2r_C} & 0 \le r \le r_C \\ \frac{\alpha}{r} & r_C < r \le a \end{cases} \tag{2.50}$$

where r_C, a and α are the radius of the core, the Earth's radius and a constant related to the total Earth mass M_E by

$$M_E = 2\,\pi\,\alpha\,a^2 \tag{2.51}$$

This choice of the initial density profile fixes the initial gravity acceleration g within the mantle to

$$g = 2\,\pi\,G\,\alpha \tag{2.52}$$

with G being the universal gravitational constant.

Depending on the bulk modulus κ, the self-compressed compressible sphere describes compressional or compositional stratifications of the mantle. Indeed, from the generalized Williamson-Adams equation (1.42) with the compositional coefficient set to zero, $\gamma = 0$, we obtain that compressional stratifications are characterized by a constant bulk modulus to which we will refer as compressional bulk modulus κ_0

$$\kappa_0 = g\,\alpha = 2\,\pi\,G\,\alpha^2 \tag{2.53}$$

Departures from this value result in compositional stratifications. Particularly, the compositional coefficient γ yields

$$\gamma = -\frac{\epsilon\,\alpha}{r^2} \tag{2.54}$$

with

$$\epsilon = \frac{\kappa - \kappa_0}{\kappa} \tag{2.55}$$

As it results from the analysis of the relaxation spectrum of the self-compressed compressible sphere, that we will discuss later in Sect. 2.5.2, the compositional stratification is stable if $\kappa > \kappa_0$ and unstable if $\kappa < \kappa_0$. This also results from the

comparison between the generalized Williamson-Adams equation (1.42) and the expression for the square of the Brunt-Väisälä frequency ω

$$\omega^2 = -\frac{g}{\rho_0}\left(\partial_r \rho_0 + \frac{g\,\rho_0^2}{\kappa}\right) = -\frac{g\,\gamma}{\rho_0} \tag{2.56}$$

The Brunt-Väisälä frequency ω characterizes the motion of a particle in the ideal fluid that adiabatically moves away from its equilibrium position. The particle will oscillate around its equilibrium position with frequency ω if $\omega^2 > 0$, while it will continue to move away from its equilibrium position if $\omega^2 < 0$. Differently, the particle remains in the new position due to the perturbation if $\omega = 0$. Although the present theoretical framework is based on the assumption of quasi-static deformations (we neglect the inertial forces in the momentum equation), the analysis of the sign of ω^2 allows to establish if the viscoelastic model is stable or unstable (Plag and Jüttner 1995; Vermeersen and Mitrovica 2000). In view of Eq. (2.56), the stability only depends on the sign of the compositional coefficient γ. The model is stable if $\gamma \leq 0$ and unstable if $\gamma > 0$. For instance layered compressible models present the unstable Rayleigh–Taylor modes (Plag and Jüttner 1995) and, indeed, their compositional coefficient becomes positive because the radial derivative of the density is zero in this case. An alternative way to describe layered compressible models consists in the assumption that they are incompressible at the initial state of hydrostatic equilibrium, i.e., they have an infinitely large bulk modulus at the initial state, $\kappa \to \infty$, and a finite bulk modulus during the perturbations. This would imply that $\gamma = 0$ from Eq. (2.56), but it is not a self-consistent with compressibility during deformation and so we reject this interpretation, which also contrasts with the presence of Rayleigh–Taylor instabilities.

In view of the way in which we have defined the self-compressed compressible sphere, we have the possibility of studying the effects of the compressional and compositional stratifications on the relaxation process of Maxwell Earth's models. Previous analytical solutions were obtained assuming material or local incompressibility and for the case of the "homogeneous compressible sphere" (Gilbert and Backus 1968). Only the latter model actually accounts for compressibility during perturbations, but all the material parameters, included the initial density, are constant from the centre to the surface of the Earth. Its analytical solution has been widely used, first, in seismology and, after, in viscoelastic modelling (Vermeersen et al. 1996b). Nevertheless, it neglects the self-compression at the initial state of hydrostatic equilibrium since it has a constant density profile: in this respect, the homogeneous compressible sphere is always unstable. Instead, our self-compressed compressible sphere (Cambiotti and Sabadini 2010) takes into account compressibility both during the perturbations and at the initial state, having a depth dependent density profile, Eq. (2.50). In addition to this qualitative improvement with respect to the homogeneous compressible sphere, our model also reproduces the density contrast at the core-mantle boundary, although it neglects other density contrasts within the mantle due to the simple Darwin-law used to describe the compressibility at the initial state. This also results into a better reproduction of the actual initial

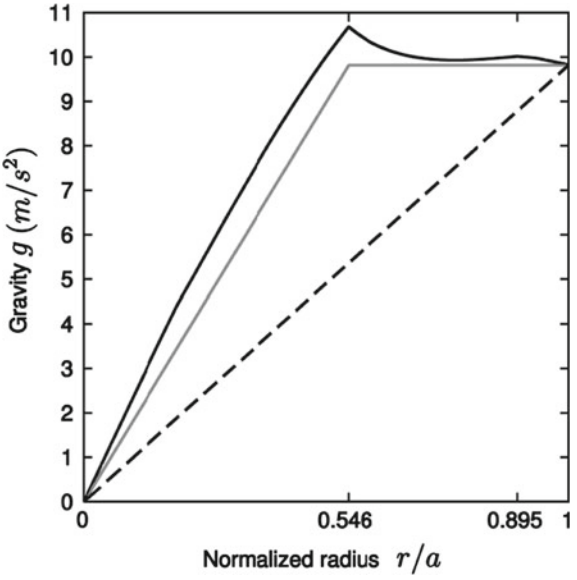

Fig. 2.6 Initial gravity acceleration g of PREM (*black solid line*), the self-compressed compressible sphere (our new model, *grey line*) and the homogeneous compressible sphere (Gilbert and Backus 1968 *black dashed line*). The core-mantle boundary corresponds to the normalized radius 0.547

gravity acceleration predicted by PREM, which is indeed almost constant within the mantle as in Eq. (2.52). We show this in Fig. 2.6 where we compare the initial gravity acceleration predicted by PREM and the gravity from the self-compressed and homogeneous compressible spheres.

2.5.1 The Analytical Solution

In order to solve the spheroidal radial and tangential components of the momentum equation and the Poisson equation, Eqs. (2.12), (2.13) and (2.15), for compressible Earth's models with constant elastic parameters κ and μ, it is convenient obtaining first two differential equations that involve only the radial and tangential displacements. This is possible owing to the specific initial density and gravity of the self-compressed compressible sphere, Eqs. (2.50) and (2.52). The first differential equation is obtained by subtracting to the radial component (2.12) of the momentum equation the derivative of the tangential component (2.13) with respect to the radial variable r

$$\left(\frac{\beta}{\alpha} - g\right) \chi_\ell + \frac{\mu}{\alpha} \left[r^2 \partial_r^2 H_\ell + 3\, r\, \partial_r H_\ell + (1 - \ell(\ell+1))\ H_\ell\right] = 0 \qquad (2.57)$$

The second differential equation is obtained by applying the operator $\partial_r + 2/r$ to the radial component Eq. (2.12) of the momentum equation and subtracting to it the tangential component Eq. (2.13) multiplied by $\ell(\ell+1)/r^2$

$$
\begin{aligned}
&-\nabla_r^2 \Phi_\ell + \nabla^2 \left(\frac{\beta}{\alpha}\, \chi_\ell - g\, U_\ell \right) \\
&+ \left(g - \frac{\beta}{\alpha} \right) \frac{1}{r}\, \partial_r \left(r^2 \chi_\ell \right) + \frac{\mu}{\alpha}\, \frac{\ell(\ell+1)}{r}\, H_\ell = 0
\end{aligned}
\tag{2.58}
$$

Here, we also substitute the Laplacian of the potential by means of the Poisson equation (2.15) together with Eqs. (2.50) and (2.52)

$$
\nabla_r^2 \Phi_\ell = -\frac{2\, g\, \alpha}{r} \left(\chi_\ell - \frac{1}{r}\, U_\ell \right) \tag{2.59}
$$

This yields

$$
\begin{aligned}
&\frac{2\, g\, \alpha}{r} \left(\chi_\ell - \frac{1}{r}\, U_\ell \right) + \nabla^2 \left(\frac{\beta}{\alpha}\, \chi_\ell - g\, U_\ell \right) \\
&+ \left(g - \frac{\beta}{\alpha} \right) \frac{1}{r}\, \partial_r \left(r^2 \chi_\ell \right) + \frac{\mu}{\alpha}\, \frac{\ell(\ell+1)}{r}\, H_\ell = 0
\end{aligned}
\tag{2.60}
$$

Let us now suppose that the six linearly independent solutions of Eqs. (2.57) and (2.60) may have the following form

$$
U_\ell = u\, r^z \tag{2.61}
$$

$$
V_\ell = v\, r^z \tag{2.62}
$$

with u, v and z as constants, and substitute these trial solutions. From Eqs. (2.57) and (2.60), we thus obtain

$$
\frac{\mu}{\alpha}\, r^{z-1} \left\{ u \left[Z - z\,(\zeta+1) - 2\,\zeta \right] - v \left[Z\, z - \ell(\ell+1)\,(1+\zeta) \right] \right\} = 0 \tag{2.63}
$$

$$
\begin{aligned}
\frac{\mu}{\alpha}\, r^{z-2} \Bigg\{ & u \left[\frac{g\,\alpha}{\mu}\, (Z+2)(z+1) + (Z-2)(z+1)\,\zeta - \ell(\ell+1)(\zeta+1) \right] \\
& - v\, \ell(\ell+1) \left[\frac{g\,\alpha}{\mu}\, (Z+2) + Z\,\zeta - (\zeta+1)(z+1) \right] \Bigg\} = 0
\end{aligned}
\tag{2.64}
$$

Here, Z is the second order polynomial in z

$$
Z = z^2 + z - \ell(\ell+1) \tag{2.65}
$$

and ζ is given by

$$
\zeta = \frac{\beta - g\,\alpha}{\mu} \tag{2.66}
$$

Since it has been possible to collect the dependence on the radial variable r in Eqs. (2.63) and (2.64), the latter can be seen as equations for the constants u, v and z. Solving Eq. (2.63) for v, we obtain

$$v = u \, \frac{Z - z\,(\zeta + 1) - 2\,\zeta}{Z\,z - \ell(\ell + 1)\,(1 + \zeta)} \tag{2.67}$$

and, using this in Eq. (2.64), after some straightforward algebra, it yields the following third-order polynomial in Z

$$a_0 + a_1\,Z + a_2\,Z^2 + Z^3 = 0 \tag{2.68}$$

with a_0, a_1 and a_2 being constant coefficients, which depend solely on the material parameters and the harmonic degree ℓ

$$a_2 = 4\,\frac{g\,\alpha}{\beta} - 2 \tag{2.69}$$

$$a_1 = \ell(\ell + 1)\left(\frac{g\,\alpha}{\beta}\,(\zeta + 3) - 4\right) \tag{2.70}$$

$$a_0 = 2\,\ell(\ell + 1)\,\frac{g\,\alpha}{\beta}\,(\zeta - 1) \tag{2.71}$$

In order to satisfy Eq. (2.68), Z has to be one of the three roots Z_j, with $j = 1, 2, 3$, of the third-order polynomial of the LHS. We do not report here the lengthy expressions for Z_j. However, we note that they only depend on the harmonic degree ℓ and on the material parameters of the self-compressed compressible sphere via $g\,\alpha/\beta$ and ζ. Then, by considering that Z is a second order polynomial in the constant z, the latter can assumes only two values z_j and z_{j+3} for each root Z_j

$$z_j = -\frac{1}{2}\left(1 + \sqrt{1 + 4\,(\ell(\ell + 1) + Z_j)}\right) \tag{2.72}$$

$$z_{j+3} = -\frac{1}{2}\left(1 - \sqrt{1 + 4\,(\ell(\ell + 1) + Z_j)}\right) \tag{2.73}$$

We thus have obtained six constants z_j that, once substituted into Eqs. (2.61), (2.62) and (2.67), yield six linearly independent solutions of the two differential Eqs. (2.63)–(2.64)

$$U_\ell = \sum_{j=1}^{6} u_j\,r^{z_j} \tag{2.74}$$

$$V_\ell = \sum_{j=1}^{6} u_j\,v_j r^{z_j} \tag{2.75}$$

where u_j are the constants of integration and, according to Eq. (2.67), v_j are given by

$$v_j = \frac{Z_j - z_j\,(\zeta+1) - 2\,\zeta}{Z_j\,z_j - \ell(\ell+1)\,(1+\zeta)} \tag{2.76}$$

Since Z_j has been defined only for $j = 1, 2, 3$, we impose that Z_4, Z_5 and Z_6 coincide with Z_1, Z_2 and Z_3.

The solution for the gravitational potential $\Phi_{\ell m}$ is obtained by substituting Eqs. (2.74)–(2.75) into the Poisson equation (2.59). This yields the following non-homogeneous differential equation of the second order in $\Phi_{\ell m}$

$$\nabla^2\Phi_\ell = -2\sum_{j=1}^{6} u_j\,r^{z_j-2}\,g\,\left[(z_j+1) - \ell(\ell+1)\,v_j\right] \tag{2.77}$$

It is solved by the particular solution

$$\Phi_\ell = \sum_{j=1}^{6} u_j\,p_j\,r^{z_j} \tag{2.78}$$

with

$$p_j = 2\,g\,\frac{\ell(\ell+1)(1-\zeta) - Z_j^2}{Z_j\,(Z_j\,z_j - \ell(\ell+1)\,(\zeta+1))} \tag{2.79}$$

and by the two solutions of the homogenenous differential equation (i.e., the Laplace equation)

$$\Phi_\ell = c\,r^\ell + c^*\,r^{-(\ell+1)} \tag{2.80}$$

with c and c^* being constants of integration. The latter, however, must not be considered. Indeed they solve neither the radial nor the tangential components of the momentum Eqs. (2.12)–(2.13), once set $U_{\ell m}$ and $V_{\ell m}$ to zero. This is due to the fact that we have already used the Poisson equation (2.59) to obtain Eq. (2.60) from Eq. (2.58).

Within the solid mantle of the self-compressed compressible model, on the basis of Eqs. (2.74), (2.75) and (2.78), the spheroidal vector solution $\boldsymbol{y}$ defined in Eq. (1.92) yields

$$\boldsymbol{y}_\ell(r) = \mathbf{Y}_\ell(r)\,\mathbf{C} \tag{2.81}$$

where $\mathbf{Y}_\ell$ and $\mathbf{C}$ are the so called fundamental matrix for the self-compressed compressible sphere and the vector of constants of integration

$$\mathbf{Y}_\ell = \left(\boldsymbol{y}_\ell^{(1)}, \boldsymbol{y}_\ell^{(2)}, \boldsymbol{y}_\ell^{(3)}, \boldsymbol{y}_\ell^{(4)}, \boldsymbol{y}^{(5)}, \boldsymbol{y}_\ell^{(6)}\right) \tag{2.82}$$

$$\mathbf{C} = (u_1, u_2, u_3, u_4, u_5, u_6)^T \tag{2.83}$$

with $\boldsymbol{y}^{(j)}$ being the six linearly independent solutions

$$\boldsymbol{y}_\ell^{(j)}(r) = \begin{pmatrix} r^{z_j} \\ v_j\, r^{z_j} \\ \left[\beta\, z_j + 2\,\lambda - \ell(\ell+1)\, v_j\, \lambda\right] r^{z_j-1} \\ \mu\left[1 + (z_j - 1) v_j\right] r^{z_j-1} \\ p_j\, r^{z_j} \\ \left[2\, g + (z_j + \ell + 1)\, p_j\right] r^{z_j-1} \end{pmatrix} \tag{2.84}$$

Note that the fundamental matrix $\mathbf{Y}_\ell$ describes the dependence on the radial distance from the Earth's centre r of the propagator matrix $\mathbf{\Pi}_\ell$, which solves the homogeneous differential system (1.159). We have

$$\mathbf{\Pi}_\ell(r, r') = \mathbf{Y}_\ell(r)\, \mathbf{Y}_\ell^{-1}(r') \tag{2.85}$$

This result can be used to solve more sophisticated models composed of different layers within the mantle, each with different (but constant) shear and bulk moduli, and viscosities. Nevertheless, the density profile must be the same given by Eq. (2.50). It is sufficient to use the fundamental matrix $\mathbf{Y}_\ell$ to obtain the propagator matrix $\mathbf{\Pi}_\ell$ in each layer and, then, impose chemical boundary conditions at the internal interfaces for propagating the solution from the inner to the outer layers. In this way, the self-compressed compressible sphere also takes into account the contrasts of the rheological parameters at the main Earth's interfaces, but not the density contrasts.

2.5.2 *The Relaxation Spectrum of the Self-compressed Compressible Sphere*

Let us now consider the self-compressed compressible sphere with compressional stratification, that we denote with CC_0, where the compositional coefficient is zero, $\gamma = 0$. The viscoelastic mantle is characterized by shear modulus $\mu = 1.45 \times 10^{11}$ Pa and viscosity $\nu = 10^{21}$ Pa s. The radius of the core is 3480 km and the Earth's radius is 6371 km. In order to respect the total Earth's mass $M_E = 5.97 \times 10^{24}$ kg, the density profile given by Eq. (2.50) is characterized by $\alpha = 2.34 \times 10^{10}\,\mathrm{kg/m^2}$ and, from Eq. (2.53), the compressional bulk modulus is $\kappa_0 = 2.23 \times 10^{11}$ Pa, which is comparable to the range of PREM bulk modulus in the transition zone, from 1.53×10^{11} Pa to 2.56×10^{11} Pa. The resulting density of the core is $10096.3\,\mathrm{kg/m^3}$, which differs by 8 % from the volume-averaged PREM density of the core and its density profile within the mantle differs from that of PREM by 9, 6 and 21 % at the Moho discontinuity, the 670 km discontinuity and the core-mantle boundary, respectively. Nevertheless, the model density differs from PREM by 41 % at the Earth's surface, due to the compositional decrease of the Earth's density within the crust.

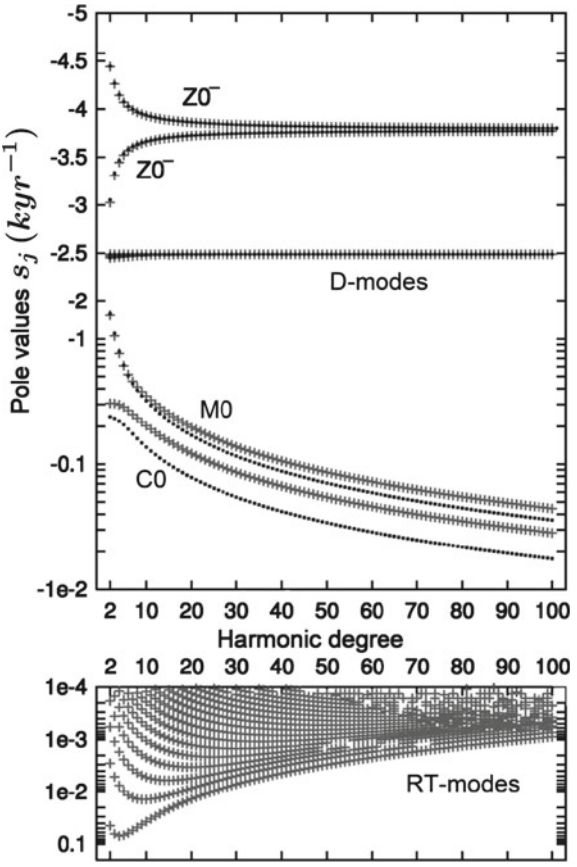

Fig. 2.7 Pole values s_j of the relaxation modes of the models CC_0 (*dot points*) and MC (*cruciform points*). The inverse Maxwell and compressional transient times of both models are $\tau^{-1} = 4.58\,\mathrm{kyr}^{-1}$ and $\varsigma^{-1} = 2.49\,\mathrm{kyr}^{-1}$

In Fig. 2.7 we compare the relaxation spectra (up to the harmonic degree $\ell = 100$) of the self-compressed compressible sphere with compressional stratification, CC_0, and of a two layered compressible model, that we denote with MC, consisting of homogeneous core and mantle, where the material parameters are constant and obtained from the model CC_0 by means of volume averages, with mantle density of $4623\,\mathrm{kg/m^3}$. Note that these two models share the $M0$ and $C0$ buoyancy modes, the pair of compressional transient modes, $Z0^+$ and $Z0^-$, and the dilatational modes (also abbreviated as D-modes). The pair of compressional transient modes, $Z0^+$ and $Z0^-$, have been identified and discussed for the first time in Cambiotti et al. (2009) in the case of layered compressible models. Nevertheless, only the layered model MC has the Rayleigh–Taylor modes (also abbreviated as RT-modes) that are, indeed, absent in the relaxation spectrum of the self-compressed model CC_0.

The transient relaxation spectra of the models CC_0 and MC, characterized by the D-modes and the pair of the modes $Z0^+$ and $Z0^-$, differ mainly at low harmonic degree, while the differences decrease at high harmonic degrees. Instead, the $C0$ buoyancy mode presents important differences at all harmonic degrees and the $M0$

buoyancy mode agrees only at the first 10 harmonic degrees. Such a circumstance is due to the different density profiles of the two models, since the elastic parameters and the viscosity are the same. We thus safely argue that the differences in the pole values are caused by the different density contrasts of the two models at the core-mantle interface and Earth's surface, respectively, which affect mainly the buoyancy modes $C0$ and $M0$.

Let us now consider two representative self-compressed compressible spheres characterized by stable and unstable compositional stratifications, where the bulk modulus κ differs from the compressional bulk modulus κ_0. Contributions from compositional and non-adiabatic stratification do not amount to more than 10–20 % of that of the compressional stratification (Birch 1952, 1964; Wolf and Kaufmann 2000); we assume bulk modulus of 2.62×10^{11} and 1.94×10^{11} Pa to describe stable and unstable compositional stratifications, respectively. They correspond to values of -0.15 and 0.15 for the parameter ϵ, Eq. (2.55), and, in this respect, we denote these two models with $\mathrm{CC}_{-0.15}$ and $\mathrm{CC}_{0.15}$.

Figure 2.8 compares the relaxation spectra of the self-compressed compressible spheres with compressional and compositional stratifications. Note that the compositional models $\mathrm{CC}_{-0.15}$ and $\mathrm{CC}_{0.15}$ share the same relaxation modes of the compressional model CC_0, but they have further relaxation modes that are infinite denumerable, with the origin of the Laplace domain as cluster point. The latter relaxation modes are stable for $\epsilon = -0.15$ and unstable for $\epsilon = 0.15$, in agreement with the analysis of the gravitational stability based on the sign of the Brunt–Väisälä frequency ω^2, Eq. (2.56). They thus describe relaxation processes involved by the compositional stratification and, for this reason, we called them compositional modes (also abbreviated as C-modes). With respect to the common relaxation modes of the three models, we note that they differ mainly in the transient region where the characteristic relaxation times of the D-modes and of the pair of transient compressional modes $\mathrm{Z0}^+$ and $\mathrm{Z0}^-$ of the models $\mathrm{CC}_{-0.15}$ and $\mathrm{CC}_{0.15}$ are greater and lower than those of the the model CC_0, reflecting the different compressional transient times ς, Eq. (1.193), that decrease for increasing bulk modulus, 0.43, 0.40 and 0.37 kyr for $\epsilon = -0.15,\ 0$ and 0.15.

2.5.3 *The Compositional Modes*

The denumerable set of C-modes originates from the oscillating behavior of the secular determinant $D_\ell(s)$ near the origin. It occurs on the positive or negative real axis of the Laplace domain, depending on the sign of the compositional coefficient γ. Such a behavior is like that of the secular determinant of layered compressible models to which the Rayleigh–Taylor modes are associated, with the exception that the RT-modes are always unstable because layered compressible Earth's models have always an unstable compositional stratification.

Let us now derive an approximated analytical expression for the pole values of the C-modes. After substitution of the analytical expression for the propagator matrix

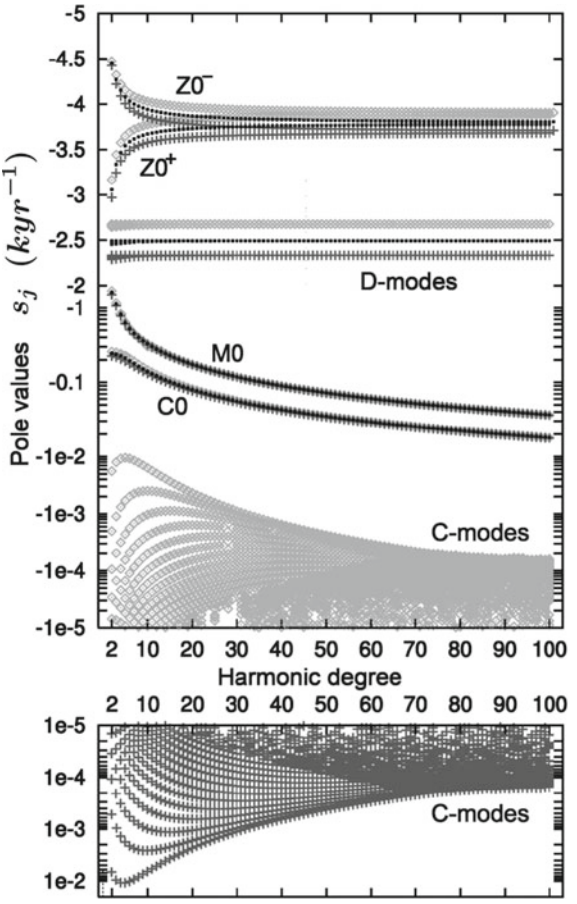

Fig. 2.8 Pole values s_j of the relaxation modes of the models CC_0 (*dot points*), $CC_{-0.15}$ (*diamond points*) and $CC_{0.15}$ (*cruciform points*). The inverse Maxwell relaxation time of all three models is $\tau^{-1} = 4.58\,\mathrm{kyr}^{-1}$ while the inverse compressional relaxation times are $\varsigma^{-1} = 2.49,\ 2.67$ and $2.33\,\mathrm{kyr}^{-1}$, respectively

$\mathbf{\Pi}_\ell$ of the self-compressed compressible sphere, Eq. (2.85) into the expression for the secular determinant D, Eq. (1.199), and after expansion in Taylor series of the function $\hat{\mu}(s)$, Eq. (1.54), we obtain that the dominant terms of the secular determinant D is proportional to

$$D_\ell(s) \propto \left(\frac{a}{r_C}\right)^{i\left(\frac{\kappa_0\,\ell(\ell+1)\,\epsilon}{\hat{\mu}(s)}\right)^{\frac{1}{4}}} - 1 \tag{2.86}$$

By equating to zero the RHS of Eq. (2.86), we thus obtain the following approximated analytical expression for the roots of the secular equation (1.200), which are the poles s_{C_m} of the compositional modes

$$s_{C_m} = -\ell(\ell+1)\,\frac{\kappa_0\,\epsilon}{\nu}\left(\frac{\log\left(\frac{r_C}{a}\right)}{\pi\, m}\right)^4 + O(m^{-6}) \tag{2.87}$$

for $m = 1, \ldots, \infty$. It confirms that the compositional modes are an infinite denumerable set of relaxation modes and that the origin of the Laplace domain, $s = 0$, is the cluster point of the poles s_{C_m} for $m \to \infty$ since they converge to zero as m^{-4}. Besides this, the dependence of Eq. (2.87) on the parameter ϵ gives us the possibility to show analytically that a little deviation from the completely compressional stratification is sufficient to activate the compositional modes. Particularly, they are stable if $\epsilon > 0$ and unstable if $\epsilon < 0$. This suggests that the Rayleigh–Taylor modes are actually a particular case of the compositional modes and that the compositional modes describe buoyancy relaxation processes arising from deviations of the stratification from the neutral state of equilibrium. This interpretation is furthermore supported by the characteristic relaxation times of the compositional and Rayleigh–Taylor modes. As shown in Figs. 2.7 and 2.8, their upper limits are of similar order of magnitude, that is greater than $10–10^2$ kyr. This short time scales, however, are due to the use of simplified models. Indeed, more realistic Earth's models based on PREM predict much larger characteristic relaxation times of order 1–100 Myr (Plag and Jüttner 1995; Vermeersen and Mitrovica 2000).

These findings contrast with the interpretation of Han and Wahr (1995) that a continuous density profile yields a continuous spectrum of buoyancy modes. This interpretation was based on the investigation of the relaxation spectrum of layered compressible models, where each density contrast contributes with a buoyancy mode Mi. For very fine layered models, where small density contrasts are introduced in order to simulate the continuous variations of the PREM density, the number of buoyancy modes Mi is large. This large number of modes was interpreted by Han and Wahr (1995) as evidence that continuous variations of the initial density imply a continuous set of buoyancy modes in the region of small Laplace variable s. In view of the relaxation spectrum of the self-compressed compressible sphere, however, we can say that this is not the case. Indeed, despite the continuous variations of the initial density described by the Darwin-law profile, Eq. (2.50), it is remarkable that no additional buoyancy modes other than the $M0$ and $C0$ modes are present in the compressional model CC_0 and that only a discrete, although infinite denumerable, set of compositional modes are triggered by compositional stratifications.

Even if Han and Wahr (1995) supported the normal mode approach, we note that their conclusion about the presence of a continuous spectrum in the buoyancy region has weakened the normal mode approach, discouraging further investigations of the relaxation spectrum for not layered Earth's models, where the continuous variations of the material parameters within the layers of the Earth are taken into account. On the contrary, our results indicate that such an analysis can be done and interesting physical knowledge of the viscoelastic relaxation processes at large timescales can be obtained as we will show in Sect. 2.6.

2.6 Viscoelastic Perturbations Due to Surface Loading

In order to investigate the role of the initial state of the viscoelastic Earth's model, characterized by compressional or compositional stratifications, we focus on Love numbers $\boldsymbol{k}$ for loads seated at the Earth's surface (we will omit the superscript L and the harmonic degree ℓ to not overwhelm the text): they are relevant in Glacial Isostatic Adjustment (GIA) studies. We consider herein perturbations within the mantle for which the Love numbers for surface loading in the Laplace s-domain read, according to Eqs. (1.172), (1.177) and (1.179)

$$\tilde{\boldsymbol{k}}(r,s) = \mathbf{N}_L^{-1}\,\mathbf{B}_\ell(r)\,\mathbf{b}^L\big|_{\mu=\hat{\mu}(s)} \tag{2.88}$$

with the tilde standing for the Laplace transform and the dimensional matrix $\mathbf{N}_L$ given by Eq. (1.174). According to Eq. (1.179), $\tilde{\boldsymbol{k}}(r,s)$ provides $\tilde{h}, \tilde{l}$ and $\tilde{k}$, the radial, tangential and gravitational viscoelastic Love numbers in the Laplace domain and their dependence on the radial distance from the Earth's centre r refers to where we calculate the perturbations. In this respect, note that the matrix $\mathbf{B}_\ell$ also depends on r, according to Eq. (1.172).

In view of the study of relaxation spectrum of the self-compressed compressible sphere, the viscoelastic Love numbers can be recast by a spectrum of relaxation modes

$$\tilde{\boldsymbol{k}}(r,s) = \boldsymbol{k}_E(r) + \sum_{j\in\mathcal{S}} \frac{\boldsymbol{k}_j(r)}{s - s_j} \tag{2.89}$$

where $\boldsymbol{k}_E$ consists of the elastic Love numbers, $\boldsymbol{k}_j$ contains the residues of the jth relaxation mode and s_j is the corresponding pole. Here, $\mathcal{S}$ denotes the whole set of relaxation modes, which is denumerable but infinite (Cambiotti and Sabadini 2010). The set $\mathcal{S}$ of relaxation modes is split into two types:

$$\mathcal{S} = \mathcal{F} \cup \mathcal{C} \tag{2.90}$$

The set $\mathcal{F}$ of fundamental modes appears both for compressional and compositional stratifications: the M0 and C0 buoyancy modes (associated with the Earth's surface and CMB), the pair of transient compressible modes, Z_- and Z_+, and the infinite and denumerable set of dilatational modes, D_m, with $m = 1, \ldots, \infty$. The set $\mathcal{C}$ of compositional modes, C_m, with $m = 1, \ldots, \infty$ is again denumerable and infinite but is triggered only in the case of compositional stratifications.

The fundamental modes describe the transition from the elastic to the Newtonian-fluid behavior, while the compositional modes control the long time-scale perturbations towards the isostatic equilibrium described by the inviscid fluid. Accordingly, we split the perturbations $\mathbf{K}$, due to a point-like surface load of unit mass with Heaviside time history, into contributions describing the elastic response, the transition to the Newtonian fluid and the final transition towards the isostatic equilibrium

$$\boldsymbol{K}(r,t) = \begin{pmatrix} U(r,t) \\ V(r,t) \\ \Phi(r,t) \end{pmatrix} =$$

$$\boldsymbol{k}_E(r) - \sum_{j\in\mathcal{F}} \frac{\boldsymbol{k}_j(r)}{s_j}\left(1 - e^{s_j t}\right) - \sum_{m\in\mathcal{C}} \frac{\boldsymbol{k}_{\mathrm{C_m}}(r)}{s_{\mathrm{C_m}}}\left(1 - e^{s_{\mathrm{C_m}} t}\right) \tag{2.91}$$

where U, V and Φ are the degree-ℓ non-dimensional radial and tangential displacements (normalized by a/M_E), and gravitational potential perturbation (normalized by $a\,g/M_E$). In view of the fact that the poles s_j of the fundamental modes are negative and that their characteristic relaxation times, $\left|1/s_j\right|$, are shorter than those of the compositional modes, $|1/s_{\mathrm{Cm}}|$, we can write the final transition towards the isostatic equilibrium as

$$\boldsymbol{K}(r,t) = \boldsymbol{k}_S(r) + \boldsymbol{K}_C(r,t) \tag{2.92}$$

where $\boldsymbol{k}_S$ is the secular perturbation due to the elastic response and the relaxation of the fundamental modes

$$\boldsymbol{k}_S(r) = \boldsymbol{k}_E(r) - \sum_{j\in\mathcal{F}} \frac{\boldsymbol{k}_j(r)}{s_j} \tag{2.93}$$

and where $\boldsymbol{K}_C$ is the perturbation due to the only compositional modes

$$\boldsymbol{K}_C(r,t) = \begin{pmatrix} U_C(r,t) \\ V_C(r,t) \\ \Phi_C(r,t) \end{pmatrix} = -\sum_{m=1}^{\infty} \frac{\boldsymbol{k}_{C_m}(r)}{s_{C_m}}\left(1 - e^{s_{C_m} t}\right) \tag{2.94}$$

As compressional stratifications have no compositional modes, the viscoelastic Love number $\tilde{\boldsymbol{k}}(s)$ is an analytic function in a neighbourhood of the origin of the Laplace domain, $s = 0$. Thus, $\tilde{\boldsymbol{k}}(s = 0)$ exists and is finite. From Eqs. (2.89) and (2.93), we obtain the following identity

$$\boldsymbol{k}_S(r) = \tilde{\boldsymbol{k}}(r, s = 0) \tag{2.95}$$

This implies that the summation over the strengths $\boldsymbol{k}_j/s_j$ of the fundamental modes entering Eq. (2.93) converges to a finite value. Furthermore, the secular perturbations describe the isostatic equilibrium to surface loading (Wu and Peltier 1982). In this respect, the secular radial displacement and gravitational-potential perturbation satisfy the isostatic conditions at the Earth's surface a

$$\lim_{t\to\infty} U(a,t) = h_S(a) = -\frac{2\,\ell + 1}{2} \tag{2.96}$$

$$\lim_{t\to\infty} \Phi(a,t) = k_S(a) = -1 \tag{2.97}$$

Perturbations below the Earth's surface, as well as the tangential displacement at the Earth's surface, are instead unconstrained due to the indeterminateness of static perturbations of the inviscid body discussed by (Longman 1962, 1963). They must be obtained solving the whole viscoelastic problem and using Eq. (2.93).

2.7 Toroidal Solution

The toroidal vector solution Eq. (1.101) does not depend whether the material is compressible or incompressible. In fact, the only material parameter entering the toroidal component of the momentum Eq. (1.86) is the rigidity μ. By assuming the latter constant within each layer of the Earth's model, $\partial_r \mu = 0$, Eq. (1.86) simplifies into

$$\mu \, \nabla_r^2 W_\ell = 0 \tag{2.98}$$

This is the Laplacian equation for $W_{\ell m}$ and the two independent solutions are

$$W_\ell = c \, r^\ell + c^* \, r^{-(\ell+1)} \tag{2.99}$$

with c and c^* as integration constants. By substituting Eq. (2.99) into Eq. (1.81), we obtain the solutions for the toroidal component of the stress

$$T_\ell = c\mu \, (\ell - 1) \, r^{\ell-1} - c^* \mu \, (\ell + 2) \, r^{-\ell-2} \tag{2.100}$$

and, thus, we can write the toroidal solution vector as follows

$$\boldsymbol{y}_\ell(r) = \mathbf{Y}_\ell(r) \, \boldsymbol{C} \tag{2.101}$$

where $\mathbf{Y}_\ell$ is the fundamental matrix for toroidal deformations

$$\mathbf{Y}_\ell = \begin{pmatrix} r^\ell & r^{-\ell-1} \\ \mu \, (\ell - 1) \, r^{\ell-1} & -\mu \, (\ell + 2) \, r^{-\ell-2} \end{pmatrix} \tag{2.102}$$

and $\boldsymbol{C}$ is the vector of integration constants

$$\boldsymbol{C} = \left(c, c^*\right)^T \tag{2.103}$$

$$\boldsymbol{y}_\ell(r_C) = \mathbf{I}_C \, \boldsymbol{C}_c \tag{2.104}$$

2.8 Time Dependent Loading Love Numbers

When our Earth's models are forced by loading or tidal forcing, the Green functions are named Love numbers, for loads and tidal potentials. Love numbers can in principle be generalized to earthquake forcing. In this Section we consider only the loading case, since the tidal case will be considered in Chap. 3 when dealing with the readjustment of the rotational bulge in Sect. 3.6. Figure 2.9 portrays the time evolution in $\log(t)$ of the convolution between the Love numbers and the Heaviside function, given by Eq. (2.94). The time interval spans a wide range of time scales, from one tenth of an year to 10^3 Gyr. The Love numbers are all amplified in time,

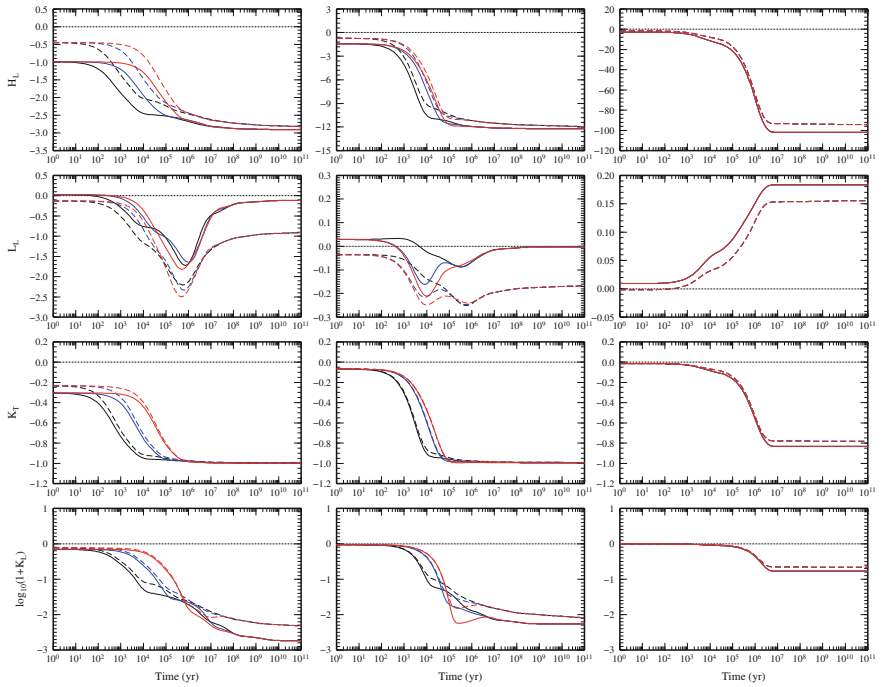

Fig. 2.9 Loading Love numbers convolved with the Heaviside function, from the elastic limit, *left*, to the fluid (long time) limit, *right*, in the abscissa. Columns from *left* to *right*, refer to the harmonic degree $\ell = 2, 10, 100$. The *first row* stands for the radial Love number H_ℓ, the *second row* for the tangential Love number L_ℓ, the *third row* for the gravitational potential Love number K_ℓ and the *bottom fourth row* stands for the gravitational potential $log(1 + K_\ell)$, including the direct effect of the unitary load. Capital letters are used since the Love numbers are convolved with the Heaviside function. *Continuous* and *dashed curves* stand for compressible and incompressible models, all based on PREM stratification. The viscosity in each layer below the 80 km thick elastic lithosphere is fixed at 10^{21} Pa s in the *upper mantle*. In the *lower mantle*, the viscosity is 10^{21} Pa s, *black*, 10^{22} Pa s, *blue* and 10^{23} Pa s, *red*

from the elastic limit in the left of the abscissa to the fluid (long time) limit, right in the abscissa, due to viscoelastic relaxation: in terms of normal modes, such an amplification is caused by the decay of the exponentials $\left(1 - e^{s_i t}\right)$ in Eq. (2.94) which sum up to the elastic contribution.

The largest differences among the various models, in terms of incompressible versus compressible or low versus high lower mantle viscosities, occur for the lowermost harmonic degree $\ell = 2$ both for the elastic limit and transients, and such differences tend to diminish for $\ell = 100$, with the three viscosity models becoming indistinguishable. The $\ell = 2$ is in fact sensitive to the global properties of the Earth, in terms of elastic, density and viscosity stratification, while the sensitivity of the highest harmonics is limited to the outermost properties of the Earth.

The $\ell = 2$ Love numbers show clearly the effects of lower mantle viscosity increase from 10^{21} to 10^{23} Pa s, causing the corresponding increase from 10^3 to 10^5 yr for global mantle relaxation, during which Love numbers are amplified. It is also notable that H_ℓ and K_ℓ portray a monotonic increase carrying the same sign, while the horizontal Love number L_ℓ portrays a non-monotonic behavior, changing also the sign when increasing the harmonic degree. It is also notable that incompressibility, dashed lines, impacts in particular the horizontal Love number, and so the component of the displacement field for surface loads, in the whole range of time windows, from the elastic limit, through the intermediate time scales when the Love numbers are amplified, to the fluid (long time) limit. It is interesting to look at the effects of viscosity changes in the outermost part of the planet, in the asthenosphere, as in Fig. 2.10. A striking difference from Fig. 2.9 is that the highest harmonic $\ell = 100$ is sensitive to the viscosity of the outermost part of the Earth as visible in the third column, to confirm that the longest wavelengths sample the deepest mantle, and the shortest ones the shallowest portion of the Earth. For $\ell = 100$, in particular the compressible Earth portrays for the three Love numbers H_l, L_l, K_l an important sensitivity to the asthenospheric viscosity, with time scales in the amplification of the Love numbers ranging from 10^1 to 10^4 yr, corresponding to a viscosity increase from 10^{19} to 10^{21} Pa s.

The horizontal Love number L_ℓ and $\ell = 10$ portrays a variability in time at shorter time scales once compared to Fig. 2.9, with the amplification starting at $t = 3$ yr instead of $t = 10^2$ yr. The Love number K_ℓ for $\ell = 2, 10$ is not sensitive to the asthenospheric viscosity, since the gravitational field is most affected by the properties of the mantle as in Fig. 2.9, while the quantity $1 + K_\ell$ is sensitive to the outermost asthenospheric viscosity, but solely when K_ℓ, for $\ell = 2, 10$, is close to its long term (fluid) value -1.

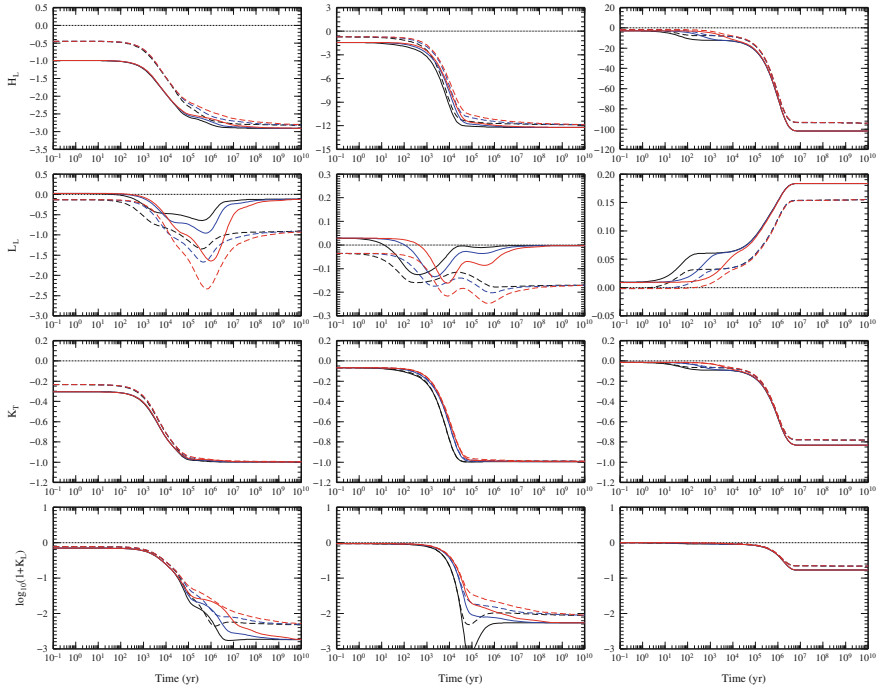

Fig. 2.10 As Fig. 2.9, except for viscosity changes in the 200 km asthenosphere below the 80 km thick elastic lithosphere. Note that the abscissa with respect to Fig. 2.9 has been lowered by one order of magnitude. *Black*, *blue* and *red curves* stand for 10^{19}, 10^{20} and 10^{21} Pa s in the asthenosphere. The viscosity is 10^{21} Pa s in the *upper mantle* below the asthenosphere and 10^{22} Pa s in the *lower mantle*

It is interesting to note that the viscosity of the asthenosphere affects to some extent also the slowest time scales, due to the interplay between the viscosity and the density stratification in the outermost part of the Earth.

References

Birch, F. (1952). "Elasticity and constitution of the Earth's interior". In: *J. Geophys. Res*. 57, pp. 227–286.

Birch, F. (1964). "Density and composition of mantle and core". In: *J. Geophys. Res*. 69, pp. 4377–4388.

Cambiotti, G., V.R. Barletta, A. Bordoni, and R. Sabadini (2009). "A comparative analysis of the solutions for a Maxwell Earth: the role of the advection and buoyancy force". In: *Geophs. J. Int.* 176, pp. 995–1006.

Cambiotti, G. and R. Sabadini (2010). "The compressional and compositional stratifications in Maxwell Earth models: the gravitational overturning and the long-period tangential flux". In: *Geophys. J. Int*. 180, pp. 475–500.

Devoti, R., V. Luceri, C. Sciarretta, G. Bianco, G. Di Donato, L.L.A. Vermeersen, and R. Sabadini (2001). "The SLR secular gravity variations and their impact on the inference of mantle rheology and lithospheric thickness". In: *Geophys. Res. Lett*. 28, pp. 855–858.

Gilbert, F. and G. Backus (1968). "Elastic-gravitational vibrations of a radially stratified sphere". In: *Dynamics of Stratified Solids*. Ed. By G. Herrmann. American Society of Mechanical Engineers, New York, pp. 82–95.

Han, D. and J. Wahr (1995). "The viscoelastic relaxation of a realistically stratified earth, and a further analysis of postglacial rebound". In: *Geo-phys. J. Int*. 120, pp. 278–311.

Karato, S. (1989). "Plasticity-crystal structure systematics in dense oxides and its implications for the creep strength of the earth's deep interior: A preliminary result". In: *Phys. Earth Planet. Inter*. 55, pp. 234–240.

Lambeck, K., P. Johnston, and M. Nakada (1990). "Holocene glacial rebound and sea-level change in NW Europe". In: *Geophys. J. Int*. 103, pp. 451–468.

Longman, I.M. (1962). "A Green's function for determining the deformation of the earth under surface mass loads-1. Theory". In: *J. Geophys. Res*. 67, pp. 845–850.

Longman, I.M. (1963). "A Green's function for determining the deformation of the earth under surface mass loads-2. Computations and numerical results". In: *J. Geophys. Res*. 68, pp. 485–496.

Love, A.E.H. (1911). *Some Problems of Geodynamics*. Dover reprint, New York, 1967.

Meade, C. and R. Jeanloz (1990). "The strength of mantle silicates at high pressures and room temperatures: Implications for the viscosity of the mantle". In: *Nature* 348, pp. 533–535.

Plag, H.-P. and H.-U. Juttner (1995). "Rayleigh-Taylor instabilities of a self-gravitating Earth". In: *J. Geodyn.* 20, pp. 267–288.

Sabadini, R., D.A. Yuen, and E. Boschi (1982). "Polar wandering and the forced responses of a rotating, multilayered, viscoelastic planet". In: *J. Geophys. Res*. 87, pp. 2885–2903.

Spada, G., R. Sabadini, D.A. Yuen, and Y. Ricard (1992). "Effects on post-glacial rebound from the hard rheology in the transition zone". In: *Geophys. J. Int*. 109, pp. 683–700.

Spada, G., D.A. Yuen, R. Sabadini, P.J. Morin, and P. Gasperini (1990). "A computer-aided, algebraic approach to the post-glacial rebound problem". In: *Mathematica J*. 1, pp. 65–59.

Vermeersen, L.L.A. and J.X. Mitrovica (2000). "Gravitational stability of spherical self-gravitating relaxation models". In: *Geophys. J. Int*. 142, pp. 351–360.

Vermeersen, L.L.A. and R. Sabadini (1999). "Polar wander, sea-level variations and Ice Age cycles". In: *Surv. Geophys*. 20, pp. 415–440.

Vermeersen, L.L.A., R. Sabadini, and G. Spada (1996b). "Compressible rotational deformation". In: *Geophys. J. Int*. 126, pp. 735–761.

Wolf, D. and G. Kaufmann (2000). "Effects due to compressional and compositional density stratification on load-induced Maxwell viscoelastic perturbations". In: *Geophys. J. Int*. 140, pp. 51–62.

Wu, P. and W.R. Peltier (1982). "Viscous gravitational relaxation". In: *Geophys. J. R. Astron. Soc*. 70, pp. 435–485.

Chapter 3
Rotational Dynamics of Viscoelastic Planets: Linear Theory

Abstract The linearized theory of rotation for viscoelastic planetary bodies, like the Earth, is developed. The MacCullagh's formula linking the inertia and gravitational perturbations is self-consistently derived within our formalism. The concept of True Polar Wander (TPW) is introduced, and attention is devoted to the physics of viscoelastic, rotational bulge readjustment. Different rotation theories that appeared in the literature are compared, including the effects of non-hydrostatic bulge contribution and compressible versus incompressible rotational bulge readjustment. The long-term behavior of the rotation equation is considered, and a linearized theory for TPW driven by mantle convection is provided. The Earth, Mars and Venus are compared in terms of the ability of their rotation axis to wander.

3.1 Introduction to Earth's Rotation

The rotation of the Earth is not regular. It changes on virtually every time scale we know in both position of the rotation axis and rotation rate. Even in our daily lives we sometimes experience the consequences of such changes, such as the second that is subtracted or added to clocks at the beginning of a new year. Although this second is not much more than a curiosity for most of us, the rotational changes that it implies can influence our lives in a more fundamental sense. There are indications that the emergence of the great ice ages some 2 million years ago was triggered by a gradual shift of the rotation axis over the Earth's surface, combined with wandering of the continents and associated changes in ocean currents (note that we are talking here about the onset of ice ages—the period of the 100,000 year cycles of ice build-up and decay is determined by astronomical causes). In the 19th century, both the rate of rotation and the position of the rotation axis were shown to be variable. Nowadays we know that these changes occur on all time scales: from shorter than a day to geological ones of hundreds of millions of years. The changes in position of the rotation axis can be divided into two main categories: those in which the position of the axis changes with respect to the distant stars but not with respect to the Earth's surface, and vice versa. For the latter category, it looks to a hypothetical observer in space as though the Earth shifts underneath its rotation axis as a solid unit while

R. Sabadini et al., *Global Dynamics of the Earth: Applications of Viscoelastic Relaxation Theory to Solid-Earth and Planetary Geophysics*,
DOI 10.1007/978-94-017-7552-6_3

the rotation axis itself remains fixed with respect to the stars, while for an observer on Earth it looks as though the rotation axis is wandering over the Earth's surface. Displacements of the axis of rotation with respect to the fixed stars (changes in which the whole planet is moving rigidly as one unit) are mainly due to external forces, notably the gravitational interactions between the Earth and the Sun, the Moon and the other planets of the Solar System. The astronomically well-known precession and nutation are examples of this. The external forces exert a net torque on the equatorial bulge of the Earth, as a consequence of which the rotation axis spins. The most important periods are about 26,000 years (precession) and 18.6 years (nutation).

Displacements of the axis of rotation with respect to a fixed position on the Earth's surface are mainly due to mass displacements in the interior of the Earth and in the hydrosphere and atmosphere. These mass displacements will generally induce changes in the moments and products of inertia. As the Earth is a deformable body, the rotation axis will readjust itself to the new situation by shifting over the surface. The rotation axis does not change its position with respect to the stars, as during these mass displacements the angular momentum of the Earth is preserved.

Apart from tidal interactions, there are a number of possible mechanisms responsible for the observed rotational variations, like growth and decay of ice sheets, changes in sea-level, ocean currents, winds and changes in the pressure distribution of the atmosphere, seasonal changes, earthquakes, tectonic plate movements, changes in convection of mantle and core, and interactions between the core and mantle. Each of these mechanisms operates on specific time scales and this is reflected in the time scales on which the rotation of the Earth changes.

Table 3.1 gives a rough indication of the observed present-day variations in position of the polar axis. The observed changes in the position of the rotation axis with respect to the Earth's surface consist of two kinds of movements: periodic and linear. The periodic motions consist mainly of two periods. The annual wobble is principally due to seasonally varying zonal winds. The cause of the Chandler wobble is a combination of processes in the oceans and atmosphere. This periodic movement, which is essentially the free precession of the Earth, was theoretically predicted in the 18th century by Euler (therefore it is also called the Eulerian free precession) but not observed until the end of the 19th century.

Figures 3.1 and 3.2 show the motion of the pole and the Length Of Day (LOD) changes. The time series are obtained at the Centro di Geodesia Spaziale (CGS) "G. Colombo" of the Agenzia Spaziale Italiana (ASI) from the Satellite Laser Ranging (SLR) observations on LAGEOS 1, LAGEOS 2, and since mid-2002, Etalon 1 and Etalon 2, applying the state-of-the-art computation models (mostly following the

Table 3.1 Variations in the position of the rotation axis with respect to the crust

Type	Magnitude	Presumed cause
Annual wobble	5 m per year	Atmospheric pressure
Chandler wobble	10 m per 14 months	Not well known
Secular drift	1 m per 10 years	Glacial rebound, mantle convection, large earthquakes

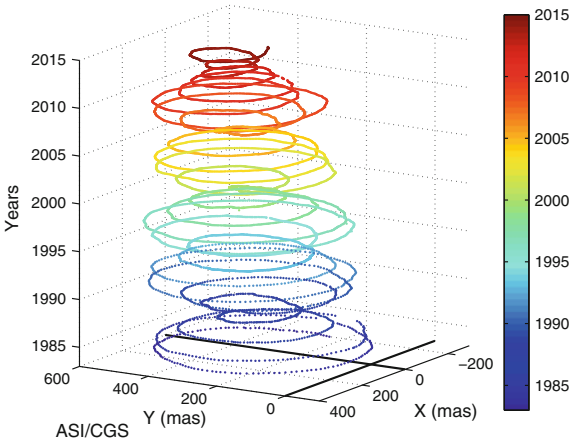

Fig. 3.1 Polar motion, from 1982 to 2015, from ASI/CGS

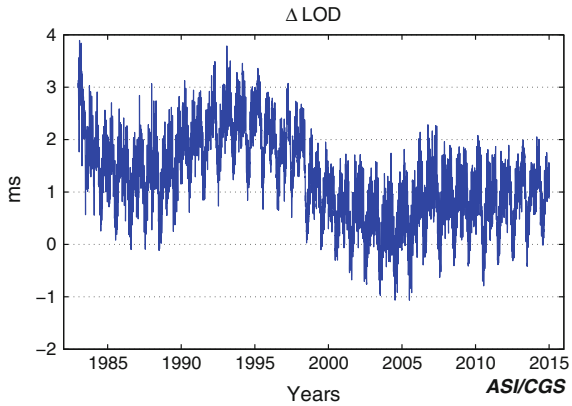

Fig. 3.2 Length of Day variations, from 1982 to 2015, from ASI/CGS

International Earth Rotation and Reference Systems Service, IERS, conventions). The observations are processed in intervals of 7 days to generate a loosely-constrained solution for station coordinates and Earth Orientation Parameters (EOP) (Xp, Yp and LOD), which is the standard solution delivered by ASI/CGS as Official IERS Analysis Centre. The EOPs shown in the figures have been rotated and translated into the ITRF2008 reference frame in order to represent the motion of the rotation axis of the Earth relative to the crust. The Chandler and the annual frequencies are the major components of the motion and give the well known pulsating shape. The contemporary secular drift, whose direction is shown in Fig. 3.1 by the red lines connecting the centre of the wobbling pole, has been determined by astrometric observation. Post Glacial Rebound (PGR), Chap. 4, resulting from the decay of huge ice sheets is thought to be the main cause of this secular drift, although mantle convection and earthquakes (Cambiotti et al. 2016) might also make a contribution.

The observed LOD changes are shown in Fig. 3.2 while the mechanisms that are thought to be responsible for them are indicated in Table 3.2.

Table 3.2 Variations in the length of day

Time scale	Magnitude	Presumed cause
Daily	ms	Atmosphere and tides
Annual	ms	Seasons
Decades	10 ms	Core-mantle coupling
>100 years	2 ms per 100 years	Tidal interaction, glacial rebound, large earthquakes

Short-time LOD fluctuations are very well explained by changes in the pressure distribution over the globe and zonal winds. Changes on time scales of a few tens of years are attributable to the exchange of angular momentum between the fluid outer core and the lower mantle, as they appear to be correlated with changes in magnetic field strength. The tidal exchange of angular momentum between the Earth and the Moon and between the Earth and the Sun is responsible for a long-term trend. The secular decrease of the rotation velocity is due to the fact that the Earth is rotating faster around its axis than the Moon is revolving around the Earth, and because the Earth is not perfectly elastic. As a result, the line connecting the Earth and the Moon does not coincide exactly with the line between the centre of the Earth and the place on the surface that shows the maximum tidal height. This gives a net torque, which brakes the Earth's rotation rate and accelerates the Moon in its orbit around the Earth. As the Earth rotates with a progressively slower rate, the centrifugal force diminishes. As a consequence, the ellipticity of the Earth decreases.

This brief overview shows that the variations in the rotation of the Earth can produce a rich ensemble of geophysical and geodetic phenomena. In this chapter we will first derive the mathematical expressions for polar wander and changes in the length of day for a rigid Earth's model. Then, we will derive the mathematical formalism for the viscoelastic adjustment of the equatorial bulge, which plays an important role in any realistic consideration about the rotation of the Earth.

3.1.1 Liouville Equations

In this section we assume that the Earth is rigidly rotating and that torques, mass displacements and relative motions can perturb the rotation.

If $\mathbf{L}$ denotes the torque, $\mathbf{H}$ the angular momentum and $\boldsymbol{\omega}$ the angular velocity, then in a reference frame co-rotating with the Earth, Euler's dynamic equation reads

$$\frac{d\mathbf{H}}{dt} + \boldsymbol{\omega} \times \mathbf{H} = \mathbf{L} \tag{3.1}$$

where

$$\mathbf{H}(t) = \mathbf{I}(t) \cdot \boldsymbol{\omega} + \mathbf{h}(t) \tag{3.2}$$

in which

$$I_{ij}(t) = \int \rho(r_k r_k \delta_{ij} - r_i r_j) dV \tag{3.3}$$

and

$$\mathbf{h}(t) = \int \rho(\mathbf{r} \times \mathbf{v}) dV \tag{3.4}$$

In these equations $\mathbf{r}$ denotes the coordinates of the mass element characterized by the density ρ, $\mathbf{I}$ is the inertia tensor, I_{ij} denotes the component of $\mathbf{I}$ and the velocity $\mathbf{v}$ occurs with respect to the coordinate system, leading to the relative angular momentum $\mathbf{h}(t)$.

In this book we assume that $\mathbf{v} = 0$, so that $\mathbf{H}$ is simply

$$\mathbf{H} = \mathbf{I} \cdot \boldsymbol{\omega} \tag{3.5}$$

Substituting Eq. (3.5) into Eq. (3.1) leads to the so-called Liouville equation

$$\frac{d}{dt}(\mathbf{I}(t) \cdot \boldsymbol{\omega}) + \boldsymbol{\omega} \times (\mathbf{I}(t) \cdot \boldsymbol{\omega}) = \mathbf{L} \tag{3.6}$$

As above, and in the following, the symbol $\int$ means integration over the volume.

3.2 MacCullagh's Formula

Near the boundary of a body departing slightly from spherical symmetry, the degree 2 contribution of the gravitational potential can be arranged in terms of the inertia tensor $\mathbf{I}$, according to MacCullagh's formula (Jeffreys 1976, p. 574), derived from now on by making use of the dyadic formalism. Within this framework, the inertia tensor reads

$$\mathbf{I} = \int \rho(\boldsymbol{r}) \left(r^2 \mathbf{1} - \boldsymbol{r} \otimes \boldsymbol{r}\right) dV = \int \rho(\boldsymbol{r}) \mathbf{M}(\theta, \varphi) r^2 dV \tag{3.7}$$

where θ and φ are the angular coordinates of $\boldsymbol{r}$ and $\mathbf{M}$ is defined as

$$\mathbf{M}(\theta, \varphi) r^2 = r^2 \mathbf{1} - \boldsymbol{r} \otimes \boldsymbol{r} = \left(\frac{2}{3}\mathbf{1} + \mathbf{Q}(\theta, \varphi)\right) r^2 \tag{3.8}$$

$$\mathbf{M}(\theta, \varphi) = \frac{2}{3}\mathbf{1} + \mathbf{Q}(\theta, \varphi) \tag{3.9}$$

where $\mathbf{Q}$ takes the form

$$\mathbf{Q}(\theta, \varphi) = \frac{1}{3}\mathbf{1} - \hat{\boldsymbol{r}} \otimes \hat{\boldsymbol{r}} \tag{3.10}$$

Exploiting the cartesian coordinates of the dyadic product $\hat{\boldsymbol{r}} \otimes \hat{\boldsymbol{r}}$ in terms of sine and cosine functions, it is shown that $\mathbf{Q}(\theta, \varphi)$ is an expansion of degree two spherical harmonics, where the isotropic term $\frac{1}{3}\,\mathbf{1}$, representing the spherical harmonic term of degree zero, is canceled by the same term with opposite sign entering the dyadic product.

Exercise 12 Expand $\mathbf{Q}(\theta, \varphi)$ in spherical harmonics, showing that they are limited to degree two, as in the following equation

$$\mathbf{Q}(\theta, \varphi) = \sum_{m=-2}^{2} \mathbf{Q}_m \, Y_{2m}(\theta, \varphi) \tag{3.11}$$

The density $\rho(\boldsymbol{r})$ in the inertia tensor is the density in the initial state $\rho_0(\boldsymbol{r})$ plus the perturbation $\rho^{\Delta}(\boldsymbol{r})$. Focusing our attention on the latter, we split the perturbation in the inertia tensor $\Delta\mathbf{I}$ in its harmonic contributions which, from the definition of $\mathbf{M}(\theta, \varphi)$ and from the expansion of the density field

$$\rho^{\Delta}(\boldsymbol{r}) = \sum_{\ell=0}^{\infty} \sum_{m=-\ell}^{\ell} \rho^{\Delta}_{\ell m}(r) \, Y_{\ell m}(\theta, \varphi) \tag{3.12}$$

becomes

$$\Delta\mathbf{I} = \Delta\mathbf{I}_0 + \Delta\mathbf{I}_2 \tag{3.13}$$

$$\Delta\mathbf{I}_0 = \int_0^a \int_{\Omega} \rho^{\Delta}(\boldsymbol{r}) \left(\frac{2}{3}\,\mathbf{1}\, Y^*_{00} \right) r^4 \, \sin\theta \, d\theta \, d\varphi \, dr$$

$$= \frac{8\pi}{3}\,\mathbf{1} \int_0^a \rho^{\Delta}_{00}(r)\, r^4 \, dr \tag{3.14}$$

$$\Delta\mathbf{I}_2 = \int_0^a \int_{\Omega} \rho^{\Delta}(\boldsymbol{r}) \left(\sum_{m=-2}^{2} \mathbf{Q}^*_m \, Y^*_{2m} \right) r^4 \, \sin\theta \, d\theta \, d\varphi \, dr$$

$$= \sum_{m=-2}^{2} \mathbf{Q}^*_m \, N_{2m} \int_0^a \rho^{\Delta}_{2m}(r)\, r^4 \, dr \tag{3.15}$$

where $\mathbf{Q}(\theta, \varphi)$ has been equivalently expanded in conjugate spherical harmonics, being a real quantity and the normalization factor $N_{\ell m}$ given by Eq. (1.72).

The inertia tensor perturbation $\Delta\mathbf{I}$ can be expressed in terms of the degree two component of the geopotential perturbation $\phi^{\Delta}_{2m}(a)$ evaluated at the Earth's surface

$$\phi^{\Delta}_{2m}(a) = -\frac{4\,\pi\,G}{5\,a^3}\int\limits_0^a \rho^{\Delta}_{2m}(r)\,r^4\,dr \tag{3.16}$$

The above expression can be demonstrated as follows. Starting from

$$\phi(\boldsymbol{r}) = -G\int \frac{\rho(\boldsymbol{r}')}{\left|\boldsymbol{r}-\boldsymbol{r}'\right|}\,dV'$$

$$= -G\int\limits_0^a\left[\int\limits_\Omega \frac{\rho(\boldsymbol{r}')}{\left|\boldsymbol{r}-\boldsymbol{r}'\right|}\,d\Omega\right] r'^2\,dr' \tag{3.17}$$

and making use of

$$\frac{1}{\left|\boldsymbol{r}-\boldsymbol{r}'\right|} = \frac{1}{r}\,\frac{1}{\sqrt{1+\left(\frac{r'}{r}\right)^2-2\,\left(\frac{r'}{r}\right)\,\cos\gamma}}$$

$$= \frac{1}{r}\sum_{\ell=0}^{\infty}\left(\frac{r'}{r}\right)^{\ell} P_\ell(\cos\gamma) \tag{3.18}$$

where $\boldsymbol{r}' < \boldsymbol{r}$ and γ denotes the angular distance between $\boldsymbol{r}$ and $\boldsymbol{r'}$

$$P_\ell(\cos\gamma) = \sum_{m=-\ell}^{\ell}\frac{(\ell-m)!}{(\ell+m)!}\,Y_{\ell m}(\theta,\varphi)\,Y^*_{\ell m}(\theta',\varphi') \tag{3.19}$$

we obtain

$$\phi^{\Delta}(r) = -\sum_{\ell=0}^{\infty}\frac{4\,\pi\,G\,r}{(2\,\ell+1)}\sum_{m=-\ell}^{\ell} Y_{\ell m}(\theta,\varphi)\int\limits_0^a \rho^{\Delta}_{\ell m}(r')\,\left(\frac{r'}{r}\right)^{\ell+2}\,dr' \tag{3.20}$$

where this expansion is applied to the perturbation $\phi^{\Delta}(r)$ rather than $\phi(r)$; we obtain

$$\phi^{\Delta}_{\ell m}(r) = -\frac{4\,\pi\,G}{(2\,\ell+1)\,r^{(\ell+1)}}\int\limits_0^a \rho^{\Delta}_{\ell m}(r')\,r'^{\ell+2}\,dr' \tag{3.21}$$

Particularly, for $\ell = 2$, we obtain

$$\phi^{\Delta}_{2m}(r) = -\frac{4\,\pi\,G}{5\,r^3}\int\limits_0^a \rho^{\Delta}_{2m}(r')\,r'^4\,dr' \tag{3.22}$$

For $r = a$ we finally obtain the MacCullagh's formula expressed within our own formalism

$$\Delta \mathbf{I}_2 = -\frac{5a^3}{4\pi G} \sum_{m=-2}^{2} N_{2m} \mathbf{Q}_m^* \, \phi_{2m}^{\Delta}(a) \tag{3.23}$$

3.2.1 Inertia Perturbations Due to Changes in the Centrifugal Potential

The centrifugal potential

$$\phi^C(\boldsymbol{r}) = \frac{1}{2}\left[(\boldsymbol{r}\cdot\boldsymbol{\omega})^2 - \omega^2 r^2\right] = \frac{\omega^2 r^2}{2}\left(\cos^2\gamma - 1\right)$$

$$= \frac{\omega^2 r^2}{3}\left(P_2(\cos\gamma) - 1\right) \tag{3.24}$$

and the addition theorem Eq. (3.19) yield

$$\phi^C(\boldsymbol{r}) = \frac{\omega^2 r^2}{3}\left[-Y_{00}^*(\hat{\mathbf{n}})\, Y_{00}(\hat{\mathbf{r}}) + \sum_{m=-2}^{2} \frac{(2-m)!}{(2+m)!}\, Y_{2m}^*(\hat{\mathbf{n}})\, Y_{2m}(\hat{\mathbf{r}})\right] \tag{3.25}$$

where

$$\boldsymbol{\omega} = \omega\, \hat{\mathbf{n}} \tag{3.26}$$

and where the spherical harmonics are expressed in terms of the normalized vectors $\hat{\mathbf{n}}$ and $\hat{\mathbf{r}}$ rather than in terms of the angular distances respect to the polar reference axis of these vectors.

The centrifugal potential induces the following perturbation in the geopotential at the radius a of the spherically symmetric Earth's model, expressed in terms of the tidal Love number

$$\phi_{2m}^{\Delta}(a) = k_2^T(t) \star \phi_{2m}^C(a,t) \tag{3.27}$$

By substitution

$$\Delta \mathbf{I}_2^{\omega} = -\frac{5\,a^3}{4\,\pi\,G} \sum_{m=-2}^{2} \mathbf{Q}_m^*\, N_{2m}\, k_2^T \star \phi_{2m}^C(a)$$

$$= -\frac{5\,a^3}{4\,\pi\,G}\, k_2^T \star \left(\sum_{m=-2}^{2} \mathbf{Q}_m^*\, N_{2m}\, \phi_{2m}^C(a)\right)$$

$$= -\frac{5\,a^3}{4\,\pi\,G}\,k_2^T \star \left(\sum_{m=-2}^{2} \mathbf{Q}_m^*\, N_{2m}\, \frac{4\,\pi}{5}\, \frac{\omega^2\, a^2}{3}\, \frac{1}{N_{2m}}\, Y_{2m}^*(\hat{\mathbf{n}}) \right) \tag{3.28}$$

$\Delta\mathbf{I}_2^\omega$ finally reads, once Eqs. (3.11) and (3.10) are used,

$$\Delta\mathbf{I}_2^\omega = -\frac{a^5\,\omega^2}{3\,G}\,k_2^T \star \left(\sum_{m=-2}^{2} \mathbf{Q}_m^*\, Y_{2m}^*(\hat{\mathbf{n}}) \right)$$

$$= -\frac{a^5\,\omega^2}{3\,G}\,k_2^T \star \left(\frac{1}{3}\,\mathbf{1} - \hat{\mathbf{n}} \otimes \hat{\mathbf{n}} \right) \tag{3.29}$$

or

$$\Delta\mathbf{I}_2^\omega = -\frac{a^5}{3\,G}\,k_2^T \star \left(\frac{\omega^2}{3}\,\mathbf{1} - \boldsymbol{\omega} \otimes \boldsymbol{\omega} \right)$$

$$= \frac{a^5}{3\,G}\,k_2^T \star \left(\boldsymbol{\omega} \otimes \boldsymbol{\omega} - \frac{\omega^2}{3}\,\mathbf{1} \right) \tag{3.30}$$

We require that the trace of the inertia tensor does not change during centrifugal deformation which makes the inertia due to the initial non rotating state plus that due to rotation to become

$$\mathbf{I}(t) = I\,\delta_{ij} + \frac{a^5}{3\,G}\,k_2^T(t) \star \left(\omega_i(t)\,\omega_j(t) - \frac{1}{3}\omega^2(t)\,\delta_{ij} \right) \tag{3.31}$$

I, G and k_2^T are the inertia of the non rotating spherical Earth, the Gravitational Constant and the degree-2 tidal gravitational Love number in the time t-domain. The MacCullagh's formula (Jeffreys 1976; Eq. (5.2.3) of Munk and MacDonald 1960) coincides with the above Eq. (3.31).

By assuming that the Earth has reached its rotating equilibrium state with the constant angular velocity before the beginning of any geophysical process $\boldsymbol{\omega} = (0, 0, \Omega)$, we get

$$\mathbf{I}(t = 0) = \mathrm{Diag}\,[A, A, C] \tag{3.32}$$

with $\mathrm{Diag}\,[A, A, C]$, C and A denoting the 3×3 diagonal matrix and the equilibrium polar and equatorial inertia moments given by

$$C = I + \frac{2}{3}\frac{a^5\,\Omega^2}{3\,G}\,k_F^T \qquad A = I - \frac{1}{3}\frac{a^5\,\Omega^2}{3\,G}\,k_F^T \tag{3.33}$$

so that

$$k_f^T = \frac{3G(C - A)}{a^5\Omega^2} \tag{3.34}$$

as it results for $\boldsymbol{\omega} = (0, 0, \Omega)$, with k_f^T being the tidal gravitational fluid limit of the Maxwell model. This latter is defined as the limit for $t \to \infty$ of the convolution of the degree-2 tidal gravitational Love number k_2^T with the Heaviside time history $H(t)$

$$k_f^T = \lim_{t \to \infty} k_2^T(t) \star H(t) \tag{3.35}$$

We note that the word "fluid" is poorly chosen when some layers are purely elastic and cannot relax their stresses. It would be less confusing to use the expression tidal "equilibrium" limit (Mitrovica et al. 2005). It is only to be in agreement with all our predecessors that we keep the inaccurate but widely used term of tidal "fluid" limit.

Equations (3.32)–(3.35) imply that before any perturbation in rotation, the Earth is subject to a constant rotation for a time scale greater than the longest characteristic relaxation Maxwell time of all the viscoelastic layers. In particular, in the case of a 120 km thick viscoelastic lithosphere with viscosity ν_L higher than 10^{24} Pa s and rigidity volume averaged from PREM (Dziewonski and Anderson 1981), this relaxation Maxwell time is greater than the characteristic time scale of 1 Myr characterizing ice age cycling, a major forcing for long term changes in rotation. This shows that the theory, based on Eq. (3.32) to estimate the initial state of rotational equilibrium, with C and A given by Eq. (3.33), can also be used on a time scale in which the elastic and the highly viscous viscoelastic lithosphere are distinguishable (see for instance Fig. 1 in Wu and Peltier (1982)).

In the perspective of studying the ice age TPW by means of compressible Maxwell Earth's models based on PREM, some remarks on the tidal fluid limit k_f^T are required. Indeed PREM has an unstable compositional stratification above the 670 km discontinuity (Plag and Jüttner 1995) corresponding to an imaginary Brunt–Väiäsala frequency (i.e., the radial density increases with depth less than what should be expected from the self-compression of the entire Earth). This unstable stratification generates growing modes which do not converge for $t \to \infty$ in Eq. (3.35). These modes similar to Rayleigh Taylor instabilities are discussed in various papers, as RT-modes in Plag and Jüttner (1995), Vermeersen and Mitrovica (2000), and included in the wider class of compositional C-modes in Cambiotti and Sabadini (2010), as discussed in Sect. 2.5.3. As shown in Vermeersen and Mitrovica (2000) these modes are characterized by long relaxation times of $10^2 - 10^3$ Myr and thus their effects are negligible on the time scale of the ice ages. In order to avoid these modes, following Chinnery (1975), we compute the tidal fluid limit k_f^T by considering the viscoelastic layers of the Maxwell Earth's model as inviscid, with the exception of the elastic layers. This approach is in agreement with the theory of the equilibrium figure of the rotating Earth at first order accuracy and it does not differ from the assumption that Maxwell Earth's models are in hydrostatic equilibrium before the loading of the last ice age, as usually done in post glacial rebound studies.

Besides this, note that we have defined k_f^T in the time t-domain. This is due to the fact that it is not possible to use its alternative definition in terms of the limit $s \to 0$ of the tidal gravitational Love number $\tilde{k}_2^T(s)$ in the Laplace s-domain. Indeed the

origin $s = 0$ of the Laplace s-domain is the cluster point of the denumerable set of the poles of the C-modes, both for stable and unstable compositional stratifications (Cambiotti and Sabadini 2010), as discussed in Sect. 2.5.

3.3 Linearized Liouville Equations

If Ω denotes the mean Earth's rotation frequency, then the components of $\boldsymbol{\omega}$ can be expressed in the dimensionless quantities m_i as

$$\boldsymbol{\omega} = (\omega_1, \omega_2, \omega_3) = \Omega(m_1, m_2, 1 + m_3). \tag{3.36}$$

The quantities m_i are small whenever the deviations from the reference axis of rotation are small. By assuming that the changes in I_{ij} are small compared to the moment of inertia in the initial state, the inertia tensor can be written as

$$I_{ij} = \begin{pmatrix} A + \Delta I_{11}(t) & \Delta I_{12}(t) & \Delta I_{13}(t) \\ \Delta I_{21}(t) & A + \Delta I_{22}(t) & \Delta I_{23}(t) \\ \Delta I_{31}(t) & \Delta I_{32}(t) & C + \Delta I_{33}(t) \end{pmatrix}, \tag{3.37}$$

in which A and C denote the moments of inertia for an equatorial principal axis and the polar principal axis, respectively. We assume that the initial mass distribution of the Earth is symmetric with respect to the rotation axis, so that the moments of inertia for the two principal equatorial axes are both equal to A. To first order

$$\begin{aligned} \mathbf{I} \cdot \boldsymbol{\omega} &= \begin{pmatrix} (A + \Delta I_{11})\omega_1 + \Delta I_{12}\omega_2 + \Delta I_{13}\omega_3 \\ \Delta I_{21}\omega_1 + (A + \Delta I_{22})\omega_2 + \Delta I_{23}\omega_3 \\ \Delta I_{31}\omega_1 + \Delta I_{32}\omega_2 + (C + \Delta I_{33})\omega_3 \end{pmatrix} \\ &\approx \begin{pmatrix} \Omega(Am_1 + \Delta I_{13}) \\ \Omega(Am_2 + \Delta I_{23}) \\ \Omega(C + Cm_3 + \Delta I_{33}) \end{pmatrix} \end{aligned} \tag{3.38}$$

so

$$\boldsymbol{\omega} \times (\mathbf{I} \cdot \boldsymbol{\omega}) \approx \begin{pmatrix} \Omega^2(Cm_2 - Am_2 - \Delta I_{23}) \\ \Omega^2(Am_1 + \Delta I_{13} - Cm_1) \\ 0 \end{pmatrix} \tag{3.39}$$

resulting, from Eq. (3.6), into

$$A\Omega\dot{m}_1 + \Omega^2(C - A)m_2 = -\Omega\Delta\dot{I}_{13} + \Omega^2\Delta I_{23} \tag{3.40}$$

$$A\Omega\dot{m}_2 - \Omega^2(C - A)m_1 = -\Omega\Delta\dot{I}_{23} - \Omega^2\Delta I_{13} \tag{3.41}$$

$$C\Omega^2 \dot{m}_3 = -\Omega^2 \Delta \dot{I}_{33} \tag{3.42}$$

where we have assumed $\mathbf{L} = 0$ and the dot denotes the time derivative. With the Eulerian free precession frequency defined as

$$\sigma_r = \frac{C - A}{A}\Omega \tag{3.43}$$

we can write

$$\frac{\dot{m}_1}{\sigma_r} + m_2 = \phi_2 \tag{3.44}$$

$$\frac{\dot{m}_2}{\sigma_r} - m_1 = -\phi_1 \tag{3.45}$$

$$\dot{m}_3 = \dot{\phi}_3 \tag{3.46}$$

in which

$$\phi_1 = \frac{1}{(C - A)}(\Delta I_{13} + \Omega^{-1} \Delta \dot{I}_{23}) \tag{3.47}$$

$$\phi_2 = \frac{1}{(C - A)}(\Delta I_{23} - \Omega^{-1} \Delta \dot{I}_{13}) \tag{3.48}$$

$$\phi_3 = \frac{1}{C}(-\Delta I_{33}) \tag{3.49}$$

are the dimensionless excitation functions.

Neglecting influences of the time variations of the inertia ($\Delta \dot{I}_{ij} = 0$), these excitation functions reduce for polar wander to the following complex notation

$$\mathbf{\Phi} = \phi_1 + i\phi_2 = \frac{\Delta I_{13}}{C - A} + i\frac{\Delta I_{23}}{C - A} \tag{3.50}$$

With this and the polar shift in complex notation $\mathbf{m} = m_1 + im_2$, the linearized Liouville equation for polar wander can be written from Eqs. (3.44) and (3.45) in complex notation, with i the imaginary unit, as

$$i\frac{\dot{\mathbf{m}}}{\sigma_r} + \mathbf{m} = \mathbf{\Phi} \tag{3.51}$$

3.4 The Concept of True Polar Wander (TPW)

At the end of the 19th century the theoretically predicted wobbling of the Earth's rotation axis with respect to the Earth's surface was observed. Two periodic movements have in fact been discerned from astronomical observations: one with a component of one year, related to seasonal influences, and one with a component of about 14 months, which was readily associated with Euler's free nutation of a rotating deformable body. From astronomical observations, Lambert (1922) and Wanach (1927) derived that the rotation axis of the Earth, besides these two periodic components, also shows a secular (linear) displacement with respect to the Earth's surface. Lambert (1922) found from an observation time series covering the period 1900–1917 that on the Northern Hemisphere the axis moves in the direction of 90°W longitude with a speed of 1.72° per million years (deg/Myr). On the basis of a somewhat longer time series (1900–1926), Wanach (1927) found a value of 1.31 deg/Myr in the direction 42°W longitude. These observations have been refined as longer time series became available and after the influence of continental drift had been recognized and was corrected for. One of the most recent values comes from McCarthy and Luzum (1996), who report a polar wander speed of $0.925° \pm 0.022°$ 1/Myr in the direction $75.0° \pm 1.1°$W longitude. To put these values in perspective: the yearly and 14-month harmonic components have amplitudes of about 10–15 m; the secular component that results after filtering these two harmonic components out has a rate of about 10 cm per year (one degree of latitude on the Earth's surface is about 111 km).

The observed polar wander is not an artificial consequence of continental drift (the plate on which an observatory is situated shifts with respect to the other plates; the plate through which the rotation axis of the Earth pierces shifts with respect to the deep mantle; etc.). That is, polar wander is corrected for these plate motions. Uncorrected polar wander is usually dubbed apparent polar wander (APW); corrected polar wander is usually called true polar wander (TPW). Thus, the secular shift of the rotation axis is not due to the continental drift of the particular plate which it pierces on the Northern or Southern Hemisphere, which would be called APW, but is supposed to reflect a true wander with respect to the deep mantle. It is therefore called TPW. The question which emerges immediately from this 'with respect to the deep mantle' is how one can determine the mantle reference frame. For long-term TPW, the hot-spot reference frame is usually taken for this fixed reference frame.

Hot-spots are point-like places on the Earth's surface that show a higher heat flow than average. They are often associated with large basaltic outpourings, both on continents and in oceans, moving relatively undisturbed through mid-ocean ridges. Whereas the rising material that forms the mid-ocean ridges (raised lineaments in the oceans that signify the places where the plates drift apart) is generally thought to have its origin in the shallow upper mantle, the relatively undisturbed movement of these hot spots through mid-ocean ridges indicates that the rising material of the hot spots comes from the deep mantle. Although there is some inter-hot-spot drift it remains limited to velocities of a few cm per year at most, whereas plates move with velocities up to 5–10 cm per year. Thus, a relatively stable (stable down to a few cm

per year) hot-spot reference frame can be established that is thought to coincide with a hypothetical deep-mantle reference frame. Here we will loosely refer to the term TPW with respect to this reference frame. Although the true nature of hot-spots is still a matter of debate, one may associate them with more or less stationary mantle convection patterns. This would imply that whenever a large change of the global convection pattern emerges, being accompanied by a large reorganization of the plates, then the concept of true polar wander becomes meaningless as the hot-spot reference frame is destroyed or reorganized. This limits the concept of TPW to periods of about 100 Myr, and one should be careful not to misinterpret a redistribution of hot-spots during plate reorganization periods as a "catastrophic turnover" of the rotation axis. Apart from this, there is evidence of TPW on timescales of both millions of years (Besse and Courtillot 1991) and thousands of years (Dickman 1977). Over the thousands of years Nakiboglu and Lambeck (1980), Sabadini and Peltier (1981) have shown that the present-day TPW can be explained by post glacial rebound due to the disappearance of the huge Pleistocene ice sheets. A number of papers have been published in recent years that argue for additional forcings being responsible for causing the observed present-day polar drift other than post glacial rebound.

On the million-year time scale, subduction (e.g. Ricard et al. 1992) and mantle convection (e.g. Steinberger and O'Connell 1997) are considered to be the major contributors to TPW, while on the thousand-year time scale the redistribution of surface loads due to the growing and melting of huge ice sheets is considered to be one of the main forcing mechanisms for TPW. Steinberger and O'Connell (1997) derive from their mantle heterogeneities advection model a contribution of 40 % to the observed secular TPW rate. Contemporary forcings might induce TPW rates comparable to the secular TPW velocity: some of the models in Vermeersen et al. (1994) on (geoid-constrained) neotectonics of the Himalayas and Tibetan Plateau and in James and Ivins (1997) on mass changes of the Greenland ice sheet induce TPW velocity rates which are comparable to the observed present-day TPW rate. Taken together, all these geophysical forcings (mantle convection, tectonics, present-day ice and water redistributions, etc.), with their associated uncertainties, make it very difficult to extract unique information about the viscosity of the Earth's mantle from TPW simulations.

We can thus conclude that starting from the work by Gold (1955), Munk and MacDonald (1960), issues related to the secular change of the Earth's rotation axis named True Polar Wander (TPW), never ceased to be discussed or questioned. Progress has been made since the sixties, on two major aspects: the first deals with the improvement in the modeling of the Earth, in terms of rheological stratification, and the second is related to the new insights on surface and deep seated density anomalies originating from ice ages and mantle convection as major sources of polar wander. After decades, we are however still in the situation in which it is necessary to come back to some basic TPW issues to dig out deeper insights into the physics of this aspect of the dynamics of our planet, focusing, in particular, on the nature, elastic or viscoelastic, of the outermost part of our planet.

Ricard et al. (1993a) first exploited the rotational behavior of elastic versus viscoelastic outermost part of the Earth, introducing the T_1 time scale characterizing

the readjustment of the equatorial bulge, based on realistically stratified viscoelastic Earth's models. Vermeersen and Sabadini (1999) pointed out the reduction in the TPW displacements for Maxwell Earth's models carrying a viscoelastic lithosphere compared to those with an elastic one. Nakada (2002) went thoroughly into the issue related to the rheology of the lithosphere by considering highly viscous viscoelastic lithospheres and he showed as the TPW rates in the lower mantle viscosity range 10^{21}–10^{22} Pa s are extremely sensitive to the choice of the rheology of the lithosphere, elastic or viscoelastic with high viscosity. This might be seen as surprising since the high viscous viscoelastic lithosphere is expected to behave as an elastic one for time scales of 1 Myr comparable to that of post glacial rebound. Mitrovica et al. (2005) named this sensitivity of the TPW predictions the "Nakada paradox" and (as cited by Nakada) "has suggested that this paradox originates from an inaccuracy in the traditional rotation theory associated with the treatment of the background equilibrium rotating form upon which any load- and rotation-induced perturbations are superimposed (e.g. Wu and Peltier 1984)".

Starting from these preliminary remarks, Mitrovica et al. (2005) suggest a new treatment of the rotational dynamics where the observed fluid Love number is used in the linearized Euler dynamic equation, rather than the tidal fluid limit deduced self-consistently from the Maxwell Earth's model used to evaluate the load-induced perturbations of the inertia tensor and the readjustment of the equatorial bulge. This apparently minor change (the discrepancy between the observed and tidal fluid limits is about 1 %) has a potentially large impact on TPW predictions and would solve the "Nakada paradox".

We enlighten in the following the differences between the so called "traditional approach" (Sabadini and Peltier 1981; Sabadini et al. 1982; Wu and Peltier 1984) and the treatment indicated by Mitrovica et al. (2005). We will show results from a newly developed compressible model, including the methodology to transform the results from the Laplace domain into the time domain. This will clarify some issues related to the use of the normal mode relaxation approach within rotational problems. We will explore the role of the non hydrostatic contribution to the fluid Love number from mantle convection calculations in order to make our estimates of TPW rates, within the scheme proposed by Mitrovica et al. (2005), as realistic as possible.

3.4.1 Reference Frame

As in a deformable Earth there are no stable reference frames in the strict sense, it is necessary to define such a reference system in a practical way. For short-term polar wander it is convenient to take the geographical frame as reference frame. It can be defined as the mean position of a number of fixed points in stable continental areas. For long-term true polar wander the choice of a reference frame becomes more complicated, as the whole mantle can change its configuration. Usually, the hot-spot reference frame is taken as the frame in which the mean mantle material is stable. The relative velocities between the hot spots are generally found to be a factor of

one tenth smaller than the relative plate velocities. m_1 and m_2 now give the resultant polar shift in radians: m_1 in the x-direction, which is chosen to be in the equatorial plane from the centre of the Earth towards the Greenwich meridian, and m_2 in the y-direction, which is chosen to be in the equatorial plane from the centre of the Earth towards 90° East longitude. m_3 gives the change in the length of day in radians per sidereal day.

For loadings that change with much smaller frequencies than σ_r, the linearization of the Liouville equation leads ultimately to

$$m_1 = \frac{\Delta I_{13}}{C - A} \text{ rad} \quad \text{x}-\text{component of polar shift} \tag{3.52}$$

$$m_2 = \frac{\Delta I_{23}}{C - A} \text{ rad} \quad \text{y}-\text{component of polar shift} \tag{3.53}$$

$$m_3 = \frac{-\Delta I_{33}}{C} \text{ rad} \quad \text{change in length of day.} \tag{3.54}$$

The equatorial flattening is of great importance: if C were equal to A, then the Eulerian free precession frequency, Eq. (3.43), would be zero, the excitation functions, Eqs. (3.47) and (3.48), would be infinite and, according to Eqs. (3.52) and (3.53), the polar shift infinitely large.

Exercise 13 For the Earth, $C = 8.0394 \times 10^{37}$ kg m^2 and $A = 8.0131 \times 10^{37}$ kg m^2, determine the period of the Eulerian free precession.

3.4.2 Adjustment of the Equatorial Bulge

Another important issue is that Eq. (3.51) does not take a shift in the equatorial bulge into account. To put it differently: it gives the polar wander for a rigid planet. If the rotation axis had to coincide with the axis perpendicular to the plane of the equatorial flattening before a mass change occurs, then, after the mass change, Eq. (3.51) would give the new position of the rotation axis that coincides with the axis of maximum moment of inertia. This new position would not be perpendicular to the plane of the equatorial flattening whenever the perturbing mass is not on the poles or the equator. A wobble ensues, which should have the frequency given by Eq. (3.43). At the end of the 19th century astronomers looked for this frequency in their observations but did not find it. However, they found a strong wobble, the so-called Chandler wobble, that had a period 4 months greater than the Eulerian free precession period. It was soon realized that the Chandler wobble is nothing else than the Eulerian free precession and that the 4-month period extension is due to the elastic properties of the Earth. The deformation of the Earth is also responsible for the decay of the wobble amplitudes on time scales of a few decades, implying that the wobbles must be maintained by geophysical forcings. And, as we have already seen in the introduction, the tidal deceleration of the Earth's rotation also requires that (visco)elastic adjustment of

the equatorial bulge be taken into account. Finally, for long-term polar wander it is obvious that the shift of the equatorial bulge has to be taken into account. There are indications that polar wander over geological times may amount up to several tens of degrees, while today the equatorial bulge is almost perpendicular to the Earth's rotation axis.

We now add to Eq. (3.31) the contributions from surface and internal loads, which allow us to subdivide the inertia tensor into three terms

$$I_{ij}(t) = I\,\delta_{ij} + \frac{a^5}{3\,G}\,k_2^T(t) \star \left(\omega_i(t)\,\omega_j(t) - \frac{1}{3}\omega^2(t)\,\delta_{ij}\right) + I_{ij}^L(t) \tag{3.55}$$

describing the inertia tensor of the spherically symmetric Earth's model, the effects of the centrifugal potential and the remaining contributions, from surface and internal loads.

Exercise 14 Show that the changes in the products of inertia ΔI_{13}^{ω} and ΔI_{23}^{ω} due to changes in the centrifugal potential can be expressed in a linear approximation as

$$\Delta I_{13}^{\omega}(t) = \frac{a^5 k_2^T(t)}{3G} * (\omega_1(t)\omega_3(t)) \approx \frac{a^5 k_2^T(t)\Omega^2}{3G} * m_1(t) \tag{3.56}$$

$$\Delta I_{23}^{\omega}(t) = \frac{a^5 k_2^T(t)}{3G} * (\omega_2(t)\omega_3(t)) \approx \frac{a^5 k_2^T(t)\Omega^2}{3G} * m_2(t) \tag{3.57}$$

The forcing function $\mathbf{\Phi}_R$ for rotational deformation can then be written in complex notation as

$$\mathbf{\Phi}_R(t) = \frac{\Delta I_{13}^{\omega}(t)}{C-A} + i\,\frac{\Delta I_{23}^{\omega}(t)}{C-A} \approx \frac{k_2^T(t)}{k_f^T} * \mathbf{m} \tag{3.58}$$

with $\mathbf{m} = m_1 + i m_2$.

3.5 Developments of Linearized Rotation Theories

The theory of relating changes in mass distribution to changes in rotation for a viscoelastic Earth has been developed over many years. Burgers (1955), acknowledging Gold (1955) as source of inspiration, built such a model in which the rheology consisted of a variation of the Kelvin-Voigt model (the Newtonian element was replaced by a Maxwell element). References to further early attempts can be found in Munk and MacDonald (1960). Multi-layer viscoelastic relaxation models for Earth's rotation driven by ice cycles were built by Sabadini et al. (1982), Wu and Peltier (1984). The simulations we present are based upon the theory of Sabadini et al. (1982), but the theory of Wu and Peltier (1984) is equivalent to Sabadini et al. (1982) after the Chandler wobble is filtered out in the theory of the latter (Sabadini et al. 1984; Vermeersen et al. 1996b; Mitrovica and Milne 1998).

The linearized Liouville equation (3.51) including both loading and tidal forcings, can be written as

$$i\frac{\dot{\mathbf{m}}}{\sigma_r} + \mathbf{m} = \mathbf{\Phi} \tag{3.59}$$

with the forcing function $\mathbf{\Phi}$ consisting of two parts: $\mathbf{\Phi} = \mathbf{\Phi}_L + \mathbf{\Phi}_R$, with $\mathbf{\Phi}_L$ the part describing the direct geodynamic forcing and $\mathbf{\Phi}_R$ the induced rotational deformation.

The linearized Liouville equation can thus be expressed as

$$i\frac{\dot{\mathbf{m}}}{\sigma_r} + (1 - \frac{k_2^T}{k_f^T})\mathbf{m} = \mathbf{\Phi}_L \tag{3.60}$$

or

$$i\frac{\dot{\mathbf{m}}}{\sigma_0} + \mathbf{m} = \mathbf{\Psi}_L \tag{3.61}$$

with

$$\sigma_0 = (1 - \frac{k_2^T}{k_f^T})\sigma_r \tag{3.62}$$

and

$$\mathbf{\Psi}_L = \frac{k_f^T}{k_f^T - k_2^T}\mathbf{\Phi}_L \tag{3.63}$$

The term σ_0 is the frequency of the Chandler wobble. Its 4-month decrease with respect to the frequency of the Eulerian free precession frequency σ_r is due to the quotient k_2^T/k_f^T.

Exercise 15 Show, assuming that k_2^T is not time-dependent, that the solution of Eq. (3.61) is

$$\mathbf{m}(t) = -i\sigma_0 e^{i\sigma_0 t}\int_{-\infty}^{t}\mathbf{\Psi}_L(\tau)e^{-i\sigma_0\tau}d\tau \tag{3.64}$$

and determine $\mathbf{m}(t)$ for the following two cases:

(1) $\mathbf{\Psi}_L(t) = \mathbf{\Psi}_0 H(t)$, with $\mathbf{\Psi}_0$ time-independent and H the Heaviside function;
(2) $\mathbf{\Psi}_L(t) = \mathbf{\Psi}_0\delta(t)$, with $\mathbf{\Psi}_0$ being time-independent.
Draw your solutions in the (m_1, m_2)-plane for both cases (1) and (2). Assume that at time $t = 0$ the rotation pole is at the origin.

We now make use of the Liouville equation in the form of Eq. (3.60) transformed into the Laplace domain

$$\frac{i\,s}{\sigma_r}\tilde{\mathbf{m}}(s) + \left(1 - \frac{k_2^T(s)}{k_f^T}\right)\tilde{\mathbf{m}}(s) = \tilde{\mathbf{\Phi}}_L(s) \tag{3.65}$$

where i and σ_r are the imaginary number and the Eulerian free precession frequency of the rigid Earth and the forcing in the RHS is cast in terms of the convolution between the direct effect of the load $\tilde{\phi}(s)$ and the response of the Earth via the loading Love number $\tilde{k}^L(s)$

$$\tilde{\mathbf{\Phi}}_L(s) = \left(1 + \tilde{k}_2^L(s)\right)\, \tilde{\phi}(s) \tag{3.66}$$

The tilde stands for the Laplace transform and $\tilde{\phi}(s) = \phi_1(s) + i\phi_2(s)$, Eqs. (3.47) and (3.48). When modal expansion of the tidal Love number $k_2^T(s)$

$$k_2^T(s) = k_E^T + \sum_{j=1}^{M} \frac{k_j^T}{s - s_j} \tag{3.67}$$

is performed in Eq. (3.65), we obtain

$$\left(i\frac{s}{\sigma_r} + 1 - \frac{1}{k_f^T}\left(k_e^T + \sum_{i=1}^{M} \frac{k_i^T}{s - s_i}\right)\right)\tilde{\mathbf{m}} = \tilde{\mathbf{\Phi}}_L(s) \tag{3.68}$$

In order to address attention solely on the rotational part, with $k_f^T = k_2^T(s = 0)$ being the tidal fluid Love number, we obtain

$$k_f^T = k_e^T + \sum_{i=1}^{M} \frac{k_i^T}{-s_i} \tag{3.69}$$

and

$$\frac{k_i^T}{s_i} + \frac{k_i^T}{s - s_i} = \frac{k_i^T s}{s_i(s - s_i)} \tag{3.70}$$

Equation (3.68) becomes

$$s\left(1 + i\frac{\sigma_r}{k_f^T}\sum_{i=1}^{M} \frac{k_i^T}{s_i(s - s_i)}\right)\tilde{\mathbf{m}}(s) = -i\sigma_r\tilde{\mathbf{\Phi}}_L(s) \tag{3.71}$$

becoming

$$s\left(1 + \sum_{i=1}^{M} \frac{x_i}{s - s_i}\right)\tilde{\mathbf{m}}(s) = -i\sigma_r\tilde{\mathbf{\Phi}}_L(s) \tag{3.72}$$

with

$$x_i = i\frac{\sigma_r k_i^T}{k_f^T s_i} \tag{3.73}$$

Now

$$1+\sum_{i=1}^{M}\frac{x_i}{s-s_i}=\frac{\prod_{j=1}^{M}(s-s_j)}{\prod_{j=1}^{M}(s-s_j)}+\sum_{i=1}^{M}x_i\frac{\prod_{j\neq i}^{M}(s-s_j)}{\prod_{j=1}^{M}(s-s_j)} \tag{3.74}$$

where $\prod_{j\neq i}^{M}$ means $\prod_{j=1}^{M}$ without the term $j=i$.

The right-hand side of the above equation

$$\frac{\prod_{j=1}^{M}(s-s_j)+\sum_{i=1}^{M}x_i\prod_{j\neq i}^{M}(s-s_j)}{\prod_{j=1}^{M}(s-s_j)} \tag{3.75}$$

can be transformed into

$$\frac{\sum_{i=0}^{M}\alpha_i s^i}{\prod_{j=1}^{M}(s-s_j)} \tag{3.76}$$

(whereby it immediately follows that $\alpha_M=1$), and consequently

$$1+\sum_{i=1}^{M}\frac{x_i}{s-s_i}=\frac{\prod_{j=1}^{M}(s-a_j)}{\prod_{j=1}^{M}(s-s_j)} \tag{3.77}$$

with a_i being the M complex roots of the equation

$$\sum_{i=0}^{M}\alpha_i s^i=0 \tag{3.78}$$

We thus obtain

$$s\frac{\prod_{j=1}^{M}(s-a_j)}{\prod_{j=1}^{M}(s-s_j)}\mathbf{m}(s)=-i\sigma_r\tilde{\mathbf{\Phi}}_L(s) \tag{3.79}$$

becoming

$$\tilde{\mathbf{m}}(s)=-i\sigma_r\frac{\prod_{j=1}^{M}(s-s_j)}{s\prod_{j=1}^{M}(s-a_j)}\tilde{\mathbf{\Phi}}_L(s) \tag{3.80}$$

that can be cast as

$$\tilde{\mathbf{m}}(s)=-i\sigma_r\left(\frac{A_0}{s}+\sum_{j=1}^{M}\frac{A_j}{s-a_j}\right)\tilde{\mathbf{\Phi}}_L(s) \tag{3.81}$$

In this expression, the terms a_j are the inverse relaxation times from the tidal problem for the M modes, having the strength given by the residues A_j. The residue A_0 gives the strength of the secular term. $\mathbf{m}(s)$ is defined in such a way that the

real-valued component gives the polar wander in the direction of the Greenwich meridian, and the imaginary-valued component the polar wander in the direction 90° to the east.

Equation (3.81) forms the basis of realistic models of Earth's rotation that takes solid-Earth's deformation and its consequential shifts in the equatorial bulge self-consistently into account (with one restriction: the Liouville expression has been linearized and therefore polar wander needs to be restricted to about 10° over the Earth's surface, or about 1000 km, at most).

The loading term entering Eq. (3.81) can be made explicit

$$\tilde{\phi}(s) = \frac{\Delta I_{13}^L(s) + i\,\Delta I_{23}^L(s)}{C - A} \tag{3.82}$$

to give

$$\tilde{\mathbf{m}}(s) = -i\sigma_r \left(\frac{A_0}{s} + \sum_{j=1}^{M} \frac{A_j}{s - a_j} \right) \left(1 + k_e^L + \sum_{j=1}^{M} \frac{k_j^L}{s - s_j} \right) \frac{\Delta I_{13}^L(s) + i\,\Delta I_{23}^L(s)}{C - A} \tag{3.83}$$

The inertia products refer to the perturbations of the rigid Earth, since the elastic and viscoelastic contribution is included in the terms within the brackets. k_e^L is the elastic load Love number and the terms k_j^L are the load Love numbers of the Mj modes, accompanied by their (negative) inverse relaxation times s_j of Chap. 1; the superscript L is used to differentiate the loading Love number from the tidal one. In this book, perturbations in rotation are due to surface or internal mass anomalies, not to earthquakes: the latter can be considered for their effects on rotation in Sabadini et al. (2007) and, most recently, in Cambiotti et al. (2016). As already observed for the tidal Love number, only the degree two harmonic component of the loading Love number enters the rotation equations.

Equation (3.83) can further be simplified to (e.g. Vermeersen et al. 1994)

$$\tilde{\mathbf{m}}(s) = -i\sigma_r \frac{\Delta I_{13}^L(s) + i\,\Delta I_{23}^L(s)}{C - A} \left(\frac{A_0^*}{s} + \sum_{i=1}^{M} \frac{\beta_i}{s - s_i} + \sum_{i=1}^{M} \frac{\gamma_i}{s - a_i} \right) \tag{3.84}$$

in which

$$\beta_i = A_0 \frac{k_i^L}{s_i} + \sum_{j=1}^{M} \frac{A_j k_i^L}{s_i - a_j}, \tag{3.85}$$

$$\gamma_i = A_i (1 + k_e^L) - \sum_{j=1}^{M} \frac{A_i k_j^L}{s_j - a_i} \tag{3.86}$$

and

$$A_0^* = A_0 (1 + k_f^L) \tag{3.87}$$

in which the fluid limit ($s = 0$) of the load Love number is given by

$$k_f^L = k_e^L - \sum_{i=1}^{M} \frac{k_i^L}{s_i} \tag{3.88}$$

Exercise 16 Show that the coefficients β_i are identically equal to zero.

3.5.1 Comparison Between Different Rotation Theories

As elucidated by Eq. (3.83), in the case of polar wander there are two relaxation mechanisms at work: load relaxation, as a consequence of a redistribution of loads over and within the Earth, and tidal-effective (or centrifugal) relaxation, as a consequence of the centrifugal force acting on a rotating Earth. This centrifugal force causes the equatorial bulge of the Earth to be displaced over the Earth's surface in a manner not unlike a wave traveling over the ocean's surface. This 'polar wander' movement goes on until the Earth's rotation axis coincides with the axis of maximum moment of inertia of the mass distribution.

The theory that is used to study changes in the second degree harmonic of the geoid $\dot{J}_2$ and polar wander can be found in a number of past publications (e.g. Nakiboglu and Lambeck 1980; Sabadini and Peltier 1981; Sabadini et al. 1982, 1984, 1988, 1993; Wu and Peltier 1984; Peltier 1985; Spada et al. 1992; Ricard et al. 1992, 1993a; Mitrovica and Peltier 1993; Vermeersen et al. 1994, 1996b, 1997; Peltier and Jiang 1996). The models in all these references employ a viscoelastic Maxwell rheology for a spherical Earth's model (that is, normal mode theory is first applied to a non-rotating spherical Earth' model, after which the required rotating ellipsoidal Earth's model is obtained by applying the centrifugal potential). Differences in the models in the above references exist in, for example, the number of layers that the Earth's model has, the way in which the differential equations are solved (analytically or numerically), whether the Lamé parameter λ is taken as finite or infinite (compressible or incompressible) and whether the models allow only for surface loads or also for internal mantle loads.

The theories developed by Sabadini et al. (1982), Wu and Peltier (1984) have been shown to be equivalent in Sabadini et al. (1984), Vermeersen and Sabadini (1996). Specifically, Sabadini et al. (1984) have shown that the secular polar wander terms are the same, while Vermeersen and Sabadini (1996) have demonstrated that when the Chandler wobble is filtered from the model of Sabadini et al. (1982), then to a high approximation the same polar wander curves are obtained compared to those found with the model of Wu and Peltier (1984) for all timescales.

In Spada et al. (1992b), an analytical theory is developed for polar wander and $\dot{J}_2$ models for Earth's stratifications with 5 layers at most. Vermeersen et al. (1996a), Vermeersen and Sabadini (1996) have developed the analytical theory for the

relaxation of an Earth's model consisting of an arbitrary number of layers. In this section we concentrate on those aspects that are specifically associated with studying rotational changes by means of analytical models in which the Earth is radially stratified with any number of layers.

3.5.2 *Omission of the M0 Rotation Mode*

A number of authors have reported during the past decade that studies on glacially induced displacement of the axis of rotation with respect to the Earth's surface named TPW, allow in general for multiple solutions for the lower mantle viscosity if the TPW is known and all the other rheological, elastic and constitutional parameters are fixed (Fig. 20 in Yuen et al. 1986; Fig. 5 in Spada et al. 1992b; Fig. 1 in Milne and Mitrovica 1996). These multiple-branch solutions are found in other geophysical signatures related to glacially induced solid-Earth deformation like post-glacial rebound, free-air gravity anomalies, and changes in the non-tidal acceleration of the Earth. We will come back to these points in detail in the following Chap. 4.

Although the theories described by Sabadini et al. (1982), Wu and Peltier (1984) appear to have a number of differences, Sabadini et al. (1984) have shown that the formulations are equivalent to some extent. The proof of the equivalence of Eqs. (16) and (17) in Sabadini et al. (1984) for the secular rotation term is an important result in this respect. Another result mentioned in Sabadini et al. (1984) is that each of the load relaxation modes has a corresponding rotational relaxation mode. This correspondence remains an important issue since, in Wu and Peltier (1984) theoretical development, one of the corresponding modes, the $M0$ rotational relaxation mode, is lacking (see also Table 1 in Sabadini et al. 1984). We show explicitly that the absence of the $M0$ rotational relaxation mode does not affect the TPW-rate behavior. As support for this result, it should be noted that the TPW predictions of Milne and Mitrovica (1996), Fig. 1, which agree with earlier analyses (e.g. Spada et al. 1992b), are based on theory which is equivalent to Wu and Peltier's (1984) approach. In this section it is first shown that Wu and Peltier's (1984) approach in deleting the Chandler wobble acts to remove the $M0$ rotational mode. A new analytical approximation formula for the $M0$ rotational relaxation mode, which incorporates the Chandler wobble frequency for a stratified Earth as the imaginary part, is derived below. It will be shown, using numerical tests, that this approximation formula is extremely accurate. It is shown that the model approach used in Sabadini et al. (1982), Wu and Peltier (1984) lead to the same secular TPW results.

Equation (64) in Wu and Peltier (1984) becomes in our notation

$$\mathbf{m}(s) = -\frac{i\sigma_r \tilde{\mathbf{\Phi}}_L(s)}{s\left(1 + i\sum_{j=1}^{M} \frac{x'_j}{s - s_j}\right)} \tag{3.89}$$

The terms $x_i' = (\sigma_r k_i^T)/(k_f^T s_i)$ do not contain the imaginary unit i as the previously defined x_i in Eq. (3.73) do and have the same dimension as s_j (parameters k_j^T are the same as the parameters t_j used in Wu and Peltier (1984)).

For inverse Laplace transformation of Eq. (3.89) the complex-valued roots of the denominator on the right hand side have to be found. At this stage, Wu and Peltier (1984) make the point that the unity term in the denominator of Eq. (3.89) can be neglected. This is only correct, however, if the imaginary parts of the roots have the same magnitude or are much smaller than the magnitude of the real parts. This is indeed the case for $M-1$ roots, but it is not true for one root which has a much larger imaginary part than real part. This root turns out to be the rotational root that gives the relaxation of the fundamental mantle mode as real part and the Chandler wobble as imaginary part.

The omission of this rotational root in Wu and Peltier (1984) will become more apparent when we rewrite the term inside the brackets of Eq. (3.89) as

$$1 + i \sum_{j=1}^{M} \frac{x_j'}{s - s_j} = \frac{\prod_{j=1}^{M}(s - s_j) + i \sum_{k=1}^{M} x_k' \prod_{j \neq k}^{M}(s - s_j)}{\prod_{j=1}^{M}(s - s_j)} \tag{3.90}$$

It is clear that if the first term of the numerator on the right hand side of Eq. (3.90) is deleted, the numerator is reduced from an expression of order M to an expression of order $M-1$. This would imply that one of the M load relaxation modes would have no rotational counterpart. Neglecting the first term of the numerator of Eq. (3.90) on the right hand side of the equation is correct for the $M-1$ roots for which the imaginary part is orders of magnitude smaller than the real part, as outlined by Wu and Peltier (1984). For these roots, the approximation

$$\sum_{k=1}^{M} x_k' \prod_{j \neq k}^{M}(s - s_j) = 0 \tag{3.91}$$

is valid, being a purely real expression resulting in $M-1$ real roots. These real roots constitute the $M-1$ rotational inverse relaxation times associated with all modes except the $M0$ mode.

For a root which has a large imaginary value, comparative in strength with the variables x_j', an argument that the first term of the numerator on the right hand side of Eq. (3.90) is negligible with respect to the second term of this numerator, is no longer valid. In fact, such a complex-valued root leads to a real part, i.e. the $M0$ rotational relaxation mode, which has the same order of magnitude as the other (real) $M-1$ roots.

This complex-valued mode, with the Chandler wobble frequency for a stratified Earth as imaginary part, has thus to be derived from the complete complex-valued equation

Table 3.3 Density and rigidity values for the 5-layer model

r (km)	ρ (kg/m^3)	μ (N/m^2)
6371 – 6250	3184	6.02×10^{10}
6250 – 5951	3434	7.27×10^{10}
5951 – 5701	3857	1.06×10^{11}
5701 – 3480	4878	2.19×10^{11}
3480 – 0	10,932	0

$$\prod_{j=1}^{M}(s - s_j) + i \sum_{k=1}^{M} x_k' \prod_{j \neq k}^{M}(s - s_j) = 0 \tag{3.92}$$

A highly-accurate analytical approximation formula can be derived from Eq. (3.92) for the $M0$ rotational relaxation mode. This approximation facilitates polar wander simulations in Earth's models with a large number of layers. Indeed, it is well known that complex rootfinding procedures are numerically more difficult to apply and are less reliable than real-valued rootfinding procedures. When an analytical formula can be obtained for the only complex root that has a non-negligible imaginary part, one can employ rootfinding procedures for real numbers using Eq. (3.91) instead of complex numbers using Eq. (3.92) in TPW calculations.

Before deriving this formula, an example concerning the foregoing remarks might be illustrative. Table 3.3 gives the values for the densities and rigidities of a 5-layer model. The mantle has a uniform viscosity of 10^{21} Pa s. In Table 3.4 the 9 inverse load relaxation times s_j and the 9 rotational relaxation roots a_j are given for this 5-layer Earth's model. The complex rotational relaxation roots a_j are determined by applying a complex rootfinding procedure to Eq. (3.78). It is clear from Table 3.4 that 8 roots have imaginary values which are negligible in strength, and that 1 root has a large imaginary value. This large imaginary value represents the Chandler wobble. The real value of this root is the $M0$ rotational relaxation mode. This mode is not negligible at all; on the contrary, it is often the strongest relaxation mode, as illustrated by the last two columns in Table 3.4. In Table 4 of Wu and Peltier (1984), where 9 load relaxation and 8 rotational relaxation roots are given, it is this $M0$ rotational relaxation mode which is lacking. The small imaginary values of the other rotational relaxation roots in Table 3.4 indicate that these modes are also characterized by wobbles. One can easily prove from Eq. (3.92) that the imaginary parts of these modes are not equal to zero, thus excluding the possibility that these imaginary values are the result of numerical inaccuracies. This is interesting from a physical point of view, although the amplitudes of these wobbles are too small to be of any immediate physical significance.

Filtering the Chandler wobble out after the rotational relaxation roots have been found is not the same as deleting the mode in which the Chandler wobble will appear before Eq. (3.92) is solved. One might thus think that the omission of the $M0$ rotational relaxation mode has marked consequences for the TPW simulations.

Table 3.4 Inverse load relaxation times s_j, inverse rotational relaxation times a_j, load Love numbers k_j^L and tidal-effective Love numbers k_j^T for the 9 relaxation modes of the 5-layer model of Table 3.3, with a uniform mantle viscosity of 10^{21} Pa s

Mode	$-s_j$ (kyr^{-1})	$-a_j$ (kyr^{-1})	k_j^L (kyr^{-1})	k_j^T (kyr^{-1})
M2	2.90×10^{-5}	$7.32 \times 10^{-5} - i9.64 \times 10^{-10}$	-1.45×10^{-7}	7.17×10^{-9}
M1	1.29×10^{-3}	$1.06 \times 10^{-2} - i1.73 \times 10^{-6}$	-7.01×10^{-5}	7.72×10^{-6}
L0	1.09×10^{-1}	$1.19 \times 10^{-1} - i1.89 \times 10^{-6}$	-1.69×10^{-4}	7.84×10^{-4}
C0	4.50×10^{-1}	$1.02 - i1.50 \times 10^{-4}$	-1.41×10^{-1}	8.08×10^{-2}
M0	2.02	$1.95 - i5.10 \times 10^{3}$	-3.32×10^{-1}	4.21×10^{-1}
T1	2.48	$2.38 - i2.19 \times 10^{-5}$	-7.82×10^{-2}	8.13×10^{-2}
T2	2.84	$2.62 - i2.45 \times 10^{-5}$	-2.80×10^{-1}	3.73×10^{-1}
T3	3.56	$3.47 - i2.60 \times 10^{-5}$	-9.95×10^{-2}	1.13×10^{-1}
T4	4.00	$3.89 - i2.94 \times 10^{-5}$	-1.15×10^{-1}	1.79×10^{-1}

The labeling of the modes agrees with the labeling in Table 4 of Wu and Peltier (1984). Note that the M0 mode is the strongest mode for both load relaxation and tidal-effective relaxation

However, Eq. (79) in Wu and Peltier (1984) contains the extra term $D_1 f(t)$ inside the square brackets, which is only created when the number of rotational relaxation modes is one less than the number of load relaxation modes. It will be shown that this term contains approximately the same contribution as is found from the relaxation of the $M0$ rotational relaxation mode after the Chandler wobble is filtered out. This equivalence will be pointed out and discussed after the analytical formula for the $M0$ rotational relaxation mode has been derived.

3.5.3 *Analytical Formula for the M0 Rotation Mode*

As shown in the last section, the numerator on the right hand side of Eq. (3.90) has $M-1$ solutions $s = a_j$ $(j = 1,..., M-1)$ for which the imaginary part can be neglected. These $M-1$ solutions can be found by applying a real-valued rootfinder procedure to Eq. (3.91). The root which contains the Chandler wobble as imaginary part and the M0 rotational relaxation mode as real part must be solved from Eq. (3.92). If we split this root $s = a_{M0}$ into its real and imaginary parts as $a_{M0} = a_R + ia_I$, then it is clear from Table 3.4 that $|a_I| \gg |a_R|$ and $|a_I| \gg |s_k|$ hold for all M load relaxation modes k_i^L.

With this, the first term of Eq. (3.92) can be approximated by

$$\prod_{j=1}^{M}(s - s_j) \approx i^M a_I^M + i^{M-1} \sum_{k=1}^{M}(a_R - s_k) a_I^{M-1} \tag{3.93}$$

while the second term of Eq. (3.92) can be approximated by

$$i\sum_{k=1}^{M} x_k' \prod_{j\neq k}^{M}(s - s_j) \approx i^M \sum_{k=1}^{M} x_k' a_I^{M-1} + i^{M-1} \sum_{k=1}^{M} x_k' \sum_{j\neq k}^{M}(a_R - s_j) a_I^{M-2} \tag{3.94}$$

The sum of Eqs. (3.93) and (3.94) has terms which all contain either i^M or i^{M-1}. Irrespective of the value of M, the terms must thus obey the relations

$$a_I^M + \sum_{k=1}^{M} x_k' a_I^{M-1} \approx 0 \tag{3.95}$$

and

$$\sum_{k=1}^{M}(a_R - s_k) a_I^{M-1} + \sum_{k=1}^{M} x_k' \sum_{j\neq k}^{M}(a_R - s_j) a_I^{M-2} \approx 0 \tag{3.96}$$

Equation (3.95) yields the expression for the imaginary part of the root as

$$a_I \approx -\sum_{k=1}^{M} x_k' \tag{3.97}$$

while Eq. (3.97) in Eq. (3.96) leads to

$$-\left(\sum_{k=1}^{M}(a_R - s_k)\right)\left(\sum_{k=1}^{M} x_k'\right) + \sum_{k=1}^{M} x_k' \sum_{j\neq k}^{M}(a_R - s_j) \approx 0 \tag{3.98}$$

and this can be reduced to

$$\sum_{k=1}^{M} x_k'(a_R - s_k) \approx 0 \tag{3.99}$$

From Eqs. (3.97) and (3.99) we thus have as Mth complex-valued root of Eq. (3.92)

$$a_{M0} \approx \left(\sum_{k=1}^{M} x_k' s_k / \sum_{k=1}^{M} x_k'\right) - i\sum_{k=1}^{M} x_k' \tag{3.100}$$

The real part of this root gives the rotational inverse relaxation time of the fundamental mantle mode $M0$, while the imaginary part gives the Chandler wobble frequency σ_0 of the stratified model (compare also with Wu and Peltier's (1984) Eq. (68))

$$\sigma_0 \approx \sum_{k=1}^{M} x_k' \tag{3.101}$$

or

$$\sigma_0 \approx \sigma_r \sum_{k=1}^{M} \frac{k_j^T}{k_f^T s_j} \tag{3.102}$$

For the 5-layer model in Table 3.3 the complex root as given by Eq. (3.100) has the value

$$a_{M0} = -1.9467033513 + 5096.94178i \text{ kyr}^{-1} \tag{3.103}$$

while from a complex rootfinder applied to Eq. (3.92) with quadruple precision the root is determined as having the value

$$a_{M0} = -1.9467033558 + 5096.94204i \text{ kyr}^{-1} \tag{3.104}$$

The analytical formula (3.100) thus gives an extremely accurate approximation of a_{M0}.

3.5.4 *Unification of the Different Approaches*

Equations (3.100) and (3.102) are not only useful in the model approach following the method of Sabadini et al. (1982), but also prove helpful in establishing the equivalence with the model approach in Wu and Peltier (1984) for secular TPW.

If we consider Eq. (79) of Wu and Peltier (1984), then the formulation of Sabadini et al. (1982) alters this equation by the following four points:

(1) The term D_1 in Wu and Peltier's (1984) Eq. (79) becomes zero. This term D_1 is an elastic term which arises from the first term (being 1) on the right hand side of Wu and Peltier's (1984) Eq. (75). The term D_1 is a direct consequence of the fact that there is one rotational relaxation mode less than the number of load relaxation modes. This term of unity would be absent if there were N rotational relaxation modes corresponding with the N load relaxation modes inside the square brackets of the last line in Wu and Peltier's (1984) Eq. (74).

(2) The term D_2 becomes $-i\sigma_0 D_2$ in Wu and Peltier's (1984) Eq. (79), but at the same time the term D_2 is divided by the extra root $-a_{M0}$ of our Eq. (3.100) in Wu and Peltier's (1984) Eq. (80). As the imaginary part is orders of magnitude larger than the real part, the effect on Wu and Peltier's (1984) Eq. (80) is that D_2 is to a high approximation divided by $-i\sigma_0$, so that the total effect on Wu and Peltier's (1984) Eq. (79) is that the original term D_2 remains unchanged (note that our roots a_i have the opposite sign of Wu and Peltier's (1984) corresponding roots λ_i).

(3) The terms E_i in Wu and Peltier's (1984) Eq. (79) become $-i\sigma_0 E_i$, but at the same time the terms E_i in Wu and Peltier's (1984) Eq. (80) are to a high approximation divided by the extra term $-i\sigma_0$, which is again a consequence of the fact that the extra rotational relaxation mode has an imaginary term in our Eq. (3.100), being orders of magnitude larger than the real part. The net effect is thus, just as in point

(2), that the terms E_i remain to a high approximation unchanged in Wu and Peltier's (1984) Eq. (79).

(4) The final change in Wu and Peltier's (1984) Eq. (79) concerns the addition of the extra term $E_N f * \exp(a_{M0}t)$. This term causes the wobble. It turns out that if this extra term is averaged over time, i.e. when the wobble is filtered out, then the contribution which remains is numerically equal to D_1 to a high approximation.

The net effect of points (1)–(4) is thus that the elastic term D_1 in Wu and Peltier's (1984) theory contains the signal due to the $M0$ rotational relaxation mode of Sabadini et al. (1982) when the Chandler wobble is filtered out. Together with points (2) and (3), one thus can conclude that to a high approximation the theoretical developments in Sabadini et al. (1982), Wu and Peltier (1984) lead to the same results for secular TPW simulations.

A first step to unify the approaches by Sabadini et al. (1982); Wu and Peltier (1984) was taken in Sabadini et al. (1984).

3.6 Non-hydrostatic Bulge Contribution

Mitrovica et al. (2005) noticed that the inertia tensor of the real Earth is not only that of a homogeneous rotating planet plus an ice load perturbation as implied by Eq. (3.55), but that perturbations due to the mantle 3D structure are also present. Coming back to the stage before the linearization of the Euler dynamic equation (3.6), this is equivalent to adding to the equilibrium inertia tensor obtained by the rotational spin-up of the model, Eq. (3.32), the perturbations ΔI^C_{11}, ΔI^C_{22} and ΔI^C_{33} in the diagonal components due to mantle convection. This choice implies that mantle convection does not directly drive polar motion, since the off-diagonal components ΔI^C_{13} and ΔI^C_{23} due to mantle convection are not added, or, alternatively, that the axis of rotation has already readjusted to the slowly evolving convection forcing so that the off-diagonal inertia perturbations are only those arising from post glacial rebound. This assumption implies that the evolution of the convective mantle is so slow that it appears frozen during the glaciation-deglaciation phases. Since the series of eight ice age cycles occurs over 800 kyr, this remains probably a reasonable approximation but not necessarily so and convection may also have contributed to the TPW during this period. According to Besse and Courtillot (1991), over geological times the TPW occurs indeed at rates not much slower than those due to glacial readjustments. This suggests that the two processes of mantle driven and surface driven TPW may interact with each other. Before Mitrovica et al. (2005), in all studies of glaciation induced TPW, the diagonal components ΔI^C_{11}, ΔI^C_{22} and ΔI^C_{33} were not introduced, and the mantle was considered without lateral density variations. The role of mantle convection was studied separately from the ice age TPW, as was done by Ricard et al. (1993a).

By keeping the assumption of symmetry around the polar axis, $\Delta I^C_{11} = \Delta I^C_{22}$, and the superscript C standing for convection, we therefore perform the changes

$$C \to C + \Delta I_{33}^C \qquad A \to A + \frac{\Delta I_{11}^C + \Delta I_{22}^C}{2} \tag{3.105}$$

Particularly, Eq. (3.34) has to be written as

$$k_{f,obs}^T = k_f^T + \beta = \frac{3\,G\,(C-A)}{a^5\,\Omega^2} \tag{3.106}$$

with $k_{f,obs}^T$ being the observed fluid Love number and

$$\beta = \frac{3\,G}{a^5\,\Omega^2}\left(\Delta I_{33}^C - \frac{\Delta I_{11}^C + \Delta I_{22}^C}{2}\right) \tag{3.107}$$

with $\beta = 0.008$, to which we refer as the β *correction* to the tidal fluid limit k_f^T following Eq. (16) in Mitrovica et al. (2005). The $k_{f\,obs}^T$ is thus an observation and k_f^T a prediction from viscoelastic modelling, while β is the contribution of mantle convection, assumed frozen during the period of ice age TPW. In view of this, Eq. (3.65) becomes

$$\frac{i\,s}{\sigma_r}\,\tilde{\mathbf{m}}(s) + \left(1 - \frac{k_2^T(s)}{k_f^T + \beta}\right)\tilde{\mathbf{m}}(s) = \left(1 + k_2^L(s)\right)\,\tilde{\phi}(s) \tag{3.108}$$

Making use of $k_{f\,obs}^T = k_f^T + \beta$, rather than k_f^T, has thus the meaning of coupling, in a simplified fashion and within a linearized scheme, the effects of the ice age TPW with those from mantle convection, but assuming for the latter only its contribution to the non hydrostatic ellipsoidal shape of the Earth (ΔI_{11}^C, ΔI_{22}^C and ΔI_{33}^C differing from zero) and not its active driving effect (ΔI_{13}^C, ΔI_{23}^C assumed equal to zero). It should be noted that Eq. (3.108) is the counterpart, within our formalism, of Eq. (6) in Mitrovica et al. (2005), based on the formalism of Wu and Peltier (1984), which we have previously demonstrated to be equivalent to ours for loadings changing slowly with respect to σ_r, that corresponds to neglecting the first term $\frac{i\,s}{\sigma_r}\,\tilde{\mathbf{m}}(s)$ in the left member of Eq. (3.108).

For layered incompressible models, in which the number of modes is known a priori, it is possible to show analytically how the β correction impacts the linearized equation for the ice age TPW. From the normal mode expansions of the gravitational tidal Love numbers in the Laplace s-domain

$$k_2^T(s) = k_E^T + \sum_{j=1}^{M} \frac{k_j^T}{s - s_j} \tag{3.109}$$

with k_E^T, k_j^T and s_j being the elastic gravitational Love number, the residues and the poles of the jth relaxation mode. The long term behavior, when $s = 0$, is controlled by

$$k_f^T = k_E^T - \sum_{j=1}^{M} \frac{k_j^T}{s_j} \tag{3.110}$$

and therefore $k_2^T(s)$ can be rearranged as follows, in agreement with Eq. (3.70)

$$k_2^T(s) = k_f^T + s \sum_{j=1}^{M} \frac{k_j^T}{s_j \left(s - s_j\right)} \tag{3.111}$$

Similarly, the loading Love number $k_2^L(s)$ can be arranged as follows

$$k_2^L(s) = k_f^L + s \sum_{j=1}^{M} \frac{k_j^L}{s_j \left(s - s_j\right)} \tag{3.112}$$

This allows us to collect in Eq. (3.65) (i.e. in the case $\beta = 0$ where the initial flattening is only due to rotation without contribution from mantle dynamics) a term linear in the Laplace variable s, in agreement with the definition given in Eq. (3.66)

$$s \left(\frac{i}{\sigma_r} - \frac{1}{k_f^T} \sum_{j=1}^{M} \frac{k_j^T}{s_j \left(s - s_j\right)} \right) \tilde{\mathbf{m}}(s) = \left(1 + k_f^L + s \sum_{j=1}^{M} \frac{k_j^L}{s_j \left(s - s_j\right)} \right) \tilde{\phi}(s) \tag{3.113}$$

as in Eq. (3.71), which is the above equation multiplied by $-i\sigma_r$. By solving this equation for $\tilde{\mathbf{m}}(s)$, we obtain

$$\tilde{\mathbf{m}}(s) = \frac{1 + k_f^L + s \sum_{j=1}^{M} \frac{k_j^L}{s_j (s - s_j)}}{s \left(\frac{i}{\sigma_r} - \frac{1}{k_f^T} \sum_{j=1}^{M} \frac{k_j^T}{s_j (s - s_j)} \right)} \tilde{\phi}(s) \tag{3.114}$$

where the factor s collected at the denominator is responsible for the so-called secular term, which characterizes the ice age TPW in such a way that it gains a net displacement at the end of each ice age cycle.

If now we want to account for the contribution of mantle convection to the inertia tensor by applying the β correction, Eq. (3.114) becomes

$$\tilde{\mathbf{m}}(s) = \frac{1 + k_f^L + s \sum_{j=1}^{M} \frac{k_j^L}{s_j (s - s_j)}}{\frac{\beta}{k_f^T + \beta} + s \left(\frac{i}{\sigma_r} - \frac{1}{k_f^T + \beta} \sum_{j=1}^{M} \frac{k_j^T}{s_j (s - s_j)} \right)} \tilde{\phi}(s) \tag{3.115}$$

The secular term is, in this case, substituted by an extra exponential decaying term, which drags the equatorial bulge and forces the ice age TPW to return to the initial position of the rotation axis, after a sufficiently long time. This can be explained in the following way. While the hydrostatic flattening readjusts during the ice age TPW, the

mantle density anomalies act as a counterweight that limits the polar excursion and ultimately control the position of the pole (Fig. 14 of Mitrovica et al. 2005). We will show that these considerations are not restricted to the simple layered incompressible models, but they extend also to the case of more realistic compressible models, used in Chap. 4, which take into account the continuous variations of the material parameters. It is noteworthy that our advanced Earth's models have a continuous relaxation spectrum (Fang and Hager 1995; Tanaka et al. 2006; Cambiotti and Sabadini 2010), which does not allow the analytical derivation of Eqs. (3.114) and (3.115) based on the discretized normal mode expansion given by Eq. (3.109).

3.7 Readjustment of the Rotational Bulge

The term $(1 - \frac{k_2^T}{k_f^T})$ entering Eq. (3.60) represents the readjustment of the rotational equatorial bulge to a new rotation axis, where the total readjustment is obtained when $k_f^T - k^T = 0$. When the Earth is elastic, this readjustment is instantaneous, otherwise it takes time, and this term tells us how fast this readjustment is. We first elucidate the role of the rheology of the lithosphere, elastic or viscoelastic. We assume that the 120 km thick viscoelastic lithosphere has a very high viscosity $\nu_{\mathrm{L}} = 10^{26}$ Pa s. The lower and upper mantle viscosities are $\nu_{\mathrm{LM}} = 10^{22}$ and $\nu_{\mathrm{UM}} = 10^{21}$ Pa s. Sections 3.7 and 3.8 are based on the material parameters, density ρ, rigidity μ and bulk modulus k as given in Table 1 of Dziewonski and Anderson (1981), interpolated in terms of polynomials depending on the radial distance r from the Earth's centre, so as to produce a continuous variation of the material parameters, without any fine layering. Rather than normal modes, anti-transformation from the s-domain to the time domain is carried out via complex contour integration, as enlightened in Sect. 1.9.

In Fig. 3.3a we compare the time evolution of the Green function $k_f^T - K^T$, with capital K^T being the convolution of the tidal gravitational Love number k_2^T with the Heaviside time history H, for the models with the elastic (E, solid line) and viscoelastic (V, dashed line) lithospheres

$$K^T(t) = k_2^T(t) \star H(t) \tag{3.116}$$

We obtain $k_{f,E}^T = 0.920$ and $k_{f,V}^T = 0.934$ for the cases of elastic and viscoelastic lithospheres. The difference between the tidal fluid limits $k_{f,V}^T - k_{f,E}^T = 0.014$ reflects a difference in the equilibrium flattening. The elastic lithosphere carries a finite strength that, instead, the model with the viscoelastic lithosphere does not have, being fully relaxed at large time (i.e., the elastic lithosphere is pre–stressed while the viscoelastic lithosphere is in hydrostatic equilibrium). Note that the Green function $k_{f,E}^T - K_E^T$ for the elastic lithosphere case (solid line) is always smaller than the Green function $k_{f,V}^T - K_V^T$ for the viscoelastic case (dashed line). Within 10 Myr, $k_{f,E}^T - K_E^T$ approaches zero, namely the equatorial bulge readjusts completely

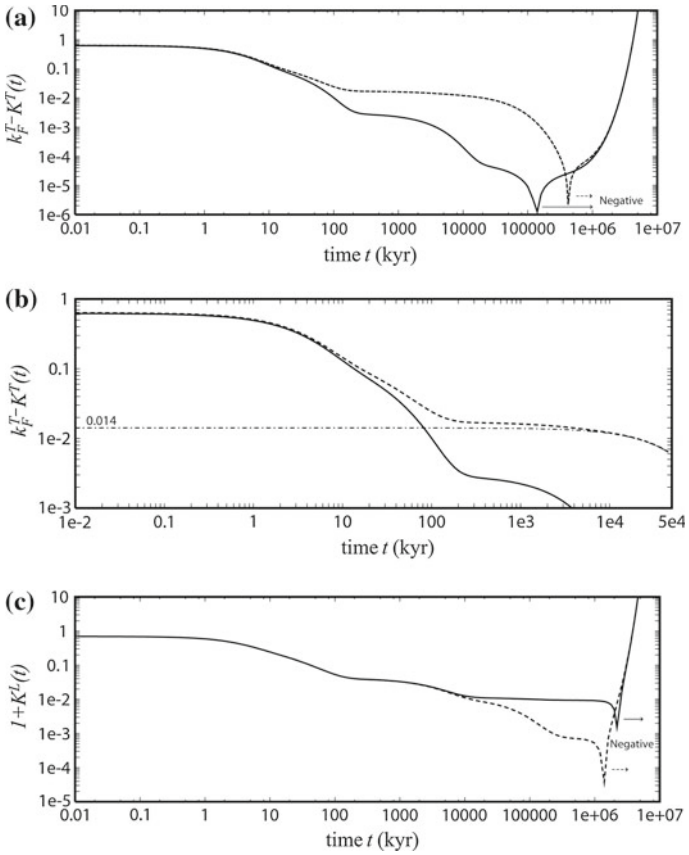

Fig. 3.3 **a**, **b** Readjustment of the equatorial bulge, $k_f^T - K^T$, and **c** load response, $1 + K^L$, for compressible PREM with elastic (*solid*) and high viscous viscoelastic (*dashed*) lithosphere and lower mantle viscosity $\nu_{\mathrm{LM}} = 10^{22}$ Pa s. In panel (**b**), enlarged from panel (**a**), the difference between the readjustment of the equatorial bulge of the model with the elastic (E) and viscoelastic (V) lithosphere is also shown, $k_{f,V}^T - K_V^T - (k_{f,E}^T - K_E^T)$ (*dash–dotted line*)

to a new rotation axis. On the contrary $k_{f,V}^T - K_V^T$ is 0.014 at 10 Myr, which is precisely the difference between the tidal fluid limits $k_{f,V}^T$ and $k_{f,E}^T$. This indicates that the accumulated stresses during the displacement of the equatorial bulge are almost completely relaxed within the viscoelastic mantle, but they are still present in the viscoelastic lithosphere with high viscosity. Indeed the viscoelastic lithosphere behaves as an elastic body at time scales lower than the lithospheric Maxwell time, 30 Myr. We show this in Fig. 3.3b for the time window of 50 Myr where, in addition to the previous Green functions, we plot also their difference $k_{f,V}^T - K_V^T - \left(k_{f,E}^T - K_E^T\right)$ (dash–dotted line). Before 10 Myr, the Green functions K_V^T and K_E^T coincide and the only difference between $k_{f,V}^T - K_V^T$ and $k_{f,E}^T - K_E^T$ is due to the difference in tidal fluid limits $k_{f,V}^T - k_{f,E}^T = 0.014$. After 10 Myr this difference is reduced since the

viscoelastic lithosphere relaxes and the rotational bulge readjusts completely to the new rotation axis. Nevertheless, as shown in Fig. 3.3a, this process is intermingled with the gravitational overturning due to the unstable compositional stratification of PREM above the 670 km discontinuity (Plag and Jüttner 1995). The unstable compositional modes (Cambiotti and Sabadini 2010) make K^T change sign. The cuspidal point at $t = 400$ Myr represents, in the logarithmic scale, this change of sign, from positive to negative, of the Green function $k^T_{f,V} - K^T_V$ for the case of viscoelastic lithosphere. For the elastic lithosphere case, the change of sign of the Green function $k^T_{f,E} - K^T_E$ occurs at 130 Myr. This overturn is a mathematical consequence of the unstable PREM stratification but has little physical consequence because TPW is anyway dominated by mantle convection on this long time scale (Spada et al. 1992b).

In Fig. 3.3c we compare the time evolution of the Green function $1 + K^L$, with K^L being the convolution of the load gravitational Love number k^L_2 with the Heaviside time history H, for models with elastic (E, solid line) and viscoelastic (V, dashed line) lithospheres

$$K^L(t) = k^L_2(t) \star H(t) \tag{3.117}$$

It expresses the return to isostatic compensation of a surface point–like load, that is obtained when $1 + K^L = 0$. The two load Green functions agree up to 10 Myr, but after this time $1 + K^L_V$ goes to zero for the viscoelastic lithosphere case as the load becomes fully compensated. Instead, $1 + K^L_E$ for the elastic lithosphere case converges to the value of 0.01, which is the gravitational anomaly $1 + k^L_{f,E}$ remaining because of the elastic support. In the end, starting from 1 Gyr, the gravitational overturn breaks the final equilibrium with the load, the cuspidal points at 2.3 and 1.3 Gyr for the elastic and viscoelastic lithosphere cases, respectively, having the same meaning as in Fig. 3.3a.

These findings show that over the time scale of post glacial rebound and until 10 Myr as well, there are no significant differences between the tidal, K^T, and load, K^L, Green functions computed with an elastic lithosphere or with a viscoelastic lithosphere with high viscosity, $\nu_{\mathrm{L}} = 10^{26}$ Pa s. However the wandering of the rotation pole involves not only the Love numbers K^T and K^L at short time period but also the limit at infinite time of the tidal Green function K^T, which is the so called tidal fluid limit k^T_f as seen in Eq. (3.69). Particularly, the rheology of the lithosphere, elastic or viscoelastic (i.e., fluid at infinite time) does affect the TPW because it controls the equilibrium figure of the Earth because $k^T_{f,V} \geq k^T_{f,E}$ (see also Fig. 1 in Mitrovica et al. 2005). The equilibrium figures are different for the two cases and the rotation of the model with the high viscous viscoelastic lithosphere is more stable since its equatorial bulge is not able to readjust to a new rotation axis on the ice age time scale (Mitrovica et al. 2005). From Fig. 3.3, we can understand that the sensitivity on the lithospheric rheology, pointed out by Nakada (2002), actually is due to the stabilizing effects of delay of the readjustment of the rotational bulge. Classically, the lower mantle viscosity ν_{LM} was considered as the main parameter controlling this delay. Instead, adopting Earth's models with the high viscous viscoelastic lithosphere allows to take into account also the delay associated with the high lithospheric viscosity ν_{L},

in addition to that associated with the lower mantle viscosity $\nu_{\rm LM}$. In view of this, models with elastic and viscoelastic lithospheres are not expected do lead to the same TPW.

3.8 Compressible and Incompressible Readjustment of the Equatorial Bulge

Incompressible Maxwell Earth's models have been widely used in the last three decades for TPW simulations. For this reason we now compare these models with the compressible Maxwell Earth's models. At the same time, we quantify the effects of the different rheologies of the lithosphere, elastic or viscoelastic.

Figure 3.4 shows the comparison between the compressible (solid line) and incompressible (dashed line) Green functions $k^T_{f,E} - K^T_E$ in the case of an elastic (E) lithosphere, 120 km thick. The lower mantle viscosity $\nu_{\rm LM}$ is increased by one order of magnitude from 10^{21} to 10^{23} Pa s from top to bottom panel. The time window considered is 10 Myr, much longer than the ice age time scale of 1 Myr. In general the compressible rotational bulge readjusts faster than the incompressible one. Indeed, the Green function $k^T_{f,E} - K^T_E$ for the compressible model is lower than that for the incompressible model, with the exception of the time intervals 3×10^2–4×10^3 kyr (panel (a)) and 10^3–10^4 kyr (panel (b)) for the lower mantle viscosities $\nu_{\rm LM} = 10^{21}$ and 10^{22} Pa s, respectively. For $\nu_{\rm LM} = 10^{23}$ Pa s (panel c) the two models predict very similar values until 1 Myr, where the compressible rotational bulge begins to readjust faster to the new rotation axis than the incompressible rotational bulge.

In Fig. 3.5, the elastic (E) lithosphere has been replaced by the viscoelastic (V) lithosphere, with viscosity $\nu_{\rm L} = 10^{26}$ Pa s. In this case, the Green function $k^T_{f,V} - K^T_V$ for the compressible model is always lower than that for the incompressible model. The vertical scale has been reduced compared to Fig. 3.4. Indeed, at 10 kyr, all the layers have significantly relaxed except for the high viscous viscoelastic lithosphere, which behaves as an elastic body as shown in Fig. 3.3b. At 10 Myr both the compressible and incompressible Green functions $k^T_{f,V} - K^T_V$ differ from zero by the discrepancy $k^T_{f,V} - k^T_{f,E}$. Since $k^T_{f,E}$ depends on the rheology of the elastic lithosphere, compressible, 0.920, or incompressible, 0.918, the discrepancy $k^T_{f,V} - k^T_{f,E}$ for the compressible model, 0.014, is smaller than that for the incompressible model, 0.016. Thus, before 10 Myr, the viscoelastic compressible lithosphere is more deformable than the incompressible lithosphere and this explains the fact that the compressible bulge readjust faster than the incompressible bulge.

Figure 3.6 shows the comparison between the compressible (solid line) and incompressible (dashed line) Green function $1 + K^L_E$ for the elastic (E) lithosphere case. As in Figs. 3.4 and 3.5, the lower mantle viscosity $\nu_{\rm LM}$ is increased of one order of magnitude from 10^{21} to 10^{23} Pa s in each panel and we consider a time window of 10 Myr. The Green function $1 + K^L_E$ for the compressible model is always lower than for the incompressible models, indicating that compressible models are more

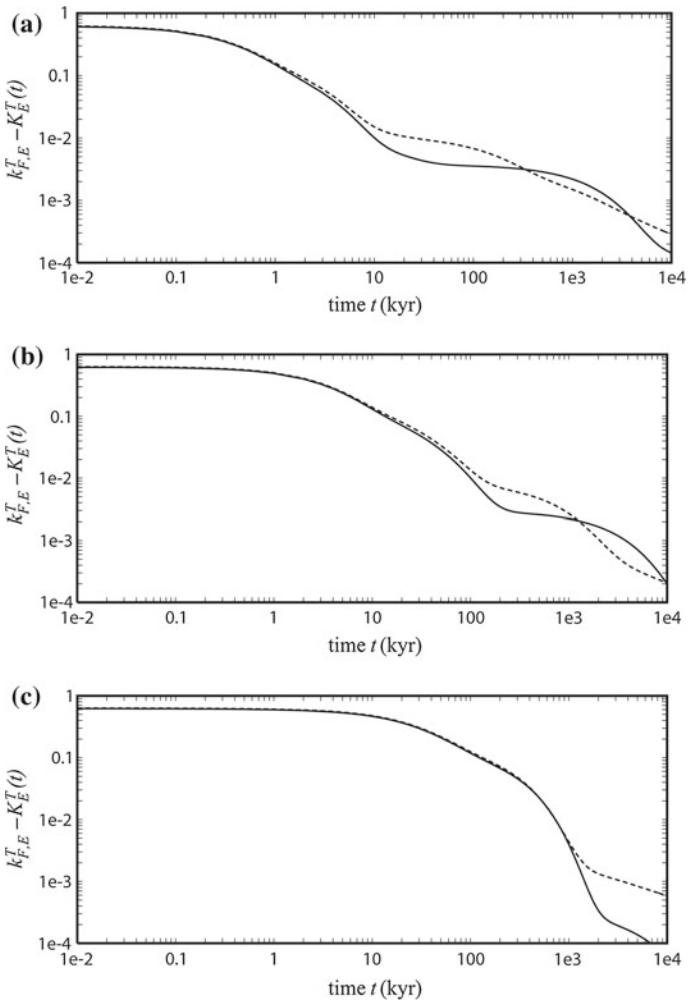

Fig. 3.4 Readjustment of the equatorial bulge, $k^T_{f,E} - K^T_E$, for compressible (*solid*) and incompressible (*dashed*) PREM with elastic lithosphere. The lower mantle viscosity ν_{LM} is **a** 10^{21} Pa s, **b** 10^{22} Pa s and **c** 10^{23} Pa s

deformable. The difference between the compressible and the incompressible cases is larger for the load response than for the equatorial bulge readjustment (compare Fig. 3.6 with Figs. 3.4 and 3.5). Particularly, in the elastic limit $t \to 0$, the readjustment of the equatorial bulge is marginally affected by the different rheologies

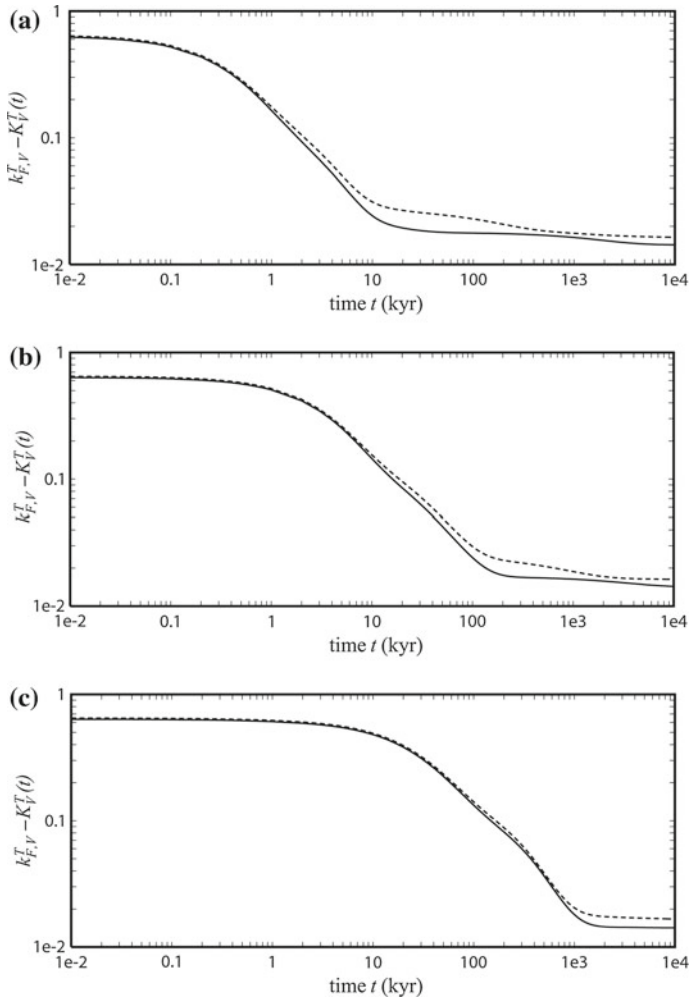

Fig. 3.5 Readjustment of the equatorial bulge, $k^T_{f,V} - K^T_V$, for compressible (*solid*) and incompressible (*dashed*) PREM with viscoelastic lithosphere. The lower mantle viscosity ν_{LM} is **a** 10^{21} Pa s, **b** 10^{22} Pa s and **c** 10^{23} Pa s, and the lithosphere viscosity ν_{L} is always 10^{26} Pa s

(see Figs. 3.4 and 3.5), while compressible and incompressible cases differ by 10 % for loading, Fig. 3.6. We do not show the results for the model with the viscoelastic lithosphere since, on the time scale of 10 Myr, they are very similar to those shown in Fig. 3.6 for the elastic lithosphere case.

By comparing the Green functions between the panels of Figs. 3.4, 3.5 and 3.6, we note that the increase of the lower mantle viscosity ν_{LM} by two orders of magnitude, from 10^{21} to 10^{23} Pa s, delays by about two orders of magnitude the time at which

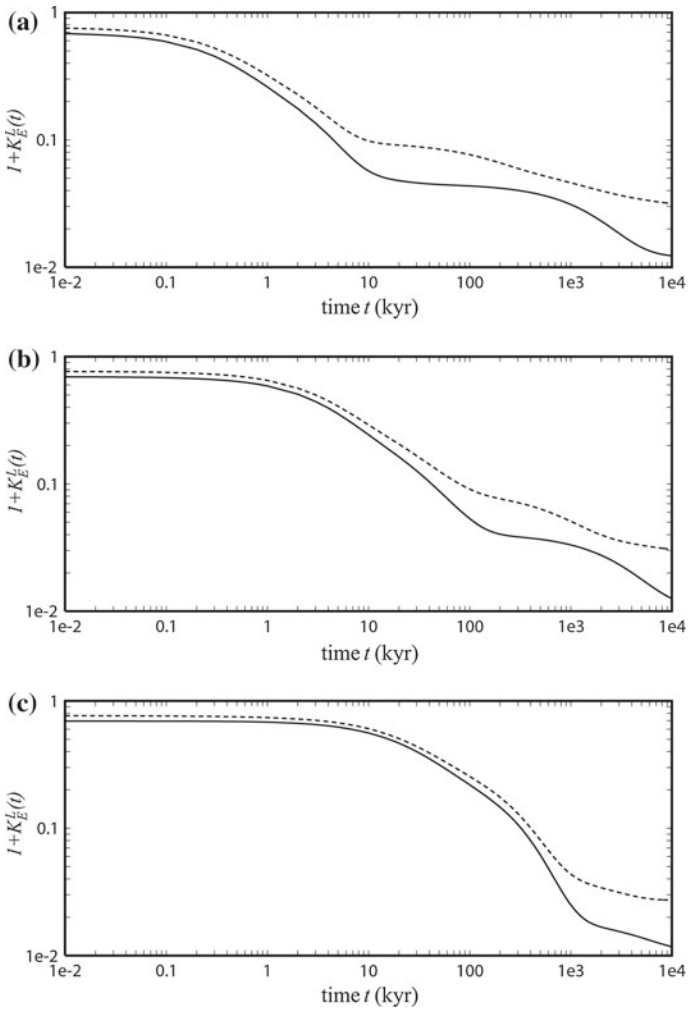

Fig. 3.6 Load response $1 + K_E^L$ of the compressible (*solid*) and incompressible (*dashed*) PREM with the elastic lithosphere. The lower mantle viscosity ν_{LM} is **a** 10^{21} Pa s, **b** 10^{22} Pa s and **c** 10^{23} Pa s

compressibility becomes effective during the transient, from 10 to 10^3 kyr, both for loading and equatorial bulge readjustments. Particularly, for the high lower mantle viscosity $\nu_{\mathrm{LM}} = 10^{23}$ Pa s (panel (c)), the compressibility is almost undistinguishable from incompressibility on time scale of the ice ages, 1 Myr.

3.9 Long-Term Behavior of the Rotation Equation

The rotation Eq. (3.114) is characterized by terms of different nature, the first one with the pole in $s = 0$ and the second one consisting of a summation over a series of poles in $s = a_i$. Independently of the strength of these two contributions, the physics of these two contributions is quite different. Once multiplied in the Laplace domain by $1/s$, denoting a constant load in time, the term in A_0 provides a polar wander which grows linearly in time, while the terms in a_i excite exponentially decaying polar shifts. The impact of the different nature of these terms on polar wander studies has not been elucidated in the literature, mainly because interest has been focussed on the present day rotational response of the Earth to the last glacial cycle of the Pleistocene deglaciation, which arises solely from the exponential terms. This section is thus devoted to the understanding of the physics underlying these two different classes of s-poles.

It is possible to get a deep insight into the physics of the $s = 0$ pole, whose strength is given by A_0, in terms of normal mode theory by studying the long-term behavior of the equation for retrieving $\mathbf{m}(s)$. In Eq. (3.71) we can take the limit for $|s| \ll |s_i|$, which makes this rotation, Eq. (3.71), to take the form

$$\mathbf{m}(s) = \frac{-i\sigma_r \mathbf{\Phi}_L(s)}{s(1 - \frac{i\sigma_r}{k_f^T} T_1)} \tag{3.118}$$

with T_1 denoting the time scale of readjustment of the equatorial bulge given by

$$T_1 = \sum_{i=1}^{N} \frac{k_i^T}{s_i^2} \tag{3.119}$$

Comparison between Eqs. (3.118) and (3.83) indicates that the explicit expression of the term A_0 is given by

$$A_0 = \frac{1}{(1 - \frac{i\sigma_r}{k_f^T} T_1)}, \tag{3.120}$$

since the $s = 0$ limit of the two equations must coincide. Equation (3.118) becomes in the time domain

$$\frac{d}{dt}\mathbf{m} = \frac{-i\sigma_r \mathbf{\Phi}_L}{1 - \frac{i\sigma_r}{k_f^T} T_1} = -i\sigma_r A_0 \mathbf{\Phi}_L \tag{3.121}$$

The basic equations for true polar wander in the $s = 0$ limit can thus be cast in terms of the time scale required for the readjustment of the rotational bulge induced by perturbation in the Earth's rotation, as shown in Sabadini and Yuen (1989) or Spada et al. (1992b). The long time scale rotational state of the Earth depends on the rheology of the mantle through the term T_1.

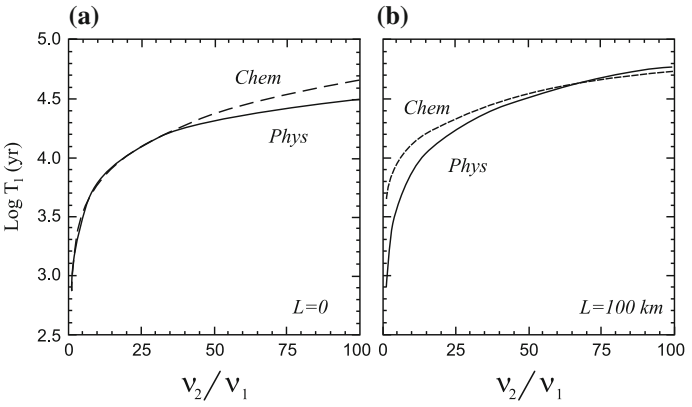

Fig. 3.7 T_1 as a function of the lower mantle-upper mantle viscosity ratio ν_2/ν_1. ν_1 is fixed at 10^{21} Pa s. The *solid line* corresponds to a mantle of uniform density to mimic the effects of a completely adiabatic mantle, while the *dashed curve* stands for a fully non-adiabatic (chemical) 670 km discontinuity. Panels **a** and **b** stand for a model without lithosphere (lithospheric thickness $L = 0$) and for a model carrying a lithosphere of 100 km ($L = 100$ km)

In the following Fig. 3.7, the time scale T_1 associated to the readjustment of the equatorial bulge is plotted for a 4-layer Earth's model, as a function of the viscosity ratio between the lower and upper mantle, for two different lithospheric thicknesses L ($L = 0$, panel (a) and $L = 100$ km, panel (b)) and for a fully adiabatic and chemical boundary at 670 km (solid and dashed curves).

Exercise 17 Taking into account the expression of the fluid tidal Love number

$$k_f^T = k_e^T - \sum_{i=1}^{M} \frac{k_i^T}{s_i} \tag{3.122}$$

and the first order approximation of the relaxing terms above, demonstrate that the long time scale version of the rotation equation takes the form in the time domain

$$\frac{d}{dt}\mathbf{m}(t) = \frac{1}{(1/k_f^T + i/R_o)} \frac{\Delta I_{13} + i\Delta I_{23}}{T_1(C-A)} \tag{3.123}$$

where the dimensionless rotational number R_o is defined by

$$R_o = \frac{\Omega T_1 J_2}{I^*}, \tag{3.124}$$

being $I^* = A/M_E a^2$, J_2 the dynamic form factor given by

$$J_2 = \frac{(C-A)}{M_E a^2} \tag{3.125}$$

and T_1 as given by Eq. (3.119).

Equation (3.123) shows that true polar wander can thus be given in terms of the dimensionless parameter R_o and contains in a simple, clear fashion, the physics underlying the long-term rotation behavior. This number depends on the separation of the two time scales $2\pi\Omega^{-1}$ and T_1, the former providing the length of the sidereal day and the latter providing the span of time required for the readjustment of the rotational bulge due to perturbations in the Earth's rotation (Sabadini and Yuen 1989). Depending on the two limits $R_o \gg 1$ and $R_o \ll 1$, it is in fact possible, as we show in Sect. 3.11 dealing with the rotational behavior of the terrestrial planets, to quantify their long-term rotational behavior. Through T_1, R_o depends on the rheology of the mantle. A precise estimate of this number for the solid planets cannot be obtained due to the large uncertainties in their rheological structure. In spite of the uncertainties due to our lack of information concerning mantle rheology, reasonable bounds for R_o can be deduced for most of the solid planets, sufficient to describe the basic characteristics of their long-term rotation. This problem will be tackled in Sect. 3.11.

3.9.1 Theory for Rotation Changes Due to Mantle Convection

TPW is generally taken as evidence of time-dependent mantle convection (Spada et al. 1992) and Pleistocene ice sheet melting (Sabadini and Peltier 1981; Mitrovica et al. 2005; Cambiotti et al. 2010). Owing to the ability of the rotational bulge to relax and readjust to perturbations of the rotation axis on a time scale T_1 that ranges from 1 to 100 kyr, depending on the internal viscoelastic stratification as shown in Fig. 3.7 (Ricard et al. 1993a), the Earth's rotation axis constantly tracks the Maximum Inertia Direction of Mantle Convection (MID-MC) on the million year time scale of mantle convection. On this long time scale, TPW simulations are often based on the assumption that the planet readjusts without delay and that the rotation axis and the MID-MC coincide (Jurdy 1978; Steinberger and O'Connell 1997; Rouby et al. 2010). We show in this section that this assumption is not correct and we quantify the offset between the rotation axis and the MID-MC in terms of the Earth's viscosity stratification.

Using mantle density anomalies observed by seismic tomography, Ricard and Sabadini (1990) showed out that the present-day rotation axis lags behind the MID-MC by some degrees. Ricard et al. (1993a) pointed out that the planet, submitted to a change of inertia of order E attributable to mantle convection, wanders with a characteristic time of order $T_1\,(C-A)/E$, where C and A are the polar and equatorial inertia moments and T_1 is given by Eq. (3.119). In view of this, the Earth can shift its rotation pole from a starting position to a new position in a time larger than a few 100 kyr or a few million years. On the basis of similar arguments, Steinberger and O'Connell (1997) estimated that the offset between the rotation axis and the MID-MC should be less than 1°, even for an high viscous mantle with lower mantle viscosity of 10^{23} Pa s. This estimate, however, was obtained assuming a MID-MC rate less than

0.2°/Myr during the past 50 Myr. Accounting for the delay of the readjustment of the rotational bulge and allowing for an offset between the geographic north pole and the present-day MID-MC, Richards et al. (1997) estimated TPW paths for different viscosity profiles of the mantle. Nevertheless, they did not quantify the offset and concluded that the influence of the delay on TPW is small.

In light of this, although Ricard et al. (1993a), Richards et al. (1997), Steinberger and O'Connell (1997) provided some insights into the long time scale rotational behavior of the Earth, a concise and complete picture of the problem has been lacking until the work by Cambiotti et al. (2011) came out, providing a new treatment of the non-linear Liouville equation to describe the long time scale rotational behavior of the Earth via a simple linear theory. This new treatment, in connection with seismic tomography, is thoroughly explored in the following.

We start with the basic laws governing the relative motion of the rotation axis with respect to the MID-MC. This relative motion is dealt with in the reference frame defined by the three eigenvectors $\boldsymbol{e}_k$ of mantle convection inertia tensor $\boldsymbol{\mathcal{C}}$

$$\boldsymbol{\mathcal{C}} = \sum_{k=1}^{3} C_k \, \boldsymbol{e}_k \otimes \boldsymbol{e}_k \tag{3.126}$$

where the algebraic product symbol is omitted in the following between two vectors, and where C_k are the inertia moments. Here C_3 is the maximum inertia moment ($C_3 \geq C_2$ and $C_3 \geq C_1$) and $\boldsymbol{e}_3$ is the MID-MC. This is a time dependent reference frame and, from geometric considerations (Ben-Menahem and Singh 2000), the time derivatives of the eigenvectors $\boldsymbol{e}_k$ yield

$$\frac{d\boldsymbol{e}_k}{dt} = \boldsymbol{\xi} \times \boldsymbol{e}_k \tag{3.127}$$

where $\boldsymbol{\xi}$ is the angular velocity of the mantle convection inertia that we write as follows

$$\boldsymbol{\xi} = -V_2 \, \boldsymbol{e}_1 + V_1 \, \boldsymbol{e}_2 + V_3 \, \boldsymbol{e}_3 \tag{3.128}$$

in such a way that V_1 and V_2 are the components of the MID-MC velocity $d\boldsymbol{e}_3/dt$ along the equatorial axes $\boldsymbol{e}_1$ and $\boldsymbol{e}_2$. V_3 describes the counterclockwise rotation rate of the equatorial axes around the MID-MC.

We write the Earth's angular velocity $\boldsymbol{\omega}$ as $\boldsymbol{\omega} = \omega \, \boldsymbol{n}$, where ω and $\boldsymbol{n}$ are the rotation rate and rotation axis. Within the reasonable assumption that the angle between the rotation axis and MID-MC is small, the rotation axis $\boldsymbol{n}$ can be expressed in terms of direction cosines m_1 and m_2 along the equatorial axes $\boldsymbol{e}_1$ and $\boldsymbol{e}_2$,

$$\boldsymbol{n} = m_1 \, \boldsymbol{e}_1 + m_2 \, \boldsymbol{e}_2 + \boldsymbol{e}_3 \tag{3.129}$$

The time variation of Earth's angular velocity $\boldsymbol{\omega}$ is therefore

$$\frac{d\boldsymbol{\omega}}{dt} = \boldsymbol{n}\frac{d\omega}{dt} + \omega\frac{d\boldsymbol{n}}{dt} \tag{3.130}$$

where the first term on the right is related to the change of the length of the day and the second term to the TPW velocity $\boldsymbol{v} = d\boldsymbol{n}/dt$ which, assuming that the time evolution of mantle convection is slow, becomes

$$\boldsymbol{v} = \left(\frac{dm_1}{dt} + V_1\right)\boldsymbol{e}_1 + \left(\frac{dm_2}{dt} + V_2\right)\boldsymbol{e}_2 \tag{3.131}$$

Equations (3.129) and (3.131) are correct to first order, for small m_1, m_2 and $\boldsymbol{\xi}$ (i.e., neglecting terms of order $m_i\, m_j$ or $m_i\, V_j$).

The rotation axis, averaged over a few Chandler periods, is aligned with the direction of maximum total inertia (Munk and MacDonald 1960), i.e., is the eigenvector of the sum of the inertia tensors due to the rotational bulge, $\boldsymbol{\mathcal{B}}$, and mantle convection, $\boldsymbol{\mathcal{C}}$,

$$\boldsymbol{n} \times (\boldsymbol{\mathcal{B}} + \boldsymbol{\mathcal{C}}) \cdot \boldsymbol{n} = 0 \tag{3.132}$$

We take into account the relaxation of the rotational bulge by means of the long-term approximation given by Eq. (7.10) first provided by Spada et al. (1992), Ricard et al. (1993a) and derived from MacCullagh's formula, Eq. (3.31), for centrifugal deformation. The second term of Eq. (7.10), pertaining to changes in the Earth's rotation, can be cast as follows

$$\boldsymbol{\mathcal{B}} = \alpha\,\omega^2\left[\left(1 - \frac{2\,T_1}{k_f^T\,\omega}\,\frac{d\omega}{dt}\right)\left(\boldsymbol{nn} - \frac{1}{3}\,\mathbf{1}\right) - \frac{T_1}{k_f^T}\,(\boldsymbol{nv} + \boldsymbol{vn})\right] \tag{3.133}$$

where ω is the Earth's rotation rate, $\mathbf{1}$ the identity matrix, T_1 the time scale of readjustment of rotational bulge given by Eq. (3.119) and $\alpha\,\omega^2$ the difference between polar and equatorial inertia moments of the hydrostatic rotational bulge. The time scale T_1 can be easily computed for any spherically symmetric viscoelastic Earth's model and is of the order of 30 kyr, as shown in Fig. 3.7 (Ricard et al. 1993a).

Equation (3.133) for the inertia of the rotational bulge is derived in the following. The long-term approximation of the MacCullagh's formula given in Eq. (10) of Ricard et al. (1993a) can be written in the dyadic formulation as follows

$$\boldsymbol{\mathcal{B}} = \alpha\left[\left(\omega_j\,\omega_k - \frac{1}{3}\,\omega^2\,\delta_{jk}\right) - \frac{T_1}{k_f^T}\left(\dot{\omega}_j\,\omega_k + \omega_j\,\dot{\omega}_k - \frac{2}{3}\,\omega_p\,\dot{\omega}_p\,\delta_{jk}\right)\right]\boldsymbol{x}_j\boldsymbol{x}_k \tag{3.134}$$

where $\boldsymbol{x}_j$ and ω_j are the unit vectors of the geographical reference frame and the corresponding components of Earth's angular velocity $\boldsymbol{\omega}$

$$\boldsymbol{\omega} = \omega\, \boldsymbol{n} = \omega_i\, \boldsymbol{x}_i \tag{3.135}$$

and

$$\alpha = k_f^T\, a^5/(3\, G) \tag{3.136}$$

with k_f^T being the degree-2 tidal gravitational fluid limit, Eq. 3.35 (Cambiotti et al. 2010; Chambat et al. 2010). The time derivative of Eq. (3.135) yields

$$\dot{\boldsymbol{\omega}} = \dot{\omega}\, \boldsymbol{n} + \omega\, \boldsymbol{v} = \dot{\omega}_i\, \boldsymbol{x}_i \tag{3.137}$$

Making use of the algebra of the dyadics, we note that

$$\omega_j\, \omega_k\, \boldsymbol{x}_j \boldsymbol{x}_k = \boldsymbol{\omega}\boldsymbol{\omega} = \omega^2\, \boldsymbol{n}\boldsymbol{n} \tag{3.138}$$

$$\omega^2\, \delta_{jk}\, \boldsymbol{x}_j \boldsymbol{x}_k = \omega^2\, \mathbf{1} \tag{3.139}$$

$$\dot{\omega}_j\, \omega_k\, \boldsymbol{x}_j \boldsymbol{x}_k = \dot{\boldsymbol{\omega}}\boldsymbol{\omega} = \omega\, \dot{\omega}\, \boldsymbol{n}\boldsymbol{n} + \omega^2\, \boldsymbol{v}\boldsymbol{n} \tag{3.140}$$

$$\omega_j\, \dot{\omega}_k\, \boldsymbol{x}_j \boldsymbol{x}_k = \boldsymbol{\omega}\dot{\boldsymbol{\omega}} = \omega\, \dot{\omega}\, \boldsymbol{n}\boldsymbol{n} + \omega^2\, \boldsymbol{n}\boldsymbol{v} \tag{3.141}$$

$$\omega_p\, \dot{\omega}_p\, \delta_{jk}\, \boldsymbol{x}_j \boldsymbol{x}_k = \omega\, \dot{\omega}\, \mathbf{1} \tag{3.142}$$

The two quantities within the round brackets of Eq. (3.134) can be cast as follows

$$\left(\omega_j\, \omega_k - \frac{1}{3}\, \omega^2\, \delta_{jk}\right) \boldsymbol{x}_j \boldsymbol{x}_k = \omega^2\, \left(\boldsymbol{n}\boldsymbol{n} - \frac{1}{3}\, \mathbf{1}\right) \tag{3.143}$$

$$\left(\dot{\omega}_j\, \omega_k + \omega_j\, \dot{\omega}_k - \frac{2}{3}\, \omega_p\, \dot{\omega}_p\, \delta_{jk}\right) \boldsymbol{x}_j \boldsymbol{x}_k$$

$$= 2\, \omega\, \dot{\omega}\, \left(\boldsymbol{n}\boldsymbol{n} - \frac{1}{3}\, \mathbf{1}\right) + \omega^2\, (\boldsymbol{v}\boldsymbol{n} + \boldsymbol{n}\boldsymbol{v}) \tag{3.144}$$

and, by using these results in Eq. (3.134), we obtain Eq. (3.133).

Exercise 18 Derive Eq. (3.134) making use of Eq. (1.45) and of the first order expansion of the tidal Love number in the s-domain.

Equation (3.133) accounts for the readjustment of the rotational bulge due to variations of the length of day via the term proportional to $d\omega/dt$. However, as we neglect the time derivative of the angular momentum in the Liouville equation averaged over a few Chandler periods, the length of day remains constant and the small quantity $(2T_1/k_f^T\omega)(d\omega/dt)$ can also be neglected.

Thus, by solving Eq. (3.132) using Eqs. (3.126), (3.129), (3.131) and (3.133), we obtain a first order differential equation for each direction cosine m_i

$$\frac{dm_i}{dt} + \frac{m_i}{T_{C_i}^{\alpha}} = -V_i \qquad (i = 1, 2) \tag{3.145}$$

where $T_{C_i}^{\alpha}$ are time scales defined by

$$T_{C_i}^{\alpha} = \frac{\alpha\,\omega^2}{k_f^T (C_3 - C_i)}\, T_1 \qquad (i = 1, 2) \tag{3.146}$$

Equations (3.145) and (3.146) show that V_i are the forcings of the relative motion of the rotation axis and that the time scales $T_{C_i}^{\alpha}$ controlling this relative motion are the time scale T_1 of the rotational bulge readjustment increased by the factor $\alpha\,\omega^2/(C_3 - C_i)$.

The difference between polar and equatorial inertia moments of the hydrostatic rotational bulge $\alpha\,\omega^2$ has been estimated (Chambat et al. 2010)

$$\alpha\,\omega^2 \approx 1.0712 \times 10^{-3}\, M_E a^2 \tag{3.147}$$

The differences between the inertia moments of mantle convection, $C_3 - C_i$, are typically of the order of the differences between the observed total inertia moments of the Earth (usually defined as A, B and C), minus the hydrostatic contribution $\alpha\,\omega^2$ (Chambat and Valette 2001)

$$\begin{aligned} C_3 - C_1 &\approx (C - A) - \alpha\,\omega^2 = 1.48 \times 10^{-5}\, M_E a^2 \\ C_3 - C_2 &\approx (C - B) - \alpha\,\omega^2 = 0.78 \times 10^{-5}\, M_E a^2 \end{aligned} \tag{3.148}$$

As already argued in Ricard et al. (1993a), the time scales $T_{C_i}^{\alpha}$ are greater than T_1 by a factor of about 100. Assuming $T_1 = 30$ kyr, the relative motion of the rotation axis is controlled by the time scales $T_{C_i}^{\alpha} \approx 3$ Myr, comparable with those of mantle convection, say greater than 1 Myr. These findings show that the previous approximation based on the assumption that the rotational bulge readjusts instantaneously to perturbations of the rotation axis is not accurate. This approximation missed in fact a fundamental aspect of TPW dynamics: the inertia perturbations due to mantle convection are two orders of magnitude smaller than those of the rotational bulge. Such a small quantity increases the time scales for viscoelastic readjustment of the rotational bulge during the TPW to values comparable to those of mantle convection. Furthermore, the two direction cosines m_1 and m_2 behave differently as $T_{C_1}^{\alpha}$ and $T_{C_2}^{\alpha}$

are likely to differ due to the dependence in Eq. (3.146) on the differences $C_3 - C_1$ and $C_3 - C_2$ (they differ by a factor of 2 at present-day). The time scales $T_{C_i}^{\alpha}$ evolve in time, potentially becoming infinite during inertial interchanges (Richards et al. 1999), a case that would invalidate our linearized approach.

The role of the time scales $T_{C_i}^{\alpha}$ becomes clear once we assume them as constants. In this case, the solution of the linearized Earth's rotation differential equations, Eq. (3.145), yields

$$m_i(t) = -e^{-t/T_{C_i}^{\alpha}} \star V_i \qquad (i = 1, 2) \tag{3.149}$$

where $\star$ stands for the time convolution: this solution shows that the time scales $T_{C_i}^{\alpha}$ are the relaxation times for the relative motion of the rotation pole forced by the MID-MC velocity components V_i. In this respect, Eq. (3.145) and its particular solution, Eq. (3.149), allow us to catch the effects on TPW dynamics due to the delay of the readjustment of the rotational bulge and to the time evolution of mantle convection. A MID-MC velocity, constant for a time greater than $T_{C_i}^{\alpha}$, drives the pole at the same velocity, $dm_i/dt = 0$, but with the pole lagging behind the MID-MC by the angle

$$m_i = -T_{C_i}^{\alpha} V_i \qquad (i = 1, 2) \tag{3.150}$$

This result has the same physical meaning as Eq. (1) of Steinberger and O'Connell (1997). Furthermore, from Eq. (3.149), it is also clear that variations of the MID-MC velocity, occurring on times comparable or smaller than $T_{C_i}^{\alpha}$, break the equilibrium of the relative position of the rotation axis with respect to the MID-MC given by Eq. (3.150). Particularly, they yield different TPW and MID-MC velocity amplitudes and directions. This result cannot be inferred within the previous framework (Ricard et al. 1993a; Richards et al. 1997; Steinberger and O'Connell 1997) and shows that estimates of TPW rates must account both for fluctuations of the Earth's inertia tensor and of the delay of readjustment of the rotational bulge.

3.10 Time-Dependent Inertia Due to Mantle Convection

Let us consider the components $\mathcal{C}_{ij} = \boldsymbol{x}_i \cdot \boldsymbol{\mathcal{C}} \cdot \boldsymbol{x}_j$ and $\mathcal{B}_{ij} = \boldsymbol{x}_i \cdot \boldsymbol{\mathcal{B}} \cdot \boldsymbol{x}_j$ of the mantle convection and rotational bulge inertia tensors in the geographical reference frame with unit vectors $\boldsymbol{x}_1$, $\boldsymbol{x}_2$ and $\boldsymbol{x}_3$ ($\boldsymbol{x}_1$ points to the Greenwich meridian, while $\boldsymbol{x}_3$ points to the north pole, i.e., coincides with the present-day rotation axis). In view of Eq. (3.132), at present time $t = 0$, the total inertia tensor (mantle convection plus rotational bulge) has zero off-diagonal components along $\boldsymbol{x}_3$

$$\mathcal{C}_{i3}(0) + \mathcal{B}_{i3}(0) = 0 \qquad (i = 1, 2) \tag{3.151}$$

and, by making use of Eq. (3.133), we obtain in the geographycal reference frame

$$\mathcal{C}_{i3}(0) = \alpha\,\omega^2\,T_1\,\boldsymbol{x}_i \cdot \boldsymbol{v}(0) \qquad (i = 1, 2) \tag{3.152}$$

corresponding to Eqs. (8)–(9) of Ricard et al. (1993b) or Eq. (3) of Steinberger and O'Connell (1997). Thus, the off-diagonal components $\mathcal{C}_{13}(0)$ and $\mathcal{C}_{23}(0)$ of the mantle convection inertia tensor are non-zero in a wandering planet (i.e., when $\boldsymbol{v}(0) \neq \boldsymbol{0}$) and cannot be estimated from observations of the total inertia of the Earth as they are compensated by the rotational bulge not yet readjusted to the north pole. They must be estimated from 3-D models of Earth's density anomalies, accounting for the effect of dynamic topography (Ricard et al. 1993b), or by solving the rotational problem as we show in the following.

We compute the mantle convection inertia tensor by means of our previously developed modelling strategy (Ricard et al. 1993b; Richards et al. 1997), assuming that largest changes in mantle density heterogeneities are likely caused by subduction. We use reconstructions of global plate motions for Cenozoic and late Mesozoic (Lithgow-Bertelloni et al. 1993), to inject cold slabs into the mantle where plates converge. In order to account for present-day geoid, for much of the observed seismic heterogeneities of the mantle and for the long term rotational stability of the Earth indicated by paleomagnetic data (Richards et al. 1997), we consider lower/upper mantle and lithosphere/upper mantle viscosity ratios of $\eta_1 = 30$ and $\eta_2 = 10$, respectively. The sinking velocity of slabs when they enter the lower mantle is reduced by a factor of 4.4 (the velocity decrease is expected to scale roughly with the logarithm of the viscosity increase). This relation between viscosity increase and velocity reduction is a crude estimate that neglects the complexity of thermal exchanges between the slabs and the transition zone (Otha 2010), but it is validated by the good fit to the geoid and to the lower mantle tomography provided by the sinking slab model (Ricard et al. 1993b). Our kinematic approach is independent of any assumed absolute mantle viscosity and yields an average sinking velocity of slabs in the lower mantle of order 1.6 cm yr^{-1}. This typical sinking velocity has been confirmed by other studies (e.g. Meer et al. 2010).

This kinematic model of the mantle time-dependent density anomalies is certainly simple but it provides a robust estimate of the inertia tensor which is related to a radial integral of the longest wavelengths of the density anomalies (harmonic degree 2). Therefore, the details of paleo-reconstructions do not impact this model. This model should provide a better estimate of the time dependent evolution of Earth's inertia than complex dynamic models (e.g. Steinberger 2000) that require many questionable assumptions (a backward in time advection of the present density anomalies that requires the choice of an absolute viscosity and assumes a depth dependent rheology in contradiction with the very existence of plates).

The kinematic slab model provides a time-dependent inertia tensor $\boldsymbol{\mathcal{C}}^{slab}(t)$. At present time, this model, $\boldsymbol{\mathcal{C}}^{slab}(0)$, maximizes the correlation with the observed inertia deduced from the geoid, $\boldsymbol{\mathcal{C}}^{obs}$, and is in good agreement with tomography. As discussed previously, the mantle inertia tensor $\boldsymbol{\mathcal{C}}^{obs}$ observed from geoid does not account for the two off-diagonal components along $\boldsymbol{x}_3$ that, according to Eq. (3.152), are related to the history of TPW. As a consequence we consider that Earth's rotation is forced by

$$\mathcal{C}(t) = \mathcal{C}^{slab}(t) + \mathcal{C}^{obs} - \mathcal{C}^{slab}(0) + \delta\mathcal{C} \tag{3.153}$$

where $\delta\mathcal{C}$ stands for the two present-day off-diagonal terms $\mathcal{C}_{13}(0)$ and $\mathcal{C}_{23}(0)$.

This inertia tensor $\mathcal{C}(t)$ is in agreement with that observed and has a time dependence estimated from slab paleo-positions. We then constrain the two unknown terms $\mathcal{C}_{13}(0)$ and $\mathcal{C}_{23}(0)$ by solving the non-linear Liouville equation (3.132) for a given time scale T_1 and by requiring that the present-day rotation axis $\boldsymbol{n}(0)$ coincides with the geographical north pole. In this way, the present-day total inertia $\mathcal{C}(0) + \mathcal{B}(0)$ has zero off-diagonal components along $\boldsymbol{x}_3$, as required by Eq. (3.151). Note also that the term $\mathcal{C}^{obs} - \mathcal{C}^{slab}(0)$ entering Eq. (3.153) accounts for any contribution other than slab subduction that can be assumed to remain constant with time, as large-scale upwellings (Rouby et al. 2010) and the two large low shear velocity provinces (LLSVPs) in Earth's lowermost mantle (Torsvik et al. 2006; Steinberger and Torsvik 2010). This term is small as the slabs by themselves explain most of the geoid, which suggests that the LLSVPs should not affect significantly the inertia tensor.

This approach is somewhat similar to the method used in Richards et al. (1997) (see their note 26). However, it does not arbitrarily assume that the present-day mantle inertia terms $\mathcal{C}_{13}(0)$ and $\mathcal{C}_{23}(0)$ are zero. The latter assumption has been made in Steinberger and O'Connell (1997), Schaber et al. (2010). It implies the coincidence between the present-day rotation axis and the MID-MC which is in contradiction with the observation of ongoing TPW as shown in Eq. (3.152). Instead, by solving for the two unknown terms, $\mathcal{C}_{13}$ and $\mathcal{C}_{23}$, we respect the correct physics of the problem. Notice also that we solve the Liouville equations from past (starting ~100 Myr ago) to present. It is incorrect to try to solve the Liouville equation backward in time as was done in Schaber et al. (2010) which results in rotation axis apparently preceding the MID-MC rather than lagging behind the MID-MC as it should (see their Fig. 5).

In the following, we will express the off-diagonal terms $\mathcal{C}_{13}$ and $\mathcal{C}_{23}$ of the mantle convection inertia tensor in terms of the C_{21} and S_{21} geoid coefficients in meters, that are due to mantle convection alone and would be observed in the absence rotation. They are related to each other as follows

$$\begin{aligned} \mathcal{C}_{13} &= -M_E\, a^2 \sqrt{\frac{5}{3}}\, \frac{C_{21}}{a} \\ \mathcal{C}_{23} &= -M_E\, a^2 \sqrt{\frac{5}{3}}\, \frac{S_{21}}{a} \end{aligned} \tag{3.154}$$

3.10.1 TPW Simulations

Figure 3.8 compares TPW paths obtained for three time scales $T_1 = 0$, 30 and 100 kyr. The case of $T_1 = 0$ corresponds to the readjustment of the rotational bulge without delay. For viscosity ratios of $\eta_1 = 30$ (lower to upper mantle) and $\eta_2 = 10$ (lithosphere to upper mantle), the time scales $T_1 = 30$ and 100 kyr correspond to

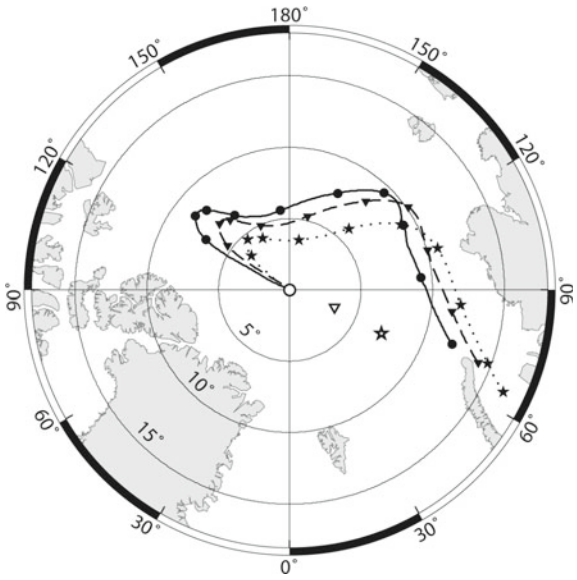

Fig. 3.8 TPW paths for three time scales $T_1 = 0$, 30 and 100 kyr (*solid*, *dashed* and *dot lines* with *circles*, *triangles* and *stars*, respectively). The *symbols* are given at intervals of 10 Myr. The present–day MID–MC positions for three time scales $T_1 = 0$, 30 and 100 kyr are also shown (*circles*, *triangles* and *stars*, respectively). Only when the rotational bulge readjusts instantaneously ($T_1 = 0$), the MID–MC coincides with the north pole

upper mantle viscosities of about 10^{21} and 3.3×10^{21} Pa s, respectively (the time scale T_1 is proportional to the upper mantle viscosity ν_M, as discussed in Ricard et al. (1993a, b). As initial condition for the Liouville equation, we assume that the rotation axis coincides with the MID-MC at 100 Myr before present. However, in view of Eq. (3.149), it should be noticed that the TPW path is affected by the initial condition only for a time of order T_{Ci}^{α} (Fig. 3.9), about 3 and 9 Myr for $T_1 = 30$ and 100 kyr.

Due to the differences in the relaxation of the rotational bulge, TPW paths differ from each other. Particularly, the polar excursion in the past 10 Myr reduces from 6.9° for $T_1 = 0$ (black dot) to 5.3°(black triangle) and 3.6° (black star) for $T_1 = 30$ and 100 kyr with respect to the north pole (circle). Furthermore, the present-day MID-MC occupies different positions, reflecting the estimated C_{21} and S_{21} geoid coefficients due to mantle convection driven by slab subduction (Table 3.5). Particularly, for $T_1 = 0$, the present-day MID-MC is at the north pole since the rotational bulge readjusts instantaneously. On the contrary, for $T_1 = 30$ and 100 kyr, the present-day MID-MC are displaced by 3.4° and 7.1° towards 68.9°E and 64.6°E, respectively.

A reduction of the polar excursion by increasing the time scale T_1 is expected on physical grounds, once the herein developed linearized differential equations and solutions, Eqs. (3.145) and (3.149), are considered to reinterpret the non-linear calculations. For the three time scales $T_1 = 0$, 30 and 100 kyr, Fig. 3.10 compares the MID-MC and TPW rates. For $T_1 = 0$, the rotational bulge readjusts instantaneously and, thus, the MID-MC and TPW rates and paths coincide. Particularly, the TPW rate is affected by every short-term fluctuation of Earth's inertia tensor. Instead, for $T_1 = 30$ and 100 kyr, the inhibition of the bulge relaxation filters out in time the

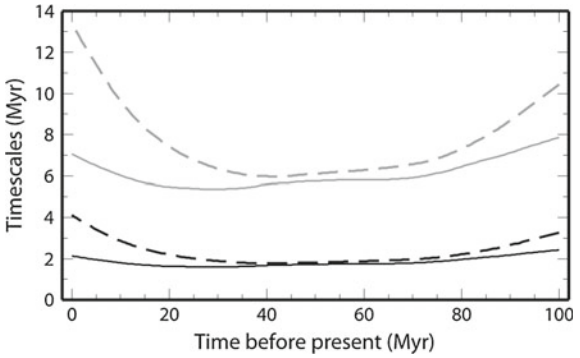

Fig. 3.9 Time scales $T_{C_1}^{\alpha}$ and $T_{C_2}^{\alpha}$ (*solid* and *dashed lines*, respectively) controlling the relative motion of the rotation axis with respect to the MID–MC, Eq. (3.146), for the time scale $T_1 = 30$ and 100 kyr (*black* and *gray lines*, respectively)

Table 3.5 Present–day C_{21} and S_{21} geoid coefficients due to mantle convection estimated from seismic tomography (top line, coefficients obtained using the tomographic model Smean of Becker and Boschi (2002) as described in Ricard et al. (1993b) or self–consistently estimated from TPW dynamics driven by the model of subduction, for the three time scales $T = 0$, 30 and 100 kyr (bottom lines)

Geoid coefficients (m)	C_{21}	S_{21}
Seismic tomography	−1.00	0.53
TPW dynamics ($T_1 = 0$)	0	0
TPW dynamics ($T_1 = 30$ kyr)	−1.05	−2.07
TPW dynamics ($T_1 = 100$ kyr)	−2.87	−4.19

short-term fluctuations of Earth's inertia, thus smoothing TPW rates. Furthermore, accordingly to Eq. (3.149), variations of TPW rates are delayed with respect to those of MID-MC by a time comparable to the time scales T_{Ci}^{α} (Fig. 3.9). Particularly, this yields an increase of the present-day TPW rate since the MID-MC rate increases by about $1^\circ\,\mathrm{Myr}^{-1}$ in the past 10 Myr. Compared to the present-day TPW rate of $1.24^\circ\,\mathrm{Myr}^{-1}$ for $T_1 = 0$, the present-day TPW rates of 0.85° and $0.55^\circ\,\mathrm{Myr}^{-1}$ for $T_1 = 30$ and 100 kyr, respectively, are reduced by 32 and 56 %.

Together with the TPW rate increase, the offset angle between the rotation axis and the MID-MC also increases, see Fig. 3.11. For $T_1 = 30$ and 100 kyr, they are about 0.8° and 2.2° in the past 50 Myr and they increase to 3.4° and 7.1° at the present-day due to the acceleration of the MID-MC in the past 10 Myr. Differently, the present-day TPW directions are only slightly affected by the readjustment of rotational bulge (Fig. 3.8) and they point towards 66.7°E, 61.5°E and 55.7°E for $T_1 = 0$, 30 and 100 kyr, respectively. Even though the estimated TPW rates are in rough agreement with the observation of $0.925 \pm 0.022^\circ\,\mathrm{Myr}^{-1}$ (McCarthy and Luzum 1996), these results are in contrast with the observed direction towards Newfoundland (75.0° ± 1.1°W). The general motion since the early Tertiary (50–60 Myr) of about $4^\circ - 9^\circ$ toward Greenland is however in agreement with paleomagnetic data (Besse and Courtillot 2002), although we do not obtain the period of (quasi) standstill at 10−50 Myr.

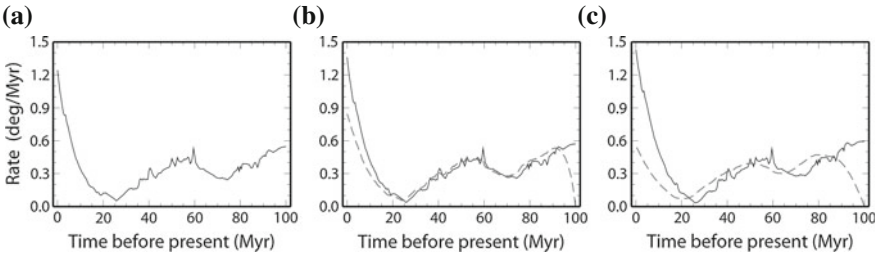

Fig. 3.10 MID–MC, $|d\boldsymbol{e}_3/dt|$, and TPW, $|\boldsymbol{v}|$, rates (*solid* and *dashed lines*, respectively) for the three time scales $T_1 = 0,\ 30$ and 100 kyr (panels **a**, **b** and **c**, respectively). The MID–MC and TPW rates coincide for $T_1 = 0$. The TPW rates for $T_1 = 30$ and 100 kyr are zero at 100 Myr before present since we have imposed as initial condition that the rotation axis and the MID–MC coincide at that time. The TPW simulations do not depend on the initial condition after a time comparable with the time scales $T_{C_i}^{\alpha}$

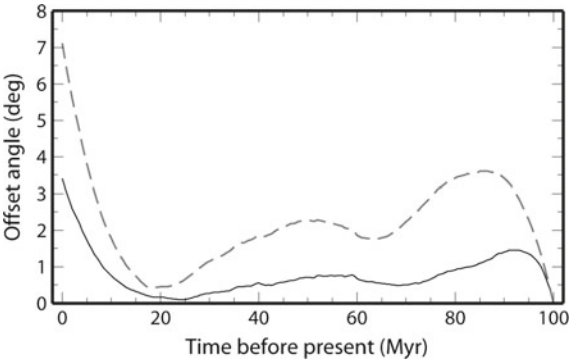

Fig. 3.11 Offset angle, $\arccos(\boldsymbol{n} \cdot \boldsymbol{e}_3)$, between the rotation axis and the MID–MC for the time scales $T_1 = 30$ and 100 kyr (*solid* and *dashed lines*, respectively). For $T_1 = 0$ the offset angle is zero at any time since the rotational bulge readjusts instantaneously

These results based on the linearization of the Liouville equation provided in Eq. (3.145) allow us to reinterpret TPW simulations. Discerning between the effects of the delay of the readjustment of the rotational bulge from those of the specific mantle convection models used in TPW simulations, we have pointed out when the former can affect significantly both TPW path and rates. Previously developed mantle circulation model (Ricard et al. 1993b; Richards et al. 1997), implemented within our new scheme, show that the delay of the readjustment of the rotational bulge can shift the TPW and MID-MC paths by several degrees and affects present-day TPW rates by about 50 %.

The slow change of the mantle convection inertia tensor remains the main factor explaining the long-term rotational stability of the Earth (Richards et al. 1997). However, as clearly indicated by Eqs. (3.145) and (3.149), the relaxation of the rotational bulge introduces a further stabilizing effect. Indeed, it filters out every short-term fluctuations of the Earth's inertia tensor and delays variations of TPW rates by the time scales $T_{C_i}^{\alpha}$, Eq. (3.146), with respect to those of the MID-MC. This yields significant differences between TPW and MID-MC rates, particularly during the past 10 Myr for our mantle convection model.

In addition to slab subduction, we have accounted also for any other contributions to mantle density anomalies that can be assumed to remain constant with time. Furthermore, the present-day C_{21} and S_{21} geoid coefficients due to mantle density anomalies alone, which cannot be observed since they are compensated by the rotational bulge not yet readjusted to the north pole, have been estimated self-consistently with TPW dynamics. Within our framework, it is possible to check whether TPW simulations are in agreement with seismic tomography. By using in Eqs. (3.152) and (3.154) the C_{21} and S_{21} geoid coefficients obtained from the tomographic model Smean of Becker and Boschi (2002) (see Table 3.5), which is an average of different recent models, we obtain a present-day TPW direction of 28°W, in rough agreement with the observed direction towards Newfoundland, and a present-day TPW rate of $0.0123°/T_1$, inversely proportional to the time scale T_1 (the observed TPW rate of $0.925° \pm 0.022°\,\mathrm{Myr}^{-1}$ is explained when $T_1 = 13\,\mathrm{kyr}$). Nevertheless, these estimates concern only the present-day and are not consistent with TPW simulations obtained using the time evolution of mantle convection inferred from global plate motions (Ricard et al. 1993b; Lithgow-Bertelloni et al. 1993).

The combined use of seismic tomography and reconstructions of global plate motions could greatly improve our understanding of both past and present-day TPW driven by mantle convection. However, these two data sets cannot be used at the same time to simulate TPW if the delay of the rotational bulge is accounted for. Furthermore, in order to fulfill observations, the contribution to TPW from Pleistocene ice sheet melting must be also considered, being comparable in magnitude with that from mantle convection and pointing towards Newfoundland (Mitrovica et al. 2005; Cambiotti et al. 2010). As it occurs on a much shorter period than mantle convection, PGR affects TPW, but its contribution to Earth's inertia tensor remains negligible compared to that of the mantle 3D structure.

3.11 Polar Wander on the Earth, Moon, Mars and Venus

Despite the uncertainties due to our lack of information concerning mantle rheology, for most of the solid planets we can deduce reasonable bounds for the rotational number R_o defined in Eq. (3.124) that are sufficient to describe the basic characteristics of their long-term rotation, as shown in this Sect. 3.11 reworked from Spada et al. (1996). Our results are summarized in Fig. 3.12, where R_o is estimated via Eq. (3.124) and plotted as a function of T_1 for various models of planetary interiors.

The first Earth's model, Ear-1 (solid squares as all the other Earth's models), is characterized by a uniform mantle with viscosity $\nu = 10^{21}$ Pa s overlaid by a 100-km-thick elastic lithosphere; model Ear-2 includes, in addition, a density increase through the 670-km-depth seismic discontinuity, with $\Delta\rho/\rho = 9\,\%$ (Sabadini and Yuen 1989). Numerical values of densities and elastic rigidities needed for the derivation of T_1 are the same as those employed in previous studies (Spada et al. 1993).

Observed values for the dynamic form factor, normalized mean inertia, and mean rotational velocity of the Earth are $J_2 = 1.08263 \times 10^{-3}$, $I^* = 0.3306$ and

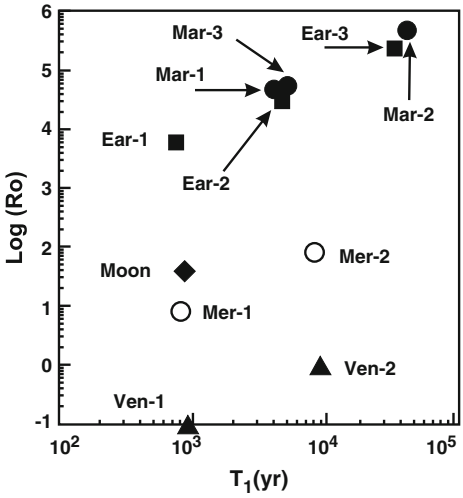

Fig. 3.12 Diagram showing the values assumed by the rotational number R_o as a function of the time-scale T_1 for different models of planetary interiors (Fig. 1 in Spada et al. 1996)

$\Omega = 7.292115 \times 10^{-5}\,\mathrm{s}^{-1}$. Values of R_o and T_1 for the Earth register their largest amplitudes for model Ear-3, characterized by the same density profile as Ear-2 but differing by a viscosity jump of a factor of 50 at 670-km depth. Values of R_o for the Earth vary between $\sim 6 \times 10^3$ for model Ear-1 and 2.5×10^5 for Ear-3; intermediate values of R_o ($\sim 2 \times 10^4$) are found for model Ear-2.

For Mars (solid circles in Fig. 3.12) we have employed two different values for mantle viscosity: $\nu = 10^{21}$ Pa s for both models Mar-1 and Mar-3 and $\nu = 10^{22}$ Pa s for Mar-2. These values were chosen on analogy with the Earth because of the large uncertainties in the rheological profile of Mars (Phillips and Lambeck 1980). Lithospheric thickness is fixed at 300 km for Mar-1 and Mar-2 and at 100 km for Mar-3 (Phillips and Lambeck 1980). The core radius for the whole set of Martian models is 1300 km with $J_2 = 1.960 \times 10^{-3}$, $I^* = 0.345$ and $\Omega = 7.09 \times 10^{-5}\,\mathrm{s}^{-1}$ (see Balmino et al. 1982; Bills, 1989; Cole, 1978). The Martian density profile is consistent with the results reported by Johnston et al. (1974). The small difference between the R_o values in models Mar-1 and Mar-3 indicates that the lithospheric thickness has a minor influence on the rotational number. While the R_o values for Mar-1 and Mar-3 are very close to those estimated for Ear-2, R_o for Mar-2 attains a value slightly exceeding Ear-3.

The two different models considered for Venus (solid triangles in Fig. 3.12) are characterized by a 100-km-thick elastic lithosphere and by a core radius of 3240 km. The reference values for mantle viscosity of Venus are $\nu = 10^{21}$ Pa s for model Ven-1 and 10^{22} Pa s for Ven-2 and are consistent with those suggested by the observed offset between its spin axis and the direction of largest inertia (Mottinger et al. 1985; Nerem et al. 1993; Konopliv and Sjogren, 1994). A commonly adopted value for the normalized mean moment of inertia of Venus is $I^* = 0.33$ (Mottinger et al. 1985). The slow rate of rotation ($\Omega = 2.9910^{-7} s^{-1}$ and small dynamic form factor ($J_2 = 4.0 \times 10^{-4}$) are responsible for the low R_o values found for Venus ($R_o \sim 10^{-1}$).

Rough estimates of R_o and T_1 for the Moon and Mercury are also shown. For the Moon (diamond) they are based on classical results about the internal constitution and rheology of this body (Toksöz 1974; Nakamura 1983). Adopted numerical values of J_2 and I^* for the Moon are 2.036×10^{-4} and 0.3905 (Bills and Ferrari 1977, 1980). The two considered models for Mercury (open circles in Fig. 3.12 are characterized by a 100-km-thick lithosphere and by a silicate mantle with viscosity of 10^{21} Pa s (Mer-1) and 10^{22} Pa s (Mer-2). The radius of the iron core is 1700 km ($\sim$0.8 % of the radius of the body), and mantle density is fixed at 3000 kg/m^3 (Cole 1978). For this model, $I^* \sim 0.337$ and we have adopted the reference values $J_2 = 80 \times 10^{-6}$ and $\Omega = 1.219 \times 10^{-6}$ s^{-1} (Zharkov and Trubistyn 1978). The most striking feature in Fig. 3.12 is that the rotational number R_o for models Ven-1 and Ven-2 ranges between $\sim 10^{-1}$ and 1, i.e. 4–6 orders of magnitude smaller than the corresponding values for the Earth and Mars. The smallness of R_o for Venus in comparison with Mars and the Earth is primarily a consequence of the small rate of rotation and the resulting small dynamical form factor J_2 (Mottinger et al. 1985), if we assume that its gross viscosity structure is similar to that of the other two planets (Phillips and Lambeck 1980; Kiefer et al. 1986).

Venus would only attain a rotational number comparable with that of the Earth and Mars if its viscosity were several orders of magnitude higher than the Earth's viscosity, which is unlikely due to the convective properties of this planet as revealed by its gravity field (Kiefer et al. 1986). Mercury and the Moon are characterized by R_o values ranging between 10 and 10^2.

We can discuss the behavior of the Liouville equations in the two limits, $R_o \ll 1$ and $R_o \gg 1$. Figure 3.13 deals with the case of a point mass δm acting within the mantle of the planet and located in the yz-plane of the non-inertial Cartesian frame rotating with the body. For $R_o \gg 1$ and constant inertia perturbation ΔI_{23}, Eq. (3.123) provides $m_x \sim 0$ and

$$m_y = k_f^T \frac{\Delta I_{23}}{(C - A)} \frac{t}{T_1}, \tag{3.155}$$

which shows that the body's pole of rotation moves in the yz-plane, toward δm if ΔI_{23} is positive and in the opposite direction if ΔI_{23} is negative. This is expected for the Earth and Mars, whose R_o exceeds 10^4 (see Fig. 3.12). The linearized Liouville equations (3.123) for $R_o \ll 1$ predict a different pole path,

$$m_x = \frac{\Omega \Delta I_{23}}{A} t, \tag{3.156}$$

which shows that the pole initially moves at right angles with respect to the plane containing the mass anomaly. For Venus, whose rotation number R_o lies in the range $10^{-1} - 1$, the pole wanders in a direction which forms an angle $\gamma = tan^{-1} R_o$ with respect to the xz-plane.

Both Eqs. (3.155) and (3.156) are valid for small excursions of the axis of rotation. Numerical analyses of the fully non-linear Liouville equations for both Mars and

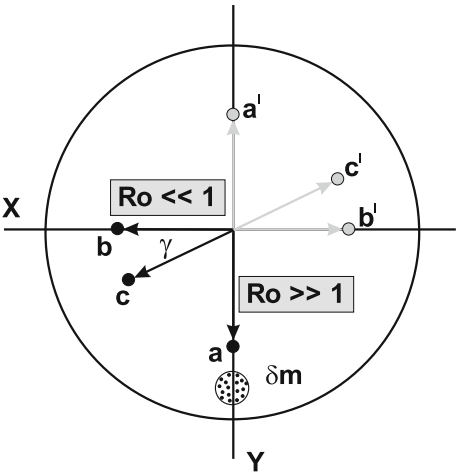

Fig. 3.13 Incipient motion of the rotation axis predicted by the Liouville equations for a planet excited by an internal mass heterogeneity δm. For large rotational numbers ($R_o \gg 1$), the pole is moved toward the source along the path Oa (*black arrow*) if the non-hydrostatic geoid anomaly associated with the dynamic compensation of δm is negative. For positive anomalies, the pole moves in the opposite direction, along Oa′ (*grey arrow*). This behavior is expected for the Earth and Mars, whose R_o clearly exceeds unity (see Fig. 3.12). The rotation axis of a planet characterized by $R_o \ll 1$ is initially forced along the direction Ob (or Ob', depending upon the sign of the geoid anomaly). Redrawn from Fig. 2 in Spada et al. (1996)

Venus, (Spada et al. 1996), show that the qualitative behavior of these asymptotic expressions are preserved in the long-term limit. Note that Eq. (3.156) provides only the initial amplitude and direction of the damped wobble which is retrieved from the non-linear Liouville equations. Figure 3.13 helps to explain the physical meaning of the rotational number R_o: it describes how the pole of rotation approaches the mass anomaly, wobbling around it with decreasing amplitude due to viscous dissipation for $R_o \ll 1$ or wandering in the plane containing the initial position of the pole and the mass anomaly for $R_o \gg 1$. This different behavior is due to the efficiency of the equatorial bulge in stabilizing the rotation of the planet, with $R_o \gg 1$ being indicative of an important equatorial bulge responsible for a slow wandering of the axis of rotation, while the opposite limit favors mega-wobbles around the mass anomaly.

If the time scale for readjustment of the equatorial bulge T_1 and the length of day $T_r = 2\pi\Omega^{-1}$ are well separated and J_2 is large, the rotational number is large, and the planets experience true polar wander; a smaller separation on these time scales and a small dynamic form factor J_2 implies, on the other hand, that TPW is inhibited. For Venus, the smallness of R_o is primarily due to the long rotational period T_r and small dynamic flattening J_2. Since in this case the centrifugal contribution to the total inertia of Venus is small, we expect that the rotational dynamics of this body is intermediate between that of a rigid body (with no rotational deformation

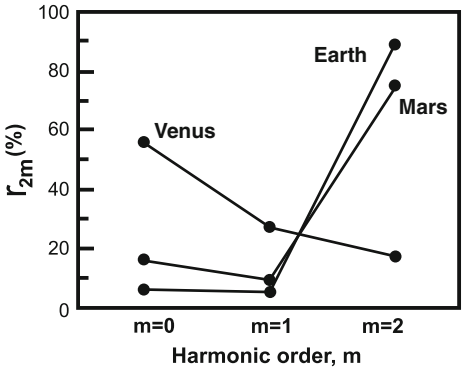

Fig. 3.14 Percentage strength r_{2m} of the harmonic degree 2 component for the topographies of the Earth, Mars and Venus. Redrawn from Fig. 7 in Spada et al. (1996)

(Lambeck 1980) or $R_o = 0$ and with the spin axis not necessarily parallel to the main inertia axis) and that of the Earth, whose bulge stabilizes the excursions of the axis of rotation by always trying to keep it parallel to the direction of the principal inertia axis (Ricard et al. 1993a). With respect to the time constant T_1 characterizing the readjustment of the equatorial bulge, the new non-dimensional rotational number R_o defined here accounts simultaneously for the rheological structure of the planet through the T_1 dependence and for the basic rotation through Ω.

The percentage strength r_{2m} of the order m components, defining the degree 2 topography for the three planets, is shown in Fig. 3.14; this strength is defined as

$$r_{2m} = \frac{|t_2^m|^2}{\sum_{k=0}^{2} |t_2^k|^2}, \tag{3.157}$$

(Spada et al. 1994) where, for the Earth and Venus, t_2^m are the spherical harmonic degree 2 components of the dynamic topography that are supported by the internal flow driven by mantle sources; for Mars, t_2^m are simply the components of the observed topography, which is not dynamic but induced by surface loads. In rotation dynamics the degree $l = 2$ geoid anomaly component controls the style of long-term polar motion, as discussed in the previous figure, so that, in order to discuss the effects of rotation on the shape of the planets, we must consider the topographic features related to the non-hydrostatic geoid for the three planets. The non-hydrostatic geoid is mostly related to internal mass anomalies for the Earth and Venus and to the observed topography due to surface lithospheric relief for Mars. In order to derive the dynamic topography for the Earth, the harmonic coefficients derived by Cazenave et al. (1989) from the observed topography has been used, after removal of the effects due to the cooling of the oceanic lithosphere and of the topography excess in continental areas. The dominant order 2 component is a feature that characterizes the degree 2 of the dynamic topography of the Earth (Cazenave et al. 1989; Ricard and Vigny 1989) and the observed topography of Mars. As shown in this figure for the Earth, the topography, induced by internal sources, carries up to 88 % of the total strength in comparison to 7 % for the order zero and 5 % of order 1 (Cazenave et al.

1989; Cazenave and Thoraval 1994; Spada et al. 1994). For Mars, this is mainly due to surface volcanic loads and does not originate from deep-seated internal dynamic processes, such as subduction or density anomalies in the mantle, as indicated by the correlation between the surface topography and the gravity field (e.g. Bills and Ferrari 1978; Phillips and Lambeck 1980). The equatorial position of the largest topographic feature of the Martian lithosphere implies a dominant order 2 component in the degree 2 of both topographies, which carries 75 % of the strength at this degree (Bills and Ferrari 1978) and the associated geoid (Sjogren et al. 1975), which shows, in fact, a significant correlation with the Martian topography (Balmino et al. 1982). Due to the topography of the Tharsis region the shape of Mars is thus elongated along an axis lying in the equatorial plane. Unlike Mars, the observed topography of Venus originates essentially from internal processes and is well correlated with the geoid (Kiefer et al. 1986), so that, to a good approximation, the topography of this planet is the dynamic topography.

This figure suggests a correlation between the dominance of the order 2 component for the Earth and Mars and TPW; Venus, where mega-wobbling is the mechanism for reaching rotation equilibrium rather than polar wander, does not in fact show this feature. As noted in the discussion of the previous figure, Mars can displace the excess topography at the equator by means of polar wander; since the topography is clustered in longitude, the displacement of the excess topography at the equator will induce a large order 2 component. This is similar to what occurs for the Earth, but in a more subtle way, because internal density anomalies rather than surface ones are responsible for the displacement of the rotation pole. On time scales of billions of years, even for the Earth long-term TPW is able to maintain the maxima of the harmonic degree 2 non-hydrostatic geoid at the equator, favoring at the same time the sectorial component of order 2 in the dynamic topography, rather than the zonal component, if the mantle is stratified in viscosity. TPW's internal origin makes the rotational behavior of the Earth extremely sensitive to the viscosity profile of the mantle; for a viscosity increase in the lower mantle of at least one order of magnitude, in agreement with global geoid models (Ricard et al. 1984; Richards and Hager 1984) and some postglacial rebound calculations (Spada et al. 1991), positive density anomalies in the mantle like subductions induce at the surface a positive geoid anomaly and a negative dynamic topography, a 'hole' that is carried at the equator together with the positive geoid anomaly. This 'hole' in the dynamic topography at the equator is, of course, responsible for a strong longitudinal dependence in the order 2 component, as observed in the previous figure for the Earth. It is thus a fact that the shape of the Earth agrees well with that of a rotating planet where subduction is the major mechanism driving long-term polar wander and where the lower mantle is stiffer than the upper mantle. This means that polar wander is a mechanism that can modify the figure of the Earth and Mars. The similarity of these two planets in the degree 2 component of the topography appears not to be a simple coincidence but rather related to long-term excursions of the rotation axis. Let us consider as an exception to this rule the case of Venus, which does not have the ability to wander and carries not this signature but rather a large order zero component in the dynamic topography and geoid (Mottinger et al. 1985; Bills and Kobrick 1985) that is

indicative of an isotropic distribution of mass anomalies within the mantle and zonal symmetry not degraded by TPW. Although the tectonics responsible for the observed morphology on the Earth, Mars and Venus is different (e.g. Head and Solomon 1981), essentially because subduction is a major mechanism on the Earth, but is inhibited on Mars and Venus by thick (Phillips and Lambeck 1980) or buoyant (Anderson 1980, 1981) lithospheres, important analogies can be found in their rotational dynamics.

This walk on terrestrial planets has shown that Mars and the Earth belong to the category that allows long-term polar wander by means of a slow drift of the pole of rotation associated with the readjustment of the equatorial bulge; Venus belongs to the second category, where a perturbation in the moment of inertia induces a mega-wobble due to the smallness of the equatorial bulge, the axis of rotation and maximum inertia not necessarily being aligned on long time-scales. Although the Earth and Venus belong to the two different categories, their driving mechanism comes from internal sources, unlike Mars, where lithospheric phenomena are the main sources of polar wander. The role played by the viscous properties of the mantle of the three planets, whose viscosities are within one or two orders of magnitude from one another, is crucial to our analysis. The similarity in the viscosity structure is the common characteristic enabling us to elucidate the peculiar features in their rotation, the other ingredient being the length of the sidereal day that determines the size of the equatorial bulge. The equatorial location of the volcanic complex on Mars is thus likely to be a consequence of polar wander, as indicated by our quantitative analysis in this section. This finding allows us to elucidate the influence of TPW on the degree 2 pattern of the topography associated with the volcanic complex (Willeman and Turcotte 1982) and to draw a comparison with the other two planets considered in our analysis. The rotation parameters and the rheology of the mantle can be conveniently expressed by means of a non-dimensional rotational number that tells us when a planet experiences TPW. There is thus a close connection between different aspects of the dynamics of terrestrial planets, which involve apparently separate realms of planetary physics such as rheology of the interiors, rotation, gravity, surface tectonics, and internal processes.

References

Anderson, D.L. (1980). "Tectonics and composition of Venus". In: *Geophys. Res. Lett*. 7, pp. 101–102.

Anderson, D.L. (1981). "Plate Tectonics on Venus". In: *Geophys. Res. Lett*. 8, pp. 309–311.

Balmino, G., B. Moynot, and Valés N. (1982). "Gravity field model of Mars in spherical harmonics up to degree and order eighteen". In: *J. Geophys. Res*. 87, pp. 9753–9746.

Becker, T.W. and L. Boschi (2002). "A comparison of tomographic and geodynamic mantle models". In: *Geochem. Geophys. Geosyst*. 3, 2001GC000168.

Ben-Menahem, A. and S.J. Singh (2000). *Seismic waves and sources*. 2nd. Dover Publications, Inc., Mineola, New York.

Besse, J. and V. Courtillot (1991). "Revised and synthetic apparent polar wander paths of the African, Eurasian, North American, and Indian Plates, and true polar wander since 200 Ma". In: *J. Geophys. Res*. 96, pp. 4029–4050.

Besse, J. and V. Courtillot (2002). "Apparent and true polar wander and the geometry of the geomagnetic field over the last 200 Myr". In: *J. Geophys. Res*. 107, p. 2300.
Bills, B.G. (1989). "The moments of inertia of Mars". In: *Geophys. Res. Lett*. 16, pp. 385–388.
Bills, B.G. and A.J. Ferrari (1977). "A lunar density model consistent with topographic, gravitational, librational, and seismic data". In: *J. Geo-phys. Res*. 82, pp. 1306–1314.
Bills, B.G. and A.J. Ferrari (1978). "Mars topography harmonics and geophysical implications". In: *J. Geophys. Res*. 83, pp. 3497–3508.
Bills, B.G. and A.J. Ferrari (1980). "A harmonic analysis of lunar gravity". In: *J. Geophys. Res*. 85, pp. 1013–1025.
Bills, B.G. and M. Kobrick (1985). "Venus topography: A harmonic analysis". In: *J. Geophys. Res*. 90, pp. 827–836.
Burgers, J.M. (1955). "Rotational motion of a sphere subject to visco-elastic deformation. I, II and III". In: vol. 58. Proc. Kon. Ned. Acad. Wet., pp. 219–237.
Cambiotti, G., Y. Ricard, and R. Sabadini (2010). "Ice age true polar wander in a compressible and non-hydrostatic Earth". In: *Geophys. J. Int*. 183, pp. 1248–1264.
Cambiotti, G., Y. Ricard, and R. Sabadini (2011). "New insights into mantle convection true polar wander and rotational bulge readjustment". In: *Earth Planet. Sci. Lett*. 310, pp. 538–543.
Cambiotti, G. and R. Sabadini (2010). "The compressional and compositional stratifications in Maxwell Earth models: the gravitational overturning and the long-period tangential flux". In: *Geophys. J. Int*. 180, pp. 475–500.
Cambiotti, G., X. Wang, R. Sabadini, and D.A. Yuen (2016). "Residual polar motion caused by coseismic and interseismic deformations from 1900 to present". In: *Geophys. J. Int*. 205, pp. 1165–1179.
Cazenave, A.A., A. Souriau, and K. Dominh (1989). "Earth surface topography: Global coupling with hotspots, geoid and mantle heterogeneities". In: *Nature* 340, pp. 54–57.
Cazenave, A.A. and C. Thoraval (1994). "Mantle dynamics constrained by degree 6 surface topography, seismic tomography and geoid: inference on the origin of the South Pacific superswell". In: *Earth Planet. Sci. Lett*. 122, pp. 207–219.
Chambat, F., Y. Ricard, and B. Valette (2010). "Flattening of the Earth: further from hydrostaticity than previously estimated". In: *Geophys. J. Int*. 183, pp. 727–732.
Chambat, F. and B. Valette (2001). "Mean radius, mass, and inertia for reference Earth models". In: *Phys. Earth Planet. Inter*. 124, pp. 237–253.
Chinnery, M.A. (1975). "The static deformation of an earth with a fluid core: a physical approach". In: *Geophys. J. R. astr. Soc*. 42, pp. 461–475.
Cole, G.H.A. (1978). *The Structure of the Planets*. Wykeham, London, p. 232.
Dickman, S.R. (1977). "Secular trend of the Earth's rotation pole: Consideration of motion of the latitude observatories". In: *Geophys. J. R. Astron. Soc*. 51, pp. 229–244.
Dziewonski, A.M. and D.L. Anderson (1981). "Preliminary reference Earth model". In: *Phys. Earth Planet. Inter*. 25, pp. 297–356.
Fang, M. and B.H. Hager (1995). "The singularity mystery associated with a radially continuous Maxwell viscoelastic structure". In: *Geophys. J. Int*. 123, pp. 849–865.
Gold, T. (1955). "Instability of the earth's axis of rotation". In: *Nature* 175, pp. 526–529.
Head, J.W. and S.C. Solomon (1981). "Tectonic evolution of the terrestrial planets". In: *Science* 213, pp. 62–75.
James, T.S. and E.R. Ivins (1997). "Global geodetic signatures of the Antarctic ice sheet". In: *J. Geophys. Res*. 102, pp. 605–633.
Jeffreys, H. (1976). *The Earth: Its Origin, History and Physical Constitution*. Cambridge Univ. Press, Cambridge, UK.
Johnston, D.H., T.R. McGetchin, and M.N. Toksöz (1974). "The thermal state and internal structure of Mars". In: *J. Geophys. Res*. 79, pp. 3959–3971.
Jurdy, D.M. (1978). "An alternative model for early Tertiary absolute plate motions". In: *Geology* 6, pp. 469–472.

Kiefer, W.S., M.A. Richards, B.H. Hager, and B.G. Bills (1986). "A dynamic model of Venus's gravity field". In: *Geophys. Res. Lett*. 13, pp. 14–17.
Konopliv, A.S. and W.L. Sjogren (1994). "Venus spherical harmonic gravity model to degree and order 60". In: *Icarus* 112, pp. 42–54.
Lambeck, K. (1980). *The Earth's Variable Rotation: Geophysical Causes and Consequences*. Cambridge Univ. Press, Cambridge, UK, p. 449.
Lambert, W.D. (1922). "The interpretation of apparent changes in mean latitude and the International Latitude Stations". In: *Astron. J*. p. 904.
Lithgow-Bertelloni, C., M.A. Richards, Y. Ricard, R. O'Connell, and D.C. Engebreston (1993). "Torodial-Poloidal partitioning of plate motions since 120 MA". In: *Geophys. Res. Lett*. 20, pp. 375–378.
McCarthy, D.D. and B.J. Luzum (1996). "Path of the mean rotational pole from 1899 to 1994". In: *Geophys. J. Int*. 25, pp. 623–629.
Meer, D.G. van der, W. Spakman, D.J.J. van Hinsbergen, M.L. Amaru, and T.H. Torsvik (2010). "Towards absolute plate motions constrained by lower-mantle slab remnants". In: *Nat. Geosci*. 3, pp. 36–40.
Milne, G.A. and J.X. Mitrovica (1996). "Post-glacial sea level change on a rotating Earth: First results from a gravitationally self-consistent sealevel equation". In: *Geophys. J. Int*. 126, pp. F13–F20.
Mitrovica, J.X. and G.A. Milne (1998). "Glaciation-induced perturbations in the Earth's rotation: A new appraisal". In: *J. Geophys. Res*. 103, pp. 985–1005.
Mitrovica, J.X. and W.R. Peltier (1993). "Present-day secular variations in the zonal harmonics of the Earth's geopotential". In: *J. Geophys. Res*. 98, pp. 4509–4526.
Mitrovica, J.X., J. Wahr, I. Matsuyama, and A. Paulson (2005). "The rotational stability of an ice-age earth". In: *Geophys. J. Int*. 161, pp. 491–506.
Mottinger, N.A., W.L. Sjogren, and B.G. Bills (1985). "Venus gravity: a harmonic analysis and geophysical implications". In: *J. Geophys. Res*. 90, pp. 739–756.
Munk, W.H. and G.J.F. MacDonald (1960). *The Rotation of the Earth*: A Geophysical Discussion. Cambridge University Press, Cambridge, UK.
Nakada, M. (2002). "Polar wander caused by the Quaternary glacial cycles and fluid Love number". In: *Earth Planet. Sci. Lett*. 200, pp. 159–166.
Nakamura, Y. (1983). "Seismic velocity structure of the lunar mantle". In: *J. Geophys. Res*. 88, pp. 677–686.
Nakiboglu, S.M. and K. Lambeck (1980). "Deglaciation effects on the rotation of the earth". In: *Geophys. J. R. Astron. Soc*. 62, pp. 49–58.
Nerem, R.S., B.G. Bills, and J.B. McNamee (1993). "A high resolution gravity model for Venus: GVM-1". In: *Geophys. Res. Lett*. 20, pp. 599–602.
Otha, K. (2010). *Electrical and Thermal Conductivity of the Earth's Lower Mantle*. PhD. Thesis, Tokyo Institute of Technology.
Peltier, W.R. (1985). "The LAGEOS constraint on deep mantle viscosity: results from a new normal mode method for the inversion of viscoelastic relaxation spectra". In: *J. Geophys. Res*. 90, pp. 9411–9421.
Peltier, W.R. and X. Jiang (1996). "Glacial isostatic adjustment and Earth rotation: Refined constraints on the viscosity of the deepest mantle". In: *J. Geophys. Res*. 101, pp. 3269–3290.
Phillips, R.J. and K. Lambeck (1980). "Gravity fields of the terrestrial planets: Long-wavelength anomalies and tectonics". In: *Rev. Geophys*. 18, pp. 27–76.
Plag, H.-P. and H.-U. Jüttner (1995). "Rayleigh-Taylor instabilities of a self-gravitating Earth". In: *J. Geodyn*. 20, pp. 267–288.
Ricard, Y., L. Fleitout, and C. Froidevaux (1984). "Geoid heights and lithospheric stresses for a dynamic Earth". In: *Ann. Geophysicae* 2, pp. 267–286.
Ricard, Y., M.A. Richards, C. Lithgow-Berteloni, and Y. Le Stunff (1993b). "A geodynamic model of mantle mass heterogeneities". In: *J. Geophys. Res*. 98, pp. 21,895–21,909.

Ricard, Y. and R. Sabadini (1990). “Rotational instabilities of the Earth induced by mantle density anomalies”. In: *Geophys. Res. Lett*. 17, pp. 627–630.
Ricard, Y., R. Sabadini, and G. Spada (1992). “Isostatic deformations and polar wander induced by internal mass redistribution”. In: *J. Geophys. Res*. 97, pp. 14,223–14,236.
Ricard, Y., G. Spada, and R. Sabadini (1993a). “Polar wandering of a dynamic Earth”. In: *Geophys. J. Int*. 113, pp. 284–298.
Ricard, Y. and C. Vigny (1989). “Mantle dynamics with induced plate tectonics”. In: *J. Geophys. Res*. 94, pp. 17,543–17,559.
Richards, M.A., H.-P. Bunge, Y. Ricard, and J.R. Baumgardner (1999). “Polar wandering in mantle convection models”. In: *Geophys. Res. Lett*. 26, pp. 1777–1780.
Richards, M.A. and B.H. Hager (1984). “Geoid anomalies in a dynamic Earth”. In: *J. Geophys. Res*. 89, pp. 5987–6002.
Richards, M.A., Y. Ricard, C. Lithgow-Bertelloni, G. Spada, and R. Sabadini (1997). “An explanation for Earth’s long-term rotational stability”. In: *Science* 275, pp. 372–375.
Rouby, H., M. Greff-Lefftz, and J. Besse (2010). “Mantle dynamics, geoid, inertia and TPW since 120 Myr”. In: *Earth Planet. Sci. Lett*. 292, pp. 301–311.
Sabadini, R. and W.R. Peltier (1981). “Pleistocene deglaciation and the Earth’s rotation: implications for mantle viscosity”. In: *Geophys. J. R. Astron. Soc*. 66, pp. 553–578.
Sabadini, R., G. Spada, and Y. Ricard (1993). “Time-dependent density anomalies in a stratified, viscoelastic mantle: implications for the geoid, Earth’s rotation and sea-level fluctuations”. In: *Surv. Geophys*. 14, pp. 537–553.
Sabadini, R. and D.A. Yuen (1989). “Mantle stratification and long-term polar wander”. In: *Nature* 339, pp. 373–375.
Sabadini, R., D.A. Yuen, and E. Boschi (1982). “Polar wandering and the forced responses of a rotating, multilayered, viscoelastic planet”. In: *J. Geophys. Res*. 87, pp. 2885–2903.
Sabadini, R., D.A. Yuen, and E. Boschi (1984). “A comparison of the complete and truncated versions of the polar wander equations”. In: *J. Geo-phys. Res*. 89, pp. 7609–7620.
Sabadini, R., D.A. Yuen, and P. Gasperini (1988). “Mantle rheology and satellite signatures from present-day glacial forcings”. In: *J. Geophys. Res*. 93, pp. 437–447.
Sabadini, R., R.E.M. Riva, and G. Dalla Via (2007). “Coseismic rotation changes from the 2004 Sumatra earthquake: the effects of Earth’s compressibility versus earthquake induced topography”. In: *Geophys. J. Int.* 171, pp. 231–243.
Schaber, K., H.-P. Bunge, B.S.A. Schubert, R. Malservisi, and A. Horbach (2010). “Stability of the rotation axis in high-resolution mantle circulation models: weak polar wander despite strong core heating”. In: *Geochem. Geophys. Geosyst*. 10, p. Q11W04.
Sjogren, W.L., J. Lorell, L. Wong, and W. Downs (1975). “Mars gravity field based on a short-art technique”. In: *J. Geophys. Res*. 80, pp. 2899–2908.
Spada, G., Y. Ricard, and R. Sabadini (1992). “Excitation of true polar wander by subduction”. In: *Nature* 360, pp. 452–454.
Spada, G., R. Sabadini, and E. Boschi (1994). “True polar wander affects the Earth dynamic topography and favours a highly viscous lower mantle”. In: *Geophys. Res. Lett*. 21, pp. 137–140.
Spada, G., R. Sabadini, and E. Boschi (1996). “Long-term rotation and mantle dynamics of the Earth, Mars, and Venus”. In: *J. Geophys. Res*. 101, pp. 2253–2266.
Spada, G., R. Sabadini, and D.A. Yuen (1991). “Viscoelastic responses of a hard transition zone: effects on postglacial uplifts and rotational signatures”. In: *Earth Planet. Sci. Lett*. 105, pp. 453–462.
Spada, G., R. Sabadini, and Y. Ricard (1993). “On a particular solution of the nonlinear Liouville equations”. In *Geophys. J. Int.* 114, pp. 399–404.
Spada, G., R. Sabadini, D.A. Yuen, and Y. Ricard (1992b). “Effects on post-glacial rebound from the hard rheology in the transition zone”. In: *Geophys. J. Int*. 109, pp. 683–700.
Steinberger, B. (2000). “Slabs in the lower mantle - results of dynamic modelling compared with tomographic images and the geoid”. In: *Phys. Earth Planet. Inter*. 118, pp. 241–257.

Steinberger, B. and R.J. O'Connell (1997). "Changes of the Earth's rotation axis owing to advection of mantle density heterogeneities". In: *Nature* 387, pp. 169–173.

Steinberger, B. and T.H. Torsvik (2010). "Toward an explanation for the present and past locations of the poles". In: *Geochem. Geophys. Geosyst*. 11, p. Q06W06.

Tanaka, Y., J. Okuno, and S. Okubo (2006). "A new method for the computation of global viscoelastic post-seismic deformation in a realistic Earth model (I) - vertical displacement and gravity variation". In: *Geophys. J. Int*. 164, pp. 273–289.

Toksöz, M.N. (1974). "Geophysical data and the interior of the Moon". In: *Ann. Rev. Earth Planet. Sci*. 2, pp. 151–177.

Torsvik, T.H., M.A. Smethurst, K. Borke, and B. Steinberger (2006). "Large igneous provinces generated from the margins of the large low-velocity provinces in the deep mantle". In: *Geophys. J. Int*. 167, pp. 1447–1460.

Vermeersen, L.L.A., A. Fournier, and R. Sabadini (1997). "Changes in rotation induced by Pleistocene ice masses with stratified analytical Earth models". In: *J. Geophys. Res*. 102, pp. 27,689–27,702.

Vermeersen, L.L.A. and J.X. Mitrovica (2000). "Gravitational stability of spherical self-gravitating relaxation models". In: *Geophys. J. Int*. 142, pp. 351–360.

VermeersenSabadini96 Vermeersen, L.L.A. and R. Sabadini (1996). "Significance of the fundamental mantle rotational relaxation mode in polar wander simulations". In: *Geophys. J. Int*. 127, pp. F5–F9.

Vermeersen, L.L.A. and R. Sabadini (1999). "Polar wander, sea-level variations and Ice Age cycles". In: *Surv. Geophys*. 20, pp. 415–440.

Vermeersen, L.L.A., R. Sabadini, and G. Spada (1996a). "Analytical viscoelastic relaxation models". In: *Geophys. Res. Lett*. 23, pp. 697–700.

Vermeersen, L.L.A., R. Sabadini, and G. Spada (1996b). "Compressible rotational deformation". In: *Geophys. J. Int*. 126, pp. 735–761.

Vermeersen, L.L.A., R. Sabadini, G. Spada, and N.J. Vlaar (1994). "Mountain building and earth rotation". In: *Geophys. J. Int*. 117, pp. 610–624.

Wanach, B. (1927). "Eine fortschreitende Lagenänderung der Erdachse". In: *Zeitschr. Geophysik* 3, p. 102.

Willeman, R.J. and D.L. Turcotte (1982). "The role of lithospheric stress in the support of the Tharsis rise". In: *J. Geophys. Res*. 87, pp. 9797–9801.

Wu, P. and W.R. Peltier (1982). "Viscous gravitational relaxation". In: *Geophys. J. R. Astron. Soc*. 70, pp. 435–485.

Wu, P. and W.R. Peltier (1984). "Pleistocene deglaciation and the Earth's rotation: A new analysis". In: *Geophys. J. R. Astron. Soc*. 76, pp. 753–791.

Yuen, D.A., R. Sabadini, P. Gasperini, and E. Boschi (1986). "On transient rheology and glacial isostasy". In: *J. Geophys. Res*. 91, pp. 11,420–11,438.

Zharkov, V.N. and V.P. Trubistyn (1978). "Interior structure of the planets". In: *Physics of Planetary Interiors*. Ed. by W.B. Hubbard. Pachart, Tucson, Arizona.

Chapter 4
TPW and $\dot{J}_2$ Induced by Ice-Sheet Loading

Abstract This chapter is devoted to the study of TPW and J_2 variations due to post glacial rebound (PGR), in practice to the modeling of the Earth's rotation and changes in the flattening driven by the melting of the huge Pleistocenic ice-sheets. The latter are herein responsible for the present-day drift of the rotation axis towards Newfoundland and for the change in the non-tidal dynamic form factor J_2. We show how this modeling allows us to obtain the viscosity profile of the mantle, discussing about two possible lower mantle viscosities, the former favoring a uniform mantle viscosity and the latter a substantially stiffer lower mantle. The path of the rotation pole is analyzed in terms of mantle viscosity and of the rheology of the lithosphere, being elastic or viscoelastic. The effects of a non-hydrostatic bulge, due to asymmetric density distribution in the mantle, is then studied in terms of its effects on TPW driven by ice-ages.

4.1 TPW and $\dot{J}_2$ from PGR

Nakiboglu and Lambeck (1980) and Sabadini and Peltier (1981) have shown that the present-day secular drift of the rotation axis of about 1 deg/Myr, roughly 10 cm every year towards Newfoundland, can be explained by post-glacial rebound due to the disappearance of the Pleistocene ice sheets. Although the rate of polar shift appears to be highly dependent on mantle viscosity, thus not being discriminative with respect to pointing out the cause behind the observed shift (changing the load, another value for the viscosity is found so that the observed polar wander drift rate is matched again), the direction of the polar shift is seen as a strong indication that post-glacial rebound is the main driving mechanism, as shown in Fig. 4.1. We will assume in this chapter, however, that polar wander during the past one million years has been caused mainly by the waxing and waning of great ice sheets.

Even with the most simple ice models, for instance containing three ice disks covering Canada, Scandinavia and Antarctica and melting 10,000 years ago, the direction of the secular drift resulting from the present-day, solid-Earth rebound is quite accurately reproduced. Although there is a high correlation, it is not the same

R. Sabadini et al., *Global Dynamics of the Earth: Applications of Viscoelastic Relaxation Theory to Solid-Earth and Planetary Geophysics*,
DOI 10.1007/978-94-017-7552-6_4

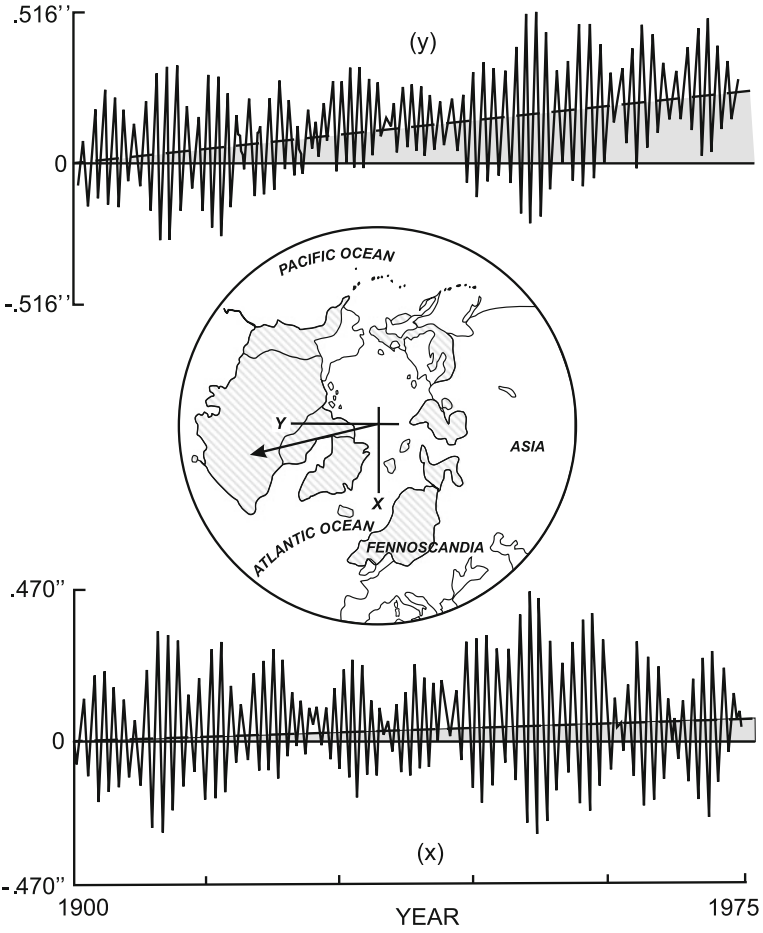

Fig. 4.1 Cartoon showing the Pleistocene ice sheets and the direction of the present-day secular wander of the rotation axis. Polar motion is given in the Conventional International Origin (CIO) coordinates (x axis through Greenwich), on the basis of the reduction of the International Latitude Service data as described by Dickman (1977). Redrawn from Fig. 1 in Sabadini and Peltier (1981)

as a proof. The possibility that the high correlation might be a coincidence cannot be excluded at the moment. Indeed, a number of papers have been published in recent years that argue for additional forcing being responsible for causing the observed present-day polar drift. Regarding this issue, it is interesting to quote the new findings by Cambiotti et al. (2016) who obtained that the two opposing processes of coseismic and interseismic deformations, due to large megathrust earthquakes at subduction zones, make the rotation axis wander around the north pole with maximum polar excursions of about one meter since 1900. Particularly, the rotation axis moves towards about Newfoundland when the interseismic deformations dominate

over coseismic ones, during phases of low seismicity or, equivalently, when most of the fault system associated with plate boundaries is locked. In the other case, when megathrust earthquakes occur, the rotation axis is suddenly shifted in the almost opposite direction, toward about 133°E. Furthermore, since interseismic and coseismic deformations do not exactly compensate each other on the time scales of decades or centuries, the rotation axis gains, at present and with respect to its initial position at the north pole at 1900, a net shift of 110 cm towards 151°E and of 86 cm toward 119° W in the cases of partial and full seismic coupling. In order to achieve these new results, it has been necessary to implement a global seismicity model from plate tectonic models, in conjunction with the seismic forcings built within the scheme of the compressible models described in Chap. 3. It is thus interesting to note that, once translated into a TPW velocity with the necessary caution since we are dealing with discontinuous events such as earthquakes, we obtain rates of about 1 cm/yr, one order of magnitude smaller than the observed one: it is also important to enlighten that when the interseimic deformation dominates, the direction is concordant with the observed one.

In parallel with the analysis of a TPW driven by post-glacial rebound, this chapter will also deal with an analysis of the degree two harmonic component of the geopotential perturbation, $\dot{J}_2$, providing a detailed analysis of the higher harmonics, including the effects of present-day ice loss in Antarctica and Greenland, in Chap. 5. The perturbation of the the dynamical form factor $J_2^{\Delta}(t) = (C^{\Delta}(t) - A^{\Delta}(t))/M_E a^2$ can be expressed in terms of the perturbation of the geopotential $\phi^{\Delta}{}_{20}$, with $C(t)$ and $A(t)$ the polar and the equatorial moments of inertia of the Earth.

Exercise 19 From the MacCullagh's formula Eq. (3.23), show that $J_2^{\Delta}(t) = \frac{a}{GM_E}\phi_{20}^{\Delta}(t)$.

In the following, the symbol Δ is omitted in $J_2(t)$ and $\dot{J}_2(t)$ in order to not overwhelm the text.

4.2 The Inference of Mantle Viscosity from TPW and $\dot{J}_2$ Data

The inference of the viscosity structure of the mantle is a basic issue in geodynamics. A variety of important geodynamical processes, from the long time scale convection in the mantle to the faster response of the Earth to Pleistocene deglaciation, depend on this parameter.

The viscosity of the Earth plays a major role in the connection between changes in surface load and changes in Earth's rotation. If the viscosity of the Earth is high, deformation does not proceed so readily as if the viscosity is low. In the case of the connection between changes in surface load and induced polar wander, there are two relaxation processes: load relaxation and centrifugal relaxation. The interplay between these two relaxation processes, elucidated in Chap. 3, is what makes the

dependence on viscosity somewhat complicated but certainly interesting to be analyzed. In spite of the efforts of several authors in the last decades, a general consensus on the viscosity profile of the mantle has not been reached yet. The use of two different classes of observables in modeling mantle deformation processes, convection and postglacial rebound, which occur on different time scales, is certainly one of the major causes for the discrepancies among the various inferences of mantle viscosity. It has been suggested that the creep properties of the mantle do not remain constant at short and long time scales. Convection and PGR may be controlled by steady-state and transient creep, respectively. If this is the case, modeling of postglacial rebound by means of a steady-state rheology causes a bias in the inference of viscosity (Sabadini et al. 1985; Peltier 1985). This point of view has been weakened by rebound analyses showing that a number of glacial isostatic adjustment data are consistent with a conspicuous viscosity increase in the lower mantle (Nakada and Lambeck 1989) that is generally found from long-wavelength geoid analyses (Richards and Hager 1984). Papers by Forte and Mitrovica (1996), Mitrovica and Forte (1997) reinforce this indication by means of a joint inversion of mantle convection and PGR data that require a significant viscosity increase with depth in the mantle. Estimated viscosity profiles differ substantially from one another, even within the various postglacial rebound analyses. Typically, some studies predict a rather uniform mantle viscosity (Richards et al. 1999; Tushingham and Peltier 1992; Spada et al. 1992b), while other analyses require a substantial viscosity contrast at the interface between the upper and lower mantle (Lambeck et al. 1990). Mitrovica (1996), to whom we refer for an exhaustive discussion of these issues, has provided a possible explanation for these apparently contradictory results. He suggests that they are consequences of a misinterpretation of the Haskell (1935) value, considered as limited to the upper mantle after the results of modern seismology. Other causes of apparent inconsistencies among the various glacial isostatic studies may be ascribed to the use of different Earth's models, different observables considered by the various authors, and insufficient search in the parameter space of the rebound models (Lambeck et al. 1996).

Other uncertainties that accompany deriving radial viscosity profiles from rotational studies are the neglect of lateral viscosity variations and uncertainties in the load history of the Pleistocene ice models. There are reasons, however, that these will affect the results to a lesser extent. Although large lateral variations in viscosity are very likely to be present in the upper mantle, their influence on second-degree harmonics is found to be small (D'Agostino et al. 1997). For low-degree phenomena like Earth's rotation and global geoid change we thus expect that volume averaging over lateral viscosity variations in the upper mantle, and using this value in our models, will give about the same results as when models are used in which these lateral viscosity variations are retained. To put this in another way, it might be very difficult to obtain information on lateral viscosity variations from degree 2 rotational data, just as it is also difficult to obtain detailed information on the radial viscosity profile for a large number of layers from studying harmonic degree 2 phenomena only. Indeed, Earth's models based on the theory developed in Chap. 2 would show that for harmonic degree 2, saturated continuum limits are reached for the Love numbers from

models with a small number of layers largely independent on the form of the radial viscosity profile. Considering this, and considering the uncertainties with respect to the forcing mechanisms, we have decided to take only two viscosity layers in the models shown in this chapter, whereas the elastic parameters and density that we use (PREM) can be more finely graded or continuously varying. From earlier studies (e.g., Wu and Peltier 1984), it is known that the last ice age has the most impact on present-day rotational changes, thereby diminishing the influence of uncertainties in the history of former Pleistocene ice cycles.

The observational data considered in this section are taken from Dickman (1977) as shown in Fig. 4.1 and McCarthy and Luzum (1996) for TPW, and from Yoder et al. (1983) and Devoti et al. (1997) for $\dot{J}_2$. For a review on how these data have been derived see the introduction to the paper by Peltier and Jiang (1996).

4.3 Loading

From oxygen isotope analysis of ocean sediments (e.g., Shackleton and Opdyke 1976), it has been deduced that the great ice sheets had a growth period of about 90,000 years and a decay period of about 10,000 years, so a total period of about 100,000 years for one complete cycle. Water contains the isotopes ^{16}O and ^{18}O; depending on the amount of ice that has accumulated on land, the relative abundance of the two isotopes which are incorporated in ocean sediments will vary due to their specific mass difference: the lighter isotope evaporates more easily from the oceans, giving an over-abundance of this isotope in ice with respect to ocean water, thus creating an over-abundance of the heavier isotope in the oceans during glacial times, which is recorded in the sediments. The period of 100,000 years is equal to the time in which the ellipticity of the orbit of the Earth around the Sun changes (one of the periods in the so-called Milankovitch cycle of harmonic variations of the Earth's orbit around the Sun), but whether there is a direct connection between ellipticity change and ice age cycles is a contentious issue at the moment. Many researchers accept the theory that the change in ellipticity can trigger and end an ice age cycle indirectly, that is, the change in solar insolation is not considered powerful enough to induce a glacial period directly but it can trigger non-linear changes in ocean currents, which can be the driving agent of the climate change. However, more recently, other theories have emerged, such as that in which changes in interplanetary dust density with a period of 100,000 years as a result of changes in orbital inclination might be the prime mover (Muller and MacDonald 1995; Farley and Patterson 1995). Whatever the cause, oxygen isotope analyses have discerned at least eight glacial cycles during the Pleistocene.

Figure 4.2 shows a cartoon of the ice load model that will be used to study the influence of ice age cycles on polar wander (Vermeersen et al. 1997; Vermeersen and Sabadini 1999).

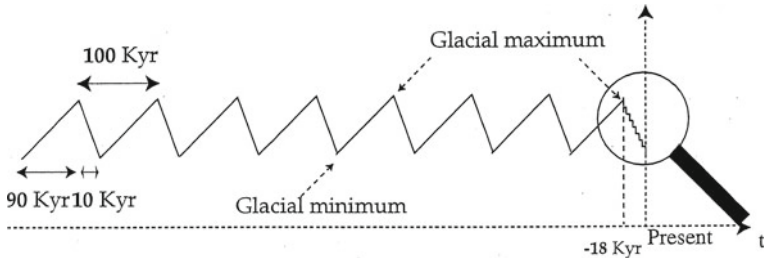

Fig. 4.2 Pleistocene glaciation and deglaciation history as used in the models. The history contains seven glacial ramp-shaped cycles followed by a linear ice accumulation period and a deglaciation period consisting of a set of discrete unloading steps, after ICE-3G (Tushingham and Peltier 1991). Each cycle has a 90 kyr glaciation period. The seven glacial pre-cycles have deglaciation periods of 10 kyr. The final glacial cycle, which starts 18 kyr before present, has a 13 kyr deglaciation period of Heaviside loadings. The ice masses are assumed to remain constant after 5 kyr before present. The maximum amount of ice accumulated at the end of a glaciation period is the same as ICE-3G gives at 18 kyr before present. The minimum amount of ice at the end of a deglaciation period is the same as ICE-3G gives at 5 kyr before present (Fig. 2 in Vermeersen et al. 1997)

In order to make use of Eq. (3.84) and of the ICE-3G model by Tushingham and Peltier (1991), we must specify the Laplace transform of the loading history $\tilde{f}(s)$. The saw-tooth function appropriate for describing the nth cycle of the load is given, in time domain, by

$$f(t) = \begin{cases} \frac{t-a(n-1)}{b} & \text{if } a(n-1) < t < a(n-1)+b \\ \frac{an-t}{a-b} & a(n-1)+b < t < an \end{cases}$$

In the Laplace domain the load time history becomes

$$\tilde{f}(s) = \sum_{n=1}^{8} \frac{e^{-a(n-1)s} - e^{-a(n-1)s-bs}}{bs^2} - \frac{e^{-a(n-1)s-bs} - e^{-ans}}{(a-b)s^2} \tag{4.1}$$

where 8 cycles of glaciation-deglaciation are considered, with the $a = 100$ kyr denoting the glaciation phase and $b = 10$ kyr the deglaciation phase.

Inserting Eq. (4.1) into Eq. (3.84) and transforming back into the time domain, we obtain first that the contribution arising from the secular term A_0^* for each cycle, after the end of the last glacial event, is given by

$$\mathbf{m}(t)_{sec} = -i\sigma_r \frac{\Delta I_{13}^L + i\Delta I_{23}^L}{C-A} \frac{A_0^* a}{2} \tag{4.2}$$

Thus, for times after the termination of ice ages, the displacement of the axis of rotation arising from the A_0^* term given by Eq. (3.87) remains constant to the net shift acquired during the active phases. This result is relevant for the interpretation of TPW driven by the continuous occurrence of ice ages, but it does not account for the

effects of stabilizing internal mass distribution contributing to the non-hydrostatic bulge, as shown afterward.

The contribution arising from the a_i poles becomes appropriate for quantifying the present-day polar wander, after the 8th cycle

$$\begin{aligned}\mathbf{m}(t) = \sum_{n=1}^{8}\Big(\sum_{i=1}^{M}\Big(-i\sigma_r\frac{\Delta I_{13}^L + i\Delta I_{23}^L}{C-A}\Big)\\ \times\Big[\frac{\gamma_i}{ba_i^2}\{e^{a_i[t-a(n-1)]} - e^{a_i[t-a(n-1)-b]}\}\\ -\frac{\gamma_i}{(a-b)a_i^2}\{e^{a_i[t-a(n-1)-b]} - e^{a_i(t-an)}\}\Big]\Big)\end{aligned} \tag{4.3}$$

where summation over n corresponds to the eight glacial cycles considered in the modeling. From this expression for $\mathbf{m}(t)$ we obtain $\lim_{t\to\infty}\mathbf{m}(t) = 0$, which shows that for long time scales there is no net polar wander associated with viscoelastic relaxation modes.

ICE-3G consists of a total of 808 circular disk loads representing the Laurentide ice sheet, the Fennoscandian ice sheet, the Northern part of Russia, Antarctica, and the southwest of South America. For all these disks, ICE-3G gives the ice decay of the last Pleistocene cycle via a set of decrements, starting 18 kyr before present and ending 5 kyr before the present. The Antarctic ice sheet starts to melt at a later stage than the ice sheets of the Northern Hemisphere. The Pleistocene glaciation-deglaciation history, as used in the modeling, is shown in Fig. 4.2, while the total ice mass of all the disks is plotted as a function of time in Fig. 4.3 for the final deglaciation phase. It might be interesting to note that there are some negligible changes from 5 to 3 kyr before present; from 3 kyr to present the ice masses of all disks remain constant.

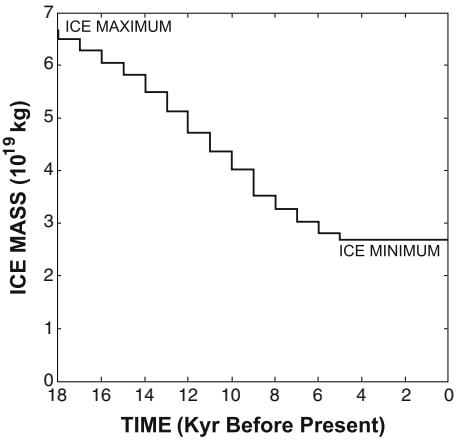

Fig. 4.3 Enlargement of the final deglaciation phase in Fig. 4.2. The discrete time steps of the ICE-3G model are shown. The ice mass on the vertical axis represents the ice of all sheets (Fig. 3 in Vermeersen et al. 1997)

Our eight complete glacial cycles consist of seven glacial saw-tooth pre-cycles, while the eighth cycle consists of a linear glaciation phase which ends 18 kyr before present, followed by ICE-3G. Each cycle is connected to its previous and following ones. Each of the seven precycles consists of a 90 kyr linear growth phase and a 10 kyr linear decay phase. The minimum amount of ice is the same as in ICE-3G at present, while the maximum amount of ice is the same as in ICE-3G 18 kyr before present. Both the polar wander rates and the $\dot{J}_2$ rates are determined at present, with $\dot{J}_2$ strictly linked to the degree 2 component of the perturbation in the geopotential.

For this temporal history the Laplace-transformed function $\tilde{f}(s)$ can be easily determined and substituted in the multidisk equivalents of the above formulations. The temporal history is simple enough, consisting of a combination of Heaviside functions and linear functions, so that performing the inverse transformations of the loading history can be done analytically, similarly to Eq. (4.1).

The TPW models can be relatively easily implemented in computer codes when all inverse relaxation times s_i and a_i are detected by a root-finding procedure, as discussed in Chap. 2. This is certainly the case with models which only have a limited number of layers, such as the five-layer incompressible models used in Spada et al. (1992b). Problems arise when not all the roots are found, as is rather the rule than the exception in models with a large number of layers. In models where only load relaxation is important, as for $\dot{J}_2$, it does not matter if modes that have far too low a strength to be of any importance are not taken into account (or remain undetected). This is the case, for instance, of those long-term buoyancy modes which are triggered by small density contrasts between two layers as discussed in Chap. 2. However, for polar wander it is necessary to take into account all the a_i rotational counterparts of the s_i modes.

4.4 Mantle Viscosity

This Sect. 4.4, reworked from Vermeersen et al. (1997), deals with the effects of viscosity variations in the mantle on TPW and $\dot{J}_2$. Figures 4.4, 4.5, 4.6, 4.7, 4.8, 4.9, 4.10, 4.11, 4.12, 4.13, 4.14, 4.15 and 4.16 are based on incompressible Earth's models described by Eqs. (2.42)–(2.47).

We consider five cases with varying layering, 5-, 31-, 56-layer models plus two with varying depth between the upper and lower mantle at 971 and 1471 km depth rather than 670 km, whose density and elastic parametrization is based on PREM (Dziewonski and Anderson 1981). These five cases have not been selected at random; all have special meanings.

To gain some insight into the effects of stratification on relaxation, we shall start with simple 5-layer models. An elastic lithosphere with a thickness of 120 km surrounds the viscoelastic mantle having a viscosity of 10^{21} Pa s.

Five-layer models have been used in the past in the context of analytical viscoelastic, incompressible relaxation modeling (e.g., Spada et al. 1992b; Ricard et al. 1993; Vermeersen et al. 1994). There is one important difference, however, in comparison

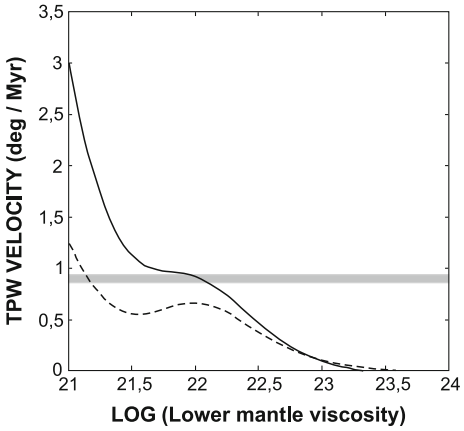

Fig. 4.4 The present-day TPW velocity as a function of the lower mantle viscosity for two 5-layer Earth's models. For this figure the ice load consisted of the Fennoscandian, Laurentian, and Antarctic ice sheets modeled as homogeneous disks. The value of the viscosity of the upper mantle is 10^{21} Pa s. The *solid curve* depicts the solution by the volume-averaged Earth's model in Table 4.2, and the *dashed curve* depicts the solution from the fixed boundary contrast Earth' model in Table 4.1 as used in Spada et al. (1992b). The *hatched area* depicts the observed present-day secular drift ranging between the error bars as given by McCarthy and Luzum (1996)

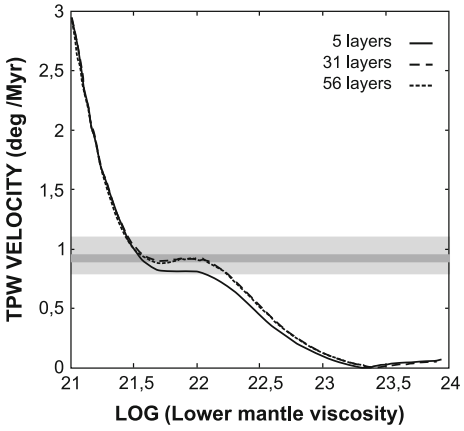

Fig. 4.5 The present-day true polar wander velocity as a function of the viscosity of the lower mantle for a volume-averaged Earth's model. The upper mantle has a viscosity of 10^{21} Pa s. The number of layers for the three curves is indicated in the *top right corner*. The *lightly hatched area* depicts the observed present-day secular drift ranging between the error bars as given by Dickman (1977). The *darkly hatched area* depicts the observed present-day secular drift ranging between the error bars as given by McCarthy and Luzum (1996)

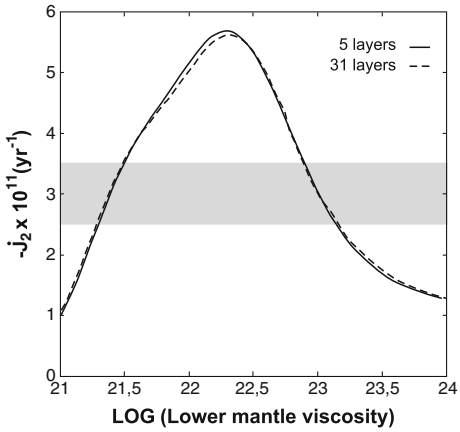

Fig. 4.6 Present-day change in the non-tidal dynamic form factor $\dot{J}_2$ as a function of lower mantle viscosity and upper mantle viscosity of 10^{21} Pa s. The *solid* and *dashed curves* correspond to volume-averaged models of 5 and 31 layers. The *hatched area* depicts the observed present-day $\dot{J}_2$ in the range $-2.5 \pm 0.7 \times 10^{-11}$ yr^{-1} where the *lower bound* corresponds to the solution CGS96 from the Centre of Space Geodesy in Matera (Italian Space Agency), derived from LAGEOS I and LAGEOS II monthly estimates over the time interval 1985–1996 (Devoti et al. 1997), and the upper bound corresponds to the the estimate obtained by Yoder et al. (1983)

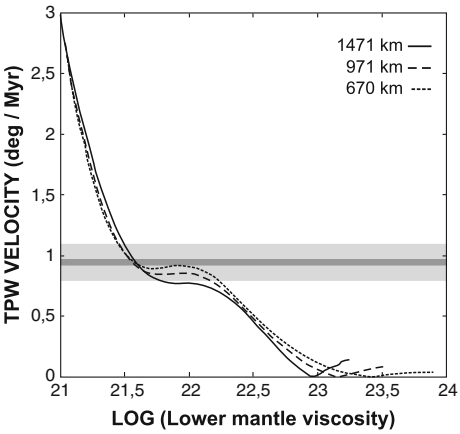

Fig. 4.7 Effects of the depth of the viscosity contrast on present-day TWP as a function of the value of the viscosity of the lower mantle. The standard 31-layer model in Table 4.3 is used as the Earth's model. The three cases depict the results for the boundary between the upper and lower mantle (upper and lower mantle defined with respect to viscosity) at 1471, 971 and 670 km depths. The upper mantle has a viscosity of 10^{21} Pa s. The hatching has the same meaning as in Fig. 4.5

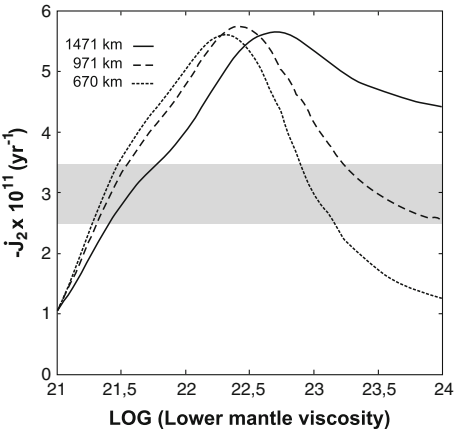

Fig. 4.8 Effects of the depth of the viscosity contrast on the present-day secular variation in $\dot{J}_2$ as a function of the value of the viscosity of the lower mantle. The standard 31-layer model in Table 4.3 is used as the Earth's model. The three cases depict the results for the boundary between the upper and lower mantles (upper and lower mantles are defined with respect to viscosity) at 1471, 971, and 670 km depth. The upper mantle has a viscosity of 10^{21} Pa s. The hatching has the same meaning as in Fig. 4.6

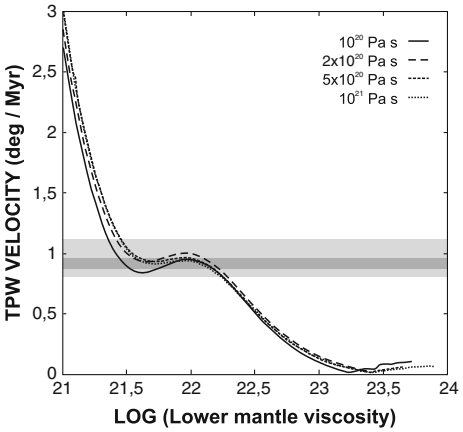

Fig. 4.9 Effects of a lower value for the upper mantle viscosity on present-day TPW as a function of the value of the viscosity of the lower mantle. The standard 31-layer model in Table 4.3 is used as the Earth's model. The *solid curve* depicts the case of an upper mantle viscosity of 10^{20} Pa s. The *dotted curve* depicts the case of an upper mantle viscosity of 10^{21} Pa s. The two cases for the upper mantle viscosity between these two values are depicted by the *short-dashed curve* for the case of 5×10^{20} Pa s and by the *long-dashed curve* for the case of 2×10^{20} Pa s. The hatching has the same meaning as in Fig. 4.5

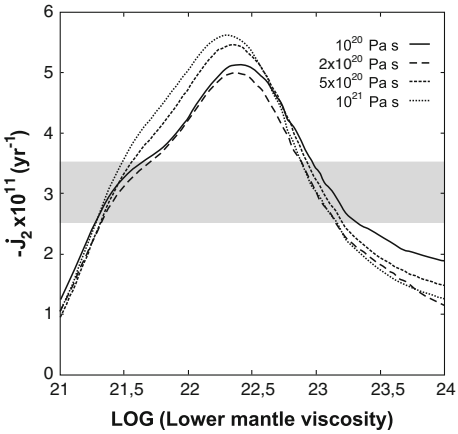

Fig. 4.10 Effects of a lower value for upper mantle viscosity on present-day secular variation in $\dot{J}_2$ as a function of the value of the viscosity of the lower mantle. The standard 31-layer model in Table 4.3 is used as the Earth' model. The *solid curve* depicts the case of an upper mantle viscosity of 10^{20} Pa s. The *dotted curve* depicts the case of an upper mantle viscosity of 10^{21} Pa s. The two cases for the upper mantle viscosity in between these two values are depicted by the *short-dashed curve* for the case of 5×10^{20} Pa s and by the *long-dashed curve* for the case of 2×10^{20} Pa s. The hatching has the same meaning as in Fig. 4.6

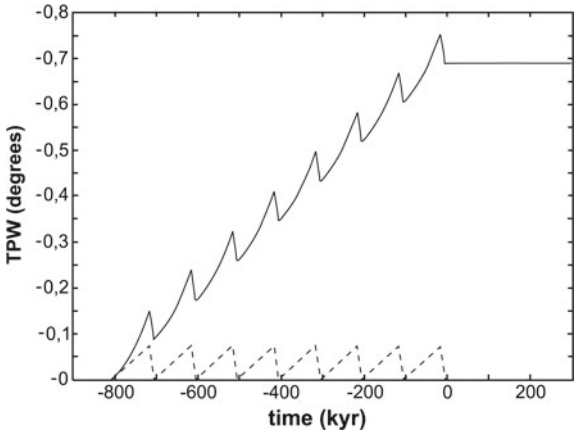

Fig. 4.11 TPW displacement during eight cycles of glaciation-delaciation, and 3×10^5 yr after the end of deglaciation at time = 0, for a 3-layer model consisting of an elastic lithosphere, a uniform viscoelastic mantle of 10^{21} Pa s and a core. All the poles in $s = 0$ and $s = a_i$ are considered for the *solid curve*, while the *dashed* one corresponds to $A_0^* = 0$. Redrawn from Fig. 9 in Sabadini et al. (2002)

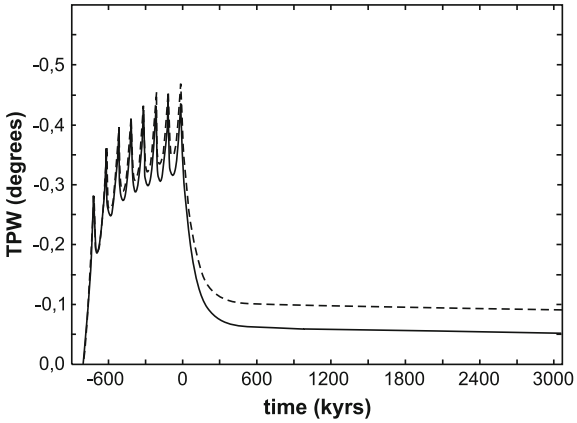

Fig. 4.12 TPW displacement during eight cycles of glaciation-deglaciation, and 3×10^6 yr after the end of deglaciation at time = 0, for the 5-layer model of Table 4.2. The upper and lower mantle viscosity is fixed at 10^{21} Pa s. All the poles in $s = 0$ and $s = a_i$ are considered for the *dashed curve*, while the *solid* one corresponds to $A_0^* = 0$. Redrawn from Fig. 10 in Sabadini et al. (2002)

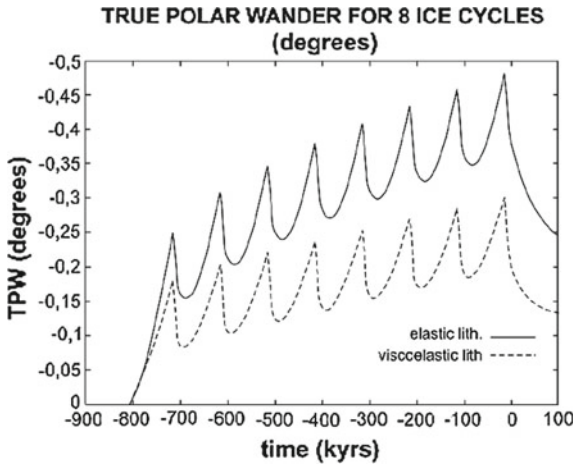

Fig. 4.13 TPW as a function of time (present is time = 0) for the ice load forcing of Fig. 4.2. The mantle viscosity is fixed at 10^{21} Pa s. The thickness of the lithosphere is 120 km. Two cases are depicted, for an elastic lithosphere, *solid curve*, and a viscoelastic one, *dashed curve*, with the same viscosity of the mantle. The horizontal scale differs from the previous two figures, ending at time = 100 kyr. The 5-layer model in Table 4.2 has been used

with the stratification that is used between the 5-layer models in this section and the one that has been used in the past. The elastic parameterization and density profile were based on what we will dub from now on fixed-boundary contrast models (e.g., Sabadini et al. 1982a; Yuen et al. 1982). The densities for the layers (lithosphere, shallow upper mantle, transition zone, lower mantle) in these models were chosen

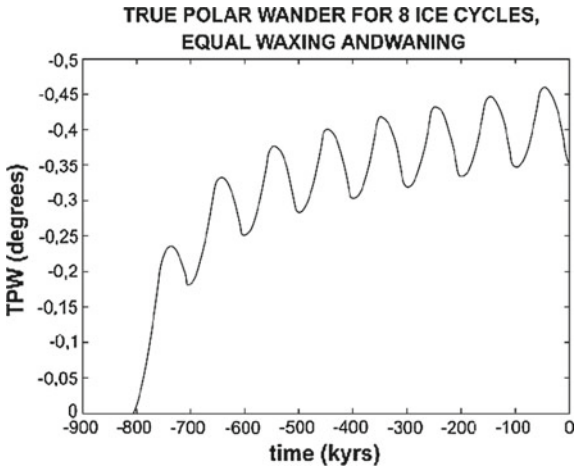

Fig. 4.14 TPW as a function of time for the ice load forcing history in Fig. 4.2 and an elastic lithosphere, but now with equal waxing and waning time scales of 50,000 years. The mantle viscosity is uniformly 10^{21} Pa s. With respect to Fig. 4.13, the end of the last deglaciation phase corresponds to the end of the horizontal scale

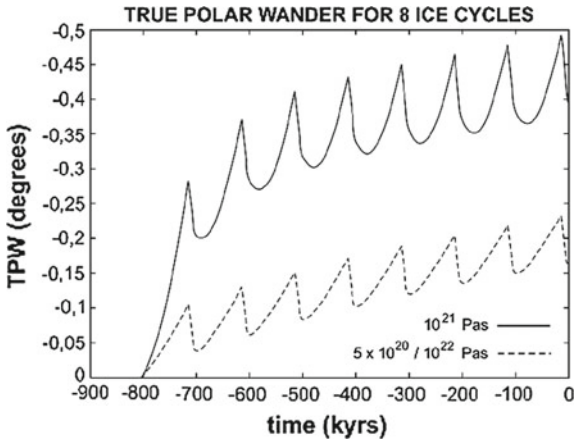

Fig. 4.15 TPW as a function of time (the present is time = 0) for the ice load forcing of Fig. 4.2 and 31-layer Earth's model in Table 4.3. Two cases are depicted: the *solid curve* for a homogeneous mantle viscosity of 10^{21} Pa s; the *dashed curve* for the case of an upper mantle viscosity of 5×10^{20} Pa s and a lower mantle viscosity of 10^{22} Pa s. As for Fig. 4.14, the end of the last deglaciation phase corresponds to the end of the horizontal scale

in such a way that the final assemblage contained density contrasts which agreed with the density contrasts given by PREM for the interfaces. Thus, for example, the density contrast at the boundary between the transition zone and the lower mantle is about 10 fixed-boundary contrast model, agreeing with the value PREM gives, but the lithosphere has, according to Table 4.1, a density of 4120 kg/m^3, which is far

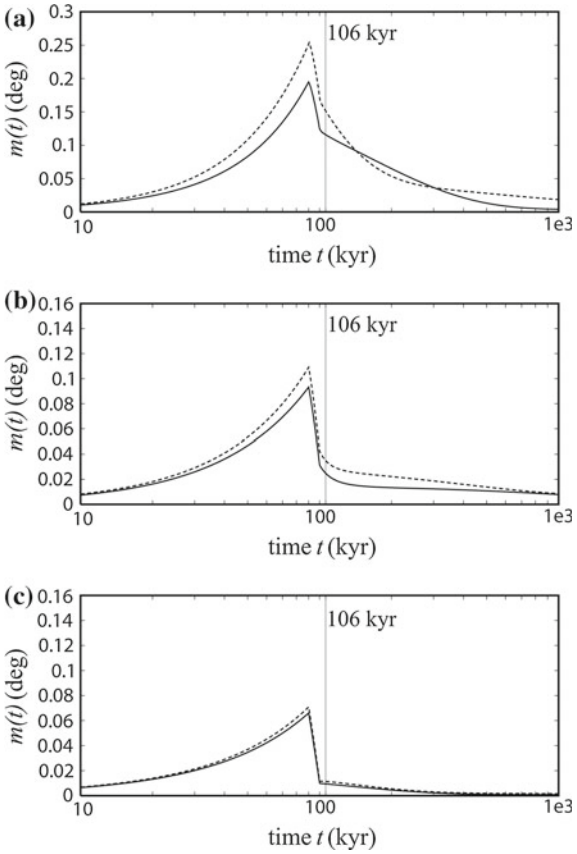

Fig. 4.16 The TPW displacement $m(t)$ due only to the last ice age for the compressible (*solid*) and incompressible (*dashed*) PREM with the elastic lithosphere. The lower mantle viscosity is $\nu_{LM} = 10^{21}$ (**a**), $\nu_{LM} = 10^{22}$ (**b**) and $\nu_{LM} = 10^{23}$ (**c**) Pa s

Table 4.1 Parameters for the 5-layer fixed-boundary contrast Earth's model

Layer	r (km)	ρ (kg/m^3)	μ (N/m^2)	
1	6371 − 6271	4120	7.28×10^{10}	Lithosphere
2	6271 − 5951	4120	9.54×10^{10}	Shallow upper mantle
3	5951 − 5701	4220	1.10×10^{11}	Transition zone
4	5701 − 3480	4508	1.99×10^{11}	Lower mantle
5	3480 − 0	10,925	0	Inviscid fluid core

r is the distance with respect to the centre of the Earth, ρ the density of the layer, and μ the rigidity

greater than the volume-averaged density of the lithosphere as given in Table 4.2 (in fact, the highest density that PREM gives for a layer in the top 120 km is less than 3381 kg/m^3). It is important to realize that the 5-layer models in the following are, unless stated explicitly otherwise, volume-averaged models. The density contrasts

Table 4.2 Parameters for the 5-layer volume-averaged Earth's model

Layer	r (km)	ρ (kg/m^3)	μ (N/m^2)	
1	6371 – 6250	3184	6.0243×10^{10}	Lithosphere
2	6250 – 5951	3434	7.2666×10^{10}	Shallow upper mantle
3	5951 – 5701	3857	1.0639×10^{11}	Transition zone
4	5701 – 3480	4878	2.1944×10^{11}	Lower mantle
5	3480 – 0	10,925	0	Inviscid fluid core

r is the distance with respect to the centre of the Earth, ρ the density of the layer, and μ the rigidity

at the boundaries are thus not fixed to the values PREM gives as they were in all 5-layer models, which, as we know, have been published in the past.

For our models, we have taken the PREM values from Tables II and III of Dziewonski and Anderson (1981). In these tables, PREM contains 55 layers between the Core Mantle Boundary (CMB) and the surface. Thus we have included the 56-layer cases in our models. In the 31-layer model the lithosphere is taken as homogeneous, while every 3 mantle layers of PREM in succession (except for the 4 layers nearest to the core: these layers are volume-averaged as pairs) are reduced by the volume-averaging procedure to two layers. Thus we end up with a minimal number of three cases (5, 31 and 56 layers), which we can posit as indicative of changes that can be expected for any other number of layers.

The TPW results for a viscosity of 10^{21} Pa s in the upper mantle and varying lower mantle viscosity are portrayed in Fig. 4.4; only for this Fig. 4.4, the Laurentide, Fennoscandian, and Antarctic ice sheets are taken into account as disks, in agreement with the analyses by Richards et al. (1999) and Spada et al. (1992b). This figure shows, within the scheme of a 5-layer model consisting of the lithosphere, three layers in the mantle and a core, the effects of constraining the average values of the density and rigidity in each layer on the basis of PREM (solid curve) or, alternatively, the effects of constraining the density and rigidity contrasts at the 420 and 670 km discontinuities in agreement with PREM (dashed curve). The latter procedure was used in the past in TPW models based on analytical schemes (Sabadini et al. 1982a; Richards et al. 1999; Spada et al. 1992b). The values used in the 5-layer models are given in Table 4.1 for the fixed boundary contrast model and in Table 4.2 for the volume-averaged model. The two schemes predict quite different TPW signals, although the major characteristics of the two curves are the same: a general decay from high TPW value for an isoviscous mantle, the vanishing of the signal for a lower mantle viscosity of 10^{23} Pa s, and a non-monotonic behavior from 3×10^{21} to 10^{22} Pa s. The fixed boundary contrast model (dashed curve) portrays a well-developed local maximum at 10^{22} Pa s. In particular, the dashed curve crosses the observational datum of McCarthy and Luzum (1996) for a lower mantle viscosity of 1.5×10^{21} Pa s. On the basis of this result an almost homogeneous mantle was deduced from previous TPW and $\dot{J}_2$ studies (Sabadini et al. 1982a; Richards et al. 1999; Spada et al. 1992b). The extra buoyancy of the model with volume-averaged densities, due to the large density contrasts at 420 and 670 km depth, is responsible

for an increase in the TPW signal in the whole range of lower mantle viscosities once compared with the fixed boundary contrast 5-layer model, which has the major effect of displacing the crossing of the TPW curve with the observed values to higher viscosities. As we will see below, this result has a major impact on the interpretation of the viscosity profile of the mantle based on TPW analysis, and is caused by the density contrasts as being non-adiabatic in nature, as discussed in Chaps. 1 and 2.

This Fig. 4.4 is a nice example of how the inference of the lower mantle viscosity depends on the hypotheses underlying the Earth's model, resulting into 1.5×10^{21} Pa s for the fixed density contrast model or 10^{22} Pa s for the 5-layer, volume averaged density model, where the dashed and solid curves cross the observational datum. The lower mantle viscosity inference depends also on how much of the observational datum is attributed to PGR: a recent, comprehensive discussion on the potential contributors to the McCarthy and Luzum (1996) datum is provided by Nakada et al. (2015), where the TPW contributions arising from PGR and present-day melting in Greenland, Antarctica and mountain glaciers is evaluated, including the effects due to the differences between the ICE-5G (Peltier 2004) and ANU (Australian National University) ice models. Keeping in mind that for TPW the contributions must be summed up vectorially, it is clear that the consequence of including other contributions beyond PGR would be to displace in the TPW figures of this chapter the observational datum up or down with respect to the model curves, which would lead to different lower mantle viscosity estimates. This chapter is instead based on the assumption that the whole observational datum is due to PGR.

Figure 4.5 shows the effects of distributing the density contrasts of the mantle in a large number of layers. PREM contains 56 layers in the lithosphere and mantle. The 31-layer model in Table 4.3 is deduced from PREM in such a way that the layers take on a progressively larger thickness from the Earth's surface to the core.

With respect to the simpler 5-layer model with volume-averaged densities, the buoyancy is now smoothly distributed over the mantle instead of being concentrated at the four major boundaries. Layering has, in fact, a major effect because it modifies the TPW curve in the proximity of the inflection of the curve at a lower mantle viscosity of 10^{22} Pa s, where crossing with the observations occurs. While for lower mantle viscosity ranging from 10^{21} to 3×10^{21} Pa s density stratification has negligible effects, PREM predicts a quite different behavior with respect to the simpler 5-layer model for viscosities higher than 3×10^{21} Pa s. In fact, the TPW signal increases in the proximity of the observational data, causing a multiplicity of lower mantle viscosity solutions. These results indicate a trade-off between density and viscosity stratification in the mantle. Another remarkable result of this figure is that differences between the curves corresponding to 31 and 56 layers are negligible, indicating that as far as rotational calculations are concerned, the continuous behavior in the sense discussed in Chap. 2 is already reached with 31-layer models. Increasing the number of layers does not provide any further information on TPW.

It is interesting to compare the sensitivity of TPW as to density stratification with that portrayed by $\dot{J}_2$ for a simplified Earth's model and load. In Fig. 4.6, $\dot{J}_2$ is shown for a 5-layer and 31-layer models with a fixed upper mantle viscosity of 10^{21} Pa s, varying lower mantle viscosity and realistic loading history. Density stratification

Table 4.3 Parameters for the standard 31-layer volume-averaged Earth's model derived from PREM

Layer	r (km)	ρ (kg/m^3)	μ (N/m^2)	
1	6371.0 – 6368.0	1020	2.66×10^{10}	Lithosphere
2	6368.0 – 6356.0	2600	2.66×10^{10}	
3	6356.0 – 6346.6	2900	4.41×10^{10}	
4	6346.6 – 6331.0	3372	6.81×10^{10}	
5	6331.0 – 6311.0	3372	6.78×10^{10}	
6	6311.0 – 6291.0	3372	6.75×10^{10}	
7	6291.0 – 6251.0	3372	6.71×10^{10}	
8	6251.0 – 6221.0	3372	6.67×10^{10}	Shallow upper mantle
9	6221.0 – 6186.0	3372	6.63×10^{10}	
10	6186.0 – 6151.0	3372	6.58×10^{10}	
11	6151.0 – 6106.0	3449	7.48×10^{10}	
12	6106.0 – 6061.0	3476	7.64×10^{10}	
13	6061.0 – 6016.0	3503	7.81×10^{10}	
14	6016.0 – 5971.0	3529	7.97×10^{10}	
15	5971.0 – 5921.0	3755	9.39×10^{10}	Transition zone
16	5921.0 – 5871.0	3819	1.01×10^{11}	
17	5871.0 – 5821.0	3882	1.09×10^{11}	
18	5821.0 – 5771.0	3945	1.17×10^{11}	
19	5771.0 – 5736.0	3980	1.21×10^{11}	
20	5736.0 – 5701.0	3988	1.23×10^{11}	
21	5701.0 – 5650.0	4397	1.59×10^{11}	Lower mantle
22	5650.0 – 5600.0	4423	1.68×10^{11}	
23	5600.0 – 5400.0	4501	1.78×10^{11}	
24	5400.0 – 5200.0	4620	1.91×10^{11}	
25	5200.0 – 4900.0	4759	2.06×10^{11}	
26	4900.0 – 4600.0	4921	2.24×10^{11}	
27	4600.0 – 4300.0	5078	2.41×10^{11}	
28	4300.0 – 4000.0	5205	2.58×10^{11}	
29	4000.0 – 3700.0	5379	2.74×10^{11}	
30	3700.0 – 3480.0	5509	2.89×10^{11}	
31	3480.0 – 0	10,932	0	Inviscid fluid core

r is the distance with respect to the centre of the Earth, ρ the density of the layer, and μ the rigidity. The outermost 3 km of water carry the same rigidity of the underlying crustal layer, for numerical stability

has no effects on $\dot{J}_2$ between a 5-layer model and PREM once volume-averaged parameters are used. This different behavior with respect to TPW is not surprising since TPW solutions have the extra viscoelastic readjustment of the equatorial bulge above the load readjustment, which is the only one present in $\dot{J}_2$.

In Chap. 5 we come back in greater details on the issue of the amount of the observed $\dot{J}_2$ which must be attributed to PGR and to present-day glacial forcing, analogously to TPW and to the analysis carried out by Nakada et al. (2015) also for $\dot{J}_2$, particularly in view of the changes in $\dot{J}_2$ obtained from SLR over the time interval 1992–2009 (Cheng et al. 2013). The figures of this chapter are based on the $\dot{J}_2$ value consistent with $-3 \pm 0.5 \times 10^{-11}$ yr^{-1} value by Stephenson and Morrison (1995). As for TPW, moving up and down the observational datum attributable to $\dot{J}_2$, the lower mantle viscosity inference varies: we refer to Nakada et al. (2015) for a very detailed discussion on these viscosity inferences depending on the observed changes in $\dot{J}_2$ after 1992 and on estimated contributions from present-day glacial forcing.

4.4.1 *Variations in Depth of the Two-Layer Mantle Viscosity Profile*

In this section we consider the possibility that the boundary where the viscosity contrast occurs does not coincide with the seismologically inferred base of the upper mantle. Two depths are considered, 971 and 1471 km, so both are deeper than the 670 km one shown for comparison. The 1471 km depth is close to the depth of 1400 km considered in the relative sea-level analysis by Mitrovica (1996) and the TPW and $\dot{J}_2$ studies by Peltier and Jiang (1996), while 971 km is an intermediate value.

For the upper layer viscosity fixed at 10^{21} Pa s, Fig. 4.7 portrays the TPW curves for the three different depths as a function of lower layer viscosity. Increasing the viscosity in the lower layer has the effect of reducing the TPW from about 3° Myr^{-1} for a viscosity of 10^{21} Pa s to zero. Although the shape of the curves is the same for the three different depths, the deepening of the viscosity contrast has the major effect of diminishing the local maximum at 10^{22} Pa s. For 1471 km this local maximum disappears and is barely visible for 971 km. The modification in the shape of the curves has the important consequence of reducing the ambiguity in the inference of the lowermost viscosity from the admissible range of 2.8×10^{21}–1.5×10^{22} Pa s for 670 km to the narrower range of 3–5 $\times 10^{21}$ Pa s for 1471 km when Dickman (1977) data are considered. The most recent TPW data by McCarthy and Luzum (1996) require a value of 4×10^{21} Pa s, being intermediate between the two previous estimates. Notice that, irrespective of the depth of the boundary, the same value of TPW is retrieved when the lowermost viscosity equals the viscosity of the upper layer, as expected. The non-monotonic decrease in TPW obtained in this chapter, with a local maximum in proximity of 10^{22} Pa s, is also shown by Yuen and Sabadini (1984), Spada et al. (1992b), consistently with the results obtained by Milne and Mitrovica (1996) based on compressible models.

Figure 4.8 deals with a similar analysis for $\dot{J}_2$. The most apparent effects of the increase with depth of the viscosity contrast are the disappearance of the high-viscosity solution branch of 2×10^{23} Pa s for 1471 km in the right portion of the

figure and the smooth increase, from 1.5–2.8 $\times 10^{21}$ to 2.5–5 $\times 10^{21}$ Pa s, of the low-viscosity branch. The increase in the $\dot{J}_2$ signal for lowermost mantle viscosities higher than 3×10^{21} Pa s when the viscosity contrast is located deeper than 670 km agrees with the results of Mitrovica and Peltier (1993). This behavior in the $\dot{J}_2$ curve has the important implication of allowing for a single solution in the lowermost viscosity and, when comparison is made with the TPW curve for 1471 km in Fig. 4.7, allowing for the simultaneous fit of the TPW and $\dot{J}_2$ data with a viscosity in the lower layer of 3–5 $\times 10^{21}$ Pa s when the TPW data by Dickman (1977) and 4×10^{21} Pa s with the latest TPW data (McCarthy and Luzum 1996) are considered. For 670 km it is not possible to obtain a simultaneous fit of both TPW and $\dot{J}_2$ for any value of the lower mantle viscosity when the new TPW data are considered. With Dickman (1977) TPW data the two viscosity solutions barely overlap at 2.5×10^{21} Pa s, degrading the simultaneous TPW and $\dot{J}_2$ fit for the depth of the viscosity contrast at 670 km with respect to 1471 km.

The important conclusion that we can draw from the results in Figs. 4.7 and 4.8 is that when self-consistent, viscoelastic, stratified Earth's models are considered, a viscosity of 10^{21} Pa s cannot be limited to the seismically defined upper mantle but must be considered appropriate for a wider region of the mantle to depths of about 1400 km. It should be emphasized that this conclusion is strongly supported by the new TPW data (McCarthy and Luzum 1996), which definitively rule out a viscosity of 10^{21} Pa s only for the upper mantle, while the TPW data by Dickman (1977) only show an indication in this sense because of the larger error bounds. This finding is only apparently inconsistent with previous analyses based on incompressible rotational deformation models, as in Sabadini et al. (1982a), Yuen and Sabadini (1984), Spada et al. (1992b). In these references a simultaneous fit of TPW and $\dot{J}_2$ data was found from an assumed value for the viscosity of the upper mantle of 10^{21} Pa s and a moderate viscosity increase in the lower mantle by a factor of 2. However, these previous results were derived from simplified 4-layer or 5-layer Earth's models, where the density contrasts at the internal boundaries were fixed according to PREM instead of the layers having volumetric density averages derived from PREM. Our findings are in complete agreement with a similar analysis of relative sea-level data by Mitrovica (1996), who, with a more rigorous scheme based on the resolving power of relative sea-level kernels, has demonstrated that the value of 10^{21} Pa s is appropriate for a region of the mantle extending to greater depths than the upper mantle defined by seismology. The value of 10^{21} Pa s, first proposed by Haskell (1935), was in fact somehow arbitrarily limited to the upper mantle after modern seismology had located the boundary between the upper and lower mantles at 670 km, as pointed out by Mitrovica (1996).

4.4.2 Upper Mantle Viscosities Lower Than 10^{21} Pa s

In the previous section we saw that within the framework of a multilayered, viscoelastic Earth's model based on PREM a simultaneous fit to TPW and $\dot{J}_2$ data is not

possible when the viscosity value of 10^{21} Pa s is limited to the upper mantle. In this section the depth of the viscosity contrast is fixed at 670 km and the upper mantle viscosity is modified in order to get a simultaneous fit with TPW and $\dot{J}_2$ data when the lower mantle viscosity is varied from 10^{21} to 10^{24} Pa s, as in the previous figures.

In Fig. 4.9 the upper mantle viscosity is reduced from 10^{21} Pa s (dotted curve) to 10^{20} Pa s (solid curve); intermediate values are 5×10^{20} Pa s (short-dashed curve) and 2×10^{20} Pa s (long-dashed curve). The reduction in the upper mantle viscosity diminishes the TPW signal in the whole range of viscosities, but it should be noted that this occurs in a non-linear fashion. A reduction factor of 2 from 10^{21} Pa s to 5×10^{20} Pa s has minor effects, except for a small increase in the proximity of the local maximum at 10^{22} Pa s. A decrease in the upper mantle viscosity from 5×10^{20} Pa s to 2×10^{20} Pa s causes a further increase in proximity of the local maximum and a decrease in the range of lower mantle viscosities from 10^{21} Pa s to 4×10^{21} Pa s. This reduction in the signal is confirmed by the upper mantle viscosity of 10^{20} Pa s, which provides the smallest TPW values for lower mantle viscosities smaller than 10^{22} Pa s. Although in a non-linear fashion, the reduction of the upper mantle viscosity has the effect of displacing the TPW curve to the left. Except for the lowest upper mantle viscosity of 10^{20} Pa s, which predicts a lower mantle of 2.5×10^{21} Pa s, the inference of the viscosity value of the lower mantle is not affected by a reduction factor of 5 from the reference value of 10^{21} Pa s. The reduction of the upper mantle viscosity has, on the other hand, the major effect of increasing the viscosity contrast at 670 km from 3 for the short-dashed curve, corresponding to 10^{21} Pa s, to 8 or 20 for the upper mantle viscosities of 5×10^{20} and 2×10^{20} Pa s, respectively.

In Fig. 4.10, the same analysis is carried out for $\dot{J}_2$. The curves are the same as in Fig. 4.9. As in the case of Fig. 4.8, the major effects of the viscosity decrease are visible in the high-value region of the lower mantle viscosities for viscosities higher than 10^{23} Pa s. Major modifications with respect to the upper mantle viscosity of 10^{21} Pa s also occur in proximity to the maximum of the curves and for lower mantle viscosities higher than 3×10^{21} Pa s.

The reduction of the peak value located at the lower mantle viscosity of 3×10^{22} Pa s and the increase in the signal for lower mantle viscosities larger than 10^{23} Pa s agree with the results obtained by Mitrovica and Peltier (1993). The reduction in the upper mantle viscosity is responsible for an increase in the range of admissible lower mantle viscosities from 1.5–3 $\times 10^{21}$ to $1.5 - 4 \times 10^{21}$ Pa s for an upper mantle viscosity of 10^{20} Pa s. With respect to the upper mantle value of 10^{21} Pa s, the $\dot{J}_2$ curves for reduced upper mantle viscosities are displaced to the right. This allows a simultaneous fit with the TPW data of McCarthy and Luzum (1996) for a viscosity increase at 670 km, which can be as high as factors of 20 and 30 for upper mantle viscosities of 2×10^{20} and 10^{20} Pa s, respectively. It should be noted that a simultaneous fit of TPW and $\dot{J}_2$ for an upper mantle viscosity of 5×10^{20} Pa s can only be obtained with the data of Dickman (1977), which have larger error bounds.

In comparison with the recent TPW data by McCarthy and Luzum (1996), those by Dickman (1977) are less discriminating in ruling out a viscosity value of 10^{21} Pa s above the 670 km discontinuity, although a clear tendency to prefer a lower value

for the upper mantle viscosity is also shown by Dickman (1977) data by means of enlarging the interval of admissible viscosity solutions for the two data sets.

The upper and lower mantle viscosities of $1 - 5 \times 10^{20}$ and $2.5 - 4 \times 10^{21}$ Pa s inferred from the McCarthy and Luzum (1996) TPW data are consistent with the estimates made by Lambeck et al. (1990) of $3 - 5 \times 10^{20}$ and $2 - 7 \times 10^{21}$ Pa s for these parameters, although our results have the tendency to remain in the lower limit of Lambeck et al. (1990) predictions. This tendency is probably attributable to model differences with Lambeck et al. (1990) analysis, where attention is focused on a different PGR signal, such as sea level in the far field, and compressible viscoelastic models with a lithospheric thickness smaller than ours. If we focus on the viscosity contrast at the boundary between the upper and lower mantles, we obtain a complete agreement with the findings of Lambeck et al. (1990), whose preferred upper and lower mantle viscosity contrast ranges between a factor of 4 and 25.

The results shown in this section indicate that the different viscosity models obtained in the past are mainly a consequence of a different way of mantle stratification. For an upper mantle viscosity varying between 10^{20} and 10^{21} Pa s, the shape of the TPW and $\dot{J}_2$ curves as a function of the viscosity of the lower mantle agrees with both previous analytical results based on simplified mantle models (Yuen and Sabadini 1984; Spada et al. 1992b) and findings by Milne and Mitrovica (1996). The TPW curves show a non-monotonic decrease in the signal from about 3° Myr^{-1} for an isoviscous mantle to zero for lower mantle viscosities higher than 10^{23} Pa s, with a characteristic upwarping in proximity of 10^{22} Pa s. The local maximum in TPW simulations is responsible for a multiplicity of solutions in the inference of lower mantle viscosity from 3×10^{21} to 10^{22} Pa s. These findings are in distinct contrast with analyses by Peltier and Jiang (1996), who, for viscosity contrasts located at 670 km, predict that TPW is negligible in the proximity of 10^{22} Pa s, where our local maximum of 0.9° Myr^{-1} is located. When the depth of the viscosity contrast is increased from 670 to 1471 km in the lower mantle, the multiplicity of solutions for both TPW and $\dot{J}_2$ in the inference of the viscosity of the lowermost portion of the mantle disappears. In the TPW curve this occurs via a reduction in the local maximum at 10^{22} Pa s at a single crossing of the observational data, while in $\dot{J}_2$ the high-branch viscosity solution disappears because of an increase in the signal beyond -3×10^{-11} yr^{-1} for viscosities in the lowermost mantle higher than 3×10^{21} Pa s. If the viscosity contrast is located at depths of about 1400 km, TPW and $\dot{J}_2$ data allow for an unambiguous viscosity solution for the upper portion of the mantle of 10^{21} Pa s, agreeing with Haskell (1935) viscosity. A viscosity of 10^{21} Pa s limited to the upper mantle has been retrieved in some previous TPW and $\dot{J}_2$ analyses because of the underestimate of mantle buoyancy in simplified five-layer fixed boundary contrast models and of the trade-off between the density and the viscosity profile (e.g., Spada et al. 1992b). If the viscosity contrast is located at 670 km depth, which defines the boundary between the upper and the lower mantles based on seismological data, TPW and $\dot{J}_2$ indicate a clear trend toward viscosities in the upper mantle lower than the Haskell value of 10^{21} Pa s. This increases the viscosity contrast to a factor of 20, in agreement with the far-field RSL analysis by Lambeck et al. (1990) and with the studies on the long-wavelength geoid anomalies supported by mantle

convection (Richards and Hager 1984). When analytical stratified models carrying all the buoyancy of PREM are considered, it becomes possible to explain some apparently contradictory results of recent inferences of mantle viscosity.

4.5 Ice Age Cycles and the Polar Wander Path: Lithospheric and Mantle Rheology

In the former section present-day polar wander as a consequence of PGR is considered. Figures 4.11, 4.12, 4.13, 4.14 and 4.15 show instead the modeled polar wander over the complete ice-age cycles period in Fig. 4.2, with the ice load of this figure as input, in the absence of any internal stabilizing mass distribution, considered later in this chapter. In Figs. 4.11, 4.12, 4.13, 4.14 and 4.15 the minus sign of the TPW displacement means that the rotation pole moves towards Russia, opposite to the present-day one shown in Fig. 4.1.

As shown by Eq. (3.84), the displacement of the axis of rotation during the active phase of loading depends not only on the viscous relaxation terms with the poles in $s = a_i$, but also on the pole in $s = 0$, which provides the secular term.

To gain insight into the physics of the Earth's rotation during the active phase of loading, we start in Fig. 4.11 with a simple but tutorial Earth's model, not containing the 670 km discontinuity, characterized by a uniform mantle density ($\rho = 4314$ kg/m^3) and viscosity ($\nu_1 = 10^{21}$ Pa s). The solid curve accounts for both the $s = 0$ and $s = a_i$ poles, while the dashed one does not contain the contribution from $s = 0$, namely $A_0^* = 0$. The solid curve shows that the axis of rotation oscillates in phase with the glacial cycles around a mean position that increases in time in a linear fashion.

Immediately after the ice begins to grow 806,000 years before the present, the direction of polar wander is toward Russia. This is understandable, as the ice load that has most effect on the rotation axis is the one over Canada, the Laurentide. When this ice sheet begins to form, there will be an excess mass over Canada. A deformable rotating body will react to an excess mass through centrifugal force by moving its rotation axis in such a way that the excess mass will be as far away from the rotation axis as possible. Thus the rotation axis moves in the direction opposite to where the surface load is until the maximum of the ice load has been reached. When the ice starts to melt, this mechanism is reversed, and the axis of rotation turns back towards Canada, giving rise to the 'saw-teeth' pattern characterizing the displacement plotted in the figures of this chapter. The direction of polar wander during ice melt is thus at 180° opposite to the direction during ice growth, that is, during periods of ice melt the rotation axis moves in the direction of Canada (as it is doing at present). The long-term TPW direction is, according to Figs. 4.11, 4.12, 4.13, 4.14 and 4.15, in the same direction as it is during periods of ice growth, so in the direction of Russia.

The $s = 0$ pole is clearly the major contributor to the net shift of the axis of rotation after the end of the last deglaciation, as indicated by the constant horizontal line. This is confirmed by the dashed curve at the bottom of this figure, which corresponds to contributions arising solely from the $s = a_i$ poles. These poles do not contribute to the net shift of the axis of rotation during the continuous occurrence of ice ages. The net shift of the axis of rotation is due to the $s = 0$ pole. Furthermore, the velocity of polar wander averaged over the complete period of ice loading can be very high, about 1 deg/Myr, at least for a mantle viscosity of 10^{21} Pa s (Sabadini et al. 1982b, 1983; Sabadini and Vermeersen 1997).

If the viscosity is increased, the velocity of polar wander is reduced accordingly. Indeed, the $s = 0$ pole contributes a large net shift of the axis of rotation only if the mantle viscosity is about 10^{21} Pa s. The relaxation terms associated with the $s = a_i$ poles do not play any role in the net shift, according to the decaying a_i exponentials of Eq. (3.84). If the mantle is not stratified in density, and the viscosity is low, large excursions of the rotation pole can be obtained, in the absence of stabilizing internal density anomalies due to long term mantle convection.

The physics underlying the $s = 0$ pole is evident in Eq. (3.87) where the loading part yields $(1 + k_f^L)$. The latter quantifies the amount of isostatic disequilibrium after complete relaxation has taken place. The $(1 + k_f^L)$ factor depends on the elastic properties of the lithosphere, and would be zero if the lithosphere is absent. The term $A_0^* = A_0(1 + k_f^L)$ shows that the contribution arising from the $s = 0$ pole depends linearly on the load, which is not isostatically compensated. The contribution from the $s = 0$ pole after the end of the last ice age is identical to that produced by a constant load that stands on the Earth's surface for a span of time corresponding to the eight cycles, with an ice mass which is one-half of the ice mass at the ice maximum, as indicated by the $1/2$ factor multiplying the term A_0^* in Eq. (4.2).

Figure 4.12 deals with the 5-layer, volume-averaged model in Table 4.2, characterized by a chemical density contrast at 420 and 670 km. In comparison with Fig. 4.11, the effect of density stratification is a reduction of the net shift of the rotation axis after the eight glacial cycles and the appearance of an exponential behavior in the mean rotational response of the Earth, as already shown by Sabadini and Vermeersen (1997). The most interesting result in Fig. 4.12, in comparison to Fig. 4.11, involves the substantial reduction of the contribution from the $s = 0$ pole on the net shift of the pole. Comparison between the dashed and solid curves, corresponding to the cases in which the $s = 0$ pole is included (dashed) or not included (solid), shows that, in contrast with the previous case of a uniform mantle, the slow $s = a_i$ poles play a major role on the long term displacement of the rotation axis. The density stratification of the mantle is responsible for a stabilization of the Earth's rotational state; in particular its rotation behavior is controlled by the density contrasts occurring in the transition zone. Density stratification in the transition zone introduces in fact the long rotational relaxation modes, as shown in Table 3.4, second column.

This decrease in the contribution from the $s = 0$ pole is accompanied by an increase in the contribution from the a_i modes, corresponding to the slowest relaxation rotational modes (which are associated with the density contrasts of the

transition zone). This slowest relaxation is responsible for the exponential decay of the displacement of the axis of rotation at the end of the glaciation-deglaciation phases and of the smoothing of the displacement pattern during the interglacial periods with respect to Fig. 4.11. It is clear that the appearance of the slow relaxation rotational modes in the 5-layer model is responsible for the increase in the strength γ_i/a_i relative to the A_0^* contribution, which causes a substantial modification of the pattern of the polar wander curves, from a linear and sharp growth to smooth exponential relaxations compared to Fig. 4.11. The net long-lasting shift remaining up to 3×10^3 kyr is due to the fact that after an ice cycle has been completed the Earth is still out of isostatic equilibrium. The relaxation times of some of the modes by which the Earth relaxes to the changed surface mass distribution are in fact longer than the periods of the ice cycles. Comparison between Figs. 4.11 and 4.12 indicates that, since the Earth is chemically stratified, the realistic pattern of polar wander is that portrayed by the 5-layer model, where the dominant role is played by the $s = a_i$ poles. This has important implications for the net shift of the axis of rotation that the Earth can gain during a finite series of ice ages. The shift that is acquired permanently is that associated with the $s = 0$ pole, while that due to relaxation is recovered after the series of cycles once a sufficiently long span of time has elapsed. This span of time is controlled by the slowest rotational mode, as shown by the part of the curve in Fig. 4.12 after the end of active glaciation phases. After the last glacial event the axis of rotation comes back to a position close to the initial one before the beginning of the first cycle, with an offset due to the net shift gained by the pole in $s = 0$. These results elucidate the major impact of density stratification on the asymptotic behavior of the rotation equations, with a reduction of a factor 14 from the 0.7° net shift of the 3-layer model to 0.05° of the 5-layer one after complete relaxation, which takes several million years.

The cases of Earth's models with the top 120 km characterized by both an elastic and a viscoelastic rheology are portrayed, solid and dashed curves, in Fig. 4.13 where the span of time after the end of the last deglaciation is 100 kyr, to enlarge the horizontal scale so that to make evident the displacement pattern during the glaciation and deglaciation phases.

The viscosity of the mantle (and lithosphere in the case of the viscoelastic top layer) is 10^{21} Pa s. The number of layers in the Earth's model is five (volume-averaged parameters for homogeneous lithosphere, shallow upper mantle, transition zone, lower mantle and core, Table 4.2). Figure 4.13 shows several interesting aspects. It is clear that the question whether the lithosphere is purely elastic or whether it has a finite viscosity is an important one: the long-term trend differs by about a factor of two. Another point that immediately strikes the eyes is that there is a short-term trend (the 'saw-tooth' profiles on time scales of about 100,000 years) and a long-term trend. The long-term trend is not zero, the average position of the rotation axis gradually shifting further away from its initial position 806,000 years ago as time proceeds up to the present. One might perhaps think that this is due to the waxing phases of the ice cycles being longer than the waning phases.

Figure 4.14 shows that this is not the case. In Fig. 4.14 the time of a phase of ice growth has been taken as being equal to the time of a phase of ice decay: both have a

period of 50,000 years. A comparison of Fig. 4.13 with Fig. 4.14 (when the case of the elastic lithosphere is considered) shows that the average polar wander (the long-term trend) is the same; only the short-term trend shows differences in the sense that the 'saw-teeth' of the corresponding curve in Fig. 4.13 have been smoothed. The reason why there is a net, almost linearly increasing, long-term TPW trend is that after an ice cycle has been completed the Earth is still out of isostatic equilibrium, as for the explanation above for Fig. 4.12. The relaxation times of some of the modes by which the Earth relaxes to the changed surface mass distribution are even longer than the periods of the ice cycles. Thus it also becomes understandable why in the case of an elastic lithosphere in Fig. 4.13 the displacement of the polar axis is greater than in the case of a viscoelastic lithosphere: an elastic lithosphere prohibits complete relaxation even on long time scales, whereas a viscoelastic lithosphere will relax completely within a finite time.

Except for the simplistic model of Fig. 4.11, Figs. 4.12, 4.13 and 4.14 portray smooth reversals from ice growing to ice melt and in particular in Fig. 4.14, with the equal waxing and waning periods, the relaxation of the solid Earth is such that the sharp teeth are replaced by smooth curves.

Whether polar wander is mainly caused by ice age cycles, by mantle convection or tectonics is thus an important question: if the present-day (secular) polar wander has to be considered, then the direction of polar wander induced by the Pleistocene ice age cycles is towards Canada; if the polar wander path over the whole Pleistocene has to be considered, then the direction is towards Russia. Note that the magnitudes of the long-term trend are an order of magnitude smaller than the magnitudes during an ice cycle. This implies that if both mantle convection and ice mass variations were to have a comparable influence on driving polar wander during ice ages on a time scale of one million years, on time scales of 10,000–100,000 years ice mass variations would have a far greater influence than mantle convection. The question of whether mantle convection, or ice age cycles, is the main driver of polar wander during recent times is as old as the first observations of the secular drift of the rotation axis. Apart from the direction discussed above, the figures of this Section might offer another observable that could distinguish between ice or mantle convection being responsible for TPW. If polar wander were triggered by subduction of ocean lithosphere, the polar wander trend would be a smooth one over millions of years (e.g., Spada et al. 1992a), without the 'saw-teeth' on a 100,000 year time scale that are triggered by ice ages. Might such saw-teeth be discerned from paleomagnetic data? Although it would be an extremely important observation, chances that we might ever detect them are very slim. If we consider the error bars in the TPW data of Besse and Courtillot (1991) and compare them with the 0.1° accuracy in Fig. 4.12 that is needed to discern the to-and-fro movements of the rotation axis, then we learn that there is a discrepancy in accuracy of one to two orders of magnitudes. A lowering of the standard deviations by one to two orders of magnitude seems to be virtually impossible. A polar wander of 0.1° might even be below the threshold of intrinsic errors of paleomagnetic field measurements (C. Duermeijer, personal communication), so it is very unlikely that such small magnitudes might ever be discernible from paleomagnetic observations. One last aspect worth mentioning concerns the behavior of polar wander in the future.

It is clear that if a new ice age period were to begin, that is, if a 'new Laurentide ice sheet' were to form over Canada, then the long-term trend before the present would resume after time = 0 in Fig. 4.13. However, if there were not to be another ice age period, then the polar wander would be as depicted in Fig. 4.13 for times after time = 0. The movement of the rotation axis would be such that it would relax towards the original position it had left 806,000 years before the present (R. Gordon, personal communication). Although it is not visible in the figure, there still would be a difference between the two cases depicted in Fig. 4.13 after a long time had elapsed: the rotation axis would go on moving in the direction it is moving at present, that is, it would move on until the negative gravity anomaly created by the vanished ice sheet over Canada were on the North Pole.

Here we see how important the question of the rheology of the lithosphere is for the movement of the rotation axis. The curves in Figs. 4.13 and 4.14 are based on a 5-layer model and a mantle with a uniform viscosity of 10^{21} Pa s. In the previous Sect. 4.4 we saw that the viscosity of the upper mantle is more likely to be lower than this value, and the viscosity of the lower mantle higher. The effects of both layering and viscosity can be seen in Fig. 4.15.

Here we have used the 31-layer Earth's model in Table 4.3. The lithosphere is elastic. The solid curve depicts the case of a uniform viscosity of 10^{21} Pa s again. Although at first sight the differences with the corresponding curve in Fig. 4.13, produced with a 5-layer Earth's model, might not seem to be dramatic, the long-term TPW rate does differ considerably between the two uniform 10^{21} Pa s cases upon closer inspection (to see this the reader might put a ruler in such a way as to connect the peaks in each of the curves). More eye-striking in Fig. 4.15 is the huge reduction of polar wander for the case of a lower mantle viscosity of 10^{22} Pa s.

4.6 Ice Age True Polar Wander in a Compressible and Non-hydrostatic Earth

This Sect. 4.6 is based on the Earth's models of Sects. 3.7 and 3.8, in which the material parameters vary continuously in terms of the Earth's distance r from the centre. Once the Green functions $k_f^T - k_2^T(t)$ and $1 + k_2^L(t)$ are introduced into the linearized rotation equations, the pole displacement $m(t)$, Eqs. (3.65) and (3.66), can be computed. For the ice loading, we consider only the last ice age, characterized by linear glaciation and deglaciation phases of 90 and 10 kyr and the same maximum ice sheet inertia perturbations as in Mitrovica et al. (2005), $\Delta I_{13}^{ice} = -6.67 \times 10^{31}$ kg m^2 and $\Delta I_{23}^{ice} = 2.31 \times 10^{32}$ kg m^2, where the self-explanatory superscript ice rather than the L of Eq. (3.83) is used. In this Sect. 4.6, TPW displacement is positive towards Russia, opposite to the sign convention of the previous TPW figures of this chapter.

Figures 4.16 and 4.17 compare the TWP displacements $m(t)$ for compressible (solid line) and incompressible (dashed line) models with the elastic and the

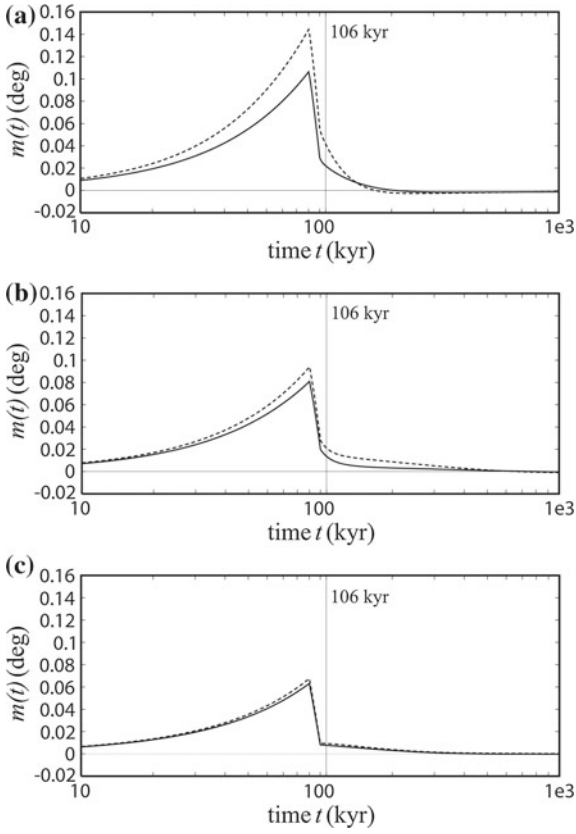

Fig. 4.17 The TPW displacement $m(t)$ due only to the last ice age for the compressible (*solid*) and incompressible (*dashed*) PREM with the viscoelastic lithosphere, $\nu_L = 10^{26}$ Pa s. The lower mantle viscosity is $\nu_{LM} = 10^{21}$ (**a**), $\nu_{LM} = 10^{22}$ (**b**) and $\nu_{LM} = 10^{23}$ (**c**) Pa s. The small negative values of $m(t)$ indicate that the rotation pole has crossed its initial position

viscoelastic lithospheres, both without considering any non hydrostatic contribution from mantle convection that will be discussed later. TPW displacements are herein computed for increasing lower mantle viscosities ν_{LM}, from 10^{21} (panel a) to 10^{23} Pa s (panel c), both in Figs. 4.16 and 4.17.

The shape of TPW displacement curves is characterized by an increasing displacement during the glaciation phase, from 10 to 90 kyr, away from Hudson bay followed by a still ongoing displacement towards Hudson Bay. Starting from the elastic lithosphere results, Fig. 4.16, the TPW displacements for the compressible models are always smaller than those for the incompressible ones, except when $\nu_{LM} = 10^{21}$ Pa s (panel a) in the time interval 120–200 kyr. This finding is in agreement with the Green functions of Fig. 3.3, illustrating that the incompressible lithosphere does not readjust to centrifugal forces and loads as fast as the more deformable compressible one, and thus the ice age loading drives more efficiently the polar wander for incompressible models.

As already observed from the Green functions, an increase of the lower mantle viscosity ν_{LM} reduces the differences between the compressible and incompressible

models, as clearly shown in Fig. 4.16c. The TPW displacements are always positive, meaning that the rotation pole never crosses the initial north pole while it moves back towards Hudson bay. Indeed the displacements $m(t)$ at $t = 1$ Myr differ significantly from the initial north pole position at zero, particularly for lower mantle viscosities 10^{21} and 10^{22} Pa s, Fig. 4.16a, b, and for the incompressible models. This shows that each glaciation cycle moves the pole by a finite amount away from Hudson bay not only for the layered incompressible models of Figs. 4.11, 4.12, 4.13 and 4.15 as the secular term of Eq. (3.87) implies within the frame of normal mode expansion, but also for continuous, compressible or incompressible models based on contour integration in the complex plane: this finite amount is on the other hand smaller for continuously stratified models, due to the overestimated density contrast between the lithosphere and the outer atmosphere within the frame of 5-layer models.

The models with the viscoelastic lithosphere are depicted in Fig. 4.17. The TPW displacements resemble those shown in Fig. 4.16 for the case of the elastic lithosphere, although with some reduction in amplitudes. This behavior is more effective for the lower mantle viscosity $\nu_{LM} = 10^{21}$ Pa s, characterized by almost a factor of 2 reduction (compare panels (a) of Figs. 4.16 and 4.17). This indicates that the difference between the viscoelastic lithosphere and the elastic one is the largest for a soft lower mantle. Differently from Fig. 4.16, now the rotation pole crosses the initial north pole at about 200 kyr, Fig. 4.17a, and at 700 kyr, Fig. 4.17b, both for compressible and incompressible models, while for the lower mantle with high viscosity, Fig. 4.17c, the crossing occurs at 500 kyr only for the compressible model. Thus the TPW displacement of models with a viscoelastic lithosphere does not end up with any finite displacement away from Hudson bay (Mitrovica et al. 2005). This drastic reduction of the TPW displacement is due to the increased delay in the readjustment of the hydrostatic equatorial bulge due to the high viscous viscoelastic rheology of the lithosphere which stabilizes rotationally the planet or, we can say, over-stabilizes the latter.

The drastic reduction of the TPW displacement when the viscosity of the viscoelastic lithosphere is reduced to that of the upper mantle, $\nu_L = 10^{21}$ Pa s, compared to the elastic case, has been shown first in Vermeersen and Sabadini (1999), their Fig. 8, for the full series of ice age cycles. Two effects are involved: first, the easier relaxation of the lithospheric stresses accumulated during the polar excursion allows the equatorial bulge to readjust faster, as shown by Fig. 3.7, and, second, the full isostatic compensation of the load over the whole ice cycles reduces the perturbation of the inertia tensor due to the ice age loading. The isostatic compensation is the most effective in stabilizing the Earth's rotation, as indicated by the reduction of the TPW displacement. The importance of the full isostatic compensation in TPW predictions can be understood by considering that the viscoelastic lithosphere nullifies the secular term responsible of a net shift of the rotation axis away from Hudson bay after the end of each ice age cycle. Indeed, the load fluid Love number being $k_f^L = 1$ for the viscoelastic lithosphere, the factor s can be simplified from the numerator and the denominator of Eq. (3.114), within the frame of normal mode analysis.

Although carried out with different values for the lithospheric viscosity ν_L, the viscoelastic TPW calculation of Vermeersen and Sabadini (1999), Nakada (2002) and

Mitrovica et al. (2005) and those given in Fig. 4.17 behave as expected on the basis of the underlying physical hypotheses and are completely coherent among themselves and the importance of the viscoelastic rheology for the lithosphere, responsible for the delay of the readjustment of the hydrostatic equatorial bulge due to the high lithospheric viscosity ν_L, is well explained within the frame of the "traditional approach", independently from any stabilizing effect of internal mass anomalies.

Another interesting observation can be drawn by comparing Fig. 4.4, based on our work of the nineties, with our latest Figs. 4.16 and 4.17. For the lower mantle viscosity of $\nu_{LM} = 10^{21}$ Pa s, the incompressible models, layered as in Fig. 4.4 or continuous as in Figs. 4.16 and 4.17, double the TPW rate of the incompressible model based on fixed density contrasts (Fig. 4.4, dashed curve) or that of the continuous compressible models (Figs. 4.16 and 4.17, solid curves), the latter carrying the same non adiabatic density contrasts as the former incompressible fixed density contrast model: we can deduce this result from the tangent to the displacement curves in Figs. 4.16 and 4.17. The TPW rates of the fixed density contrast incompressible model and those of the continuous compressible models are around the same, which leads us to conclude that a) continuous or layered density profiles are equivalent, b) incompressible models mimic the behavior of realistic compressible models once only the major non adiabatic density discontinuities are taken in account and c) density increase for incompressible models is non adiabatic away from these density discontinuities, as we can more rigorously argue on the basis of Sect. 1.2.2. Equation (1.42) shows in fact that when the bulk modulus k goes to infinity, γ is necessarily different from zero to sustain a density stratification, which is in this case non adiabatic. These findings show that non adiabaticity makes the Earth rotationally unstable in the lower mantle viscosity range $\nu_{LM} = 10^{21} - 10^{22}$ Pa s.

4.6.1 The Role of Mantle Heterogeneities

In order to estimate the correction β, Eq. (3.107), Mitrovica et al. (2005) consider the difference between the observed fluid Love number $k^T_{f,obs}$ and the tidal fluid limit $k^T_{f,\mathrm{II}}$ coming from the second-order theory of the hydrostatic equilibrium figure of the rotating Earth (Nakiboglu 1982). These authors found that $\beta = k^T_{f,obs} - k^T_{f,\mathrm{II}} = 0.008$: this difference represents the non-hydrostatic contribution due to the lateral density variations and dynamic topography sustained by convection.

Nakiboglu's hydrostatic flattening is close to the values given by other authors (Denis 1989; Alessandrini 1989). However as the β parameter is the small difference between two large numbers (observed fluid Love number and tidal fluid limit), the β deduced from these different authors only agree within 10 %; notice that all these papers are based on PREM (Dziewonski and Anderson 1981) which was in agreement with an Earth's mass and inertia that have been sligthly reevaluated since then. The hydrostatic flattening according to Clairaut's first order theory is essentially controlled by I/Ma^2 (Radau's result, where I, M and a are the Earth's, inertia, mass and radius), a parameter equal to 0.3308 in PREM while the most recent estimate is

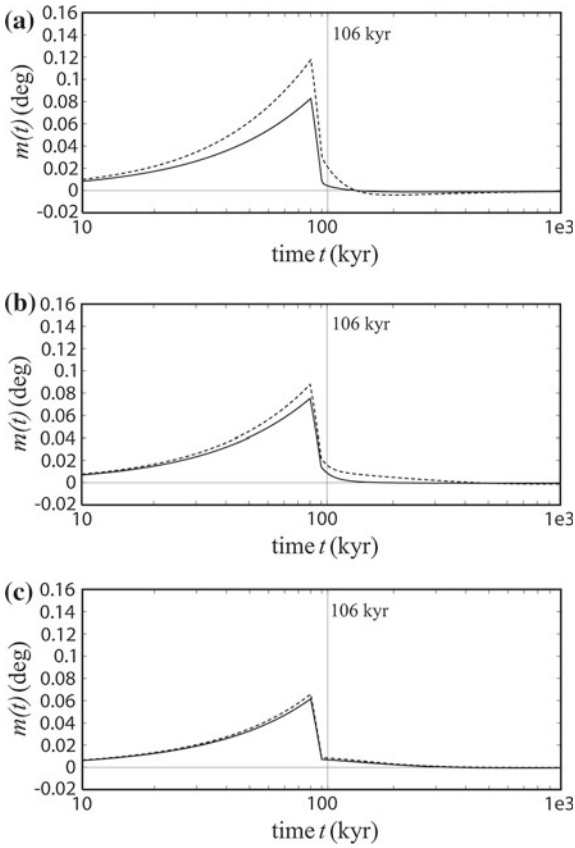

Fig. 4.18 The TPW displacement $m(t)$ due to the last ice age only of the compressible (*solid*) and incompressible (*dashed*) PREM with the viscoelastic lithosphere, $\nu_L = 10^{26}$ Pa s, and the non-hydrostatic correction $\beta = 0.008$. The lower mantle viscosity is $\nu_{LM} = 10^{21}$ Pa s (**a**), $\nu_{LM} = 10^{22}$ Pa s (**b**) and $\nu_{LM} = 10^{23}$ Pa s (**c**). The negative values of $m(t)$ indicate that the rotation pole has already crossed its initial position

0.33069 (Chambat and Valette 2001). This reevaluation should reduce the predicted hydrostatic flattening and, by consequence, increase β. Clearly a more rigorous estimate of the hydrostatic flattening is needed but is beyond the goal of this book (see Chambat et al. 2010). It seems qualitatively that the β parameter chosen by Mitrovica et al. (2005) might be a conservative value that could be increased up to $\beta = 0.01$. Mitrovica et al. (2005) were aware of the possible uncertainity on the β parameter and indeed they consider the reasonable range $0.006 < \beta < 0.01$ in their Fig. 10.

We now quantify the effects of the slow mantle convection for models with a highly viscous viscoelastic lithosphere, $\nu_L = 10^{26}$ Pa s, by making use of the same β correction as in Mitrovica et al. (2005), namely $\beta = 0.008$ in Eq. (3.106). Figure 4.18 shows the effects of this non hydrostatic contribution to the equatorial bulge, to be compared with Fig. 4.17. For the soft lower mantle $\nu_{LM} = 10^{21}$ Pa s (panels a of Figs. 4.17 and 4.18), the minor differences during the active loading glaciation-deglaciation phase, from 10 to 100 kyr, are accompanied by large deviations at the end of the unloading. At 100 kyr, the displacement is reduced by a factor of 3 with respect to the compressible model and almost by a factor of 2 with respect to the incompressible one. For

the higher lower mantle viscosities $\nu_{LM} = 10^{22}$ Pa s (panels b) and $\nu_{LM} = 10^{23}$ Pa s (panels c), the effects of the non hydrostatic contribution are not as important. The TPW displacement for $\nu_{LM} = 10^{21}$ Pa s is severely affected by the non hydrostatic contribution and both compressible and incompressible models predict a change of sign in the displacement $m(t)$ at about 15 kyr after the end of deglaciation, Fig. 4.18a, with the axis of rotation being displaced toward the deglaciated region with respect to the initial north pole. The crossing of the initial north pole occurs earlier in time also for the higher viscosity cases, Fig. 4.18b, c, but not as dramatically as for the models with the soft lower mantle of $\nu_{LM} = 10^{21}$ Pa s.

This crossing of the initial north pole occurs both for the high viscosity lithosphere and in the presence of a non hydrostatic correction β. It is a completely different process than that due to the coupling in the linearized rotation equations of the direction cosines $m_1(t)$ and $m_2(t)$ involved by the first term of the right side of Eqs. (3.65) and (3.108), neglected in the present work following Mitrovica and Milne (1998). This coupling explains the 14 month Chandler wobble and a small amplitude wobble with a period much larger than the 1 Myr considered in Figs. 4.17 and 4.18.

We now investigate the sensitivity of the present-day TPW predictions to the rheology of the lithosphere and to the β correction. Figure 4.19 shows the present-day TPW rate, namely the time derivative of the displacements of Figs. 4.16, 4.17 and 4.18 evaluated at 6 kyr after the end of unloading, as a function of the lower mantle

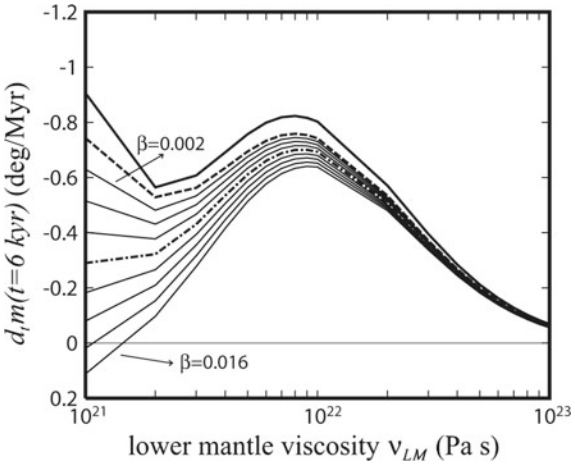

Fig. 4.19 The present-day TPW rate, here denoted by $d_t m(t)$, with β correction due to a single ice age, evaluated at 6 kyr after the end of the deglaciation, as function of the lower mantle viscosity ν_{LM}, for PREM with the elastic lithosphere (*thick solid line*), the high viscosity viscoelastic lithosphere, (*dashed line*), $\nu_L = 10^{26}$ Pa s, and with the non-hydrostatic contribution $\beta = 0.008$ (*dash-dotted line*). The *thin solid lines* refer to the PREM with the hard viscoelastic lithosphere and the non hydrostatic correction β varying from 0.002 to 0.016 by steps of 0.002, from *top* to *bottom*. The sign of $d_t m(t)$ indicates whether the rotation pole moves forward to, negative, or go away from, positive, the Hudson Bay

viscosity ν_{LM}. We use the compressible model with a viscoelastic lithosphere (dashed line) and we vary the β correction (thin solid lines) by steps of 0.002 from 0.002 to 0.016, around the value of 0.008 (dash-dotted line) used in Mitrovica et al. (2005). The case with an elastic lithosphere is indicated by the thick solid line. In this figure, only one ice cycle is considered. The largest sensitivity of TPW rates to lithospheric rheology and β correction occurs for lower mantle viscosities ν_{LM} smaller than 10^{22} Pa s. At $\nu_{LM} = 10^{21}$ Pa s the predicted rates vary from -0.91 deg/Myr, for the model with the elastic lithosphere (thick solid line), to -0.29 deg/Myr, for the model with the viscoelastic lithosphere and the correction $\beta = 0.008$ (dash-dotted line). As first shown by Mitrovica et al. (2005), the effects of the non hydrostatic bulge is to dampen TPW rates when the lower mantle viscosity ν_{LM} is in the range 10^{21}–10^{22} Pa s. For very large β corrections, 0.014 and 0.016, the damping effect of the non hydrostatic bulge is made evident by the change of sign of the TPW rate, indicating that the rotation pole crosses its initial position and is going now away from Hudson bay once again. The non hydrostatic contribution from convection is so effective in fixing the rotation axis that the pole of rotation comes back to its initial position without any finite displacement of the pole or even over-shooting the initial north pole.

A better comparison with Mitrovica et al. (2005) results, and a more realistic estimate of present-day TPW rates, is obtained by considering the full series of eight ice age cycles, as shown in Fig. 4.20. For the elastic lithosphere case and when $\nu_{LM} = 10^{21}$ Pa s, adding the seven previous ice age cycles to the single one of Fig. 4.19, increases the TPW rates by a factor of 2, while for ν_{LM} greater than 10^{22} Pa s the increase is only of 10 % or less. On the contrary, for the model with the viscoelastic lithosphere, both with or without the non hydrostatic contribution, the previous seven ice ages have a negligible effect, the differences being lesser than 5 % for the whole range of lower mantle viscosity. This shows that the TPW rate remains mostly sensitive to only the last ice age.

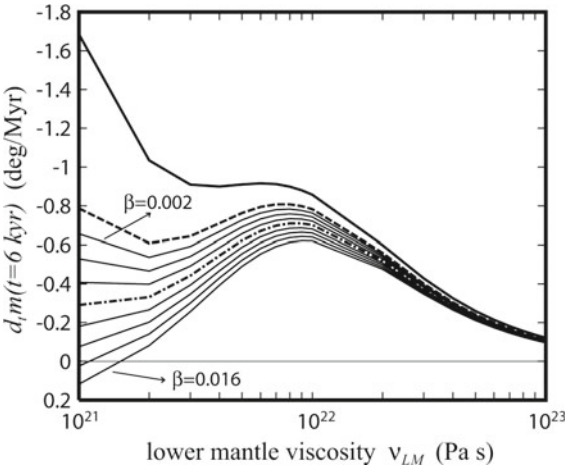

Fig. 4.20 The same as Fig. 4.19, but for the full series of eight ice ages

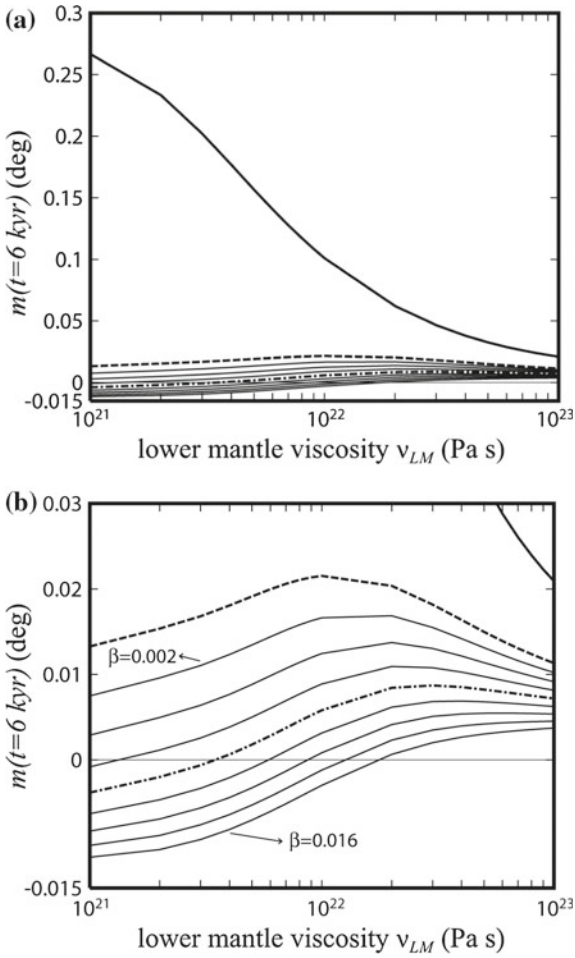

Fig. 4.21 The present TPW displacement $m(t)$ due to the full series of eight ice ages, evaluated at 6 kyr after the end of the deglaciation, as function of the lower mantle viscosity ν_{LM}, for PREM with the elastic lithosphere (*thick solid line*), the high viscosity viscoelastic lithosphere, (*dashed line*), $\nu_L = 10^{26}$ Pa s, and with the non hydrostatic correction $\beta = 0.008$ (*dashed-dot line*). The *thin lines* refer to PREM with the viscoelastic lithosphere and the non hydrostatic correction β varying from 0.002 to 0.016 by steps of 0.002, from *top* to *bottom*. The negative values of $m(t)$ indicates that the rotation pole has already crossed its initial position. The panel (**b**) shows the enlargement of the panel (**a**) in the range of -0.015 to 0.03°

TPW predictions are sensitive to the previous seven ice ages mainly for lower mantle viscosity in the range $10^{21} - 10^{22}$ Pa s as it results from the comparison of Figs. 4.19 and 4.20 for the model with the elastic lithosphere (thick solid lines). Without a high viscosity viscoelastic lithosphere or without a non hydrostatic contribution from mantle convection, the only stabilizing effect is the delay in the readjustment of the hydrostatic equatorial bulge to the axis of instantaneous rotation controlled by the lower mantle viscosity ν_{LM}, which becomes smaller and smaller decreasing ν_{LM} so making TPW sensitive to the previous ice cycles.

The damping effect due to the high viscosity of the lithosphere and to the non hydrostatic contribution is more evident in the displacement of the rotation axis than in the TPW rate, as we show in Fig. 4.21. After the eight ice age cycles, in the case of the elastic lithosphere (thick solid line), the axis of rotation is displaced from its

initial position by 0.27°, at $\nu_{LM} = 10^{21}$ Pa s, and this value diminishes gradually with the lower mantle viscosity to about 0.02 deg/Myr at $\nu_{LM} = 10^{23}$ Pa s. The rheology change from elastic (thick solid line) to viscoelastic (dashed line) lithosphere causes reductions in the TPW displacements by factors ranging from 20, at $\nu_{LM} = 10^{21}$ Pa s, to 2, at $\nu_{LM} = 10^{23}$ Pa s. The value obtained for our compressible model with the elastic lithosphere and the low lower mantle viscosity of $\nu_{LM} = 10^{21}$ Pa s is very similar to what is obtained in Vermeersen and Sabadini (1999) for a simpler 5-incompressible model. The TPW displacements are subjected to further reductions when a β correction is added. Particularly, for $\beta = 0.008$ (dash-dotted line), the rotation pole crosses the initial north position. Generally, as shown in Fig. 4.21b, the TPW displacements for the viscoelastic lithosphere range in a narrow interval of $-0.011°$ to $0.022°$ for any values of the lower mantle viscosity ν_{LM}, even without the β correction.

The present-day TPW rates obtained by using the correction $\beta = 0.008$ reaches at most -0.71 deg/Myr for a lower mantle viscosity $\nu_{LM} = 8 \times 10^{21}$ Pa s. This is -0.29 deg/Myr lower than the observed rate of -1 deg/Myr. Our findings fully support the results obtained by Mitrovica et al. (2005) and, having been obtained on the basis of compressible Earth's models which take into account continuous variations of the material parameters, and thus relying on the contour integration rather than on normal mode summation, they provide an independent confirmation. Even if we consider models with elastic lithosphere we obtain the same TPW predictions once the tidal fluid limit $k^T_{f,E} = 0.920$ from modeling is replaced by the estimate $k^T_{f,obs} = 0.942$ of Mitrovica et al. (2005), their Eq. (16). Indeed the stabilizing effect of the larger non hydrostatic bulge for models with elastic lithosphere, $\beta = k^T_{F,obs} - K^T_{F,E} = 0.022$, would be quantitatively the same of the two stabilizing effect acting in the case of models with the highly viscous viscoelastic lithosphere: the delayed readjustment of the equatorial bulge together with the smaller non hydrostatic bulge, $\beta = k^T_{f,obs} - k^T_{f,V} = 0.008$. This means that TPW studies cannot discriminate between the effects of the lithospheric rheology and of the lateral density variations and dynamic topography sustained by convection. In any case, the parameter β has to be consistent with mantle convection models.

TPW predictions using the traditional approach where the equilibrium flattening is self consistently computed (Sabadini and Peltier 1981; Sabadini et al. 1982a; Wu and Peltier 1984) and the scheme proposed by Mitrovica et al. (2005) where the observed tidal fluid number is considered differ in the lower mantle viscosity range $\nu_{LM} = 10^{21} - 10^{22}$ Pa s. The motion of the rotation axis, given by the linearized Liouville equation (3.65), depends on the load-induced perturbation, $1 + \tilde{k}^L_2(s)$, and on the readjustment of the equatorial bulge, $k^T_F - \tilde{k}^T_2(s)$. Over the time of ice age, the load, $\tilde{k}^L_2(s)$, and tidal, $\tilde{k}^T_2(s)$, Love numbers, computed for models with an elastic and high viscous viscoelastic lithosphere are the same. Nevertheless, the traditional approach leads to different TPW predictions due to the fact that the high viscous viscoelastic lithosphere implies an extra delay of the readjustment of the equatorial bulge, compared to the elastic lithosphere. The elastic and viscoelastic lithospheres are indeed associated with different stress patterns. Frozen stresses are present in the

elastic lithosphere before and after the glaciation, while the viscoelastic lithosphere is initially stress free and it builds up stress that cannot relax during the polar motion for high lithospheric viscosities.

In order to take into account the difference between observed and modelled tidal fluid numbers, Mitrovica et al. (2005) introduce the β-correction, Eq. (3.107). This scheme represents a first attempt to couple mantle convection with ice age TPW within a linear rotation theory. As first enlightened by Mitrovica et al. (2005), this ice age-convection coupling dampens present-day ice age TPW rates since the non hydrostatic extra bulge, frozen within the planet, stabilizes the planet by slowing down the displacement of the axis of rotation away from this fixed orientation so effectively that the rotation pole goes back to its initial position at large time.

With the extra degree of freedom given by the parameter β, models with elastic and highly viscous elastic lithosphere lead to the same ice age TPW prediction. It is therefore difficult to choose the most appropriate lithospheric rheology when the distinction is made between the actual shape of the Earth and its equilibrium shape. We agree however with Mitrovica et al. (2005) that using a viscoelastic lithosphere in the framework of the traditional theory seems reasonable because it is simpler (but not necessary true) to start from a relaxed lithospheric stress and because the tidal fluid limit from the viscoelastic modelling is closer to observation and thus a smaller mantle contribution β needs to be introduced.

The present-day value of β, related to the excess flattening due to mantle convection, cannot be best evaluated than by subtracting the computed hydrostatic tidal fluid limit to the observed fluid Love number, Eq. (3.107). On geological time scale, as the Earth is constantly reorienting to maximize its equatorial inertia, i.e., to be more flattened than the hydrostatic estimate, β should always remain positive except maybe during exceptional inertial interchange polar excursion (Richards et al. 1999). The value of the non hydrostatic contribution β due to convection can be estimated by means of convection models or, for the last hundred million years, from paleo-reconstruction of plate tectonics (Ricard et al. 1993b). The difference between the time dependent inertia terms remains of the same order than Mitrovica et al. (2005) estimate of 0.008 within a factor 2. This means that the Earth's rotation axis is always very stable with respect to short term forcings like glaciations: as soon as the forcing vanishes, the mantle anomalies force the rotation axis to come back to its initial position. Mantle convection, can drive large TPW displacements (Spada et al. 1992b).

Once the Mitrovica et al. (2005) estimate of the correction $\beta = 0.008$ is taken into account, the highest present-day TPW rate of 0.71 deg/Myr from glacial forcing is obtained for a lower mantle viscosity of 10^{22} Pa s, which means that at least 30 % of the observed value of 1 deg/Myr remains unexplained. This implies that mantle convection, or other mechanisms such as large earthquakes must contribute to polar motion to be compliant with observations. Recent mantle circulation models by Schaber et al. (2010), characterized by a large heat flux at the core-mantle boundary, require a lower mantle viscosity of 10^{23} Pa s to stabilize the planet rotation, leading to TPW rates of about 0.5 deg/Myr in rough agreement with the direction towards Newfoundland in the last 100 Myr. The first self-consistent TPW calculations from

mantle convection have been obtained by Ricard et al. (1993) and already required a substantial increase in the lower mantle viscosity, 10^{22} Pa s at least, to rotationally stabilize the planet. The ice age TPW in addition to the TPW driven by mantle convection and earthquakes are thus needed to fulfill observations, requiring lower mantle viscosity ranging from 10^{22} to 10^{23} Pa s. If this is the case, the β-correction proposed by Mitrovica et al. (2005) would only impact marginally the estimate of ice age TPW rates, as it would be the high viscosity of the lower mantle that would control the TPW. It is notable that an inconsistency for lower mantle viscosity predictions between glacial and convection forcing continues to exist. Indeed, for the Schaber et al. (2010) estimate of 10^{23} Pa s lower mantle viscosity, glacial forcing would provide at most TPW rates of 0.1 deg/Myr that, summed to the convection TPW rate of 0.5 deg/Myr, would not explain the observation of 1 deg/Myr. The exact balance of the TPW, between deglaciation and other forcing, is therefore not yet understood.

References

Alessandrini, B. (1989). "The hydrostatic equilibrium figure of the Earth - an interative approach". In: *Phys. Earth Planet. Inter.* 54, pp. 180–192.

Besse, J. and V. Courtillot (1991). "Revised and synthetic apparent polar wander paths of the African, Eurasian, North American, and Indian Plates, and true polar wander since 200 Ma". In: *J. Geophys. Res.* 96, pp. 4029–4050.

Cambiotti, G., X. Wang, R. Sabadini, and D.A. Yuen (2016). "Residual polar motion caused by coseismic and interseismic deformations from 1900 to present". *In: Geophys. J. Int.*

Chambat, F., Y. Ricard, and B. Valette (2010). "Flattening of the Earth: further from hydrostaticity than previously estimated". In: *Geophys. J. Int.* 183, pp. 727–732.

Chambat, F. and B. Valette (2001). "Mean radius, mass, and inertia for reference Earth models". In: *Phys. Earth Planet. Inter.* 124, pp. 237–253.

Cheng, M.K., B.D. Tapley, and J.C. Ries (2013). "Deceleration in the Earth's oblateness". In: *J. Geophys. Res.* 118, pp. 740–747.

D'Agostino, G., G. Spada, and R. Sabadini (1997). "A semi-analytical approach for a laterally varying viscoelastic mantle". In: *Geophys. J. Int.* 129, pp. F1–F5.

Denis, C. (1989). "The hydrostatic figure of the Earth, in Gravity and Low Frequency Geodynamics (chap. 3)". In: ed. by R. Teisseyre. Vol. 4. Elsevier, Amsterdam.

Devoti, R., M. Fermi, V. Luceri, P. Rutigliano, C. Sciarretta, and G. Bianco (1997). "Estimation of low degree geopotential coefficients using SLR data". In: *Ann. Geophysicae* 15(I), p. C126.

Dickman, S.R. (1977). "Secular trend of the Earth's rotation pole: Consideration of motion of the latitude observatories". In: *Geophys. J. R. Astron. Soc.* 51, pp. 229–244.

Dziewonski, A.M. and D.L. Anderson (1981). "Preliminary reference Earth model". In: *Phys. Earth Planet. Inter.* 25, pp. 297–356.

Farley, K.A. and D.B. Patterson (1995). "A 100-kyr periodicity in the flux of extraterrestrial 3He to the sea floor". In: *Nature* 378, pp. 600–603.

Forte, A.M. and J.X. Mitrovica (1996). "New inferences of mantle viscosity from joint inversion of long-wavelength mantle convection and postglacial rebound data". In: *Geophys. Res. Lett.* 23, pp. 1147–1150.

Haskell, N.A. (1935). "The motion of a fluid under a surface load". In: *Physics* 6, pp. 265–269.

Lambeck, K., P. Johnston, and M. Nakada (1990). "Holocene glacial rebound and sea-level change in NW Europe". In: *Geophys. J. Int.* 103, pp. 451–468.

Lambeck, K., P. Johnston, C. Smither, and M. Nakada (1996). "Glacial rebound of the British Isles - III, Constraints on mantle viscosity". In: *Geophys. J. Int.* 125, pp. 340–354.
McCarthy, D.D. and B.J. Luzum (1996). "Path of the mean rotational pole from 1899 to 1994". In: *Geophys. J. Int.* 25, pp. 623–629.
Milne, G.A. and J.X. Mitrovica (1996). "Post-glacial sea level change on a rotating Earth: First results from a gravitationally self-consistent sealevel equation". In: *Geophys. J. Int.* 126, pp. F13–F20.
Mitrovica, J.X. (1996). "Haskell [1935] revisited". In: *J. Geophys. Res.* 101, pp. 555–569.
Mitrovica, J.X. and A.M. Forte (1997). "Radial profile of mantle viscosity: Results from the joint inversion of convection and postglacial rebound observables". In: *J. Geophys. Res.* 102, pp. 2751–2769.
Mitrovica, J.X. and G.A. Milne (1998). "Glaciation-induced perturbations in the Earth's rotation: A new appraisal". In: *J. Geophys. Res.* 103, pp. 985–1005.
Mitrovica, J.X. and W.R. Peltier (1993). "Present-day secular variations in the zonal harmonics of the Earth's geopotential". In: *J. Geophys. Res.* 98, pp. 4509–4526.
Mitrovica, J.X., J. Wahr, I. Matsuyama, and A. Paulson (2005). "The rotational stability of an ice-age earth". In: *Geophys. J. Int.* 161, pp. 491–506.
Muller, R.A. and G.J. MacDonald (1995). "Glacial cycles and orbital inclination". In: *Nature* 377, pp. 107–108.
Nakada, M. (2002). "Polar wander caused by the Quaternary glacial cycles and fluid Love number". In: *Earth Planet. Sci. Lett.* 200, pp. 159–166.
Nakada, M. and K. Lambeck (1989). "Late Pleistocene and Holocene sealevel change in the Australian region and mantle rheology". In: *Geophys. J. Int.* 96, pp. 497–517.
Nakada, M., J. Okuno, K. Lambeck, and A. Purcell (2015). "Viscosity structure of Earth's mantle inferred from rotational variations due to GIA process and recent melting events". In: *Geophys. J. Int.* 202, pp. 976–992.
Nakiboglu, S.M. (1982). "Hydrostatic theory of the Earth and its mechanical applications". In: *Phys. Earth planet. Int.* 28, pp. 302–311.
Nakiboglu, S.M. and K. Lambeck (1980). "Deglaciation effects on the rotation of the earth". In: *Geophys. J. R. Astron. Soc.* 62, pp. 49–58.
Peltier, W.R. (1985). "The LAGEOS constraint on deep mantle viscosity: results from a new normal mode method for the inversion of viscoelastic relaxation spectra". In: *J. Geophys. Res.* 90, pp. 9411–9421.
Peltier, W.R. (2004). "Global glacial isostasy and the surface of the ice-age Earth: the ICE-5G (VM2) model and GRACE. " In: *Ann. Rev. Earth Planet. Sci.* 32, pp. 111–149.
Peltier, W.R. and X. Jiang (1996). "Glacial isostatic adjustment and Earth rotation: Refined constraints on the viscosity of the deepest mantle". In: *J. Geophys. Res.* 101, pp. 3269–3290.
Ricard, Y., M.A. Richards, C. Lithgow-Berteloni, and Y. Le Stunff (1993b). "A geodynamic model of mantle mass heterogeneities". In: *J. Geophys. Res.* 98, pp. 21895–21909.
Ricard, Y., G. Spada, and R. Sabadini (1993). "Polar wandering of a dynamic Earth". In: *Geophys. J. Int.* 113, pp. 284–298.
Richards, M.A. and B.H. Hager (1984). "Geoid anomalies in a dynamic Earth". In: *J. Geophys. Res.* 89, pp. 5987–6002.
Richards, M.A., H.-P. Bunge, Y. Ricard, and J.R. Baumgardner (1999). "Polar wandering in mantle convection models". In: *Geophys. Res. Lett*. 26, pp. 1777–1780.
Sabadini, R., A.M. Marotta, R. De Franco, and L.L.A. Vermeersen (2002). "Style of density stratification in the mantle and true polar wander induced by ice loading". In: *J. Geophys. Res.* 107, p. 2258.
Sabadini, R. and W.R. Peltier (1981). "Pleistocene deglaciation and the Earth's rotation: implications for mantle viscosity". In: *Geophys. J. R. Astron. Soc.* 66, pp. 553–578.
Sabadini, R. and L.L.A. Vermeersen (1997). "Ice-age cycles: Earth's rotation instabilities and sealevel changes". In: *Geophys. Res. Lett.* 24, pp. 3041–3044.

Sabadini, R., D.A. Yuen, and E. Boschi (1982a). "Polar wandering and the forced responses of a rotating, multilayered, viscoelastic planet". In: *J. Geophys. Res.* 87, pp. 2885–2903.

Sabadini, R., D.A. Yuen, and E. Boschi (1982b). "Interaction of cryospheric forcings with rotational dynamics has consequences for ice ages". In: *Nature* 296, pp. 338–341.

Sabadini, R., D.A. Yuen, and E. Boschi (1983). "Dynamic effects from mantle phase transitions on true polar wander during ice ages". In: *Nature* 303, pp. 694–696.

Sabadini, R., D.A. Yuen, and R. Widmer (1985). "Constraints on shortterm mantle rheology from the $\dot{J}_2$ observation and the dispersion of the 18.6 yr tidal Love number". In: *Phys. Earth Planet. Inter.* 38, pp. 235–249.

Schaber, K., H.-P. Bunge, B.S.A. Schubert, R. Malservisi, and A. Horbach (2010). "Stability of the rotation axis in high-resolution mantle circulation models: weak polar wander despite strong core heating". In: *Geochem. Geophys. Geosyst.* 10, p. Q11W04.

Shackleton, N.J. and N.D. Opdyke (1976). "Oxygen isotope and paleomagnetic stratigraphy of Pacific core V28-239 late Pliocene to latest Pleistocene". In: *Geol. Soc. Am. Mem.* 145, pp. 449–464.

Spada, G., Y. Ricard, and R. Sabadini (1992a). "Excitation of true polar wander by subduction". In: *Nature* 360, pp. 452–454.

Spada, G., R. Sabadini, D.A. Yuen, and Y. Ricard (1992b). "Effects on post-glacial rebound from the hard rheology in the transition zone". In: *Geophys. J. Int.* 109, pp. 683–700.

Stephenson, F.R. and L.V. Morrison (1995). "Long-term fluctuations in the Earth's rotation - 700-BC to AD-1990". In: *Phil. Trans. R. Soc. Lond. A* 351, pp. 165–202.

Tushingham, A.M. and W.R. Peltier (1991). "ICE-3G: A new global model of late Pleistocene deglaciation based upon geophysical predications of postglacial relative sea level change". In: *J. Geophys. Res.* 96, pp. 4497–4523.

Tushingham, A.M. and W.R. Peltier (1992). "Validation of the ICE-3G model of Wurm-Wisconsin deglaciation using a global data base of relative sea level histories". In: *J. Geophys. Res*. 97, pp. 3285–3304.

Vermeersen, L.L.A., A. Fournier, and R. Sabadini (1997). "Changes in rotation induced by Pleistocene ice masses with stratified analytical Earth models". In: *J. Geophys. Res.* 102, pp. 27689–27702.

Vermeersen, L.L.A. and R. Sabadini (1999). "Polar wander, sea-level variations and Ice Age cycles". In: *Surv. Geophys.* 20, pp. 415–440.

Vermeersen, L.L.A., R. Sabadini, G. Spada, and N.J. Vlaar (1994). "Mountain building and earth rotation". In: *Geophys. J. Int.* 117, pp. 610–624.

Wu, P. and W.R. Peltier (1984). "Pleistocene deglaciation and the Earth's rotation: A new analysis". In: *Geophys. J. R. Astron. Soc.* 76, pp. 753–791.

Yoder, C.F., J.G. Williams, J.O. Dickey, B.E. Schutz, B.J. Eanes, and B.D. Tapley (1983). "Secular variation of the Earth's gravitational harmonic J2 coefficient from Lageos and non tidal acceleration of Earth rotation". In: *Nature* 303, pp. 757–762.

Yuen, D.A. and R. Sabadini (1984). "Secular rotational motions and the mechanical structure of a dynamical viscoelastic Earth". In: *Phys. Earth. Planet. Inter.* 36, pp. 391–412.

Yuen, D.A., R. Sabadini, and E. Boschi (1982). "Viscosity of the lower mantle as inferred from rotational data". In: *J. Geophys. Res.* 87, pp. 10745–10762.

Chapter 5
Detection of the Time-Dependent Gravity Field and Global Change

Abstract In this chapter we consider the effects on $\dot{J}_\ell$ due to both the deglaciation of the Pleistocene and present-day ice loss in Antarctica and Greenland. The secular drift up to degree 6 from time series of the zonal coefficients of the Earth's gravity field from Satellite Laser Ranging (SLR) data are compared with predictions from viscoelastic Earth's models forced by PGR, to infer the mantle viscosity and the present-day ice instabilities in Antarctica and Greenland. The cumulative effects of the spherical harmonic perturbations on the gravity field is analyzed on the basis of the GRACE space gravity mission, to enlighten the importance of a precise PGR modeling for a correct interpretation of the anomalous gravity pattern from GRACE. Global deformation patterns from PGR are shown, in terms of vertical and horizontal displacements. We show how it is possible to make use of GRACE data to develop a new branch of seismology, which we name "gravitational" seismology, to retrieve the source parameters of giant, thrust earthquakes at subduction zones, as the Sumatran, 2004, and Tohoku-Oki, 2011, earthquakes. We develop the Gravitational Centroid Moment Tensor solution (GCMT) for a point source, for the Tohoku-Oki earthquake, comparing it with classical solutions from wave seismology.

5.1 Changes in the Long-Wavelength Geoid Components from Satellite Laser Ranging Techniques

In the dynamic Satellite Laser Ranging (SLR) data analysis, the satellite's orbit can be used as a gravity probe to monitor the time-varying gravity field. A long history of SLR observations of the geodetic satellites LAGEOS-I, LAGEOS-II, Starlette and Stella have been analyzed by Devoti et al. (2001) to estimate the time series of the low degree zonal coefficients in the Earth's gravity field and derive their secular drifts up to 6 degrees. Comparison of these zonal rates with the results of the viscoelastic Earth's models in Chaps. 1 and 2, forced by PGR, shows that the SLR-retrieved even and odd zonals can be used today to infer the mantle viscosity and the lithospheric thickness. The a-dimensional components of the perturbation of the gravitational potential of the Earth are defined as $J_\ell(t) = -\frac{a}{G}\phi^{\Delta}{}_{\ell 0}(t)$, which means that $\phi^{\Delta}{}_{\ell 0}(t)$ is divided by the gravitational potential of a unitary mass located at the north pole

R. Sabadini et al., *Global Dynamics of the Earth: Applications of Viscoelastic Relaxation Theory to Solid-Earth and Planetary Geophysics*,
DOI 10.1007/978-94-017-7552-6_5

at the Earth's surface, according to Eq. (1.219) for $M_L = 1$ kg and $r_L = a$, in order to make $J_\ell(t)$ a-dimensional. In the following, the symbol Δ for the perturbation of the $J_\ell(t)$ or $\dot{J}_\ell(t)$ is omitted, to not overwhelm the writing.

In Devoti et al. (2001) the observations of four geodetic satellites are analyzed for the period 1987–1998, spanning 11 years of LAGEOS-1 and Starlette observations and 5 and 4 years of LAGEOS-2 and Stella observations. Unmodeled and mismodeled tidal and non-gravitational perturbations could in principle affect the long-term gravity signal and may partly explain the discrepancies between the time derivatives of the zonals given in Tables 5.1 and 5.2.

Another critical point in treating a long period of tracking data arises from the lack of homogeneity in data quality and distribution. Devoti et al. (2001) provide a detailed description of the techniques applied to recover the zonals given in Tables 5.1 and 5.2. Figure 5.1 shows the characteristics of the satellites which have been used to retrieve the SLR solution analyzed in this chapter. Figure 5.2 shows the MLRO (Matera Laser Ranging Observatory) of the Centre of Space Geodesy "G. Colombo" in Matera (Italy) (Italian Space Agency, ASI) for SLR analyses.

Exercise 20 Making use of the $\ell = 2$ loading Love number k_2^L for the uniform viscoelastic Earth's model obtained from the Exercise 11 in Chap. 2, and $a = 6.371 \times 10^6$ m, $\rho = 5517\,\mathrm{kg/m^3}$, $g = 9.8\,\mathrm{m/s^2}$ and $M_E = 5.976 \times 10^{24}$ kg, evaluate the mantle viscosity ν so that it fits the modeled $\dot{J}_2$ with the observed value -2.9×10^{-11} yr^{-1}

Table 5.1 Even degree zonal secular drift estimated by different authors, units: 10^{-11} yr^{-1}

Author	$\dot{J}_2$	$\dot{J}_4$	$\dot{J}_6$
Yoder et al. (1983)	-3.0		
Rubincam (1984)	-2.6 ± 0.6		
Cheng et al. (1989)	-2.5 ± 0.3	0.3 ± 0.6	
Gegout and Cazenave (1993)	-2.8 ± 0.4		
Eanes (1995)	-2.4 ± 0.2		
Nerem and Klosko (1996)	-2.8 ± 0.3	0.2 ± 1.5	
Cazenave et al. (1996)	-3.0 ± 0.5	-0.8 ± 1.5	
Cheng et al. (1997)	-2.7 ± 0.4	-1.4 ± 1.0	0.3 ± 0.7
Devoti et al. (2001)	-2.9 ± 0.2	0.6 ± 0.5	0.3 ± 0.3

Table 5.2 Odd degree zonal secular drift estimated by different authors, units: 10^{-11} yr^{-1}

Author	$\dot{J}_3$	$\dot{J}_5$	$\dot{J}_{odd}$	$\dot{J}_{odd}$
			$(\dot{J}_3 + 0.837\dot{J}_5)$	$(\dot{J}_3 + 0.9\dot{J}_5)$
Nerem and Klosko (1996)			1.6 ± 0.4	
Cheng et al. (1997)	-1.3 ± 0.5	2.1 ± 0.6	0.5	0.6
Devoti et al. (2001)				0.5 ± 0.2

Regarding Cheng et al. (1997), the $\dot{J}_{odd}$ data are obtained from the merging of the two separate odd zonals according to the coefficients appearing in the first row

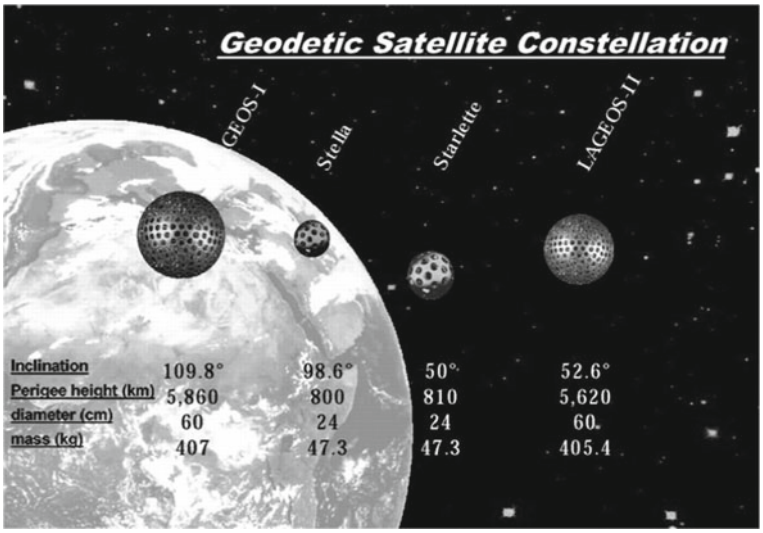

Fig. 5.1 Satellites for laser tracking used in the SLR analyses of this chapter, with the Earth in the background

obtained by Devoti et al. (2001), with the mass of the ice load being $M_I = 2 \times 10^{20}$ kg, assuming for simplicity $\theta = 0°$ and that the whole ice sheet melted instantaneously 12×10^3 yr ago (Answer: $\nu = 1.78 \times 10^{21}$ Pa s, lower branch, and 8.5×10^{23} Pa s, upper branch).

In order to explore the capability of our SLR-retrieved zonals to infer the mantle viscosity and the lithospheric thickness L, we model the viscoelastic response of our planet to Pleistocene deglaciation, the major contributor to the zonal rates given in Tables 5.1 and 5.2; the ice model is the ICE-3G by Tushingham and Peltier (1991), as appropriate as the ICE5G (Peltier 2004) and ANU (Australian National University) (Nakada et al. 2015) ice models when dealing with the geophysical observables which depend on the gross features of the loading history, as the low harmonics of the gravity field. In this section, present-day forcing is not included in the modeling, and we thus assume that Pleistocene deglaciation is the only forcing contributor. We can look for discrepancies in the results of the modeling as possible indicators for present-day ice melt or growth. In Figs. 5.3 and 5.4 a χ^2 analysis is carried out for each of the zonals in Tables 5.1 and 5.2 estimated by Devoti et al. (2001) in order to explore their preferred lower and upper mantle viscosities, ν_2 and ν_1, and lithospheric thickness, L, and to elucidate possible discrepancies among these best-fit parameters. The χ^2 analysis for each zonal separately is given by

$$\chi^2 = \left(\frac{\dot{J}_l^{mod} - \dot{J}_l^{obs}}{\sigma_l^{obs}}\right)^2, \tag{5.1}$$

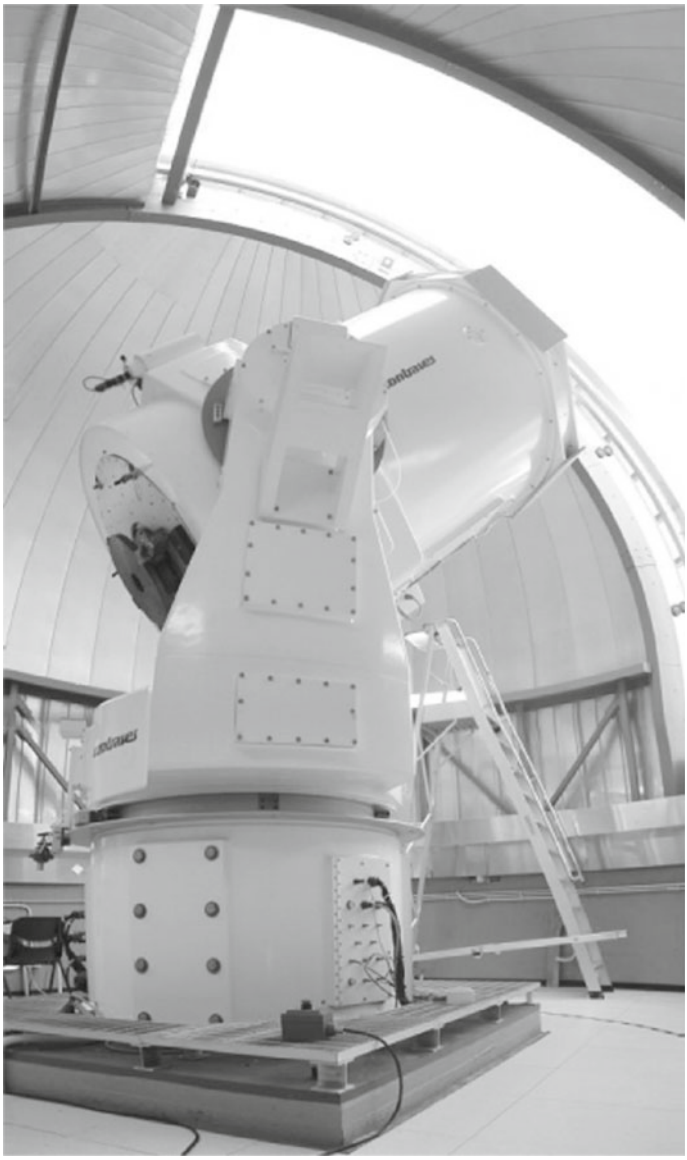

Fig. 5.2 MLRO (Matera Laser Ranging Observatory) of the Centre of Space Geodesy "G. Colombo" in Matera, Italy (Italian Space Agency, ASI.)

where $\dot{J}_{obs}$ and $\dot{J}_{mod}$ correspond to the zonal in the tables and that retrieved from the models, respectively; σ_l represents the standard deviation of the observed value.

The region where χ^2 attains its (local) minimum gives the best fit between observed and modeled values. In agreement with Vermeersen et al. (1998) where,

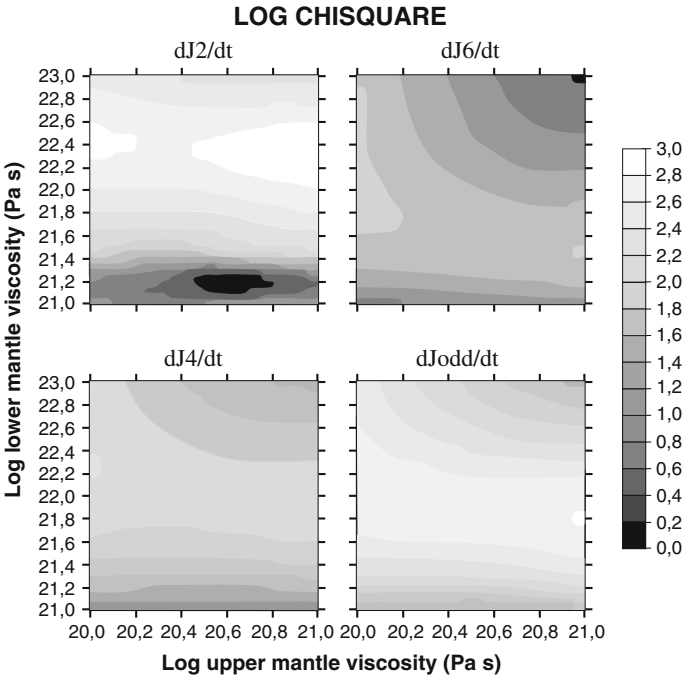

Fig. 5.3 χ^2 analysis for the time derivatives of the zonals by Devoti et al. (2001) given in Tables 5.1 and 5.2 for varying upper and lower mantle viscosities

except for the odd one, the χ^2 analysis was carried out for all the zonals simultaneously or the zonal plus TPW, the best fit in Fig. 5.3 falls into two main regions, one in which the lower mantle viscosity ν_2 is high, of the order of 10^{23} Pa s or higher, and another one in which it is of the order of 10^{21} Pa s or lower.

Figure 5.3 shows that the tendency of this multiplicity of solutions is a characteristic of each zonal. The best-fit ν_2 varies among the zonals, with a clear tendency for $\dot{J}_{odd}$, $\dot{J}_4$ and $\dot{J}_6$ towards lower mantle viscosities that fall beyond the limits stated above, with $\nu_2 < 10^{21}$ Pa s and $\nu_2 > 10^{23}$ Pa s. By contrast, the best-fit lower mantle viscosity for $\dot{J}_2$ is 21.2 in the logarithmic scale. This discrepancy between $\dot{J}_2$ and the other zonals indicates that, beyond post-glacial rebound, another mechanism of mass redistribution must be active. Another interesting result in Fig. 5.3 is that the best-fit upper mantle viscosity is lower than 10^{21} Pa s, for $\nu_2 = 10^{21.2}$: in particular, $\nu_1 = 10^{20.6}$ Pa s for $\dot{J}_2$. For the best-fit corresponding to $\nu_2 > 10^{23}$ Pa s, it is interesting to note that the upper mantle viscosity should be higher than 10^{21} Pa s.

These results indicate an upper mantle viscosity considerably lower than 10^{21} Pa s for a lower mantle viscosity of the order of $10^{21}-10^{22}$ Pa s, in good agreement with previous findings (Nakada and Lambeck 1989; Forte and Mitrovica 1996). The zonal analysis carried out in Fig. 5.3 shows that the sensitivity to lower mantle viscosity variation is highest for $\dot{J}_2$ and $\dot{J}_{odd}$, lowest for $\dot{J}_6$ and somehow intermediate for $\dot{J}_4$.

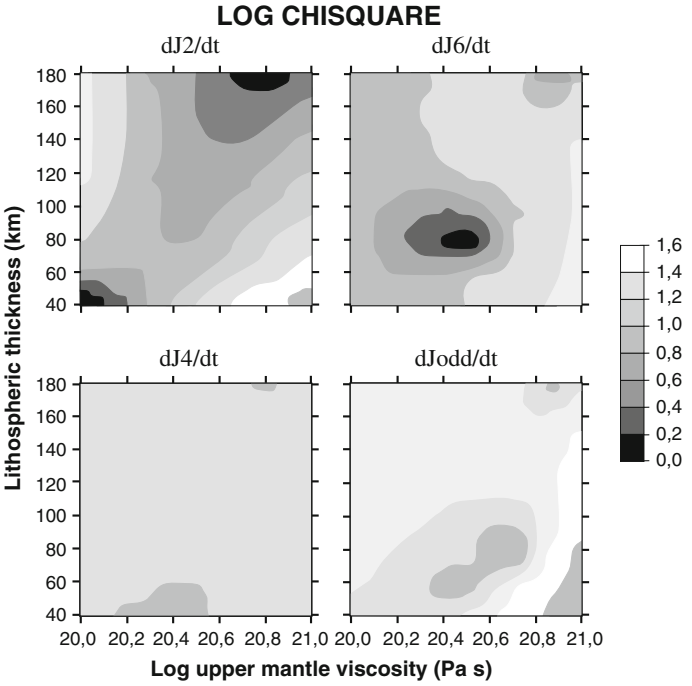

Fig. 5.4 χ^2 analysis for the time derivatives of the zonals by Devoti et al. (2001) given in Tables 5.1 and 5.2 for varying upper mantle viscosity and lithospheric thickness

The highest sensitivity to upper mantle viscosity variations is portrayed by $\dot{J}_2$ for ν_2 of the order of 10^{21} Pa s, and by the other zonals for ν_2 of the order of 10^{23} Pa s.

The same χ^2 analysis is carried out in Fig. 5.4 for lithospheric thickness and upper mantle viscosity. As observed in Fig. 5.3, the preferred upper mantle viscosity is generally lower than 10^{21} Pa s. In particular, a local minimum in $\dot{J}_6$ corresponds to an upper mantle viscosity of 20.5 in logarithmic scale.

Consistent with $\dot{J}_6$, the log of upper mantle viscosities of about 20.5 are indicated by $\dot{J}_{odd}$. This tendency to upper mantle viscosities lower than 10^{21} Pa s is portrayed by $\dot{J}_2$ and $\dot{J}_4$ too, although the sensitivity to upper mantle viscosity variations is lowest for $\dot{J}_4$. When we consider the best-fit lithospheric thickness, it is remarkable that $\dot{J}_6$ and $\dot{J}_{odd}$ are sensitive to lithospheric thickness variations and favour a lithosphere of 60–100 km. This finding is in contrast with $\dot{J}_2$, where local minima indicate a lithospheric thickness lower than 40 km, as also preferred by $\dot{J}_4$, or higher than 180 km. This discrepancy could also be interpreted as an indication of ongoing mass redistribution over the Earth.

Some interesting observations arise if we compare the viscosity values that fit the various harmonics or we test the mutual consistency of the different SLR analyses in Tables 5.1 and 5.2. For an upper mantle viscosity of 10^{21} Pa s, $\dot{J}_2$ can be fitted

by a lower mantle viscosity of 1.5×10^{21} Pa s, while $\dot{J}_{odd}$ in this section or in Cheng et al. (1997) requires a lower mantle viscosity of $2-6 \times 10^{20}$ Pa s; the datum in Nerem and Klosko (1996) for $\dot{J}_{odd}$ requires 1.0×10^{21} Pa s. The $\dot{J}_4$ from Nerem and Klosko (1996) and the SLR analysis carried out in this section agree within 2σ, but the sign is opposite with respect to the model predictions. Our modeling, with a mantle viscosity of 10^{21} Pa s, agrees in amplitude and sign with Cheng et al. (1997) but only in amplitude with the SLR analysis by Devoti et al. (2001). For $\dot{J}_6$, our SLR analysis agrees with Cheng et al. (1997) and is coherent with our model predictions as far as the amplitude is concerned, but is opposite in sign. These findings show that discrepancies still exist between model predictions and the various SLR analyses, as well as among the SLR analyses themselves.

These results show that SLR-retrieved low degree geoid components J_2 and J_{odd} can be used in principle to constrain the rheology of the mantle and lithospheric thickness. Discrepancies in the viscosity values needed to fit the zonal rates when Pleistocene deglaciation is the only forcing mechanism are a strong indication that mass redistribution is actually occurring over the Earth, eventually being associated with mass instabilities in Greenland and Antarctica, as also suggested by Johnston and Lambeck (1999): these arguments are explored in the following section.

5.2 Trade-Off Between Lower Mantle Viscosity and Present-Day Mass Imbalance in Antarctica and Greenland

Two major mechanisms are responsible for the secular changes in the gravitational field: the Pleistocene deglaciation, as shown in Fig. 4.2, and the present-day mass instability in Antarctica, Greenland and Alpine glaciers. The Earth is affected today by the first mechanism because of the viscous memory of the mantle and by the second due to ongoing surface mass redistribution.

In the previous section, comparison between SLR-retrieved zonals and predictions from viscoelastic models driven solely by Pleistocene deglaciation showed that this mechanism cannot be the only source of time variations of the gravity field. In fact, discrepancies in the viscosity profiles required to reproduce the different zonals when the only forcing mechanism is PGR seem to indicate ongoing mass redistribution over the Earth as related to global change and eventually associated with mass instabilities in Antarctica and Greenland. Both the even and odd zonal geopotential components of the gravity field, up to harmonic degree $l = 6$, are used in this section in conjunction with the modeled ones to infer the key parameters that control the two major mechanisms above: the viscosity, characterizing the flow properties of the mantle, and the ice mass imbalance in Antarctica and Greenland, which are thought to be the contributors to ongoing mass redistribution.

The $\dot{J}_{odd}$ contribution by Devoti et al. (2001) in Table 5.2 can be better estimated by the following expression appropriate for a single satellite solution (Starlette) (Schutz et al. 1993)

$$\dot{J}_{odd} = \dot{J}_3 + 1.04\dot{J}_5 - 0.53J_7 - 0.81\dot{J}_9 + 0.13\dot{J}_{11} + 0.52\dot{J}_{13} + 0.06\dot{J}_{15} - 0.3\dot{J}_{17} - 0.11\dot{J}_{19} + 0.14\dot{J}_{21}. \quad (5.2)$$

The highest odd zonals are not considered since they would enter Eq. (5.2) with coefficients smaller than 0.1. Except for $\dot{J}_{odd}$ of Eq. (5.2), we will assume in our study that all the other zonals are sufficiently well separated so as to draw sound geophysical conclusions. In this section, we make use of the zonal secular drifts of Cheng et al. (1997) and Devoti et al. (2001) given in Tables 5.1 and 5.2, except for $\dot{J}_{odd}$ in Devoti et al. (2001) now based on Eq. (5.2). These data are used to constrain the upper and lower mantle viscosities and the amount of mass imbalance in Antarctica and Greenland by means of the χ^2 analysis for each zonal separately, as discussed in the previous section, in order to emphasize that the simultaneous fit of all the zonals can occur only for a specific range of lower mantle viscosity values and ice mass imbalance, which allows the minima in χ^2 for the different $\dot{J}_l$ to overlap in the viscosity space.

Ice mass imbalance in Antarctica and Greenland is varied until the best-fit lower mantle viscosities obtained from Eq. (5.1) are the same for all the zonals. Ice mass in Antarctica is varied in our modeling within the bounds of -500 to $+400$ Gt/yr, as per previous observations of grounded ice (Warrick et al. 1996; Bentley and Giovinetto 1991; Jacobs 1992). For Greenland we have considered the case of ice loss from 0 to -144 Gt/yr, the latter corresponding to a sea-level rise of 0.4 mm/yr for a 1 °C warming (Oerlemans 1991). The viscoelastic part of the Earth's model is only needed for the Pleistocene deglaciation, while present-day mass imbalance in Antarctica and Greenland requires the elastic component. A better physical insight into the results of the viscosity inversion can be gained if we show first the dependence of the $\dot{J}_l$ on the lower mantle viscosity and on the rate of melting in the polar regions. In Fig. 5.5 the $\dot{J}_l$ are shown as a function of lower mantle viscosity for Pleistocene (solid), Pleistocene plus ice loss in Antarctica of -500 Gt/yr (dashed), and Pleistocene plus ice loss in Antarctica and Greenland of -500 and -144 Gt/yr (dotted), with $\dot{J}_{odd}$ based on the Eq. (5.2). Note the sensitivity of the zonals to lower mantle viscosity variations and the dominant effect of ice loss in Antarctica with respect to Greenland. The peak value in the $\dot{J}_2$ in the solid curves for the Pleistocene deglaciation is displaced from 2×10^{22} hboxPa s, corresponding to $\dot{J}_2$, towards lower values of lower mantle viscosity for increasing harmonic order, in agreement with Mitrovica and Peltier (1993), down to 3×10^{21} Pa s for $\dot{J}_6$. The modeled zonals show the tendency to admit two intersections of the model results, with the horizontal stripes depicting the Cheng et al. (1997), Devoti et al. (2001) zonal secular drifts, light and dark gray, respectively, thus providing two possible lower mantle viscosities. The lower viscosity solution corresponds to a situation of sustained flow in the mantle and a present-day configuration which is close to global post-glacial isostatic equilibrium,

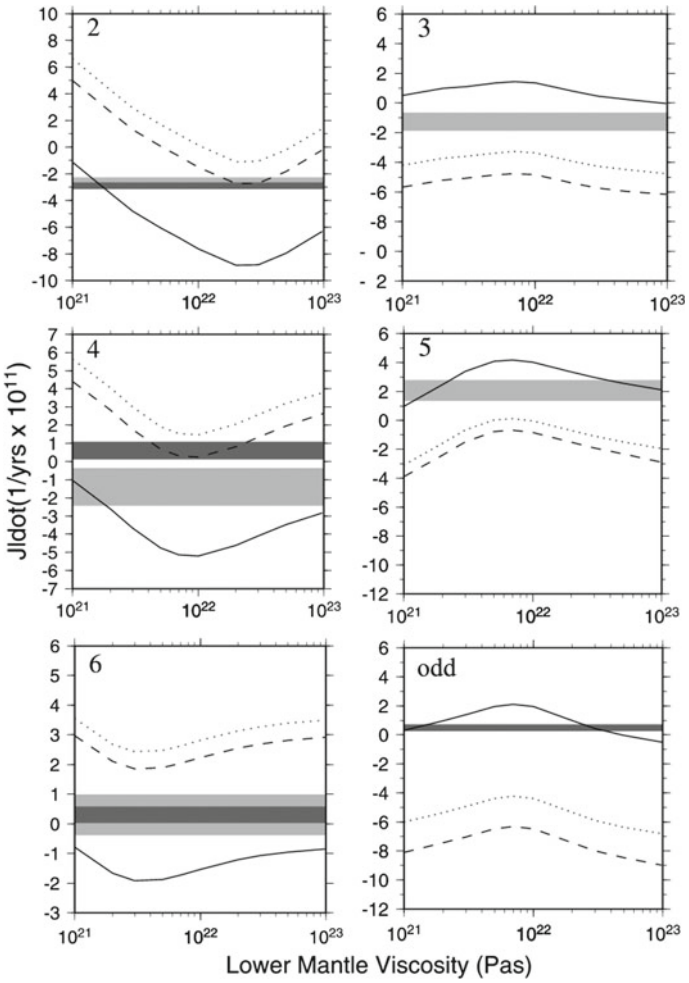

Fig. 5.5 $\dot{J}_l$ as a function of lower mantle viscosity, ranging from 10^{21} to 10^{23} Pa s. The *numbers* in the *top*, *left part of the panels* indicate the harmonic degree or the cumulative odd degrees as in Eq. (5.2), in the *bottom*, *right panel*. Upper mantle viscosity is fixed at 5×10^{20} Pa s. The *light* and *dark gray* stripes stand for the Cheng et al. (1997), Devoti et al. (2001) solutions. *Solid curves* correspond to Pleistocene deglaciation, *dashed ones* to Pleistocene plus maximum ice loss in Antarctica and the *dotted ones* include maximum ice loss in Greenland. The modeled results for $\dot{J}_{odd}$ stand for the combination of zonals given by Eq. (5.2)

while the higher viscosity solution corresponds to reduced mantle flow and large isostatic disequilibrium. The solid curves show that Pleistocene forcing does not allow a simultaneous fit of the SLR data for all the zonals with the same lower mantle viscosity. The scenarios of ice mass imbalance in Antarctica and Greenland suggest that this inconsistency, already noted in the previous section, could be due to some amount of ice mass instability occurring today in these two regions but not

included in the solid curves. The dashed and dotted curves show how ice loss in Antarctica and Greenland impacts the results of the Pleistocene deglaciation.

With respect to the Pleistocene solid curves, the effects of melting in Antarctica are to displace the peak values in $\dot{J}_l$ in the direction of the Cheng et al. (1997), Devoti et al. (2001) data for the even and odd zonals, eventually exceeding the data themselves as shown by the dashed curves for $\dot{J}_6$ and the odd zonals because of the extreme value of -500 Gt/yr used in the simulations. Comparison between the dashed and dotted curves shows that ice loss in Greenland reinforces the effects of Antarctica on the even zonals and counteracts Antarctica on the odd ones (Mitrovica and Peltier 1993; James and Ivins 1997). These results indicate that ice growth in Antarctica must be excluded because it would cause a displacement of the Pleistocene curves in the opposite direction with respect to Cheng et al. (1997) and Devoti et al. (2001), while at the same time suggesting that present-day mass imbalance may make possible to solve for the inconsistencies in the lower mantle viscosity inferences noted above.

In the following figures, both SLR solutions are used within a χ^2 approach, where ice mass loss in Antarctica and Greenland is added to Pleistocene deglaciation; the effects of Alpine glaciers are negligible and have not been considered. Since Antarctica is the largest contributor, we have adopted the strategy of constraining ice loss in Antarctica first by means of Cheng et al. (1997), where the odd zonals are not contaminated by higher harmonic components; the effects of ice loss in Greenland on viscosity estimates are then analyzed. After having explored all the possibilities for ice loss in Antarctica between 0 and -500 Gt/yr, we find that the best-fit lower mantle viscosities from the different zonals in Cheng et al. (1997) are the same if ice mass imbalance is close to -250 Gt/yr, which will be used throughout. The left columns in Figs. 5.6 and 5.7 correspond to this scenario and provide the χ^2 patterns for the zonal secular drifts of Cheng et al. (1997) and Devoti et al. (2001), respectively; melting in Greenland at the rate of -144 Gt/yr is added in the right columns. χ^2 varies as a function of upper and lower mantle viscosity, horizontal and vertical scales, respectively. The grey scale provides the χ^2 values, with the minima providing the best-fit solutions given by the darkest gray. Figure 5.6, left column, shows that for -250 Gt/yr of ice loss in Antarctica the best-fit lower mantle viscosity log solutions overlap for all the zonals and that for the best resolved zonals $\dot{J}_2$, $\dot{J}_3$ and $\dot{J}_5$ the χ^2 minimum does not coincide with 21.2, corresponding to the first intersection of the $\dot{J}_2$ solid curve with SLR data, top left panel in Fig. 5.5, but is displaced to higher values, 21.6–22.0 in logarithmic scale; $\dot{J}_4$ and $\dot{J}_6$ are coherent with this picture, although less resolved. A substantial change in the rate of melting in Antarctica with respect to -250 Gt/yr would not allow a simultaneous fit of the zonals with the same viscosity profile. This imbalance of -250 Gt/yr is within the range of -500 to 400 Gt/yr resulting from observations of grounded ice but is higher than the -60 ± 76 Gt/yr, mainly from West Antarctica, obtained from 5 yrs of satellite radar altimeter data (Wingham et al. 1998). This discrepancy could arise from the adopted Pleistocene forcing model ICE-3G or from the underestimation, in the treatment of radar altimeter data, of the accumulation rate that could have hidden an imbalance larger than the -60 Gt/yr (Wingham et al. 1998). When Greenland is added, right column, the tendency to higher lower mantle viscosities is reinforced. $\dot{J}_2$ portrays a

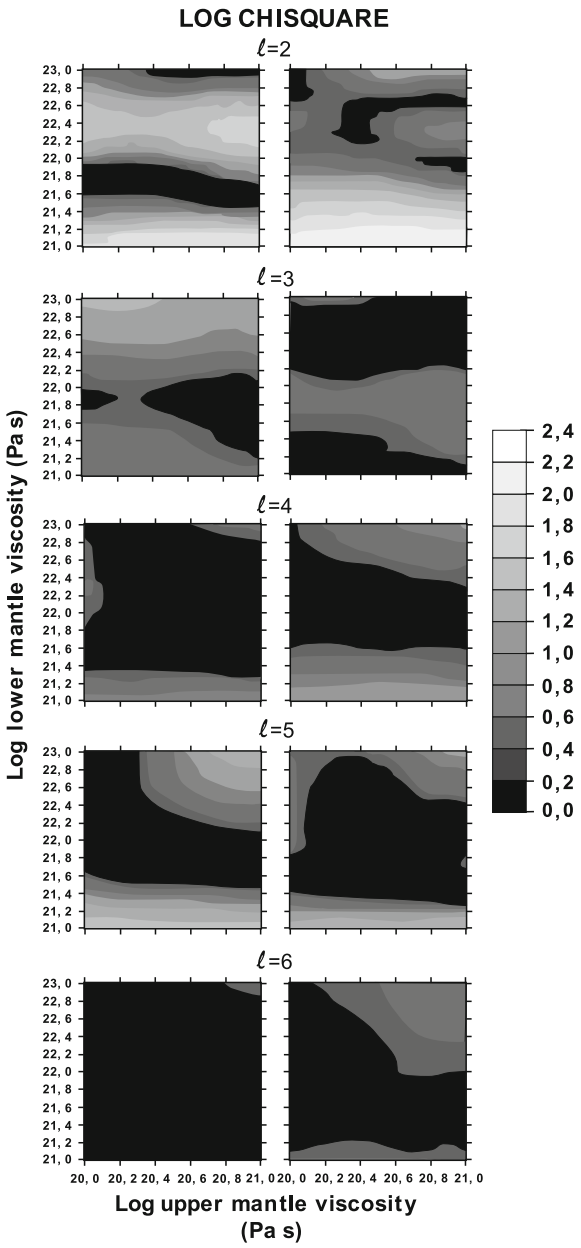

Fig. 5.6 χ^2 patterns for the $\dot{J}_l$, Eq. (5.1), as a function of upper and lower mantle viscosities, these parameters varying as shown by the *horizontal* and *vertical scales*. Observational data are taken from the Cheng et al. (1997) solution, Tables 5.1 and 5.2. The minima correspond to the *darkest gray*. Pleistocene plus ice loss in Antarctica (−250 Gt/yr) are considered in the *left column*. In the *right column* ice loss of −144 Gt/yr in Greenland is added

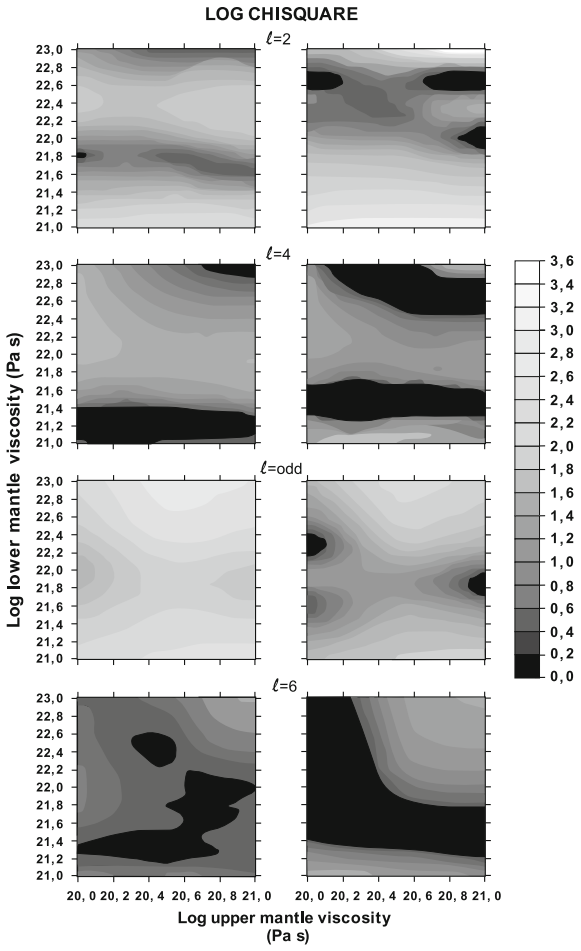

Fig. 5.7 χ^2 patterns for the $\dot{J}_l$, as in Fig. 5.6, for the Devoti et al. (2001) solution, with $\dot{J}_{odd}$ given by the combination of Eq. (5.2). The *left* and *right columns* correspond to the same forcing in Fig. 5.6

single minimum at 22.0–22.8 for the log of the lower mantle viscosity, in agreement with the now better defined minima of $\dot{J}_4$ and $\dot{J}_6$. $\dot{J}_3$ now splits into two possible viscosity solutions, with the highest viscosity still coherent with the patterns of the other zonals. χ^2 portrays a weak dependence on the upper mantle viscosity for all the zonals. Cheng et al. (1997) provide a clear indication for ice loss in Antarctica and for a further viscosity increase in the lower mantle once ice loss in Greenland is added to that in Antarctica. Intermediate values of ice loss in Greenland between 0 and -144 Gt/yr would provide values of the log of the lower mantle viscosities between 21.6–22.0 and 22.0–22.8. The χ^2 patterns relative to the Devoti et al. (2001) solution, Fig. 5.7, are in close agreement with Cheng et al. (1997) as far as $\dot{J}_2$ and $\dot{J}_6$ are concerned, with higher resolution in the location of the minima, but differ in $\dot{J}_4$, portraying two possible viscosity solutions as expected, on the other hand, on

the basis of Fig. 5.3. $\dot{J}_{odd}$ cannot be directly compared with the separate $\dot{J}_3$ and $\dot{J}_5$ in Cheng et al. (1997), being a summation of a larger number of odd zonals, but it is remarkable that it portrays some similarities with the Cheng et al. (1997) odd components. The lowest χ^2 value region in fact overlaps in the two SLR solutions, with a better defined minimum in Cheng et al. (1997) of $\chi^2 = 0.0-0.2$ with respect to 1.4–1.6 in Devoti et al. (2001), contaminated by several odd zonals. When ice loss in Greenland is added in the right column, the tendency towards higher lower mantle viscosities also appears in Fig. 5.7. The lowest χ^2 value for $\dot{J}_{odd}$ and upper mantle viscosities of the order of 10^{20} Pa s now overlaps with the minima of the other zonals, improving the coherence with Cheng et al. (1997).

The $\dot{J}_l$ results can be strengthened by TPW simulations. Historical and modern polar motion data, as given in McCarthy and Luzum (1996), are now compared with modeled TPW predictions to validate, by means of an independent source, the results obtained solely on the basis of the SLR analysis. Figure 5.8 shows the TPW χ^2 patterns when the observational datum of 0.333 ± 0.008 arcsec/century is considered (McCarthy and Luzum 1996) with the top and bottom panels corresponding to the same forcing of the left and right columns in Figs. 5.6 and 5.7, respectively. Note the overlapping of the TPW and $\dot{J}_2$ χ^2 minima for the log of the lower mantle viscosity of 21.8 when ice loss is limited to Antarctica, top panel. This finding solves the apparent

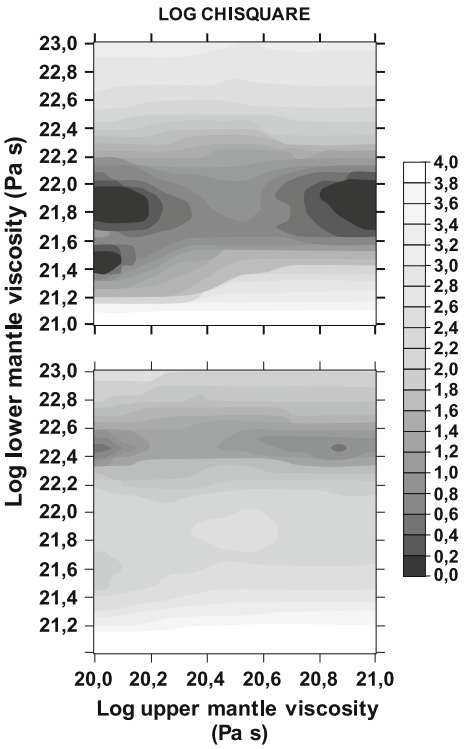

Fig. 5.8 χ^2 patterns for TPW. The *top panel* corresponds to Pleistocene deglaciation and ice loss in Antarctica, while ice loss in Greenland is added in the *bottom panel*

paradox noted in the past consisting of TPW data systematically requiring higher values of lower mantle viscosities with respect to $\dot{J}_2$ when Pleistocene deglaciation is the only forcing mechanism (Vermeersen et al. 1997). In the bottom panel, the TPW pattern favors an increase of the log of the lower mantle viscosity to 22.4–22.6, in agreement with $\dot{J}_l$ simulations for melting in Greenland of -144 Gt/yr. Ice mass imbalance in Greenland does not degrade the coherence between the lower mantle viscosity inferred from the $\dot{J}_l$ and TPW obtained in the top panel.

We have thus obtained that the χ^2 viscosity patterns based on the low degree $\dot{J}_l$ in Cheng et al. (1997) are the same if the rate of melting in Antarctica is constrained to -250 Gt/yr, corresponding to a sea-level rise of 0.7 mm/yr, and if the lower mantle is more viscous than the upper mantle. This scenario is coherent with Devoti et al. (2001), even if the $\dot{J}_3$ and $\dot{J}_5$ zonals are contaminated by higher degree contributions. The tendency of the lower mantle viscosity solutions towards values higher than 10^{21} Pa s when melting in Antarctica is added to Pleistocene deglaciation agrees with previous indications based on the temporal variations of the gravity field (Mitrovica and Peltier 1993; Nerem and Klosko 1996). In particular, our inference of lower mantle viscosity when Antarctica is the major contributor to present mass imbalance is in close agreement with the findings of a previous analysis by Johnston and Lambeck (1999) based solely on $\dot{J}_2$, on the assumption that the non-steric component of sea-level rise is 1 mm/yr. The novelty of our analysis stands on the release of this assumption on sea-level rise thanks to the joint use of the accurately detected even and odd zonal components of the SLR-retrieved gravity field. The non-steric component of sea-level rise that results from our study is at most 1.1 mm/yr, of which 0.7 from Antarctica and 0.4 mm/yr from Greenland, within the best estimate total sea level rise of 1.8 mm/yr, which includes 0.4 mm/yr of thermal expansion of the oceans. Our analysis reconciles lower mantle viscosity inferences from Pleistocene deglaciation with those based on the long-wavelength, static components of the geoid anomalies and true polar wander driven by internal mass heterogeneities, which indicate a lower mantle more viscous than the upper mantle (e.g. Hager 1984; Sabadini and Yuen 1989; Ricard et al. 1993; Forte and Mitrovica 1996). This unification of the viscosity inferences resulting from geodynamical processes spanning different time scales, from thousands to hundreds of millions of years, is made possible nowadays by means of the accurate detection of the even and odd zonal components of the time-dependent gravity field, proving that the SLR technique will remain a fundamental tool to constrain the global dynamics of our planet.

5.3 Time Dependent Gravity Field from the GRACE Space Mission: The Importance of PGR Models

Dedicated satellite gravity missions like GRACE contribute substantial improvements towards the higher harmonics, with respect to the previous sections of this chapter (e.g. Kaufmann 2000; Velicogna and Wahr 2002; Wahr and Davis 2002). This section enlightens the importance of the PGR models built on the incompressible

fundamental solution $\mathbf{Y}_\ell$, Eq. (2.42), for a correct interpretation of the secular components of the time dependent gravity field derived from GRACE. Any kind of geophysical process, that is responsible for the redistribution of mass over the Earth and within the mantle, changes the gravity field whose variations are monitored by GRACE space gravity mission, at higher wavelengths with respect to those considered in the previous sections.

The correct identification of the gravitational spatial and temporal signature of each geophysical process, from hydrology, from the atmoshpere, the oceans, and from the solid Earth, is thus extremely important to correctly estimate the most important phenomena related to global changes, such as the present-day ice mass loss in Greenland and Antarctica and the related effect on sea-level changes: the latter in fact depend on an accurate determination of PGR, which in turn depends on the assumed solid Earth's parameters entering the fundamental solution $\mathbf{Y}_\ell$ and on the deglaciation model.

The time dependent surface density anomalies due to PGR can be converted into water equivalent (w.e.) units, as in Fig. 5.9, where the w.e. PGR mass variation trend in cm/yr is given for the 5-layer, viscoelastic incompressible model depicted in Table 5.3, in agreement with the most appropriate mantle viscosities of 10^{22} Pa s as in Sect. 5.2 and in agreement with Tosi et al. (2005). As far as ice loading hystory is concerned, this figure is based on the ICE-3G ice-sheet model for the Pleistocene deglaciation by Tushingham and Peltier (1991). Deglaciation centres produce spots of geoid increase over Hudson bay and Antarctica that can be as large as 2 mm/yr, as well as over the Gulf of Bothnia, due to the uplift of the Earth's crust, where crustal material substitutes the air or the water, of lower density.

Over the deglaciation centres, the Earth's crust uplifts, which is translated into an increase in water equivalent ranging between 4 cm/yr over Hudson Bay and

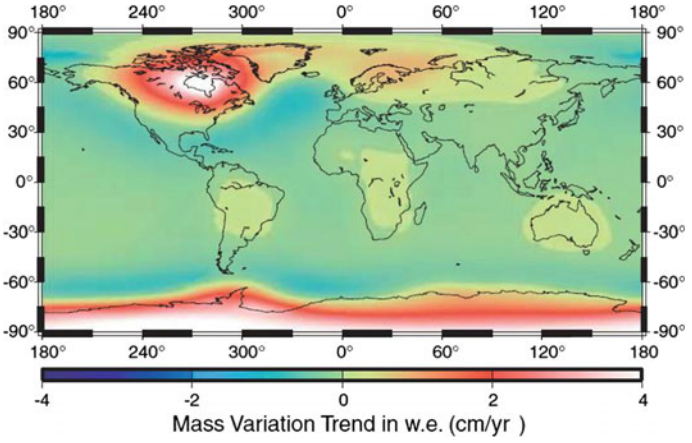

Fig. 5.9 PGR mass variation trend in water equivalent (cm/yr). The Earth's model parameters are given in Table 5.3. This figure is taken from Barletta et al. (2008), their Fig. 5.8

Table 5.3 Parameters for the 5-layer Earth's model

Layer	r (km)	ρ (kg/m^3)	μ (Pa)	ν (Pa s)
1	6371.0	3196.9	5.98×10^{10}	1.00×10^{50}
2	6250.0	3457.7	7.41×10^{10}	1.00×10^{20}
3	5951.0	3882.3	1.09×10^{11}	1.00×10^{20}
4	5701.0	4890.6	2.21×10^{11}	1.00×10^{22}
5	3480.0	10925.	0.0	0.0

r is the distance with respect to the centre of the Earth, ρ the density of the layer, μ the rigidity and ν the viscosity

Antarctica, or about 2 cm/yr over the Gulf of Bothnia, while over the peripheral oceanic and continental areas we note a decrease of 0.5–1.0 cm/yr, due to the down-flexure of the portion of the lithosphere in the periphery of the uplifting deglaciation centres. Over continental areas, such as central Africa, south America and Australia, water equivalent increases slightly, by about 2–3 mm/yr, due to a slight uplift of the continents caused by the levering effects of the subsiding oceanic basins, as described in Mitrovica and Peltier (1991).

The incompressible viscoelastic model results of Fig. 5.9 can be compared with the map of mass variation linear trends in water equivalent (w.e.) of Fig. 5.10, expressed in cm/yr as for Fig. 5.9, based on the linear regression of individual gravity coefficients from GRACE, then summed together, according to the methodology of Barletta et al. (2008), to whom we refer for details regarding the data treatment procedures which have allowed to obtain the results of Fig. 5.10.

These figures from the real gravity observations show major features, such as the red spots of mass growing over Hudson bay and Gulf of Bothnia, in Scandinavia, clearly due to the PGR induced uplift of the crust seen also in the model results of Fig. 5.9, the mass decrease in Greenland, at its southeastern edge, and the blue and red spots of decreasing and increasing mass in Antarctica, close to each other, at 240° and 290° longitude. Other features are related to hydrological effects. It is worthwhile noting that both Figs. 5.9 and 5.10 have been obtained by truncating the series of harmonic coefficients at $l = 70$, in agreement with GRACE resolution, and the gravity time series cover the period December 2002 to March 2006.

Subtracting the PGR contribution of Fig. 5.9 from the GRACE trends of Fig. 5.10, the following Fig. 5.11 is obtained which, once compared with Fig. 5.10a, shows that the large spot over Hudson Bay disappears, making this region stable, and the gravity gain over Scandinavia is also reduced, as expected since the PGR contribution has been removed. In Antarctica, the increase in water equivalent seen in GRACE data at 290° longitude is disrupted by subtraction of PGR effects, and the decrease observed in Fig. 5.10 in the blue spot of Western Antarctica at 240° is enhanced. This figure shows that mass variations trends over Antarctica and Greenland from GRACE time series trade off with mass estimates from PGR over these regions, particularly in Antarctica. It has already been shown, by means of previous SLR and GRACE analyses (Tosi et al. 2005; Chen et al. 2006a, b; Luthcke et al. 2006;

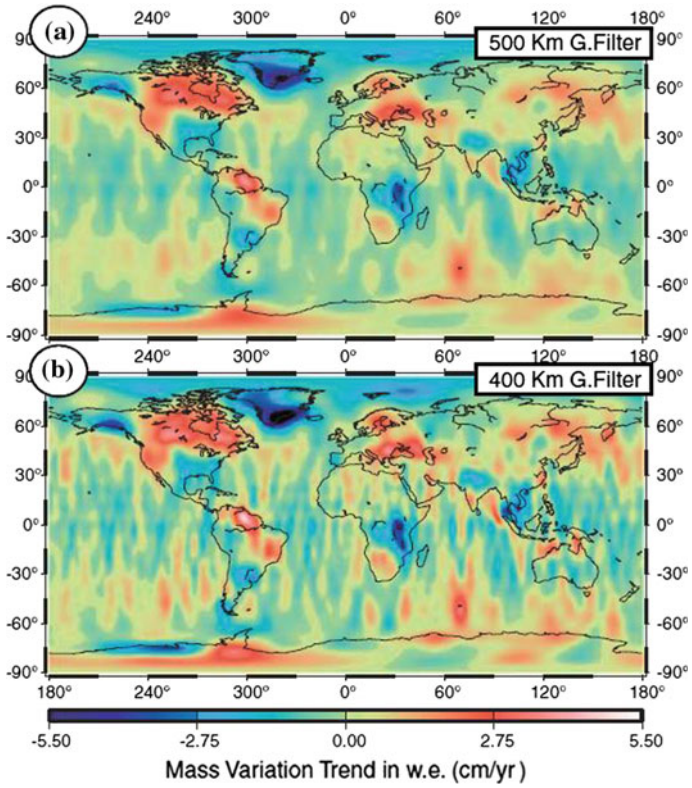

Fig. 5.10 Map of mass variation trend in water equivalent (w.e.), expressed in cm/yr. This map is smoothed with a 500 km Gaussian filter, panel (**a**), and with a 400 km one, panel (**b**). This figure is taken from Barletta et al. (2008), their Fig. 5.6

Velicogna and Wahr 2005, 2006a, b), that PGR trades off with present-day mass imbalance in Antarctica and Greenland, as also shown in Sect. 3.2, which means that mantle viscosity, controlling the present-day mass variation from PGR, impacts the estimates of present-day ice mass, the latter depending only on the elastic properties of the Earth.

Once the updated upper and lower mantle viscosities of Table 5.3, 10^{20} and 10^{22} Pa s, nowadays considered the most realistic, in the incompressible, viscoelastic model are used as in Barletta et al. (2008), a substantial mass loss in both Antarctica and Greenland is obtained, of -171 ± 39 and -101 ± 22 Gt/yr, or 10^9 tons per year: this scenario is portrayed by Fig. 5.11, although realistic constraints to the trend in ice mass loss derived from GRACE provide a range of variations wider that that commonly stated, ranging from -209 Gt/yr to an accumulation of 88 Gt/yr for Antarctica, and from -122 to -50 Gt/yr for Greenland, as shown in Barletta et al. (2008). It is remarkable that the upper bounds of this GRACE derived ice mass loss in Antarctica and Greenland are only slightly lower, by the 16 and

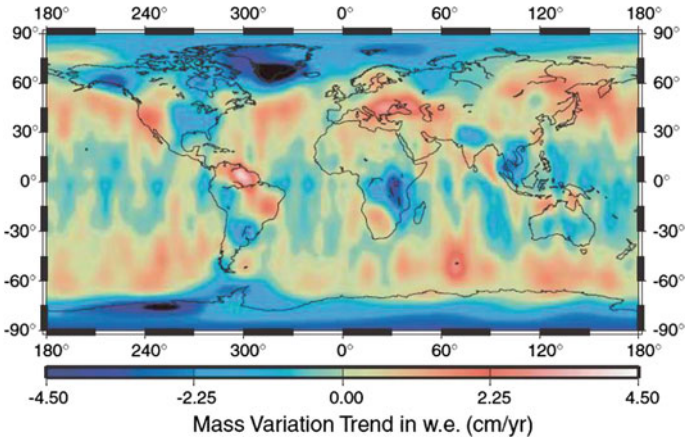

Fig. 5.11 GRACE mass variation trend in water equivalent, after removal of PGR contribution, based on the model parameters of Table 5.3. This figure is taken from Barletta et al. (2008), their Fig. 5.9

15 % respectively, than those of −250 and −144 Gt/yr inferred in Sect. 5.2 from the $\dot{J}_\ell$ low degrees. These deviations are expected, due to the different time coverage of the two SLR and GRACE data sets of Sects. 5.2 and 5.3, which may be affected by possible changes in the rate of ice mass loss for Antarctica and Greenland. The reader should be made aware, on the other hand, that the fate of these estimates is to be continuously updated, due to the improvement in the accuracy of the gravity data and to the increase on the time interval spanned by the gravity time series.

The results of this section clearly show the major step-ahead made in our understanding of the time dependent gravity field at high harmonics from the GRACE space gravity mission with respect to the SLR time series of previous sections, limited at the lowermost harmonics, although the accuracy in the estimate of the latter has not been taken over yet.

5.3.1 Global Vertical and Horizontal Displacements from PGR

It is interesting to look at PGR not only from the perspective of gravity changes as in the previous sections, but also from that of vertical and horizontal displacements at the Earth's surface. The results in Fig. 5.12, portraying the modeled global deformation pattern induced by PGR from Marotta (2003), show that vertical and horizontal velocities associated with PGR are sensitive to the rheological or viscosity stratification of the mantle, where the viscosity describes the flow properties of the mantle. Figure 5.12a corresponds to an upper mantle viscosity $\nu_{UM} = 0.5 \times 10^{21}$ Pa s and a lower mantle viscosity $\nu_{LM} = 1.0 \times 10^{21}$ Pa s defining the PGR-21 model; the

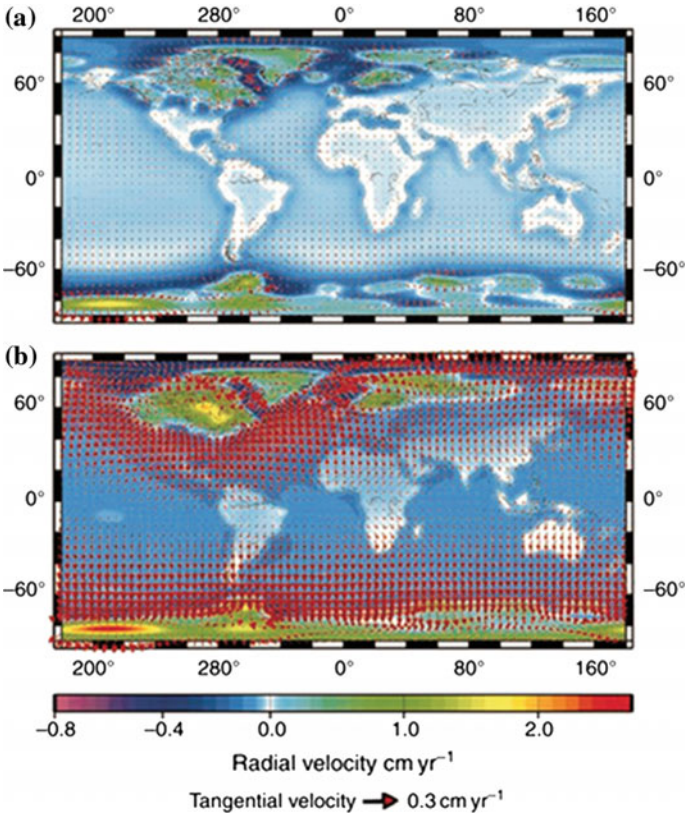

Fig. 5.12 **a** corresponds to an upper mantle viscosity $\nu_{UM} = 0.5 \times 10^{21}$ Pa s and a lower-mantle viscosity $\nu_{LM} = 1.0 \times 10^{21}$ Pa s (PGR-21). **b** corresponds to $\nu_{UM} = 0.5 \times 10^{21}$ Pa s and $\nu_{LM} = 1.0 \times 10^{22}$ Pas (PGR-22). The elastic lithosphere is 80 km thick, and both lithosphere and mantle are incompressible. Redrawn from Fig. 1 of Marotta (2003)

bottom panel corresponds to $\nu_{UM} = 0.5 \times 10^{21}$ Pa s and $\nu_{LM} = 1.0 \times 10^{22}$ Pa s, defining the PGR-22 model. These results are based on the normal-mode relaxation and propagator theory described in Chaps. 1 and 2, within the frame of the incompressible models based on Eq. (2.42). The redistribution of the glacial melt water on the viscoelastic Earth is solved within the ICE-3G model by Tushingham and Peltier (1991), by using the spectral analysis first implemented by Mitrovica and Peltier (1991), appropriate for sea-level change calculations, as discussed in Chap. 6. The elastic lithosphere is 80 km thick, and both lithosphere and mantle are incompressible, as stated above, which means that density remains constant within each layer of the radially stratified Earth's model and that, at a fixed position in space, density changes can occur only via displacements of interfaces separating material

with different density. The lithosphere, the upper mantle, and the lower mantle are subdivided into thinner layers such that, taken collectively, these parts of the planet contain 31 layers whose physical properties are volumetrically averaged from realistic, seismologically retrieved Earth's stratification (Dziewonski and Anderson 1981): this stratification is realistic and is also used for some models of Chap. 4.

The vertical deformation represented by the colors is characterized by uplifting centres over deglaciated areas in North America, Northern Europe, and Antarctica, where ice-sheet complexes where located, in agreement with ICE-3G, and by subsidence in the periphery of these deglaciation centres. It should be recalled that these global deformation patterns represent, in terms of vertical and horizontal velocities in millimeter per year, the mathematical simulation of present-day deformation of the Earth, forced by ice-sheet disintegration during the Pleistocene, and is going on today because of the viscous memory of the Earth, as sketched by the dashpot in Fig. 1.2. The horizontal velocity field is characterized by two different components: a global one, directed northward or southward with respect to the Earth's equatorial region because of the suction effect of the mantle material towards the deglaciated regions of the Northern and Southern Hemispheres, and a regional one directed radially outward from the centre of the different deglaciation zones. The relative strengths of these components, as the intensity of vertical motions, depend on the viscosity ratio between the upper and lower mantle, as comparison of panel (b) and panel (a) shows. Increasing the viscosity in the lower mantle to 10^{22} Pa s, with respect to 10^{21} Pa s, makes mantle material more difficult to relax after deglaciation, which maintains larger horizontal and vertical velocities for the present-day situation, as portrayed in Fig. 5.12b. For lower-mantle viscosity of 10^{21} Pa s, it is remarkable that the outward horizontal velocity from deglaciation centres is larger than the global velocity due to material flow from the equatorial region of the mantle, particularly visible in North America. Increasing the lower-mantle viscosity makes the global flow from the equatorial region larger, as anticipated above, which in turn dampens, at deglaciation centres, the outward velocity directed towards the equator. This effect can be better visualized in Fig. 5.13, which focuses on PGR velocity patterns in Europe from Marotta and Sabadini (2002).

Figure 5.13 is an enlargement of the Fennoscandia region from Fig. 5.12, showing vertical and horizontal velocity fields in Europe for the two Earth's models introduced in Fig. 5.12, namely PGR-21 (a) and PGR-22 (b). Two different components of the horizontal velocity field can be distinguished, a global north-trending one, due to the suction effect of mantle material from the equator towards the deglaciated regions of the Northern Hemisphere, as anticipated above, and a regional one directed radially outward from the centre of deglaciation in the Gulf of Bothnia. Each component prevails over the other depending on the viscosity ratio between the upper and lower mantle. For PGR-21, top panel, the two deformation styles in the deglaciated region and in the far field are well separated, as indicated by the outward horizontal velocities of at most 0.6 mm/yr in proximity of the deglaciated region, and by

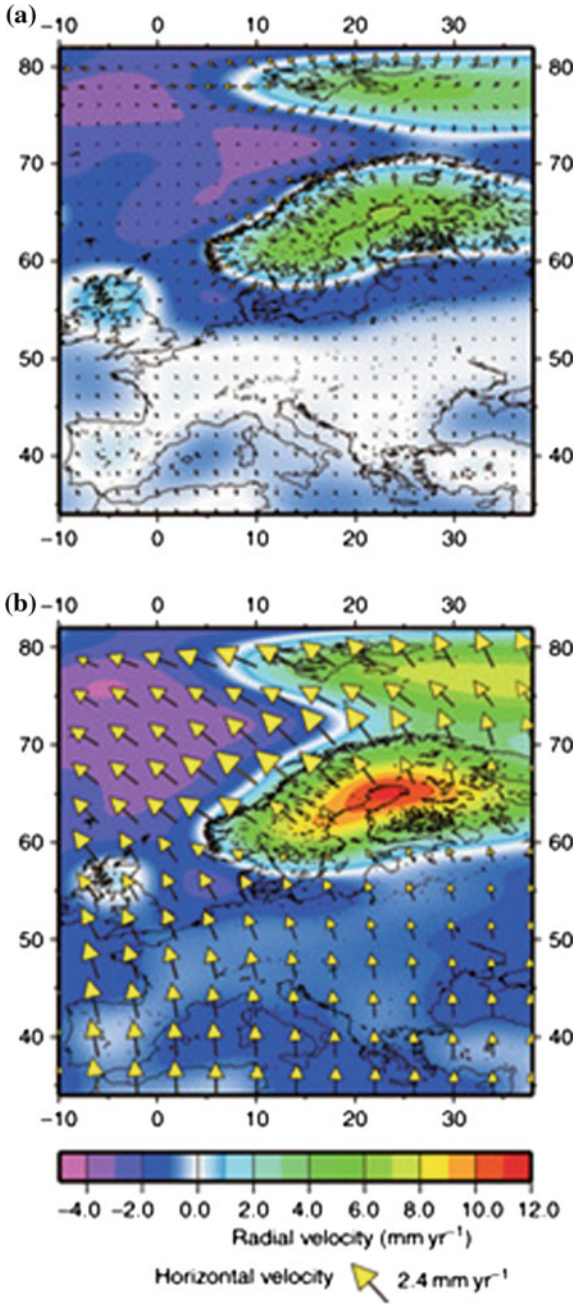

Fig. 5.13 **a**, **b** Enlargements of the European region from Fig. 5.12 (Fig. 2 in Marotta and Sabadini 2002)

the north-trending lower values, less than 0.2 mm/yr, in the far field. The vertical deformation is characterized by two uplifting centres in the north-eastern region where ice-sheet complexes were located. The Mediterranen region is affected by a subsidence of −1 mm/yr, which will become important in the sea-level calculations of Chap. 6, with the adjacent European continental region essentially unaffected by vertical motions. The deformation pattern portrayed in panels (a) of Figs. 5.12 and 5.13 agrees with the findings of Mitrovica et al. (1994) (their Fig. 3), except for the slightly smaller rates due to the overall reduction in the upper- and lower-mantle viscosity by a factor 2 in our case. For PGR-22, bottom panel, the high north-trending component of the horizontal velocity, exceeding the local outward velocity in the southern part of the deglaciation region, is caused by the larger global isostatic disequilibrium of the planet with respect to PGR-21 due to the higher viscosity. The latter induces a substantial increase in the horizontal velocity, up to 2.4 mm/yr in the north and 1.2–1.6 mm/yr in the far field. In comparison with the top panel, there is a notably substantial intensification of the uplift, affecting a wider region. Subsidence increases in the Mediterranean region to −2 mm/yr, extending its influence even in Central Europe, at a rate of −1 mm/yr. Generally speaking, these PGR patterns of 3-D deformation predicted by models have proved to be consistent among the various studies (James and Ivins 1997; Mitrovica et al. 1993).

5.4 The 2004 Sumatran and 2011 Tohoku-Oki Giant Earthquakes

Similar to surface and internal loads, also the mass redistribution caused by great earthquakes affects the Earth's gravity field in terms of long-wavelength permanent signatures, nowadays detectable by space gravity missions, as GRACE (Gross and Chao 2006): these gravity data provide new insights for understanding the physics of extreme natural events, such as the giant earthquakes of magnitude Mw higher than 8.5, which struck our planet in the past decade, the 2004 Sumatran (Han et al. 2006; Panet et al. 2007; Linage et al. 2009; Cambiotti et al. 2011; Broerse et al. 2011), the 2010 Maule (Han et al. 2010; Heki and Matsuo 2010) and the 2011 Tohoku-Oki (Matsuo and Heki 2011; Han et al. 2011; Cambiotti and Sabadini 2012; Zhou et al. 2012) earthquakes. These megathrust earthquakes occur within subduction environments of fast converging oceanic and continental plates, and cause volume changes of rocks in the region surrounding the fault, as well as deformation of the Earth's surface and internal layer boundaries carrying density contrasts. Due to the uplift of the ocean floor, they also displace ocean water away from the near field, causing a gravitational signature whose amplitude is comparable with that from mass rearrangement within the solid Earth (Linage et al. 2009; Cambiotti et al. 2011; Broerse et al. 2011).

5.4.1 Modeling the 2004 Sumatran Earthquake

The coseismic geoid and gravity anomalies from the 2004 Sumatran earthquake build on our new, compressible, self-gravitating Earth's model described in Sect. 3.8. This new model, based on PREM (Dziewonski and Anderson 1981), represents the elastic limit of viscoelastic models, recently used for post-glacial rebound studies (Cambiotti et al. 2010) and developed for coseismic studies by Smylie and Mansinha (1971) and Sun and Okubo (1993). Our approach differs from that followed by Gross and Chao (2006) and Linage et al. (2009), the latter using compressible models based on a free oscillation scheme. The gravitational part of the phenomenon is dealt with self-consistently and, in this respect, the modeling is similar to that used by Pollitz et al. (2006) for the study of postseismic relaxation following the 2004 Sumatran earthquake. The effects of compressibility are taken into account both in the initial state and during the perturbations (Cambiotti et al. 2010), on the basis of Runge-Kutta integration in the radial variable of the differential equations describing momentum conservation and self-gravitation, as described in Chap. 1. The gravitational effect of the sea-level feedback is important for the 2004 Sumatran earthquake (Linage et al. 2009) and is thus self-consistently included in the treatment of the global ocean layer of PREM. In this way, the approaches used by Han et al. (2006) and Linage et al. (2009) are refined in the results shown in this section although, from a quantitative point of view, the approach used in the present analysis does not significantly change the results presented by these authors. This novel theoretical treatment in the modeling is accompanied by new efforts in the treatment of the GRACE data time series that are aimed at optimizing the estimate of the coseismic gravitational component of the 2004 Sumatran earthquake, thus providing a realistic comparison between observations and models, as described in detail in Cambiotti et al. (2011). The 2004 Sumatran earthquake was one of the strongest non-periodic gravity variations that occurred at the Earth's surface in the last decade. However, the analysis of the earthquake signature in GRACE data is quite challenging because of the step-like shape of the phenomenon. Additional contamination may originate from other phenomena occurring in the Sumatran region, such as hydrological and residual ocean circulation cycles. Particular attention has thus been devoted at removing those signals other than the coseismic jump from GRACE data time series. Gravity data from GRACE are then exploited to help constraining the seismic source model of the 2004 Sumatran earthquake obtained by the multiple Centroid Momentum Tensor (CMT) source analysis of Tsai et al. (2005). In the following, in fact, the results are based on the seismic source model of Tsai et al. (2005), which is composed of five point-like sources with total seismic moment of 1.17×10^{23} Nm, and on the use of an isotropic 350 km Gaussian filtering (Wahr et al. 1998). Although more realistic slip distributions over the fault are typically used to explain seismic waves and ground motions from GPS (Ammon et al. 2005), the along strike five seismic source model used by Tsai et al. (2005) is used since at the limited spatial resolution of GRACE data the difference with respect to more realistic slip distributions is expected to be small. Slip distribution along dip affects instead the long wavelength seismic signal,

a sensitivity that can be used to obtain information about the depth at which the largest seismic moment has been released.

Figure 5.14 shows the coseismic geoid anomalies for our compressible self-gravitating Earth's model, after we eliminate (Fig. 5.14a) or we include (Fig. 5.14b) the 3 km thick ocean layer of PREM; these models are named S-PREM (Solid PREM) and O-PREM (Ocean PREM). In order to gain insight into the physics of the coseismic gravitational perturbations due to the 2004 Sumatran earthquake, particularly regarding the asymmetry between the negative and positive gravitational anomalies observed in GRACE data (Han et al. 2006; Linage et al. 2009) we consider the geoid anomalies rather than the gravity ones. This choice allows us to compare geoid anomalies and radial displacements in terms of sea level variations describing the water redistribution responsible for the sea-level feedback on the geoid anomalies themselves. The sea-level variation is in fact the difference between the geoid variation and the radial displacement of the sea-bottom.

To better isolate the main features of the coseismic phenomenon and the main physical processes affecting it, we focus out attention on the asymmetry coefficient AS, defined as the ratio between the absolute values of the minimum negative and maximum positive geoid anomalies. For S-PREM, maximum and minimum geoid anomalies are +2.57 and −2.28 mm, respectively, and the asymmetry coefficient is AS = 0.88. The bipolar shape of the geoid anomalies of S-PREM closely resembles that of the gravity anomalies of Sun and Okubo (1993), their Fig. 7, for a dip-slip source within a spherically symmetric, self-gravitating Earth's model as in the present case. The positive geoid anomaly is slightly higher in absolute value than the negative

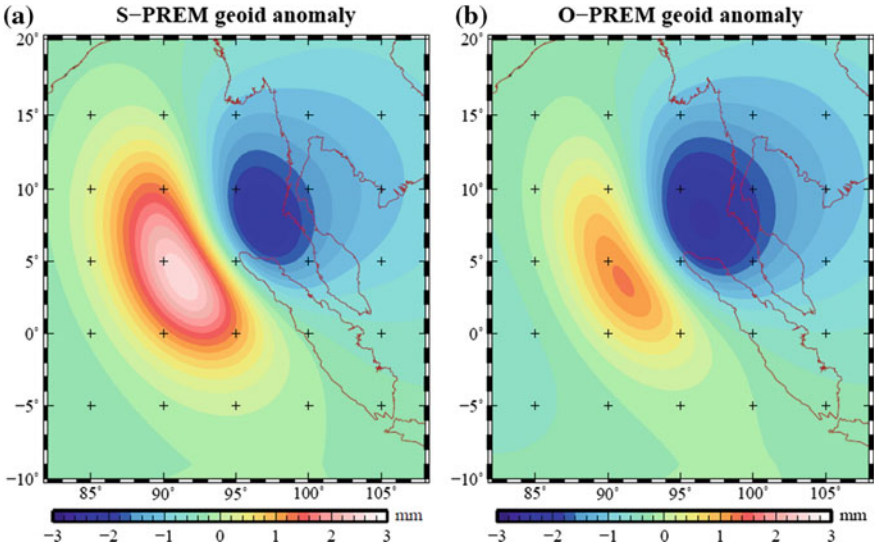

Fig. 5.14 Coseismic geoid anomalies for compressible. **a** S-PREM and **b** O-PREM, after the 350 km Gaussian filtering

one. For O-PREM maximum and minimum geoid anomalies of +1.24 and −2.52 mm are obtained leading to an asymmetry coefficient AS = 2.03.

Indeed, as shown in Fig. 5.15, the geoid anomalies due to the sea-level feedback, obtained by subtracting the geoid anomalies for O-PREM (Fig. 5.14b) from those for S-PREM (Fig. 5.14a), is negative almost everywhere and is of the same order of magnitude as the geoid anomalies for S-PREM, with a minimum value of −1.33 mm. In order to better understand this issue, in Fig. 5.16 we show the radial displacements at the solid Earth's surface for both S-PREM (Fig. 5.16a) and O-PREM (Fig. 5.16b), after the 350 km Gaussian filtering for the sake of comparison with the geoid anomalies shown in Fig. 5.14. Note that the predicted maximum uplift, +93.1 mm, has an absolute value that is much larger than the maximum down-drop, −18.3 mm, by about a factor of 5 for S-PREM. Furthermore, the loading due to water redistribution has a negligible effect on the radial displacement because the maximum uplift, +97.0 mm, and down-drop, −18.6 mm, for O-PREM differ from those for S-PREM by less than 3 %. These differences are, however, comparable with the geoid anomalies shown in Fig. 5.14. The radial displacement is larger than the geoid anomaly by almost two order of magnitude, indicating that the coseismic sea-level variation is mainly due to the variation of the topography rather than that of the geoid and that the uplifted crust displaces away the ocean water thus reducing the geoid anomalies in the near field of the Sumatran earthquake as visible from Fig. 5.14b compared to Fig. 5.14a, in agreement with Linage et al. (2009) who first suggested that the asymmetry towards the negative pole of the coseismic gravity anomalies observed in GRACE data is due the sea-level feedback.

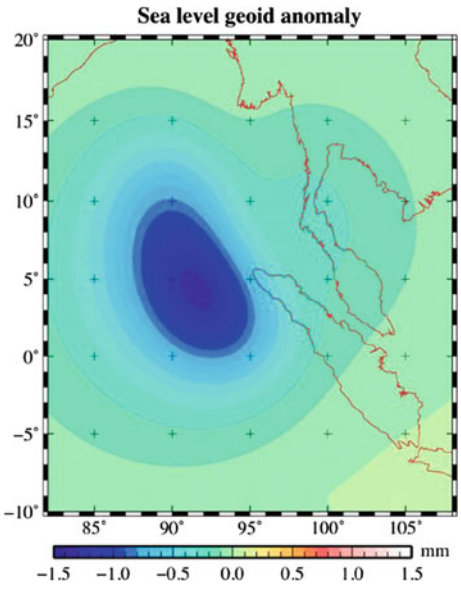

Fig. 5.15 Coseismic geoid anomalies due to the sea-level feedback, obtained by subtracting the compressible O-PREM and S-PREM geoid anomalies shown in Fig. 5.14, after the 350 km Gaussian filtering

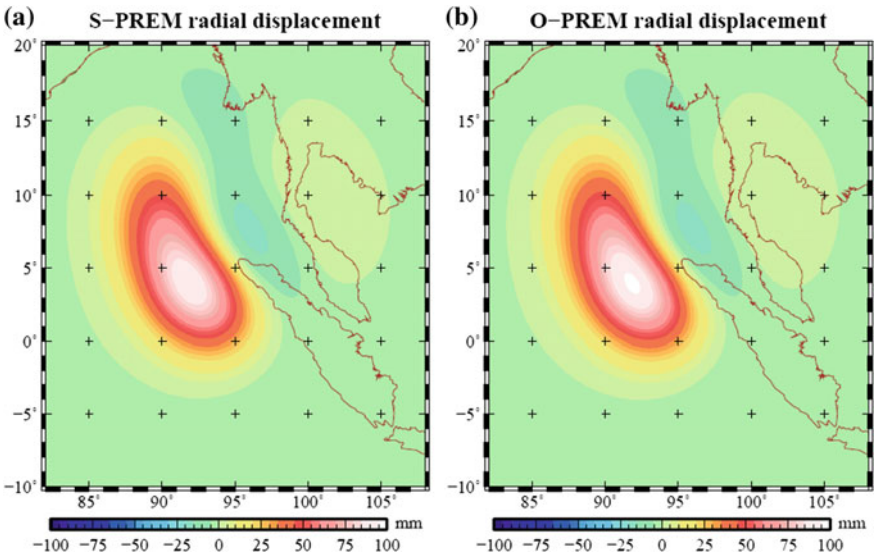

Fig. 5.16 Coseismic radial displacements for compressible **a** S-PREM and **b** O-PREM, after the 350 km Gaussian filtering for the sake of comparison with the geoid anomalies shown in Fig. 5.14 in terms of sea-level variations

5.4.2 The GRACE Data

The peculiar step-like shape of the signature due to an earthquake is quite difficult to resolve in gravitational data analyses using standard approaches. The time resolution of the GRACE data is the highest ever achieved by a satellite only campaign on gravity variations, but it still poorly resolves coseismic phenomena in detail. The 1-month time resolution is adequate, but it does not allow discrimination of very short time-scale phenomena and the coseismic signal is clearly contaminated by postseismic effects and by any other phenomena that occurred in the same geographical area during and immediately after the earthquake. Moreover, the peculiar noise of GRACE data, the so called stripes, is particularly strong at equatorial latitudes; thus, its typical north–south shape can affect the quality of the data in the Sumatran region. A good treatment of the stripes is therefore important. Among the various solutions proposed, we make use of the DDK3 anisotropic filtering described by Kusche (2007) and Kusche et al. (2009) to extract the earthquake gravity signal. Kusche et al. (2009) provide three anisotropic filters with different spatial resolutions. To better address the main features of the local scale signature of the 2004 Sumatran earthquake, the DDK3 filter is used at the highest spatial resolution. Depending on the comparison criterion, this filter is roughly equivalent to an isotropic Gaussian filter of about 240–330 km half width, close to the limit of the GRACE nominal resolution; the main features of the 2004 Sumatran earthquake as recorded in GRACE data are provided on the basis of the gravity anomaly representation in μGal. The

other natural choice, the geoid representation, which is more global, is prone to leakage of signals from nearby regions as for the case of hydrology: the gravity anomaly representation is less sensitive to this kind of contamination. GRACE Level 2 data have been processed and provided to the scientific community by three official analysis centres: the Centre for Space Research (CSR, University of Texas), the GeoForschungsZentrum (GFZ, Potsdam) and the Jet Propulsion Laboratory (JPL, California Institute of Technology). In order to optimize the information from these different solutions, the analysis is performed on the average of CSR and GFZ data, for each (common) month of the two time series (i.e. present in the series of both processing centres), although separate usage of the two time series is not expected to impact the results of the study. The average is done after applying the corrections prescribed to the Stokes coefficients of the two data sets and replacing the degree-2 order-0 Stokes coefficient with its more stable estimate from the Satellite Laser Ranging constellation satellites as recommended. The GFZ solution is truncated at the harmonic degree 60 in order to conform to the lower spatial resolution of the CSR solution. Figure 5.17 shows the original GRACE data time series in gravity anomaly representation (thin solid line, cross-shaped points) at the two points (94.2°E, 2.1°N) and (97.0°E, 7.7°N) in the south-west and north-east near field of the Sumatran trench. GRACE data time series are then smoothed in the time domain by means of a Gaussian filter, to reduce the variability due to seasonal and interannual signals due to hydrology from the continent and to the residual ocean circulation component present in the data, while preserving permanent co- and postseismic signatures and signals due to medium and long-period hydrological cycles of periods greater than 2 years. After the Gaussian smoothing in the time domain, black-solid line in Fig. 5.17, the latter shows evident long-term signals that cannot be considered as only coseismic jumps. Therefore, in order to remove these signals and to estimate only the coseismic jump, the smoothed time series are fitted by means of a coseismic discontinuity and a linear trend, representing the simplest approximation before implementing the exponential one. On this basis, Fig. 5.18 is generated, representing the coseismic jump, Fig. 5.18a and the postseismic signal, Fig. 5.18b. Figure 5.18 shows the estimated coseismic jump and postseismic contribution 5 years after the earthquake. The maximum coseismic gravity anomaly is $+6.1 \pm 1.5\,\mu$Gal and the minimum is $-12.7 \pm 0.9\,\mu$Gal at (95.6°E, 0.7°N) and (97.0°E, 6.3°N). The peak-to-peak coseismic jump is thus $+18.8 \pm 1.7\,\mu$Gal, while the asymmetry coefficient is $AS = 2.1 \pm 0.5$. The postseismic contribution can be as important as the coseismic one, with maximum, $+8.7 \pm 0.7\,\mu$Gal, and minimum, $-7.1 \pm 1.6\,\mu$Gal, values at (94.2°E, 4.9°N) and (99.8°E, 9.1°N).

5.4.3 Constraining the 2004 Sumatran Earthquake

In order to make the comparison between coseismic jump estimates from observations with those from models significant, it is important to apply the same spatial filter used to deal with GRACE data to models because the spatial features of the seismic

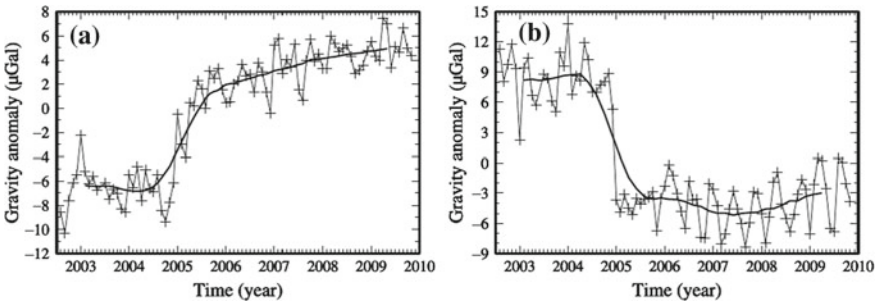

Fig. 5.17 Original (*thin solid lines*, *cross-shaped points*) and smoothed (*thick solid lines*) DDK3-filtered GRACE data time series at points (94.2°E, 2.1°N) and (97.0°E, 7.7°N), in the **a** south-west and **b** north-east near field of the Sumatran trench

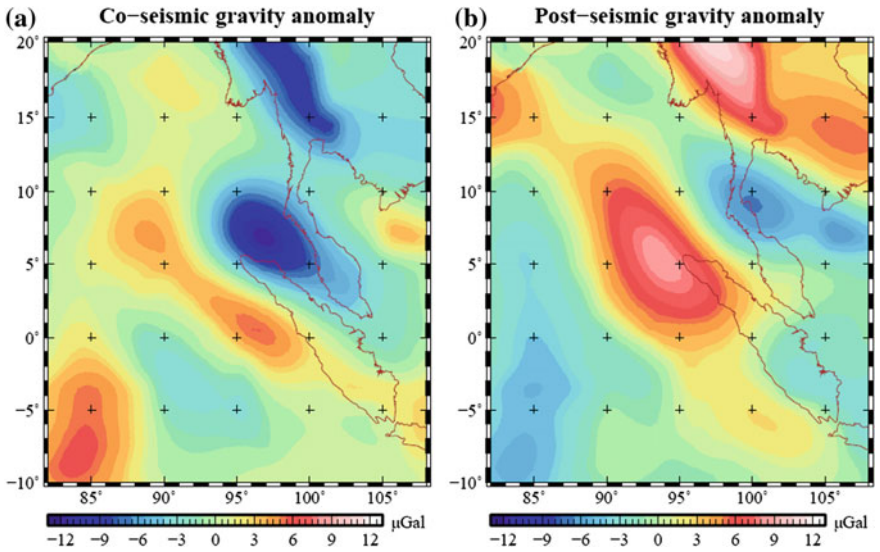

Fig. 5.18 Coseismic gravity anomalies, (**a**), and **b** postseismic contribution, 5 years after the earthquake obtained by the non-linear fitting to the smoothed DDK3-filtered GRACE data time series

signature make the gravity anomalies very sensitive to the type of filtering. The use of different filters would yield unphysical differences, which would make the comparison less effective. For this reason and owing to the easy implementation of the filter DDK3, made available by Kusche et al. (2009), DDK3-filtered CSR-GFZ solutions are compared with equivalently filtered coseismic models. To compare with the coseismic jump obtained from observations, Fig. 5.19a shows the coseismic gravity anomalies obtained for compressible O-PREM including the sea level feedback and based on the seismic source model of Tsai et al. (2005), after the DDK3 filtering. A maximum of +8.6 μGal and a minimum of −10.0 μGal gravity anomalies at points (92.8°E, 2.1°N) and (97.0°E, 6.3°N) are obtained in Fig. 5.19a from the modeling.

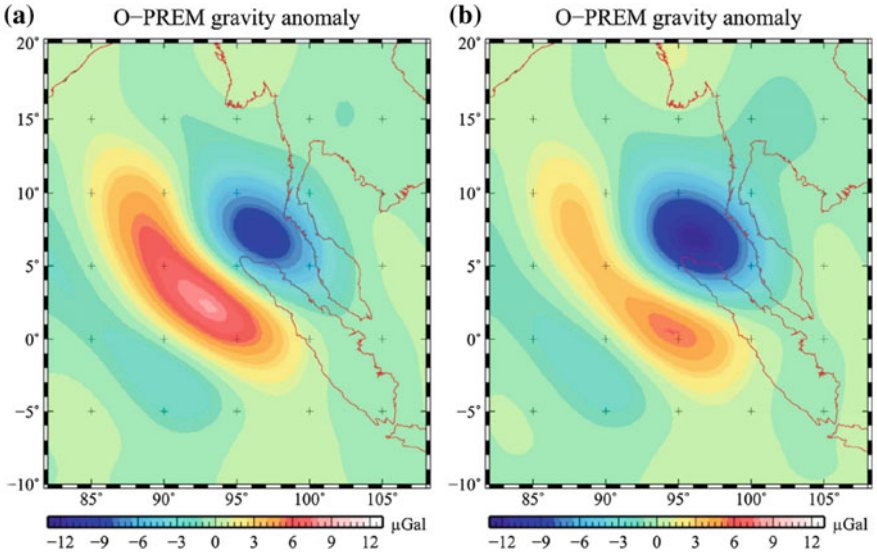

Fig. 5.19 DDK3-filtered coseismic gravity anomalies for compressible O-PREM, obtained using the **a** original and **b** modified seismic source models of Tsai et al. (2005), with source depth below, 25 km, and above, 15 km, the Moho discontinuity, respectively. The dip angles for the modified seismic source models have been increased by 50 %

The peak-to-peak gravity anomaly obtained from the model, +18.6 μGal, is in agreement, within one sigma error, with the observed one, +18.8 ±1.7 μGal, while the asymmetry coefficient AS = 1.2 differs from the observed one, AS = 2.1 ± 0.5, by about two-sigma error. The asymmetry coefficient AS depends mainly on the sea level feedback and the latter is sensitive to changes of the topography at the bottom of the ocean, which is in turn dependent on the depth of the source. Once we set at 15 km the depth of the source as in Fig. 5.19b, shallower than the original Tsai et al. (2005) solution at 25 km depth, the agreement with observations is improved. In this case, both the peak-to-peak gravity anomaly and the asymmetry coefficient AS from modeling match the best estimates from observations, 18.8 μGal and 2.1, suggesting that the physics of this giant earthquake is represented correctly.

Compressibility is an important feature of co-seismic perturbations, as shown in the following by comparing compressible and incompressible Earth's models in order to catch the role of compressibility in co-seismic studies. In Fig. 5.20 we compare DDK3-filtered co-seismic gravity anomalies for compressible (a) and incompressible (b) S-PREM by using the modified seismic source model. The peak-to-peak gravity anomalies are 22.8 and 23.4 μGal, while the asymmetry coefficients AS are 0.8 and 0.6, for compressible (a) and incompressible (b) S-PREM, respectively. The two bipolar patterns are asymmetric towards the positive co-seismic gravity anomaly, particularly in the incompressible case once compared to the compressible model. A detailed discussion on the shortcomings of incompressibility versus

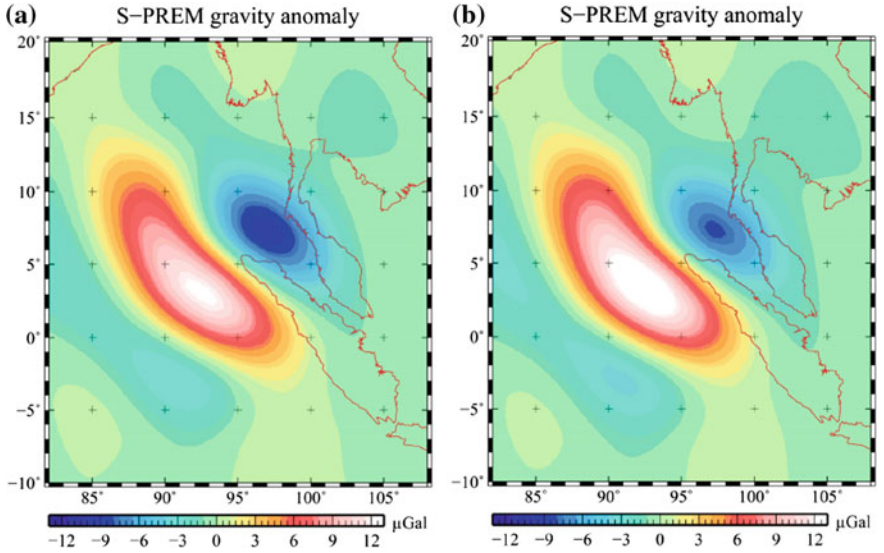

Fig. 5.20 **a** Compressible, **b** incompressible

realistic compressible Earth's models is found in Cambiotti et al. (2011), clearly showing the necessity of incorporating compressibility in co-seismic models, not only for these megathrust earthquakes. In particular, incompressibility severely affects the gravity anomaly caused by the sea-level feedback associated with the amount of sea water that is washed out from the epicentral region, which is of importance in order to correctly interpret the gravity patterns due to thrust earthquakes in oceanic environments.

5.4.4 The 2011 Tohoku-Oki Earthquake: Gravitational Seismology

A novel procedure for estimating the principal seismic source parameters (hypocentre and moment tensor) relying solely on space gravity data from GRACE and our new compressible Earth's model, has been applied for the first time to the 2011 Tohoku earthquake in Cambiotti and Sabadini (2013). It yields a seismic source model that is consistent with a thrust earthquake and geological information of the subduction zone, closely resembling the Global CMT (Centroid-Moment-Tensor) Project solution based on teleseismic wave inversion: the moment magnitude Mw is slightly higher, 9.13 ± 0.11 compared to the CMT 9.08 one, and the hypocentre is further offshore by about 40 km within the oceanic plate. This procedure has thus become an important tool in seismology, complementing centroid-moment-tensor analyses by

exploiting the new gravity data from GRACE. Within the context of a CMT solution, coseismic gravity changes is now modelled for a point-like seismic source by means of our compressible model described in Chap. 3 (Cambiotti et al. 2011) based on PREM (Dziewonski and Anderson 1981), as for the previous sections on the Sumatran eartquake, but with the crust and lithospheric mantle substituted by a regional average of CRUST2.0 (Bassin et al. 2000). Following the probabilistic approach to the nonlinear inverse problem by Mosengard and Tarantola (2002) and localizing in space the DDK3-filtered GRACE and synthetic gravity anomalies on the basis of the Slepian, optimally concentrated functions as described in Cambiotti and Sabadini (2012), the earthquake CMT parameters are obtained for the best model, thus providing the first self-consistent GCMT (Gravitational Centroid Moment Tensor) solution, as given in Table 5.4. The synthetic gravity pattern based on these inverted parameters is given in Fig. 5.21b, closely resembling that from GRACE data given in Fig. 5.21a. It is worthwhile to note that the bipolar shape of the gravity is the same of the 2004 Sumatran earthquake, with minima and maxima inverted with respect to Fig. 5.14b due to the opposite direction of plate convergence of the Indian and

Table 5.4 Best principal seismic source parameters of GCMT, global CMT project and USGS solutions

	GCMT	Global CMT Project	USGS
Hypocentre			
Depth (km)	16.1	20.0	10.0
Latitude	$37.75° \pm 0.46°$N	37.5°N	38.5°N
Longitude	$143.47° \pm 0.46°$E	143.1°E	142.6°E
Moment tensor (10^{22} N m)			
M_{rr}	2.45 ± 1.15	1.730	2.03
$M_{\theta\theta}$	-0.12 ± 0.70	−0.281	−0.16
$M_{\varphi\varphi}$	-2.33 ± 0.91	−1.450	−1.87
$M_{r\theta}$	2.17 ± 0.59	2.120	2.06
$M_{r\varphi}$	5.33 ± 0.95	4.550	3.49
$M_{\theta\varphi}$	-1.07 ± 0.31	−0.657	−0.60
Seismic moment (10^{22} N m)			
Double couple	6.32 ± 2.94	5.31	4.54
Residual dipoles	0.32 ± 0.55	0.01	−0.05
Moment magnitude			
Double couple	9.13 ± 0.11	9.08	9.04
Residual dipoles	8.34 ± 0.32	7.27	7.73
Fault plane geometry			
Dip	$12.2° \pm 3.1°$	10°	14°
Slip	$89.7° \pm 8.5°$	88°	68°
Strike	$201.9° \pm 7.8°$	203°	187°

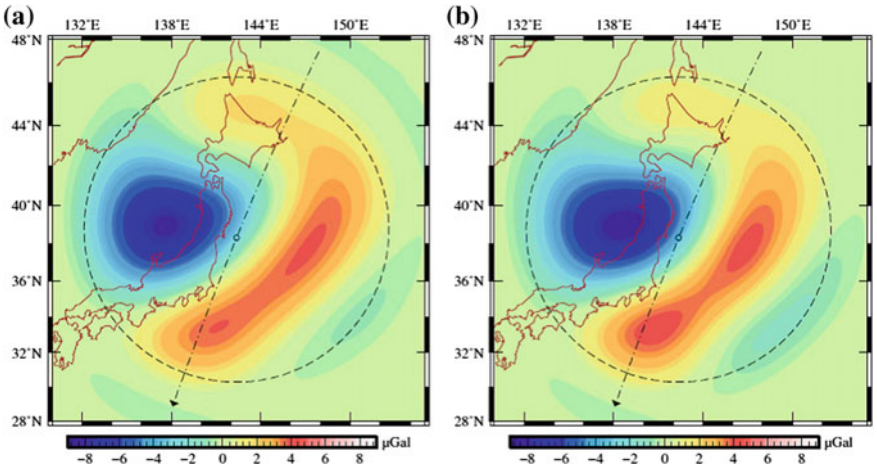

Fig. 5.21 Coseismic gravity anomalies **a** estimated from GRACE gravity data and **b** modeled using the GCMT solution, after DDK3 filtering and spatial localization within a *circular cup* (*dashed circle*) of half-width 8° and centered at the USGS mainshock

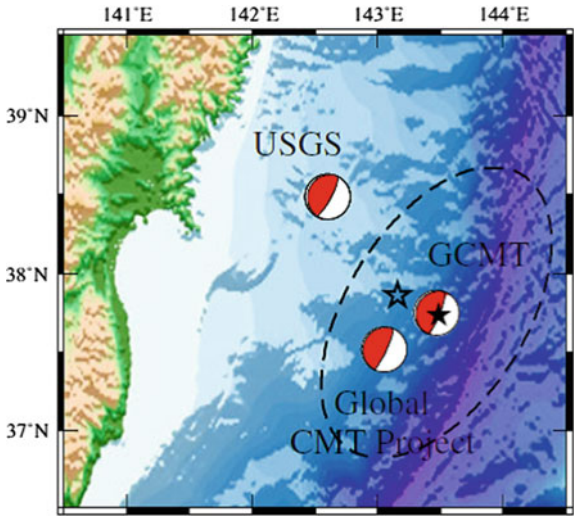

Fig. 5.22 GCMT, Global CMT Project and USGS focal mechanisms and mean epicentres within the crust and the lithospheric mantle (*white* and *black stars*, respectively). The *dashed ellipse* indicates the two-sigma errors of the GCMT solution

Pacific Oceans underneath Eurasia. The negative pole in the hanging-wall side has the minimum gravity anomaly of $-8.3 \pm 1.6\,\mu$Gal at (138.6° E, 38.9° N), and the positive pole in the foot-wall side that is characterized by two maxima of $+4.2 \pm 1.5$ μGal and $+4.1 \pm 1.1$ μGal at (140.8° E, 33.3° N), and (146.9° E, 37.8° N). Note that this two-dome structure of the positive pole in the offshore region is also present in the observations of Fig. 5.21a. It is due to the use of the anisotropic DDK3-filter and to the gravity reduction caused by ocean water removal from the uplifted crust,

a phenomenon that leaves two small domes, remnants of the broader and higher central positive pole caused by mass rearrangement of the solid Earth, as first shown in Cambiotti and Sabadini (2012).

Table 5.4 compares our solution, which we name Gravitational Centroid Moment Tensor (GCMT) solution, with two classical seismological CMT solutions, the Global CMT Project one and the USGS (United States Geological Survey) one. The GCMT and Global CMT Project solutions well agree with each other within one-sigma error: the GCMT moment magnitude $\mathrm{Mw} = 9.1 \pm 0.11$ is slightly higher compared to the 9.08 Global CMT Project solution. Our higher estimate of the moment magnitude may, in part, reflect the influence of afterslip in GRACE measurements. This afterslip is thought to be a substantial fraction of the seismic moment in the weeks following the main shock (Ozawa et al. 2011).

The GCMT solution instead differs from the USGS solution especially for the location of the epicentre, as shown in Fig. 5.22 and the geometry of the fault discontinuity. The USGS solution is indeed characterized by a strike angle of 187°, which is not well aligned with the local trench and by a significant along-strike component of slip, the rake angle being 68°.

References

Ammon, C.J., C. Ji, H.K. Thio, D. Robinson, S. Ni, V. Hjorleifsdottir, H. Kanamori, T. Lay, S. Das, D. Helmberger, G. Ichinose, J. Polet, and D. Wald (2005). "Rupture process of the 2004 Sumatra-Andaman earthquake". In: *Science* 308, pp. 1133–1139.

Barletta, V.R., R. Sabadini, and A. Bordoni (2008). "Isolating the PGR signal in the GRACE data: impact on mass balance estimates in Antarctica and Greenland". In: *Geophys. J. Int.* 172, pp. 18–30.

Bassin, C., G. Laske, and G. Masters (2000). "The current limits of resolution for surface wave tomography in North America". In: *EOS Trans. AGU* 81, pp. S12A–03.

Bentley, C.R. and M.B. Giovinetto (1991). "Mass balance of Antarctica and sea level change". In: *International Conference on the Role of Po-lar Regions in Global Change*. Ed. by C.L. Wilson G. Weller and B.A. Severin. Vol. II. University of Alaska, Fairbanks, AK, pp. 481–488.

Broerse, D.B.T., L.L.A. Vermeersen, R.E.M. Riva, and W. van der Wal (2011). "Ocean contribution to co-seismic crustal deformation and geoid anomalies: Application to the 2004 December 26 Sumatran-Andaman earthquake". In: *Earth Planet. Sci. Lett*. 305, pp. 341–349.

Cambiotti, G., A. Bordoni, R. Sabadini, and L. Colli (2011). "GRACE gravity data help constraining seismic models of the 2004 Sumatran earthquake". In: *J. Geophys. Res*. 116, p. B10403.

Cambiotti, G., Y. Ricard, and R. Sabadini (2010). "Ice age true polar wander in a compressible and non-hydrostatic Earth". In: *Geophys. J. Int*. 183, pp. 1248–1264.

Cambiotti, G. and R. Sabadini (2012). "A source model for the great 2011 Tohoku earthquake (MW = 9.1) from inversion of GRACE gravity data". In: *Earth Planet. Sci. Lett*. 335, pp. 72–79.

Cambiotti, G. and R. Sabadini (2013). "Gravitational seismology retrieving Centroid-Moment-Tensor solution of the 2011 Tohoku earthquake". In: *J. Geophys. Res*. 118, pp. 183–194.

Cazenave, A.A., P. Gegout, G. Ferhat, and R. Biancale (1996). "Temporal variations of the gravity field from Lageos 1 and Lageos 2 observations". In: *Global Gravity Field and Its Temporal Variations, IAG Symp*. Ed. By A.A. Cazenave R.H. Rapp and R.S. Nerem. Vol. 116. Springer Verlag, Berlin - New York, pp. 141–151.

Chen, J.L., C.R. Wilson, D.D. Blankenship, and B.D. Tapley (2006b). “Antarctic mass rates from GRACE”. In: *Geophys. Res. Lett*. 33, p. L11502.

Chen, J.L., C.R. Wilson, and B.D. Tapley (2006a). “Satellite gravity measurements confirm accelerated Melting of Greenland Ice sheet”. In: *Science* 313, p. 1958.

Cheng, M.K., R.J. Eanes, C.K. Shum, B.E. Schutz, and B.D. Tapley (1989). “Temporal variations in low-degree zonal harmonics from Starlette orbit analysis”. In: *Geophys. Res. Lett*. 16, pp. 393–396.

Cheng, M.K., C.K. Shum, and B.D. Tapley (1997). “Determination of longterm changes in the Earth’s gravity field from satellite laser ranging observations”. In: *J. Geophys. Res*. 102, pp. 22,377–22,390.

Devoti, R., V. Luceri, C. Sciarretta, G. Bianco, G. Di Donato, L.L.A. Vermeersen, and R. Sabadini (2001). “The SLR secular gravity variations and their impact on the inference of mantle rheology and lithospheric thickness”. In: *Geophys. Res. Lett*. 28, pp. 855–858.

Dziewonski, A.M. and D.L. Anderson (1981). “Preliminary reference Earth model”. In: *Phys. Earth Planet. Inter*. 25, pp. 297–356.

Eanes, R.J. (1995). “A study of temporal variations in Earth’s gravitational field using Lageos-1 laser range observations”. In: *CSR Report*. Vol. 95–8. University of Texas, Austin.

Forte, A.M. and J.X. Mitrovica (1996). “New inferences of mantle viscosity from joint inversion of long-wavelength mantle convection and postglacial rebound data”. In: *Geophys. Res. Lett*. 23, pp. 1147–1150.

Gegout, P. and A.A. Cazenave (1993). “Temporal variations of the Earth’s gravity field for 1985-1989 from Lageos”. In: *Geophys. J. Int*. 114, pp. 347–359.

Gross, R.S. and B.F. Chao (2006). “The rotational and gravitational signature of the December 26, 2004 Sumatran earthquake”. In: *Surv. Geo-phys*. 27, pp. 615–632.

Hager, B.H. (1984). “Subducted slabs and the geoid: Constraints on mantle rheology and flow”. In: *J. Geophys. Res*. 89, pp. 6003–6015.

Han, S.C., C.K Shum, M. Bevis, C. Ji, and C.Y. Kuo (2010). “Regional gravity decrease after the 2010 Maule (Chile) earthquake indicates largescale mass redistribution”. In: *Geophys. Res. Lett*. 37, p. LL23307.

Han, S.C., J. Sauber, and R. Riva (2011). “Contribution of satellite gravimetry to understanding seismic source processes of the 2011 Tohoku-Oki earthquake”. In: *Geophys. Res. Lett*. 38, p. L24312.

Han, S.C., C.K. Shum, M. Bevis, C. Ji, and C.Y. Kuo (2006). “Crustal dilatation observed by GRACE after the 2004 Sumatran-Andaman earthquake”. In: *Science* 313, pp. 658–662.

Heki, K. and K. Matsuo (2010). “Coseismic gravity changes of the 2010 earthquake in central Chile from satellite gravimetry”. In: *Geophys. Res. Lett*. 37, p. L24306.

Jacobs, S. (1992). “Is the Antarctic ice sheet growing?” In: *Nature* 360, pp. 29–33.

James, T.S. and E.R. Ivins (1997). “Global geodetic signatures of the Antarctic ice sheet”. In: *J. Geophys. Res*. 102, pp. 605–633.

Johnston, P. and K. Lambeck (1999). “Postglacial rebound and sea level contributions to changes in the geoid and the Earth’s rotation axis”. In: *Geophys. J. Int*. 136, pp. 537–558.

Kaufmann, G. (2000). “Ice-ocean mass balance during the Late Pleistocene glacial cycles in view of CHAMP and GRACE satellite missions”. In: *Geophys. J. Int*. 143, pp. 142–156.

Kusche, J. (2007). “Approximate decorrelation and non-isotropic smoothing of the time-variable GRACE-type gravity field models”. In: *J. Geod*. 81, pp. 733–749.

Kusche, J., R. Schmidt, S. Petrovic, and R. Rietbroek (2009). “Decorrelated GRACE time-variable gravity solutions by GFZ, and their validation using a Hydrological Model”. In: *J. Geod*. 83, pp. 903–913.

Linage, C. de, L. Rivera, J. Hinderer, J.P. Boy, Y. Rogister, S. Lambotte, and R. Biancale (2009). “Separation of coseismic and postseismic gravity changes for the 2004 Sumatran earthquake from 4.6 yr of GRACE observations and modelling of the coseismic change by normal mode summation”. In: *Geophys. J. Int*. 176, pp. 695–714.

Luthcke, S.B., H.J. Zwally, W. Abdalati, D.D. Rowlands, R.D. Ray, R.S. Nerem, F.G. Lemoine, J.J. McCarthy, and D.S. Chinn (2006). "Recent Greenland Ice mass loss by drainage system from satellite gravity observations". In: *Science* 314, pp. 1286–1289.

Marotta, A.M. and R. Sabadini (2002). "Tectonic versus glacial isostatic deformation in Europe". In: *Geophys. Res. Lett.* 29, pp. 73-1–73-4.

Marotta, A.M. (2003). "Benefits from GOCE within Solid Earth Geophysics". In: *Space Science Reviews* 108, pp. 95–104.

Matsuo, K. and K. Heki (2011). "Coseismic gravity changes of the 2011 Tohoku-Oki earthquake from satellite gravimetry". In: *Geophys. Res. Lett*. 38, p. L00G12.

McCarthy, D.D. and B.J. Luzum (1996). "Path of the mean rotational pole from 1899 to 1994". In: *Geophys. J. Int*. 25, pp. 623–629.

Mitrovica, J.X., J.L. Davis, and I.I. Shapiro (1993). "Constraining proposed combinations of ice history and Earth rheology using VLBI determined base-line length rates in North-America". In: *Geophys. Res. Lett*. 20, pp. 2387–2390.

Mitrovica, J.X., J.L. Davis, and I.I. Shapiro (1994). "A spectral formalism for computing 3-dimensional deformations due to surface loads. 2. Present-day Glacial Isostatic Adjustment". In: *J. Geophys. Res*. 99, pp. 7075–7101.

Mitrovica, J.X. and W.R. Peltier (1991). "On postglacial geoid subsidence over the equatorial oceans". In: *J. Geophys. Res*. 96, pp. 20,053–20,071.

Mitrovica, J.X. and W.R. Peltier (1993). "Present-day secular variations in the zonal harmonics of the Earth's geopotential". In: *J. Geophys. Res*. 98, pp. 4509–4526.

Mosengard, K. and A. Tarantola (2002). "Probabilistic Approach to Inverse Problems". In: *International Handbook of Earthquake & Engineering Seismology (Part A)*. Academic Press, pp. 237–265.

Nakada, M. and K. Lambeck (1989). "Late Pleistocene and Holocene sealevel change in the Australian region and mantle rheology". In: *Geophys. J. Int*. 96, pp. 497–517.

Nakada, M., J. Okuno, K. Lambeck, and A. Purcell (2015)."Viscosity structure of Earth's mantle inferred from rotational variations due to GIA process and recent melting events". In: *Geophys. J. Int.* 202, pp. 976–992.

Nerem, R.S. and S.M. Klosko (1996). "Secular variations of the zonal harmonics and polar motions as geophysical constraints". In: *Global Gravity Field and Its Temporal Variations*. Ed. by A.A. Cazenave R.H. Rapp and R.S. Nerem. Springer Verlag, Berlin - New York, pp. 152–163.

Oerlemans, J. (1991). "The mass balance of the Greenland ice sheet: sensitivity to climate change as revealed by energy balance modelling". In: *The Holocene* 1, pp. 40–49.

Ozawa, S., T. Nishimura, H. Munekane, H. Suito, T. Kobayashi, M. Tobita, and T. Imakiire (2012). "Preceding, coseismic, and postseismic slips of the 2011 Tohoku earthquake, Japan". In: *J. Geophys. Res*. 117, p. B07404.

Panet, I., V. Mikhailov, M. Diament, O. de Viron, G. King, F. Pollitz, M. Holschneider, and R. Biancale (2007). "Co-seismic and post-seismic signatures of tha Sumatra December 2004 and March 2005 earthquakes in GRACE satellite gravity". In: *Geophys. J. Int*. 171, pp. 171–190.

Pollitz, F.F., R. Bürgmann, and P. Banerjee (2006). "Post-seismic relaxation following the great 2004 Sumantran-Andaman earthquake on a compressible self-gravitating Earth". In: *Geophys. J. Int*. 167, pp. 397–420.

Ricard, Y., G. Spada, and R. Sabadini (1993). "Polar wandering of a dynamic Earth". In: *Geophys. J. Int*. 113, pp. 284–298.

Rubincam, D.P. (1984). "Postglacial rebound observed by LAGEOS and the effective viscosity of the lower mantle". In: *J. Geophys. Res*. 89, pp. 1077–1087.

Sabadini, R. and D.A. Yuen (1989). "Mantle stratification and long-term polar wander". In: *Nature* 339, pp. 373–375.

Schutz, B.E., M.K. Cheng, R.J. Eanes, C.K. Shum, and B.D. Tapley (1993). "Geodynamic results from Starlette orbit analysis". In: *Contributions of Space Geodesy to Geodynamics: Earth Dynamics*. Ed. by D.E. Smith and D.L. Turcotte. Vol. 24. AGU Geodynamics Series, p. 175.

Smylie, D.E. and L. Mansinha (1971). "The elasticity theory of dislocations in real earth models and changes in the rotation of the earth". In: *Geophys. J. Roy. Astron. Soc*. 23, pp. 329–354.

Sun, W. and S. Okubo (1993). "Surface potential and gravity changes due to internal dislocations in a spherical Earth, 1, Theory for a point dislocation". In: *Geophys. J. Int*. 114, pp. 569–592.

Tosi, N., R. Sabadini, A.M. Marotta, and L.L.A. Vermeersen (2005). "Simultaneous inversion for the Earth's mantle viscosity and ice mass imbalance in Antarctica and Greenland". In: *J. Geophys. Res*. 110, p. B07402.

Tsai, V.C., M. Nettles, G. Ekstrom, and A.M. Dziewonsi (2005). "Multiple CMT source analysis of the 2004 Sumatran earthquake". In: *Geophys. Res. Lett*. 32, p. L17304.

Tushingham, A.M. and W.R. Peltier (1991). "ICE-3G: A new global model of late Pleistocene deglaciation based upon geophysical predications of postglacial relative sea level change". In: *J. Geophys. Res*. 96, pp. 4497–4523.

Velicogna, I. and J.Wahr (2002). "Postglacial rebound and Earth's viscosity structure from GRACE". In: *J. Geophys. Res*. 107(B12).

Velicogna, I. and J. Wahr (2005). "Greenland mass balance from GRACE". In: *Geophys. Res. Lett*. 32, p. L18505.

Velicogna, I. and J. Wahr (2006a). "Measurement of time-variable gravity show mass loss in Antarctica". In: *Science* 311, p. 1754.

Velicogna, I. and J. Wahr (2006b). "Acceleration of Greenland ice mass loss in spring 2004". In: *Nature* 443, p. 329.

Vermeersen, L.L.A., A. Fournier, and R. Sabadini (1997). "Changes in rotation induced by Pleistocene ice masses with stratified analytical Earth models". In: *J. Geophys. Res*. 102, pp. 27,689–27,702.

Vermeersen, L.L.A., R. Sabadini, R. Devoti, V. Luceri, P. Rutigliano, C. Sciarretta, and G. Bianco (1998). "Mantle viscosity inferences from joint inversion of Pleistocene deglaciation-induced changes in geopotential with a new SLR analysis and polar wander". In: *Geophys. Res. Lett*. 25, pp. 4261–4264.

Wahr, J., M. Molenaar, and F. Bryan (1998). "Time variability of the Earth's gravity field: Hydrological and oceanic effects and their possible detection using GRACE". In: *J. Geophys. Res*. 108, pp. 30,205–30,229.

Wahr, J.M. and J.L. Davis (2002). "Geodetic constraints on glacial isostatic adjustment". In: *Ice Sheets, Sea Level and the Dynamic Earth*. Ed. By J.X. Mitrovica and L.L.A. Vermeersen. Vol. 29. AGU Geodynamics Series, pp. 3–32.

Warrick, R.A., Le Provost, C., Meier, M.F., Oerlemans, J. and P.L. Woodworth (1996) "Changes in sealevel" In: Climate Change 1995: the science of climate change, J.T. Houghtou, L.G. Meira Filho, B.A. Callender, N. Harris, A. Kattenberg and K. Maskell (eds). Cambridge Univ. Press, Cambridge, pp. 359–405.

Wingham, D.J., A.J. Ridout, R. Scharroo, R.J. Arthern, and C.K. Shum (1998). "Antarctic elevation change 1992 to 1996". In: *Science* 282, pp. 456–458.

Yoder, C.F., J.G. Williams, J.O. Dickey, B.E. Schutz, B.J. Eanes, and B.D. Tapley (1983). "Secular variation of the Earth's gravitational harmonic J2 coefficient from Lageos and non tidal acceleration of Earth rotation". In: *Nature* 303, pp. 757–762.

Zhou, X., W. Sun, G. Zhao, G. Fu, J. Dong, and Nie Z. (2012). "Geodetic observations detecting coseismic displacements and gravity changes caused by the Mw=9.0 Tohoku-Oki earthquake". In: *J. Geophys. Res.* 117, p. B05408. 355.

Chapter 6
Sea-Level Changes

Abstract Sea-level changes, geoid and gravity anomalies due to PGR are first considered on the global scale. The effects of TPW on sea-level changes is studied, focusing on the effects of radial viscosity variations in the mantle. The Mediterranean Sea is then taken as a test area to simulate the simultaneous effects on sea-level changes from PGR and active tectonics. The first, self-consistent simulations of sea-level changes due to subduction within a viscoelastic framework are also provided, to enlighten the effects on sea-level changes due to the transient relative motion between the geoid surface and the sea-bottom topography, for the global subduction pattern.

6.1 The Issue of Sea-Level Change, a Present-Day Concern

To the general public it seems a rather obvious fact that if the ice sheets of Antarctica and Greenland melted, sea level would rise. In fact, there is wide-spread concern that global warming of the Earth might induce melt of the present-day large ice sheets and thereby induce a global sea-level rise, leading to flooding of lowlands. Although the link between ice melt and sea-level rise might seem obvious, the relation between ice mass changes and sea-level variations is more complicated. It might sound strange when one first hears about it, but ice melt could actually induce a sea-level drop at some places on the Earth's surface. And perhaps it is even more surprising that this has been known for more than a century.

In this oversimplified picture of ice melt and sea-level rise we neglect that ice has mass. Mass has the property of attracting other masses around it. So an ice sheet on a continent attracts the water of the oceans. Thus, the water near an ice sheet will be elevated with respect to a situation in which this gravitational interaction does not occur. If the ice sheet melts, this gravitational attraction effect, or self-gravitation, disappears too. Woodward (1998) showed that it is not a small, negligible effect. He derived the following formula for the ratio of the change in sea level with self-gravitation taken into account and the sea-level change without the self-gravitation of the ice sheet taken into account. If the ice sheet, modeled as a point source, were to melt, this ratio is:

R. Sabadini et al., *Global Dynamics of the Earth: Applications of Viscoelastic Relaxation Theory to Solid-Earth and Planetary Geophysics*,
DOI 10.1007/978-94-017-7552-6_6

$$\left(\frac{1}{2\sin(\theta/2)} - 1 - \frac{\rho_E}{3\rho_w}\right) / \frac{\rho_E}{3\rho_w}. \tag{6.1}$$

In Eq. (6.1) θ is the angular distance from the ice sheet, ρ_E the mean density of the Earth, and ρ_w the density of the water. Equation (6.1) shows that the ratio is not dependent on the total mass of the ice sheet. A derivation of Eq. (6.1) can also be found in Farrell and Clark (1976). From Eq. (6.1) one can easily compute that sea level will drop in the oceans as a result of ice melt within a distance of about 20° (on the Earth's surface equal to about 2200 km) from the former ice sheet. Even within 60° (equal to about 6700 km), sea level will rise less than if the amount of water from the ice sheet had been distributed uniformly ('eustatically') over the oceans. But, on the other hand, at distances exceeding 60° sea level will rise more than the eustatic value. So if all the Greenland ice were concentrated on the southern tip of Greenland and were to melt, then the effect of self-gravitation would cause a sea-level drop at the coast of Iceland, a smaller sea-level rise than the eustatic one at the coast near New York and a larger sea-level rise than the eustatic one at the coast of Australia.

The relation between ice melt and sea-level change is clearly not so simple as we generally might think. Although the total amount of ice that melts is equal to the total amount of water that is added to the oceans, the redistribution of the melt water is not uniform. The situation becomes even more complicated if one considers the fact that the solid Earth is not rigid. Placing a load on the Earth's surface will cause an immediate (elastic) subsidence of the surface underneath the load, followed by a time-dependent and spatially dependent subsidence and uplift pattern caused by viscoelastic flow in the Earth's interior, as we have learned from Chaps. 1 and 2. This implies that if ice and water are redistributed over the Earth's surface, the solid Earth will react to it. Solid-Earth deformation due to a changed surface load can still be observed today in Canada and Scandinavia. Some 10,000 years ago the last of the great Ice Ages ended with the melt-down of the Laurentide and Fennoscandian ice sheet complexes, which covered these regions with a maximum height of about 3 km. Today the Earth is still rebounding to the disappearance of the Pleistocene ice-sheets, with maximum uplift rates of about 1 cm per year near the center of the Bothnic Gulf and near the south of Hudson Bay. So the relation ice melt = sea-level rise, which we have had to modify because of the effect of self-gravitation, must be expanded to a three-component relation (continental) ice/sea level/solid Earth. Ice melt will cause a sea-level change and both components will induce solid-Earth deformation. But solid-Earth deformation in turn will induce a sea-level change again. Whereupon this sea-level change will induce solid-Earth deformation, and so on. It is clear that this relationship is a non-linear one. The formulations for this relationship were derived in the 1970s and have become known as the 'sea-level equation', which is an integral equation. In a very condensed form the equation for the relative sea-level change reads (Farrell and Clark 1976)

$$S = \rho_I \frac{\phi}{g} * L + \rho_w \frac{\phi}{g} * S + C, \tag{6.2}$$

in which S denotes the change in sea level, L the change in (continental) ice thickness, ϕ the Green function for the variation in the gravitational potential, ρ_I the density of the ice and g the surface gravity. C is a constant which is to be determined by invoking the condition that the total amount of ice change is equal to the total amount of sea-level change. The asterisk denotes time convolution. Note that the sea-level change S is both on the left-hand side and on the right-hand side of Eq. (6.2).

With this sea-level equation, by which the sea-level change and solid Earth's deformation interrelationship as function of ice mass variations (and solid Earth's models) can be handled, present-day sea-level variations can be modeled adequately, both for sea-level changes due to Pleistocene deglaciation and to recent continental ice mass changes (Farrell and Clark 1976; Peltier and Andrews 1976; Wu and Peltier 1983; Nakada and Lambeck 1987; Lambeck et al. 1990; Mitrovica and Peltier 1991; Johnston 1993; Di Donato et al. 2000; Mitrovica and Vermeersen 2002).

Melting ice causes a redistribution of mass of the rotating Earth. A redistribution of mass affects the moments and products of inertia. A deformable rotating body will react to such changes by adjusting rotation rate and position of its rotation axis with respect to the body's geography. For the Earth it implies that the three components ice-mass changes/sea level variations/solid Earth's deformation will affect the Earth's rotation. But changes in the Earth's rotation in turn could affect the three components again, as described in Chap. 3. Sea level and solid-Earth deformation can be affected by the change in centrifugal force accompanying rotation changes. Ice can be affected as a redistribution of mass of a rotating body will generally affect the position of the rotation axis with respect to the body's geography, so the position of the latter with respect to the Sun (the position of the rotation axis does not change with respect to its surroundings: to an outside observer it looks as if the body is shifting underneath its rotation axis, while the rotation axis remains fixed with respect to the inertial system of its surroundings). For the Earth this implies that the distribution of oceans and (partly ice-covered) land over the planet's surface will change with respect to the plane of the Earth's orbit around the Sun, although the angle of the rotation axis with respect to this plane remains fixed. Such a global shift can induce changes in the ocean's currents, enhance or reduce the amount of continental areas around the poles available for ice to settle on, and increase or decrease ice melt due to changes in insolation angle. It is clear that in order to be self-consistent we have to extend the three-component relationship ice/sea level/solid Earth's deformation with a fourth component: polar wander.

6.2 Sea-Level Variations, Geoid and Gravity Anomalies Due To Pleistocene Deglaciation

The importance of Pleistocene deglaciation on the interpretation of sea-level variabilities has been addressed by several authors. For example, Lambeck and Nakiboglu (1984) find that post glacial rebound may contribute between 30 and 50 % of the

present-day secular rise in sea level of 1.8 mm/yr (Douglas 1995). Although there are many uncertainties in estimating such a percentage, such figures show the potential importance of including solid-Earth deformation processes in studies on sea-level variations.

Both the absolute value of the contemporary global (eustatic) sea-level rise and the effect that PGR has on contemporary sea-level variations are not well known at the moment. Whereas the former is mainly a matter of measurements, the uncertainty in the contribution that post-glacial rebound has on present-day global sea-level variations is mainly due to insufficient knowledge about the Pleistocene ice sheets and the rheological properties of the Earth. However, differences in modeling approaches for establishing the relationship between PGR and sea-level variations can also be a source of discrepancies.

The results shown in this chapter make use, for the first time in glacial-rebound induced sea-level studies, of an analytical scheme described in previous chapters in dealing with stratified, incompressible Earth's models.

6.2.1 Mathematical Formulation

In the present analysis we show some results mainly focussed on the sensitivity of density and viscosity stratification in sea-level modeling.

The sea-level variations and geoid are based on the following equations, in relation to the herein defined Green functions Φ and Γ for the gravitational potential perturbation and radial displacement of the solid surface.

The geoid anomaly G and the vertical displacement R are given by Mitrovica and Peltier (1989), whose expressions are reproduced to adapt our formalism to their sea-level change theory

$$G(\theta, \varphi, t) = \frac{1}{g} \int_{-\infty}^{t} \iint_{\Omega} a^2 \, \sigma(\theta', \varphi', t') \, \Phi(\gamma, t - t') \, d\Omega' \, dt' \tag{6.3}$$

$$R(\theta, \varphi, t) = \int_{-\infty}^{t} \iint_{\Omega} a^2 \, \sigma(\theta', \varphi', t') \, \Gamma(\gamma, t - t') \, d\Omega' \, dt' \tag{6.4}$$

where a is the mean radius of the Earth, g is the gravity, γ represents the angular distance between the impulse load point (θ, φ') and the observation point (say θ, φ), t is the time, Ω represents the complete solid angle and σ is the surface load whose spherical harmonic coefficients are

$$\sigma_{\ell m}(t) = \sum_{n=1}^{N} \delta\sigma_{\ell m}^{n} H(t - t_n), \tag{6.5}$$

with N denoting the number of time steps in which the surface load is subject to a change; H is the Heaviside step function and

$$\delta\sigma_{\ell m}^{n} = \rho_I \delta I_{\ell m}^{n} + \rho_W \delta S_{\ell m}^{n,e}, \tag{6.6}$$

where ρ_I and ρ_W are, respectively, the densities of ice and water, $\delta I_{\ell m}^{n}$ and $\delta S_{\ell m}^{n,e}$ denote the spherical harmonic coefficients of the increments in the ice masses and eustatic sea level at the various time steps

$$\delta S_{\ell m}^{n,e} = \frac{\rho_I}{\rho_W} \frac{4\pi a^2}{A_o} \delta I_{00}^{n} C_{\ell m}, \tag{6.7}$$

where $C_{\ell m}$ are the spherical harmonic coefficients of the ocean function, defined to be unity over the ocean and zero over the remaining surface of the Earth, and A_o is the present area of the oceans; Eq. (6.7) is Eq. (53) in Mitrovica and Peltier (1991).

The Green functions Φ, Γ are given by

$$\Phi(\gamma, t) = \frac{ag}{M_E} \sum_{\ell=0}^{\infty} \left\{ (1 + k_{\ell e}^{L}) \delta(t) + \sum_{j=1}^{M} k_{\ell j}^{L} \exp(s_{\ell j} t) \right\} P_\ell(\cos\gamma), \tag{6.8}$$

$$\Gamma(\gamma, t) = \frac{a}{M_E} \sum_{\ell=0}^{\infty} \left\{ h_{\ell e}^{L} \delta(t) + \sum_{j=1}^{M} h_{\ell j}^{L} \exp(s_{\ell j} t) \right\} P_\ell(\cos\gamma) \tag{6.9}$$

which are Eq. (8) by Mitrovica and Peltier (1991), except Eq. (6.8) includes the direct effect of the load, namely the term 1 in the first brackets; $P_\ell(\gamma)$ is the Legendre polynomial given by Eq. (1.68), M_E is the mass of the Earth, δ is the Dirac delta function and $k_{\ell e}^{L}$, $h_{\ell e}^{L}$ denote the spherical harmonic components of the elastic load Love numbers for the perturbation to the gravitational potential and the radial displacement, defined in Eqs. (1.179) and (1.180). The terms $k_{\ell j}^{L}$, $h_{\ell j}^{L}$ represent the viscous components of the same numbers for the individual modes j with negative inverse relaxation times $s_{\ell j}$, with the ℓ dependence explicitly given.

Solving the integration in time and over the surface of the Earth in Eqs. (6.3) and (6.4) yields

$$G(\theta, \varphi, t) = G^{E}(\theta, \varphi, t) + G^{V}(\theta, \varphi, t) \tag{6.10}$$

$$R(\theta, \varphi, t) = R^{E}(\theta, \varphi, t) + R^{V}(\theta, \varphi, t) \tag{6.11}$$

where the superscripts E and V denote the elastic and viscous components, as given below (Di Donato et al. 2000)

$$G^E(\theta,\varphi,t) = \frac{4\pi a^3}{M_E}\sum_{\ell=2}^{\infty}\frac{(1+k^L_{\ell e})}{(2\ell+1)}\sum_{m=-\ell}^{\ell}\sigma_{\ell m}(t)Y_{\ell m}(\theta,\varphi) \tag{6.12}$$

$$R^E(\theta,\varphi,t) = \frac{4\pi a^3}{M_E}\sum_{\ell=2}^{\infty}\frac{h^L_{\ell e}}{(2\ell+1)}\sum_{m=-\ell}^{\ell}\sigma_{\ell m}(t)Y_{\ell m}(\theta,\varphi) \tag{6.13}$$

$$G^V(\theta,\varphi,t) = \frac{4\pi a^3}{M_E}\sum_{\ell,m}\left\{\sum_{j=1}^{M}\frac{k^L_{\ell j}}{(-s_{\ell j})(2\ell+1)}\sum_{n=1}^{N}\delta\sigma^n_{\ell m}\left[1-\exp\left(s_{\ell j}(t-t_n)\right)\right]\right\}Y_{\ell m}(\theta,\varphi) \tag{6.14}$$

$$R^V(\theta,\varphi,t) = \frac{4\pi a^3}{M_E}\sum_{\ell,m}\left\{\sum_{j=1}^{M}\frac{h^L_{\ell j}}{(-s_{\ell j})(2\ell+1)}\sum_{n=1}^{N}\delta\sigma^n_{\ell m}\left[1-\exp\left(s_{\ell j}(t-t_n)\right)\right]\right\}Y_{\ell m}(\theta,\varphi), \tag{6.15}$$

with $Y_{\ell m}$ given in Eq. (1.67).

The relative sea-level change, which will be denoted by RSL from now on instead of S as in Mitrovica and Peltier (1989), is the difference between the changes in the geoid and radial displacement projected over the surface of the oceans (Farrell and Clark 1976), namely

$$RSL(\theta,\varphi,t) = C(\theta,\varphi)\left(G(\theta,\varphi,t) - R(\theta,\varphi,t)\right) \tag{6.16}$$

The sea-level change has the following explicit expression (Eq. (18) in Di Donato et al. (2000))

$$RSL(\theta,\varphi,t) = C(\theta,\varphi)\sum_{\ell,m}\left\{E_\ell\, T_\ell\, \sigma_{\ell m}(t) + T_\ell\sum_{n=1}^{N}\delta\sigma^n_{\ell m}\,\beta_\ell(t-t_n)\right\}Y_{\ell m}(\theta,\varphi), \tag{6.17}$$

with

$$E_\ell = 1 + k^E_\ell - h^E_\ell \tag{6.18}$$

$$\beta_\ell(t-t_n) = \sum_{j=1}^{M}\frac{(k^L_{\ell j} - h^L_{\ell j})}{(-s_{\ell j})}\left[1-\exp\left(s_{\ell j}(t-t_n)\right)\right], \tag{6.19}$$

$$T_\ell = \frac{4\pi a^3}{M_E(2\ell+1)}. \tag{6.20}$$

Equations (6.18), (6.19) and (6.20) are Eqs. (16) and (22) in Mitrovica and Peltier (1991).

The self-consistent sea-level calculation requires the solution of an integro-differential equation that can be solved by means of the pseudo-spectral approach first outlined and implemented by Mitrovica and Peltier (1991), where a detailed and clear discussion of the method can be found. The sea-level rates due to glacial isostatic adjustment that we present here have been calculated by means of this formalism, while the geoid computations are based on the so-called eustatic approximation in which the water is distributed uniformly in the oceans (Wu and Peltier 1983). In order to make estimates of the geoid and free-air gravity anomalies due to post-glacial rebound, the eustatic approximation is certainly satisfactory as these global signatures are relatively insensitive to the detailed history of water redistribution in the oceans.

6.2.2 *Sea-Level Variations, the Geoid and Free-Air Gravity Anomalies*

In the computations that follow, 5- and 31-layer incompressible Earth's models are considered, Eqs. (2.42)–(2.47), whose parameters will be those in Tables 4.2 and 4.3. The lithospheric thickness is fixed at 120 km and the upper mantle viscosity at 10^{21} Pa s, while the viscosity of the lower mantle will be 10^{21} Pa s for model 1, 5×10^{21} Pa s for model 2 and 10^{22} Pa s for model 3. Models 1 and 3 represent two end-members for a homogeneous and stratified mantle, while model 2 is an intermediate case. Model 3 is in closer agreement with mantle convection results (Ricard and Vigny 1989) and with the $\dot{J}_\ell$ results from the SLR analyses of Chap. 5.

For the loading history, the ICE-3G model by Tushingham and Peltier (1991), shown in Fig. 4.3, is adopted. In the calculations of the geoid and gravity anomalies, summation is carried up to degree 80. This is a truncation high enough to estimate the major signal and its pattern.

Figure 6.1 provides the present-day geoid anomaly due to Pleistocene deglaciation for the 5-layer Earth's model 1. The peak anomalies of -9, -4 and -10 m are located over Hudson Bay, the Gulf of Bothnia and the Antarctic region, respectively, where the largest ice sheets were located. As already observed by Mitrovica and Peltier (1989) for the northern regions, these anomalies are comparable with the observed geoid in the range of harmonic degrees $10 < \ell < 22$. Longer wavelengths are in fact correlated with geoid anomalies due to mantle convection (Mitrovica and Peltier 1989). The pattern of geoid anomalies is rather smooth, in agreement with the dominant low frequency content of geopotential perturbation. This issue will be considered later on when dealing with gravity anomalies and their richer content at high harmonic degrees. A remarkable feature of this geoid is the positive anomaly of about 1 m located in the Atlantic and Pacific oceans, clearly due to the mantle material which has flowed away from the glaciated regions during the phase of glaciation towards the equatorial regions. In these oceanic regions, where the geoid anomaly is positive, the present-day rates of change of the geoid predicted by Mitrovica and

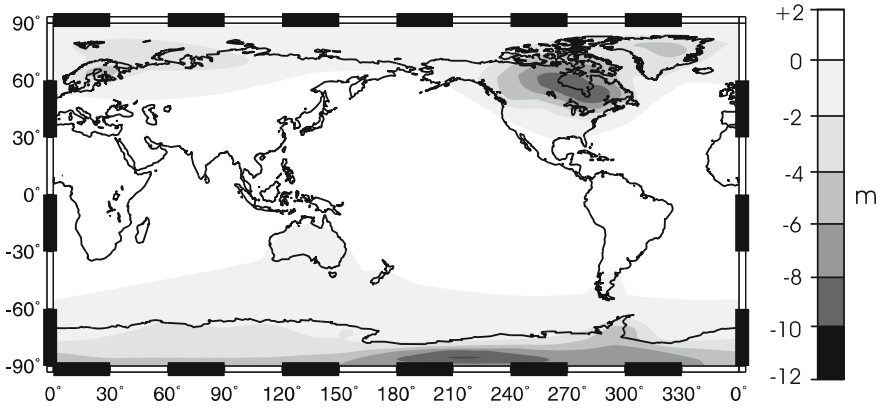

Fig. 6.1 Global map of the present-day geoid anomaly due to Pleistocene deglaciation for Earth's model 1 ($\ell = 2, 80$)

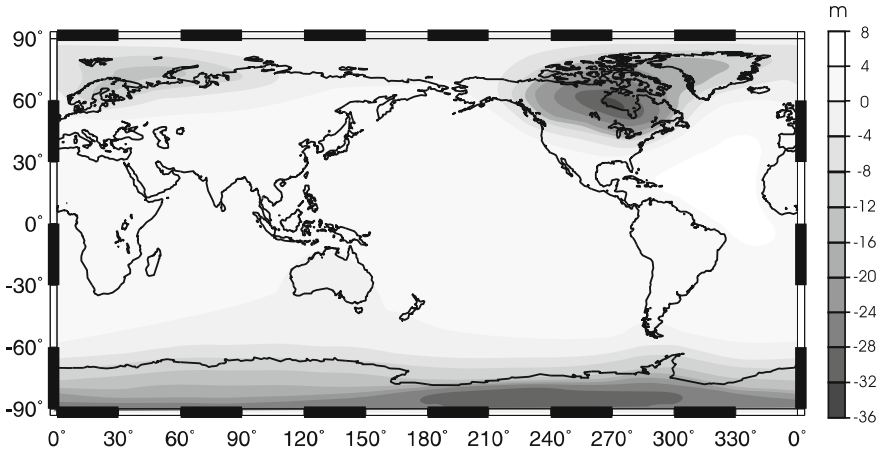

Fig. 6.2 Global map of the present-day geoid anomaly due to Pleistocene deglaciation for Earth's model 3 ($\ell = 2, 80$)

Peltier (1991), using the same ice model and mantle viscosity profile are negative, indicating that this geoid anomaly is decreasing to restore isostatic equilibrium.

Figure 6.2 provides the geoid anomaly for the 5-layer Earth's model 3. With respect to Fig. 6.1, it is remarkable that the geoid pattern is maintained, except for the peak values of the anomalies, which are larger than in the homogeneous model. The highest anomaly is of course caused by the larger amount of isostatic disequilibrium maintained by the high viscosity of model 3, in comparison with the homogeneous one. The peak values of the anomalies are now -36, -12 and -30 m, about a factor four larger than for model 1. It is also remarkable that even the positive anomalies in the oceans are larger than the corresponding ones in Fig. 6.1, in agreement with

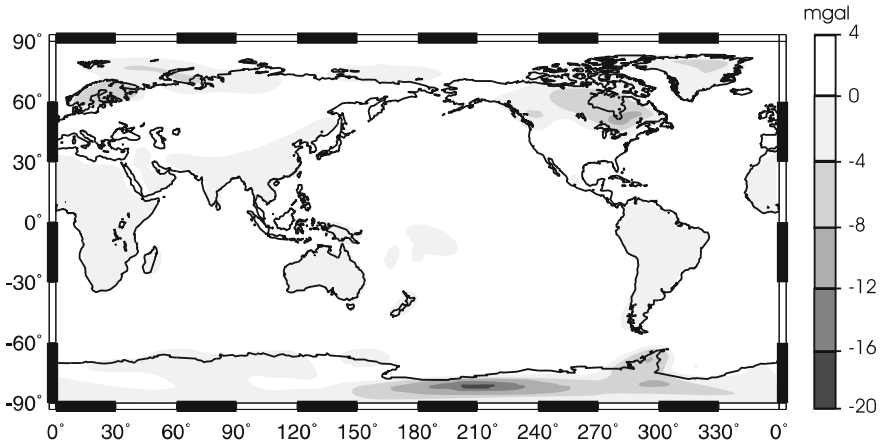

Fig. 6.3 Global map of the present-day free-air gravity anomaly computed using Earth's model 1 ($\ell = 2, 80$)

the larger amount of mantle material stored beneath the ocean basins that, due to the higher viscosity, has not flowed yet under the continental areas to fill the large mass deficit.

In Fig. 6.3, the free-air gravity anomaly is provided for model 1. The peak values of the gravity anomalies are located, as expected, in the centre of the deglaciated areas and are, respectively, -18 mgal over Antarctica, -10 mgal over Hudson Bay and -6 mgal over the Northern part of Europe in agreement with the findings first reported by Mitrovica and Peltier (1989). The pattern of the gravity anomalies has a close resemblance to the geoid. As expected, the pattern of the free-air gravity anomalies is not as smooth as the pattern of the geoid, due to the faster decay with distance of the signal from the anomalous masses, indicating a richer high-frequency content in the free-air gravity anomalies in comparison to the geoid ones.

In order to appreciate the high-frequency content in the free-air gravity anomaly, the case in which only spherical harmonic coefficients in the degree range $l = 80, 200$ have been retained is considered in Fig. 6.4. A signal of -3 mgal is obtained in the Antarctic region and -1 mgal in the other deglaciated centres.

Figure 6.5a, b show the predicted present-day rates of sea-level change for the 31-layer Earth's model 2, in northern Europe and in the Mediterranean region, respectively. The lower mantle viscosity of model 2 is consistent with inferences based on post-glacial relative sea-level variations in northern Europe (Lambeck et al. 1990) and numerical predictions of post-glacial sea-level change in southern Europe (Mitrovica and Davis 1995). The sea-level Eq. (6.16) is solved using the pseudo-spectral algorithm by Mitrovica and Peltier (1991) with a truncation at degree and order 256, so the spatial resolution is sufficient to model sea-level increase in small regions. The highest rates are obtained of course in the centre of deglaciation, the Gulf of Bothnia. The uplift of the land causes a sea-level fall of -11 mm/yr there. On

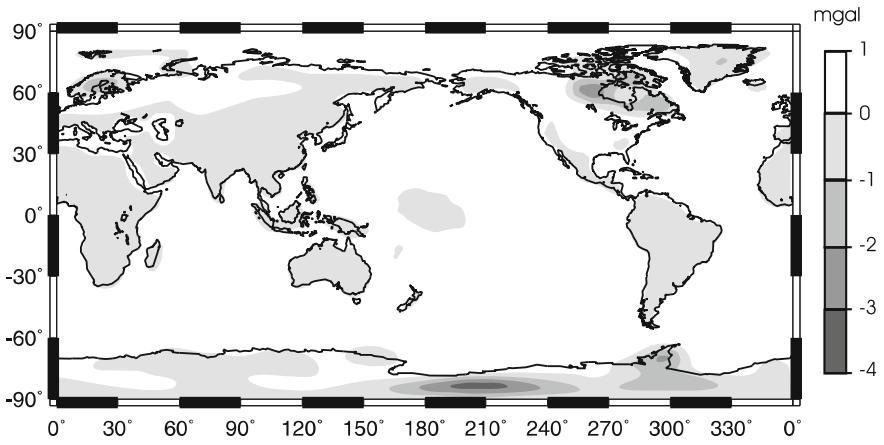

Fig. 6.4 Global map of the present-day free-air gravity anomaly computed for Earth's model 1 by retaining only the spherical harmonic coefficients in the degree range $\ell = 80, 200$

the periphery of the uplifting region, the land is subsiding due to the collapse of the peripheral bulge, causing a sea-level increase that, along the coastal areas of northern Europe, can be as high as 1–2 mm/yr. Sea-level increase along the coasts of northern continental Europe is subject to large variabilities, from 0.4 mm/yr near the French coast to 1–1.5 mm/yr along the coasts of The Netherlands and Germany. It should be noted that the collapse of the peripheral bulge decreases in central Europe. Further to the south, sea level is actually increasing, with rates in the order of 0.6–0.8 mm/yr in the central Mediterranean due to the subsidence of the sea bottom caused by the water load. The periphery of the Mediterranean Sea is characterized by a weak sea-level rise with rates from 0.2 to 0.4 mm/yr in the Adriatic Sea and about 0.4 mm/yr along the Mediterranean coast of France. Here the rates of sea-level change have small values due to the levering effect (Nakada and Lambeck 1989): the subsidence of sea basins is contoured by the uplift of the surrounding continents. This sea-basin subsidence is due to mantle material presently flowing from the Mediterranean region towards the Fennoscandian region in northern Europe. These last values are comparable with the sea-level changes due to active tectonics in the central Mediterranean: finite-element calculations of active tectonics in peninsular Italy have indicated that overthrusting of the Apennines onto the Adriatic plate is responsible for a sea-level increase of 0.4 mm/yr (Negredo et al. 1997). The peak value in the central Mediterranean due to post-glacial rebound is thus comparable with that due to active tectonics (Di Donato et al. 1999).

The model results indicate that glacial isostatic readjustment of the solid Earth can induce sea-level variations in sea basins located in the far field with respect to the centres of deglaciated regions in the order of 1 mm/yr, of the same order of magnitude as those induced by tectonic processes in the Mediterranean, as shown in the following section.

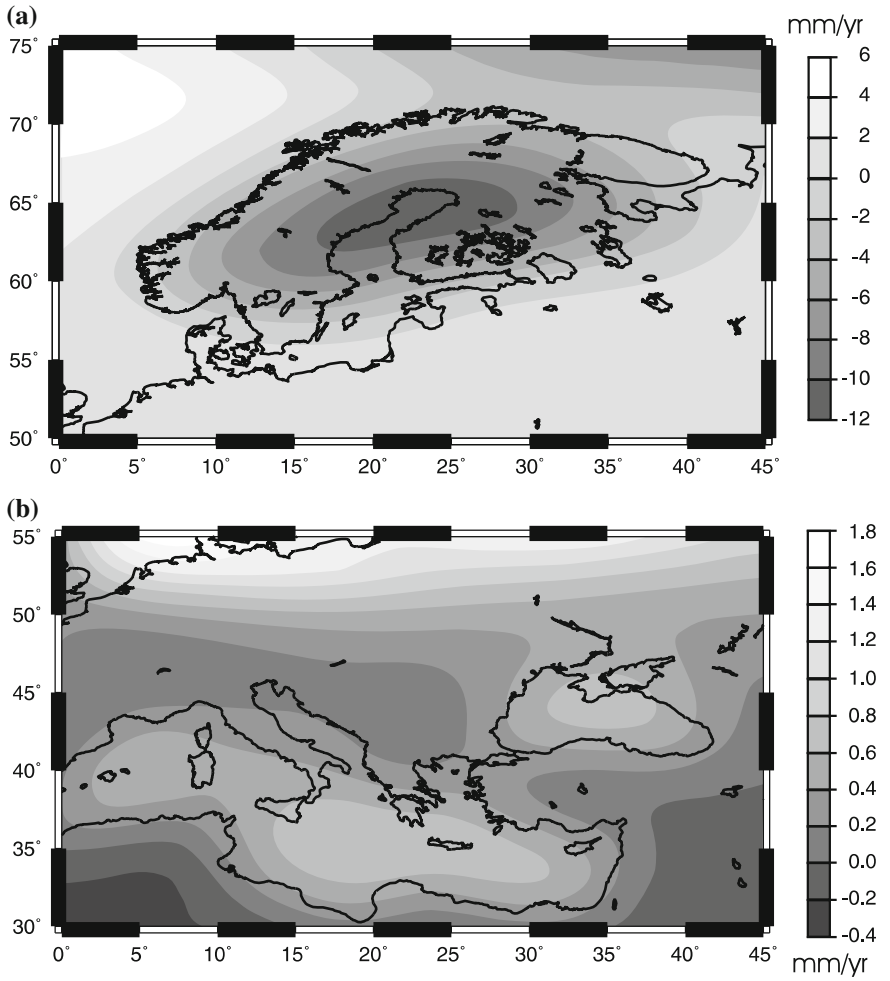

Fig. 6.5 The present-day rates of sea-level change. **a** In northern Europe and **b** in the Mediterranean region due to Pleistocene deglaciation for Earth's model 2 ($\ell = 2, 256$)

6.3 Glacial Isostatic Adjustment (GIA) Versus Tectonic Processes: The Example of the Mediterranean Sea

The Adriatic Sea and the coastlines of peninsular Italy represent an important area for studying sea-level changes because model predictions can be used to gauge the risk of sea-level rise on the historically important cities of Venice and Ravenna. Furthermore, the current level of ancient Roman ruins in this part of the Mediterranean, relative to present-day sea-level, provide high-quality sea-level records (Pirazzoli 1998) (see Fig. 6.6).

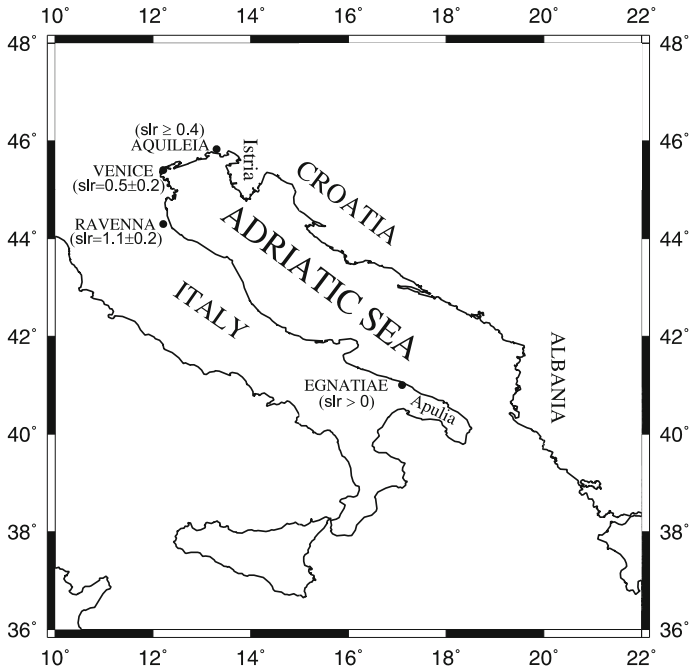

Fig. 6.6 Map of the study area with site locations and observational sea-level rates in millimeters per year superimposed. Error bars for Venice and Ravenna are also included (Fig. 1 in Di Donato et al. (1999))

For example, archaeological evidence in the Istria promontory, in the north Adriatic coast of Croatia, indicates a sea-level rise of 0.7 mm/yr (Pirazzoli 1998; Degrassi 1955). At the Roman fluvial harbor of Aquileia. in the northernmost part of the Adriatic, sea-level has risen by at least 0.8 m since the first half of the first century A.D., providing a lower bound for the rate of sea-level rise of 0.4 mm/yr (Schmiedt 1979). In Ravenna, Roman ruins are currently located 2–3 m below sea level (Roncuzzi 1970), suggesting a rate of sea-level rise in the range of 1.0–1.5 mm/yr, or 1.1 ± 0.2 mm/yr (Pirazzoli 1998), while Flemming (1992) estimates a sea-level rise of 0.5 mm/yr in Venice, to which we can safely attribute conservative error bounds of ± 0.2 mm/yr following Flemming (1992). At Egnatiæ, in Apulia, graves, harbor constructions and a partially submerged Roman caldarium indicate a net sea-level rise in the southern part of the Adriatic coasts of Italy (Pirazzoli 1998). These sea-level data are all based on archaeological ruins and are not affected by the subsidence induced by water extraction, which has hit the cities of Ravenna and Venice in the last 40 years, or by neotectonic faulting, absent in the area.

These archaeological constraints are characterized by some potentially significant geographic variability, although they indicate a remarkably coherent sea-level rise in the northern Adriatic sea in the order of 1.0 mm/yr in the last 2000 years. This change is unlikely to reflect a global signal, since the estimated present-day eustatic sea-level

rise of 1.8 mm/yr has not persisted over the last two millennia (Douglas 1995). It is reasonable, therefore, to look for other causes to explain these data, and the most obvious candidates are active tectonics and GIA. Although the impact of both active tectonics and GIA on sea-level changes is widely recognized (Mitrovica and Peltier 1991; Pirazzoli 1997), the tectonic contribution to sea-level data has to date been quantified only indirectly on the basis of residuals between sea-level observations and modeled GIA effects (Lambeck 1995). In contrast to this indirect approach, in the following the effects of both these processes are self-consistently taken into account using tectonic and GIA models, as first shown in Di Donato et al. (1999). The resulting pattern of predicted sea-level changes can be compared directly with sea-level observations. This modeling is appropriate for time scales ranging between 10^3 and 10^5 yr and, thus, the results can be compared with the above archaeological data, which have a 10^3 yr time scale.

Active tectonic processes in the central Mediterranean, namely the Africa-Eurasia convergence and subduction in the southern Tyrrhenian, are modeled by means of finite-element solutions in a half-space domain. The model, which extends earlier work by Negredo et al. (1997), allows lateral variations in the rheology of the lithosphere and mantle which are consistent with tectonic structures in the central Mediterranean. Figure 6.7 is a cartoon representing the mesh of the finite-element model of peninsular Italy, which includes the deep tectonic structures of the central Mediterranean Sea.

In comparison to that study (Negredo et al. 1997), the present tectonic model is characterized by a realistic geometry of the Apennine chain overthrusting onto the Adriatic domain (Fig. 6.7). The push of the African continent is indicated by the thick arrows, directed roughly to the north, in agreement with VLBI solutions (Lanotte et al. 1996). The Tyrrhenian subduction is portrayed by the deep lithospheric structure beneath the Calabrian Arc, with geometric characteristics in agreement with seismic tomography (Spakman 1990). The tectonic structures, based on geological and seismological data, are sufficiently well constrained so as not to require a sensitivity analysis based on the parameters characterizing the tectonic model. The active push of Africa and the slab pull underneath the Calabrian Arc are responsible for deformation of the whole domain situated between the African block and the Alps, in particular of the coastlines of peninsular Italy.

The redistribution of water due to ice-sheet disintegration is a global process. Predictions of sea-level variations due to GIA are based on the formulation provided at the beginning of this chapter. The predictions incorporate the effects of deglaciation, based on the ICE-3G reconstruction of Tushingham and Peltier (1991), on crustal and sea surface changes in the Mediterranean Sea.

The glacially induced sea-level variations in the area arise from various coupled processes: loading associated with Pleistocene meltwater filling the Mediterranean Sea, the rebound in Fennoscandia that drives mantle flow from the Mediterranean region to the uplifting area centered in the Gulf of Bothnia and long-wavelength motion of the water away from the Mediterranean and towards subsiding regions at the periphery of previously glaciated areas (Mitrovica and Davis 1995), as shown in Sect. 6.2.2. The tectonic and postglacial rebound models have consistent values

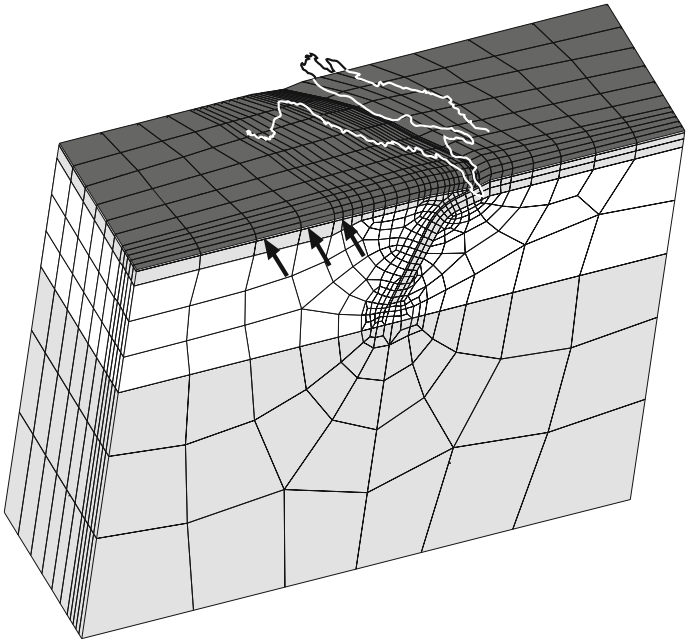

Fig. 6.7 Cartoon portraying the mesh of the finite element tectonic model of the central Mediterranean Sea. The lithosphere, *upper* and *lower* mantle are indicated. The dipping plate is the subducted oceanic lithosphere beneath the Calabrian Arc in the southern part of peninsular Italy. The coastlines of Italy are drawn on the *top*, with the thick curve with the finer mesh indicating the decoupling zone of the Apennines with respect to the Adriatic plate on the *right*. The *horizontal arrows* indicate the push of Africa; slab pull is activated in the subducted lithosphere. Redrawn from Fig. 2 in Di Donato et al. (1999)

for the thickness and rheology of the lithosphere and the viscosity within the upper and lower mantle. The elastic structure is constrained by the seismic model PREM (Dziewonski and Anderson 1981) and the Earth's model has a 120 km-thick elastic lithosphere for modeling the GIA. Both the models are characterized by an upper mantle viscosity of 10^{21} Pa s and a viscosity increase in the lower mantle of a factor 30, in agreement with long-wavelength geoid modeling (Ricard and Vigny 1989) and the results in Chap. 5. This viscosity profile reconciles the inference derived from long-term tectonic processes (Ricard and Vigny 1989) with glacio-isostatic analyses that indicate substantial viscosity increase in the lower mantle (Mitrovica and Forte 1997). Equations of Sect. 6.2.1 and the iterative pseudo-spectral formalism described in Mitrovica and Peltier (1991) have been used in order to determine the gravitationally self-consistent sea-level changes described hereafter. The tectonic model, which is not self-gravitating, assumes that the geoid does not change during deformation. The sea-level change is, in this case, due to the motion of the sea floor. This assumption is justified by results from studies of sea-level changes due to slow

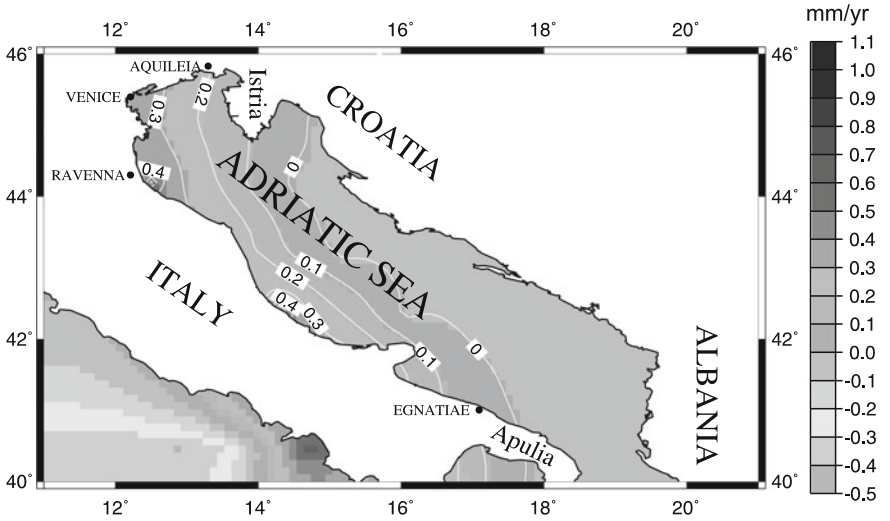

Fig. 6.8 Present-day rates of sea-level change due to active tectonics in the Adriatic Sea, the basin surrounded by Albania, Croatia and Italy. Redrawn from Fig. 3 in Di Donato et al. (1999)

tectonic forcings (Piromallo et al. 1997), which will be described in the last section of this chapter.

Figure 6.8 reproduces the sea-level rates accounting only for the effects of active tectonics.

The pattern of sea-level change along the Adriatic coasts shows a high variability due to the geometrical complexity of the tectonic structures activated by the interaction between the Apennine mountain belt, the Adriatic plate to the east and the Alps to the north, as visualized in Fig. 6.7. Active tectonics is responsible for significant rates of sea-level rise in the western coasts of the Adriatic sea. This sea-level rise is due to the downflexure of the Adriatic plate underneath the overthrusting Apennine belt, whose eastern border is represented by the thick line in Fig. 6.7 separating the Tyrrhenian sector of the Italian peninsula to the west and the Adriatic domain to the east. Overthrusting of the Apennines is caused by the push of Africa from the south and by the decoupling, on geological time scales, of the western and eastern parts of the peninsula via a megafault. Figure 6.8 clearly indicates that active tectonics alone cannot explain archaeologically inferred sea-level records within the Adriatic. At Aquileia and the Istria promontory the tectonic model provides at most 0.1–0.2 mm/yr, which is at least 0.3 mm/yr lower than the observed trend in this region (Schmiedt (1979)). The highest predicted sea-level rise in the Adriatic Sea due to active tectonics is 0.4–0.5 mm/yr, occurring in the Po delta plain, although at Ravenna even in this case the model predictions are significantly below the sea-level rise of 1.1 ± 0.2 mm/yr recorded at this site (Pirazzoli 1998). The predicted sea-level rise at Ravenna achieves a maximum because the Adriatic platform experiences the largest subsidence at this site due to the arquated geometry of the Apennines, and our

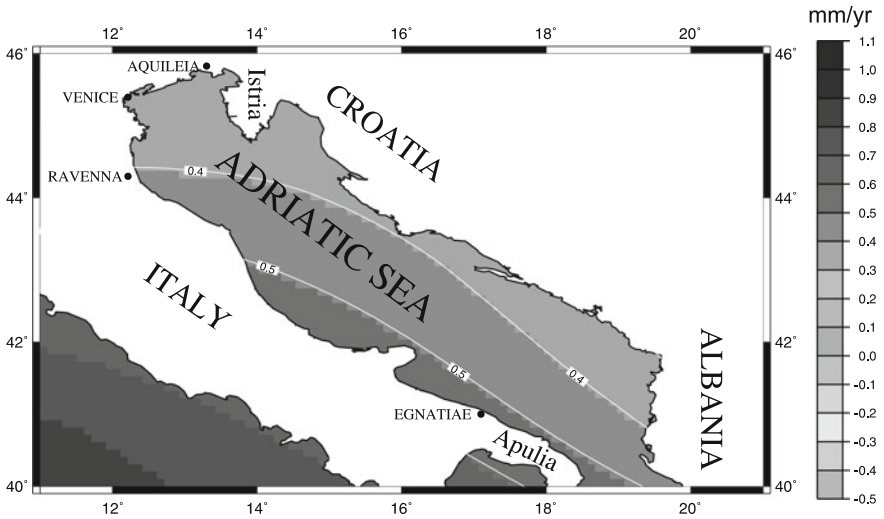

Fig. 6.9 Present-day rates of sea-level change due to GIA in the Adriatic Sea. Redrawn from Fig. 4 in Di Donato et al. (1999)

predictions therefore reflect the three-dimensional geometry of the tectonic regime. In Apulia active tectonics yields a sea-level fall of about 0.1 mm/yr due to crustal uplift. This fall is consistent with the tectonic uplift of Apulia occurring on the time scale of millions of years (Pirazzoli 1998).

Figure 6.9 deals with the effects of GIA. The most noticeable effect of the water load is a long-wavelength sea-level rise in the Adriatic Sea, increasing from 0.3–0.4 mm/yr in the northern part of the basin and along the coasts of Albania and Croatia to 0.5–0.6 mm/yr in Apulia. The large subsidence of the sea basin causes a slight uplift of the surrounding continental areas due to the flexural behavior of the lithosphere, which is thus ultimately responsible for the decrease in the sea-level signal in the eastern part of the Adriatic coast. Although the amplitude of this signal is somewhat dependent on the viscosity model assumed for the upper and lower mantle and on the thickness of the lithosphere, the pattern agrees well with previous results by Mitrovica and Davis (1995), with whom our results have been checked for stratified viscosity models in the Mediterranean Sea up to harmonic degree 256. The GIA model alone cannot entirely explain the datum at Aquileia and the Istria promontory, since the model prediction reaches only 0.3–0.4 mm/yr at this site; the discrepancy between GIA prediction and observation is large at Ravenna, where the GIA simulation predicts rates of only 0.4–0.5 mm/yr. In Apulia, our GIA model correctly predicts the sea-level rise at Egnatiæ, indicating that GIA is the dominant mechanism for sea-level change over the last thousand years at this site (as opposed to the above noted dominant tectonic effects in Apulia over time scales of millions of years). Figures 6.8 and 6.9 show that active tectonics and GIA are unable to account for the observed sea-level rise when taken separately.

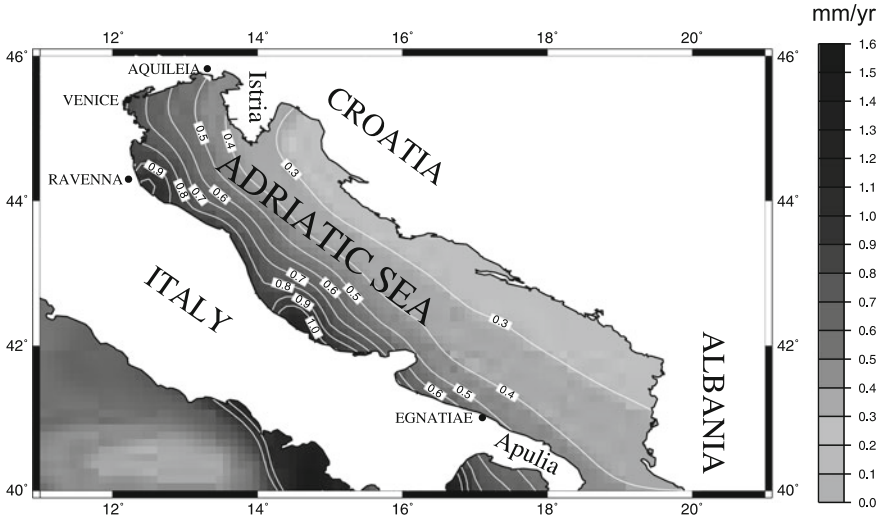

Fig. 6.10 Present-day rates of sea-level change due to GIA and active tectonics. Redrawn from Fig. 5 in Di Donato et al. (1999)

Figure 6.10 shows the combined sea-level effects of active tectonics and GIA. In the northernmost part of the Adriatic Sea, where the Istria promontory and Aquileia are located, our combined models of GIA and active tectonics predict a sea-level rise of 0.4–0.5 mm/yr, in good agreement with archaeological data in Aquileia and, to a somewhat lesser extent, with the data in the Istria promontory. It is remarkable that such a conclusion on the necessity to incorporate both active tectonics and GIA in the northernmost sector of the Adriatic Sea can be drawn on the basis of the lower bound for sea-level rise of 0.4 mm/yr at the site of Aquileia. If we move to the south, along the western part of the Adriatic Sea in proximity to Venice and Ravenna, the modeling accounts for a substantial amount of the variation in the sea-level records from Venice to Ravenna; as noted already, sea-level records vary from 0.5 ± 0.2 mm/yr in Venice (Flemming 1992) to 1.1 ± 0.2 mm/yr in Ravenna (Pirazzoli 1998), in agreement with our results, varying from 0.75 to 0.95 mm/yr between these two localities. Model results tend to underestimate the geographical variations in sea-level changes, perhaps due to small-scale tectonic features not taken into account in the modeling. It is remarkable, nevertheless, that the simulations reproduce the correct geographical trend, from which it is possible to conclude that the dependence of sea-level records on geographic location is due, in large part, to active tectonics. Compaction of the sediments, not modeled in the present analysis, could contribute to the sea-level record at Ravenna, and thus increase our prediction toward the higher bound on the observed trend. At Egnatiæ, a sea-level rise of 0.5 mm/yr agrees with the observed trend at this site.

Simultaneous modeling of active tectonics and Pleistocene ice-sheet disintegration in the central Mediterranean Sea makes it possible predictions on the trends in

sea-level rise due to slow geodynamical processes. Consistency between data and model results in trends and magnitude of sea-level rise indicates that the major contributors to sea-level rise have been properly taken into account. A major finding is that contributions to sea-level rise due to GIA and active tectonics are comparable in the studied area, since active tectonics here is characterized by horizontal velocities at sub-centimeter level (Lanotte et al. 1996). In other tectonic environments in the Mediterranean Sea, with more significant horizontal velocities, active tectonics would provide higher sea-level signals, as in the island of Crete in the Aegean Sea (Lambeck 1995). The results in this section clearly show that it is possible to quantify the effects of active tectonics and GIA on sea-level rise in an area of great interest not only for the presence of cities like Venice and Ravenna, witnesses of a unique historical past, but also for the impact that climatic changes and anthropogenic activities, such as water and gas extraction, could have on the acceleration of sea-level rise.

6.4 Sea-Level Fluctuations Induced by Polar Wander

Glacial isostatic adjustment and tectonics are responsible for sea-level fluctuations at the regional scale, as shown in the previous Section. Polar wander of a viscoelastic stratified Earth can induce, instead, global sea-level fluctuations comparable to the short-term component in the eustatic sea-level curves that show a characteristic pattern where sea-level rise and fall can occur simultaneously, depending on the geographical location (Sabadini et al. 1990). This simultaneous occurrence of sea-level rise and fall, visible as episodes of deposition or non-deposition of marine sediments in different parts of the world, has led to the proposal that at least some sea-level rises and falls must be global, or eustatic, in character. This simultaneous occurrence of sea-level rise and fall is in distinct contrast to the main assumption underlying the reconstruction of eustatic curves, i.e., that global sea-level events produce the same depositional sequence everywhere. This apparent contradiction may be due to the poor time resolution of the stratigraphic records in the distant past, which is comparable to the timescale of polar motion, and to non-uniform data coverage. The results presented in this Section show that polar wander should be added to the list of geophysical mechanisms (the others are glacial instabilities, plate tectonic mechanisms, subduction, sea-floor spreading, and thermal and compaction-induced subsidence) that can control the third-order cycles in sea level. RSL fluctuations due to variations in the centrifugal force associated with long-term wander of the Earth's rotation axis can be predicted theoretically for radially stratified viscoelastic Earth's models. The possible causes for these long-term displacements of the rotation axis can originate in the mantle, as suggested by the rotational responses of the Earth to the tectonic mechanisms described in Chap. 7, or can be caused by the surface redistribution of melt water from ice ages, as shown in Chap. 4. In this section the possible dynamic sources of polar wander are disregarded and attention is drawn instead to the effects on RSL induced by polar wander rates that agree with those induced by the geophysical processes considered in the other chapters of this book.

In the Laplace transform domain, the perturbation in the centrifugal potential depends, to first order, on the s-dependent direction cosines $m_1(s)$, $m_2(s)$ of the unitary rotation axis $\hat{\mathbf{n}}(s)$ as for Eq. (3.129), which means that it depends on the $m = -1, m = 1$ harmonic order

$$\phi^C(\theta, \varphi, s) = \frac{\Omega^2 a^2}{3} \left[\frac{1}{6} Y^*_{2,-1}(\hat{\mathbf{n}}(s))\, Y_{2,-1}(\hat{\mathbf{r}}) + \frac{1}{6} Y^*_{21}(\hat{\mathbf{n}}(s))\, Y_{21}(\hat{\mathbf{r}}) \right] \tag{6.21}$$

as obtained from Eq. (3.25), where Ω is the rotation rate of the Earth, a is the Earth's radius and $\hat{\mathbf{r}}$ depends on the colatitude and longitude θ, φ of the observer. Because our model is radially symmetric, and the distribution of the ocean is assumed uniform, this $\ell = 2, m = -1, m = 1$ perturbation potential induces a signal in the relative sea-level fluctuation of the same angular degree and order, as for Eqs. (3.56) and (3.57) for the inertia perturbation due to the centrifugal potential. Neglecting the effects of self-attraction of the uniform ocean and of the geographical distribution of the coastlines, the RSL from Eq. (6.16) is then

$$RSL(\theta, \varphi, s) = (1 + k_2^T(s) - h_2^T(s))\phi^C(\theta, \varphi, s)/g, \tag{6.22}$$

where k_2^T and h_2^T are the $\ell = 2$ components of the tidal Love numbers for the gravitational potential and vertical displacement, respectively, obtained from the boundary conditions at the Earth's surface given by Eq. (1.127) and g is the gravity. Neglecting the self-attraction of the ocean has the effect of producing an increase of at most 10 % on our results. The term $1 + k_2^T(s)$ yields the deformation of the ocean surface relative to the Earth's centre, whereas h_2^T controls the vertical displacement of the sea-bottom.

Owing to the lag between these two contributions, perturbations in the centrifugal potential induce sea-level fluctuations, as shown by the drawing in Fig. 6.11. The white arrow indicates the direction of the polar wander, and the solid and dashed curves depict the shift of the equipotential surface (geoid). Highstands and lowstands are generated depending on the latitude and longitude of the observation points with respect to the polar motion. To quantify these sea-level fluctuations for incompressible Earth's models, it is necessary to make use of the spectral decomposition of the tidal Love numbers, which are recoverable by means of the normal mode theory, as shown in Sects. 1.8 and 2.3. The model used for the following simulations is a 4-layer model as in Table 7.1 of the following Chap. 7 on TPW forced by sinking slabs, with viscosity ν_1 and ν_2 in the upper and lower mantle. The upper-lower mantle interface is located at a depth of 670 km and modeled in such a way as to simulate the mechanical behavior of phase-change or chemical transitions, which are assumed fully adiabatic and non-adiabatic. The fully adiabatic mantle is modeled by deleting the M1 buoyancy mode. Polar wander rate in the following simulations is 1 Deg/Myr, of the same order of TPW induced by post-glacial rebound or tectonic mechanisms (Chaps. 4 and 7). The results for different polar wander rates can be obtained by means of linear scaling.

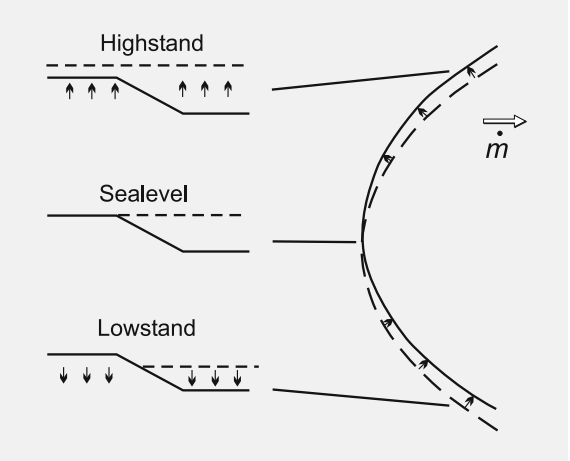

Fig. 6.11 Pictorial representation of sea-level fluctuation induced by polar wander. The *white arrow* denotes the direction of polar drift at a rate $\dot{m} = 1$ Deg/Myr. The *solid and dashed curves* represent the deformation of geoid and topography of the sea floor at time $t = t_0$, when the perturbation is initially imposed, and at a subsequent time $t = t_1$. Sea level is unperturbed at the equator, but rises and falls occur in the northern and southern hemispheres

In Fig. 6.12 the perturbative potential is applied at time $t = 0$; the evolution of the sea level at mid-latitudes, where the effects are larger owing to the latitudinal dependence of the perturbation, is depicted. Sea-level fluctuations are extremely sensitive to viscosity stratification and lithospheric thickness. These curves are characterized by transient behavior, more pronounced for high lower mantle viscosities, followed by a linear trend, which is connected to a constant rate of polar wander. For smooth viscosity contrasts, phase-change models (dashed curves) produce a smaller signal than chemically stratified ones (solid curves). For the chemically stratified models, deflections of the 670 km discontinuity induce a buoyant restoring force which inhibits viscous relaxation in the mantle. This, in turn, reduces the vertical uplift of the sea floor and helps to maintain the offset between sea-floor topography and the geoid. For high viscosity contrasts ($\nu_2 = 10^{23}$ Pa s), the stiffening of the lower mantle overcomes the dynamic effects associated with the nature of the 670 km discontinuity. Thus phase-change and chemically stratified models exhibit the same behavior. The dotted curve, corresponding to a model with a reduced lithospheric thickness of 50 km, shows the sensitivity of sea-level fluctuations induced by polar wander to variations in lithospheric thickness. High viscosity contrast models thus predict sea-level fluctuations in the order of several tens of meters on timescales of 1 Myr, which are comparable to the third-order cycle in the eustatic curves.

It is useful to analyze the behavior of the rate of sea-level fluctuations (Fig. 6.13). Rates in the order of 0.05–0.1 mm yr^{-1} are maintained for timescales of 0.5 Myr if the viscosity contrast is sufficiently high ($\nu_2/\nu_1 = 50$–100). For uniform models, or mild viscosity contrasts ($\nu_2/\nu_1 = 1$–10), rates of sea-level fluctuations decay in a few tens

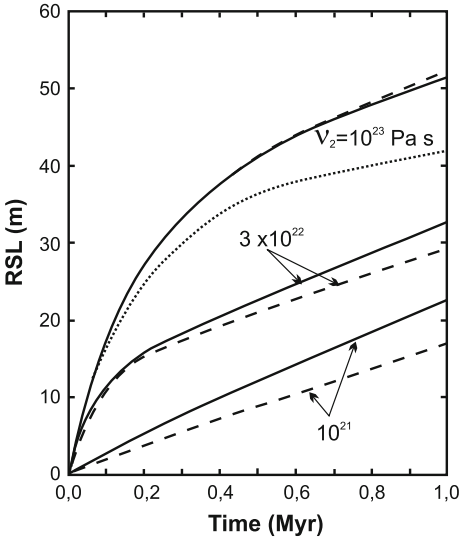

Fig. 6.12 Time dependence of relative sea-level fluctuations at mid-latitudes ($\theta = 45°$, $\phi = 0°$), corresponding to $\dot{m} = 1$ Deg/Myr and polar motion toward Greenwich. The perturbative potential is applied at time $t = 0$. *Solid curves* correspond to chemically stratified models (fully non-adiabatic) and *dashed* ones correspond to fully adiabatic phase changes. Lithospheric thickness is 100 km, except for the *dotted curve*, which corresponds to 50 km. The upper mantle viscosity ν_1 is 10^{21} Pa s, and the lower mantle viscosity ν_2 is varied from 10^{21} Pa s (*bottom*) to 10^{23} Pa s (*top*)

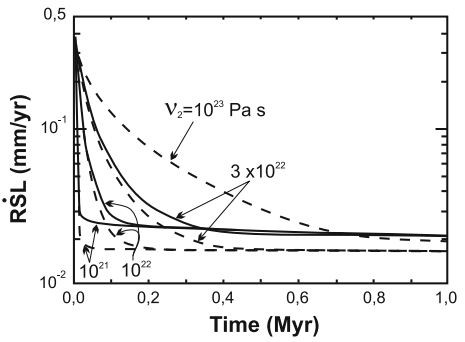

Fig. 6.13 Time dependence of $\dot{RSL}$ in mm/yr. *Solid curves* correspond to chemically stratified models and *dashed* ones correspond to fully adiabatic phase changes. For $\nu_2 = 10^{23}$ Pa s, the chemical transition and phase-change models are indistinguishable. Results for $\nu_2 = 10^{22}$ Pa s are also shown

of thousands of years. After the decay of the initial transient, the rates reach a final value of 0.02 mm/yr, irrespective of the rheological stratification. As expected, phase-change models produce lower rates, except for high viscosity contrasts, in which case these models are indistinguishable from chemically stratified ones. We find that rates of sea-level fluctuations are around one order of magnitude smaller than those associated with vertical deformation of the sea floor, which are 1–1.5 mm/yr. The rates predicted by our model are of the same order of magnitude as the short-wavelength ones associated with temporal variations of the horizontal tectonic stress field in the

lithosphere (Sect. 6.3). From these results, it is clear that the proposed mechanism of polar wander is efficient in inducing sea-level fluctuation, especially during epochs of rotational instabilities, caused by mantle flows. Significant shift of the rotation pole occurred, for example, during the Late Cretaceous. The results shown in this section indicate that the highstand or lowstand system tracts observed in one part of the world are not necessarily correlated with the same depositional sequence in another geographic location. A highstand in a marine package in the Northern Hemisphere can, in fact, be coeval with a lowstand in the Southern Hemisphere at the same longitude if the only active mechanism that induced the eustatic sea level event was polar wander.

6.5 Sea-Level Changes Induced by Subduction

The effects of tectonics on relative sea-level changes have been shown at the regional scale. In this section we explore the effects of tectonics, in particular subduction, at the global scale. As in the case of the effects of rotation, we neglect the self-attraction of the oceans and the geographical distribution of the coastlines.

RSL is determined by the difference in height between the surface of the non-hydrostatic geoid and the surface of dynamic topography: in Fig. 6.14 we illustrate the different contributions to the determination of RSL. The direct contribution of internal mass anomalies to the gravity potential is given by the term that would constitute the only contribution to the potential in the case of a rigid Earth (Lambeck 1980). However, in a viscoelastic Earth, an additional compensating effect is induced by the deflection of the interfaces. The internal masses and the deflected interfaces

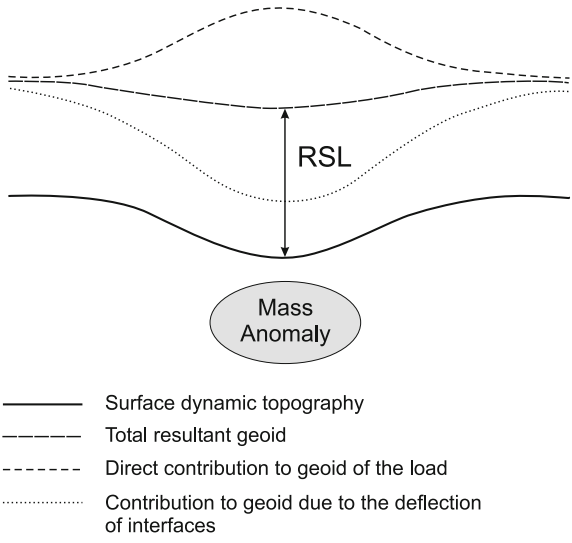

Fig. 6.14 Schematic representation for the various contributions to RSL determination. RSL is determined by the offset in height between the surface of the resultant geoid and the dynamic topography, as shown by the arrow (adapted from Ricard and Vigny (1989))

together modify the sea water surface. In Fig. 6.14, the resultant geoid and dynamic topography appear to be highly correlated both in amplitude and sign. However, this is only to be considered as a schematic representation and not as a general rule, since geoid and topography usually have much different amplitudes, as we will point out later on, and they may also be opposite in sign.

The generalized Love numbers used in this section are those appropriate for internal loads, Eq. (1.179) (Ricard et al. 1992; Sabadini et al. 1990, 1993); they display an elastic response and various viscoelastic relaxation contributions, as in the case of the Love numbers for surface loads introduced in Sects. 1.7.1 and 1.7.2.

6.5.1 Sea-Level Variations, Geoid Anomalies and The Long-Wavelength Dynamic Topography

The study of geophysical observables related to the geoid and dynamic topography is fundamental for the understanding of relative fluctuations in the mean sea level. Several works have already analyzed in detail the geoid anomalies as in Ricard et al. (1992), while we will focus our attention on the dynamic topography in the present Section. Since dynamic topography shows a strong degree 2 content well correlated with the non-hydrostatic geoid and with hot anomalies in the lower mantle (Cazenave et al. 1989; Ricard and Vigny 1989), the study of the degree 2 Love number for the topography turns out to be particularly interesting. Moreover, long-wavelength responses clearly illustrate the effects of mantle rheology and stratification on geoid and dynamic topography. We will develop our analysis up to a higher harmonic degree, $\ell = 20$, which is more appropriate to describe features such as subduction zones. The 4-layer, incompressible Earth's model described in Table 7.1 is employed as in Sect. 6.4, with both phase-change and chemical interface at 670 km. A pure phase change interface implies a whole mantle convection, since the mantle material is allowed to flow across the boundary. A fully non-adiabatic density jump across the discontinuity (chemical interface), on the contrary, separates the mantle flow and generates a layered convection with two superimposed convective cells (e.g., Ricard et al. 1992; Piromallo et al. 1997).

Figure 6.15 shows the degree 2 dynamic topography as a function of depth. We locate a point mass anomaly characterized by a Heaviside time-history at a depth d in the mantle in order to compare the effects of loads positioned at various depths. The different curves represent the dimensionless values of the topography computed at the time indicated (expressed in kiloyears) and normalized to the spectral amplitude of the load (Piromallo et al. 1997). In this figure the viscosities of the lower and upper mantles are both fixed at 10^{21} Pa s. No lithosphere is included in the results portrayed in the left column panels (Fig. 6.15a, c, e and g), while a 100 km thick elastic lithosphere is present in the right column (Fig. 6.15b, d, f and h). The 670 km depth interface is characterized by a physical discontinuity in the four top panels and by a chemical change in the four bottom panels. While models (a), (b), (e) and

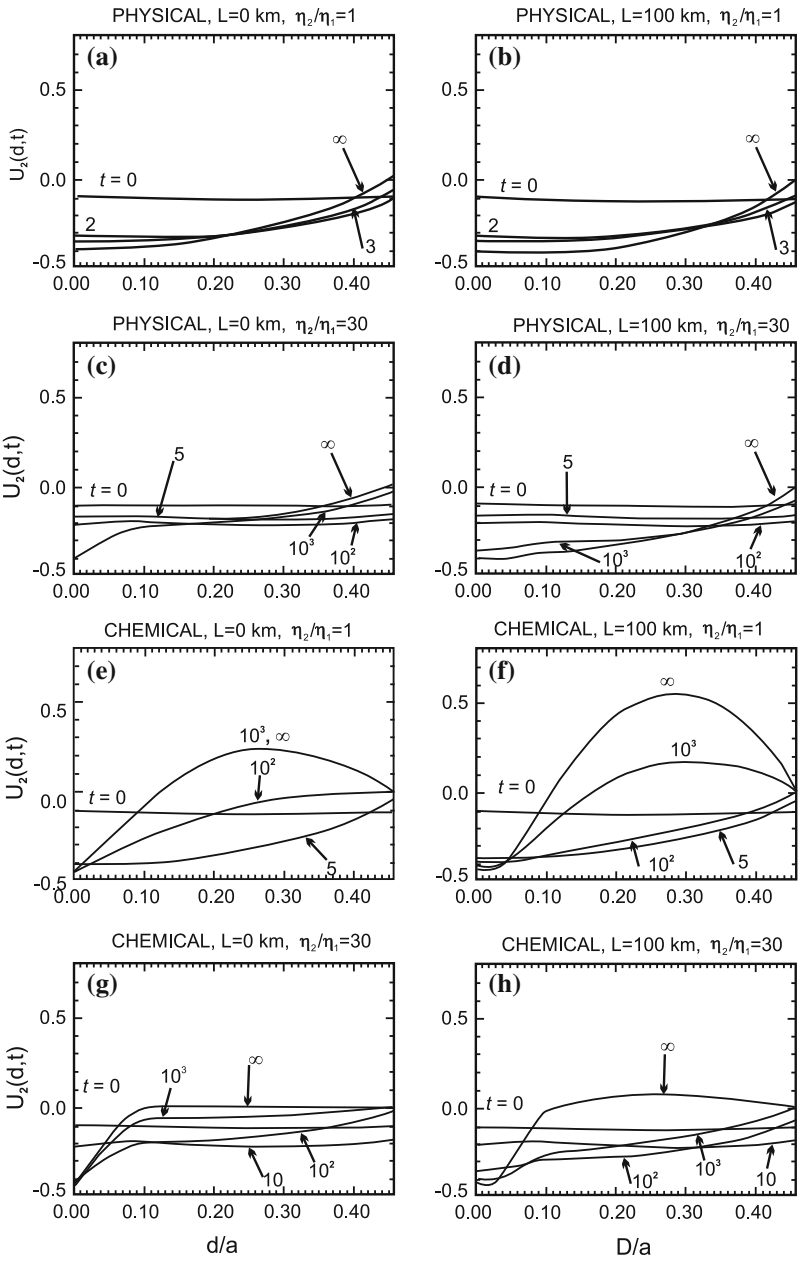

Fig. 6.15 Time evolution for topography as a function of the point source depth d (normalized to the Earth's radius a) and time t. A physical interface is assumed at 670 km of depth in the four *top panels*, while a chemical change is considered in the four *bottom panels*. A 100 km-thick lithosphere (L) is present in the *right column panels*. A viscosity contrast between the *lower* and the *upper* mantle ($\nu_2/\nu_1 = 30$) is assumed in models c, d, g and h. The curves have been computed at different times, expressed in kiloyears after the initiation of loading (Fig. 2 in Piromallo et al. 1997)

(f) are isoviscous, models c, d, g and h are characterized by the presence of a sharp viscosity contrast between the lower and the upper mantle ($\nu_2/\nu_1 = 30$). The upper mantle viscosity is kept fixed at 10^{21} Pa s. The elastic response ($t = 0$) induces a negative surface topography and does not show large differences among the various models since the mass is not compensated, thus causing a downward deflection of the surface. As time increases up to the fluid limit ($t = \infty$), the characteristic features of the different models are clearly displayed. For a physical discontinuity at 670 km (Fig. 6.15a, b, c and d) the dynamic topography is always negative. Topography vanishes for masses located at the core-mantle boundary in the asymptotic regime: for long time-scales, the masses are isostatically compensated by the density jump between the core and the mantle.

The time required to reach the isostatic regime is a few thousand years in the case of an isoviscous mantle (Fig. 6.15a, b), while it rises to values in the order of 10^4 yr when the lower mantle is 30 times more viscous (Fig. 6.15c, d). For a chemical transition (Fig. 6.15e, f) masses located at 670 km depth are locally compensated, while those in the lower mantle cause a topographic high at the surface. In these latter models the asymptotic value is reached after a longer time interval due to the influence of the slower relaxation mode associated with the weak density jump at 670 km of depth. The viscosity increase causes a depression of the surface topography associated with lower mantle loads (Fig. 6.15g, h). It is worth noting that topography values are larger in the models with the lithosphere due to the stress concentration in the vicinity of an elastic element. Note, too, that a mass, when situated close to the surface, induces a topography which is approximately independent on mantle stratification: this corresponds to the usual concept of isostasy.

In Fig. 6.16 the same kind of analysis for $\ell = 2$ is performed for RSL curves. It clearly appears that RSL shows a trend which is opposite to that of the dynamic topography at the surface. We generally observe, above a mass excess, a highstand of the sea level, except in the case of chemical transition, in which a lowstand is possible for lower mantle heterogeneities. The fact that RSL curves are roughly opposite to those of the topography shows that the contribution of the latter overwhelms the signal due to the geoid. Gurnis (1990a), by means of a one-dimensional kinematic model, studied the influence of the admittance (ratio of geoid to dynamic topography) on continental flooding. He has shown that the maximum allowable admittance is close to 0.11 for long wavelengths (Gurnis 1990b). Our results reinforce these findings.

6.5.2 A Single Sinking Slab

We shall now consider RSL variations associated with a mass anomaly which mimics the effects of a slab sinking in the mantle at a constant velocity. The main assumptions of our model are: (i) the head of the mass sinks vertically, (ii) the mass extends from the surface to its head and thus increases with time, (iii) the sinking velocity corresponds to a typical velocity of subduction, (iv) the total mass of the anomaly is 2×10^{19} kg, corresponding to a slab pull of 5×10^{13} N/m along a trench 4000 km long

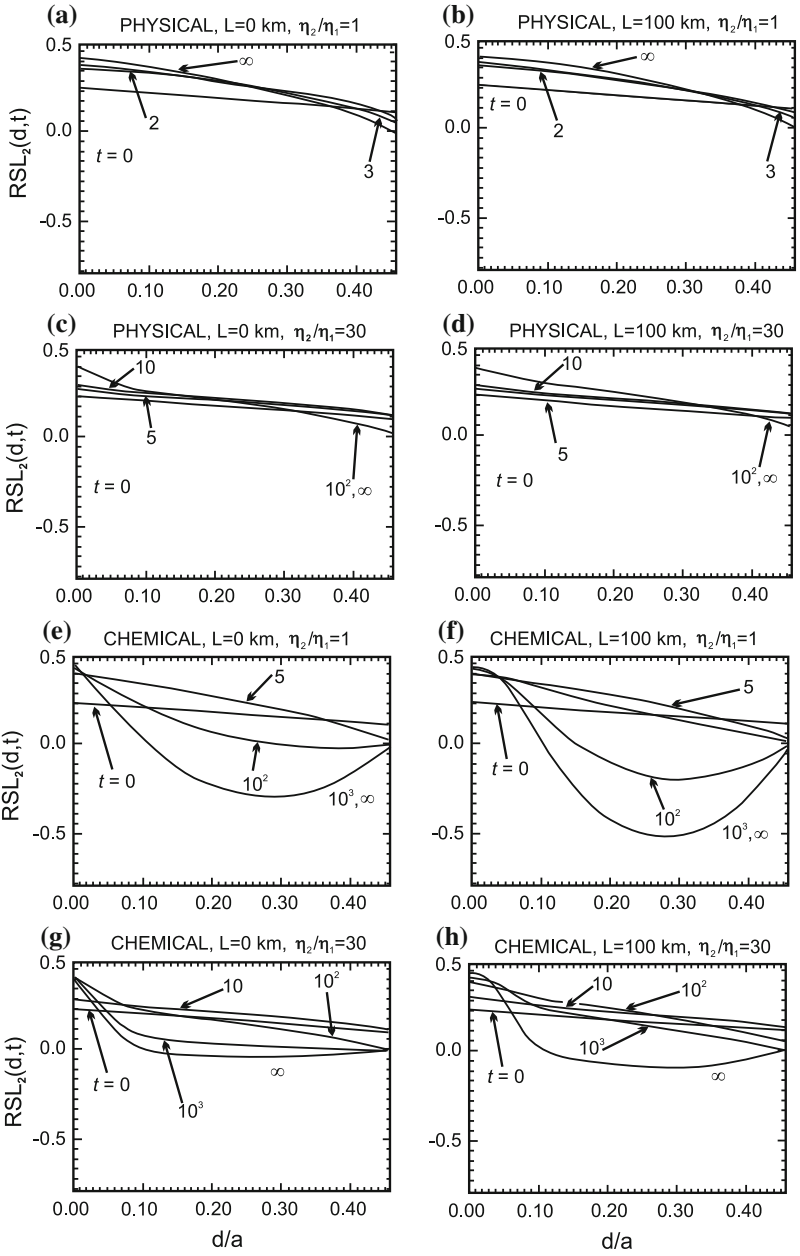

Fig. 6.16 Time evolution for RSL (d, t) as a function of depth of the point source d (normalized to the Earth's radius) and time t. A physical interface is assumed at 670 km depth in the four *top* panels, while a chemical change is considered in the four *bottom* panels. A 100 km-thick lithosphere is present in the *right* column panels. A viscosity contrast between the *lower* and the *upper* mantle ($\nu_2/\nu_1 = 30$) is assumed in models c, d, g and h. The curves have been computed at different times, expressed in kiloyear, after the initiation of loading (Fig. 3 in Piromallo et al. 1997)

(see Turcotte and Schubert 1982). We consider a total mass of the anomaly, which is of the same order of magnitude as the ice sheets in the northern hemisphere during the Pleistocene deglaciation. This allows for a direct comparison of RSL variations due to various geophysical processes. For the sake of simplicity, we simulate the mass as a column composed of identical point elements progressively switching on at increasing depths from the surface down to the 670 km depth discontinuity.

In each panel of Fig. 6.17 three values for the velocity of subduction are considered (2, 5 and 10 cm/yr). The $\ell = 2$ harmonic degree RSL is expressed in meters. We obtain only positive variations for RSL, thus showing that a subducting mass produces a highstand in sea level for each of our eight models. Another feature common to all models is the monotonically increasing trend of the three curves from the initial instant up to the point where subduction stops (with a gradient clearly depending on the subduction velocity). We observe an exponential decay in the condition of isostatic equilibrium (Fig. 6.17e–h), governed by the relaxation of the chemical upper-lower mantle interface (see Spada et al. 1992; Ricard et al. 1992). For the models with a physical interface (Fig. 6.17a–d) the asymptotic regime is reached on shorter time-scales. The fastest process (Fig. 6.17a, b and d with $v = 10$ cm/yr) produces the largest variation, with 8 m of RSL in a time span of about 7 million years. In each figure, the three curves share the same asymptotic limit, independent of the velocity of subduction. For different models the fluid limit varies considerably, ranging from larger amplitudes for isoviscous models with a physical discontinuity (Fig. 6.17a, b) to smaller ones for models with a chemical interface and no lithosphere (Fig. 6.17e, g). In two-layered convective models, we notice that RSL varies rapidly at the beginning of subduction and progressively slows down as time increases. This trend is likely explained by the decrease in amplitude with depth of the Green function for dynamic topography, which mostly contributes to RSL as we already observed. RSL fluctuations are inhibited by viscosity contrasts, unlike in uniform models.

6.5.3 A Distribution of Slabs

RSL is now portrayed for a realistic distribution of slabs along the present-day convergent margins. The sinking slabs are discretized by means of point loads (slablets) subducting with the same constant velocity (following the approach in Ricard et al. 1993). In the following simulations, it is assumed that no anomalies are present in the mantle before the initiation of subduction, which starts simultaneously along all the margins. All the slabs are then introduced at the same time, sinking into the mantle at a constant velocity, $v = 5$ cm/yr, and stopping when they have reached the 670 km interface. Figures 6.18 and 6.19 depict the RSL variations expanded up to harmonic degree $\ell = 20$, 15 Myr after the beginning of subduction. At this time, all the slabs have reached the 670 km depth and a steady-state situation is achieved by the complete relaxation of the viscoelastic flow. The harmonic degree $\ell = 20$ corresponds to a wavelength of about 2000 km, which allows a satisfactory spatial

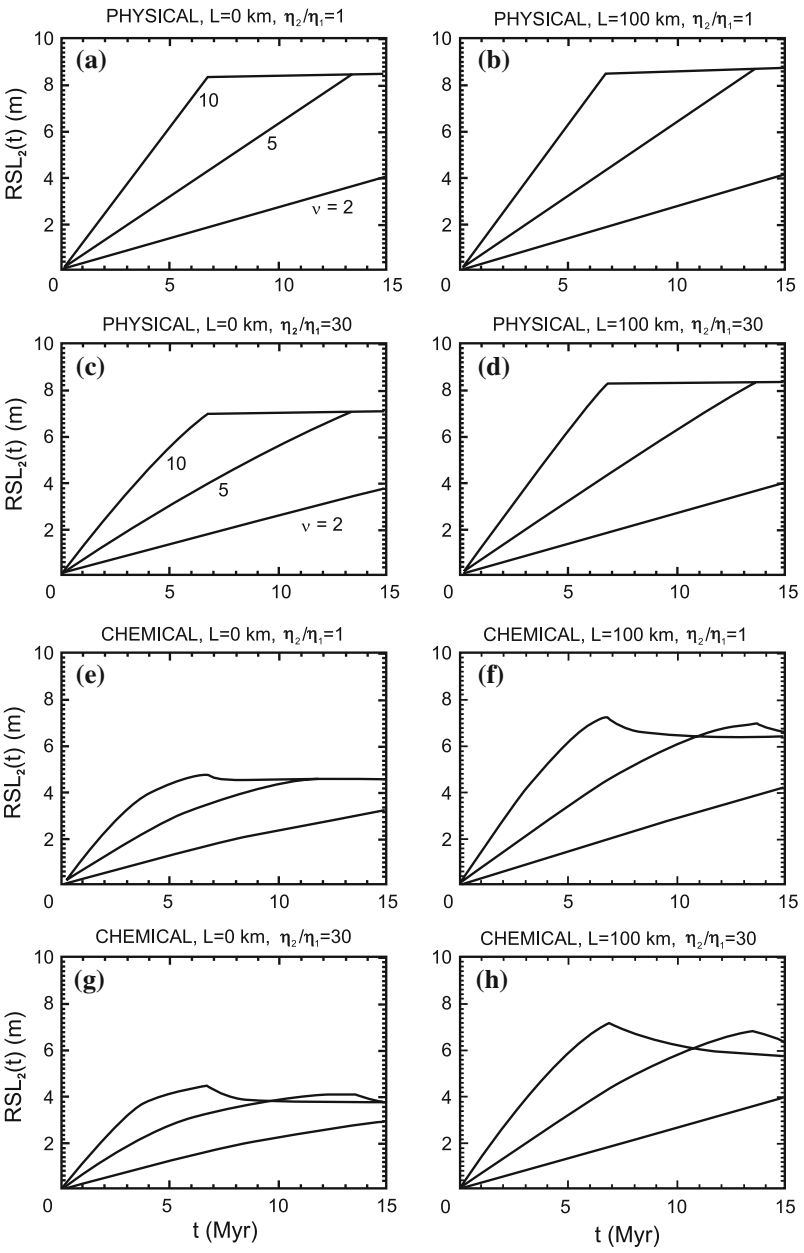

Fig. 6.17 RSL variations, expressed in meters, as a function of time from the starting of subduction for a single slab sinking down to 670 km. The three curves for each panel correspond to the different values of average velocity of subduction $v = 2, 5, 10$ cm/yr, as indicated in panels (**a**) and (**c**). The succession of models is the same as described in the previous figures (Fig. 4 in Piromallo et al. 1997)

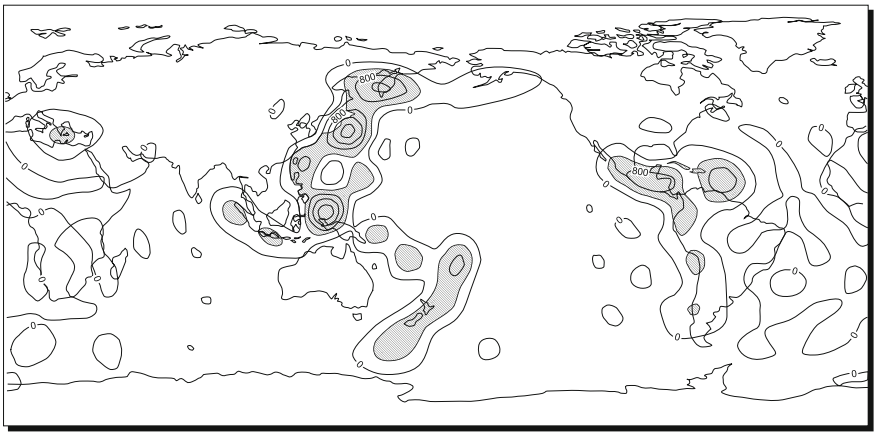

Fig. 6.18 Map of the RSL variation induced by a realistic distribution of slabs up to degree 20, 15 Myr after the beginning of subduction. The model has a 100 km thick elastic lithosphere, a physical interface at 670 km and an isoviscous mantle. Contours are 400 m apart. Redrawn from Fig. 5 in Piromallo et al. (1997)

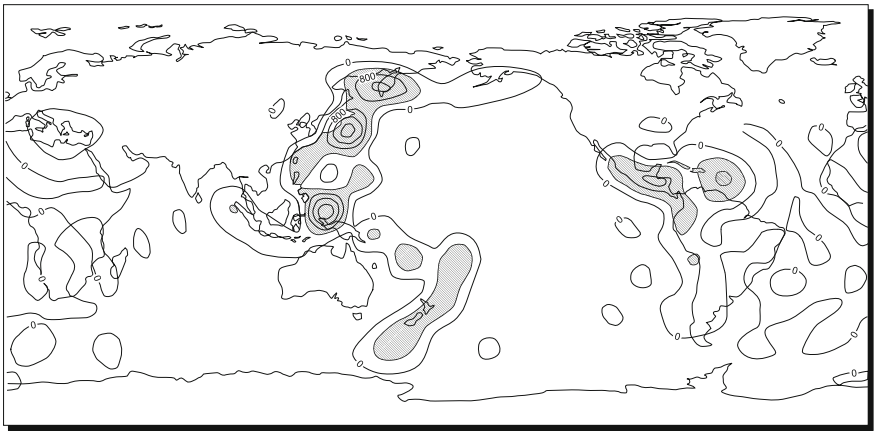

Fig. 6.19 Same as in Fig. 6.18, but with a viscosity contrast ($\nu_2/\nu_1 = 30$) between the lower and the upper mantle (model d). Redrawn from Fig. 6 in Piromallo et al. (1997)

resolution. The two maps display the results for models including a lithosphere and a physical change at the 670 km depth discontinuity.

In Fig. 6.18 the mantle is isoviscous and corresponds to the model of Figs. 6.15b and 6.16b, while in Fig. 6.19 a $\nu_2/\nu_1 = 30$ viscosity contrast is assumed, as in Figs. 6.15d and 6.16d. Since RSL is solely induced by slabs, the resulting patterns are strongly influenced by subduction margins, where large positive RSL variations are found, associated with small signals in the surrounding ocean basins. The contrast of viscosity within the mantle notably inhibits the variations in RSL. An upper bound

for RSL variations induced by subduction yields values in the order of 0.1 mm/yr and is in agreement with previous studies by Gurnis (1992) based on two-dimensional models and comparable with the value attributed to changes in the large-scale tectonic regime of the Earth.

The contribution of the dynamic topography is by far more relevant than geoid variations in the assessment of RSL changes. Results from different models bear evidence of the impact, in terms of time-scales and amplitudes, of the overall viscosity profile and of the nature of the seismic discontinuities in the mantle in determining RSL. The presence of exponentially decaying viscoelastic relaxation times is clearly evident in the models with a chemical interface. RSL rates are enhanced by the elastic lithosphere, the physical interface at 670 km depth and uniform mantle viscosity. Subduction is an important geophysical mechanism controlling long-term sea-level curves in addition to glacial variations, polar wander, plate tectonic mechanisms, thermal and compaction-induced subsidence. We refer to the work by Austermann and Mitrovica (2015) where the effects of shoreline migrations in sea-level calculations are considered, within the frame of fluid Love numbers resulting from viscoelastic Earth's modeling, combining the effects of mantle convection, ice mass changes and sediment redistribution, for a simple but physically sound example.

References

Austermann, J. and J.X. Mitrovica (2015). "Calculating gravitationally self-consistent sea level changes driven by dynamic topography". In: *Geophys. J. Int.* 203, pp. 1909–1922.

Cazenave, A.A., A. Souriau, and K. Dominh (1989). "Earth surface topography: Global coupling with hotspots, geoid and mantle heterogeneities". In: *Nature* 340, pp. 54–57.

Degrassi, A. (1955). *I porti romani dell'Istria.* Sansoni, Firenze, pp. 119–169.

Di Donato, G., A.M. Negredo, R. Sabadini, and L.L.A. Vermeersen (1999). "Multiple processes causing sea level rise in the central Mediterranean". In: *Geophys. Res. Lett.* 26, pp. 1769–1772.

Di Donato, G., L.L.A. Vermeersen, and R. Sabadini (2000). "Sea-level changes, geoid and gravity anomalies due to Pleistocene deglaciation by means of multilayered, analytical Earth model". In: *Tectonophysics* 320, pp. 409–418.

Douglas, B.C. (1995). "Global sea level change: determination and interpretation". In: *Rev. Geophys., Suppl.* (July), pp. 1425–1432.

Dziewonski, A.M. and D.L. Anderson (1981). "Preliminary reference Earth model". In: *Phys. Earth Planet. Inter.* 25, pp. 297–356.

Farrell,W.E. and J.A. Clark (1976). "On postglacial sea-level". In: *Geophys. J. R. Astron. Soc.* 46, pp. 647–667.

Flemming, N.C. (1992). "Predictions of relative coastal sea-level change in the Mediterranean based on archeological historical and tide-gauge data". In: *Climatic change in the Mediterranean.* Ed. by J.D. Milliman L. Jeeftic and G. Sestini. London, pp. 247–281.

Gurnis, M. (1990a). "Plate-mantle coupling and continental flooding". In: *Geophys. Res. Lett.* 17, pp. 623–626.

Gurnis, M. (1990b). "Ridge spreading, subduction and sea level fluctuations". In: *Science* 250, pp. 970–972.

Gurnis, M. (1992). "Rapid continental subsidence following the initiation and evolution of subduction". In: *Science* 253, pp. 1556–1558.

Johnston, P. (1993). "The effect of spatially non-uniform water loads on prediction of sea-level change". In: *Geophys. J. Int.* 114, pp. 615–634.
Lambeck, K. (1980). *The Earth's Variable Rotation: Geophysical Causes and Consequences*. Cambridge Univ. Press, Cambridge, UK, p. 449.
Lambeck, K. (1995). "Late Pleistocene and Holocene sea-level change in Greece and south-western Turkey: A separation of eustatic, isostatic and tectonic contributions". In: *Geophys. J. Int.* 122, pp. 1022–1044.
Lambeck, K., P. Johnston, and M. Nakada (1990). "Holocene glacial rebound and sea-level change in NW Europe". In: *Geophys. J. Int.* 103, pp. 451–468.
Lambeck, K. and S.M. Nakiboglu (1984). "Recent global changes in sealevel". In: *Geophys. Res. Lett.* 11, pp. 959–961.
Lanotte, R., G. Bianco, M. Fermi, P. Rutigliano, and G.R. Verdone (1996). "The CGS VLBI EUR96 geodetic solution". In: *11-th Working Meeting on European VLBI for Geodesy and Astrometry.* Ed. by G. Elgered. Chalmers Univ. of Technology, Goteborg.
Mitrovica, J.X. and J.L. Davis (1995). "Present day post-glacial sea level change far from the late Pleistocene ice sheets: implications for recent analyses of tide gauge record". In: *Geophys. Res. Lett.* 18, pp. 2529–2532.
Mitrovica, J.X. and A.M. Forte (1997). "Radial profile of mantle viscosity: Results from the joint inversion of convection and postglacial rebound observables". In: *J. Geophys. Res.* 102, pp. 2751–2769.
Mitrovica, J.X. and W.R. Peltier (1989). "Pleistocene deglaciation and the global gravity field". In: *J. Geophys. Res.* 94, pp. 13,651–13,671.
Mitrovica, J.X. and W.R. Peltier (1991). "On postglacial geoid subsidence over the equatorial oceans". In: *J. Geophys. Res.* 96, pp. 20,053–20,071.
Mitrovica, J.X. and L.L.A. Vermeersen (2002). "Ice Sheets, Sea Level and the Dynamic Earth". In: *AGU Geodynamics Series* 29, p. 310.
Nakada, M. and K. Lambeck (1987). "Glacial rebound and relative sealevel variations: a new appraisal". In: *Geophys. J. R. Astron. Soc.* 90, pp. 171–224.
Nakada, M. and K. Lambeck (1989). "Late Pleistocene and Holocene sealevel change in the Australian region and mantle rheology". In: *Geophys. J. Int.* 96, pp. 497–517.
Negredo, A.M., R. Sabadini, and C. Giunchi (1997). "Interplay between subduction and continental convergence: a three-dimensional dynamic model for the Central Mediterranean". In: *Geophys. J. Int.* 131, pp. F1–F5.
Peltier, W.R. and J.T. Andrews (1976). "Glacial isostatic adjustment, I. The forward problem". In: *Geophys. J. R. Astron. Soc.* 46, pp. 605–646.
Pirazzoli, P.A. (1997). "Mobilité verticale des côtes méediterranéennes à la fin de l'Holocene: une comparaison entre données de terrain et modélisation isostatique". In: *Transformations and Evolution of the Mediterranean Coastline.* Ed. by F. Briand and A. Maldonado. CIESM Science Series B03, 18. Bull. Inst. Oceanogr, Monaco., pp. 15–33.
Pirazzoli, P.A. (1998). "A comparison between postglacial isostatic predictions and Late Holocene sea-level field data from Mediterranean and Iranian coastal areas". In: *Dynamics of the Ice Age Earth: A Modern Perspective.* Ed. by P. Wu. Trans Tech Publications, Ütikon-Zürich, pp. 401–420.
Piromallo, C., G. Spada, R. Sabadini, and Y. Ricard (1997). "Sea-level fluctuations due to subduction: The role of mantle rheology". In: *Geophys. Res. Lett.* 24, pp. 1587–1590.
Ricard, Y., R. Sabadini, and G. Spada (1992). "Isostatic deformations and polar wander induced by internal mass redistribution". In: *J. Geophys. Res.* 97, pp. 14,223–14,236.
Ricard, Y., G. Spada, and R. Sabadini (1993). "Polar wandering of a dynamic Earth". In: *Geophys. J. Int.* 113, pp. 284–298.
Ricard, Y. and C. Vigny (1989). "Mantle dynamics with induced plate tectonics". In: *J. Geophys. Res.* 94, pp. 17,543–17,559.
Roncuzzi, A. (1970). "Rapporti fra ricerca archeologica e studio dell'abbassamento del suolo nel ravennate". In: ed. by C. Matha. Vol. 4. Studi Idrogeologici dei Territori Padani Inferiori, Atti Casa Matha, Ravenna, Italy, pp. 33–53.

Sabadini, R., C. Doglioni, and D.A. Yuen (1990). “Eustatic sea-level fluctuations induced by polar wander”. In: *Nature* 345, pp. 708–709.

Sabadini, R., G. Spada, and Y. Ricard (1993). “Time-dependent density anomalies in a stratified, viscoelastic mantle: implications for the geoid, Earth’s rotation and sea-level fluctuations”. In: *Surv. Geophys.* 14, pp. 537–553.

Schmiedt, G. (1979). “Contributo della fotografia aerea alla conoscenza del territorio di Aquileia”. In: *Antichitá Altoadriatiche* 15, pp. 145–188.

Spada, G., R. Sabadini, D.A. Yuen, and Y. Ricard (1992). “Effects on post-glacial rebound from the hard rheology in the transition zone”. In: *Geophys. J. Int.* 109, pp. 683–700.

Spakman, W. (1990). “Tomographic images of the upper mantle below central Europe and the Mediterranean”. In: *Terra Nova* 2, pp. 542–553.

Turcotte, D.L. and G. Schubert (1982). *Geodynamics. Applications of Con-tinuum Physics to Geological Problems.* John Wiley and Sons Inc., New York, p. 450.

Tushingham, A.M. and W.R. Peltier (1991). “ICE-3G: A new global model of late Pleistocene deglaciation based upon geophysical predications of postglacial relative sea level change”. In: *J. Geophys. Res.* 96, pp. 4497–4523.

Woodward, R.S. (1998). “On the form and position of mean sea level”. In: *United States Geol. Survey Bull.* 48, pp. 87–170.

Wu, P. and W.R. Peltier (1983). “Glacial isostatic adjustment and the free air gravity anomaly as a constraint on deep mantle viscosity”. In: *Geophys. J. R. Astron. Soc.* 74, pp. 377–449.

Chapter 7
TPW Driven by Subduction: Non-linear Rotation Theory

Abstract This chapter deals with the development of a non-linear rotation theory, driven by internal density anomalies, as for those due to mantle convection, for a stratified, viscoelastic, incompressible Earth. We show how mantle convection TPW represents a very powerful constraint for the mantle viscosity profile, and our finding is that the lower mantle has to be definitively stiffer than the upper mantle.

7.1 Formulation of the Non-linear Rotation Problem

When dealing with marked excursions of the rotation axis, such as TPW driven by subduction, we must use, as shown in this section reworked from Ricard et al. (1993), the fully non-linear Eq. (3.6), where the inertia tensor $\mathbf{I}$ can be divided into three contributions of decreasing amplitudes

$$\mathbf{I(t)} = I\delta_{ij} + \frac{a^5 {k_2}^T(t)}{3G} * (\omega_i(t)\omega_j(t) - \frac{1}{3}\omega^2(t)\delta_{ij}) + (\delta(t) + k_2^L(t)) * \Delta I_{ij}(t) \quad (7.1)$$

where the asterisk denotes the time convolution and the first two terms are those of Eq. (3.31). The three terms on the right-hand side are of the order of 0.33 $M_E a^2$, 1.08×10^{-3} $M_E a^2$ and 10^{-5} $M_E a^2$, where M_E and a are the mass and the radius of the Earth.

The degree $\ell = 2$ Love numbers ${k_2}^T(t)$ and $k_2^L(t)$ are based on the fundamental matrix $\mathbf{Y}_2(a)$ for an incompressible Earth's model, as for Eqs. (2.42)–(2.47).

The first term $I\delta_{ij}$ denotes the tensor of a spherical non-rotating Earth and is equal to 0.33 $M_E a^2$. The second term results from the centrifugal potential deforming the Earth. This means that any change in rotation is equivalent to a new potential applied to the Earth's surface. When under such a boundary condition, the planet matches an inertia tensor equal to the convolution of $k_2^T(t)$, the tidal Love number of harmonic degree 2, with the time history of the centrifugal potential. As we have already seen in Eqs. (3.32)–(3.34), the contribution related to the rotation shows that a planet,

R. Sabadini et al., *Global Dynamics of the Earth: Applications of Viscoelastic Relaxation Theory to Solid-Earth and Planetary Geophysics*,
DOI 10.1007/978-94-017-7552-6_7

rotating at a constant velocity Ω, reaches a steady-state axi-symmetrical shape with a polar inertia

$$C = I + \frac{2k_f^T a^5}{9G}\Omega^2 \tag{7.2}$$

and two equatorial inertia

$$A = I - \frac{k_f^T a^5}{9G}\Omega^2 \tag{7.3}$$

where k_f^T denotes the fluid tidal Love number defined in Eq. (3.35) and the amplitude of the rotational contribution to inertia is

$$C - A = \frac{k_f^T a^5}{3G}\Omega^2 \tag{7.4}$$

If we assume that the Earth is close to hydrostatic equilibrium, we find that this value can be identified with the observed dynamic flattening $C - A = 1.08 \times 10^{-3}\ M_E a^2$.

The third term in the inertia tensor $\mathbf{I}$, Eq. (7.1) is related to the mass redistribution due to geophysical processes inside the Earth or at its surface, with k_2^L denoting the loading Love number appropriate for surface loading, or internal loads; in Eq. (7.1), $\Delta I_{ij}(t)$ represents the inertia changes due to a given geophysical process, without taking into account any dynamic deformation. These inertia changes act directly on the planet through the Dirac delta function and $\Delta I_{ij}(t)$ generalizes, also for internal loads, the terms ΔI_{13}^L, ΔI_{23}^L entering Eq. (4.2) or (4.3) for surface ice loads, and include the time dependent part of the inertia perturbation, so leading to the complete inertia perturbation tensor. The convolution accounts for the effects of isostatic compensation. The amplitude of ΔI_{ij} can be estimated for the excitation sources. For example, the Pleistocene deglaciation in Chap. 4 corresponds to a change of inertia with an amplitude of about $10^{-5}\ M_E a^2$.

In Chaps. 3 and 4 we made use of linearized rotation equations, so that only the perturbations of ω with respect to a starting vector Ω were considered. The general non-linear problem governed by the fully non-linear rotational equations has been solved for very simple models and for constant excitation sources (Lefftz et al. 1991; Munk and MacDonald 1960). This section deals with the effects of a time-dependent mantle mass redistribution on the Earth's rotation. The impact of slow varying processes on rotation was first considered within a self-consistent fully non-linear approach by Ricard et al. (1993). Internal mass redistribution could induce a TPW velocity comparable to the observed value of around 1 Deg/Myr and eventually move the Earth's pole to a great extent. The practical problem in dealing with these issues is to compute realistic Love numbers and to efficiently perform the convolutions in the previous equations.

When dealing with large excursions of the rotation axis, it is necessary to overcome the numerical difficulties of solving the non-linear problem arising from the interaction of different time scales spanning various decades. These time constants range from zero (the elastic impulse) to a relaxation time of several million years associated with the $M1$ mode, the slowest relaxation mode in the four-layer Earth's model considered in this chapter, Table 7.1.

Such a very large $M1$ time span also holds for the geophysical excitations, preventing any direct approach to the integro-differential system above. The complexity of numerical integration is further increased by the fact that $\omega(t)$ does not monotonously vary but revolves at a Chandler period of about 435 days around an average solution. An approximate solution of these equations is thus necessary. Since this Section deals with very slow geophysical processes like plate motions and mantle convection, our excitation function varies with time constants larger than 1 Myr. To begin with, let us assume that our Earth's model has no internal non-adiabatic density discontinuity, so that the $M1$ mode is not excited and the slowest relaxation time is much smaller than 1 Myr. In this case, $|s_i t| \gg 1$ or $|s| \ll s_i$ and we can thus approximate the loading Love number as

$$k_2^L(t=\infty) = k_E^L - \sum_{i=1}^{M} \frac{k_i^L}{s_i}. \tag{7.5}$$

This enables us to identify the time-dependent isostatic Love number $k_2^L(t)$ with its fluid limit k_f^L.

We cannot directly make use of the fluid limit k_f^T for the tidal case because the time-dependent readjustment of the equatorial bulge during polar wander must be self-consistently taken into account. Since the approximation is somewhat more complex here, we must allow for the possibility of a time-dependent readjustment of the equatorial bulge during polar wander. Thus, in the Laplace domain

$$k_2^T(s) = k_E^T + \sum_{i=1}^{M} \frac{k_i^T}{s - s_i} \tag{7.6}$$

Table 7.1 Parameters for the 4-layer fixed-boundary contrast Earth's model

Layer	r (km)	ρ (kg/m^3)	μ (N/m^2)	
1	6371 – 6271	2689	2.82×10^{10}	Lithosphere
2	6271 – 5951	4430	8.37×10^{10}	Upper mantle
3	5701 – 3480	4919	2.17×10^{11}	Lower mantle
4	3480 – 0	10,927	0	Inviscid fluid core

r is the distance with respect to the centre of the Earth, ρ the density of the layer, and μ the rigidity

as Eq. (3.109) and $|s| \ll s_i$ to first order in s/s_i, we make the first order approximation

$$k_2^T(s) = k_E^T - \sum_{i=1}^{M} \frac{k_i^T}{s_i}\left(1 + \frac{s}{s_i}\right) \tag{7.7}$$

which leads to Eq. (3.134) once included in Eq. (7.1) in the s-domain, and then anti-transformed from the s- to the t-domain.

By defining the fluid tidal Love number as in Eq. (7.5), we have

$$k_2^T(s) = k_f^T - T_1 s \tag{7.8}$$

where T_1 is defined as in Eq. (3.119).

It should be noted that in Ricard et al. (1993) the time scale for the readjustment of the equatorial bulge is defined by $T_1^* = T_1/k_f^T$ which makes in the quoted paper this time scale to appear as $k_f^T T_1$ rather than T_1, according to our herein definition, which has to be taken into account when comparing the equations of this chapter, which agrees with the definition given in Eq. (3.119), with those of Ricard et al. (1993).

The expansion given by Eq. (7.8) is valid for $|s| \ll |s_{M1}|$, meaning that our approximation holds for geophysical processes slower than the relaxation time controlling the readjustment of the non-adiabatic discontinuity at the 670 km depth. The quality of the approximation for the tidal Love number is reinforced by the fact that, for most of the realistic models of the Earth's mantle, the amplitude of the residue k_{M1}^T is negligible. Put in another way, this vanishing strength means that a change in the Earth's centrifugal potential induces no appreciable displacement of the 670 km depth interface.

$M1$ plays a major role in the loading problem. When $k^L(s)$ is computed for masses found inside the mantle, the amplitude k_{M1}^L associated with the $M1$ mode can be large. We thus separate the slowest mode from the fast relaxing ones and use the following equation for $k_2^L(t)$

$$k_2^L(t) = k_f^L + \frac{k_{M1}^L}{s_{M1}} e^{s_{M1} t}. \tag{7.9}$$

In this equation, expressing the convolution of the loading Love number with a Heaviside function, it is assumed that on the given time scale all the modes, except possibly the $M1$ mode, have already relaxed and the convolution entering Eq. (7.1) between the exponential part of $k_2^L(t)$ and ΔI_{ij} can thus be easily performed numerically.

The quantity $1 + k_f^L$, for the harmonic degree $\ell = 2$, as a function of depth of the excitation source is shown in Fig. 7.1 for a number of Earth's models.

These functions are zero for mass anomalies close to the core-mantle boundary. For non-adiabatically stratified models (bottom row), the mass anomalies are also perfectly compensated for when they are close to the density jump at 670 km depth. For masses at the surface, $1 + k_f^L$ is also zero in the case without the lithosphere (left

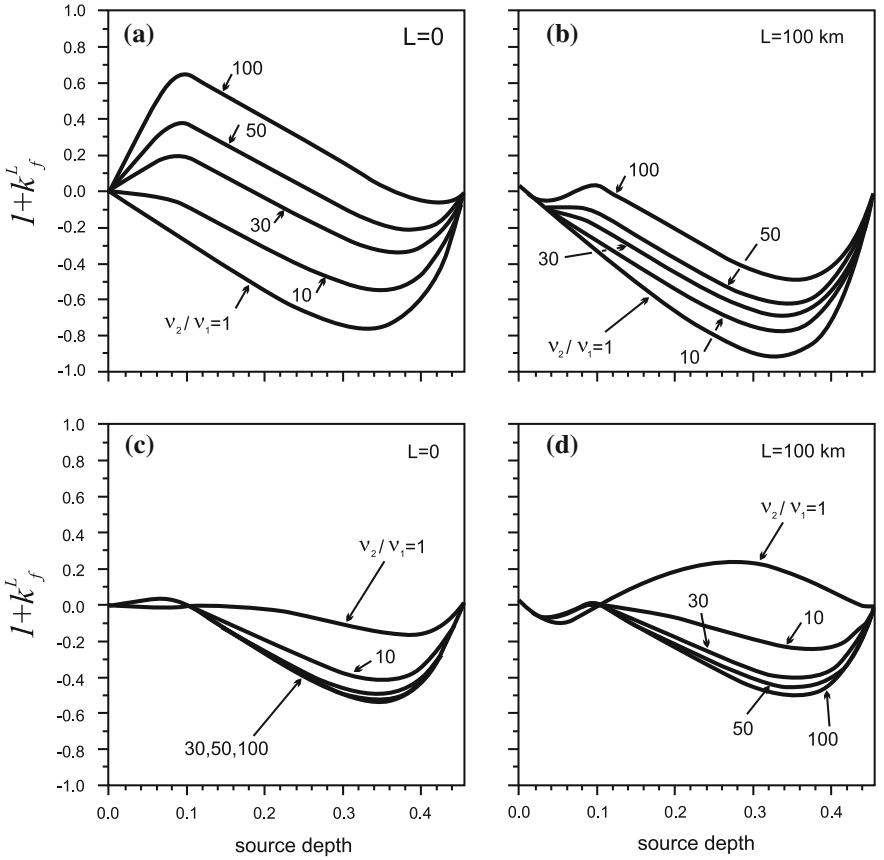

Fig. 7.1 Perturbation in the inertia in the long-term approximation due to an inertia source of unit amplitude introduced at time $t = 0$ in the mantle. This perturbation $1 + k_f^L$ is plotted as a function of the mass anomaly depth, from the normalized Earth's surface at 0.0 to the CMB, for a viscosity jump at the upper-lower mantle interface by a factor of 1, 10, 30, 50 or 100. In the *first row*, the mantle density is uniform, in the *second row* it increases by 9 % at 670 km depth. A lithosphere is present in the *right column*. Redrawn from Fig. 4 in Ricard et al. (1993)

column), while a slight undercompensation is supported by elastic stresses when the lithosphere is present (right column). In the case of moderate viscosity increases in the mantle, a positive mass anomaly gives rise to a negative $1 + k_f^L$; larger viscosity variations can impose a positive $1 + k_f^L$. As the inertia tensor is related to the geoid of degree 2, the excitation functions $1 + k_f^L$ only differ from the geoid kernels by a normalization factor (Ricard et al. 1984; Richards and Hager 1984). The long-term limits of the viscoelastic models without purely elastic lithospheres exactly reproduce what has been found for purely viscous steady-state models.

The equivalence between long-term viscoelastic models and viscous steady-state models needs some clarification. That is, when $t \to \infty$ or $s \to 0$, our viscoelastic model assumes the character of a Newtonian viscous fluid (Wu and Peltier 1982) and has the same surface Love numbers. For internal loads, the displacements inside the viscoelastic mantle tend to infinity when $s \to 0$, but the associated velocities approach finite values equal to those obtained via steady-state viscous models. When $s \to 0$, the viscous limit of a viscoelastic model cannot be directly obtained by setting $s = 0$ in the rheological law, which would correspond to the rheology of an inviscid fluid. That steady-state viscous models can be used even for time-dependent loads is due to the fact that interface deformations are generally faster than the time-varying positions of the loads. However, the expression of $k_2^L(t)$, which explicitly includes the time dependence of the $M1$ mode, allows us to take into account the upper-lower mantle interface, which readjusts slowly. The need for keeping the $M1$ mode in the convolution of the load history with the isostatic Love numbers is illustrated in Fig. 7.2. We computed the time-dependent excitation function $1 + k_f^L$ for four chemically stratified models. While in the top row of Fig. 7.2 the mantle viscosity is uniform, it increases by a factor of 50 in the lower row. The right column differs from the left by the presence of a lithosphere. The corresponding Love numbers are plotted by a dashed line, 0.2 Myr (panel (a)) or 1 Myr (panels (b), (c) and (d)) after the imposition of a Heaviside load. Since at such time the Love numbers are far from reaching their asymptotic values (full lines), it is necessary to account for the explicit time-dependence of the $M1$ mode when chemically stratified models are used.

Inserting Eq. (7.8) into Eq. (7.1), the latter transformed into the s-domain, and taking into account that the image of a time derivative $\dot{f}(t)$ is $sf(s)$ in the s-domain, we can express the total inertia tensor in the time domain after anti-Laplace transformation as

$$\mathbf{I} = I\delta_{ij} + \frac{a^5 k_f^T}{3G}\left(\omega_i\omega_j - \frac{1}{3}\omega^2\delta_{ij}\right) - \frac{a^5 T_1}{3G}\left(\dot{\omega}_i\omega_j + \omega_i\dot{\omega}_j - \frac{2}{3}\omega_l\dot{\omega}_l\delta_{ij}\right) + E_{ij} \tag{7.10}$$

where

$$E_{ij} = (\delta(t) + k_2^L(t)) * \Delta I_{ij}(t) \tag{7.11}$$

consistently with Eq. (7.1) and with Eqs. (3.134)–(3.136).

By neglecting the terms $\ddot{\omega}$ and $\dot{\omega}^2$ for consistency with the previous approximations, and remembering that ω_3 contains the zero-order term as in Eq. (3.129), these definitions and the basic Eq. (3.6) with $\mathbf{L} = \mathbf{0}$ give us (Ricard et al. 1993)

$$\Delta_{ij}(\omega)\dot{\omega}_j + \Gamma_{ij}(\omega, E, \dot{E})\omega_j = 0 \tag{7.12}$$

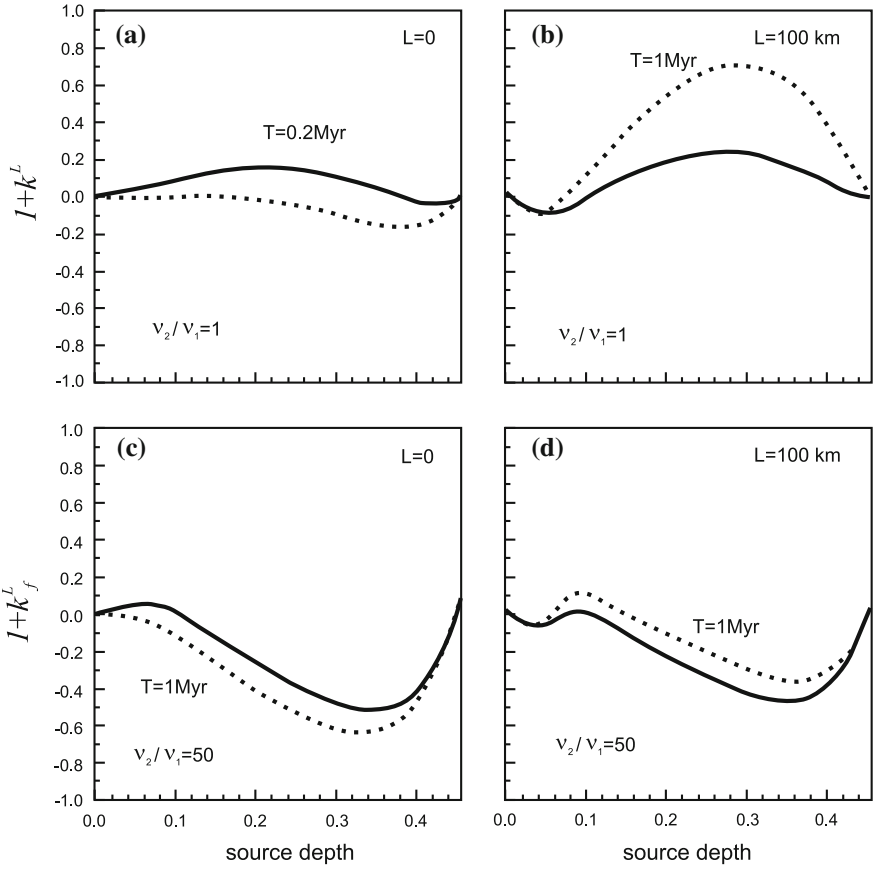

Fig. 7.2 Inertia perturbation $1 + k_f^L$ computed at time $t = 0.2$ Myr or $t = 1$ Myr after the introduction of a mass anomaly (*dashed line*). A *solid line* depicts the fluid limit obtained at very long times. The models used in the four panels are stratified in density and the long-term behavior is controlled by the $M1$ mode. *On top*, the mantle viscosity is uniform, at *bottom* it increases by a factor of 50. A lithosphere is present in the *right column*. For cases (**b–d**) the asymptotic regime is only reached after millions of years. Redrawn from Fig. 5 of Ricard et al. (1993)

where

$$\Delta = \begin{pmatrix} I & \frac{T_1 a^5}{3G}\omega^2\omega_3 & -\frac{T_1 a^5}{3G}\omega^2\omega_2 \\ -\frac{T_1 a^5}{3G}\omega^2\omega_3 & I & \frac{T_1 a^5}{3G}\omega^2\omega_1 \\ \frac{T_1 a^5}{3G}\omega^2\omega_2 & -\frac{T_1 a^5}{3G}\omega^2\omega_1 & I \end{pmatrix} \tag{7.13}$$

$$\Gamma = \begin{pmatrix} \dot{E}_{11} & \Sigma_3 & -\Sigma_2 \\ -\Sigma_3 & \dot{E}_{22} & \Sigma_1 \\ \Sigma_2 & -\Sigma_1 & \dot{E}_{33} \end{pmatrix} \tag{7.14}$$

and

$$\Sigma_i = E_{ij}\omega_j. \tag{7.15}$$

Exercise 21 Derive Eq. (7.12), starting from Eqs. (7.10) and (7.11) and from the definitions given in Eqs. (7.13) to (7.15).

These equations can also be found in Ricard et al. (1993), their Eqs. (11)–(15). Since the diagonal terms of Δ are smaller than the non-diagonal terms, a further approximation might neglect them (Lefftz et al. 1991). In such a case, Δ is not invertible and the conservation of ω^2 must be imposed. Even by including its diagonal terms, the matrix Γ is not numerically ill-conditioned. The approximation, i.e. neglecting the diagonal terms, provides insight into the basic physics of polar wander on a long-term scale. This approximation is equivalent to replacing Eq. (3.6) by

$$\mathbf{I} \cdot \omega = \alpha\omega, \tag{7.16}$$

where α is unknown. The Euler equation degenerates into an eigenvalue problem: the angular momentum $\mathbf{I} \cdot \omega$ remains constantly parallel to the angular velocity ω. Likewise, the equation above indicates that the non-diagonal terms of $\mathbf{I}$, namely ΔI_{13} and ΔI_{23}, in a reference frame where z coincides with ω, are zero in the long-term approximation. Note, of course, that the inertia matrix $\mathbf{I}$ includes not only the effects of internal masses in a dynamic non-rotating Earth but also the rotational deformations. The main inertia of the exciting source is not necessarily parallel to the rotation axis. We can check the validity of our equations by computing the change in the rotation vector $(0, 0, \Omega)$ when perturbed at time $t = 0$ by a change in inertia. By taking into account that

$$C - A = \frac{k_f^T a^5}{3G}\Omega^2 \tag{7.17}$$

by disregarding the terms that include ω_1 and ω_2, since we start from an initial configuration $(0, 0, \Omega)$ in which these are zero, and by assuming that ω_3 is equal to Ω, the previous matrix Eq. (7.12) yields

$$\dot{\omega}_1 + i\dot{\omega}_2 = \Omega\left(\frac{1}{T_1/k_f^T + iI/[\Omega(C-A)]}\right)\frac{E_{13} + iE_{23}}{C - A} \tag{7.18}$$

$$\dot{\omega}_3 = -\Omega\frac{\dot{E}_{33}}{I}. \tag{7.19}$$

Exercise 22 Derive the linearized Eqs. (7.18) and (7.19) from Eq. (7.12).

Polar motion and change in length of day are governed by these equations, decoupled as in Eqs. (3.51) and (3.46). In fact, the first equation above, appropriate for

long time scales, coincides with Eqs. (3.51) and (3.46) once the explicit expression of T_1 given by Eq. (3.119) is considered, except for the appearance of the moment of inertia I, instead of the equatorial moment of inertia A, due to our approximations.

This equation affords a better understanding of the differences between the inertia tensor of the non-rotating dynamic Earth $I\delta_{ij} + E_{ij}$ and the rotating dynamic Earth $\mathbf{I}$. The observed present-day polar wander has a velocity of 1 Deg/Myr, is directed toward Hudson Bay and is mainly related to post-glacial rebound (Vermeersen and Sabadini 1997). Although the elapsed time since the deglaciation is too short for a complete relaxation of the modes involved in the tidal relaxation process, we can use this equation to estimate the order of magnitude of the excitation presently driving the pole. For $T_1 = 20$ kyr, which corresponds to a viscosity increase in the mantle of around 25, as shown in Fig. 3.7, the excitation $E/(C - A)$ amounts to 3.5×10^{-4}, a value which can be translated into terms of a geoid anomaly of degree 2 and order 1 of about 7 m. While the tensor E of the non-rotating Earth presents non-diagonal terms E_{31} and E_{32} associated with a 7-m high geoid anomaly of degree 2 and order 1, the tensor $\mathbf{I}$ of the rotating Earth is purely axi-symmetrical and associated with a geoid without terms of degree 2 and order 1. The very existence of the tensor E only arises from the observation of polar wander. We can see from this linearized equation that the planet, subjected to a change of inertia of order E, will wander with a characteristic time of order $T_1(C - A)/E$. A lower bound for this time scale can be estimated from the ratio of the Earth's flattening (=21 km) to the geoid height anomalies of degree 2 (=100 m). This characteristic time is thus larger than 200 T_1. That is, under a change of inertia, the Earth can shift its rotation pole from a starting position to a new position on a time scale larger than a few 100 kyr or 1 Myr, depending upon its internal stratification.

Resolving the non-linear equations above can be performed by a standard Runge-Kutta algorithm, as done in Ricard et al. (1993), which generalizes for a stratified Earth and a complex load history the solution obtained by Milankovitch (1934) in a discussion of possible polar wander induced by the distribution of continents on top of a homogeneous viscoelastic Earth.

7.2 Polar Wander Velocity for a Distribution of Slabs

An idealized model for mass redistribution within the mantle, first modeled in Ricard et al. (1993), is now presented to show the effects of convection on the Earth's rotation, based on the formulation of the previous Sect. 7.1. This simple model catches some of the basic features of mantle convection and is inspired by Goldreich and Toomre (1969). We assume that slabs randomly distributed on the sphere, the analogues of Gold (1955) beetles, are falling inside the mantle with a new slab sinking every two million years. Their velocity in the upper mantle is equal to 10 cm/yr and is reduced according to the increase in mantle viscosity in the lower mantle. On average, eight slabs are present at the same time in the upper mantle and all have the same mass of 2×10^{19} kg. We computed from this mantle convection model, the inertia tensor of

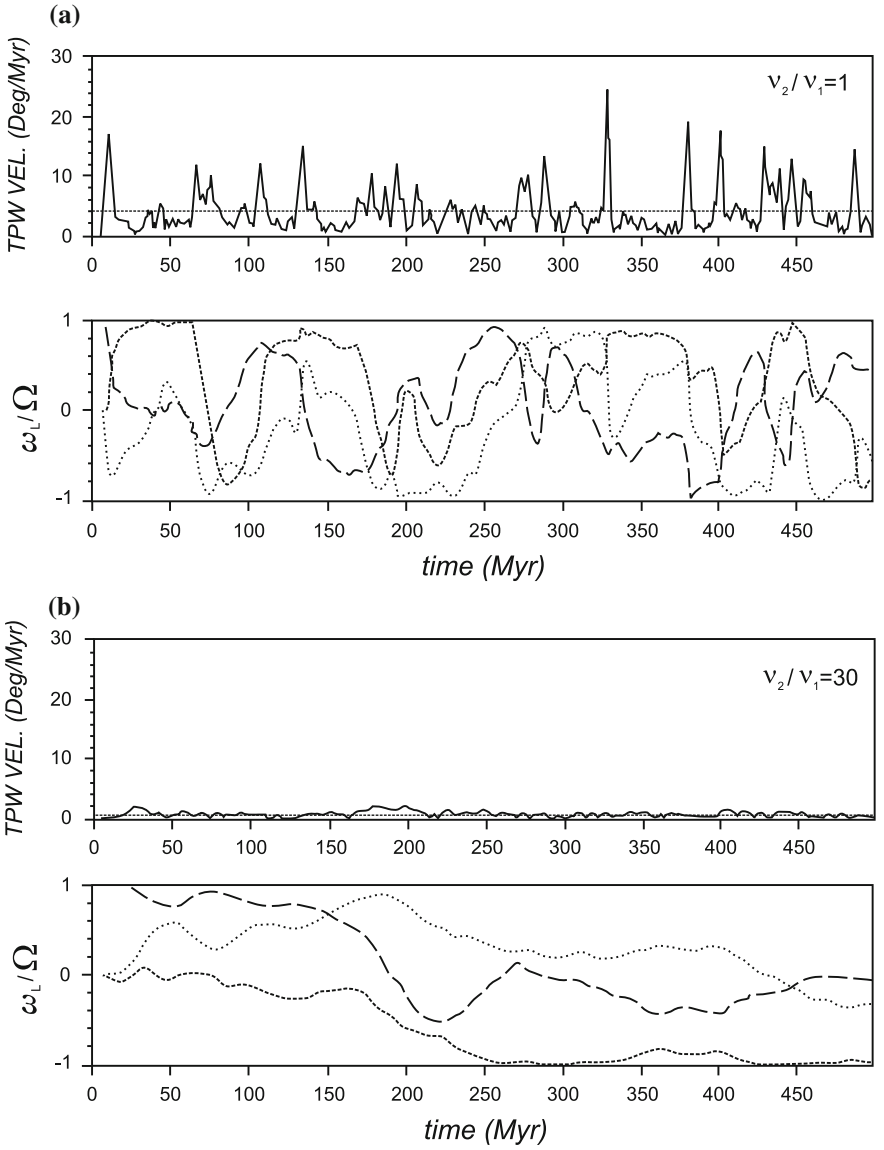

Fig. 7.3 Velocity of polar wander and normalized components of the angular velocity vector in an Earth-fixed reference frame induced by a random distribution of sinking slabs. In *panel* **a** the mantle is uniform and the Earth rotation axis is highly unstable. Increasing viscosity by a factor 30 in the *lower mantle* **b** drastically reduces the amplitude of TPW rate. The 670 km depth interface is supposed to be a phase-change discontinuity. Redrawn from Fig. 9 in Ricard et al. (1993)

our Earth's model in a constant geographical framework for a time span of 500 Myr. The results are depicted in the following Fig. 7.3, panels (a) and (b), for two different rheological stratifications. Our Earth's model is adiabatically stratified in both cases. In panel (a), the mantle is uniform, whereas in panel (b) the lower mantle viscosity is increased by a factor 30. The bottom part of each panel shows the variations of the three components of the rotation vector in a geographical framework.

The amplitude of the initial rotation vector has been used to normalize the velocity components. The top part of each panel shows the rate of TPW in Deg/Myr; the dashed line represents the average TPW velocity. Note the striking differences in the rotation behavior between a uniform and a stratified mantle, panels (a) and (b). A viscosity increase at 670 km depth inhibits mantle flow and slows the average TPW velocity below 1 Deg/Myr. This slow-down is due to three concurrent effects, related to the viscosity increase. First, the viscosity increase reduces the slab velocities and, hence, the amplitudes of the time derivatives of the inertia tensor. Second, the viscosity increase reduces the amplitude of the loading excitation term $1 + k_f^L$, at least for a viscosity increase lower than 100. And, third, it increases the time T_1 of the rotational response by channeling the flow into the upper mantle. Each slab in the model with a homogeneous mantle crosses the whole mantle in about 30 Myr, so that, after a transient regime of 30 Myr, our model reaches a steady-state behavior where the slabs are uniformly distributed in the mantle.

References

Gold, T. (1955). "Instability of the earth's axis of rotation". In: *Nature* 175, pp. 526–529.

Goldreich, P. and A. Toomre (1969). "Some remarks on polar wandering". In: J. *Geophys*. Res. 74, pp. 2555–2567.

Lefftz, M., H. Legros, and J. Hinderer (1991). "Non-linear equations for the rotation of a viscoelastic planet taking into account the influence of a liquid core". In: *Celest. Mech. Dynamical Astron*. 52, pp. 13–43.

Milankovitch, M. (1934). "Der Mechanismus der Polverlagerungen und die daraus sich ergebenden Polbahnkurven". In: *Gerlands Beitr. z. Geophys*. 42, pp. 70–97.

Munk, W.H. and G.J.F. MacDonald (1960). *The Rotation of the Earth: A Geophysical Discussion*. Cambridge University Press, Cambridge, UK.

Ricard, Y., L. Fleitout, and C. Froidevaux (1984). "Geoid heights and lithospheric stresses for a dynamic Earth". In: *Ann. Geophysicae* 2, pp. 267–286.

Ricard, Y., G. Spada, and R. Sabadini (1993). "Polar wandering of a dynamic Earth". In: *Geophys. J. Int.* 113, pp. 284–298.

Richards, M.A. and B.H. Hager (1984). "Geoid anomalies in a dynamic Earth". In: *J. Geophys. Res.* 89, pp. 5987–6002.

Vermeersen, L.L.A. and R. Sabadini (1997). "A new class of stratified viscoelastic models by analytical techniques". In: *Geophys. J. Int.* 129, pp. 531–570.

Wu, P. and W.R. Peltier (1982). "Viscous gravitational relaxation". In: *Geophys. J. R. Astron. Soc.* 70, pp. 435–485.

Chapter 8
Post-seismic Deformation

Abstract This chapter deals with the mechanism of stress relaxation due to the viscous flow after the occurrence of an earthquake, leading to post-seismic deformation. We consider stress relaxation operating both in the Earth's mantle or in the low viscosity layers of the crust. We elucidate the influence of lithospheric and mantle stratification on post-seismic deformation, both at the global scale and the the local scale. The aim is to provide a powerful tool for the interpretation of GNSS (Global Navigation Satellite System), SAR (Synthetic Aperture Radar) and GRACE data sampled at seismically active regions, where earthquakes occur within the plates or at their boundaries. Particular attention is devoted to some seismically active regions in the Mediterranean area, where we first discovered the signatures of post-seismic deformation.

8.1 Global Post-seismic Deformation

The occurrence of faulting in the lithosphere is responsible for an instantaneous deformation of the Earth's surface, which is called co-seismic deformation. In response to the induced elastic stress in the mantle and in the crust, creep occurs in this deep portion of the planet, or in the ductile portion of the crust, via viscoelastic stress relaxation. Immediately after the occurrence of the earthquake, the mechanism of stress release due to viscous flow in the ductile part of the Earth's crust starts to operate, leading to post-seismic deformation. The delayed deformation of the lithosphere caused by stress relaxation in the mantle or in the low viscosity layers of the crust is called post-seismic deformation. In this section, and within the frame of an incompressible Earth's model based on the fundamental matrix given by Eq. (2.42), we deal with the effects of a realistic PREM-based Dziewonski and Anderson (1981) lithosphere and mantle stratification on post-seismic deformation after a series of preliminary analyses based on simplified models carrying at most four layers, namely the lithosphere, the upper and lower mantle and the core. Relaxation is here considered

R. Sabadini et al., *Global Dynamics of the Earth: Applications of Viscoelastic Relaxation Theory to Solid-Earth and Planetary Geophysics*,
DOI 10.1007/978-94-017-7552-6_8

to occur in the mantle, while in the following section the effects of stress relaxation in the ductile portion of the crust will be considered. As we saw in Chap. 5, the implementation of compressibility as discussed in Sects. 2.5–2.8 is key for a correct modeling of co-seismic deformation, as shown in Sect. 5.4.3, Fig. 5.20 for example, but incompressibility can be considered a reasonable approximation when dealing with post-seismic deformation, when the Earth's material behaves as a viscous fluid. Our analysis is key to the understanding of plate-mantle interaction, especially for the correct interpretation of geodetic VLBI and GPS data of plate deformation when earthquakes occur within the plate or at its boundaries. Improvements in satellite differential radar interferometry (Massonnet et al. 1993) or in precise GPS monitoring of crustal motions necessitate realistic and precise models of co-seismic and post-seismic effects, which must include sphericity, self-gravitation and stratification of the lithosphere and mantle, as first outlined in the present analysis based on a completely analytical approach. In order to study post-seismic deformation we have to go up to harmonic degrees of the order of 10^3, one order of magnitude higher than in post-glacial rebound, as the peaks of the total strength of the modes as a function of zonal degree can be situated at zonal degrees of several thousands for shallow earthquakes in the upper crust, as considered in this section.

With respect to post glacial rebound, the toroidal solutions must also be considered. The procedure for solving post-seismic problems in viscoelasticity was first described by Sabadini et al. (1994a).

Figure 8.1, dealing with the relaxation times as a function of harmonic degree, shows that the modes form nice continuous-like patterns with increasing harmonic degree. The model used in this calculation is a 10-layer model, averaged from PREM, in which the uppermost mantle is stratified into four viscoelastic layers, with varying density and rigidity but uniform viscosity of 10^{20} Pa s, in agreement with the findings of Chap. 5; the transition zone and lower mantle are homogeneous. The model is presented in Table 8.1, where the viscosity is volume-averaged from the convex viscosity profile given in Fig. 1 of Vermeersen and Sabadini (1997).

The fastest transient viscoelastic modes superimpose at the bottom of the scale. For all the models shown here carrying a different number of layers, all the theoretically predicted modes have been successfully detected, which guarantees that the basis upon which our fields are developed is complete. It should be noted too that not all of the theoretically predicted 17 modes are important. For example, the top four modes for each harmonic degree in Fig. 8.1, which are the internal-mantle buoyancy modes, have extremely long relaxation times (some even exceed the age of the Earth) and extremely small strengths. Still, their detection is useful in checking that all modes which do have non-negligible strengths have been detected.

In order to elucidate the influence of lithospheric and mantle stratification on post-seismic deformation, we show in the following figures the displacement pattern for a vertical, point-like, dip-slip source embedded at 100-km depth at the base of the lithosphere; the seismic moment of the source is fixed at 10^{22} Nm, characteristic of a large earthquake. Radial displacement fields are sampled at an azimuth of 90° with respect to the strike of the fault, in the subsiding portion of the Earth's surface; tangential displacements are sampled at 45°. At 180° from the direction that

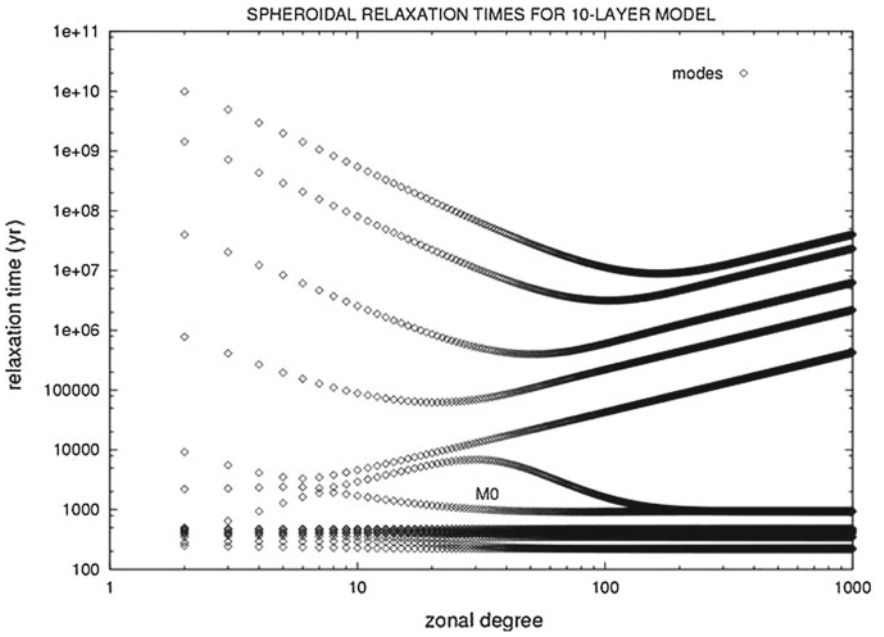

Fig. 8.1 Relaxation times, in years, as a function of the harmonic zonal degree for the 10-layer model averaged from PREM and described in Table 8.1; the elastic lithosphere has three layers and the uppermost mantle is divided into four viscoelastic layers with a viscosity of 10^{20} Pa s. The fundamental mantle modes are indicated by $M0$ (Fig. 1 in Sabadini and Vermeersen (1997a))

Table 8.1 Parameters for the 10-layer volume-averaged Earth's model. r is the distance with respect to the centre of the Earth, ρ the density of the layer, and μ the rigidity

Layer	r (km)	ρ (kg/m^3)	μ (N/m^2)	ν (Pa s)	
1	6371–6356	2283	2.66×10^{10}		
2	6356–6331	3194	5.91×10^{10}		Elastic lithosphere
3	6331–6251	3372	6.77×10^{10}		
4	6251–6221	3372	6.69×10^{10}	1.5×10^{20}	
5	6221–6151	3372	6.61×10^{10}	2.5×10^{20}	Uppermost mantle
6	6151–6061	3462	7.56×10^{10}	4.5×10^{20}	
7	6061–5971	3515	7.89×10^{10}	7.0×10^{20}	
8	5971–5701	3857	1.06×10^{11}	3.0×10^{21}	Transition zone
9	5701–3480	4878	2.19×10^{11}	2.4×10^{22}	Lower mantle
10	3480–0	10, 932			Inviscid fluid core

The viscosity ν is volume-averaged from the convex viscosity profile provided by Vermeersen and Sabadini (1997)

we have considered, we would have obtained the same displacement patterns, but with the reversed sign. Figure 8.2 shows, for a fixed distance of 200 km from the epicentre of the fault and varying time after the occurrence of the earthquake, the radial and tangential displacement components, (a) and (b) respectively. Remarkable differences can be observed among the 4- and 10-layer volume-averaged models and model P1 as used in previous analyses by Piersanti et al. (1995) and Sabadini et al. (1995), in which the rigidity and density parameters were taken from fixed-boundary contrast models. The parameters for the 4-layer volume-averaged model are given in Table 8.2; the parameters for model P1 can be found in Table 1 of Piersanti et al. (1995).

For radial displacement, panel (a), the volume-averaged models predict an increase in the post-seismic deformation; model P1 (short-dashed curve) predicts the opposite behavior, a reduction in the post-seismic signal. Although similar to the 10-layer model in the amplification of the post-seismic deformation, the 4-layer model (solid curve) predicts, both in the elastic and long time-scale limit, a radial displacement which is higher by a factor two in comparison to the 10-layer models (dashed curve). While the behavior of the old P1 model is due to the absence of elastic stratification between the lithosphere and the mantle, responsible for an overestimated lithospheric rigidity, deviations in the 4-layer model with respect to the 10-layer one are due to the absence of stratification in the elastic lithosphere in the 4-layer model. This finding clearly indicates the necessity of stratifying the lithosphere in global post-seismic deformation models.

This result is not surprising, since the final state, after relaxation has taken place in the mantle, depends solely on the elastic properties of the lithosphere. We have verified that a further refinement of the lithospheric layering does not modify the results with respect to the 10-layer model. The largest rigidity and density contrasts within the lithosphere are located at the base of the upper and of the lower crust, with the remaining portion of the lithosphere essentially homogeneous, which guarantees that a three-layered lithosphere is sufficient to provide realistic estimates of the effects of earthquakes on global co-seismic and post-seismic deformation.

In panel (b) of Fig. 8.2, a similar analysis is carried out for the tangential displacement, measured in the outward direction with respect to the dislocation, at 45° from the strike of the fault. On analogy with what is obtained in panel (a), the tangential displacement of the P1 model is also subject to a substantial reduction during post-seismic deformation. This is in distinct contrast with the results of the volume-averaged models, which show a small reduction in the signal with respect to the co-seismic deformation. Comparison between the 4- and 10-layer models reinforces the conclusion drawn from the analysis in panel (a) of the importance of stratifying the outer elastic layer of the Earth for realistic estimates of post-seismic displacements.

Figure 8.3 shows the displacement as a function of the distance from the epicentre for the same models in Fig. 8.2, but for fixed time intervals after the earthquake; the 4- and 10-layer viscosity models are averaged from the convex viscosity profile of Fig. 1 in Vermeersen and Sabadini (1997). The viscosity values can be found in Tables 8.1 and 8.2. The panels depict three snapshots of the deformation: panel (a) for the elastic

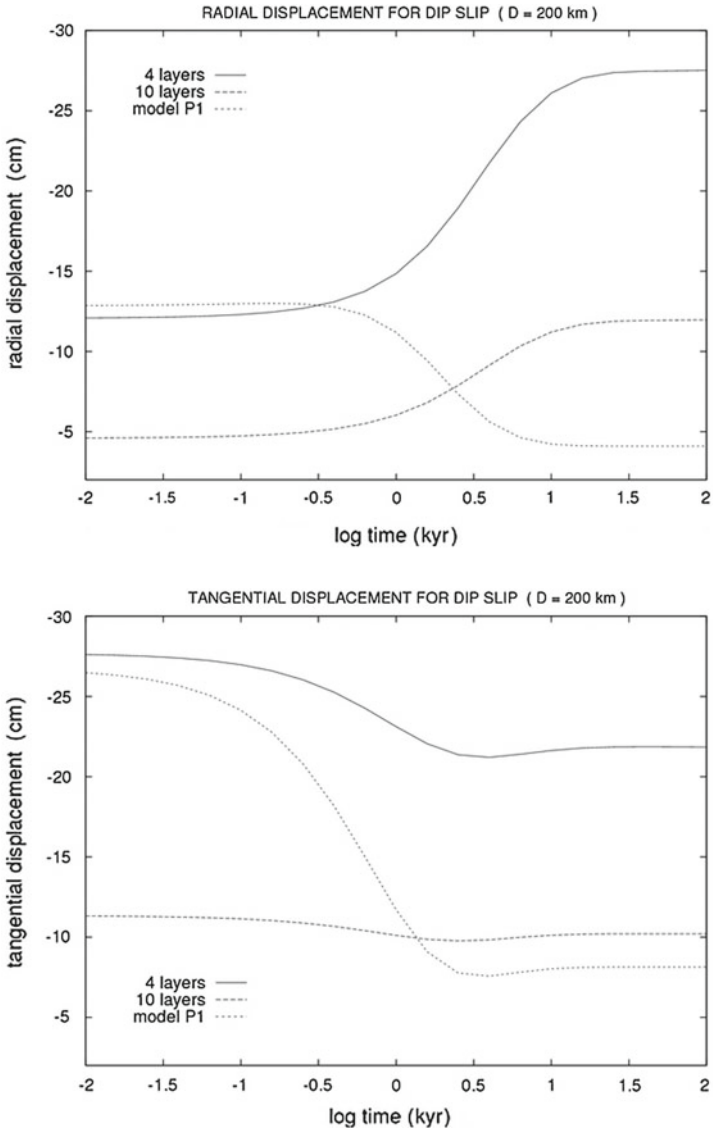

Fig. 8.2 Radial displacement, *top panel*, and tangential displacement, *bottom panel*, in centimeters as a function of time in years after the occurrence of the faulting, at t = 0 year; the source is a *vertical*, point-like dip-slip, with a seismic moment of 10^{22} Nm. Negative values denote subsidence; the distance from the epicentre of the fault is $D = 200$ km. The parameters for the 4- and 10-layer volume-averaged models are given in Tables 8.1 and 8.2; model P1 is given in Table 1 of Piersanti et al. (1995). (Fig. 2 in Sabadini and Vermeersen 1997a)

Table 8.2 Parameters for the 4-layer volume-averaged Earth's model

layer	r (km)	ρ (kg/m^3)	μ (N/m^2)	ν (Pa s)	
1	6371–6250	3234	5.99×10^{10}		Elastic lithosphere
2	6250–5701	3631	8.60×10^{10}	1.6×10^{21}	Upper mantle
3	5701–3480	4878	2.17×10^{11}	2.4×10^{22}	Lower mantle
4	3480–0	10, 932			Inviscid fluid core

r is the distance with respect to the centre of the Earth; ρ the density of the layer, and μ the rigidity. The viscosity ν is volume averaged from the convex profile models, as for Table 8.1

limit, and panel (b) for an intermediate time at which the post-seismic deformation is still evolving and for the long time-scale limit. The most striking result in this figure is that the 10-layer model behaves in a completely different fashion from the simplified P1 and 4-layer models, in all three time snapshots. In the elastic limit, the P1 and 4-layer model overestimate the radial displacement by more than a factor of two. During the transient at t = 10^3 year, the P1 model predicts a substantial reduction rather than a smooth amplification of the post-seismic signal, as predicted by the volume-averaged 4- and 10-layer models. In the far field, we notice an upwarping of the lithosphere for the 10-layer model, which is not predicted by the 4-layered model, due to the overestimated rigidity of the outer elastic layer. In the long time-scale configuration, the 10-layer model does not show a visible increase in the deformation in the near field, while in the far field this model has rebounded with an annihilation of the upwarping that was noted during the transient regime. This result indicates, as expected, that mantle relaxation has a strong control of post-seismic deformation in the far field from the epicentre of large earthquakes, and thus ultimately controls plate-mantle interaction. In this final state, the old P1 model predicts a pattern which does not show any resemblance to the more realistically stratified models, providing a smooth deformation of a few centimeters, in comparison with the 50 cm at 50 km from the epicentre as predicted by the 10-layer model. Except for the post-seismic deformation in the far field noted above, the drastically different behavior of the three models is due to whether the lithosphere has been stratified or not.

Figure 8.4 shows the effects of mantle viscosity stratification based on the comparison between two 10-layer models, with the same lithospheric stratification, for a uniform mantle viscosity of 10^{21} Pa s and convex viscosity profile. The elastic and long time-scale limits of the homogeneous and convex viscosity mantle are the same (short-dashed and dotted curves, respectively): being identical, the elastic profiles of the mantle and lithosphere control the initial and final configurations. While in proximity to the epicentre, at distances of the order of 10–100 km, the two models behave in a similar fashion (except for a 10 per cent smaller signal at 50 km for the homogeneous model caused by a higher viscosity in the upper mantle), in the far field the homogeneous and convex mantle viscosity models produce a quite different response at intermediate time-scales of 1–1000 year. As already noted in the discussion of panel (b) in Fig. 8.3, displacement in the far field occurs in the opposite direction with respect to that experienced in the near field. The convex viscosity

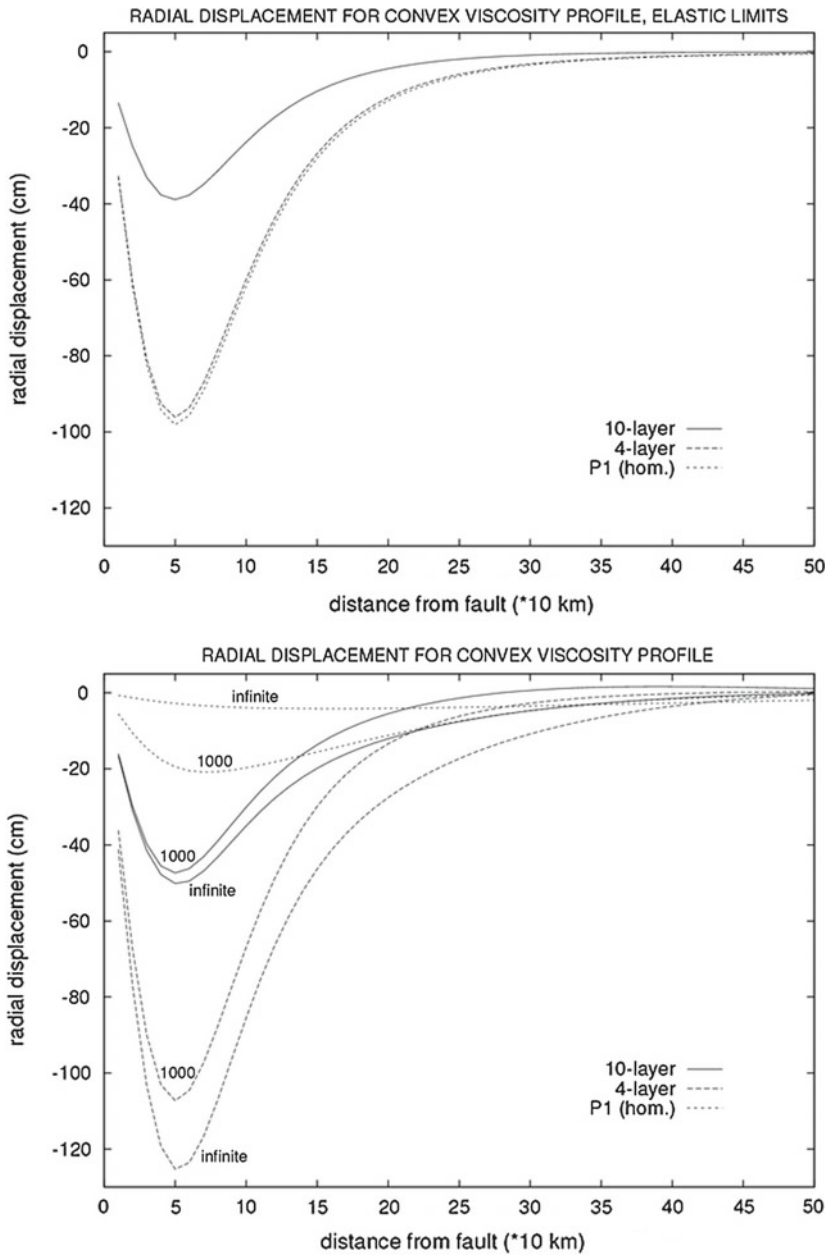

Fig. 8.3 Radial displacement as a function of the distance from the fault in the elastic limit, *top panel*, and at t = 1,000 year after the earthquake together with the long time-scale t = ∞ limit, *bottom panel*. The curves depict the cases for the 10-layer model, *solid curve*, 4-layer model, *dashed curve*, and model P1, *short-dashed curve*. The mantle viscosity of the 4- and 10-layer models is given in Tables 8.1 and 8.2. Model P1 has a uniform mantle viscosity of 10^{21} Pa s. In all cases the lithosphere is elastic (Fig. 3 in Sabadini and Vermeersen 1997a)

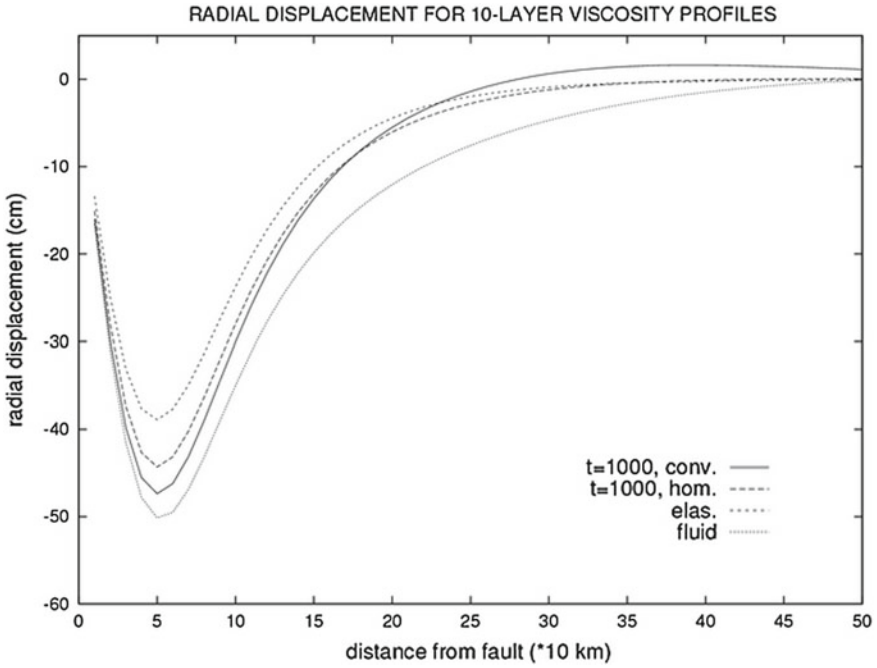

Fig. 8.4 Comparison between a 10-layer model with a uniform viscosity of 10^{21} Pa s, *dashed curve*, and convex viscosity, *solid curve*, at t = 1,000 year after the earthquake. The *short-dashed* and *dotted curves* denote the elastic and long time-scale limits of the two models (Fig. 4 in Sabadini and Vermeersen 1997a)

profile model predicts, in fact, positive vertical displacements of about 3 cm, while the homogeneous viscosity mantle model does not show any visible evidence of relaxation, still providing the values of co-seismic deformation. This result clearly indicates the importance of mantle rheological stratification in controlling the deformation of the plate in the far field during post-seismic deformation. The upward deflection of the lithosphere in the far field caused by the convex viscosity mantle is due to the upper mantle, which is softer than in the homogeneous model.

The elastic stratification of the lithosphere has a major influence on post-seismic deformation; at least three layers in the lithosphere, averaged from PREM, are necessary to obtain a correct estimate of the deformation following large earthquakes, both in the near field and in the far field. We have verified that a further increase in the eleven lithospheric layers of PREM produces a minor refinement in post-seismic deformation estimates in comparison with the major improvement that is gained from one to three lithospheric layers. The modification in the deformation pattern during the evolution from the initial elastic state to the long time-scale one is controlled by mantle rheology: viscoelastic stratification of the mantle has a major influence on the rebound of the lithosphere in the far field following the earthquake. In comparison with the required stratification of the lithosphere, the same fineness of layering is

not needed in the mantle, in agreement with the result that mantle rheological stratification controls the global pattern of post-seismic deformation in the far field, not being sensitive to the short wavelength features of the mantle structure.

8.2 Post-seismic Deformation for Shallow Earthquakes

In the previous section large and deep earthquakes were considered in order to elucidate the global properties of post-seismic deformation by focusing in particular on stress relaxation in the mantle. In this section the normal mode method is applied to carry out the effects of stress relaxation in the lower crust. By dealing with shallow sources and rheologically stratified crusts, the normal mode expansion must be performed to high harmonic degrees, up to $l = 6000$, to resolve post-seismic displacements for earthquakes whose faults cut a thin upper elastic crust overlying a viscoelastic lower crust. It is possible to show that the high resolution in co-seismic displacements necessitates summation to over 4×10^4 spherical harmonics, while for estimating rates of deformation, due to stress relaxation in the lower crust, summation over spherical harmonics of a few times 10^3 is sufficient. The models shown in this chapter are totally new with respect to those which stemmed from Piersanti et al. (1995) in terms of both the large number of layers dealt with in the present book, first made possible by the grid-spacing procedures described at the end of Sect. 1.8, representing the real heart of this new family of post-seismic deformation models.

8.2.1 The Umbria-Marche (1997) Earthquake

So as to show the effects of stress relaxation in the lower crust, the Umbria-Marche ($M_w = 6.0$) 1997 moderate-size earthquake, characteristic of a slowly deforming plate boundary in the central Mediterranean, is modeled in this Sect. 8.2.1, reworked from Riva et al. (2000), by means of the normal mode method. Central Italy is undergoing continental extension and experienced the moderate Umbria-Marche 1997 normal faulting earthquake sequence. Deep seismic reflection studies (CROP03) and the 1997 earthquake sequence clearly show a seismogenic layer decoupled from the lower crust by a sizeable transition zone. In accord with these observations, the modeling is based on a crust divided into three layers: an elastic upper crust, a transition zone and a low-viscosity lower crust, as shown in Fig. 8.5.

The fault is embedded in the upper crust. The calculation of post-seismic deformation requires the assumption of a layered viscoelastic Earth's model. Nearly all viscoelastic relaxation studies (Ma and Kusznir 1995; Pollitz 1996) assume a three-layer model schematizing the brittle upper crust (UC), the lower crust (LC) and the mantle. Seismological and geological observations from regions of active faulting suggest that the seismogenic UC is likely to be separated from the LC by a transition zone (TZ) where both brittle and ductile processes can occur (Chen and Molnar 1983;

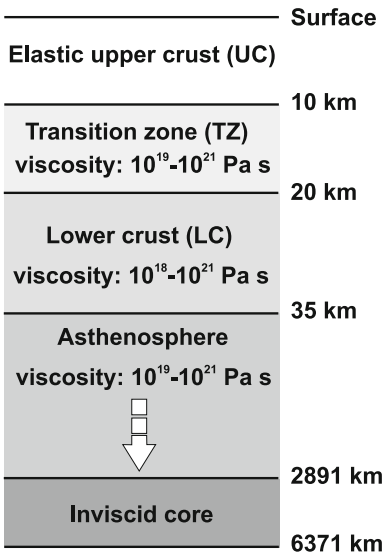

Fig. 8.5 Earth's model and viscosity parameters used for the Umbria-Marche earthquake, redrawn from Fig. 1 in Riva et al. (2000)

Meissner and Strehlau 1982; Scholz 1990; Sibson 1989). These observations are more frequent in regions of active continental extension (Jackson and White 1989). The recent CROP03 seismic reflection profile (Pialli et al. 1998), designed for the study of the deep crust in the northern Apennines, imaged the top of the fully ductile LC using regional high-amplitude reflectors. Below the Umbria-Marche extensional belt, the top of the LC is about 20 km deep, with a Moho around 35 km (Coli 1988). Cattaneo et al. (2000) show an abrupt cutoff of the 1997 aftershock sequence at about 9 km of depth. Thus the seismic activity is largely restricted to the uppermost 10 km of the deforming continental crust and leaves room for a 10 km-thick TZ above 15 km of LC as imaged by the CROP03 section (Fig. 8.5). The TZ acts in the normal mode modeling as a layer which decouples the elastic UC from the low-viscosity LC. Accordingly, the modeling is based on five layers (Fig. 8.5). The relevant stratification is consistent with the range of regional velocity models estimated via the analysis of surface-wave dispersion (Calcagnile and Panza 1981) and regional gravity and heat flow anomalies (Della Vedova et al. 1991; Marson et al. 1995) and other relevant geological and geophysical data (Du et al. 1998). The Umbria-Marche earthquake sequence started on September 26, 1997, and took place in a complex deforming zone along a normal fault system in the central Apennines. This shallow sequence was followed by a mantle event on March 26, 1997 (Mw 5.2) located at a depth of 46 km (Aoudia et al. 2000; Saraó et al. 1998). Only the strongest earthquake of the Umbria-Marche sequence that took place on the 26 September 1997 at 9:40 (Mw = 6.0) is considered in the modeling. The seismic moment is based on the solution in Saraó et al. (1998) retrieved by broad-band waveform inversion, in good agreement with the CMT solution (Ekstrom et al. 1998). The application below makes it

possible to elucidate the characteristics of post-seismic deformation in the studied region and to provide a first-order estimate of the expected vertical velocities.

To illustrate the sensitivity of the results on the depth of the source, the finiteness of the source in the vertical direction is neglected, and besides the source depth of 7 km (Aoudia et al. 2003; Saraó et al. 1998), a case in which the source is embedded at a depth of 3 km is also considered to simulate the effects of a fault nearly reaching the surface. We distribute the seismic moment along a line of dislocations whose length along strike is 10 km; the source has thus an infinitesimal extension (a point) in the down dip direction. The dip of the fault is 37°, in agreement with the Saraó et al. (1998) solution. In order to resolve the deformation produced by this fault, summation of 4000 normal modes is performed, which ensures convergence of the solution. The vertical deformation is considered in the following simulations, being most relevant to normal faults; the results are evaluated at the surface along a line perpendicular to the strike of the fault, crossing its centre. In the whole set of panels, the fault is dipping to the left, and the distance is measured from the intersection of the upward prolongation of the fault with the Earth's surface. In Fig. 8.6, the depth is fixed at 7 km.

Figure 8.6a portrays the co-seismic and post-seismic vertical deformation, measured at the surface. The co-seismic component (solid line) shows the deformation pattern characteristic of normal faulting, with an uplifted, localized footwall and a broad subsidence in the hanging wall. The post-seismic component (dashed line), which includes the co-seismic one plus the extra deformation resulting from the relaxation in the viscoelastic medium, is responsible for a broadening of the subsidence, which also affects the footwall. Post-seismic displacements are recorded after complete relaxation occurred in the viscoelastic layers. The largest co-seismic displacement is −8 cm 10 km from the fault. Due to the relaxation, the maximum displacement increases to −12 cm, and a broad area, which remained at rest during the co-seismic deformation, is now subject to subsidence at distances of tens of kilometers. This effect is due to the decoupling of the uppermost part of the crust with respect to the lower layers. The occurrence of normal faulting and the extension at the bottom of the UC, below the neutral plane, is responsible for the down flexure of this layer, visible in the broad subsidence in Fig. 8.6a.

Figure 8.6b provides another perspective to this physics, with the vertical velocities expected at different times after the earthquake. The wide region of negative velocity marks the broad down-flexure of the UC. The two regions of low velocity represent the peripheral response of the layer to the subsidence. Another interesting characteristics in Fig. 8.6b is the short wavelength feature at the centre of the subsiding area: we can recognize the relative maximum corresponding to the footwall and the largest subsidence of the hanging wall, within a generalized subsidence. The highest velocity is −0.85 mm/yr in the hanging wall, immediately after the earthquake, at $t = 0$. Due to the relatively high viscosity of the TZ (10^{19} Pa s), this velocity shows a minor reduction after 10 year, and after 50 year there is still a visible signal of −0.25 mm/yr. If, for the TZ, a viscosity of 10^{18} Pa s is also considered, hence coupled with the LC, the highest velocity increases by one order of magnitude to −8.5 mm/yr. Since the viscosity of the TZ and LC is largely uncertain, probably

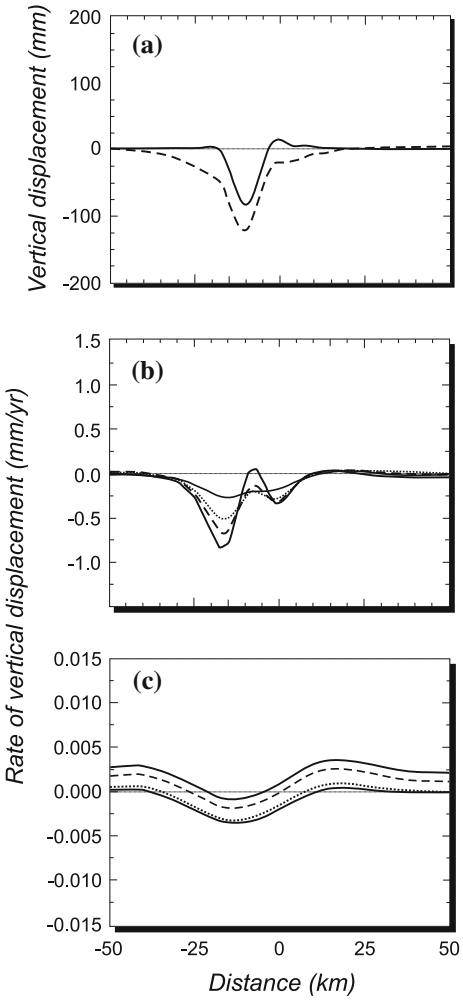

Fig. 8.6 Co-seismic and post-seismic vertical surface displacements and rates calculated for a 7-km deep normal faulting line-source, redrawn from Fig. 2 in Riva et al. (2000). The profiles are across the centre of the fault (x = 0 km) and perpendicular to its strike. The fault is dipping to the left and is buried in the upper layer of Fig. 8.5. **a** Co-seismic (*solid line*) and post-seismic (*dashed line*) displacements. **b** Post-seismic rates due to relaxation in the TZ expected at different times after the earthquake, with t = 0, 10, 20, 50 year, *solid*, *dashed*, *dash-dotted* and *dotted*, respectively. **c** Post-seismic rates due to relaxation in the mantle expected at t = 0, 100, 500, 1000 year, *solid*, *dashed*, *dash-dotted* and *dotted*, respectively, after the earthquake

ranging between 10^{18} and 10^{19} Pa s, it is likely that the largest subsidence rates in the highly deforming area of the hanging wall vary in the range that we have estimated. Comparison between the ongoing GPS campaigns and model predictions is crucial in estimating the effective viscosity of the TZ and LC.

Figure 8.6c deals with stress relaxation limited to the mantle, with sampling times increased with respect to the previous cases. The deformation pattern is broadened since stress relaxation involves a larger portion of the Earth and the global subsidence disappears because the whole crust is now coupled. The amplitude of the vertical velocity in the earthquake area is substantially reduced since the whole planet is now involved in the deformation, as indicated by the slow decay at increasing distance from the epicentral area and longer relaxation times with respect to Fig. 8.6b.

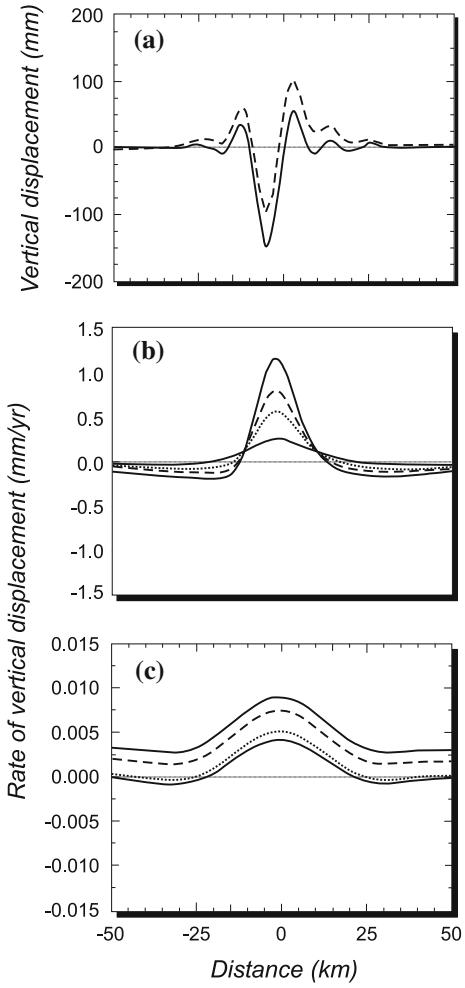

Fig. 8.7 Co-seismic and post-seismic vertical surface displacements and rates calculated for a 3-km deep normal faulting line-source, redrawn from Fig. 3 in Riva et al. (2000). Terminology as in Fig. 8.6

Figure 8.6b, c show that for shallow normal faulting the TZ and LC play a major role in comparison to stress relaxation in the mantle, which is actually negligible.

In Fig. 8.7 the source is embedded at a depth of 3 km, in the top half of the UC. In comparison with Fig. 8.6, the pattern of both co-seismic and post-seismic displacement in Fig. 8.7 becomes sharper, and the largest co-seismic subsidence in the hanging wall is increased by a factor of two with respect to the case of 7 k of depth (Fig. 8.6a). The uplift in the footwall, with respect to Fig. 8.6a, is subject to a larger increase, by a factor of three. The difference between the highest uplift in the footwall and subsidence in the hanging wall is thus doubled with respect to Fig. 8.6a. This increase in the amplitude of the displacement and sharpening of its pattern is attributable to the decrease in the wavelength caused by the shallower source depth in comparison with Fig. 8.6. The most interesting difference with respect to Fig. 8.6

is the upward migration of the post-seismic displacement pattern with respect to the co-seismic one. An extensional source located above the neutral plane of the UC causes a bending moment opposite to the one induced by the deeper source in Fig. 8.6, and the Earth's surface is thus subject to a general uplift, rather than subsidence. From Figs. 8.6a and 8.7a, depending on the location of the source beneath or above the neutral plane, the post-seismic curves lie completely above or below the co-seismic one. These findings differ from those reported by Ma and Kusznir (1995) where, due to the finiteness of the source in the vertical direction, the fault cuts the whole UC through its neutral plane, which causes the crossing of the curves depicting the post-seismic and co-seismic vertical displacement.

When attention is drawn to the velocity pattern in Fig. 8.7b, the global upwarping observed in the post-seismic displacement also affects the vertical velocity, in agreement with the previous observations on the flexural properties of the UC. Uplift velocities of 1.2 mm/yr are in fact obtained in the hanging wall region, close to the footwall. This tendency of a general upwarping is visible also in Fig. 8.7c, where relaxation involves only the mantle. In comparison with Fig. 8.6c, we note an increase in the uplift velocity. For Fig. 8.7c the same observations about Fig. 8.6c can be made, except that now the uplift of the footwall is enhanced with respect to the subsidence in the hanging wall.

The detection of post-seismic deformation in the Umbria-Marche area is an extremely challenging task due to the smallness of the expected signal, of the order of a few millimeters per year, for both vertical and horizontal components. In order to reveal post-seismic effects in the area, a series of GPS campaigns has been undertaken in order to detect in particular the horizontal deformation components. The results of this surveying, along a baseline perpendicular to the major fault activated during the 1997 Umbria-Marche seismic sequence, is shown in Fig. 8.8. In order to provide results independent from the reference system, the displacements are evaluated with respect to the town of Spello, indicated by A_0. These results represent a first evidence of horizontal post-seismic deformation for shallow earthquakes in the Mediterranean region, as shown in Aoudia et al. (2003). Figure 8.8, redrawn from Aoudia et al. (2003), provides the comparison between the GPS baseline variations and the modeled ones as a function of the baseline length in kilometers from the reference site of Spello (A_0). All baseline variations are positive, except $A_0 - A_1$, which indicates a general trend of post-seismic extension across the fault. Bernese 4.2 and GIPSY 2.6 estimates are shown as one sigma error bars and the model results correspond to a transition zone viscosity of 10^{18} Pa s and a lower crust viscosity of 10^{17} Pa s using different fault models, indicated by FM1, FM2 and FM3, as indicated in the caption. FM1 (dotted) is not adequate to explain the observations at different sites and does not reproduce the general pattern of baseline variations shown by the two GPS analyses. FM2 (dashed) reproduces only part of the observations and the general trend, while FM3 (solid) is the best performing one, being able to reproduce almost all the observations and the general baseline variation pattern. These findings demonstrate the important role of GPS survey in seismogenic zones in revealing the physics of post-seismic deformation and providing a fundamental tool in modern seismic hazard studies.

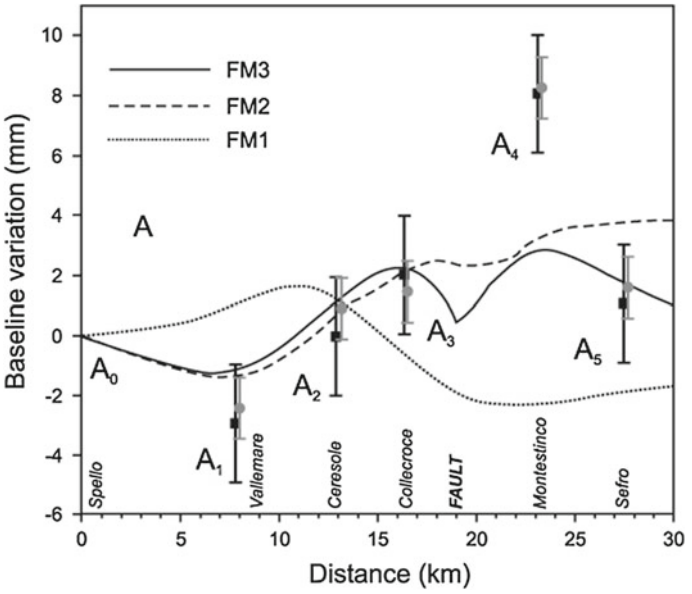

Fig. 8.8 2002–1999 baseline length variations along the GPS section with respect to the A_0 site using GIPSY and Bernese solutions, *gray* and *black vertical bars*, respectively, versus viscoelastic model predictions for the fault model FM1 (Salvi et al. 2000), FM2 (Zollo et al. 1999) and FM3 (Basili and Meghraoui 1999) fault models, using a viscosity of 10^{18} and 10^{17} Pa s for the transition zone and lower crust, respectively

The results of this section provide a first estimate of the expected rates of post-seismic deformation in the Umbria-Marche epicentral area. Fine rheological layering in the crust plays a major role in the interplay between relaxation in the TZ and LC with respect to relaxation in the mantle as shown in Sect. 8.1 when shallow and moderate normal faulting earthquakes are considered in the relaxation theory. Unlike large and generally deep earthquakes (Melosh 1983; Pollitz and Sacks 1997; Suito and Hirahara 1999; Thatcher and Rundle 1979), shallow and moderate normal-faulting earthquakes are free of the influence of lower lithospheric viscous coupling, while the TZ and low-viscosity LC impose a pattern and a scale on post-seismic deformation. For normal faulting, these applications show the relevance of the depth of the source with respect to the thickness of the elastic layer in controlling post-seismic upwarping or downwarping, as emphasized by Thatcher and Rundle (1979) and Melosh (1983) for thrust faults. Since the elastic layer is the upper crust rather than the whole lithosphere, these findings show that the results obtained by Thatcher and Rundle (1979) and Melosh (1983) are scale-invariant and applicable to dip-slip sources embedded in an elastic layer of any thickness overlying a viscoelastic one. Furthermore, the pattern of widening and narrowing of the deformation due to stress relaxation at different depths (Figs. 8.6 and 8.7) is in agreement with the results obtained by King et al. (1988) using a simpler model. These findings show

that an appropriate test area for applying the viscoelastic relaxation theory at high harmonic degrees and for studying the effects of the TZ and LC in Italy's central Apennines, where a clear cutoff in the depth distribution of earthquakes indicates that the seismogenic layer is limited to the first ten kilometers of the crust and a well-developed TZ lies below this depth, above a low-viscosity LC.

8.2.2 The Irpinia (1980) Earthquake

Comparison of measured vertical displacements from two leveling campaigns performed in 1981 and 1985 in the epicentral area of the 1980 Irpinia earthquake ($M_w = 6.9$) and predictions from viscoelastic Earth' models reveals the occurrence of post-seismic deformation due to stress relaxation in the ductile part of the crust, south of the area explored in the previous Sect. 8.2.1. In proximity of the major fault, the leveling lines show a peculiar upwarping of the crust, accumulated during the time interval 1981–1985.

Here we test the mechanism of stress relaxation in the ductile parts of the crust after the occurrence of the shallow, normal-fault 1980 Irpinia earthquake, following the study by Dalla Via et al. (2003). The joint studies of local and world-wide seismological data, static deformations and geological evidences have provided a detailed picture of the complex mechanism of this event (De Natale et al. 1988; Pantosti and Valensise 1990; Pingue and De Natale 1993; Westaway and Jackson 1984). The main event consisted of three distinct subfaults at least, ruptured at intervals of about 20 s from each other. Surface faulting linked to this earthquake was well evident at several places and in particular on the main fault (first subevent), with dislocation up to 1.2 m. The total seismic moment inferred for this event is 3×10^{19} Nm.

The asymptotic expression of the fundamental solutions of the incompressible, self-gravitating, spherical, viscoelastic Earth for high harmonic degree described in Dalla Via et al. (2003) makes possible, for this 1980 Irpinia application, to sum 40,000 spherical harmonic contributions in the co-seismic part and 6000 ones in the post-seismic part, which guarantees the attainment of the highest resolution both in the co-seismic and post-seismic components. The Earth's model, described in Table 8.3, consists of 5 layers including a purely elastic upper crust (UC), a viscoelastic lower crust (LC), the mantle (M) and the core (IC).

The depths of the crustal layers and their elastic values have been taken from the average depths of the seismogenic crust and MOHO in the southern Apennine area (Mostardini and Merlini 1986), while the deeper layers are based on standard global Earth's models. The upper limit of the lower crust, 18.5 km, has been chosen to match the maximum depths of earthquakes in this area on the basis of the assumption that the viscoelastic, ductile lower crust inhibits seismic fracture.

Viscosity in the lower crust has been varied from typical values of 10^{19} Pa s (Pollitz et al. 1998). In order to mimic the reduction of the viscosity within the lower crust and the decoupling between the lower crust and the mantle, as expected on the basis of strength reduction with depth for the continental lithosphere under extension

Table 8.3 Viscoelastic model parameters for the 1980 Irpinia earthquake

Layer	Depth (km)	ρ (kg/dm^3)	ν (Pa s)	μ (GPa)
UC	0–18.5	2.65	∞	32.5
LC	18.5–28.5	2.75	$1 \cdot 10^{18}$	33.7
			$0.75 \cdot 10^{19}$	
			$1 \cdot 10^{19}$	
			∞	
LCB	28.5–32.5	2.90	10^{18}	35.5
			∞	
M	32.5–2891	3.39	10^{21}	73.5
IC	2891–6372	10.93	–	–

UC Upper crust; *LC* Lower crust; *LCB* Lower crust bottom; *M* Mantle; *IC* Inviscid core

(Cosgrove 1997; Lynch and Morgan 1987), the bottom of the lower crust, LCB in Table 8.3, has been reduced by one order of magnitude with respect to the normal value of 10^{19} Pa s. Due to the simplified viscosity profile within the lower crust, only the effective viscosity resulting from the volumetric average within the two viscoelastic layers characterizing the lower crust can be compared with post-seismic results from other tectonic environments (Pollitz et al. 1998, 2000). A standard mantle (M) of 10^{21} Pa s below the lower crust does not portray any sizeable deformation over the time-scale of post-seismic deformation.

The assumed fault system consists of three normal subfaults as shown in Fig. 8.9, including the three leveling lines considered, namely CZT2 (diamonds), CZT3 (crosses) and IGM81 lines (circles), measured immediately after the main shock and four years later; the thin curve in Fig. 8.9, starting from Eboli and routing to Grottaminarda through Potenza and the IGM81 profile, represents the leveling line along which the co-seismic vertical displacement has been measured (Arca et al. 1983; De Natale et al. 1988). The surface projections of the three faults F1, F2 and F3 are shown by the light gray; the fault parameters of this model, shown in Table 8.4, are taken from Pingue and De Natale (1993). The total seismic moment has been inferred from seismological and geodetic data; for the main fault F1 the seismic moment M_0 is fixed at 24.4×10^{18} Nm, at 2.5×10^{18} Nm for F2 and at 3.2×10^{18} Nm for F3. The slip angle is fixed at $-90°$ for each fault. Slip on the three sub-faults has been considered homogeneous in the first tests. Subsequently, by maintaining the seismic moment constant to $M_0 = 3.0 \times 10^{19}$ Nm, the slip distribution on the main fault has been varied with depth in order to reduce the misfit between model predictions and observations.

Fig. 8.10 shows the observed displacements resulting from the leveling lines in Fig. 8.9, where the black vertical bars reproduce the observations and their average errors; the curves represent the modeled vertical displacements due to viscoelastic relaxation without the co-seismic component, computed for various combinations of slip distribution and viscosities. In order to carry out a comparison independent of

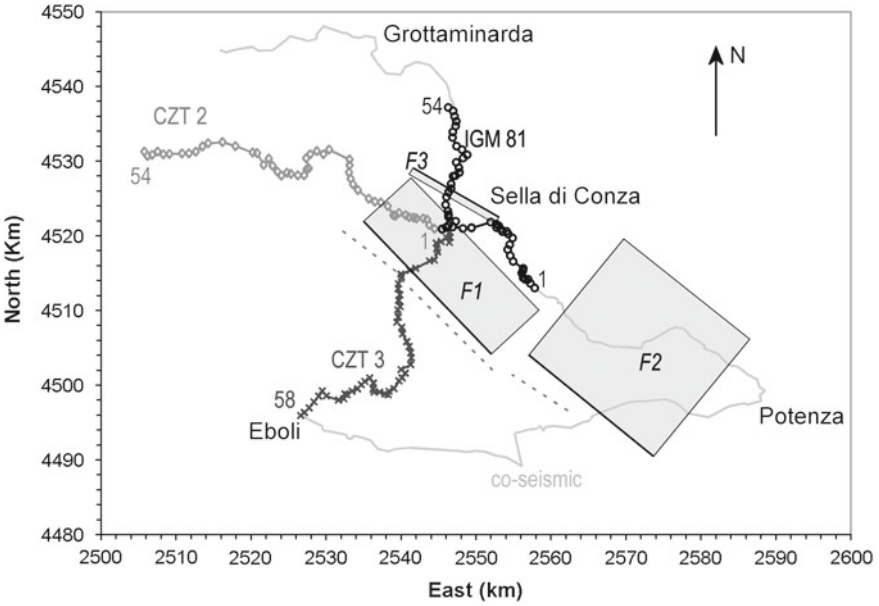

Fig. 8.9 Fault model of the Irpinia 1980 earthquake. The leveling lines IGM81 (*black dots*), CZT2 (*squares*) and CZT3 (*gray dots*) are also indicated. F1, F2 and F3 indicate the three faults, at 0, 18 and 40 s, respectively, as given in Table 8.4; the *dashed lines* provide the surface evidence of the faults. The first (1) and last (54, 58) benchmarks of each leveling line are also shown. Redrawn from Fig. 1 in Dalla Via et al. (2003)

Table 8.4 $L1$ fault length

Sub Event	$L1$ (km)	$L2$ (km)	Top (km)	Disl. (cm)	Str. (°)	Dip (°)
$F1$(0 s)	25	20	1.0	150	317	60
$F2$(18 s)	22	14	1.0	25	310	20
$F3$(40 s)	13	10	1.3	75	120	85

$L2$ fault width along slip direction. *Top* depth of fault top margin. *Disl*. mean dislocation. *Str*. strike

the choice of the zero in the leveling, each model result has been uniformly shifted in such a way that the mean residual vanishes. The grey curves correspond to the reference model characterized by a uniform distribution of the seismic moment over the fault and by a lower crust viscosity, between 18.5 and 28.5 km depth, of 10^{19} Pa s (Table 8.3). Although the trends shown by this model agree with some basic features of the three lines, such as the subsidence along points 1–20 and the following uplift of IGM81, the general uplift along CZT2 and the uplift between points 1–50 of CZT3, the gray curves always underestimate the observations, especially the upward bulge of 20–30 mm of CZT3 and the drastic increase in the uplift at point 20 of IGM81. In order to increase the upwarping of the crust along CZT3, where this line crosses the

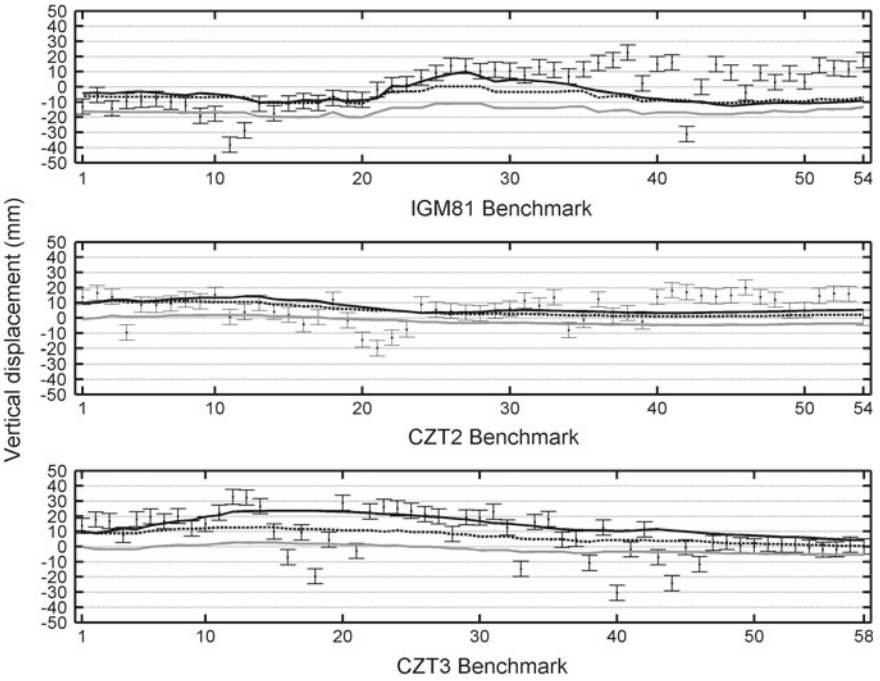

Fig. 8.10 Leveling data for the three lines and modeling results: the *gray curves* correspond to a transition zone viscosity of 10^{19} Pa s and a uniformly distributed seismic moment, the *dotted* ones to the same viscosity but non-homogeneous seismic moment according to Table 8.5. The *black solid curves* correspond to a lower crust (LC) viscosity of 0.75×10^{19} Pa s and the seismic moment distribution in Table 8.5. Redrawn from Fig. 2 in Dalla Via et al. (2003)

Table 8.5 Seismic moment distribution along the fault width ($L2$); M = $M_0/5$ where M_0 is given in the text; the fault description is given in Table 8.4

Fault fraction	$F1$	$F2$	$F3$
1/5	0.8 × M	2.0 × M	2.0 × M
2/5	1.2 × M	2.0 × M	2.0 × M
3/5	1.5 × M	1.0 × M	1.0 × M
4/5	1.0 × M	0.0 × M	0.0 × M
5/5	0.5 × M	0.0 × M	0.0 × M

major fault, it is necessary to distribute the seismic moment in such a way that the maximum slip occurs at depths of about 10 km, as shown in Table 8.5, resulting in the dotted curves in Fig. 8.10.

This best-fit seismic moment distribution has been chosen by minimizing the L^1 norm of the residuals between observations and model predictions for all the three lines simultaneously. The long-wavelength uplift between points 1–35 of CZT3

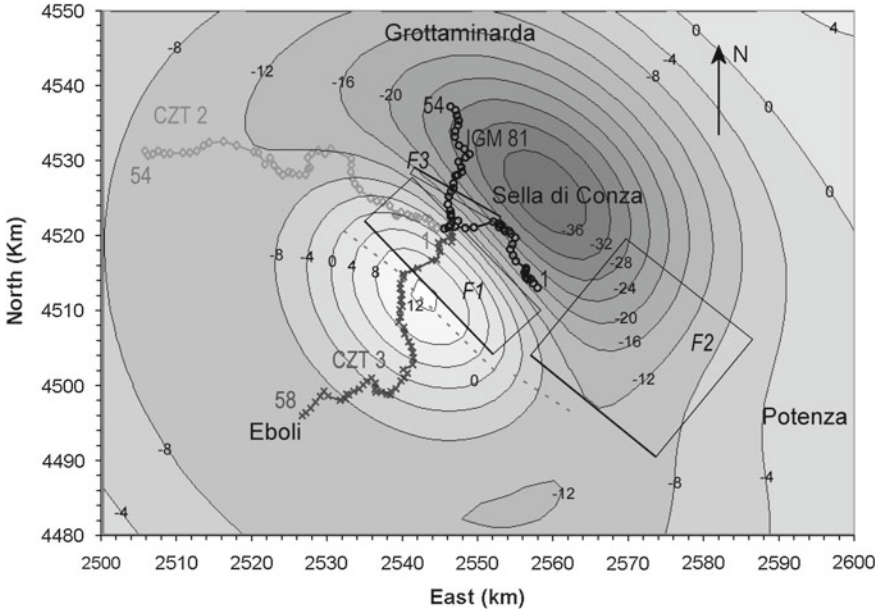

Fig. 8.11 Modeling results superimposed on the leveling lines and faults in Fig. 8.9, corresponding to the post-seismic displacement accumulated in the period 1981–1985 (in mm) due to crustal relaxation; fault parameters and lower crust viscosity are those corresponding to the *black curves* in Fig. 8.10. Redrawn from the top panel of Fig. 3 in Dalla Via et al. (2003)

increases with respect to the dotted curve to 12 mm; the same is true for CZT2 for points 1–25, where uplift reaches 10 mm. Particularly evident is the tendency to reproduce the change from subsidence into uplift along IGM81 from the benchmarks 15 to 35. The fit between the observations and model results can be substantially improved by reducing the viscosity in the lower crust from 10^{19} to 0.75×10^{19} Pa s, as shown in Table 8.3 for the LC layer in the case of non-uniform seismic moment distribution, as indicated by the black solid curves. The increase to 23 mm in the maximum along CZT3 is accompanied by an increase to 15 mm and 10 mm along CZT2 and IGM81, respectively. The general trend of observed displacements now appears well reproduced by the best-fit model, except for some high frequency signals at very localized zones and a rather systematic underestimation of displacements in the northernmost zone of the IGM81 line.

Figure 8.11 provides an areal view of the post-seismic vertical displacement accumulated in the period 1981–1985, with characteristic zones of uplift and subsidence; this figure corresponds to the same viscosity model of Fig. 8.10, characterized by lower crust relaxation (solid curves). Two major features are notable: the broadness of the area affected by subsidence and uplift and the amplitude of the displacement, of the order of 10 and 40 mm for uplift and subsidence. These effects are indicative of stress release at depth and of the ability of the viscoelastic part of the crust to

channel the flow at large distances from the fault. The expected present-day peak-to-peak post-seismic vertical displacement, 22 years after the earthquake, is 120 cm, characterized by the same pattern as in Fig. 8.11.

In the case of the 1980 Irpinia earthquake area, we thus have evidence that, once averaged over the thickness of the lower crust of 14 km, the effective average viscosity of 0.6×10^{19} Pa s agrees within the order of magnitude with the 'normal' lower crust viscosity of about 10^{19} Pa s obtained by Pollitz et al. (1998) from post-seismic relaxation following the 1989 Loma Prieta earthquake.

The characteristic wavelength of the post-seismic deformation in the Irpinia area is supporting evidence for viscoelastic relaxation in the lower crust rather than in the uppermost part of the mantle, unlike the 1992 Landers earthquake where there are indications that relaxation also involves a weak upper mantle. An additional result from post-seismic displacement modeling in this area consists of further details about the fault slip with respect to the previous results. It appears that higher slip concentration at around 10 km depth is able to give a best fit to the observed data.

References

Aoudia, A., A. Borghi, R. Riva, R. Barzaghi, B.A.C. Ambrosius, R. Sabadini, L.L.A. Vermeersen, and G.F. Panza (2003). "Postseismic deformation following the 1997 Umbria-Marche (Italy) moderate normal faulting earthquakes". In: *Geophys. Res. Lett.* 30, p. 1390.

Aoudia, A., G. Chimera, G. Costa, C. Nunziata, G.F. Panza, F. Romanelli, A. Saraó, P. Suhadolc, and F. Vaccari (2000). "Modelling of the seismic ground motion for the Umbria-Marche earthquake sequence". In: *Pro-ceedings 12-th World Conference on Earthquake Engineering*. Auckland, CDrom Paper-ID 2500.

Arca, S., V. Bonasia, R. Gaulon, F. Pingue, J.C. Ruegg, and R. Scarpa (1983). "Ground movements and faulting mechanism associated to the November 23, 1980 southern Italy earthquake". In: *Boll. Geodesia Scienze Affini* XLII(2).

Basili, R. and M. Meghraoui (1999). "Coseismic and postseismic displacements related with the 1997 earthquake sequence in Umbria-Marche (central Italy)". In: *Geophys. Res. Lett.* 28, pp. 2695–2698.

Calcagnile, G. and G.F. Panza (1981). "The main characteristics of the litho-sphere-asthenosphere system in Italy and surrounding regions". In: *Pure Appl. Geophys*. 119, pp. 865–879.

Cattaneo, M., P. Augliera, G. De Luca, A. Gorini, A. Govoni, S. Marcucci, A. Michelini, G. Monachesi, D. Spallarossa, L. Trojani, and XGUMS (2000). "The 1997 Umbria-Marche (Italy) earthquake sequence: analysis of the data recorded by the local and temporary networks". In: *J. Seismology* 4, pp. 401–414.

Chen, W. P. and P. Molnar (1983). "Focal depths of intracontinental and intraplate earthquakes and their implications for the thermal and mechanical properties of the lithosphere". In: *J. Geophys. Res.* 88, pp. 4183–4214.

Coli, M. (1988). "Considerations on the crustal modelling along the CROP-3 Profile". In: *Mem. Soc. Geol. It.* 52, pp. 401–412.

Cosgrove, J. W. (1997). "The influence of mechanical anisotropy on the behaviour of the lower crust". In: *Tectonophys*. 280, pp. 1–14.

Dalla Via, G., G. De Natale, C. Troise, F. Pingue, F. Obrizzo, R. Riva, and R. Sabadini (2003). "First evidence of post-seismic deformation in the central Mediterranean: crustal viscoelastic relaxation in the area of the 1980 Irpinia earthquake (Southern Italy)". In: *Geophys. J. Int.* 154(3), pp. F9–F14.

De Natale, G., F. Pingue, and R. Scarpa (1988). "Seismic and ground deformation monitoring in the seismogenetic region of Southern Apennines, Italy". In: *Tectonophys.* 152, pp. 165–178.

Della Vedova, B., I. Marson, G.F. Panza, and P. Suhadolc (1991). "Upper mantle properties of the Tuscan-Tyrrhenian area: a key for understanding the recent tectonic evolution of the Italian region". In: *Tectonophys.* 195, pp. 311–318.

Du, Z.J., A. Michelini, and G.F. Panza (1998). "EurID: a regionalised 3- D seismological model of Europe". In: *Phys. Earth Planet. Inter.* 105, pp. 31–62.

Dziewonski, A.M. and D.L. Anderson (1981). "Preliminary reference Earth model". In: *Phys. Earth Planet. Inter.* 25, pp. 297–356.

Ekstrom, G., A. Morelli, and A.M. Dziewonski (1998). "Moment tensor analysis of the Central Italy earthquake sequence of September-October 1997". In: *Geophys. Res. Lett.* 25, pp. 1971–1974.

Jackson, J.A. and N.J. White (1989). "Normal faulting in the upper continental crust: observations from regions of active extension". In: *J. Struct. Geol.* 11, pp. 15–36.

King, G.C.P., R.S. Stein, and G.B. Rundle (1988). "The growth of geological structures by repeated earthquakes: Conceptual framework". In: *J. Geophys. Res.* 93, pp. 13,307–13,318.

Lynch, H.D and P. Morgan (1987). "The tensile strength of the lithosphere and the localization of extension". In: *Continental Extensional Tecton- ics*. Ed. by J.F. Dewey M.P. Coward and P.L. Hancock. Vol. 28. Geological Society Special Publication, pp. 53–65.

Ma, X.Q. and N.J. Kusznir (1995). "Coseismic and postseismic subsurface displacements and strains for a dip-slip normal fault in a three layer elastic-gravitational medium". In: *J. Geophys. Res.* 100, pp. 12,813–12,828.

Marson, I., G.F. Panza, and P. Suhadolc (1995). "Crust and upper mantle models along the active Tyrrhenian rim". In: *Terra Nova* 7, pp. 348– 357.

Massonnet, D., M. Rossi, C. Carmona, F. Adragna, G. Peltzer, K. Feigl, and T. Rabaute (1993). "The displacement field of the Landers earthquake mapped by radar interferometry". In: *Nature* 364, pp. 138–142.

Meissner, R. and J. Strehlau (1982). "Limits of stress in continental crust and their relation to the depth-frequency relation of shallow earthquakes". In: *Tectonics* 1, pp. 73–89.

Melosh, H.J. (1983). "Vertical movements following a dip-slip earthquake". In: *Geophys. Res. Lett.* 10, pp. 47–50.

Mostardini, P. and S.Merlini (1986). "Appennino centro-meridionale: sezioni geologiche e proposta di modello strutturale". In: *Mem. Soc. Geol. Ital.* 35, pp. 177–202.

Pantosti, D. and G. Valensise (1990). "Faulting mechanism and complexity of the 23 November 1980, Campania-Lucania, earthquake, inferred from surface observations". In: *J. Geophys. Res.* 95, pp. 15,319–15,341.

Pialli, G., M. Barchi, and Minelli G. (1998). "Results of of the CROP03 Deep Seismic Reflection Profile". In: *Mem. Soc. Geol. It.* LII, p. 657.

Piersanti, A., G. Spada, R. Sabadini, and M. Bonafede (1995). "Global post-seismic deformation". In: *Geophys. J. Int.* 120, pp. 544–566.

Pingue, F. and G. De Natale (1993). "Fault mechanism of the 40 s subevent of the 1980 Irpinia (Southern Italy) earthquake from levelling data". In: *Geophys. Res. Lett.* 20, pp. 911–914.

Pollitz, F.F. (1996). "Coseismic deformation from earthquake faulting on a layered spherical earth". In: *Geophys. J. Int* 125, pp. 1–14.

Pollitz, F.F., R. Bürgmann, and P. Segall (1998). "Joint estimation of afterslip rate and post-seismic relaxation following the 1989 Loma Prieta earthquake". In: *J. Geophys. Res.* 103, pp. 26,975–26,992.

Pollitz, F.F., G. Peltzer, and R. Bürgmann (2000). "Mobility of continental mantle: Evidence from postseismic geodetic observations following the 1992 Landers earthquake". In: *J. Geophys. Res.* 105, pp. 8035–8054.

Pollitz, F.F. and I.S. Sacks (1997). "The 1995 Kobe, Japan, Earthquake: A long-delayed aftershock of the offshore 1944 Tonankai and 1946 Nankaido earthquakes". In: *Bull. Seism. Soc. Am.* 87, pp. 1–10.

Riva, R.E.M., A. Aoudia, L.L.A. Vermeersen, R. Sabadini, and G.F. Panza (2000). "Crustal versus asthenospheric relaxation and post-seismic deformation for shallow normal faulting earthquakes: the Umbria-Marche (central Italy) case". In: *Geophys. J. Int.* 141, pp. F7–F11.

Sabadini, R., A. Piersanti, and G. Spada (1995). "Toroidal/poloidal partitioning of global post-seismic deformation". In: *Geophys. Res. Lett.* 22, pp. 985–988.

Sabadini, R. and L.L.A. Vermeersen (1997a). "Influence of lithospheric and mantle layering on global post-seismic deformation". In: *Geophys. Res. Lett.* 24, pp. 2075–2078.

Sabadini, R., D.A. Yuen, and E. Boschi (1994a). "The effects of postseismic motions on the moment of inertia of a stratified viscoelastic earth with an asthenosphere". In: *Geophys. J. R. Astron. Soc.* 79, pp. 727–745.

Salvi, S., S. Stramondo, M. Cocco, M. Tesauro, I. Hunstad, M. Anzidei, P. Briole, P. Baldi, E. Sansosti, G. Fornaro, R. Lanari, F. Doumaz, A. Pesci, and A. Galvani (2000). "Modeling coseismic displacements resulting from SAR interferometry and GPS measurements during the 1997 Umbria-Marche seismic sequence". In: *J. Seismology* 4, pp. 479– 499.

Saraó, A., F. Romanelli, G. Costa, and G.F. Panza (1998). "Source inversion and macroseismic modelling for the Umbria-Marche main events". In: *Ann. Geophysicae* 16(I), p. C164.

Scholz, C.H. (1990). *The Mechanics of Earthquakes and Faulting*. Cambridge Univ. Press, Cambridge, UK, p. 439.

Sibson, R.H. (1989). "Earthquake faulting as a structural process". In: *J. Struct. Geol.* 11, pp. 1–14.

Suito, H. and K. Hirahara (1999). "Simulation of postseismic deformations caused by the 1896 Riku-u earthquake, Northeast Japan: Re-evaluation of the viscosity in the upper mantle". In: *Geophys. Res. Lett.* 26, pp. 2561– 2564.

Thatcher, W. and J.B. Rundle (1979). "A model for the earthquake cycle in underthrust zones". In: *J. Geophys. Res.* 84, pp. 5540–5556.

Vermeersen, L.L.A. and R. Sabadini (1997). "A new class of stratified viscoelastic models by analytical techniques". In: *Geophys. J. Int.* 129, pp. 531–570.

Westaway, R. and J. Jackson (1984). "Surface faulting in the Southern Italy Campania-Basilicata earthquake of 23 November 1980". In: *Nature* 312, pp. 436–438.

Zollo, A., S. Marcucci, G. Milana, and P. Capuano (1999). "The 1997 Umbria-Marche (Central Italy) earthquake sequence: Insights on the mainshock ruptures from near source strong motion records". In: *Geo- phys. Res. Lett.* 26, pp. 3165–3168.

Chapter 9
Icy Moons

Abstract This chapter is devoted to the influence of a viscoelastic interior and a non-zero obliquity on diurnal and non-synchronous rotation (NSR) stresses shaping the tectonic features of the icy moons around the giant planets in our Solar System, like Europa, Ganymede and Callisto around Jupiter, and Titan and Enceladus around Saturn. Since the late 1970s, the icy moon became one of the most interesting planetary objects of study. Flybys of the Voyager I and II spacecraft and recent missions to Europa (Galileo) and Titan and Enceladus (Cassini-Huygens) have shown us that these moons are intricate and fascinating worlds on their own. Many might possess liquid layers under their icy crusts and with tidal energy and volcanism present they might even offer the best chances for natural habitats and perhaps even of existing extra-terrestrial lifeforms in our Solar System. Induced effects of tidal deformation and stresses might give us clues about the interior of these icy moons, especially about the existence and properties of shallow fluid or low-viscous layers. In this chapter the viscoelastic normal mode theory is further developed by including shallow low-viscosity layers in the models for icy moons in general, and for Jovian moon, Europa in particular. As an example, we apply the developed theory to the modeling of surface stresses on Europa. This chapter is derived from the work by Hermes M. Jara-Orué and Bert L.A. Vermeersen entitled 'Effects of low-viscous layers and a non-zero obliquity on surface stresses induced by diurnal tides and non-synchronous rotation: the case of Europa (Jara-Orué and Vermeersen 2011).

9.1 Diurnal and Non-synchronous Rotation (NSR) Stresses Acting on Europa's Surface

The determination of Europa's second-degree gravitational coefficients J_2 and C_{22} from the Doppler shift of Galileo's radio signal during four close flybys has allowed us to have a better understanding about the internal structure of this peculiar icy moon. Under the assumption of hydrostatic equilibrium, the measured values for J_2 and C_{22} imply a differentiated interior consisting of at least three material layers: a Fe

R. Sabadini et al., *Global Dynamics of the Earth: Applications of Viscoelastic Relaxation Theory to Solid-Earth and Planetary Geophysics*,
DOI 10.1007/978-94-017-7552-6_9

or Fe–FeS metallic core, a silicate mantle and a 80–70 m thick H_2O layer (Anderson et al. 1998; Sohl et al. 2002; Schubert et al. 2009). Due to the similar densities of liquid water and solid ice, it is not possible to determine unambiguously from the gravity data whether Europa's H_2O shell is subdivided into a global liquid ocean and an overlying ice shell (Anderson et al. 1998; Sohl et al. 2002). However, the existence of a global subsurface ocean below Europa's ice shell is essentially confirmed by the detection of an induced magnetic field by Galileo's magnetometer (Khurana et al. 1998; Kivelson et al. 2000; Zimmer et al. 2000; Hand and Chyba 2007; Schilling et al. 2007), and by the existence of a complex network of intersecting cracks, bands and ridges on Europa's surface (e.g. Geissler et al. 1998; Greeley et al. 1998; Hoppa et al. 1999b, c; Pappalardo et al. 1999; Kattenhorn and Hurford 2009). Europa's liquid ocean would be in direct contact with the underlying silicates, as the pressure at the rock-water interface is too low for the formation of high-pressure ice phases (e.g. Sotin and Tobie 2004). The currently undetected, but plausible, existence of hydrothermal seafloor systems would then allow for a mechanism to supply energy and nutrients to Europa's ocean (Hand et al. 2009), increasing the habitability potential of this Jovian moon.

The formation of tectonic features (cracks, bands and ridges) has been attributed to various sources of stresses acting at different timescales. On a 3.55-days timescale, stresses at the icy surface are induced by the diurnal tides induced by the non-zero eccentricity of Europa's orbit (Greenberg et al. 1998; Hoppa et al. 1999b, c; Greenberg et al. 2003; Harada and Kurita 2006; Wahr et al. 2009), the non-zero obliquity of Europa's spin axis (Bills 2005; Hurford et al. 2009; Rhoden et al. 2010, 2011), and physical librations of a decoupled shell (Van Hoolst et al. 2008; Rhoden et al. 2010). Diurnal stresses have been mainly used to model the formation of cycloidal features (Hoppa et al. 1999b; Hurford et al. 2007, 2009; Rhoden et al. 2010) and strike-slip faults (Hoppa et al. 1999c; Preblich 2007; Rhoden et al. 2011) on Europa's surface. On a much longer timescale, stresses may be induced by true polar wander (TPW) of the spin axis with respect to the icy surface (Ojakangas and Stevenson 1989a; Leith and McKinnon 1996; Matsuyama and Nimmo 2008; Schenk et al. 2008) and/or by non-synchronous rotation (NSR) of a decoupled shell (Leith and McKinnon 1996; Greenberg et al. 1998; Kattenhorn 2002; Greenberg et al. 2003; Hurford et al. 2007; Harada and Kurita 2007; Wahr et al. 2009). These slow stressing mechanisms lead to large ($\sim$MPa) stresses, which have been used to model the formation of global-scale surface features (Leith and McKinnon 1996; Geissler et al. 1998; Greenberg et al. 1998; Schenk et al. 2008). In addition, large isotropic stresses (up to $\sim$0 MPa) can result from thickening of the ice shell (Nimmo 2004).

Diurnal stresses acting on Europa's surface have been usually computed by means of the thin shell approximation (Leith and McKinnon 1996; Greenberg et al. 1998; Hoppa et al. 1999b; Hurford et al. 2007, 2009; Rhoden et al. 2010, 2011). In this method, which is based on the work of Melosh (1980b), Europa is assumed to be a thin elastic icy shell floating on a global liquid ocean (Hurford et al. 2007). A more realistic model by Harada and Kurita (2006) analyzes the influence of a differentiated internal structure on the surface diurnal stress, focusing on the relation between the magnitude of surface stresses and the thickness of the material layers.

Harada and Kurita (2006) show that surface diurnal stresses only depend on the thickness of the ice shell, hence supporting the assumption made by the thin shell approximation regarding the effect of the deep interior. The methods discussed above inherently assume that Europa's ice shell behaves elastically when forced by diurnal tides. However, as suggested by thermal models (e.g. Hussmann et al. 2002; Tobie et al. 2003) and impact crater models (Schenk 2002), the lower portion of Europa's ice shell most probably behaves in a viscoelastic way under the influence of diurnal tides. Recent modeling by (Wahr et al. 2009) includes the effect of viscoelasticity on surface diurnal stresses, thereby offering a potential method to study the effect of such a layer. However, the discussion in Wahr et al. (2009) only focuses on cases for which Europa's interior behaves nearly elastically with respect to diurnal tides.

Europa's decoupled ice shell can experience slow non-synchronous rotation as a result of the acting tidal torque and lateral thickness variations in the shell (Greenberg and Weidenschilling 1984; Ojakangas and Stevenson 1989b; Bills et al. 2009). If existing, NSR would be a slow periodic process with a period ($>11,000$ years) comparable to the characteristic Maxwell relaxation time (τ = viscosity/rigidity) of the lithospheric shell (see Sect. 9.7). Hence, viscoelastic relaxation in the lithospheric shell is expected to have an important influence on the magnitude and orientation of NSR stresses at Europa's surface. Nevertheless, NSR stresses acting on Europa's surface have been often computed through application of the thin shell approximation to determine the elastic stress fields induced by the current tidal bulge and by the original tidal bulge (Leith and McKinnon 1996; Greenberg et al. 1998; Hurford et al. 2007). The rotation angle between the two elastic stress fields, usually referred to as the accumulated degrees of NSR, defines the amount of NSR stress that accumulates in the shell (e.g. Greenberg et al. 1998). More realistic models of surface NSR stresses by Harada and Kurita (2007) and Wahr et al. (2009) have focused on the determination of the stress directly from the Maxwell viscoelastic equations of motion and the acting NSR tidal potential. This kind of modeling has two main advantages with respect to the simpler thin shell approximation: (1) it includes viscoelastic relaxation effects into the computation of NSR stresses, and (2) it allows to relate the obtained stress field to the rheological properties of the interior. Both aforementioned studies obtain similar results for the relation between the simulated NSR stress and the rheological properties of the icy shell. However, both studies take a different approach to analyze the effect of viscoelastic relaxation on surface NSR stresses. The work by Harada and Kurita (2007) constrains the magnitude of diurnal and NSR stresses to be comparable, as previously suggested by Greenberg et al. (1998). As a result, Harada and Kurita (2007) implicitly assume that NSR stresses are severely affected by viscoelastic relaxation in the lithospheric shell. This assumption inherently leads to a westward shift of 45° in the surface distribution of the NSR stress field; the same as the one predicted in Greenberg et al. (1998). On the other hand, the work by Wahr et al. (2009) takes into consideration that NSR stresses could be larger in magnitude than diurnal stresses. Therefore, the westward shift of the NSR stress field does not necessarily have to be equal to 45°. This conclusion has a large effect on the determination of the time elapsed since the

formation of a surface feature (Wahr et al. 2009), especially if the relaxation state of the NSR stress field changes with time.

Although the studies by Harada and Kurita (2007) and Wahr et al. (2009) already discussed the influence of viscoelasticity on surface stresses, their treatment is mostly focused on NSR stresses. Viscoelastic effects on diurnal stresses have often been neglected by considering quasi-elastic interior models. However, thermal models of Europa's ice shell have often assumed that the lower convective portion of the ice (asthenosphere) has a Newtonian viscosity in the range 10^{13}–10^{15} Pa s (see e.g. Hussmann et al. 2002; Sotin and Tobie 2004; Nimmo and Manga 2009). In this range, not only tidal heat dissipation becomes largest but also the viscoelastic effect on diurnal stresses. As a result, we aim to extend the determination of diurnal stresses to interior models with a 2-layered ice shell, in which the Maxwell time of the lower icy sublayer is smaller or comparable to the orbital period, as suggested by thermal modeling. In addition we will take into account the effect of a non-zero obliquity on diurnal stresses from a viscoelastic perspective. Regarding NSR stress modeling, we will discuss the effect of the viscosity of the lower ice layer as a function of the amount of relaxation. In addition, we allow NSR stresses to be larger, comparable and smaller than diurnal stresses in order to infer the possible relation between the resulting NSR-diurnal stress field and the observed features.

The viscoelastic modeling of tidal deformation and stresses on Europa's surface is based on three aspects: determination of the tidal forcing, assumptions on Europa's internal configuration and determination of Europa's viscoelastic response being underlain by a shallow-viscosity layer to tidal forces.

9.2 The Tidal Potential

The shape and orientation of the tidal bulge would remain fixed to the satellite's figure if the satellite would always show exactly the same face to the tide-raising planet. This particular configuration would take place if: (1) the satellite's orbit around the planet would be circular (zero eccentricity), (2) the spin axis of the satellite would be perpendicular to its orbital plane (zero obliquity), and (3) the spin rate of the satellite would be synchronous to its orbital motion (synchronous rotation).

None of these requirements apply to Europa, as shown in Fig. 9.1. In fact, in the top panel of this figure we observe that the tidally locked orbit of Europa around Jupiter is slightly eccentric. While completing one orbit around Jupiter, Europa has rotated once around its own rotation axis. The eccentricity causes that Jupiter librates diurnally in the sky as seen from the surface of Europa. The angle alpha is thus not constant along the orbit, as Europa rotates with a constant angular velocity around its own rotation axis, but with a varying orbital velocity around Jupiter due to the eccentricity. Thus, also the tidal bulge of Europa will librate diurnally, as portrayed by the bottom panel, resulting in differential tidal friction within the interior of Europa and thus in heat dissipation. This tidal friction will decrease the eccentricity

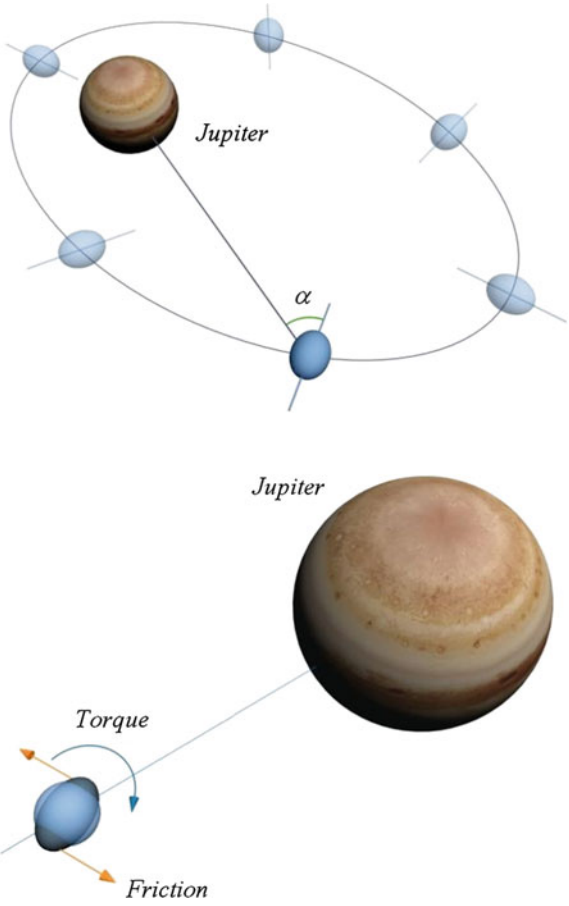

Fig. 9.1 *Top* tidally locked orbit of Europa around Jupiter. *Bottom* diurnal libration of the tidal bulge of Europa

of the orbit of Europa around Jupiter. It is the 1:2:4 orbital resonance of Europa with neighboring Io and Ganymede that maintains the eccentricity.

First of all, the 1:2:4 Laplace resonance between the orbital motions of Io, Europa and Ganymede prevents the orbit of Europa to become circular. In addition, the obliquity of Europa's spin axis cannot be exactly equal to zero as a consequence of precession of Europa's orbital plane (Bills 2005). Furthermore, a global subsurface ocean might decouple the rotational motion of Europa's ice shell from the rotational motion of the rocky interior. As a result, the positive net tidal torque experienced by the satellite might only affect the spin rate of the decoupled ice shell whereas the rocky interior remains tidally locked (e.g. Greenberg and Weidenschilling 1984; Ojakangas and Stevenson 1989b). Although non-synchronous rotation (NSR) of Europa's ice shell is strongly favored by the orientation of tectonic features (e.g. Greenberg et al. 1998; Hoppa et al. 2001; Kattenhorn 2002; Greenberg et al. 2003; Hurford et al. 2007; Rhoden et al. 2010), the torque caused by Jupiter's gravitational attraction on

permanent asymmetries in Europa's figure might counteract the net tidal torque and maintain synchronicity of the spin rate (Greenberg and Weidenschilling 1984; Bills et al. 2009). The contribution of the permanent asymmetries to the evolution of the spin rate depends on the difference between the two principal equatorial moments of inertia (i.e. $B - A$) and the orientation of the longest axis (related to moment of inertia A) with respect to the direction of the planet (see e.g. Goldreich et al. 1966).

The tidal force field acting on Europa's surface is subjected to periodic variations on a diurnal timescale ($\approx$3.55 days), which are mainly the result of the slightly elliptical shape of Europa's orbit around Jupiter (with eccentricity $e = 0.0094$). Diurnal changes in the magnitude of the tidal forces acting on Europa, which are caused by periodic variations in the distance between Europa and Jupiter, lead to continuous stretching and squeezing of the tidal bulge. On the other hand, diurnal changes in the orientation of the tidal field with respect to the surface, which are caused by differences between Europa's spin rate and the instantaneous orbital rate, lead to periodic longitudinal migrations of the tidal bulge. In both cases, the materials composing the interior of Europa will continuously try to deform accordingly to the shape dictated by the acting diurnal tidal field. This periodic reshaping of Europa's interior leads to the generation of frictional heat in the interior and $\sim$100 kPa stresses at the surface (see Sect. 9.7 for a more detailed analysis).

Also on a diurnal timescale, the tidal force field acting on Europa's surface experiences additional periodic variations as the obliquity of Europa's spin axis is non-zero ($\varepsilon \approx 0.1°$). The most important effect of Europa's non-zero obliquity is that it causes diurnal changes in the latitudinal orientation of the tidal bulge. As a result, the obliquity introduces an additional source of heat dissipation in the interior and stresses at the surface of Europa. For example, Europa's non-zero obliquity might have played a substantial role in the formation of cycloidal cracks crossing the equator, as suggested by Hurford et al. (2009).

In addition, the tidal field acting on the surface of Europa might be subjected to (periodic) variations on timescales much larger than one Europan day. Here we assume that the spin rate of Europa's decoupled ice shell is slightly faster than synchronous, in accordance with the geological evidence (Greenberg et al. 1998; Hoppa et al. 2001; Kattenhorn 2002; Greenberg et al. 2003; Hurford et al. 2007; Rhoden et al. 2010). As a consequence, the tidal bulge exerted by Jupiter on Europa would slowly migrate in westward direction with respect to a meridian attached to the icy surface. A complete revolution of the tidal bulge with respect to Europa's surface (i.e. the period of NSR) would take more than 12,000 years (Hoppa et al. 1999a). Non synchronous rotation is a very important process in the analysis of surface stresses for two reasons: (1) it might be a source of large $\sim$MPa stresses (Harada and Kurita 2007; Wahr et al. 2009) and (2) it changes the longitude of tectonic features. NSR stresses have been often related to the formation of global lineaments on Europa's surface (see e.g. Greenberg et al. 1998; Harada and Kurita 2007; Hurford et al. 2007; Wahr et al. 2009).

In this book tidal forces are expressed as minus the gradient of a scalar field, Eqs. (1.2) and (1.3) and the tidal potential Φ^T, on the basis of Eqs. (1.60) and (1.219), can then be expressed as a series of spherical harmonics

$$\phi^T = -GM_T \frac{1}{R} \sum_{\ell=2}^{\infty} \left(\frac{a}{R}\right)^{\ell} P_\ell(\cos\theta) \tag{9.1}$$

where G, M_T, a and R are defined as the universal gravitational constant, the mass of the primary, the mean radius of Europa and the distance from the centre of Europa to the primary (r_L in Eq. (1.219)). The function P_ℓ is defined as the Legendre polynomial of spherical harmonic degree ℓ. The angle θ is now the angular distance of a point on the surface of Europa with respect to the line connecting the centres of Europa and Jupiter. With respect to Jara-Orué and Vermeersen (2011) the tidal potential carries the opposite sign, to make all the perturbed potentials considered in this book consistent with Eqs. (1.2) and (1.60). The series of spherical harmonics given by Eq. (9.1) converges rapidly as the term $(a/R)^{\ell}$ decreases exponentially when the harmonic degree ℓ increases. In the case of Jupiter's tide on Europa, the contribution of the second degree term is already about 430 times larger than the contribution of the third degree term. Hence, we can safely express the tidal potential exerted by Jupiter on Europa by only taking into account the second degree term.

Thereafter, we apply the method of Kaula (1964) to express the tidal potential in terms of the Keplerian elements describing the motion of Jupiter with respect to a reference frame attached to Europa's rotating surface, in which the z-axis coincides with Europa's spin axis and the x-axis points towards Jupiter at pericenter. We simplify the resulting expression by taking into account that Europa's eccentricity and obliquity are small, i.e. we consider terms only up to first order in eccentricity and obliquity and neglect any cross terms of the eccentricity and obliquity. Moreover, we neglect the effect of NSR on the eccentricity tide and obliquity tide because these terms are approximately two orders of magnitude smaller than the effect of NSR on the main "static" tide. Then, the resulting expression for the tidal potential Φ_T exerted by Jupiter on Europa becomes

$$\phi^T = (na)^2 \left\{\phi_T^0 + \phi_T^{ns} + \phi_T^{e1} + \phi_T^{e2} + \phi_T^{o1}\right\} \tag{9.2}$$

where

$$\phi_0^T = -\frac{1}{2} P_{20}(\theta) + \frac{1}{4} P_{2,2}^{\theta} \cos(2\varphi)\,, \tag{9.3}$$

$$\phi_{ns}^T = -\frac{1}{2} P_{22}(\theta) \sin(2\varphi + \Omega_{ns} t) \sin(\Omega_{ns} t)\,, \tag{9.4}$$

$$\phi_{e1}^T = -\frac{3e}{2} P_{20}(\theta) \cos(nt), \tag{9.5}$$

$$\phi_{e2}^T = \frac{e}{4} P_{22}(\theta) \left[3\cos(2\varphi)\cos(nt) + 4\sin(2\varphi)\sin(nt)\right], \tag{9.6}$$

$$\phi_{o1}^T = P_{21}^{\theta} \cos(\varepsilon) \sin(\varepsilon) \cos(\varphi) \sin(\omega + nt), \tag{9.7}$$

where e and n are respectively the eccentricity and the mean motion of Europa's orbit, ε is the obliquity of Europa's spin axis and ω is the argument of pericentre measured

Table 9.1 Physical parameters: tidal potential acting on Europa

Parameter	Symbol	Value	Unit	Reference
Mean radius	a	1562	km	(Seidelmann et al. 2007)
Mean motion	n	101.37472	°/day	(e.g. Bills 2005)
Eccentricity	e	0.0094	–	(e.g. Wahr et al. 2009)
Obliquity	ε	0.1	°	(Bills 2005)
Argument of pericenter	ω	345	°	(Hurford et al. 2009)
Angular rate of NSR	Ω_{ns}	<0.03	°/year	(Hoppa et al. 1999a)
Period of NSR	T_{ns}	>12, 000	years	(Hoppa et al. 1999a)

with respect to the ascending node where Europa's orbital plane crosses Europa's equatorial plane. The variable Ω_{ns} describes the constant angular rate of NSR, i.e. the difference between Europa's angular spin rate and Europa's mean orbital rate. The numerical values corresponding to the aforementioned parameters are listed in Table 9.1.

Furthermore, the angles θ and φ are, respectively, the colatitude and longitude of a point on Europa's surface. Finally, the associated Legendre polynomials $P_{20}(\theta)$, $P_{21}(\theta)$ and $P_{22}(\theta)$ are, according to Eq. (1.68), given by

$$P_{20}(\theta) = \frac{3\cos^2(\theta) - 1}{2}, \tag{9.8}$$

$$P_{21}(\theta) = 3\sin(\theta)\cos(\theta), \tag{9.9}$$

$$P_{22}(\theta) = 3\sin^2(\theta). \tag{9.10}$$

Equations (9.2)–(9.7) show that the tidal potential acting on Europa consists of a static component and several time-dependent components. The term ϕ_0^T represents the time invariant potential, although the second term of Eq. 9.3 would contain a time variable component if physical librations of the ice shell (Van Hoolst et al. 2008; Baland and Van Hoolst 2010) would be taken into account. The term ϕ_0^T would completely define the tidal potential acting on Europa's surface if Europa's orbit would be circular, its rotation synchronous and its obliquity zero. In that particular case, the stresses induced by the formation of the bulge would have had sufficient time to relax completely and tidal heat would not be dissipated in the interior of Europa. The term ϕ_{ns}^T describes the contribution of NSR to the tidal potential. This term is only non-zero and time dependent if the ice shell rotates non-synchronously with respect to the orbital motion, i.e. when $\Omega_{ns} \neq 0$. Finally, the terms ϕ_{e1}^T, ϕ_{e2}^T and ϕ_{o1}^T represent the diurnal tidal potential resulting form the non-zero eccentricity of Europa's orbit (first two terms) and the non-zero obliquity of Europa's spin axis (last term).

9.3 The Interior of Europa

The materials composing the interior of Europa and other planetary satellites do not respond in a perfectly elastic way to the acting tidal forces at either diurnal timescales nor at timescales relevant to NSR. Part of the interior's response is delayed with respect to the onset time of the tidal forcing as a result of viscous relaxation effects. Therefore, the interior of a planetary satellite will most probably behave as a viscoelastic body rather than as a purely elastic or fluid body (see e.g. Tobie et al. 2005).

The internal structure of Europa has been assumed to consist of five homogeneous and incompressible spherical layers: a fluid metallic core of Fe and/or FeS, a large silicate mantle, a liquid ocean, a warm low-viscous ice-I layer and a cold high-viscous ice-I layer on top. The radius r and density ρ of each of these concentric spherical layers needs to be such that the complete model of Europa's interior satisfies the conditions on average density ($\rho_{av} = 2989$ kg/m^3) and normalized mean moment of inertia ($\frac{I}{Ma^2} = 0.346$) (Anderson et al. 1998). The methodology used to model the layered structure of Europa's interior follows the approach outlined in Sohl et al. (2002) and Harada and Kurita (2006).

Although the entire ice shell is assumed to have a constant density ρ and rigidity μ, we subdivide the ice shell in two layers with different viscosities ν. The introduced viscosity contrast leads to the existence of two ice layers with different mechanical and thermal properties (viscosity is a function of temperature). The subdivision of the ice shell in two layers is consistent with thermal models dealing with stagnant lid convection in the ice shell (e.g. Hussmann et al. 2002; Tobie et al. 2003) and with the morphology of impact craters on Europa's surface (Schenk 2002).

Here we will make use of various models of Europa's interior to analyze the relation between tidal stresses at the surface and the parameters defining the interior. To reduce the number of plausible models, we do not change the size of the core (600 km), the thickness of the H_2O layer (130 km), the thickness of the lithosphere (5 km), the densities of ice and liquid water (937 and 1000 kg/m^3, respectively), the rigidity of the silicate mantle (65 GPa) and the viscosities of the mantle and the lithosphere (10^{19} and 10^{21} Pa s, respectively). We vary the total thickness of the ice shell from 5 to 130 km (no ocean), the rigidity of ice-I from 1 to 10 GPa, and the viscosity of the asthenosphere from 10^{12} to 10^{17} Pa s. However, we will limit the

Table 9.2 Reference 5-layer model of Europa's interior

Layer	Outer radius (km)	Density (kg/m^3)	Rigidity (GPa)	Viscosity (Pa s)
Lithosphere	1562	937.0	3.487	10^{21}
Asthenosphere	1557	937.0	3.487	10^{14}
Ocean	1532	1000.0	0	0
Silicate mantle	1432	3453.6	65.000	10^{19}
Core	600	5565.8	0	0

graphical representation of spatial and temporal variations of surface stresses to our standard model of Europa's interior, which is defined by the physical parameters listed in Table 9.2.

9.4 The Impulse Tidal Response of Europa

9.4.1 The Impulse Response of Interior Models with a Global Subsurface Ocean

Whereas in this book the Laplace transform has been used, since the tidal forcing exerted by Jupiter on Europa shows a harmonic behavior, it would seem more appropriate to use the Fourier approach to determine the tidal response of a Maxwell viscoelastic body (see e.g. Moore and Schubert 2000; Tobie et al. 2005; Harada and Kurita 2007; Rappaport et al. 2008; Roberts and Nimmo 2008; Wahr et al. 2009). Nevertheless, in the remaining of this Chapter we proceed our treatment of the tidal response by means of the Laplace transform, herein indicated explicitly by tilde overlying the fields. This choice is based on two reasons: (1) to analyze the characteristics of the relaxation process in more detail, and (2) to avoid the presence of complex-valued variables prior to the determination of the rotation modes from the linearized Liouville equation (relevant for the treatment of True Polar Wander).

The classical propagator matrix method as dealt with in Sect. 2.1.2 inherently implies propagation of the radial functions $\tilde{y}_1$ to $\tilde{y}_6$ from the core-mantle boundary (CMB) to the surface through exclusively viscoelastic material layers. However, as suggested in Sect. 9.3, our models of Europa's interior include a material layer with zero rigidity between two viscoelastic layers: the subsurface ocean. The presence of a liquid ocean between the mantle and the ice shell changes the dynamics of the interior's response as fluid layers are not able to propagate mechanical quantities, such as deformations and stresses, from the top of the silicate mantle to the base of the ice shell. Therefore, the response of the ice shell is mechanically decoupled from the response of the silicate mantle, although remaining gravitationally coupled.

The presence of a liquid inviscid ocean in the interior of Europa introduces a challenge to the application of the propagator matrix method. An internal fluid material layer (with $\tilde{\mu} = 0$) would cause a singularity in the radial propagation of the tangential displacement $\tilde{y}_2$. This singularity degenerates the propagation of the remaining mechanical quantities ($\tilde{y}_1$, $\tilde{y}_3$ and $\tilde{y}_4$) and the potential stress $\tilde{y}_6$ through the liquid ocean. In order to circumvent this problem, we assume that Europa's subsurface ocean is in a state of hydrostatic equilibrium in both the undeformed and deformed cases and that the deformations of the fluid follow equipotential surfaces (based on Chinnery 1975). In this way, the physical behavior of Europa's putative subsurface ocean is fully determined by Poisson's equation. If we further assume that Europa's ocean is incompressible and non-stratified, Poisson's equation (1.87) reduces to

Laplace's equation because $\tilde{\chi}_\ell$ and $\frac{\partial \rho_0}{\partial r}$ become equal to zero. Then, from Eqs. (1.142) and (1.91) the relevant set of differential equations can be written as

$$\frac{\mathrm{d}\tilde{y}_5}{\mathrm{d}r} = \tilde{y}_7, \tag{9.11}$$

$$\frac{\mathrm{d}\tilde{y}_7}{\mathrm{d}r} = \frac{\ell(\ell+1)}{r^2}\tilde{y}_5 - \frac{2}{r}\tilde{y}_7, \tag{9.12}$$

which depend only on the degree ℓ as the tidal potential given by Eq. (9.1) and where the auxiliary radial function $\tilde{y}_7$ is simply defined as the radial derivative of the perturbed potential, i.e.

$$\tilde{y}_7 = \frac{\partial \tilde{\Phi}_\ell}{\partial r} \tag{9.13}$$

or, alternatively, in terms of the potential stress $\tilde{Q}_\ell$ (compare Eq. (1.93))

$$\tilde{y}_7 = \tilde{Q}_\ell - \frac{\ell+1}{r}\tilde{\Phi}_\ell - 4\pi G\rho_0\tilde{U}_\ell = \tilde{Q}^*_\ell. \tag{9.14}$$

The same equations would hold if the subsurface ocean would be stratified in several layers with different densities. From Eqs. (9.14) and (1.153) we obtain

$$\tilde{Q}^{*(i)}_\ell = \tilde{Q}^{*(i+1)}_\ell - 4\pi G\left(\rho_0^{(i+1)} - \rho_0^{(i)}\right)\frac{\Phi_\ell^{(i+1)}}{g(r_{i+1})}. \tag{9.15}$$

where i is a fluid layer overlying fluid layer $i+1$ and r is the outer radius of a given fluid layer. Equation (9.15) also takes into account that the radial deformation of fluid layers follows the shape of an equipotential surface, as Eq. (1.53) tells us.

The introduction of a subsurface ocean decouples the propagation of the tidal response from the core-mantle boundary to the surface in three parts: propagation through the mantle, propagation through the ocean and propagation through the ice shell. The first and last propagation steps obey the equations of motion for viscoelastic bodies, while the second propagation obeys the equations of motion for fluid layers (Eqs. (9.11) and (9.12)). In order to couple the three parts of the propagation, we need to provide a set of boundary conditions at the interfaces between the ocean and both the underlying silicate mantle and the overlying ice shell. Then, the general structure of the adapted propagator matrix method becomes:

- The solution vector at the core-mantle boundary (CMB) is propagated through the silicate mantle by means of the viscoelastic propagator matrix,
- At the mantle-ocean interface, a set of boundary conditions relates the solution vector at the top of the silicate mantle to the solution vector at the bottom of the ocean,
- The solution vector at the bottom of the ocean is propagated through the liquid ocean by means of the fluid propagator matrix,

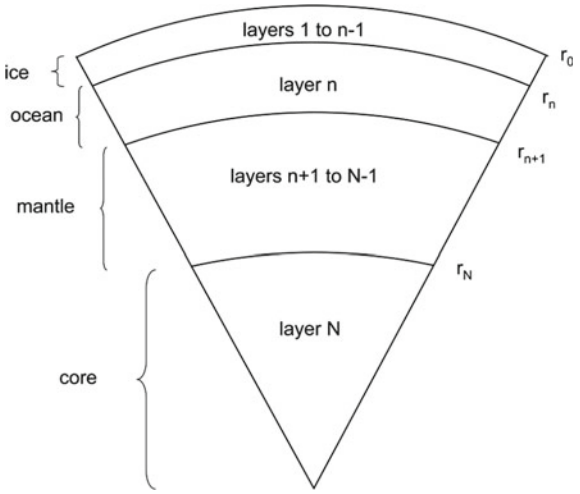

Fig. 9.2 Definition of the nomenclature used to describe the internal layers of Europa. Layers $1 \leq i \leq n-1$ are the ice shell, layer $i = n$ is the ocean, layers $n+1 \leq i \leq N-1$ are the *solid mantle and layer* $i = N$ is the fluid core

- At the ocean-ice interface, we again link the solution vector at the top of the ocean to the solution vector at the bottom of the ice shell by a set of boundary conditions,
- The solution vector at the base of the ice shell can be further propagated up to the surface by means of the viscoelastic propagator matrix.

In our tidal modeling, the layered internal structure of an icy moon with N layers is presented in the following way: layers $1 \leq i \leq n-1$ represent the ice shell, layer $i = n$ represents the liquid ocean, layers $n+1 \leq i \leq N-1$ represent the silicate mantle and layer $i = N$ is the fluid core (see Fig. 9.2).

The presence of a subsurface ocean precludes the propagation of mechanical quantities (i.e. deformations and stresses) from the top of the mantle to the base of the ice shell, thereby implying that only the perturbed gravitational potential ($\tilde{y}_5 = \tilde{\Phi}_\ell$) and its radial derivative ($\tilde{y}_7 = \tilde{Q}^*_\ell$) can be propagated through the liquid ocean. As a result, the response of the ice shell is mechanically decoupled from the response of the mantle, albeit remaining gravitationally coupled.

The propagation of the gravity-related radial functions $\tilde{y}_5$ and $\tilde{y}_7$ through a liquid layer is governed by the set of differential equations (9.11) and (9.12). This set of equations can alternatively be written as

$$\begin{pmatrix} \tilde{\Phi}_\ell \\ \tilde{Q}^*_\ell \end{pmatrix} = \begin{pmatrix} r^\ell & r^{-(\ell+1)} \\ \ell r^{\ell-1} & -(\ell+1) r^{-(l+2)} \end{pmatrix} \begin{pmatrix} C_1 \\ C_2 \end{pmatrix} = \tilde{\mathbf{Y}}_\ell(r, s) \tilde{\mathbf{C}}_\ell. \tag{9.16}$$

where $\tilde{\mathbf{Y}}_\ell$ is the fundamental matrix and $\tilde{\mathbf{C}}_\ell$ is a vector of integration constants. The Laplace variable s could be omitted in the fluid fundamental matrix, since no s-dependent term enters its definition, Eq. (9.16).

In contrast to all other radial functions, $\tilde{Q}_\ell^*$ is characterized by being discontinuous at the interface between two fluid layers with different densities and at the boundaries with viscoelastic layers. Since we want to keep the number of discontinuous boundaries as low as possible (i.e. two boundaries), we simplify the modeling by assuming that the density is constant throughout the entire ocean layer. As a result, we can relate the solution vector at the top of the ocean to the solution vector at the bottom of the ocean by

$$\begin{pmatrix} \tilde{\Phi}_\ell^{(n)}(r_n) \\ \tilde{Q}_\ell^{*(n)}(r_n) \end{pmatrix} = \tilde{\mathbf{B}}_\ell^f \begin{pmatrix} \tilde{\Phi}_\ell^{(n)}(r_{n+1}) \\ \tilde{Q}_\ell^{*(n)}(r_{n+1}) \end{pmatrix} \tag{9.17}$$

in which $\tilde{\mathbf{B}}_\ell^f$ is the fluid propagator matrix, as for the first term in the right hand member of Eq. (1.157), defined by

$$\tilde{\mathbf{B}}_\ell^f = \tilde{\mathbf{Y}}_\ell^{(n)}(r_n, s) \left(\tilde{\mathbf{Y}}_\ell^{(n)}(r_{n+1}, s) \right)^{-1} \tag{9.18}$$

as for Eq. (2.9) and where the fundamental matrix $\tilde{\mathbf{Y}}_\ell^{(n)}(r_n, s)$ is built over the appropriate terms of Eq. (2.42) defining the incompressible fundamental matrix. The situation would be slightly more complicated for stratified oceans, as each additional boundary would result in an additional discontinuity in $\tilde{Q}_\ell^*$.

9.4.2 Boundary Conditions

As can be seen from Eq. (9.17) only two elements of the solution vector are propagated through fluid layers, whereas propagation through viscoelastic layers requires all six elements of the solution vector. A proper set of boundary conditions is required to express the conditions at the viscoelastic side of a fluid-solid interface in terms of the conditions at the fluid side of the same interface. In the case of a subsurface ocean, we need to define such boundary conditions at two interfaces:

1. At the ocean-ice interface: the radial deformation of the ocean $\tilde{U}_\ell^{(n)}(r_n)$ cannot follow an equipotential surface as the icy shell prevents such a radial displacement. A constant term K_4 takes into account the difference between the shape of the ideal equipotential surface at the top of the ocean layer and the shape of the icy shell at its base. Furthermore, the pressure induced by this constant term K_4 defines the radial stress $\tilde{\sigma}_{rr,\ell}^{(n)}(r_n)$ at the top of the ocean. The tangential deformation $\tilde{V}_\ell^{(n-1)}(r_n)$ at the base of the icy shell is assumed to be decoupled from the motion of the ocean and equal to a constant K_5. The tangential stress at the interface is zero in the absence of acting tangential traction. By taking into account continuity of the six elements across the ocean-ice interface and the boundary condition for

the tangential deformation, we can define the set of boundary conditions at the ocean-ice interface as (adapted from Greff-Lefftz et al. 2000):

$$\begin{pmatrix} \tilde{U}_\ell^{(n-1)}(r_n) \\ \tilde{V}_\ell^{(n-1)}(r_n) \\ \tilde{\sigma}_{rr,\ell}^{(n-1)}(r_n) \\ \tilde{\sigma}_{r\theta,\ell}^{(n-1)}(r_n) \\ \tilde{\Phi}_\ell^{(n-1)}(r_n) \\ \tilde{Q}_\ell^{(n-1)}(r_n) \end{pmatrix} = \begin{pmatrix} \frac{\tilde{\Phi}_\ell^{(n)}(r_n)}{g(r_n)} + K_4 \\ K_5 \\ \rho_0^{(n)} g(r_n) K_4 \\ 0 \\ \tilde{\Phi}_\ell^{(n)}(r_n) \\ \tilde{Q}_\ell^{(n)}(r_n) + 4\pi G \rho_0^{(n)} K_4 \end{pmatrix} \tag{9.19}$$

where the sixth element of the solution vector at the base of the icy shell, $\tilde{Q}_\ell^{(n-1)}(r_n)$, can alternatively be expressed as

$$\tilde{Q}_\ell^{(n-1)}(r_n) = \tilde{Q}_\ell^{*(n)}(r_n) + \frac{\ell+1}{r_n}\tilde{\Phi}_\ell^{(n)} + 4\pi G \rho_0^{(n)} \left(\frac{-\tilde{\Phi}_\ell^{(n)}(r_n)}{g(r_n)} + K_4 \right) \tag{9.20}$$

2. At the mantle-ocean interface: the set of boundary conditions at this interface slightly differs from the set corresponding to the ocean-ice interface (Eq. (9.19)). The first difference is related to the tangential deformation at the top of the mantle $\tilde{V}_\ell^{(n+1)}(r_{n+1})$, which does not propagate further to the base of the ocean as the tangential motion of both layers is assumed to be decoupled (free-slip boundary condition). The second difference is related to the radial deformation at the top of the mantle $\tilde{U}_\ell^{(n+1)}(r_{n+1})$, which at this boundary is defined as the difference between the equipotential shape and a constant K_6 (Greff-Lefftz et al. 2000). By taking these observations into account, the set of boundary conditions at the mantle-ocean interface can be written as (adapted from Greff-Lefftz et al. 2000):

$$\begin{pmatrix} \frac{\tilde{\Phi}_\ell^{(n)}(r_{n+1})}{g(r_{n+1})} \\ \tilde{V}_\ell^{(n)}(r_{n+1}) \\ \tilde{\sigma}_{rr,\ell}^{(n)}(r_{n+1}) \\ \tilde{\sigma}_{r\theta,\ell}^{(n)}(r_{n+1}) \\ \tilde{\Phi}_\ell^{(n)}(r_{n+1}) \\ \tilde{Q}_\ell^{(n+1)}(r_{n+1}) \end{pmatrix} = \begin{pmatrix} \tilde{U}_\ell^{(n+1)}(r_{n+1}) + K_6 \\ - \\ -\rho_0^{(n)} g(r_{n+1}) K_6 \\ 0 \\ \tilde{\Phi}_\ell^{(n+1)}(r_{n+1}) \\ \tilde{Q}_\ell^{(n)}(r_{n+1}) - 4\pi G \rho_0^{(n)} K_6 \end{pmatrix} \tag{9.21}$$

where the sixth element of the solution vector at the top of the mantle, $\tilde{Q}_\ell^{(n+1)}(r_{n+1})$, can also be written as

$$\tilde{Q}_\ell^{(n+1)}(r_{n+1}) = \tilde{Q}_\ell^{*(n)}(r_{n+1}) + \frac{\ell+1}{r_{n+1}}\tilde{\Phi}_\ell^{(n)}(r_{n+1}) + 4\pi G \rho_0^{(n)} \left(\frac{-\tilde{\Phi}_\ell^{(n)}(r_{n+1})}{g(r_{n+1})} - K_6 \right) \tag{9.22}$$

These additional boundary conditions increase the level of complexity of the propagator matrix technique, as will be shown in the following Sect. 9.4.3.

9.4.3 Application to Icy Moons I: Normal Modes

In order to determine which relaxation modes are applicable to our interior models, we need to find the M non-zero roots of the secular determinant (compare with Eq. (1.200))

$$\det(\tilde{\mathbf{W}}_1) = 0. \tag{9.23}$$

These roots are defined as the inverse relaxation times s_j ($j = 1, 2, \ldots M$) of the interior model or, alternatively, as the free oscillations of the model. The roots are the solutions of the characteristic equation

$$\mathbf{0} = \tilde{\mathbf{W}}_1 \tilde{\mathbf{C}}_\ell, \tag{9.24}$$

where $\tilde{\mathbf{C}}_\ell = (K_1\ K_2\ K_3\ K_4\ K_5)^T$ is the 5×1 vector of unknowns and $\tilde{\mathbf{W}}_1$ is the 5×5 propagator matrix defined by (see C.1 for derivation)

$$\tilde{\mathbf{W}}_1 = \begin{pmatrix} 0 & 0 & L_{\ell,1} & L_{\ell,2} & L_{\ell,3} \\ 0 & 0 & \tilde{\mathbf{B}}^{sm}_{\ell,41} & \tilde{\mathbf{B}}^{sm}_{\ell,42} & \tilde{\mathbf{B}}^{sm}_{\ell,43} \\ R_{\ell,3} & \tilde{\mathbf{B}}^{si}_{\ell,32} & G_{\ell,11} & G_{\ell,12} & G_{\ell,13} \\ R_{\ell,4} & \tilde{\mathbf{B}}^{si}_{\ell,42} & G_{\ell,21} & G_{\ell,22} & G_{\ell,23} \\ R_{\ell,6} & \tilde{\mathbf{B}}^{si}_{\ell,62} & G_{\ell,31} & G_{\ell,32} & G_{\ell,33} \end{pmatrix}. \tag{9.25}$$

Equation (9.25) contains four groups of elements, each of them having a specific relation to the unknown constants K_1 to K_5. The first group includes the nine terms $G_{\ell,vw}$ (row $1 \le v \le 3$ and column $1 \le w \le 3$), which are explicitly defined by Eq. (C.11). These terms describe the propagation of the conditions at the CMB to the surface. The second group includes the terms $R_{\ell,y}$ and $\tilde{\mathbf{B}}^{si}_{\ell,y2}$ ($y \in \{3, 4, 6\}$). These terms together describe the propagation of the conditions at the ocean-ice boundary to the surface. The third group contains the terms $\tilde{\mathbf{B}}^{sm}_{\ell,4x}$ ($x \in \{1, 2, 3\}$). This group of terms denotes the boundary condition on the tangential stress at the mantle-ocean boundary. Finally, the fourth group includes the terms $L_{\ell,x}$ ($x \in \{1, 2, 3\}$), which are defined by Eq. (C.16). These terms represent the boundary condition on the radial deformation at the mantle-ocean boundary. The last two conditions can be safely used as both the tangential stress and the radial deformation at the mantle-ocean boundary cannot be propagated through the ocean layer.

9.4.4 Application to Icy Moons II: Impulse Response to Tidal Forces

After determining the M normal modes of our interior model and their corresponding relaxation times and modal strengths, we proceed with the computation of the

response of our interior model to a unit impulse tidal forcing. This so-called unit impulse response of the interior to the acting tides is a property of the interior and hence it does not depend on the forcing itself.

Tidal forces constrain the parameters $\tilde{\sigma}_{rr,\ell}$, $\tilde{\sigma}_{r\theta,\ell}$ and $\tilde{Q}_\ell$ of the solution vector at the surface, such that the boundary condition vector $\tilde{\mathbf{b}}$ becomes

$$\tilde{\mathbf{b}} = \begin{pmatrix} 0 & 0 & 0 & 0 & \dfrac{(2\ell+1)}{a} \end{pmatrix}^T \tag{9.26}$$

as for Eq. (1.130) where the last three elements refer to the boundary conditions at the surface and the first two refer to the additional boundary conditions at the mantle-ocean boundary (see C.1 for a more detailed explanation).

The boundary condition vector $\tilde{\mathbf{b}}$ provides five constraints, which can be related to the unknown constants K_1 to K_5 by means of the propagator matrix $\tilde{\mathbf{W}}_1$ Eq. (9.25); i.e.

$$\tilde{\mathbf{b}} = \tilde{\mathbf{W}}_1 \tilde{\mathbf{C}}_\ell \tag{9.27}$$

In a similar way, we can relate the remaining three elements of the solution vector at the surface (i.e. $\tilde{U}_\ell$, $\tilde{V}_\ell$ and $\tilde{\Phi}_\ell$) to the conditions at the CMB and ocean-ice boundary (i.e. K_1 to K_5) by means of a different propagator matrix, which we will denote as $\tilde{\mathbf{W}}_2$. After some analytical manipulation we can express the unconstrained part of Eq. (C.1) as

$$\tilde{\mathbf{X}}_\ell(s) = \begin{pmatrix} \tilde{U}_\ell(R,s) \\ \tilde{V}_\ell(R,s) \\ \tilde{\Phi}_\ell(R,s) \end{pmatrix} = \mathbf{P}_{35} \tilde{\mathbf{W}}_2 \tilde{\mathbf{C}}_\ell \tag{9.28}$$

where $\tilde{\mathbf{X}}_\ell(s)$ is the impulse response at the surface, $\tilde{\mathbf{W}}_2$ is the propagator matrix defined by Eq. (C.20) and $\mathbf{P}_{35}$ is a projection matrix that filters out the first two elements of the product between $\tilde{\mathbf{W}}_2$ and $\tilde{\mathbf{C}}_\ell$. The derivation of the propagator matrix $\tilde{\mathbf{W}}_2$, which basically follows the same steps as the derivation of $\tilde{\mathbf{W}}_1$, is shortly outlined in C.11.

Thereafter, we substitute Eq. (9.27) into Eq. (9.28) in order to obtain a more convenient expression for the unit impulse response $\tilde{\mathbf{X}}_\ell(s)$ at the surface, i.e.:

$$\tilde{\mathbf{X}}_\ell(s) = \begin{pmatrix} \tilde{U}_\ell(R,s) \\ \tilde{V}_\ell(R,s) \\ \tilde{\Phi}_\ell(R,s) \end{pmatrix} = \mathbf{P}_{35} \tilde{\mathbf{W}}_2 \left(\tilde{\mathbf{W}}_1 \right)^{-1} \tilde{\mathbf{b}} \tag{9.29}$$

where the inverse of the propagator matrix $\tilde{\mathbf{W}}_1$ can alternatively be written as the ratio between its matrix of complementary minors $\tilde{\mathbf{W}}_1^\dagger$ and its determinant, i.e.

$$\left(\tilde{\mathbf{W}}_1 \right)^{-1} = \frac{\tilde{\mathbf{W}}_1^\dagger}{\det\left(\tilde{\mathbf{W}}_1 \right)} \tag{9.30}$$

Equation (9.30) clearly shows that each of the M relaxation modes produces a singularity in the unit impulse response, because the determinant of the matrix $\tilde{\mathbf{W}}_1$ becomes zero for all $s = s_j$. As a final step, we apply complex contour integration to Eq. (9.29) to obtain the following expression for the unit impulse response to tidal forces

$$\tilde{\mathbf{X}}_\ell(s) = \begin{pmatrix} \tilde{U}_\ell(R,s) \\ \tilde{V}_\ell(R,s) \\ \tilde{\Phi}_\ell(R,s) \end{pmatrix} = \mathbf{K}_\ell^e(R) + \sum_{j=1}^{M} \frac{\mathbf{K}_\ell^j(R)}{s - s_j} \tag{9.31}$$

in which the elastic limit parameter $\mathbf{K}_\ell^e(R)$ is given by

$$\mathbf{K}_\ell^e(R) = \lim_{s\to\infty} \mathbf{P}_{35}\tilde{\mathbf{W}}_2 \left(\tilde{\mathbf{W}}_1\right)^{-1} \tilde{\mathbf{b}} \tag{9.32}$$

and the vector residues $\mathbf{K}_\ell^j(R)$ are given by

$$\mathbf{K}_\ell^j(R) = \mathbf{P}_{35} \left(\frac{\tilde{\mathbf{W}}_2 \left(\tilde{\mathbf{W}}_1\right)^\dagger}{\frac{d}{ds} \det\left(\tilde{\mathbf{W}}_1\right)} \right)_{s=s_j} \tilde{\mathbf{b}} \tag{9.33}$$

where the derivative to s of the function $\det\left(\tilde{\mathbf{W}}_1\right)$ at $s = s_j$ is calculated by Ridder's method of polynomial extrapolation (Press et al. 1996).

Although Eqs. (9.31)–(9.33) already give a representation of the viscoelastic response of a planetary body to tidal forces, it is common to express the unit response in terms of the Love numbers h_2, l_2 and k_2.

Application of the adapted propagator matrix technique to Europa leads to the determination of the unit impulse response $\tilde{\mathbf{X}}_\ell(s)$ of Europa's interior to tidal forces. The unit impulse response of a planetary body, which is formally defined as the response of the body to a unit impulse excitation applied at $t = 0$, depends only on the structural and rheological properties of the interior. The actual tidal response of Europa follows from the product between the calculated unit impulse response $\tilde{\mathbf{X}}_\ell(s)$ and the acting tidal potential $\tilde{\phi}^T(s)$; both expressed in the Laplace domain according to the correspondence principle. The equivalent response in the time domain can then be determined by applying the inverse Laplace transform to the outcome of the aforementioned product.

As can be observed from Eqs. (9.2) and (9.31), both the unit impulse response and the tidal potential are expanded in spherical harmonics. However, as can be seen from Eq. (9.2), the tidal potential acting on Europa is completely defined by its second harmonic degree. Therefore, we only need the second-degree term of the unit impulse response expansion in order to determine the tidal response of Europa at its surface. This term, i.e. $\tilde{\mathbf{X}}_2(s)$, follows directly from Eq. (9.31)

$$\tilde{\mathbf{X}}_2(s) = \begin{pmatrix} \tilde{U}_2(R,s) \\ \tilde{V}_2(R,s) \\ \tilde{\Phi}_2(R,s) \end{pmatrix} = \mathbf{K}_2^e(R) + \sum_{j=1}^{M} \frac{\mathbf{K}_2^j(R)}{s - s_j} \tag{9.34}$$

where R is the mean radius of Europa, s is the Laplace variable and $j = 1, 2, \ldots M$ are the M relaxation modes of Europa's interior and surface. Each of these relaxation modes is characterized by an inverse relaxation time s_j, which can be found by computing the non-zero roots of Eq. (9.23). The elastic limit parameter $\mathbf{K}_2^e(R)$ and the vector residues $\mathbf{K}_2^j(R)$ are mathematically defined by Eqs. (9.32) and (9.33), respectively.

9.5 Radial Deformation at the Surface

At any point on Europa's surface, the deformation induced by the continuously acting diurnal tides can be subdivided in three orthogonal components: radial deformation u_r, tangential deformation along meridians u_θ and tangential deformation along circles of latitude u_φ. Each of these deformation components depends on the properties of the interior and the diurnal tidal potential accordingly to the following relations (adapted from e.g. Alterman et al. 1959):

$$u_r(a,\theta,\varphi,t) = \mathcal{L}^{-1}\left(\frac{-\tilde{h}_2}{g_0}\tilde{\phi}^T(a,\theta,\varphi,s)\right) \tag{9.35}$$

$$u_\theta(a,\theta,\varphi,t) = \mathcal{L}^{-1}\left(\frac{-\tilde{l}_2}{g_0}\frac{\partial\tilde{\phi}^T(a,\theta,\varphi,s)}{\partial\theta}\right) \tag{9.36}$$

$$u_\phi(a,\theta,\varphi,t) = \mathcal{L}^{-1}\left(-\frac{\tilde{l}_2}{g_0\sin(\theta)}\frac{\partial\tilde{\phi}^T(a,\theta,\varphi,s)}{\partial\varphi}\right) \tag{9.37}$$

where the symbol $\mathcal{L}^{-1}$ represents the inverse Laplace transform.

Henceforth we focus on the radial deformation u_r at the surface caused by diurnal tides, as future missions carrying an altimeter could be able to determine the existence of a subsurface ocean from direct measurements of the radial deformation at the surface (Moore and Schubert 2000; Wahr et al. 2006; Rappaport et al. 2008; Clark et al. 2010). We expand Eq. (9.35) by making use of the analytical expressions for the Love number $\tilde{h}_2$ and the diurnal potential $\tilde{\phi}_T(R,\theta,\varphi,s)$ (Laplace transform of Eq. (9.2)). After some analytical manipulation, the radial deformation u_r at a given time t can be defined as the sum of an elastic component u_r^e and a viscous component u_r^v, defined by

$$u_r^e = \frac{1}{4}(na)^2 \left\{ \frac{h_2^e}{g_0} \Big(-6eP_{20}(\theta)\cos(nt) + 4P_{21}(\theta)\cos(\epsilon)\sin(\epsilon)\Big[\cos(\varphi)\sin(\omega+nt)\Big] + eP_{22}(\theta)\Big[4\sin(2\varphi)\sin(nt) + 3\cos(2\varphi)\cos(nt)\Big]\Big) \right. \tag{9.38}$$

$$u_r^v = \frac{1}{4}(na)^2 \sum_{j=1}^{M} \frac{h_{2,j}^v}{g_0} \frac{1}{\sqrt{1+\Gamma_j^2}} \Big(-6eP_{20}(\theta)\cos\big(nt - \arctan(\Gamma_j)\big) + 4P_{21}(\theta)\cos(\epsilon)\sin(\epsilon)\Big[\cos(\varphi)\sin\big(\omega + nt - \arctan(\Gamma_j)\big)\Big] + eP_{22}(\theta)\Big[4\sin(2\varphi)\sin\big(nt - \arctan(\Gamma_j)\big) + 3\cos(2\varphi)\cos\big(nt - \arctan(\Gamma_j)\big)\Big]\Big)\Big\} \tag{9.39}$$

We observe that the elastic deformation u_r^e, which is defined by Eq. (9.38) is directly proportional to the diurnal tidal potential by a constant $\frac{h_2^e}{g_0}$. On the other hand, the viscous deformation (Eq. (9.39)) is characterized by a phase delay and attenuation of the diurnal tide. Both effects are unambiguously related to the dimensionless parameter Γ_j, which is formally defined as the ratio between the mean angular velocity of Europa's orbit (n) and the inverse relaxation time ($-s_j$) of the jth relaxation mode, i.e.

$$\Gamma_j = \frac{n}{-s_j} = \frac{2\pi\tau_j}{T} \tag{9.40}$$

where τ_j is the relaxation time of the jth relaxation mode and T is the orbital period.

Although every relaxation mode j contributes in a characteristic way to the radial deformation at the surface, not all modal contributions are large enough to introduce an observable viscoelastic effect on the total radial deformation. In order to analyze which relaxation modes dominate the viscoelastic response, we present in Fig. 9.3 a graphical representation of the influence of the ratio Γ_j on the attenuation of a modal strength h_{2j}^v and consequently on the amplitude of the radial deformation.

If one takes into consideration that complete attenuation is represented by a value of zero in Fig. 9.3 and no attenuation is represented by a value of one, we observe: (1) the radial deformation induced by a relaxation mode j becomes independent from the relaxation time τ_j for values of Γ_j smaller than 0.1, i.e. for relaxation times τ_j shorter than 1.36 h in Europa's case, (2) the radial deformation induced by a relaxation mode vanishes almost completely for values of Γ_j larger than 100, i.e. for relaxation times τ_j larger than 52.5 days in Europa's case. Consequently, only relaxation modes with a strong modal strength h_{2j}^v and a short relaxation time ($\tau_j < 52.5$ days) will have a non-negligible effect on the magnitude of the radial deformation. In a similar way, Fig. 9.3 clearly shows that relaxation modes with a very short relaxation time ($\Gamma_j < 0.01$ or $\tau_j < 8$ min in Europa's case) contribute in a practically elastic way to the radial deformation, as their corresponding phase-lag becomes negligibly small.

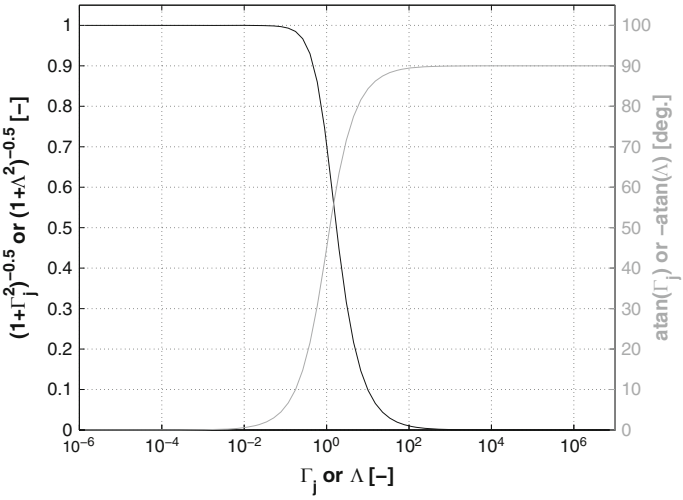

Fig. 9.3 Theoretical effect of the ratio $\Gamma_j = \frac{n}{-s_j}$ on the contribution of a relaxation mode j to the surface diurnal stress at the surface, and effect of the ratio $\Lambda = \frac{\mu/\eta}{n}$ on the relaxation state of diurnal stresses at the surface. Regarding the ratio Γ_j, the dark curve represents the attenuation of the corresponding modal strength h_{2j}^{v} (1 is no attenuation and 0 is complete attenuation) and the *light curve* shows the phase-lag of the contribution of mode j to the diurnal stress. Regarding the ratio Λ, the *dark curve* presents the importance of viscous relaxation on the magnitude of diurnal stresses at the surface (1 means that stresses are elastically stored, whereas 0 means complete relaxation of the stresses) and the *light curve* gives the phase-lead caused by relaxation

The phase-lag of the contribution of a given relaxation mode to the radial deformation increases significantly for larger relaxation times, becoming 90° for values of Γ_j larger than 100. However, such slow relaxation modes do not affect the phase of the deformation field due to the strong attenuation they experience.

In agreement with (Moore and Schubert 2000), we can conclude that viscoelasticity has two important effects on Europa's radial deformation due to diurnal tides: (1) it might increase the magnitude of the deformation at the surface, and (2) it causes a delay in the tidal response. If we assume that the density and rigidity of ice-I are constant throughout the entire ice shell, the adopted five layer model of Europa's interior (see Sect. 9.3) will trigger six relaxation modes in accordance with the discussion at the end of Sect. 9.4.3: the core mode C_0, the surface mode M_0, the buoyancy modes M_2 and M_3 at the ocean-ice and ocean-mantle interfaces, and the transient modes T_1 and T_2 at the boundary between the two ice layers (see Table 9.3).

From these relaxation modes, only the transient modes might have relaxation times which are sufficiently fast to have an effect on the radial deformation induced by tides. In other words, the viscoelastic character of the radial deformation at the surface is governed by the structural and rheological properties of the ice layers.

Table 9.3 Tidal response of the reference model of Europa's interior to diurnal tidal forces

Mode	$\boldsymbol{\tau}_j$ (s)	$\boldsymbol{\Gamma}_j$ (–)	$\mathbf{h}_2^e$ or $\mathbf{h}_{2j}^v$ (–)	$\mathbf{l}_2^2$ or $\mathbf{l}_{2j}^v$ (–)
Elastic	–	–	1.15100×10^{0}	3.07996×10^{-1}
C_0	7.02026×10^{10}	1.43745×10^{6}	5.17509×10^{-2}	1.40296×10^{-2}
M_3	9.15741×10^{9}	1.87504×10^{5}	7.16925×10^{-1}	1.94722×10^{-1}
M_2	9.75577×10^{10}	1.99756×10^{6}	1.38050×10^{-3}	2.35200×10^{-4}
M_0	2.91957×10^{11}	5.97802×10^{6}	3.69559×10^{-2}	1.00498×10^{-2}
T_1	1.73366×10^{5}	3.54978×10^{0}	7.19132×10^{-5}	6.00107×10^{-3}
T_2	3.07948×10^{4}	6.30543×10^{-1}	8.49611×10^{-2}	2.26471×10^{-2}

9.6 Stresses at the Surface of Europa

9.6.1 Diurnal Stresses at the Surface

Here we develop a method to derive the diurnal stress field at Europa's surface from the tidal viscoelastic response given by Eq. (9.34). This method is broadly similar to the one by (Wahr et al. 2009), however some important differences arise from the way both methods calculate the tidal Love numbers. Due to the subdivision of the non-elastic response into several relaxation modes, our method enables us to get a deeper insight into the physics of relaxation by studying the contribution of each relaxation mode to the tidal response. In addition, our method remains stable in the fluid limit. This allows us to determine the tidal response and subsequent stresses of interior models containing viscoelastic layers with a very small Maxwell time (i.e. low viscosity and low rigidity).

$$\sigma_{ij} = \mathcal{L}^{-1}\left(\tilde{\Pi}\delta_{ij} + 2\tilde{\mu}(s)\tilde{\epsilon}_{ij}(s)\right) \tag{9.41}$$

where δ_{ij} is the Kronecker delta, $\mathcal{L}^{-1}$ is the inverse Laplace transform, $\tilde{\epsilon}_{ij}(s)$ is the strain tensor and $\tilde{\Pi}$ is the product between the compliance $\tilde{\lambda}(s)$ and the dilatation $\nabla \cdot \tilde{\mathbf{u}}$. The strain tensor $\tilde{\epsilon}_{ij}(s)$ at the surface is related to the tidal response through the strain-displacement relations:

$$\tilde{\epsilon}_{rr} = \frac{1}{g_0}\frac{\partial}{\partial r}\left(-\tilde{h}_2(a,s)\tilde{\phi}^T\right) \tag{9.42}$$

$$\tilde{\epsilon}_{r\theta} = 0 \tag{9.43}$$

$$\tilde{\epsilon}_{r\varphi} = 0 \tag{9.44}$$

$$\tilde{\epsilon}_{\theta\theta} = \frac{1}{rg_0}\left(-\tilde{l}_2(a,s)\ \frac{\partial^2\tilde{\phi}^T}{\partial\theta^2}\ -\ \tilde{h}_2(a,s)\ \tilde{\phi}^T\right) \tag{9.45}$$

$$\tilde{\epsilon}_{\varphi\varphi} = \frac{1}{rg_0}\left(-\left[\tilde{h}_2(a,s) - 6\tilde{l}_2(a,s)\right]\ \tilde{\phi}^T\ +\ \tilde{l}_2(a,s)\ \frac{\partial^2\tilde{\phi}^T}{\partial\theta^2}\right) \tag{9.46}$$

$$\tilde{\epsilon}_{\theta\varphi} = \frac{1}{rg_0}\tilde{l}_2(a,s)\left(-\frac{1}{\sin\theta}\ \frac{\partial^2\tilde{\phi}^T}{\partial\theta\partial\varphi}\ +\ \frac{\cos\theta}{\sin^2\theta}\ \frac{\partial\tilde{\phi}^T}{\partial\varphi}\right) \tag{9.47}$$

where the Laplace-transform of the diurnal tidal potential at the surface ($\tilde{\phi}^T$) is a function of s, θ and φ, i.e. $\tilde{\phi}^T = \tilde{\phi}^T(a, s, \theta, \varphi)$. The diurnal tidal potential is defined by the terms $\tilde{\phi}^T_{e1}$, $\tilde{\phi}^T_{e2}$ and $\tilde{\phi}^T_{o1}$ in Eq. (9.2).

Furthermore, the mean normal stress $\tilde{\Pi} = \sum_{\ell=0}^{\infty}\tilde{\lambda}\tilde{\chi}_\ell Y_\ell(\theta,\varphi)$ is related to the tidal response by the surface boundary condition regarding the radial stress (i.e. $\tilde{\sigma}_{rrl}(R,s) = 0$). We can write:

$$\tilde{\Pi} = \frac{2\tilde{\mu}(s)}{rg_0}\left(-2\tilde{h}_2(a,s)\ +\ 6\tilde{l}_2(a,s)\right)\ \tilde{\phi}^T \tag{9.48}$$

The non-zero elements of the stress tensor acting on the surface of an incompressible Maxwell body can then be retrieved by substituting Eqs. (9.42)–(9.48) into Eq. (9.41), i.e.

$$\sigma_{\theta\theta} = \mathcal{L}^{-1}\left(2\tilde{\mu}(s)\frac{1}{rg_0}\left\{-\tilde{l}_2(a,s)\ \frac{\partial^2\tilde{\phi}_T}{\partial\theta^2} - 3\left(\tilde{h}_2(a,s) - 2\tilde{l}_2(a,s)\right)\ \tilde{\phi}^T\right\}\right) \tag{9.49}$$

$$\sigma_{\varphi\varphi} = \mathcal{L}^{-1}\left(2\tilde{\mu}(s)\frac{1}{rg_0}\left\{-3\left(\tilde{h}_2(a,s) - 4\tilde{l}_2(a,s)\right)\ \tilde{\phi}^T + \tilde{l}_2(a,s)\ \frac{\partial^2\tilde{\phi}^T}{\partial\theta^2}\right\}\right) \tag{9.50}$$

$$\sigma_{\theta\varphi} = \mathcal{L}^{-1}\left(2\tilde{\mu}(s)\frac{\tilde{l}_2(a,s)}{rg_0}\left\{-\frac{1}{\sin\theta}\ \frac{\partial^2\tilde{\phi}^T}{\partial\theta\partial\varphi} + \frac{\cos\theta}{\sin^2\theta}\ \frac{\partial\tilde{\phi}^T}{\partial\varphi}\right\}\right) \tag{9.51}$$

Equations (9.49)–(9.51) show that viscoelasticity influences the state of stresses at the surface in two ways: (1) through the compliance $\tilde{\mu}(s)$, which is related to the rheological properties of the lithosphere, and (2) by the viscoelastic response itself, which is represented by the Love numbers $\tilde{h}_2(a,s)$ and $\tilde{l}_2(a,s)$. If we redefine the compliance $\tilde{\mu}(s)$ as

$$\tilde{\mu}(s) = \mu - \frac{\mu\cdot\frac{\mu}{\nu}}{s+\frac{\mu}{\nu}} = \mu\left(1 - \frac{1}{1+s\tau_M}\right) = \mu\Big(1 - \eta(s,\tau_M)\Big) \tag{9.52}$$

where $\tau = \nu/\mu$ is defined as the characteristic Maxwell time of the lithosphere. This parameter gives an indication of the time scale at which the rheological behavior of a material shows a transition from elastic to viscous. The term $\eta(s, \tau_M)$ represents the relaxation of the elastic shear modulus as a function of s and the Maxwell time τ_M. A close inspection of Eq. (9.52) shows that relaxation becomes more important for time scales much larger than the characteristic Maxwell time (i.e. $s \ll 1/\tau_M$). Based on these definitions, we can also refer to the compliance $\tilde{\mu}(s)$ as the effective shear modulus of the lithosphere.

Explicit analytical expressions for the diurnal stresses $\sigma_{\theta\theta}$, $\sigma_{\varphi\varphi}$ and $\sigma_{\theta\varphi}$ can be derived by substituting the Laplace transform of Eq. (9.2) (only the diurnal terms ϕ^T_{e1}, ϕ^T_{e2} and ϕ^T_{o1}) into Eqs. (9.49)–(9.51). After some rather lengthy analytical manipulations, we obtain

$$\sigma_{\theta\theta} = \sigma^e_{\theta\theta} + \sigma^v_{\theta\theta} \tag{9.53}$$

$$\sigma_{\varphi\varphi} = \sigma^e_{\varphi\varphi} + \sigma^v_{\varphi\varphi} \tag{9.54}$$

$$\sigma_{\theta\varphi} = \sigma^e_{\theta\varphi} + \sigma^v_{\theta\varphi} \tag{9.55}$$

where the contribution of the elastic response (superscript e) and relaxation modes (superscript v) to the diurnal stress tensor are given by

$$\begin{aligned}\sigma^e_{\theta\theta} = \frac{1}{2}\frac{n^2 a\mu}{g_0}\frac{1}{\sqrt{1+\Lambda^2}}\Big\{ &-6e\beta^{\theta\theta}_{2,0}(\theta)\cos\Big(nt+\arctan(\Lambda)\Big)\\ &+e\beta^{\theta\theta}_{2,2}(\theta)\Big[4\sin(2\varphi)\sin\Big(nt+\arctan(\Lambda)\Big)+3\cos(2\varphi)\cos\Big(nt+\arctan(\Lambda)\Big)\Big]\\ &+4\cos(\varepsilon)\sin(\varepsilon)\beta^{\theta\theta}_{2,1}(\theta)\Big[\cos(\varphi)\sin\Big(\omega+nt+\arctan(\Lambda)\Big)\Big]\Big\}\end{aligned} \tag{9.56}$$

$$\begin{aligned}\sigma^v_{\theta\theta} = \frac{1}{2}\frac{n^2 a\mu}{g_0}\frac{1}{\sqrt{1+\Lambda^2}}\sum_{j=1}^{M}\Bigg(\frac{1}{\sqrt{1+\Gamma_j^2}}\cdot\Big\{ &-6e\beta^{\theta\theta,j}_{2,0}(\theta)\cos\Big(nt-\arctan(\Gamma_j)+\arctan(\Lambda)\Big)\\ &+4e\beta^{\theta\theta,j}_{2,2}(\theta)\sin(2\varphi)\sin\Big(nt-\arctan(\Gamma_j)+\arctan(\Lambda)\Big)\\ &+3e\beta^{\theta\theta,j}_{2,2}(\theta)\cos(2\varphi)\cos\Big(nt-\arctan(\Gamma_j)+\arctan(\Lambda)\Big)\\ &+4\cos(\varepsilon)\sin(\varepsilon)\beta^{\theta\theta,j}_{2,1}(\theta)\Big[\cos(\varphi)\sin\Big(\omega+nt-\arctan(\Gamma_j)+\arctan(\Lambda)\Big)\Big]\Big\}\Bigg)\end{aligned} \tag{9.57}$$

$$\begin{aligned}\sigma^e_{\varphi\varphi} = \frac{1}{2}\frac{n^2 a\mu}{g_0}\frac{1}{\sqrt{1+\Lambda^2}}\Big\{ &-6e\beta^{\varphi\varphi}_{2,0}(\theta)\cos\Big(nt+\arctan(\Lambda)\Big)\\ &+e\beta^{\varphi\varphi}_{2,2}(\theta)\Big[4\sin(2\varphi)\sin\Big(nt+\arctan(\Lambda)\Big)+3\cos(2\varphi)\cos\Big(nt+\arctan(\Lambda)\Big)\\ &+4\cos(\varepsilon)\sin(\varepsilon)\beta^{\varphi\varphi}_{2,1}(\theta)\Big[\cos(\varphi)\sin\Big(\omega+nt+\arctan(\Lambda)\Big)\Big]\Big\}\end{aligned} \tag{9.58}$$

$$\sigma^{v}_{\varphi\varphi} = \frac{1}{2}\frac{n^2 a\mu}{g_0}\frac{1}{\sqrt{1+\Lambda^2}}\sum_{j=1}^{M}\left(\frac{1}{\sqrt{1+\Gamma_j^2}}\cdot\left\{-6e\beta^{\varphi\varphi,j}_{2,0}(\theta)\cos\left(nt-\arctan(\Gamma_j)+\arctan(\Lambda)\right)\right.\right.$$
$$+\,4e\beta^{\varphi\varphi,j}_{2,2}(\theta)\sin(2\varphi)\sin\left(nt-\arctan(\Gamma_j)+\arctan(\Lambda)\right)$$
$$+\,3e\beta^{\varphi\varphi,j}_{2,2}(\theta)\cos(2\varphi)\cos\left(nt-\arctan(\Gamma_j)+\arctan(\Lambda)\right)$$
$$\left.\left.+\,4\cos(\varepsilon)\sin(\varepsilon)\beta^{\varphi\varphi,j}_{2,1}(\theta)\left[\cos(\varphi)\sin\left(\omega+nt-\arctan(\Gamma_j)+\arctan(\Lambda)\right)\right]\right\}\right) \quad (9.59)$$

$$\sigma^{e}_{\theta\varphi} = \frac{1}{2}\frac{n^2 a\mu}{g_0}\frac{1}{\sqrt{1+\Lambda^2}}\cdot$$
$$\left\{e\beta^{\theta\varphi}_{2,2}(\theta)\left[8\cos(2\varphi)\sin\left(nt+\arctan(\Lambda)\right)\;-\;6\sin(2\varphi)\cos\left(nt+\arctan(\Lambda)\right)\right]\right.$$
$$\left.+\,4\cos(\varepsilon)\sin(\varepsilon)\beta^{\theta\varphi}_{2,1}(\theta)\left[\sin(\phi)\sin\left(\omega+nt+\arctan(\Lambda)\right)\right]\right\} \quad (9.60)$$

$$\sigma^{v}_{\theta\varphi} = \frac{1}{2}\frac{n^2 a\mu}{g_0}\frac{1}{\sqrt{1+\Lambda^2}}\sum_{j=1}^{M}\left(\frac{1}{\sqrt{1+\Gamma_j^2}}\cdot\right.$$
$$\left\{8e\beta^{\theta\varphi,j}_{2,2}(\theta)\cos(2\phi)\sin\left(nt-\arctan(\Gamma_j)+\arctan(\Lambda)\right)\right.$$
$$-\,6e\beta^{\theta\varphi,j}_{2,2}(\theta)\sin(2\varphi)\cos\left(nt-\arctan(\Gamma_j)+\arctan(\Lambda)\right)$$
$$\left.\left.+\,4\cos(\varepsilon)\sin(\varepsilon)\beta^{\theta\varphi,j}_{2,1}(\theta)\left[\sin(\varphi)\sin\left(\omega+nt-\arctan(\Gamma_j)+\arctan(\Lambda)\right)\right]\right\}\right) \quad (9.61)$$

where the Beta-functions depend on the elastic Love numbers h^e_2a and l^e_2, the modal strengths $h^v_{2,j}$ and $l^v_{2,j}$, and the co-latitude θ. These functions are listed in C.2. The dimensionless ratios Λ and Γ_j are defined as

$$\Lambda = \frac{\mu/v}{n} = \frac{T}{2\pi\tau_M}, \quad (9.62)$$

and

$$\Gamma_j = \frac{n}{-s_j} = \frac{2\pi\tau_j}{T}, \quad (9.63)$$

where n is the mean angular velocity of Europa's orbit, T is the orbital period, $-s_j$ is the inverse relaxation time of the mode j, and $\tau_j = -1/s_j$ is the corresponding relaxation time.

From a theoretical point of view, the dimensionless ratio Λ describes the relaxation state of diurnal stresses at Europa's surface. As can be observed from Fig. 9.3, relaxation at the surface starts to become important for values of Λ larger than 0.1.

In the case of Europa's lithosphere, $\Lambda > 0.1$ would correspond to viscosities smaller than 1.7×10^{15} Pa s for a rigidity $\mu = 3.487$ GPa, or to viscosities smaller than 4.9×10^{14} Pa s for a rigidity $\mu = 1$ GPa. Such low viscosities are, however, more representative for the lower portion of the icy shell and are several orders of magnitude smaller than the plausible values for the viscosity of a cold, conducting lithosphere (Hussmann et al. 2002; Nimmo and Manga 2009). For this reason, we can state that diurnal stresses are elastically stored in the lithosphere due to the high viscosity of the upper ice layer and/or the high frequency of the forcing function. This statement is in agreement with (Wahr et al. 2009).

On the other hand, viscoelasticity could have an important effect on the magnitude and geographical distribution of surface diurnal stresses. As shown by Eqs. (9.57), (9.59) and (9.61), every relaxation mode j contributes in a non-elastic way to the surface diurnal stress. However, not all modal contributions are large enough to induce an observable viscoelastic effect on the diurnal stress field. Figure 9.3 depicts a graphical representation of the influence of the ratio Γ_j on the contribution of a relaxation mode j to the surface diurnal stress. The dark curve in Fig. 9.3 gives the effect of Γ_j on the modal strengths (h^v_{2j} and l^v_{2j}), and hence on the magnitude of the viscoelastic contribution to the surface diurnal stress. We observe that the contribution of relaxation modes with Γ_j larger than 100 (i.e. τ_j larger than 52.5 days in Europa's case) can be safely neglected, as their corresponding modal strengths are reduced by more than two orders of magnitude. Therefore, the slow-relaxing modes C_0, M_3, M_2 and M_0 (see the numerical values presented in Table 9.3 for an example) will not have an influence on diurnal stresses. Only the fast-relaxing transient modes T_1 and T_2 remain as potential candidates, with T_2 as the most influential mode due to its larger modal strengths and its faster relaxation time. In addition, Γ_j introduces a phase delay in the tidal response which generates a westward shift of the stress patterns at the surface. The light curve in Fig. 9.3 shows that relaxation modes with a very short relaxation time ($\Gamma_j < 0.01$ or $\tau_j < 8$ min in Europa's case) contribute in an effectively elastic way to the surface diurnal stress, as their corresponding phase-lag becomes negligibly small. The phase-lag increases significantly for larger relaxation times, becoming 5.82° for $\Gamma_j = 0.1$, 45° for $\Gamma_j = 1$ and 84.3° for $\Gamma_j = 10$. Since the ratio Γ_j has opposite effects on the magnitude and phase-lag (Fig. 9.3), the viscoelastic effect on surface diurnal stresses will be largest for strong modes with $\Gamma_j \sim 1$. In our modeling, the relaxation time of the strong transient mode T_2 satisfies the condition $\Gamma_j \sim 1$ only if the viscosity of the asthenosphere ranges between 10^{14} and 10^{15} Pa s. These are typical values for the viscosity of a high-dissipative and convective asthenosphere, hence viscoelastic effects on Europa's diurnal stress field are plausible. The effect of viscoelasticity is enhanced by thick ice layers and high values for the rigidity of ice, as both parameters lead to an increase of the modal strengths. Although not directly relevant to Europa, viscoelastic effects on the diurnal stress field become dominant for oceanless models with an extremely low-viscous asthenosphere (less than 10^{13} Pa s). In these cases, the diurnal stress field at the surface will be considerably different than in all cases with a subsurface ocean.

9.6.2 NSR Stresses at the Surface

Based on the interpretation of tectonic features, non synchronous rotation (NSR) of Europa's ice shell has been widely suggested as an important mechanism to generate large stresses (∼MPa) on the surface (Leith and McKinnon 1996; Greenberg et al. 1998; Gleeson et al. 2005; Harada and Kurita 2007; Hurford et al. 2007; Kattenhorn and Hurford 2009; Sotin et al. 2009; Wahr et al. 2009). From a dynamical perspective, NSR would take place if tidal torques acting on the decoupled shell would drive the rotation of the shell to a slightly faster than synchronous state (Greenberg and Weidenschilling 1984). However, as shown by Bills et al. (2009), the tidal torque acting on Europa cannot be large enough to overcome the counteracting gravitational torque exerted by Jupiter on permanent asymmetries in the figure of Europa (represented by the difference between the equatorial moments of inertia, i.e. $B - A$). In addition, recent research by Goldreich and Mitchell (2010) points out that the tidal torque is counteracted by an elastic torque resulting from rotation of the shell with respect to the equilibrium figure of the ocean. Despite the occurrence of NSR cannot be precluded from this study, the resulting stresses on the surface would be too small to create a crack (Goldreich and Mitchell 2010). Although NSR of Europa's ice shell is strongly opposed by the dynamical considerations discussed above, NSR is still possible if driven by mass displacements in the interior of the body (Ojakangas and Stevenson 1989b; Bills et al. 2009).

Here we compute the NSR stress field at Europa's surface from the Maxwell viscoelastic response (Eq. (9.34)) and the NSR forcing function (term $\tilde{\phi}_T^{ns}$ in Eq. (9.2)) by applying the methodology introduced in Sect. 9.6.1. As a result, we are allowed to write each non-zero element of the NSR stress tensor in the form given by Eqs. (9.49)–(9.51). Before using these equations to compute NSR surface stresses, we need to remark that the Love numbers $\tilde{h}_2$ and $\tilde{l}_2$ required for NSR calculations differ from the Love numbers used to derive the diurnal response (compare Tables 9.3 and 9.4).

The different set of tidal Love numbers results from our assumption to keep the rocky interior synchronously locked while the ice shell experiences NSR. As the rocky mantle remains tidally locked, the stresses induced by the formation of the mantle's bulge had sufficient time to relax completely and, therefore, the response of

Table 9.4 Tidal response of the reference model of Europa's interior to NSR forces

Mode[a]	$\boldsymbol{\tau}_j$ (yr)	$\boldsymbol{\gamma}_j$ [b]	$\mathbf{h}_2^e$ or $\mathbf{h}_{2j}^v$ (–)	$\mathbf{l}_2^e$ or $\mathbf{l}_{2j}^v$ (–)
Elastic	–	–	1.85155×10^{0}	4.95366×10^{-1}
M_2	9.24992×10^{3}	9.68650×10^{0}	3.60537×10^{-2}	9.80448×10^{-3}
M_0	3.09117×10^{3}	3.23707×10^{0}	1.80231×10^{-3}	3.07295×10^{-4}
T_1	5.49324×10^{-3}	5.75251×10^{-6}	1.16432×10^{-4}	9.28203×10^{-3}
T_2	9.84029×10^{-4}	1.03047×10^{-6}	1.53522×10^{-1}	4.09211×10^{-2}

[a]The core-mode C_0 and the mantle-mode M_3 vanish from the NSR response, since we assumed that the synchronously locked rocky interior behaves as a fluid with respect to NSR forces
[b]Corresponds to the minimum period of NSR, i.e. $T_{ns} = 12{,}000$ years ($\Delta \approx 0.1$)

the rocky interior to the NSR forcing function can be described as being purely fluid. From a modeling perspective, we can describe this physical behavior by decreasing the rigidity of the mantle μ to values relevant for near-fluid materials, i.e. $\mu \approx 0$ (see also Wahr et al. 2009). After taking these observations into account, we can proceed to express the NSR stress field at Europa's $\hat{\sigma}_{ij}$ as a combination of a purely elastic part (superscript e) and the contribution from the relaxation modes (superscript v):

$$\hat{\sigma}_{\theta\theta} = \hat{\sigma}^{e}_{\theta\theta} + \hat{\sigma}^{v}_{\theta\theta} \tag{9.64}$$

$$\hat{\sigma}_{\varphi\varphi} = \hat{\sigma}^{e}_{\varphi\varphi} + \hat{\sigma}^{v}_{\varphi\varphi} \tag{9.65}$$

$$\hat{\sigma}_{\theta\varphi} = \hat{\sigma}^{e}_{\theta\varphi} + \hat{\sigma}^{v}_{\theta\varphi} \tag{9.66}$$

where the individual stress components in Eqs. (9.64)–(9.66) are defined by

$$\hat{\sigma}^{e}_{\theta\theta} = \frac{1}{2}\frac{n^2 r\mu}{g_0}\,\frac{1}{\sqrt{\Delta^2+1}}\alpha^{\theta\theta}_{2,2}(\theta)\,\cos\left(2\varphi + 2\Omega_{ns}t + \arctan(\Delta)\right) \tag{9.67}$$

$$\hat{\sigma}^{v}_{\theta\theta} = \frac{1}{2}\frac{n^2 r\mu}{g_0}\,\frac{1}{\sqrt{\Delta^2+1}}\sum_{j=1}^{M}\left\{\frac{1}{\sqrt{1+\gamma_j^2}}\,\alpha^{\theta\theta,j}_{2,2}(\theta)\cdot \cos\left(2\varphi + 2\Omega_{ns}t + \arctan(\Delta) - \arctan(\gamma_j)\right)\right\} \tag{9.68}$$

$$\hat{\sigma}^{e}_{\varphi\varphi} = \frac{1}{2}\frac{n^2 r\mu}{g_0}\,\frac{1}{\sqrt{\Delta^2+1}}\alpha^{\varphi\varphi}_{2,2}(\theta)\,\cos\left(2\varphi + 2\Omega_{ns}t + \arctan(\Delta)\right) \tag{9.69}$$

$$\hat{\sigma}^{v}_{\varphi\varphi} = \frac{1}{2}\frac{n^2 r\mu}{g_0}\,\frac{1}{\sqrt{\Delta^2+1}}\sum_{j=1}^{M}\left\{\frac{1}{\sqrt{1+\gamma_j^2}}\,\alpha^{\varphi\varphi,j}_{2,2}(\theta)\cdot \cos\left(2\varphi + 2\Omega_{ns}t + \arctan(\Delta) - \arctan(\gamma_j)\right)\right\} \tag{9.70}$$

$$\hat{\sigma}^{e}_{\theta\varphi} = -\frac{n^2 r\mu}{g_0}\,\frac{1}{\sqrt{\Delta^2+1}}\alpha^{\theta\varphi}_{2,2}(\theta)\,\sin\left(2\varphi + 2\Omega_{ns}t + \arctan(\Delta)\right) \tag{9.71}$$

$$\hat{\sigma}^{v}_{\theta\varphi} = -\frac{n^2 r\mu}{g_0}\,\frac{1}{\sqrt{\Delta^2+1}}\sum_{j=1}^{M}\left\{\frac{1}{\sqrt{1+\gamma_j^2}}\,\alpha^{\theta\varphi,j}_{2,2}(\theta)\cdot \sin\left(2\varphi + 2\Omega_{ns}t + \arctan(\Delta) - \arctan(\gamma_j)\right)\right\} \tag{9.72}$$

where the alpha functions describe the dependence of NSR stresses on the interior's response (Love numbers) and the co-latitude (see C.2). Furthermore, the dimensionless ratio Δ, which describes the relaxation state of NSR stresses at Europa's surface, is defined by

$$\Delta = \frac{\mu/\nu}{2\Omega_{ns}} = \frac{T_{ns}}{4\pi\,\tau_M}, \tag{9.73}$$

and the ratio γ_j, which describes the influence of a relaxation mode to NSR stresses, is defined by

$$\gamma_j = \frac{2\Omega_{ns}}{-s_j} = \frac{4\pi\,\tau_j}{T_{ns}}. \tag{9.74}$$

In Eqs. (9.73) and (9.74), the frequency of the NSR forcing function is defined as twice the constant angular rate of NSR, i.e. $2\Omega_{ns}$. This definition is motivated by the fact that a fixed point on the surface of Europa's rotating shell crosses the tidal bulge twice during one period of NSR, under the assumption that the angular rate Ω_{ns} remains constant.

The combined effect of Δ and γ_j on the various components of the NSR stress field can be analyzed with support of Figs. 9.4 and 9.5, in which the relaxation behavior of very fast relaxation modes (i.e. $\gamma_j \ll 0.1$) provides a good approximation to the behavior of the purely elastic contribution to NSR stresses.

Both figures show that viscoelastic relaxation in the lithospheric shell starts to strongly influence the behavior of NSR stresses when Δ becomes larger than $\sim$0.1. However, as shown by Fig. 9.4, viscoelastic relaxation has a relatively larger effect on nearly-elastic contributions to NSR stresses (γ_j <0.1) than on contributions from

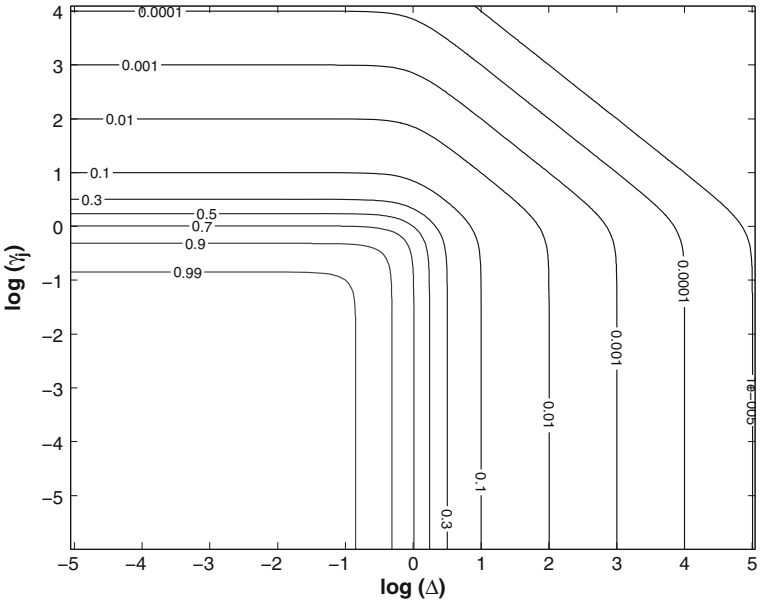

Fig. 9.4 Viscoelastic relaxation state of the contribution of a relaxation mode j to NSR stresses as a function of the dimensionless parameters $\Delta = \frac{\mu/\eta}{2\Omega_{ns}}$ and $\gamma_j = \frac{2\Omega_{ns}}{-s_j}$

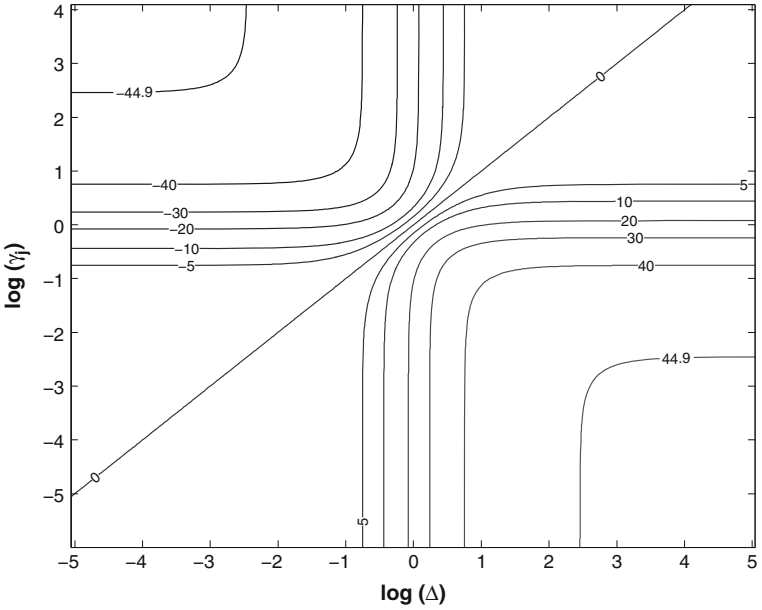

Fig. 9.5 Westward longitudinal shift of NSR stress patterns at the surface as a function of the dimensionless parameters $\Delta = \frac{\mu/\eta}{2\Omega_{ns}}$ and $\gamma_j = \frac{2\Omega_{ns}}{-s_j}$

slow relaxation modes. This behavior is logical, as stresses related to slow relaxation modes are already attenuated by the viscoelastic character of the response itself. Besides attenuation of the magnitude, viscoelastic relaxation also introduces a westward shift on the spatial distribution of stress patterns at the surface. Figure 9.5 shows that the longitudinal shift in westward direction can become as large as 45° for $\Delta < 100$ and $\gamma_j < 0.1$, i.e. in a regime where NSR stresses are being severely relaxed away.

In the particular case of our reference model of Europa's interior (see Table 9.2), the Maxwell relaxation time of the lithosphere is about 9,000 years and $\Delta = 1$ would correspond to $T_{ns} \approx 110{,}000$ years. The suggested minimum for the period of NSR ($T_{ns} = 12,000$ years) would then correspond to $\Delta \approx 0.1$, and hence we can state that viscoelastic relaxation would always play an important role in the study of stresses induced by NSR of Europa's ice shell. Furthermore, we can deduce from Table 9.4 that the contributions from the slower relaxation modes M_0 and M_3 are already attenuated at $\Delta \approx 0.1$ as their γ_j's exceed the imposed threshold of 0.1. For values of Δ in the vicinity of the fluid limit, all relaxation modes would be affected in the same way (Figs. 9.4 and 9.5), and therefore the relative contribution of the slow relaxation modes M_0 and M_3 to the total stress at the surface will increase.

9.7 Stress Patterns on Europa's Surface

The diurnal and NSR stress fields acting on Europa's surface are important factors in the study of the formation and evolution of tectonic features on Europa's surface. Stress fields on planetary surfaces are commonly expressed in location-dependent coordinates defined by the so-called principal axes. These axes are aligned in such a way that the planes normal to them are not affected by shear stresses (Ranalli 1995). The normal stresses working along the principal axes are defined as the principal stresses. The derivation of principal stresses and axes is a typical eigenvalue problem applied to the diurnal stress tensor (Eqs. 9.53–9.61) and/or NSR stress tensor Eqs. (9.64)–(9.72), where the principal stresses are given by the eigenvalues and the principal axes by the corresponding eigenvectors. The resulting diurnal stress field acting at the surface of the reference model of Europa's interior is graphically presented in Fig. 9.6 at four different positions along Europa's orbit.

As expected, the diurnal stress field closely follows the radial displacement field, showing tension where Europa's figure stretches (red lines in Fig. 9.6) and compression where Europa's figure squeezes (blue lines in Fig. 9.6). This result is rather expected because diurnal stresses acting on Europa's surface are always elastically stored in the lithosphere, i.e. $\Lambda \ll 0.1$ (see Fig. 9.3).

Although the largest part of diurnal stresses is caused by the eccentricity, we cannot neglect the effect of a small non-zero obliquity. As can be observed from Fig. 9.6, a small obliquity of $0.1°$ already breaks the symmetric distribution of stress patterns

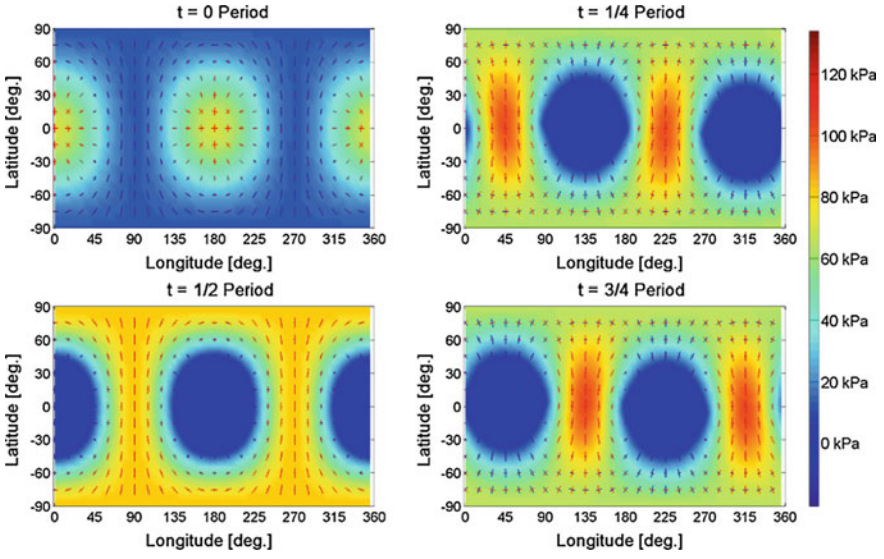

Fig. 9.6 Diurnal stress field at the surface of the reference model of Europa's interior (Table 9.2) for an eccentricity $e = 0.0094$ and an obliquity $\varepsilon = 0.1°$. The stress patterns are given at four different positions on Europa's orbit around Jupiter

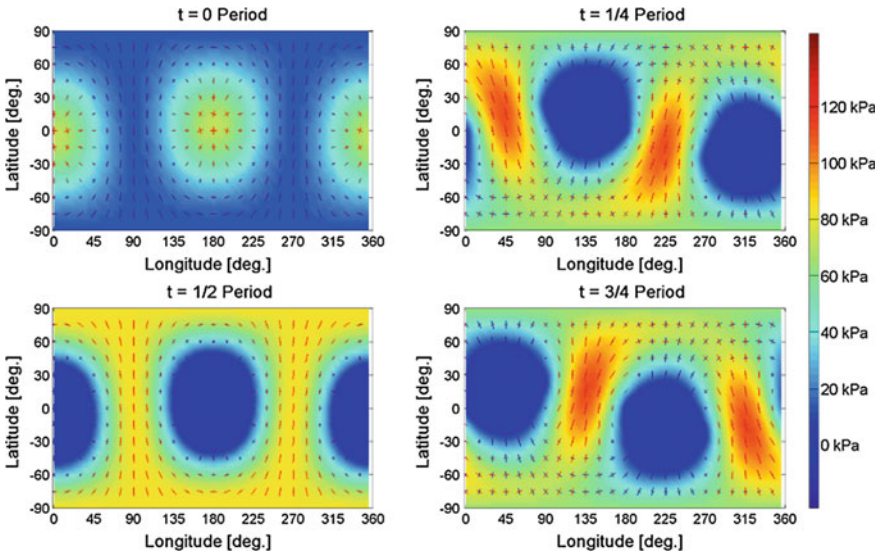

Fig. 9.7 Diurnal stress field at the surface of the reference model of Europa's interior (Table 9.2) for an eccentricity $e = 0.0094$ and an obliquity $\varepsilon = 0.5°$. The stress patterns are given at four different positions on Europa's orbit around Jupiter

with respect to the equator. This effect is enhanced for larger values for the obliquity, as is clearly shown by Fig. 9.7 for a hypothetical obliquity of 0.5°.

The rupture of the symmetry with respect to the equator leads latitudinal shifts of the tensile and compressive bulges, thereby yielding changes in the orientation and magnitude of the diurnal stress patterns (see Fig. 9.7). In our example, increasing the obliquity from 0.1° to 0.5° leads, on average, to ∼9 % larger stresses at Europa's surface, wheras the effect on the spatial distribution is clearly visible from Figs. 9.6 and 9.7. At mid-latitudes, where the influence of a non-zero obliquity is largest, diurnal stresses can locally become even twice as large after increasing the value of the obliquity from 0.1° to 0.5°.

Diurnal stresses at the surface of Europa depend on the rheological and structural properties of the interior through the tidal Love numbers h_2 and l_2. From all physical parameters of the interior, the largest effect on the tidal response, deformations and stresses is caused by the existence or non-existence of a subsurface ocean below the ice shell. As shown by Figs. 9.8 and 9.9, diurnal stresses are often much larger (more than one order of magnitude) when a subsurface ocean is present below the ice shell.

However, as shown by Fig. 9.8, diurnal stresses might become even larger if an extremely low-viscous asthenosphere (i.e. $\eta_{ast} = 10^{12}$ Pa s) extends down to the upper boundary of the silicate mantle. This peculiar behavior is caused by a decrease in the relaxation time of the strong transient modes T_1 and T_2 towards values comparable to the inverse of Europa's mean motion (keep in mind that the relaxation time of the transient modes T_1 and T_2 does not necessarily need to be comparable to

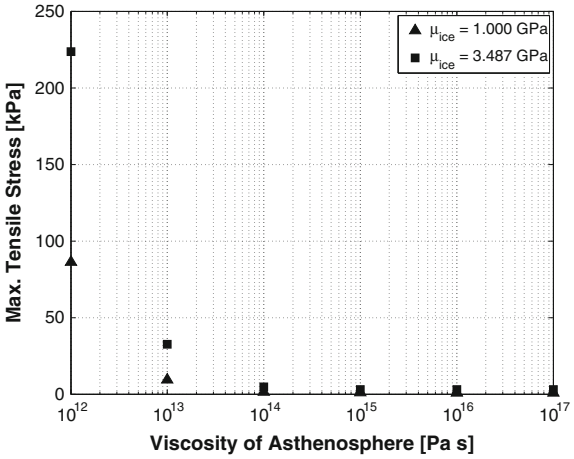

Fig. 9.8 Magnitude of the largest tensile stresses acting on Europa's surface as a function of the viscosity of the asthenosphere for interior models without a subsurface ocean (ice shell is 130 km *thick*). The squares correspond to an ice rigidity of $\mu_{ice} = 3.487$ GPa and the *triangles* to an ice rigidity of $\mu_{ice} = 1$ GPa. In all cases, the eccentricity is set at $e = 0.0094$ and the obliquity at $\varepsilon = 0.1°$

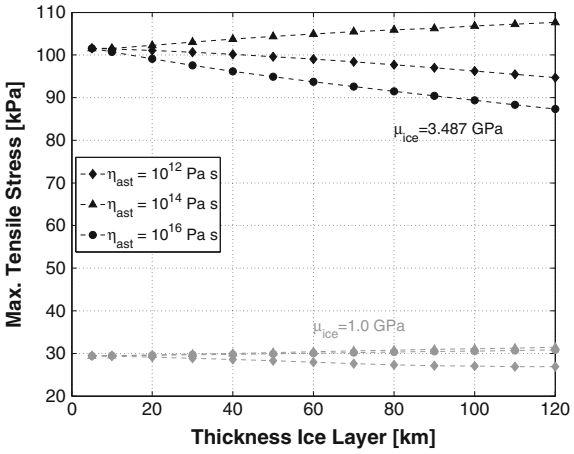

Fig. 9.9 Magnitude of the largest tensile stresses acting on Europa's surface as a function of the rigidity of ice, thickness of the ice shell and viscosity of the asthenosphere. The *black dashed curves* correspond to an ice rigidity of $\mu_{ice} = 3.487$ GPa and the *gray dashed curves* to an ice rigidity of $\mu_{ice} = 1$ GPa. In all cases, the *bottom* of the ocean is set at 130 km from the surface, the eccentricity at $e = 0.0094$ and the obliquity at $\varepsilon = 0.1°$

the Maxwell time of the asthenosphere). Since also the modal strengths of T_1 and T_2 become larger than the elastic Love numbers, the diurnal stress field at the surface will be characterized by a large longitudinal phase shift which can exceed the 40°.

The influence of a subsurface ocean on the surface diurnal stresses is by far the largest, but certainly not the only one. As shown by Fig. 9.9, the magnitude of surface diurnal stresses depends roughly linearly on the elastic rigidity of the lithospheric shell, especially for models with a thin ice shell (less than 10 km). However, deviations from a perfect linear relation are clearly observable as the thickness of the shell increases. These deviations are caused by the combined effect of the asthenosphere's thickness and viscosity, and are enhanced at larger values for the elastic rigidity of ice-I. As shown in Fig. 9.9, the largest deviations from the elastic state (represented by the curves for $\eta_{ast} = 10^{16}$ Pa s) occur for values of the asthenosphere's viscosity for which the Maxwell relaxation time of this layer approaches the inverse of Europa's mean motion (i.e. $\eta_{ast} = 10^{14}$ Pa s to $\eta_{ast} = 10^{15}$ Pa s). For extremely low values for the asthenosphere's viscosity (i.e. $\eta_{ast} = 10^{12}$ Pa s), the asthenosphere behaves as a fluid. Hence, as can be observed from Fig. 9.9, the magnitude of surface diurnal stresses is nearly independent of the ice thickness.

The combined effect of the asthenosphere's viscosity and thickness also leads to a westward shift in the surface distribution of the surface stress patterns. The amount of phase shift ζ depends on the ratio Γ_j of the dominant relaxation mode T_2, and is therefore strongest when the relaxation time of T_2 is comparable to the inverse of Europa's mean angular velocity. This effect is illustrated in Fig. 9.10, where we observe that phase shifts up to $\zeta = 7°$ are plausible for interior models with a thick ice shell and highly dissipative asthenosphere (i.e. $\eta_{ast} = 10^{14}$ Pa s).

The value of the phase shift, however, does not indicate the actual longitudinal shift of the stress patterns at Europa's surface. Instead, it denotes the time delay of the shell's response expresses as a difference in true anomaly. Due to eccentricity of Europa's orbit, the actual westward shift of the surface patterns will oscillate around the value of the phase shift during one orbital revolution. Figure 9.10 also shows that the phase shift becomes negligibly small as the behavior of the asthenosphere

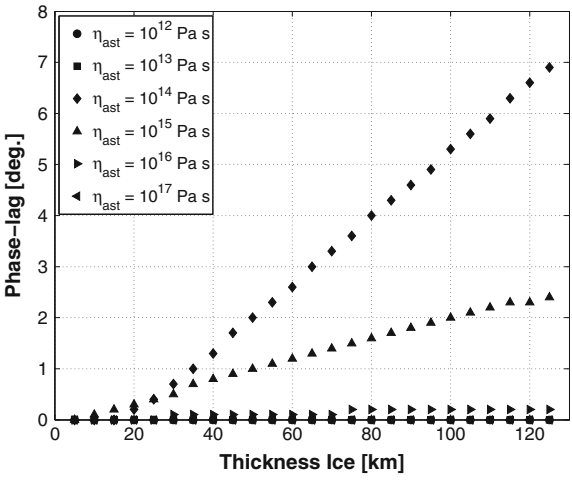

Fig. 9.10 Phase shift of diurnal stress field as a function of the thickness of the entire ice layer and of different values of the viscosity of the asthenosphere. In all cases, the *bottom* of the ocean is set at 130 km from the surface, the rigidity of ice at $\mu_{ice} = 3.487$ GPa, the eccentricity at $e = 0.0094$ and the obliquity at $\varepsilon = 0°$

becomes nearly elastic ($\eta_{ast} \geq 10^{16}$ Pa s) or nearly fluid ($\eta_{ast} \leq 10^{13}$ Pa s). As a result, we can conclude that viscoelasticity only influences the diurnal stress field if the characteristic Maxwell time of the asthenosphere does not deviate by approximately one order of magnitude from the inverse mean motion $1/n$.

The diurnal stress field resulting from our modeling closely resembles the results published in previous studies (Greenberg et al. 1998; Harada and Kurita 2006; Wahr et al. 2009). However, some differences arise from the Maxwell viscoelastic treatment of the interior's rheology, the non-zero obliquity, incompressibility and the use of different interior models. As partially shown in Fig. 9.9, the viscoelastic representation of the tidal response leads to variations up to 20 % in the magnitude of diurnal stresses. As mentioned above, viscoelasticity might also shift the entire stress field in westward direction, especially if the relaxation time of the strong transient mode T_2 is comparable to the inverse of Europa's mean motion. These typical viscoelastic effects are not observed in the surface stress modeling by Greenberg et al. (1998) and Harada and Kurita (2006), as they assume a perfectly elastic tidal response; neither in the modeling by Wahr et al. (2009), as they only explicitly show cases for which viscoelasticity becomes unimportant. In addition, our modeling of the obliquity's effect on surface diurnal stresses resembles the modeling by Rhoden et al. (2010) for nearly elastic bodies. Obviously, some differences arise from our viscoelastic treatment.

In contrast to diurnal stresses, NSR stresses at the surface of Europa might experience severe relaxation effects depending on the rheological properties of the lithosphere. The relaxation state of NSR stresses at Europa's surface depends on the dimensionless parameter Δ, which is proportional to the ratio between the period of NSR and the Maxwell relaxation time of the lithosphere see Eq. (9.73). As shown by Figs. 9.4 and 9.5, viscoelastic relaxation starts to affect the magnitude and spatial distribution of NSR stresses for $\Delta > 0.1$ and becomes more severe as Δ increases. At $\Delta = 100$, viscoelastic relaxation already reduces the magnitude of NSR stresses by two orders of magnitude and shifts the entire stress field by nearly 45° in westward direction.

In the particular case of our reference model of Europa's interior, the Maxwell relaxation time of the lithosphere is equal to about 9,100 years and hence $\Delta = 0.1$ would correspond to a period of NSR approximately equal to 11,500 years. This value for T_{ns} is slightly smaller than the assumed minimum value for T_{ns} (12,000 years), meaning that the NSR stress field at the surface of our reference model will always show signs of viscoelastic relaxation. The effects of viscoelastic relaxation are clearly visible in Fig. 9.11, where the NSR stress field at Europa's surface is depicted for $\Delta = 0.1$, 1, 10 and 100.

There, we clearly observe that an increasing Δ leads to a gradual decrease of the magnitude of NSR stresses and a gradual shift of the entire stress field in westward direction. For $\Delta = 100$, in accordance with our theoretical expectations, the magnitude of NSR stresses becomes nearly two orders of magnitude smaller than for $\Delta = 0.1$ and the entire stress field is shifted by approximately 45° in westward

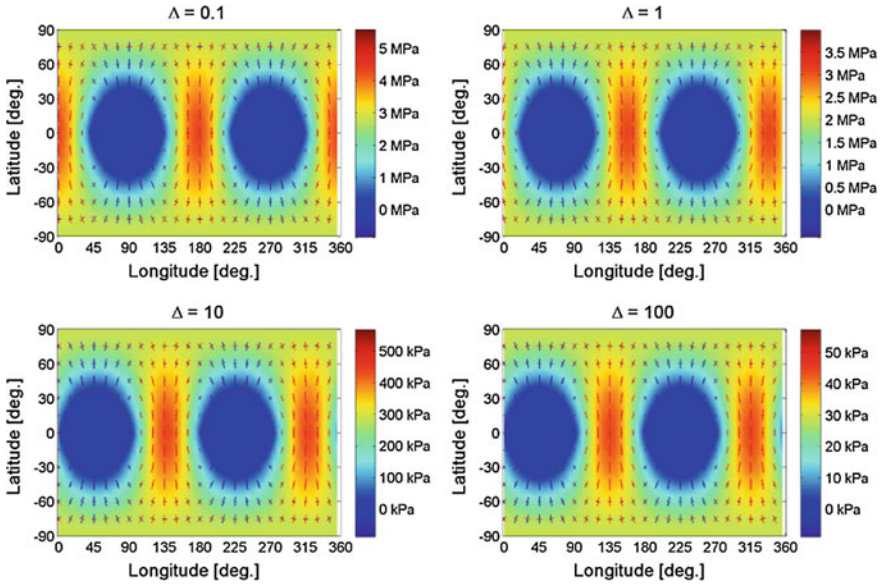

Fig. 9.11 NSR stress field at the surface of the reference model of Europa's interior as a function of the ratio $\Delta = \frac{\mu/\eta}{2\Omega_{ns}}$. For the rheological properties of the reference model of Europa's interior, $\Delta = 0.1$ corresponds to $T_{ns} = 11,419$ years, $\Delta = 1$ to $T_{ns} = 114,188$ years, $\Delta = 10$ to $T_{ns} \approx 1.14$ million years and $\Delta = 100$ to $T_{ns} \approx 11.4$ million years

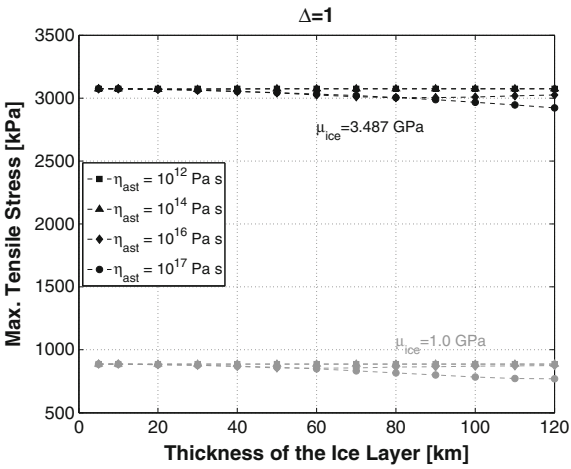

Fig. 9.12 Magnitude of largest NSR tensile stresses at Europa's surface as a function of the ice thickness, ice rigidity and viscosity of the asthenosphere for $\Delta = 1$. The *black dashed lines* correspond to a rigidity of $\mu_{ice} = 3.487$ GPa and the *gray dashed lines* to a rigidity of $\mu_{ice} = 1$ GPa

direction. The exact value of the longitudinal shift does not depend on the viscoelastic response of Europa's interior, as shown by Figs. 9.12 and 9.13; at least for our reference model of Europa's interior.

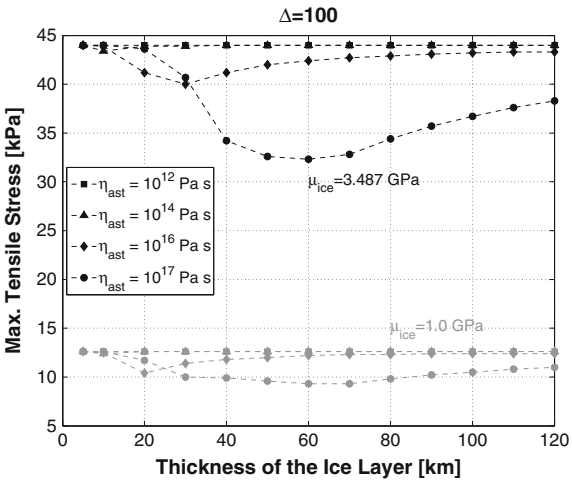

Fig. 9.13 Magnitude of largest NSR tensile stresses at Europa's surface as a function of the ice thickness, ice rigidity and viscosity of the asthenosphere for $\Delta = 100$. The *black dashed lines* correspond to a rigidity of $\mu_{ice} = 3.487\,\text{GPa}$ and the *gray dashed lines* to a rigidity of $\mu_{ice} = 1\,\text{GPa}$

However, Figs. 9.12 and 9.13 also show that the situation is different for other models of Europa's interior, especially if the viscosity of the asthenosphere is increased towards 10^{16} Pa s or more. In the high-viscous range, i.e. $\eta_{ast} \geq 10^{16}$ Pa s, the magnitude of the largest NSR stresses will strongly depend on the thickness and viscosity of the asthenosphere, as shown by Figs. 9.12 and 9.13. The strong dependence on the properties of the asthenosphere is caused by the relaxation of the ocean/ice boundary, represented by the buoyancy mode M_2. In the high-viscous range (i.e. $\eta_{ast} \geq 10^{16}\,\text{Pa s}$), this relaxation mode is characterized by having the slowest relaxation of all induced modes and by having a notoriously large tangential modal strength l_{2j}^{v}. As a result, the effect of M_2 on NSR stresses is negligibly small for values of Δ corresponding to elastic storage of stresses or even moderate relaxation (i.e. $\Delta < 1$). The effect of M_2 on NSR stresses clearly increases as relaxation becomes more severe, leading to the large deviations observed in Fig. 9.13 for $\Delta = 100$. In our modeling, the relaxation mode M_2 can become sufficiently strong for $\eta_{ast} \geq 10^{17}$ Pa s and $\Delta \geq 100$ to shift the entire NSR stress field by more than 45° in westward direction, altering the usual orientation of the NSR stress patterns.

Although viscoelastic relaxation severely reduces the magnitude of NSR stresses, the NSR stress field remains larger than the ever-acting diurnal stress field for $\Delta < 43°$ (i.e. $T_{ns} < 4.9$ million years in the case of our reference model). That means that NSR stresses will dominate the state of stresses at Europa's surface if the lithosphere is viscous enough to prevent strong viscoelastic relaxation or if NSR is sufficiently fast to reduce the value of the ratio Δ. In other cases, the state of stresses at Europa's surface will be dominated by the diurnal stress field.

9.8 Morphology of the Europa Icy Moon

The main goal for modeling tidal stresses at Europa's surface is to study the origin and formation of the observed tectonic features. These features are thought to have formed as a result of tensile failure of Europa's icy surface (Greenberg et al. 1998). Tensile failure most probably initiates when the acting tensile stresses exceed the tensile strength of the surface ice. Estimates of the poorly known tensile strength of ice-I at conditions relevant to Europa range from 40 kPa to several MPa, depending on porosity and contamination of the surface ice (Hoppa et al. 1999b; Schulson 2001; Lee et al. 2005). Here we have dealt with the modeling of diurnal and NSR stresses acting at Europa's surface. Diurnal stresses are often related to the origin and formation of multi-arc cycloidal features on Europa's surface, whereas NSR stresses are often required to explain the formation of long arcuate lineaments (e.g. Wahr et al. 2009).

As shown by Fig. 9.8, diurnal stresses at the surface of oceanless models of Europa's interior are usually much smaller than the plausible values for the tensile strength of ice (40 kPa to several MPa). Failure of the icy surface due to solely diurnal stresses, as suggested by the existence of numerous cycloidal lineaments on Europa's surface, would therefore require the existence of a subsurface ocean. However, diurnal stresses might exceed the tensile strength of ice if the silicate mantle would be in direct contact with an extremely low-viscous asthenosphere (η_{ast} less than $\sim 10^{12}$ Pa s). The resulting surface stress field, although large in magnitude (>100 kPa, see Fig. 9.8), will considerably differ from the stress field at the surface of interior models with a subsurface ocean. The question remains whether the orientation of existing cycloids can be explained by the diurnal stress field at the surface of an oceanless Europa.

The presence of a subsurface ocean, however, does not inherently guarantee that the acting diurnal stresses can be large enough to cause failure of the icy surface. As shown in Fig. 9.9, diurnal stresses do not exceed the tensile strength of ice when the rigidity of the icy lithosphere is assumed to be as low as 1 GPa. However, due to our poor knowledge regarding the mechanical strength of Europa's surface ice, we cannot preclude the possibility that diurnal cracking would occur for such a low rigidity. On the other hand, the sole effect of diurnal stresses could lead to mechanical failure of a 10 GPa icy lithosphere, but only if the tensile strength of the surface ice remains lower than ≈ 300 kPa. This result strongly suggests that diurnal formation of cycloidal features would preclude the existence of a non-contaminated, non-porous upper lithosphere. In addition, as shown by Fig. 9.7, a non-zero obliquity breaks the north-south symmetry of the diurnal stress field, allowing for an explanation for equator-crossing cycloidal features (Hurford et al. 2009).

If one takes into account that Europa's ice shell would rotate faster than synchronous, tensile stresses up to several MPa might be induced at the surface, depending on the rheological properties of the lithosphere and the rate of non-synchronous rotation. Since NSR is assumed to be a slow process ($>10^4$ years), the magnitude of NSR stresses at Europa's surface can be severely reduced by viscoelastic relaxation

(see Sect. 9.7). The amount of viscoelastic relaxation acting on NSR stresses is physically described by the parameter Δ, which is directly proportional to the ratio between the period of NSR and the Maxwell time of the lithosphere. As a result, slow NSR and low-values for the viscosity of the icy lithosphere would lead to an increase of the ratio Δ, enhancing viscoelastic relaxation of NSR stresses.

NSR stresses, if present, do not act alone on Europa's surface but superimpose upon the ever-acting diurnal stresses. Variations in the value of Δ, i.e. in the relaxation state of NSR stresses, can reduce or enhance the importance of NSR stresses relative to diurnal stresses and lead to changes in the spatial and temporal distribution of the combined stress field. Without the effect of viscoelastic relaxation (i.e. $\Delta < 0.1$), NSR stresses would be much larger than diurnal stresses (approximately a factor 42 in the case of our standard model as shown by Figs. 9.6 and 9.11 for $\Delta = 0.1$). Hence, the spatial and temporal distribution of the NSR-diurnal stress patterns will hardly change on a diurnal scale. Increasing the effect of viscoelastic relaxation on NSR stresses towards $\Delta \approx 30$ gradually enhances the effect of diurnal stresses on the combined field. The combined NSR-diurnal stress field experiences periodic longitudinal oscillations on a diurnal timescale, which gradually become larger as Δ increases. When Δ becomes larger than $\sim$30 (depending on the interior's model), longitudinal oscillations of the combined stress field can no longer be sustained by the strongly relaxed NSR stress field. The combined stress field would then become diurnal-like, as can be observed from Fig. 9.14.

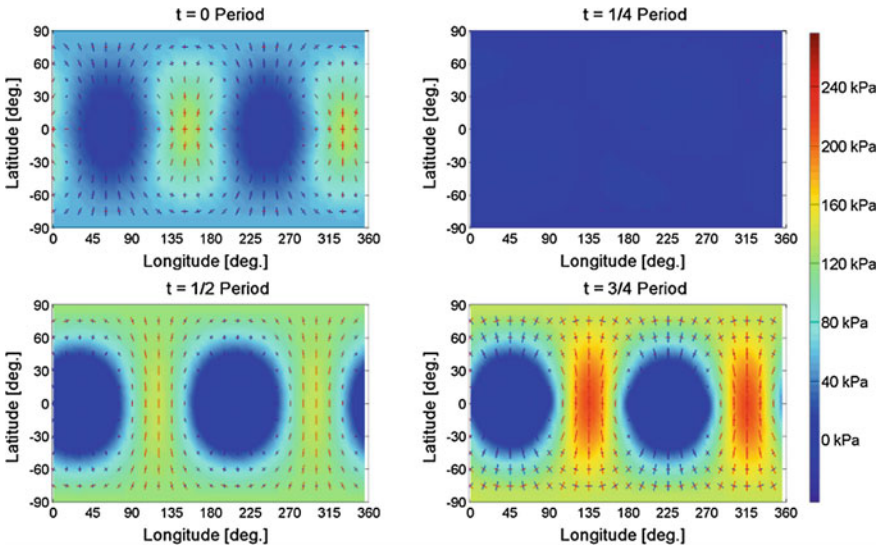

Fig. 9.14 Combined diurnal-NSR stress field at the surface of our reference model of Europa for $\Delta = 40$, $e = 0.0094$ and $\varepsilon = 0.1°$. The stress patterns are given at four different positions on Europa's orbit around Jupiter

We can use the combined NSR-diurnal stress field to analyze the formation of the diverse lineament morphologies observed on Europa's surface. The formation of long arcuate lineaments requires either a slowly-changing stress field or unrealistically fast crack propagation speeds. The combined NSR-diurnal stress field remains nearly static as long as the NSR component clearly dominates the spatial-temporal distribution of the surface stress patterns. In our modeling, the NSR component keeps the combined stress field nearly static for values of Δ approximately smaller than 5 (equivalent to about 8° of NSR). On the other hand, the formation of cycloidal features requires a highly-variable stress field and slow crack propagation speeds. The combined NSR-diurnal stress field becomes highly-variable (diurnal-like) for values of Δ larger than 30 (equivalent to about 2° of NSR). An interesting characteristic of Europa's surface is that cycloidal features coexist with global arcuate lineaments, implying variations of the relaxation parameter Δ throughout the geological history of Europa's surface. Temporal variations of the relaxation parameter Δ can either be caused by secular variations in the rotation rate of Europa's ice shell, changes in the rheological properties of the surface ice, or both of them. Changes in tidal heat dissipation with time, due to e.g. the time evolution of the orbit's eccentricity (Hussmann and Spohn 2004), could then lead to changes in the ice shell thickness distribution with time, affecting Europa's rotation rate (through the principal moments of inertia of the shell) and thereby the relaxation parameter Δ. Moreover, the same changes in tidal dissipation could also induce variations in the viscosity of the icy surface and Δ (Wahr et al. 2009). Consequently, variations of the relaxation parameter Δ as a function of time would require the existence of a dynamic ice layer covering a subsurface ocean.

It is worth to mention that the methodology presented in Sects. 9.4 and 9.6 implicitly assumes that Europa's interior behaves as an incompressible Maxwell body. However, the effects of compressibility are known to be generally less than about 20 % in magnitude. At the same time, we consider the assumption of linear rheology of more severe influence as the rheology of planetary ices is known to be best described by non-Newtonian rheological models (Durham et al. 1997, 2001; Goldsby and Kohlstedt 2001) and all materials are known to be compressible. The study of Europa's surface stress field from a non-Newtonian perspective is inherently numerical and depends strongly on the poorly known properties of ice-I at Europan conditions. Nevertheless, the dependence of the effective viscosity on the stress (non-linear effect) is small compared to the dependence on the temperature (Showman and Han 2004), as diffusion creep might be the dominating flow mechanism for all grain sizes (Moore 2006). By comparing our results with simulations from the viscoelastic SatStress software of Wahr et al. (2009), we obtain differences in magnitude up to ~20 % for equivalent interior models; i.e. much less than the differences caused by the poorly constrained rigidity of ice (see Fig. 9.9). We assign the obtained differences in magnitude to compressibility and partially to the fact that we treated Europa's inner structure as differentiated into a liquid metallic core and a rocky mantle, whereas Wahr et al. (2009) considered a single homogeneous core/mantle layer with a higher density than our silicate mantle. Although the effect of compressibility on the magnitude of surface tidal stresses is similar to e.g. the

influence of a low-viscous asthenosphere, it is less important for our purposes as compressibility does not affect the orientation of the global stress patterns.

Diurnal stresses at Europa's surface might experience the effects of viscoelastic relaxation of the asthenosphere, mainly in the form of a longitudinal shift of the surface stress patterns. However, as discussed in Sect. 9.7, the relevance of the viscoelastic effect is limited to interior models with a thick and highly dissipative asthenosphere. On timescales relevant for NSR ($>10^4$ years) the magnitude and phase shift of NSR surface stresses can be affected by viscoelastic relaxation of the ice/shell boundary. This effect, however, becomes only important when NSR stresses experience strong viscoelastic relaxation in the lithospheric shell (i.e. $\Delta \sim 100$ or larger). The combination of NSR and diurnal stresses for different amounts of viscoelastic relaxation of NSR stresses in the lithosphere leads to a large variety of global stress fields that might explain the formation of the large diversity of lineament morphologies observed on Europa's surface.

In addition, we have shown that even a small obliquity breaks the symmetric distribution of surface stress patterns with respect to the equator. The effect of a small obliquity on the local magnitude and orientation of diurnal stress patterns is largest at mid-latitudes and when Europa is located 90° away from the nodes formed by the intersection of Europa's orbital and equatorial planes (see Fig. 9.7). In those cases, local differences in magnitude up to more than 100 % with respect to the eccentricity-only case are possible, even for very small obliquities ($<0.25°$). Diurnal stresses induced by the obliquity can offer an explanation for the existence of equator-crossing cycloids and the southern shift of the Wedges region, as suggested by (Hurford et al. 2009; Rhoden et al. 2010).

References

Alterman, Z., H. Jarosch, and C.L. Pekeris (1959). "Oscillations of the Earth". In: *Proceedings of the Royal Society of London. Series A, Mathematical and Physical Sciences (1934–1990)* 252, pp. 80–95.

Anderson, J.D., G. Schubert, R.A. Jacobson, E.L. Lau, W.B. Moore, and W.L. Sjogren (1998). "Europa s differentiated internal structure: Inferences from four Galileo encounters". In: *Science* 281, pp. 2019–2022.

Baland, R.M. and T. Van Hoolst (2010). "Librations of the Galilean satellites: The influence of global internal liquid layers". In: *Icarus* 209.2, pp. 651–664.

Bills, B.G. (2005). "Free and forced obliquities of the Galilean satellites of Jupiter". In: *Icarus* 175.1, pp. 233–247.

Bills, B.G., F. Nimmo, O. Karatekin, T. Van Hoolst, N. Rambaux, B. Levrard, and J. Laskar (2009). "Rotational dynamics of Europa". In: *Europa*. Ed. by R.T. Pappalardo, W.B. McKinnon, and K. Khurana. Arizona Press Space Science Series, pp. 119–134.

Chinnery, M.A. (1975). "The static deformation of an earth with a fluid core: a physical approach". In: *Geophys. J. R. astr. Soc.* 42, pp. 461–475.

Clark, K., J. Boldt, R. Greeley, K. Hand, I. Jun, R. Lock, R. Pappalardo, T. Van Houten, T. Yan, and M. Gregory (2010). "Return to Europa: overview of the Jupiter Europa orbiter mission". In: *Advances in Space Research.*

Durham, W.B., S.H. Kirby, and L.A. Stern (1997). “Creep of water ices at planetary conditions: A compilation”. In: *J. Geophys. Res.* 102, pp. 16–293.

Durham, W.B., L.A. Stern, and S.H. Kirby (2001). “Rheology of ice I at low stress and elevated confining pressure”. In: *J. Geophys. Res*. 106.B6, pp. 11,031–11,042.

Geissler, P.E., R. Greenberg, G. Hoppa, A. McEwen, R. Tufts, C. Phillips, B. Clark, M. Ockert-Bell, P. Helfenstein, J. Burns, *et al*. (1998). “Evolution of Lineaments on Europa: Clues from Galileo Multispectral Imaging Observations”. In: *Icarus* 135.1, pp. 107–126.

Gleeson, D., Z. Crawford, A.C. Barr, M.C. Mullen, R.T. Pappalardo, L.M. Prockter, M.M. Stempel, and J. Wahr (2005). “Wavy and cycloidal lineament formation on Europa from combined diurnal and nonsynchronous stresses”. In: *36-th Lunar and Planetary Science Conference*. Vol. XXXVI. Abstract 2364.

Goldreich, P. and S. Peale (1966). “Spin-orbit coupling in the solar system”. In: *The Astronomical Journal* 71.6, pp. 425–438.

Goldreich, P.M. and J.L. Mitchell (2010). “Elastic ice shells of synchronous moons: Implications for cracks on Europa and non-synchronous rotation of Titan”. In: *Icarus* 209, pp. 631–638.

Goldsby, D.L. and D.L. Kohlstedt (2001). “Superplastic deformation of ice: Experimental observations”. In: *J. Geophys. Res.* 106.B6, pp. 11,017–11,030.

Greeley, R., R. Sullivan, J. Klemaszewski, K. Homan, J.W. Head, *et al*. (1998). “Europa: Initial Galileo Geological Observations* 1”. In: *Icarus* 135.1, pp. 4–24.

Greenberg, R., P. Geissler, G. Hoppa, B.R. Tufts, D.D. Durda, R. Pappalardo, J.W. Head, R. Greeley, R. Sullivan, and M.H. Carr (1998). “Tectonic processes on Europa: Tidal stresses, mechanical response, and visible features”. In: *Icarus* 135, pp. 64–78.

Greenberg, R., G.V. Hoppa, G. Bart, and T. Hurford (2003). “Tidal stress patterns on Europa’s crust”. In: *Celestial Mechanics and Dynamical Astronomy* 87, pp. 171–188.

Greenberg, R. and S.J.Weidenschilling (1984). “How fast do Galilean satellites spin?” In: *Icarus* 58, pp. 186–196.

Greff-Lefftz, M., H. Legros, and V. Dehant (2000). “Influence of the inner core viscosity on the rotational eigenmodes of the Earth”. In: *Physics of the Earth and Planetary Interiors* 122, pp. 187–204.

Hand, K.P. and C.F. Chyba (2007). “Empirical constraints on the salinity of the europan ocean and implications for a thin ice shell”. In: *Icarus* 189.2, pp. 424–438.

Hand, K.P., C.F. Chyba, J.C. Priscu, R.W. Carlson, and K.H. Nealson (2009). “Astrobiology and the potential of life on Europa”. In: *Europa*. Ed. by R.T. Pappalardo, W.B. McKinnon, and K. Khurana. Arizona Press Space Science Series, pp. 589–629.

Harada, Y. and K. Kurita (2006). “The dependence of surface tidal stress on the internal structure of Europa: The possibility of cracking of the icy shell”. In: *Planetary and Space Science* 54, pp. 170–180.

Harada, Y. and K. Kurita (2007). “Effect of non-synchronous rotation on surface stress upon Europa: Constraints on surface rheology”. In: *Geophys. Res. Lett*. 34.11, p. L11204.

Hoppa, G., R. Greenberg, P. Geissler, B.R. Tufts, J. Plassmann, and D.D. Durda (1999a). “Rotation of Europa: Constraints from terminator and limb positions”. In: *Icarus* 137.2, pp. 341–347.

Hoppa, G., B.R. Tufts, R. Greenberg, and P. Geissler (1999b). “Formation of cycloidal features on Europa”. In: *Science* 285, pp. 1899–1902.

Hoppa, G., B.R. Tufts, R. Greenberg, and P. Geissler (1999c). “Strikeslip faults on Europa: Global shear patterns driven by tidal stress”. In: *Icarus* 141.2, pp. 287–298.

Hoppa, G.V., B.R. Tufts, R. Greenberg, T.A. Hurford, D.P. O’Brien, and P.E. Geissler (2001). “Europa’s rate of rotation derived from the tectonic sequence in the Astypalaea region”. In: *Icarus* 153.1, pp. 208–213.

Hurford, T.A., A.R. Sarid, and R. Greenberg (2007). “Cycloidal cracks on Europa: Improved modeling and non-synchronous rotation implications”. In: *Icarus* 186.1, pp. 218–233.

Hurford, T.A., A.R. Sarid, R. Greenberg, and B.G. Bills (2009). “The influence of obliquity on europan cycloid formation”. In: *Icarus* 202.1, pp. 197–215.

Hussmann, H. and T. Spohn (2004). "Thermal-orbital evolution of Io and Europa". In: *Icarus* 171.2, pp. 391–410.

Hussmann, H., T. Spohn, and K. Wieczerkowski (2002). "Thermal equilibrium states of Europa's ice shell: Implications for internal ocean thickness and surface heat flow". In: *Icarus* 156, pp. 143–151.

Jara-Orué, H.M. and L.L.A. Vermeersen (2011). "Effects of low-viscous layers and a non-zero obliquity on surface stresses induced by diurnal tides and non-synchronous rotation: the case of Europa". In: *Icarus* 215, pp. 417–438.

Kattenhorn, S.A. (2002). "Nonsynchronous rotation evidence and fracture history in the Bright Plains region, Europa". In: *Icarus* 157.2, pp. 490–506.

Kattenhorn, S.A. and T. Hurford (2009). "Tectonics of Europa". In: *Europa*. Ed. by R.T. Pappalardo, W.B. McKinnon, and K. Khurana. Arizona Press Space Science Series, pp. 199–236.

Kaula, W.M. (1964). "Tidal dissipation by solid friction and the resulting orbital evolution". In: *Review of Geophysics and Space Physics*, 2, pp. 661–685.

Khurana, K.K., M.G. Kivelson, D.J. Stevenson, G. Schubert, C.T. Russell, R.J. Walker, and C. Polanskey (1998). "Induced magnetic fields as evidence for subsurface oceans in Europa and Callisto". In: *Nature* 395, pp. 777–780. issn: 0028-0836.

Kivelson, M.G., K.K. Khurana, C.T. Russell, M. Volwerk, R.J. Walker, and C. Zimmer (2000). "Galileo magnetometer measurements: A stronger case for a subsurface ocean at Europa". In: *Science* 289.5483, p. 1340.

Lee, S., R.T. Pappalardo, and N.C. Makris (2005). "Mechanics of tidally driven fractures in Europa's ice shell". In: *Icarus* 177.2, pp. 367–379.

Leith, A.C. and W.B. McKinnon (1996). "Is There Evidence for Polar Wander on Europa?" In: *Icarus* 120.2, pp. 387–398.

Matsuyama, I. and F. Nimmo (2008). "Tectonic patterns on reoriented and despun planetary bodies". In: *Icarus* 195.1, pp. 459–473. issn: 0019–1035.

Melosh, H.J. (1980b). "Tectonic patterns on a tidally distorted planet". In: *Icarus* 43.3, pp. 334–337.

Moore, W.B. (2006). "Thermal equilibrium in Europa's ice shell". In: *Icarus* 180.1, pp. 141–146.

Moore, W.B. and G. Schubert (2000). "The tidal response of Europa". In: *Icarus* 147, pp. 317–319.

Nimmo, F. (2004). "Stresses generated in cooling viscoelastic ice shells: Application to Europa". In: *J. Geophys. Res* 109, p. E12001.

Nimmo, F. and M. Manga (2009). "Geodynamics of Europa's icy shell". In: *Europa. Ed*. by R.T. Pappalardo, W.B. McKinnon, and K. Khurana. Arizona Press Space Science Series, pp. 119–134.

Ojakangas, G.W. and D.J. Stevenson (1989a). "Polar wander of an ice shell on Europa". In: *Icarus* 81.2, pp. 242–270.

Ojakangas, G.W. and D.J. Stevenson (1989b). "Thermal state of an ice shell on Europa". In: *Icarus* 81.2, pp. 220–241.

Pappalardo, R.T., M.J.S. Belton, H.H. Breneman, M.H. Carr, C.R. Chapman, G.C. Collins, T. Denk, S. Fagents, P.E. Geissler, B. Giese, R. Greeley, R. Greenberg, J.W. Head, P. Helfenstein, G. Hoppa, S.D. Kadel, K.P. Klaasen, J.E. Klemaszewski, K.Magee, A.S. McEwen, J.M. Moore, G. Neukum, C.B. Phillips, L.M. Prockter, G. Schubert, D.A. Senske, R.J. Sullivan, B.R. Tufts, E.P. Turtle, R. Wagner, and K.K. Williams (1999). "Does Europa have a subsurface ocean? Evaluation of the geological evidence". In: *J. Geophys. Res*. 104, pp. 24,015–24,055.

Preblich, B., R. Greenberg, J. Riley, and D. O'Brien (2007). "Tidally driven strike-slip displacement on Europa: Viscoelastic modeling". In: *Planetary and Space Science* 55, pp. 1225–1245.

Press, W.H., S.A. Teukolsky, W.T. Vetterling, and B.P. Flannery (1996). *Numerical Recipes in Fortran 77: the Art of Scientific Computing*. Cambridge University Press.

Ranalli, G. (1995). *Rheology of the Earth: Deformation and Flow Processes in Geophysics and Geodynamics*. Chapman and Hall.

Rappaport, N.J., L. Iess, J. Wahr, J.I. Lunine, J.W. Armstrong, S.W. Asmar, P. Tortora, M. Di Benedetto, and P. Racioppa (2008). "Can Cassini detect a subsurface ocean in Titan from gravity measurements?" In: *Icarus* 194.2, pp. 711–720.

Rhoden, A.R., T.A. Hurford, and M. Manga (2011). “Strike-slip fault patterns on Europa: Obliquity or polar wander?” In: *Icarus* 211.1, pp. 636–647.

Rhoden, A.R., B. Militzer, E.M. Huff, T.A. Hurford, M. Manga, and M.A. Richards (2010). “Constraints on Europa’s rotational dynamics from modeling of tidally-driven fractures”. In: *Icarus* 210.2, pp. 770–784.

Roberts, J.H. and F. Nimmo (2008). “Tidal heating and the long-term stability of a subsurface ocean on Enceladus”. In: *Icarus* 194.2, pp. 675–689.

Schenk, P.M. (2002). “Thickness constraints on the icy shells of the galilean satellites from a comparison of crater shapes.” In: *Nature* 417, pp. 419–421.

Schenk, P.M., I. Matsuyama, and F. Nimmo (2008). “True polar wander on Europa from global-scale small-circle depressions”. In: *Nature* 453.7193, pp. 368–371.

Schilling, N., F.M. Neubauer, and J. Saur (2007). “Time-varying interaction of Europa with the jovian magnetosphere: Constraints on the conductivity of Europa’s subsurface ocean”. In: *Icarus* 192.1, pp. 41–55.

Schubert, G., F. Sohl, and H. Hussmann (2009). “Interior of Europa”. In: *Europa*. Ed. by R.T. Pappalardo, W.B. McKinnon, and K. Khurana. Arizona Press Space Science Series, pp. 353–367.

Schulson, E.M. (2001). “Brittle failure of ice”. In: *Engineering Fracture Mechanics* 68.17-18, pp. 1839–1887.

Seidelmann, P.K., B.A. Archinal, M.F. A’Hearn, A. Conrad, G.J. Consolmagno, D. Hestroffer, J.L. Hilton, G.A. Krasinsky, G. Neumann, J. Oberst, *et al*. (2007). “Report of the IAU/IAG Working Group on cartographic coordinates and rotational elements: 2006”. In: *Celestial Mechanics and Dynamical Astronomy* 98.3, pp. 155–180.

Showman, A.P. and L. Han (2004). “Numerical simulations of convection in Europa’s ice shell: Implications for surface features”. In: *J. Geophys. Res*. 109.10.1029.

Sohl, F., T. Spohn, D. Breuer, and K. Nagel (2002). “Implications from Galileo observations on the interior structure and chemistry of the Galilean satellites”. In: *Icarus* 157, pp. 104–119.

Sotin, C. and G. Tobie (2004). “Internal structure and dynamics of the large icy satellites”. In: *Comptes Rendus-Physique* 5, pp. 769–780.

Sotin, C., G. Tobie, J. Wahr, and W.B. McKinnon (2009). “Tides and tidal heating on Europa”. In: *Europa*. Ed. by R.T. Pappalardo, W.B. McKinnon, and K. Khurana. Arizona Press Space Science Series, pp. 85–117.

Tobie, G., G. Choblet, and C. Sotin (2003). “Tidally heated convection: Constraints on Europa’s ice shell thickness”. In: *J. Geophys. Res*. 108.E11, p. 5124.

Tobie, G., A. Mocquet, and C. Sotin (2005). “Tidal dissipation within large icy satellites: Applications to Europa and Titan”. In: *Icarus* 177.2, pp. 534–549.

Van Hoolst, T., N. Rambaux, O. Karatekin, V. Dehant, and A. Rivoldini (2008). “The librations, shape, and icy shell of Europa”. In: *Icarus* 195.1, pp. 386–399.

Wahr, J., Z.A. Selvans, M.C.E. Mullen, A.C. Barr, G.C. Collins, M.M. Selvans, and R.T. Pappalardo (2009). “Modeling stresses on satellites due to nonsynchronous rotation and orbital eccentricity using gravitational potential theory”. In: *Icarus* 200.1, pp. 188–206.

Wahr, J.M., M.T. Zuber, D.E. Smith, and J.I. Lunine (2006). “Tides on Europa, and the thickness of Europa’s icy shell”. In: *J. Geophys. Res* 111.E12, p. E12005.

Zimmer, C., K.K. Khurana, and M.G. Kivelson (2000). “Subsurface oceans on Europa and Callisto: Constraints from Galileo magnetometer observations”. In: *Icarus* 147.2, pp. 329–347.

Appendix A
Dyads and Vector Identities

This Appendix is partially based on Appendix A-Algebra and Calculus of Dyadics in Ben-Menahem and Singh (2000), to whom we refer for details. We recall herein only the basic definition of a dyad, and provide those vector identities that are necessary to expand in spherical harmonics the momentum equation. The dyad formulation is useful since these vector identities are valid for any coordinate system.

The most general dyad is the juxtaposition of any two vector $\boldsymbol{a}$ and $\boldsymbol{b}$ defined as

$$\boldsymbol{ab} = \sum_{\alpha,\,\beta} a_\alpha\, b_\beta\, \boldsymbol{e}_\alpha \boldsymbol{e}_\beta \tag{A.1}$$

where α and β vary from 1 to 3 and $\boldsymbol{e}_\alpha, \boldsymbol{e}_\beta$ denote the unit vectors along the respective x_α, x_β axes; Eq. (A.1) is known as the algebric product between $\boldsymbol{a}$ and $\boldsymbol{b}$, different from the scalar, $\boldsymbol{a} \cdot \boldsymbol{b}$, and cross, $\boldsymbol{a} \times \boldsymbol{b}$, products.

The first vector of the dyad is called antecedent and the second one the consequent; if we reverse the order of the vectors in the dyad we obtain its transpose, herein indicated by the superscript T, as for example the transpose of the dyad entering the definition of the strain Eq. (1.26), as for the following $\boldsymbol{f}$ vector and the $\boldsymbol{\nabla}$ gradient

$$(\boldsymbol{\nabla f})^T = \boldsymbol{f\nabla} \tag{A.2}$$

where the symbol $\otimes$ of the algebraic product is now on omitted, to make easier the comparison with Appendix A of Ben-Menahem and Singh (2000) where the former is also omitted.

We now list the vector identities for deriving Eq. (1.83)

$$\boldsymbol{\nabla}(uv) = (\boldsymbol{\nabla}u)v + u(\boldsymbol{\nabla}v) \tag{A.3}$$

$$\boldsymbol{\nabla f} - \boldsymbol{f\nabla} = -\mathbf{1} \times (\boldsymbol{\nabla} \times \boldsymbol{f}) \tag{A.4}$$

R. Sabadini et al., *Global Dynamics of the Earth: Applications of Viscoelastic Relaxation Theory to Solid-Earth and Planetary Geophysics*,
DOI 10.1007/978-94-017-7552-6

where **1** denotes the unitary dyad.

$$\nabla \cdot (u\boldsymbol{D}) = u(\nabla \cdot \boldsymbol{D}) + (\nabla u) \cdot \boldsymbol{D} \tag{A.5}$$

where $\boldsymbol{D}$ denotes a dyad.

$$\nabla \cdot (u\mathbf{1}) = \nabla u \tag{A.6}$$

$$\nabla \cdot (\nabla \boldsymbol{f}) = \nabla^2 \boldsymbol{f} \tag{A.7}$$

$$\nabla \cdot (\nabla \boldsymbol{f})^T = \nabla(\nabla \cdot \boldsymbol{f}) \tag{A.8}$$

A.1 Divergence and Volume Changes

The divergence of the spherical harmonic vectors yields

$$\nabla \cdot \boldsymbol{R}_{\ell m} = \frac{2}{r} Y_{\ell m} \tag{A.9}$$

$$\nabla \cdot \boldsymbol{S}_{\ell m} = -\frac{\ell(\ell+1)}{r} Y_{\ell m} \tag{A.10}$$

$$\nabla \cdot \boldsymbol{T}_{\ell m} = 0 \tag{A.11}$$

when the following identities are considered

$$\nabla \cdot (u\boldsymbol{f}) = u\nabla \cdot \boldsymbol{f} + (\nabla u) \cdot \boldsymbol{f} \tag{A.12}$$

$$\nabla \times (u\boldsymbol{f}) = u\nabla \times \boldsymbol{f} + (\nabla u) \times \boldsymbol{f} \tag{A.13}$$

$$\nabla \cdot \boldsymbol{e}_r = \frac{2}{r} \tag{A.14}$$

$$\nabla \cdot (\boldsymbol{f} \times \boldsymbol{g}) = (\nabla \times \boldsymbol{f}) \cdot \boldsymbol{g} - \boldsymbol{f} \cdot (\nabla \times \boldsymbol{g}) \tag{A.15}$$

It is noteworthy that toroidal deformations have no radial components and does not involve volume changes Δ. In fact the divergence of the toroidal part of the displacement, which is given by Eqs. (1.63) and (1.66), yields, on the basis of Eq. A.5

$$\nabla \cdot \boldsymbol{u}_T = \sum_{\ell m} (\partial_r W_{\ell m}\, \boldsymbol{e}_r \cdot \boldsymbol{T}_{\ell m} + W_{\ell m} \nabla \cdot \boldsymbol{T}_{\ell m}) = 0 \tag{A.16}$$

On the contrary, the divergence of the spheroidal part of the displacement, which is given by Eqs. (1.62), (1.64) and (1.65), yields, on the basis of Eq. A.5

$$\nabla \cdot \boldsymbol{u}_S = \sum_{\ell m} (\partial_r U_{\ell m}\, \boldsymbol{e}_r \cdot \boldsymbol{R}_{\ell m} + U_{\ell m} \nabla \cdot \boldsymbol{R}_{\ell m} + \partial_r V_{\ell m}\, \boldsymbol{e}_r \cdot \boldsymbol{S}_{\ell m} + U_{\ell m} \nabla \cdot \boldsymbol{S}_{\ell m}) = \sum_{\ell m} \chi_{\ell m}\, Y_{\ell m} \tag{A.17}$$

with $\chi_{\ell m}$ given by

$$\chi_{\ell m} = \partial_r U_{\ell m} + \frac{2}{r}\, U_{\ell m} - \frac{\ell\,(\ell+1)}{r}\, V_{\ell m} \tag{A.18}$$

The spherical harmonic expansion of the volume change Δ can thus be written as follows

$$\Delta = \sum \chi_{\ell m}\, Y_{\ell m} \tag{A.19}$$

A.2 Laplacian Entering the Divergence of the Cauchy Stress Tensor

From

$$\nabla^2\,(f\,\boldsymbol{a}) = \boldsymbol{a}\,\nabla^2 f + f\,\nabla^2 \boldsymbol{a} + 2\,\nabla f \cdot (\nabla \boldsymbol{a}) \tag{A.20}$$

$$\nabla \boldsymbol{e}_r = \frac{1}{r}\,\left(\boldsymbol{e}_\theta \boldsymbol{e}_\theta + \boldsymbol{e}_\phi \boldsymbol{e}_\phi\right) \tag{A.21}$$

$$\nabla^2 \boldsymbol{e}_r = -\frac{2}{r^2}\,\boldsymbol{e}_r \tag{A.22}$$

the Laplacian of the spherical harmonic vector $\boldsymbol{R}_{\ell m}$ reads

$$\nabla^2 \boldsymbol{R}_{\ell m} = \frac{1}{r^2}\,[2\,(\boldsymbol{S}_{\ell m} - \boldsymbol{R}_{\ell m}) - \ell(\ell+1)\,\boldsymbol{R}_{\ell m}] \tag{A.23}$$

Making use of

$$\nabla^2 \nabla f = \nabla \nabla^2 f \tag{A.24}$$

we obtain the Laplacian of the spherical harmonic vector $\boldsymbol{S}_{\ell m}$

$$\nabla^2 \boldsymbol{S}_{\ell m} = -\frac{\ell(\ell+1)}{r^2}\,(\boldsymbol{S}_{\ell m} - 2\,\boldsymbol{R}_{\ell m}) \tag{A.25}$$

From

$$\nabla^2 \boldsymbol{\nabla} \times \boldsymbol{f} = \boldsymbol{\nabla} \times \nabla^2 \boldsymbol{f} \tag{A.26}$$

$$\nabla \boldsymbol{r} = \mathbf{1} \tag{A.27}$$

$$\nabla \times (\nabla \boldsymbol{f}) = 0 \tag{A.28}$$

we obtain the Laplacian of the spherical harmonic vector $\boldsymbol{T}_{\ell m}$

$$\nabla^2 \boldsymbol{T}_{\ell m} = -\frac{\ell(\ell+1)}{r^2} \boldsymbol{T}_{\ell m} \tag{A.29}$$

A.3 Vector Product Entering the Divergence of the Cauchy Stress Tensor

Making use of

$$\boldsymbol{\nabla} \times \boldsymbol{\nabla} \times \boldsymbol{f} = \boldsymbol{\nabla}(\boldsymbol{\nabla} \cdot \boldsymbol{f}) - \nabla^2 \boldsymbol{f} \tag{A.30}$$

we obtain

$$\boldsymbol{e}_r \times (\nabla \times (U_{\ell m} \boldsymbol{R}_{\ell m})) = \frac{U_{\ell m}}{r} \boldsymbol{S}_{\ell m} \tag{A.31}$$

$$\boldsymbol{e}_r \times (\nabla \times (V_{\ell m} \boldsymbol{S}_{\ell m})) = -\left(\frac{V_{\ell m}}{r} + \partial_r V_{\ell m} \right) \boldsymbol{S}_{\ell m} \tag{A.32}$$

$$\boldsymbol{e}_r \times (\nabla \times (W_{\ell m} \boldsymbol{T}_{\ell m})) = -\left(\frac{W_{\ell m}}{r} + \partial_r W_{\ell m} \right) \boldsymbol{T}_{\ell m} \tag{A.33}$$

Appendix B
Analytical Functions

A function $f(z)$ in the complex plane is called analytical in a point $z = z_0$ if $f(z)$ is differentiable in $z = z_0$ and in a small surrounding area. Mathematically stated: the derivative

$$\frac{df}{dz} = \lim_{\delta z \to 0} \frac{\delta f}{\delta z} = \lim_{\delta z \to 0} \frac{f(z + \delta z) - f(z)}{z + \delta z - z} \tag{B.1}$$

should exist. If we split the function f into real and imaginary parts as $f = u + iv$ and z into $z = x + iy$, then we get

$$\frac{\delta f}{\delta z} = \frac{\delta u + i\delta v}{\delta x + i\delta y} \tag{B.2}$$

Setting $(\delta x \to 0,\ \delta y = 0)$ gives:

$$\lim_{\delta z \to 0} \frac{\delta f}{\delta z} = \lim_{\delta x \to 0} \left(\frac{\delta u}{\delta x} + i \frac{\delta v}{\delta x} \right) = \frac{\partial u}{\partial x} + i \frac{\partial v}{\partial x} \tag{B.3}$$

while setting $(\delta x = 0, \delta y \to 0)$ gives:

$$\lim_{\delta z \to 0} \frac{\delta f}{\delta z} = \lim_{\delta y \to 0} \left(-i \frac{\delta u}{\delta y} + \frac{\delta v}{\delta y} \right) = -i \frac{\partial u}{\partial y} + \frac{\partial v}{\partial y} \tag{B.4}$$

Existence of df/dz thus leads to the following two conditions:

$$\frac{\partial u}{\partial x} = \frac{\partial v}{\partial y} \quad \text{and} \quad \frac{\partial u}{\partial y} = -\frac{\partial v}{\partial x} \tag{B.5}$$

which are called the *Cauchy-Riemann conditions*.

The Cauchy theorem states the following: if $f(z)$ is analytical inside a region bounded by the closed contour C, then

R. Sabadini et al., *Global Dynamics of the Earth: Applications of Viscoelastic Relaxation Theory to Solid-Earth and Planetary Geophysics*,
DOI 10.1007/978-94-017-7552-6

$$\oint_C f(z)dz = 0 \tag{B.6}$$

We can proof the Cauchy theorem by using the *Stokes' theorem* for converting a line integral over a closed contour into a surface integral:

$$\oint_C f(z)dz = \oint_C (udx - vdy) + i \oint_C (vdx + udy) \tag{B.7}$$

The Gauss lemma states that

$$\oint_C f(x, y)dx = -\int_S \frac{\partial f}{\partial y} dxdy \tag{B.8}$$

$$\oint_C f(x, y)dy = \int_S \frac{\partial f}{\partial x} dxdy \tag{B.9}$$

where the surface S is contoured by C. Applying the Gauss lemma to Eq. (B.7) we obtain

$$\begin{aligned} \oint_C f(z)dz = &\int_S \left(-\frac{\partial v}{\partial x} - \frac{\partial u}{\partial y}\right) dxdy \\ &+ i \int_S \left(\frac{\partial u}{\partial x} - \frac{\partial v}{\partial y}\right) dxdy \end{aligned} \tag{B.10}$$

Applying the Cauchy-Riemann conditions to the above equation we obtain

$$\oint_C f(z)dz = 0. \tag{B.11}$$

B.1 Cauchy Integral Representation

Let us assume that $f(z)$ is an analytical function within the domain R. We can show that, if C is a closed curve in R, the following Cauchy integral representation holds

$$f(z) = \frac{1}{2\pi i} \oint_C \frac{f(z')}{z' - z} dz' \tag{B.12}$$

for any z internal to C.

We consider the quantity

$$\frac{f(z^{'}) - f(z)}{z^{'} - z} \tag{B.13}$$

Since f is a continuous function, for any $\epsilon > 0$ we can find $\delta(\epsilon) > 0$ such that for

$$|z^{'} - z| < \delta(\epsilon) \tag{B.14}$$

we have

$$|f(z^{'}) - f(z)| < \epsilon \tag{B.15}$$

C denotes a circle in the $z^{'}$ plane centered on z of radius $r < \delta(\epsilon)$ expressed by

$$z^{'} = z + re^{i\theta} \tag{B.16}$$

The modulus of the integral of equation (B.13) over C satisfies

$$\left| \oint_C \frac{f(z^{'}) - f(z)}{z^{'} - z} dz^{'} \right| < \frac{\epsilon}{r} 2\pi r. \tag{B.17}$$

In fact, over C we have that $|z^{'} - z| = r$ which results into

$$\left| \oint_C \frac{f(z^{'}) - f(z)}{z^{'} - z} dz^{'} \right| = \left| \oint_C \frac{f(z^{'}) - f(z)}{r} dz^{'} \right|. \tag{B.18}$$

The Darboux inequality for functions of complex variables states that the above modulus of the integral over C is always smaller than the maximum of the value attained by the function which is integrated, $\frac{\epsilon}{r}$ in our case, multiplied by the length of the arc along which the function is integrated, $2\pi r$ in our case, leading to equation Eq. (B.17) from Eq. (B.18).

If we take the limit $\epsilon \to 0$, the right part of Eq. (B.17) vanishes, leading to

$$\oint_C \frac{f(z^{'}) - f(z)}{z^{'} - z} dz^{'} = 0 \tag{B.19}$$

We thus obtain

$$\oint_C \frac{f(z^{'})}{z^{'} - z} dz^{'} = f(z) \oint_C \frac{dz^{'}}{z^{'} - z}. \tag{B.20}$$

From Eq. (B.16) we obtain

$$\oint_C \frac{dz'}{z'-z} = i \oint_C d\theta = 2\pi i \tag{B.21}$$

that finally leads to

$$f(z) = \frac{1}{2\pi i} \oint_\gamma \frac{f(z')}{z'-z} dz' \tag{B.22}$$

which finally proves the result, since the curves γ and C are equivalent for the Cauchy Theorem, being obtained one from the other by continuous deformation within the domain R where $f(z)$ is analytical.

From the Cauchy integral representation of the function $f(z)$ it is straightforward to obtain the following representation of the nth derivative of $f(z)$

$$\frac{d^n f(z)}{dz^n} = \frac{n!}{2\pi i} \oint_\gamma \frac{f(z')}{(z'-z)^{n+1}} dz'. \tag{B.23}$$

B.2 Residue Theorem

If $f(z)$ is analytical within the domain D, except for a number of isolated singularities, the Residue Theorem holds, which states that the integral of $f(z)$ extended to any closed curve γ in D, not passing through any singular point of $f(z)$, is equal to $2\pi i$ the sum of the residues of the singularities of $f(z)$ internal to γ.

Let us consider the function

$$f(z) = \frac{g(z)}{(z-z_0)^k} \tag{B.24}$$

where $g(z)$ is analytical; $f(z)$ is singular with a pole of kth order in $z = z_0$. On the basis of the integral representation of the derivatives of an analytical function, we obtain

$$\oint_\gamma \frac{g(z)}{(z-z_0)^k} dz = \frac{2\pi i}{(k-1)!} \frac{d^{k-1}}{dz^{k-1}} g(z)|_{z=z_0}. \tag{B.25}$$

By definition,

$$|Res f(z)|_{z=z_0} = \frac{1}{2\pi i} \oint_\gamma f(z) dz \tag{B.26}$$

which gives on the basis of equation (B.23)

$$|Resf(z)|_{z=z_0} = \frac{1}{2\pi i} \oint_{\gamma} \frac{g(z)}{(z-z_0)^k} dz. \tag{B.27}$$

Taking into account the Cauchy representation of the kth derivative of an analytical function $g(z)$, the above expression becomes

$$|Resf(z)|_{z=z_0} = \frac{1}{(k-1)!} \frac{d^{k-1}g(z)}{dz^{k-1}}|_{z=z_0} \tag{B.28}$$

or

$$|Resf(z)|_{z=z_0} = \frac{1}{(k-1)!} \lim_{z \to z_0} \frac{d^{k-1}}{dz^{k-1}} (z-z_0)^k f(z) \tag{B.29}$$

If we have a simple pole in $z = z_0$, the above expression becomes

$$|Resf(z)|_{z=z_0} = \lim_{z \to z_0} (z-z_0) f(z) \tag{B.30}$$

Appendix C
Icy Moons

C.1 Derivation of the Propagator Matrices $\tilde{\mathbf{W}}_1$ and $\tilde{\mathbf{W}}_2$

The presence of an internal liquid ocean divides the propagation process into three regions of application, namely: the silicate mantle, the liquid ocean and the ice shell. Here, we combine the propagation within each of these separate regions into one single propagator matrix by explicit application of the boundary conditions given by Eqs. (9.19) and (9.21).

We start the combination process by relating the conditions at the free (unforced) surface to the solution vector at the base of the ice shell, i.e.

$$\begin{pmatrix} \tilde{U}_\ell^{(1)}(R) \\ \tilde{V}_\ell^{(1)}(R) \\ 0 \\ 0 \\ \tilde{\Phi}_\ell^{(1)}(R) \\ 0 \end{pmatrix} = \tilde{\mathbf{B}}_\ell^{si} \begin{pmatrix} \tilde{U}_\ell^{(n-1)}(r_n) \\ \tilde{V}_\ell^{(n-1)}(r_n) \\ \tilde{\sigma}_{rr,\ell}^{(n-1)}(r_n) \\ \tilde{\sigma}_{r\theta,\ell}^{(n-1)}(r_n) \\ \tilde{\Phi}_\ell^{(n-1)}(r_n) \\ \tilde{Q}_\ell^{(n-1)}(r_n) \end{pmatrix} \tag{C.1}$$

where $\tilde{\mathbf{B}}_\ell^{si}$ is the ice propagator matrix within the icy layers from surface of Europa to the bottom of the ocean, according to the scheme of Fig. 9.2, based on Eqs. (2.9), (2.10) where the fundamental matrix $\tilde{\mathbf{Y}}_\ell$ is that of an incompressible viscoelastic material given by Eq. (2.42).

Equation (C.1) introduces three constraints to the propagation problem, as both stress elements ($\tilde{\sigma}_{rr,\ell}$ and $\tilde{\sigma}_{r\theta,\ell}$) and the so-called potential stress ($\tilde{Q}_\ell$) are by definition equal to zero at the surface in the free surface case. Here, we recall that the free surface case is used to determine the normal modes or free oscillations of our interior model. The determination of these modes and their corresponding relaxation times and strengths is a very important step in the calculation of the viscoelastic response of an icy moon to tidal forces, because these modes describe the effect of viscoelastic

R. Sabadini et al., *Global Dynamics of the Earth: Applications of Viscoelastic Relaxation Theory to Solid-Earth and Planetary Geophysics*,
DOI 10.1007/978-94-017-7552-6

relaxation on the response at the surface. Consequently, we proceed our discussion by only taking into account the constrained part of the solution vector, i.e.

$$\mathbf{0} = \mathbf{P}_1 \, \tilde{\mathbf{B}}_\ell^{si} \begin{pmatrix} \tilde{U}_\ell^{(n-1)}(r_n) \\ \tilde{V}_\ell^{(n-1)}(r_n) \\ \tilde{\sigma}_{rr,\ell}^{(n-1)}(r_n) \\ \tilde{\sigma}_{r\theta,\ell}^{(n-1)}(r_n) \\ \tilde{\Phi}_\ell^{(n-1)}(r_n) \\ \tilde{Q}_\ell^{(n-1)}(r_n) \end{pmatrix} \tag{C.2}$$

where the projector operator $\mathbf{P}_1$ is given by

$$\mathbf{P}_1 = \begin{pmatrix} 0\,0\,1\,0\,0\,0 \\ 0\,0\,0\,1\,0\,0 \\ 0\,0\,0\,0\,0\,1 \end{pmatrix} \tag{C.3}$$

Thereafter, we apply the set of boundary conditions at the ocean-ice interface (Eq. (9.19)) to the right side of Eq. (C.2). This step leads to the following expression

$$\tilde{\mathbf{d}}_s = \tilde{\mathbf{B}}_\ell^{R1} \begin{pmatrix} \frac{\tilde{\Phi}_\ell^{(n)}(r_n)}{g(r_n)} \\ \tilde{\Phi}_\ell^{(n)}(r_n) \\ \tilde{Q}_\ell^{(n)}(r_n) \end{pmatrix} \tag{C.4}$$

where the matrix $\tilde{\mathbf{B}}_\ell^{R1}$ is defined as

$$\tilde{\mathbf{B}}_\ell^{R1} = \mathbf{P}_1 \tilde{\mathbf{B}}_\ell^{si} \begin{pmatrix} 1\,0\,0 \\ 0\,0\,0 \\ 0\,0\,0 \\ 0\,0\,0 \\ 0\,1\,0 \\ 0\,0\,1 \end{pmatrix} \tag{C.5}$$

and the vector $\tilde{\mathbf{d}}_s$ as

$$\tilde{\mathbf{d}}_s = \begin{pmatrix} -R_{\ell,3} K_4 - \tilde{\mathbf{B}}_{\ell,32}^{si} K_5 \\ -R_{\ell,4} K_4 - \tilde{\mathbf{B}}_{\ell,42}^{si} K_5 \\ -R_{\ell,6} K_4 - \tilde{\mathbf{B}}_{\ell,62}^{si} K_5 \end{pmatrix} \tag{C.6}$$

with $R_{\ell,y}$ ($y \in \{3, 4, 6\}$) defined by

$$R_{\ell,y} = \tilde{\mathbf{B}}_{\ell,y1}^{si} + \rho_0^{(n)} g(r_n) \tilde{\mathbf{B}}_{\ell,y3}^{si} + 4\pi G \rho_0^{(n)} \tilde{\mathbf{B}}_{\ell,y6}^{si} \tag{C.7}$$

In Eqs. (C.6) and (C.7) the subscripts refer to an individual element of the ice propagator matrix $\tilde{\mathbf{B}}_\ell^{si}$. By convention, the first digit in the subscript indicates the row and the second digit the column.

The next step is to express the right hand side of Eq. (C.4) in terms of the conditions at the bottom of the ocean layer. Substitution of Eqs. (9.19) and (9.20) into Eq. (C.4) yields

$$\tilde{\mathbf{d}}_s = \tilde{\mathbf{B}}_\ell^{R1} \begin{pmatrix} \frac{1}{g(r_n)} \left(-\tilde{\mathbf{B}}_{\ell,11}^f \tilde{\Phi}_\ell^{(n)}(r_{n+1}) - \tilde{\mathbf{B}}_{\ell,12}^f \tilde{Q}_\ell^{*(n)}(r_{n+1}) \right) \\ \tilde{\mathbf{B}}_{\ell,11}^f \tilde{\Phi}_\ell^{(n)}(r_{n+1}) + \tilde{\mathbf{B}}_{\ell,12}^f \tilde{Q}_\ell^{*(n)}(r_{n+1}) \\ \tilde{\mathbf{B}}_{\ell,21}^f \tilde{\Phi}_\ell^{(n)}(r_{n+1}) + \tilde{\mathbf{B}}_{\ell,22}^f \tilde{Q}_\ell^{*(n)}(r_{n+1}) + J \end{pmatrix} \tag{C.8}$$

where $\tilde{\mathbf{B}}_\ell^f$ is defined in Eq. (9.18) and where the auxiliary variable J is defined by

$$J = \left(\frac{\ell+1}{r_n} - \frac{4\pi G \rho_0^{(n)}}{g(r_n)} \right) \left(\tilde{\mathbf{B}}_{\ell,11}^f \tilde{\Phi}_\ell^{(n)}(r_{n+1}) + \tilde{\mathbf{B}}_{\ell,12}^f \tilde{Q}_\ell^{*(n)}(r_{n+1}) \right) \tag{C.9}$$

Moreover, the radial functions $\tilde{\Phi}_\ell^{(n)}(r_{n+1})$ and $\tilde{Q}_\ell^{*(n)}(r_{n+1})$ at the bottom of the ocean can be expressed in terms of the conditions at the CMB by applying the set of boundary conditions at the mantle-ocean interface (Eq. 9.21) and the viscoelastic propagation through the silicate mantle. Then, we can write Eq. (C.8) as follows

$$\tilde{\mathbf{d}}_s = \begin{pmatrix} G_{\ell,11} & G_{\ell,12} & G_{\ell,13} \\ G_{\ell,21} & G_{\ell,22} & G_{\ell,23} \\ G_{\ell,31} & G_{\ell,32} & G_{\ell,33} \end{pmatrix} \tilde{\mathbf{C}}_{c,\ell} \tag{C.10}$$

where the elements $G_{\ell,vw}$ (row $1 \le v \le 3$ and column $1 \le w \le 3$) are defined by

$$\begin{aligned} G_{\ell,vw} = & - \frac{\tilde{\mathbf{B}}_{\ell,v1}^{R1}}{g(r_n)} \left(\tilde{\mathbf{B}}_{\ell,11}^f \tilde{\mathbf{B}}_{\ell,5w}^{sm} + \tilde{\mathbf{B}}_{\ell,12}^f Z_{\ell,w} \right) \\ & + \tilde{\mathbf{B}}_{\ell,v2}^{R1} \left(\tilde{\mathbf{B}}_{\ell,11}^f \tilde{\mathbf{B}}_{\ell,5w}^{sm} + \tilde{\mathbf{B}}_{\ell,12}^f Z_{\ell,w} \right) \\ & + \tilde{\mathbf{B}}_{\ell,v3}^{R1} \left(\tilde{\mathbf{B}}_{\ell,21}^f \tilde{\mathbf{B}}_{\ell,5w}^{sm} + \tilde{\mathbf{B}}_{\ell,22}^f Z_{\ell,w} \right) \\ & + \tilde{\mathbf{B}}_{\ell,v3}^{R1} \left(\frac{\ell+1}{r_n} - \frac{4\pi G \rho_0^{(n)}}{g(r_n)} \right) \left(\tilde{\mathbf{B}}_{\ell,11}^f \mathbf{B}_{\ell,5w}^{sm} + \tilde{\mathbf{B}}_{\ell,12}^f Z_{\ell,w} \right) \end{aligned} \tag{C.11}$$

in which

$$Z_{\ell,w} = \tilde{\mathbf{B}}_{\ell,6w}^{sm} + \left(\frac{4\pi G \rho_0^{(n)}}{g(r_{n+1})} - \frac{\ell+1}{r_{n+1}} \right) \tilde{\mathbf{B}}_{\ell,5w}^{sm} - \frac{4\pi G}{g(r_{n+1})} \tilde{\mathbf{B}}_{\ell,3w}^{sm} \tag{C.12}$$

where $\tilde{\mathbf{B}}_\ell^{sm}$ denotes the propagator within the mantle layers from the bottom of the ocean to the core mantle boundary, according to the scheme of Fig. 9.2, based on Eqs. (2.9), (2.10) and (1.164) where the fundamental matrix $\tilde{\mathbf{Y}}_\ell$ is that of an incompressible viscoelastic material given by Eq. (2.42) and the core-mantle boundary conditions are based on Eq. (1.150), but for the core of Europa.

As can be seen from Eq. (C.10), we only applied three constraints to a problem having six unknowns (K_1 to K_6). The additional constraints can be obtained from the radial functions that cannot be propagated through the ocean layer, but that are related to the CMB-constants K_1 to K_3 through the set of boundary conditions at the mantle-ocean interface. The first additional constraint is defined by taking into account continuity of radial stress at the mantle-ocean boundary. We can express the constant K_6 in terms of the CMB-constants,

$$K_6 = -\frac{1}{\rho_0^{(n)} g(r_{n+1})}\begin{pmatrix}\tilde{\mathbf{B}}_{\ell,31}^{sm} & \tilde{\mathbf{B}}_{\ell,32}^{sm} & \tilde{\mathbf{B}}_{\ell,33}^{sm}\end{pmatrix}\tilde{\mathbf{C}}_{c,\ell} \tag{C.13}$$

thereby reducing the number of unknowns to five (K_1 to K_5).

A second additional constraint can be introduced by taking into account continuity of tangential stress at the mantle-ocean boundary by the following expression:

$$0 = \begin{pmatrix}\tilde{\mathbf{B}}_{\ell,41}^{sm} & \tilde{\mathbf{B}}_{\ell,42}^{sm} & \tilde{\mathbf{B}}_{\ell,43}^{sm}\end{pmatrix}\tilde{\mathbf{C}}_{c,\ell} \tag{C.14}$$

The third and last additional constraint can be obtained from the boundary condition regarding the radial displacement at the mantle-ocean interface. We can write the following relation

$$0 = \begin{pmatrix}L_{\ell,1} & L_{\ell,2} & L_{\ell,3}\end{pmatrix}\tilde{\mathbf{C}}_{c,\ell} \tag{C.15}$$

where the elements $L_{\ell,w}$ are defined by

$$L_{\ell,w} = \tilde{\mathbf{B}}_{\ell,1w}^{sm} - \frac{1}{\rho_0^{(n)} g(r_{n+1})}\tilde{\mathbf{B}}_{\ell,3w}^{sm} + \frac{1}{g(r_{n+1})}\tilde{\mathbf{B}}_{\ell,5w}^{sm} \tag{C.16}$$

Finally, combination of Eqs. (C.10), (C.14) and (C.15) allows us to write out the propagator matrix $\tilde{\mathbf{W}}_1$ that relates the five defined constraints to the five unknowns, i.e.

$$\tilde{\mathbf{W}}_1 = \begin{pmatrix} 0 & 0 & L_{\ell,1} & L_{\ell,2} & L_{\ell,3} \\ 0 & 0 & \tilde{\mathbf{B}}_{\ell,41}^{sm} & \tilde{\mathbf{B}}_{\ell,42}^{sm} & \tilde{\mathbf{B}}_{\ell,43}^{sm} \\ R_{\ell,3} & \tilde{\mathbf{B}}_{\ell,32}^{si} & G_{\ell,11} & G_{\ell,12} & G_{\ell,13} \\ R_{\ell,4} & \tilde{\mathbf{B}}_{\ell,42}^{si} & G_{\ell,21} & G_{\ell,22} & G_{\ell,23} \\ R_{\ell,6} & \tilde{\mathbf{B}}_{\ell,62}^{si} & G_{\ell,31} & G_{\ell,32} & G_{\ell,33} \end{pmatrix} \tag{C.17}$$

which satisfies the characteristic equation

$$\mathbf{0} = \tilde{\mathbf{W}}_1 \tilde{\mathbf{C}}_\ell \tag{C.18}$$

where $\tilde{\mathbf{C}}_\ell = (K_1\ K_2\ K_3\ K_4\ K_5)^T$.

In a similar way as for the constrained part of Eq. (C.1), we can express the unconstrained parameters at the surface directly in terms of the unknown constants K_1 to K_5. After some analytical manipulation we obtain

$$\tilde{\mathbf{X}}_\ell(s) = \begin{pmatrix} \tilde{U}_\ell(R,s) \\ \tilde{V}_\ell(R,s) \\ \tilde{\Phi}_\ell(R,s) \end{pmatrix} = \mathbf{P}_{35} \tilde{\mathbf{W}}_2 \tilde{\mathbf{C}}_\ell \tag{C.19}$$

where $\tilde{\mathbf{X}}_\ell(s)$ is defined as the unit impulse response, $\tilde{\mathbf{W}}_2$ is the propagator matrix, $\tilde{\mathbf{C}}_\ell$ is the vector of unknown constants and $\mathbf{P}_{35}$ is a projection matrix that filters out the first two elements of the product between $\tilde{\mathbf{W}}_2$ and $\tilde{\mathbf{C}}_\ell$. The propagator matrix $\tilde{\mathbf{W}}_2$ itself is defined by

$$\tilde{\mathbf{W}}_2 = \begin{pmatrix} 0 & 0 & L_{\ell,1} & L_{\ell,2} & L_{\ell,3} \\ 0 & 0 & \tilde{\mathbf{B}}^{sm}_{\ell,41} & \tilde{\mathbf{B}}^{sm}_{\ell,42} & \tilde{\mathbf{B}}^{sm}_{\ell,43} \\ R_{\ell,1} & \tilde{\mathbf{B}}^{si}_{\ell,12} & G'_{\ell,11} & G'_{\ell,12} & G'_{\ell,13} \\ R_{\ell,2} & \tilde{\mathbf{B}}^{si}_{\ell,22} & G'_{\ell,21} & G'_{\ell,22} & G'_{\ell,23} \\ R_{\ell,5} & \tilde{\mathbf{B}}^{si}_{\ell,52} & G'_{\ell,31} & G'_{\ell,32} & G'_{\ell,33} \end{pmatrix} \tag{C.20}$$

where the elements $G'_{\ell,vw}$ (row $1 \le v \le 3$ and column $1 \le w \le 3$) are defined by

$$\begin{aligned} G'_{\ell,vw} = & -\frac{\tilde{\mathbf{B}}^{R2}_{\ell,v1}}{g(r_n)} \left(\tilde{\mathbf{B}}^{f}_{\ell,11} \tilde{\mathbf{B}}^{sm}_{\ell,5w} + \tilde{\mathbf{B}}^{f}_{\ell,12} Y_{\ell,w} \right) \\ & + \tilde{\mathbf{B}}^{R2}_{\ell,v2} \left(\tilde{\mathbf{B}}^{f}_{\ell,11} \tilde{\mathbf{B}}^{sm}_{\ell,5w} + \tilde{\mathbf{B}}^{f}_{\ell,12} Y_{\ell,w} \right) \\ & + \tilde{\mathbf{B}}^{R2}_{\ell,v3} \left(\tilde{\mathbf{B}}^{f}_{\ell,21} \tilde{\mathbf{B}}^{sm}_{\ell,5w} + \tilde{\mathbf{B}}^{f}_{\ell,22} Y_{\ell,w} \right) \\ & + \tilde{\mathbf{B}}^{R2}_{\ell,v3} \left(\frac{\ell+1}{r_n} - \frac{4\pi G \rho_0^{(n)}}{g(r_n)} \right) \left(\tilde{\mathbf{B}}^{f}_{\ell,11} \tilde{\mathbf{B}}^{sm}_{\ell,5w} + \tilde{\mathbf{B}}^{f}_{\ell,12} Y_{\ell,w} \right) \end{aligned} \tag{C.21}$$

with

$$\tilde{\mathbf{B}}^{R2}_{\ell} = \mathbf{P}_2 \tilde{\mathbf{B}}^{si}_{\ell} \begin{pmatrix} 1 & 0 & 0 \\ 0 & 0 & 0 \\ 0 & 0 & 0 \\ 0 & 0 & 0 \\ 0 & 1 & 0 \\ 0 & 0 & 1 \end{pmatrix} \tag{C.22}$$

and $\mathbf{P}_2$ given by

$$\mathbf{P}_2 = \begin{pmatrix} 1\,0\,0\,0\,0\,0 \\ 0\,1\,0\,0\,0\,0 \\ 0\,0\,0\,0\,1\,0 \end{pmatrix} \tag{C.23}$$

C.2 Auxiliary Variables in Stress Equations

The elements of the diurnal stress tensor at the surface, which are mathematically defined by Eqs. (9.56) to (9.61), depend on the Love numbers (i.e. on the properties of the interior) and the co-latitude through the Beta-functions. These functions are listed below

$$\beta_{2,0}^{\theta\theta}(\theta) = \frac{3}{4}\left(3h_2^e - 10l_2^e\right)\cos(2\theta) + \frac{3}{4}\left(h_2^e - 2l_2^e\right) \tag{C.24}$$

$$\beta_{2,0}^{\theta\theta,j}(\theta) = \frac{3}{4}\left(3h_{2j}^v - 10l_{2j}^v\right)\cos(2\theta) + \frac{3}{4}\left(h_{2j}^v - 2l_{2j}^v\right) \tag{C.25}$$

$$\beta_{2,1}^{\theta\theta}(\theta) = \frac{3}{2}\left(3h_2^e - 10l_2^e\right)\sin(2\theta) \tag{C.26}$$

$$\beta_{2,1}^{\theta\theta,j}(\theta) = \frac{3}{2}\left(3h_{2j}^v - 10l_{2j}^v\right)\sin(2\theta) \tag{C.27}$$

$$\beta_{2,2}^{\theta\theta}(\theta) = -\frac{3}{2}\left(3h_2^e - 10l_2^e\right)\cos(2\theta) + \frac{9}{2}\left(h_2^e - 2l_2^e\right) \tag{C.28}$$

$$\beta_{2,2}^{\theta\theta,j}(\theta) = -\frac{3}{2}\left(3h_{2j}^v - 10l_{2j}^v\right)\cos(2\theta) + \frac{9}{2}\left(h_{2j}^v - 2l_{2j}^v\right) \tag{C.29}$$

$$\beta_{2,0}^{\varphi\varphi}(\theta) = \frac{3}{4}\left(3h_2^e - 8l_2^e\right)\cos(2\theta) + \frac{3}{4}\left(h_2^e - 4l_2^e\right) \tag{C.30}$$

$$\beta_{2,0}^{\varphi\varphi,j}(\theta) = \frac{3}{4}\left(3h_{2j}^v - 8l_{2j}^v\right)\cos(2\theta) + \frac{3}{4}\left(h_{2j}^v - 4l_{2j}^v\right) \tag{C.31}$$

$$\beta_{2,1}^{\varphi\varphi}(\theta) = \frac{3}{2}\left(3h_2^e - 8l_2^e\right)\sin(2\theta) \tag{C.32}$$

$$\beta_{2,1}^{\varphi\varphi,j}(\theta) = \frac{3}{2}\left(3h_{2j}^v - 8l_{2j}^v\right)\sin(2\theta) \tag{C.33}$$

$$\beta_{2,2}^{\varphi\varphi}(\theta) = -\frac{3}{2}\left(3h_2^e - 8l_2^e\right)\cos(2\theta) + \frac{9}{2}\left(h_2^e - 4l_2^e\right) \tag{C.34}$$

$$\beta_{2,2}^{\varphi\varphi,j}(\theta) = -\frac{3}{2}\left(3h_{2j}^v - 8l_{2j}^v\right)\cos(2\theta) + \frac{9}{2}\left(h_{2j}^v - 4l_{2j}^v\right) \tag{C.35}$$

$$\beta_{2,1}^{\theta\varphi}(\theta) = 3l_2^e\sin(\theta) \tag{C.36}$$

$$\beta_{2,1}^{\theta\varphi,j}(\theta) = 3l_{2j}^v\sin(\theta) \tag{C.37}$$

$$\beta_{2,2}^{\theta\varphi}(\theta) = 3l_2^e\cos(\theta) \tag{C.38}$$

$$\beta_{2,2}^{\theta\varphi,j}(\theta) = 3l_{2j}^v\cos(\theta) \tag{C.39}$$

In a similar way, the NSR stress tensor at Europa's surface (Eqs. (9.67) to (9.72)) depends on the Love numbers and co-latitude through the following alpha-functions

$$\alpha_{2,2}^{\theta\theta}(\theta) = -\frac{3}{2}\left(3\hat{h}_2^e - 10\hat{l}_2^e\right)\cos(2\theta) + \frac{9}{2}\left(\hat{h}_2^e - 2\hat{l}_2^e\right) \tag{C.40}$$

$$\alpha_{2,2}^{\theta\theta,j}(\theta) = -\frac{3}{2}\left(3\hat{h}_{2j}^v - 10\hat{l}_{2j}^v\right)\cos(2\theta) + \frac{9}{2}\left(\hat{h}_{2j}^v - 2\hat{l}_{2j}^v\right) \tag{C.41}$$

$$\alpha_{2,2}^{\varphi\varphi}(\theta) = -\frac{3}{2}\left(3\hat{h}_2^e - 8\hat{l}_2^e\right)\cos(2\theta) + \frac{9}{2}\left(\hat{h}_2^e - 4\hat{l}_2^e\right) \tag{C.42}$$

$$\alpha_{2,2}^{\varphi\varphi,j}(\theta) = -\frac{3}{2}\left(3\hat{h}_{2j}^v - 8\hat{l}_{2j}^v\right)\cos(2\theta) + \frac{9}{2}\left(\hat{h}_{2j}^v - 4\hat{l}_{2j}^v\right) \tag{C.43}$$

$$\alpha_{2,2}^{\theta\varphi}(\theta) = 3\hat{l}_2^e\cos(\theta) \tag{C.44}$$

$$\alpha_{2,2}^{\theta\varphi,j}(\theta) = 3\hat{l}_{2j}^v\cos(\theta) \tag{C.45}$$

where the elastic Love numbers $\hat{h}_2^e$ and $\hat{l}_2^e$, and modal strengths $\hat{h}_{2j}^v$ and $\hat{l}_{2j}^v$ refer to the tidal response of interior models in which the silicate mantle has been assumed to behave as a fluid with respect to NSR (see Sect. 9.6.2).

Index

R. Sabadini et al., *Global Dynamics of the Earth: Applications of Viscoelastic Relaxation Theory to Solid-Earth and Planetary Geophysics*,
DOI 10.1007/978-94-017-7552-6